Numerical Simulation of Intense Multi-Scale Vortices Generated by Supercell Thunderstorms

by
Catherine A. Finley

PI: Roger A. Pielke

Department of Atmospheric Science
Colorado State University
Fort Collins, Colorado

NSF ATM-9306754 and ATM-9420045

Colorado State University

Department of Atmospheric Science

Paper No. 640

NUMERICAL SIMULATION OF INTENSE MULTI-SCALE VORTICES GENERATED BY SUPERCELL THUNDERSTORMS

by

Catherine A. Finley

Department of Atmospheric Science

Colorado State University

Fort Collins, CO 80523

Research Supported by

National Science Foundation under

Grants ATM-9306754 and ATM-9420045

December 19, 1997

Atmospheric Science Paper No. 640

ABSTRACT

NUMERICAL SIMULATION OF INTENSE MULTI-SCALE VORTICES GENERATED BY SUPERCELL THUNDERSTORMS

A nested grid primitive equation model (RAMS version 3b) is used to study various aspects of tornadoes and the thunderstorms that produce them. A unique aspect of these simulations is that the model was initialized with synoptic data, and telescoping grids allow atmospheric flows ranging from the synoptic-scale down to sub-tornado-scale vortices to be represented in the model.

Two different case studies were simulated in this study: June 30, 1993, and May 15, 1991. The June 30, 1993, simulation produced a classical supercell storm which developed at the intersection between a stationary front and an outflow boundary generated by previous convection. As the simulation progressed, additional storms developed west of the main storm along the stationary front. One of these storms interacted with the main storm to produce a single supercell storm. This storm had many characteristics of a high-precipitation (HP) supercell, and eventually evolved into a bow-echo. The transition of the storm into a bow-echo is discussed and possible physical processes responsible for the transition are presented.

The June 30, 1993, simulated supercell produced two weak tornadoes. The first tornado developed along the flanking line of the storm to the southeast of the mesocyclone. The second tornado developed along a strong horizontal shear zone beneath the rotating comma-head structure of the HP supercell. Neither tornado was clearly linked to the mesocyclone in the parent storm, and both tornadoes formed first near the surface and then developed upward with time. Circulation and vorticity analyses were used to investigate the tornadogenesis process in this case. Results from these analyses indicated that the

circulation associated with both tornadoes was already present at low-levels in the storm environment 15-20 minutes before the tornadoes developed. Although the baroclinic term associated with the downdraft air made a negligible contribution to the circulation in this case, the downdraft played an important role in tilting horizontal vorticity into the vertical just above the surface in the near tornado environment where horizontal convergence could then act to amplify it. A comparison with the proposed tornadogenesis process(es) in classical supercells is also presented.

The May 15, 1991, simulation produced a classical supercell which developed along the dryline in the Texas panhandle. This supercell in turn produced a tornado which lasted for 50 minutes in the simulation. During a ten minute period toward the end of the simulation, six secondary vortices developed within the main tornado vortex. The simulated secondary vortices had many features in common with multiple-vortex tornadoes and secondary vortices produced in laboratory vortices. The evolution and structure of the simulated secondary vortices is presented, and physical mechanisms responsible for their development and dissipation are discussed.

Catherine A. Finley
Department of Atmospheric Science
Colorado State University
Fort Collins, Colorado 80523
Spring 1998

ACKNOWLEDGEMENTS

There are many people who have contributed greatly to my graduate experience here at CSU. First I would like to thank my advisor, Roger Pielke, for allowing me to pursue my own path through my graduate studies. Bill Cotton, Sonia Kreidenweis and Bob Meroney are thanked for taking the time to serve on my committee. Special thanks are given to Bill Cotton who also acted in the unofficial role of co-advisor. Without his support, completion of this work would not have been possible.

John Lee is thanked for 'showing me the ropes' with the RAMS model. His willingness to share his knowledge of numerical modeling benefited me greatly throughout the course of this work. I would also like to thank Bob Walko for patiently answering questions about the model, and for his help and advice when model problems arose or when code modifications were needed.

Louie Grasso and Bob Walko are thanked for many thought-provoking discussions on tornadoes, tornadogenesis and related topics, from which I benefited greatly. Ligia Bernardet and Jason Nachamkin are thanked for their moral support, and for many enlightening discussions on the dynamical and modeling aspects of convective systems. My office mates Tom Chase, Jerry Harrington and Mark Sellers are thanked for providing comic relief in times of extreme stress, and for insightful discussions on science, philosophy, and the MRHLF. I would also like to thank the following people who have provided moral and/or technical support during the course of my graduate work: Donna Chester, James Cizek, Jeff Copeland, Brian Gaudet, Louie and Karen Grasso, Richard and Margaret Finley, Abby Hodges, Tara Jensen, Dallas McDonald, Brenda Thompson, Bill Thorson and Jane Wilkins.

Finally I would like to acknowledge the people who have had the greatest impact on my life. I would like to thank my parents, Emil and Mary Hamann, for supporting and encouraging me to 'take the road less traveled' and pursue a career in science. Lastly and

most importantly, I would like to thank my husband Steve for his unwaivering support and love during this long and arduous journey.

TABLE OF CONTENTS

LIST OF ABBREVIATIONS

API	Antecedent Precipitation Index
BLV	Boundary Layer Vortices
BRN	Convective Bulk Richardson Number
BWER	Bounded Weak Echo Region
CAPE	Convective Available Potential Energy
CCOPE	Cooperative Convective Precipitation Experiment
DPE	Dynamic Pipe Effect
FFD	Forward Flank Downdraft
HP	High Precipitation
HSI	Horizontal Shear Instability
LCL	Lifting Condensation Level
LFC	Level of Free Convection
LP	Low Precipitation
MCC	Mesoscale Convective Complex
MCS	Mesoscale Convective System
NCEP	National Center for Environmental Prediction
NST	Non-Supercell Tornado
PBL	Planetary Boundary Layer
PV	Parent Vortex
RAMS	Regional Atmospheric Modeling System
Re	Reynolds Number
RFD	Rear Flank Downdraft
SREH	Storm-Relative Environmental Helicity
SST	Sea Surface Temperature
SV	Secondary Vortex
TVS	Tornado Vortex Signature
UTC	Universal Time Coordinate
VORTEX	Verifications of the Origins of Rotation in Tornadoes EXperiment

Chapter 1

INTRODUCTION

We were among the first to arrive at the scene of the disaster; and our pen fails entirely to depict the sight which met our view. We found the town, as the messenger had reported, literally blown to pieces, and destruction and death scattered everywhere with the sweep of destruction. The first pile that met our eye was the ruins of the Millard House, occupied by H.G. Sessions, formerly of Erie, Pa. This was a three-story brick hotel; and it could not have been more effectively destroyed had a barrel of gunpowder exploded within its walls. The inmates were all more or less hurt. From this we proceeded to look about the town, and we found that hardly a house was left uninjured, and that many of them were swept entirely away.

-Press report printed in the Lyons City Advocate (Iowa), June 4, 1860

The above quotation was taken from a press report describing the scene in the town of Camanche, Iowa, following the passage of a tornado late in the day on June 3, 1860 (Stanford 1987). Tornadoes are among the most violent storms on earth. Winds associated with tornadoes can reach in excess of $100ms^{-1}$ (225 mph) leaving damage paths 3km wide in extreme cases (Davies-Jones 1983). Fortunately, less than 10% of all reported thunderstorms produce severe weather (Doswell 1985) and few of these actually produce tornadoes. The small size and relatively short lifetime of most tornadoes confines damage to very limited regions, but also makes it very difficult to study them in the field. Even if instruments were 'fortunate' enough to have a tornado pass over them, the tornado's strong winds and incredible shears would most likely destroy them. As a result, we have been forced to observe tornadoes from afar using Doppler radar or photogrammetry.

Our current understanding of tornadogenesis and tornado dynamics is quite limited. Obtaining observations over the time and space scales needed to address these issues would be extremely difficult at best. Another approach to understanding tornadoes and tornadogenesis is through modeling, either in the laboratory or in the computer. While laboratory experiments have aided our understanding of the dynamics of intense vortices (including

tornadoes), they do not provide any insights into how tornadoes develop in actual thunderstorms. To address this issue, primitive equation models have been used to simulate both the parent thunderstorm and the tornado(es). These modeling studies have been successful in this regard. However, until recently, all numerical simulations of severe storms have been performed starting with horizontally homogeneous initial conditions in which a single 'typical' sounding is used to initialize the entire model domain. Since there are no inhomogeneities to drive convergence in the model, the convective storm must be initiated with a warm bubble. These numerical studies have been able to simulate many aspects of classical supercell storms, but as yet have not been able to capture the evolution of other types of supercell storms, such as high-precipitation (HP) supercells. Recently Grasso (1996) used a nested grid primitive equation model which was initialized with actual synoptic data to simulate two classical supercell storms and the tornadoes they produced. This is also the approach taken here.

In this study, a nested grid primitive equation model (RAMS version 3b) which was initialized with synoptic data from two different case studies is used to study tornadoes and the storms that produce them. A unique aspect of these simulations is that atmospheric flows ranging from the synoptic-scale down to the tornado-scale can all be represented in the model. A total of six grids were used in the simulations. Grids #1-2 were used to capture the evolution of the the synoptic-scale features while Grid #3 captured the mesoscale features in the environment. Grids #4-5 were used to resolve the supercell storms which developed, and Grid #6 captured the evolution of the tornadoes.

This dissertation is basically broken into three parts. The first part investigates storm-scale processes, specifically the evolution of a simulated classical supercell into a high-precipitation (HP) supercell. One of the main purposes of this study is to extend the work of previous modeling studies by examining the tornadogenesis process in this simulated HP supercell and comparing it to the proposed tornadogenesis process(es) in classical supercells. To this end, the second part of the dissertation documents the evolution of two weak tornadoes produced within the HP supercell, and investigates the tornadogenesis process. The third part of the dissertation describes the development and evolution of secondary

vortices within a tornado vortex produced in a simulated classical supercell. Because of the wide range of scales of motion investigated in this dissertation, Chapter 2 provides a fairly extensive review of our current knowledge of vortices produced by severe storms ranging from mesocyclones down to suction vortices in tornadoes. Chapter 3 gives an overview of the two different cases simulated in this study: June 30, 1993, and May 15, 1991. A brief description of the RAMS model is given in Chapter 4 along with the model configurations used in the simulations. Chapter 5 contains a discussion of the storm evolution in the June 30, 1993 case. The simulated June 30 storm produced two weak tornadoes, and the evolution of these tornadoes along with an analysis of the tornadogenesis process is provided in Chapter 6. The May 15, 1991, simulation produced a tornado which contained smaller sub-vortices. A brief description of the May 15, 1991 simulation along with an analysis of the 'secondary vortices' is presented in Chapter 7. A summary of the major findings in this study along with suggestions for future research are given in Chapter 8.

Chapter 2

BACKGROUND

2.1 Environmental Factors

It is impossible to discuss supercell thunderstorms without discussing the environmental conditions which favor their development. Supercells usually develop in environments which are convectively unstable and have large vertical shears of the horizontal winds (especially at low-levels). The relationship between these two environmental properties appears to be instrumental in determining whether a given environment is capable of supporting supercells, and there has been a significant effort by the atmospheric science community to quantify these parameters. The convective instability is usually quantified in the form of Convective Available Potential Energy (CAPE) which is defined here as:

$$CAPE = g \int_{LFC}^{EL} \frac{\theta' - \theta_0}{\theta_0} dz \tag{2.1}$$

where θ_0 is the environmental potential temperature, θ' is the potential temperature a boundary layer parcel would have if it were lifted dry adiabatically until saturated, and then lifted moist adiabatically to its Equilibrium Level (EL). CAPE values are generally greater than 2000 $J(kg)^{-1}$ in supercell environments, but cases where CAPE values were as low as 800-1000 $J(kg)^{-1}$ have been recorded. Note that CAPE can vary significantly in space and time, especially under rapidly changing synoptic conditions.

The significance of the relationship between CAPE and shear was quantified using idealized model simulations by Weisman and Klemp (1982, 1984). These studies investigated the effects of different values of CAPE and wind shear profiles (both unidirectional and directionally varying) on storm evolution in a model. They found that multicell thunderstorms tended to form in low to moderate values of CAPE and shear, while supercells were

favored in high shear and high CAPE environments. At intermediate shear and CAPE values, cumulonimbi take on multicell characteristics with many storms having characteristics of both supercells and multicell storms. They defined a convective bulk Richardson number (abbreviated BRN) which is given by:

$$BRN = \frac{CAPE}{0.5(\overline{u}^2 + \overline{v}^2)} \tag{2.2}$$

where $\overline{u}$, $\overline{v}$ are the density weighted mean wind calculated over the lowest 6 km of the atmosphere. They found that BRN between 15 and 45 favored supercell development while multicell storm development was favored for BRN greater than 45. Although these values of BRN were derived with the use of a model initialized with a single idealized sounding, the value ranges of BRN for multicell and supercell storm regimes seem to work fairly well as a 'general rule of thumb' in realistic atmospheric conditions (Weisman and Klemp, 1982; Rasmussen and Wilhelmson, 1983).

Observations of severe storm environments also indicate that not only is the magnitude of the low-level environmental wind shear large, but the shear vector usually turns clockwise with height (Rasmussen and Wilhelmson, 1983; Barnes and Newton, 1986). A typical hodograph associated with supercells is shown in Figure 2.1. Although the calculation of Ri utilizes the magnitude of the low-level shear, it does not take into account directional changes of the shear vector with height.

A quantity which in some respect accounts for the curvature in the environmental flow is helicity. Helicity is defined in general as $H = \mathbf{v} \cdot \vec{\omega}$ where $\mathbf{v}$ is the three-dimensional environmental wind vector, and $\vec{\omega}$ is the three-dimensional vorticity vector. Both observations and simulations of long-lived rotating storms show large correlations between velocity and vorticity within the storm. Lilly (1986) proposed that supercells owe their long life, stability and predictability to the helical nature of their flow. There is evidence from turbulence theory that helicity suppresses the down-scale energy cascade in the inertial subrange, isolating large energy and helicity containing scales from the dissipation scales. Thus rotating storms which contain and produce helicity are less susceptible to dissipation than other thunderstorms.

Another related quantity which plays a very important role in severe storm dynamics is storm-relative environmental helicity (SREH). Storm-relative environmental helicity is defined mathematically as:

$$SREH(\mathbf{c}) = \int_0^h (\mathbf{v} - \mathbf{c}) \cdot \vec{\omega} dz \tag{2.3}$$

where h is the depth of the storm inflow layer, **c** is the velocity of the storm, **v** is the velocity of the environmental winds, and $\vec{\omega}$ is the 3-dimensional vorticity vector. SREH depends on the strength of the storm-relative winds and the component of environmental vorticity in the direction of the storm relative winds (known as 'streamwise vorticity'). Note that storm motion must either be known or estimated to calculate any storm-relative quantity. A rough threshold value for supercell development is somewhere between SREH $\geq 150 m^2 s^{-2}$ (Davies-Jones and Burgess, 1990) to SREH $\geq 250 m^2 s^{-2}$ (Droegemeier et al., 1993).

Droegemeier et al. (1993) used a numerical model to investigate the influence of storm-relative environmental helicity on convective storm structure and evolution. They tried to identify characteristics of ambient wind profiles that are conducive to the development of long-lived rotating storms. They ran many (horizontally homogeneous) simulations, systematically changing the depth of the shear layer and the hodograph curvature, while keeping the magnitude of the shear vector constant. The results indicated that several different types of convection were possible for environments which contained the same magnitudes of CAPE and shear, indicating that the mean shear (and hence the BRN) is not a precise predictor of the rotational characteristics of convective storms. They found the shear *profile* and storm motion determined the storm rotational characteristics, and hence SREH was a much better predictor of net updraft rotation than the BRN.

2.2 Supercell Thunderstorms

The term 'supercell' was first coined by Browning (1964, 1968). It referred to a subset of storms which contained inflow and outflow circulation branches that did not interfere with

each other and which exhibited evidence of strong rotation when viewed with time-lapse photography.

Observations and radar studies over the past 40 years have lead to the following general characteristics associated with supercell storms:

- Most supercells rotate cyclonically, although anticyclonically rotating supercells have been observed (Achtemeier, 1975; Knupp and Cotton, 1982).
- Cyclonically rotating storms move to the right of the mean environmental wind vector, while anticyclonically rotating storms move to the left. In general, the more storm motion deviates from the mean wind vector, the stronger the storm rotation is.
- Supercells often produce severe weather (strong winds, large hail) and sometimes produce large and intense tornadoes.
- Radar signatures associated with supercells include 'bounded weak echo regions' and 'hook echoes'. Bounded weak echo regions (abbreviated BWER–sometimes referred to as 'echo-free vaults') are regions in the storm reflectivity field where weak echo regions at low levels extend upward and are surrounded by regions of high reflectivity at upper levels. These regions are usually associated with strong updrafts in the storm. Hook echoes (although not seen in all supercell storms) sometimes form along the right-rear flank of the storm. They are thought to be associated with an intense cyclonic circulation (called a 'tornado cyclone' or 'mesocyclone') which draws precipitation around it producing a hook pattern in the radar reflectivity field.
- Supercells sometimes form after 'storm splitting', a process in which a single updraft splits into two counter-rotating updrafts. The environmental wind profile determines which of the two storms is 'favored' for further development (if either is favored). Although a complete discussion of this process is beyond the scope of this study, observational and modelling studies have shown that when the environmental vertical wind shear vector turns clockwise (counterclockwise) with height, the cyclonically (anticyclonically) rotating storm is favored for further development. If the shear vector is unidirectional, neither storm is favored, and both storms may continue to develop. For further discussion of the splitting process, refer to Klemp and Wilhelmson (1978a,1978b), Thorpe and Miller (1978), Schlesinger (1980) and Wilhelmson and Klemp (1978,1981).

The fundamental idea behind categorizing storms into 'multi-cells' and 'supercells' is that the two types of storms are dynamically different. However, the wide spectrum of storm structures in the atmosphere sometimes blurs our imposed categories and definitions. For example, multi-cell storms can evolve into supercells and visa versa. Other observations have shown that some multi-cell storms briefly exhibit characteristics associated with supercells (such as storm rotation and motion that deviates from the mean wind vector) (Foote and Frank, 1983).

At what point does a storm become (or cease to be) a supercell? One criteria that has often been used to define supercells is the presence of a single 'steady' rotating updraft.

However, Doswell and Burgess (1993) argue that this may not be a good criteria since detailed radar observations have shown that multicellular structure can be seen superimposed on most supercells. In this study (following Weisman and Klemp (1984) and Doswell and Burgess (1993)), supercells will be defined as storms with persistent[1] spatial correlations between updraft centers and vorticity centers.

2.2.1 The Supercell Spectrum

Although it is better to think of a 'storm spectrum' rather than well defined boundaries between storm types, supercells can generally be broken into three different categories depending on their precipitation structure and characteristics (Moller et al., 1988; Doswell et al., 1990; Doswell and Burgess, 1993; Moller et al., 1994): low-precipitation (LP) supercells, high-precipitation (HP) supercells, and 'classical' supercells which produce moderate amounts of precipitation. Each type of supercell is discussed in more detail below.

'Classical' Supercells

Classical supercells are perhaps the most studied of the supercell spectrum. The conceptual model of a 'classical' supercell was first introduced by Browning (1964) and has changed little in the last 20 years. A conceptual model of a classical supercell is shown in Figure 2.2. At the surface during the mature phase of the storm, there are two low-level outflow boundaries: one to the north of the updraft associated with the forward flank downdraft (FFD), and another to the south and west of the updraft associated with the rear flank downdraft (RFD). New convective towers usually develop along the rear flank outflow boundary and are known as the 'flanking line'. Most of the precipitation in the storm falls to the north and west of the main updraft. The main updraft generally lies above the intersection of the forward flank and rear flank gust fronts. It is in this region of the storm which separates the inflow air from the storm outflow which is the preferred region for tornado development.

---

[1] on time scales much larger than the convective time scale which is on the order of $\sim$ 20-30 minutes

In addition to the general characteristics of supercells listed above, classical supercells have the following properties:

- frequently develop well away from competing storms
- radar signature frequently shows hook echo structure
- large outbreaks of tornadoes are often associated with these storms
- moderate precipitation rates
- often produce large hail.

The two most common locations for tornado development are along the periphery of the mesocyclone, and at the nose of the gust front as shown in Figure 2.2. Sometimes a supercell will produce several mesocyclones (and possibly tornadoes) in succession (Burgess, et al, 1982, 1993). A conceptual model of the mesocyclone evolution in these cases is shown in Figure 2.3. As the first mesocyclone matures, the gust front wraps cyclonically around the mesocyclone core, similar to extra-tropical cyclone development. The gust front continues to accelerate around the first mesocyclone core until the first core occludes. The first mesocyclone then begins to weaken as it gets 'cut off' from the storm inflow air, and a new mesocyclone begins to develop in the region of strong convergence near the point of occlusion. The second mesocyclone core intensifies rapidly in the vorticity rich environment and eventually becomes the storm's new mesocyclone. Some supercells undergo this process many times during there life (on average about once every 40 minutes), and the mesocyclone can persist for several hours. These storms frequently produce 'tornado families' in which at least one tornado is associated with each successive mesocyclone.

Low-Precipitation (LP) Storms

Low-Precipitation (LP) supercells have been documented visually by Burgess and Davies-Jones (1979), Bluestein and Parks (1983), Bluestein (1984), and with Doppler radar by Bluestein and Woodall (1990). Since these storms produce little (if any) precipitation, they are difficult to detect on conventional radar and their severe weather potential often goes unrecognized. Observations indicate that LP supercells have the following general characteristics:

- usually form along the surface dryline in the western plains (although the author has observed them on one occasion in west-central Minnesota)
- produce little rain, but often produce large hail
- show strong visual evidence of rotation
- difficult to detect storm severity with radar
- only produce tornadoes occasionally
- tend to be smaller in diameter than classical supercells
- show no evidence of any strong downdraft at the surface
- always form as isolated cells
- have been observed to rotate both cyclonically and anticyclonically. Cyclonic rotation is much more prevalent.

A conceptual model of an LP supercell is shown in Figure 2.4. Although these storms generally produce weak tornadoes (Bluestein and Parks, 1983), Burgess and Davies-Jones (1979) documented a case where an LP storm produced a significant tornado in Oklahoma, even though radar reflectivities did not indicate the storm was severe.

The physical mechanisms favoring LP supercell development are not well understood. Bluestein and Woodall (1990) speculated that LP storms are a type of supercell in which hail production is favored over rain production for some reason (which they did not speculate on). Bluestein and Parks (1983) hypothesize that the size of the initial 'convective bubble' (or thermal which generates the first convective updraft) may be smaller for LP storms than for other supercells, and that the size of the initial convective updraft could play an important role in subsequent storm evolution. They noticed that the difference between the Level of Free Convection (LFC) and Lifting Condensation Level (LCL) was smaller in their observed LP storm environments than it was in classical supercell environments. They reasoned that parcels in the classical supercell environment must 'work harder' to reach the LFC, so there would be a tendency for more gravity wave activity and broader thermals in the classical supercell environment, and hence broader convective updrafts.

High-Precipitation (HP) Storms

High-Precipitation (HP) supercells occur most frequently in the eastern half of the U.S. and western High Plains (Doswell and Burgess, 1993), and may be the predominant type of

supercell in these regions. Doswell (1985), Nelson (1987), Moller et al. (1988), and Doswell et al. (1990), Moller et al. (1990), Doswell and Burgess (1993), Moller et al. (1994) have documented the following general characteristics of HP supercells:

- extensive precipitation (including torrential rain and hail) along the right rear flank of storm
- mesocyclone often embedded within significant precipitation
- storms may not be clearly isolated from surrounding convection, but remain distinctive in character
- often associated with widespread damaging hail or wind events, with damage occurring over relatively long and broad swaths. It has been suggested that derecho events (mesoscale convective systems that produce long swaths of damaging winds) may have HP supercells embedded in them (Johns and Hirt, 1987).
- tend to be larger than 'classical' supercells
- updrafts often take on an 'arc' shape as new updrafts form at the southern end of the gust front
- tornadoes may occur with the mesocyclone (which is often found on the northern or eastern side of the storm), or along the leading edge of the gust front
- may exhibit multicell characteristics such as several high reflectivity cores, multiple mesocyclones and multiple bounded weak echo regions[2].

Like LP storms, HP storms are more difficult to recognize on radar than classical supercells. Their radar characteristics can take varied forms including:

- kidney-bean shaped configurations
- exceptionally large hook echoes
- weak echo notches along the forward and rear flank of the storm (indicating the probable location of the rotating updraft)
- persistent low-level reflectivity gradient adjacent to a front flank notch
- spiral or 'S' shaped structure
- multiple high reflectivity cores and multiple bounded weak echo regions.

Moller et al. (1990) developed a conceptual model of HP supercells which is based on over 50 HP supercell cases from 1973-1990. This conceptual model is shown in Figure 2.5. When HP supercells were the dominant mode of convection, they found that most of the events were characterized by:

---

[2]This characteristic lead Nelson (1987) and Nelson and Knight (1987) to call HP supercells 'hybrid' storms.

1. significant instability, but helicity only marginal for supercells

2. storms tended to move along a pre-existing thermal boundary, usually an old outflow boundary, or a stationary front.

Their results indicated that significant low-level warm advection across the thermal boundary may play a major role in the development of mesoscale vertical motion on HP supercells days, as a shortwave at upper levels did not appear to be a necessary ingredient (although if present, would certainly aid convective development). They also suggested that HP storms may spin up a mesocyclone from either solenoidal effects along a thermal boundary, or from the increased vertical wind shear along the boundary.

HP supercells can also undergo several different kinds of life cycles as shown in Figure 2.6. Frames 1-4 show the transition of a classical supercell into an HP supercell which takes a 'kidney bean' shape on radar. Note that the mesocyclone is located on the forward flank of the HP supercell, not along the right-rear flank as with classical supercells. The storm then may either evolve into a bow- echo storm with a 'rotating comma head' (5a-8a) (an evolution which usually occurs in a rapid transition), or develop a new mesocyclone along the right rear flank as the old mesocyclone moves northward along the leading edge of the storm and dissipates. Cyclic mesocyclone development has been observed to occur with either life cycle (Moller et al., 1990) as patterns 2-8a or 2-7b are repeated during the storm evolution.

In addition to the composite studies of HP supercells, there have been many individual case studies reported in the literature. Vasiloff et al. (1986) document a case where a multicell storm developed into an HP supercell. The storm developed a large 'background updraft' and then changed direction. The storm maintained multi-cell characteristics even during its supercell phase.

Nelson (1987) documented several HP supercells which produced large hail in Oklahoma. Data collected from one of the cases indicated that the transition to the HP supercell stage was coincident with the formation of an intense downdraft. Nelson speculated that

the formation of this strong rear flank downdraft was necessary for the development and maintenance of the hybrid storm.

Przybylinski (1989) presented an HP supercell case which produced a tornado near Raleigh, North Carolina. The storm was part of a squall-line, and followed the rotating comma head life cycle. The storm produced multiple mesocyclones which tended to weaken as they moved northward through the storm. New updrafts formed to the south of older updrafts ahead of the rear flank downdraft. The storm produced a tornado late in its life cycle, and is somewhat unique in that the tornado was associated with the rotating comma head structure in the storm. They also found evidence of a 'pulsating' rear flank downdraft, as multiple outflow 'surges' could be detected.

A tornado outbreak which occurred in Indiana June 2, 1990, was documented by Przybylinski el.al. (1993). This outbreak was unique because both classical and HP supercells were present in a line of strong convection. The HP storms were aligned in a NE-SW orientation such that each storm moved along the outflow boundary of its downwind neighbor. The radar also showed weak echo notches along the trailing flank of the HP storms which the authors were able to correlate with some damaging wind reports.

Other HP supercell cases have also been documented by Foote and Frank (1983), Moller et al. (1990), Przybylinski (1990), Imy and Pence (1993) and Calianese et al. (1996).

So why do supercells have such a wide range of precipitation characteristics? Rasmussen and Strake (1996) hypothesize that the precipitation intensity beneath a supercell updraft is strongly influenced by the amount of hydrometeors that are re-ingested into the updraft after being transported into the anvil. They investigated the environments associated with 43 (isolated) supercell cases (they did not address cases where two (or all three) types of supercells occur in relatively close proximity to one another). They constructed what they believed were 'representative' soundings for each case (note that this procedure implies a horizontally homogeneous environment). They found that HP storm environments contained more precipitable water than other supercell environments, although the relative humidities are not much different implying that the HP storm environment is generally warmer than other cases. HP storm environments also featured the driest mid-level air,

implying HP environments have the largest evaporative potential (and hence may produce the strongest rear-flank downdrafts). The authors also examined composite hodographs for each storm type and found the most striking differences occurred in the upper level (above 7km) winds. The turning of the wind vectors in the upper troposphere appeared to be a good discriminator between LP and HP storm environments. LP storms occurred only when the hodograph turned counterclockwise between 5-9km, while HP storms were more likely when the hodograph turned clockwise between 5-9km (although there were a few exceptions). When the storm-relative upper level flow was $\leq 12ms^{-1}$, supercells were exclusively of the HP variety regardless of the storm-relative helicity, while LP storms were dominant when the upper levels winds were $\geq 30ms^{-1}$. Their results also indicated that HP environments had the weakest low-level shear, and that HP supercells tended to propagate along the PBL-4km shear vector.

2.2.2 Origins of Updraft Rotation

Mid-levels

Barnes (1968) and Browning (1968) were the first to speculate that vertical shear of the horizontal wind (which produced horizontal vorticity in the environment) could be a source of rotation for thunderstorms. They observed that the storm inflow carried with it horizontal vorticity which could be tilted into the vertical by the storm updraft. It wasn't until the advent of cloud resolving models that this idea was widely accepted. To date, most modelling studies of supercell storms have used horizontally homogeneous initial conditions (Klemp and Wilhelmson, 1978a,b; Klemp et al., 1981; Weisman and Klemp, 1982, 1984; Droegemeier et al., 1993 just to name a few). However, Doswell et al. (1990) state that '...the mesoscale variations necessitating inhomogeneous initial conditions may well have been an important factor in the convective evolution.' They also point out that it is not necessarily true that *all* forms of supercell behavior can be simulated well with horizontally homogeneous initial conditions (note lack of HP supercell simulations in the literature).

Never-the-less, horizontally homogeneous model simulations have provided much insight into the basic dynamics of supercell storms.

The importance of vertical shear of the horizontal wind in the severe storms' environment has long been recognized, as was discussed earlier. Klemp and Wilhelmson (1978a) used 3-D model simulations with idealized initial conditions to show that storms could become self-sustaining with even small amounts of vertical shear present in the environment. They also found that by changing the strength of the low-level shear, the model produced a storm which split with the cyclonically (anticyclonically) rotating storm propagating the the right (left) of the mean wind.

Klemp and Wilhelmson (1978b) further investigated the effects of shear on supercell storms using idealized initial conditions. When the environmental shear was unidirectional, the initial storm split into two counter-rotating storms which were mirror images of each other, one propagating to the right of the mean environmental winds, the other to the left. The right moving storm rotated cyclonically, while the left moving storm rotated anticyclonically. When the shear vector turned clockwise with height, the initial storm split again, but the right moving storm continued to develop while the left moving storm weakened. Their simulated right-moving storm exhibited many characteristics observed in classical supercells such as a 'hook' pattern in the precipitation field, a bounded weak echo region and a mesocyclone. They also found the flow fields in the right moving storm looked similar to the conceptual model developed by Browning (1964) with mid-level air approaching the storm from the right flank, wrapping around the front side of the updraft and flowing into the downdraft. Their results suggest that the environmental wind *shear* can determine whether a right or left moving storm will be favored in a particular environment. These results are consistent with observations in that the climatological wind profile in mid-latitudes produces a hodograph which turns clockwise, and most observed supercells rotate cyclonically and move to the right of the mean wind.

Klemp et al. (1981) used a numerical model and radar observations to study a supercell which produced a tornado near Del City, Oklahoma. Although the model was initialized with horizontally homogeneous initial conditions, the simulated storm showed many of the

same characteristics that were observed with radar until the storm became tornadic. Both the observed and modelled storms produced a downdraft which rotated around the original updraft. The downdraft then generated a second updraft as it moved eastward. Storm relative trajectory analysis also showed that individual parcels in the storm updraft rotated anticyclonically as they moved through the storm, even though the updraft was rotating cyclonically. The success of their (relatively simple) numerical simulation suggests that the larger-scale environment plays a dominant role in structuring many features in the storm.

Rotunno (1981) proposed a conceptual model to explain the initial rotational properties of the storm. The model utilized a uni-directional shear profile in which all initial vorticity was in the horizontal. The initial updraft tilted some of the horizontal vorticity into the vertical, creating a vorticity dipole. A vector pointing from the positive to the negative center of the dipole had the same direction as the horizontal vorticity vector. The conceptual model does not explain why some storms rotate cyclonically (or anticyclonically) since it predicts loops of vorticity are drawn into the updraft and hence the updraft would have no net circulation. However, the results indicate that tilting/stretching of ambient vorticity can account for the production of vertical vorticity in the midlevels of storms.

Davies-Jones (1984) emphasized the importance of streamwise vorticity in the inflow region of storms for maintaining their cyclonic circulation (the same argument can be applied to anticyclonically rotating storms). Streamwise vorticity is defined mathematically as:

$$\vec{\omega_s} = \vec{\omega} \cdot \mathbf{p} \tag{2.4}$$

where $\mathbf{p}$ is the unit vector in the direction of the local storm-relative wind. Put into words, streamwise vorticity is simply the component of environmental vorticity in the direction of the storm-relative winds.

This idea is shown conceptually in Figure 2.7. Consider two extreme cases–one where the vorticity vectors are perpendicular to the low level storm-relative winds, and one where the vorticity vectors are parallel to the low level storm-relative winds. In the perpendicular case, as the air flows into the updraft, the horizontal vorticity gets tilted into the vertical, creating a vorticity dipole, and hence no net circulation in the updraft. In the parallel case,

the horizontal vorticity again gets tilted into the vertical as air flows into the updraft, but in this case, the updraft acquires a net cyclonic circulation. Thus changes in storm motion can affect the storm rotation by modifying the angle between the storm relative winds and the environmental vorticity.

Rotunno and Klemp (1982) used linear theory and a numerical model to show how an initially symmetric updraft can grow preferentially to the right side of the shear vector and acquire cyclonic rotation when the environmental shear vector veers with height. They derived a perturbation pressure equation to explain how vertical wind shear and buoyancy gradients can interact to produce pressure perturbations. The linearized perturbation pressure equation is given by:

$$\pi' \sim \frac{\partial \mathbf{V}}{\partial z} \cdot \nabla w'. \tag{2.5}$$

According to (2.5), the storm updraft and environmental wind shear interact to produce a horizontal perturbation pressure gradient across the updraft in the direction of the environmental wind shear vector. When the shear vector veers (turns clockwise) with height, a vertical perturbation pressure gradient is also created which is directed upward on the storm's southern flank, and downward on the storm's northern flank. This idea is illustrated in Figure 2.8. The authors proposed that the enhanced upward forcing on the updraft's southern flank could force the low level air to its level of free convection. Thus the storm updraft continually 'redevelops' along the southern flank, and this explains why supercells tend to move to the right of the mean winds. When the shear vector turns clockwise with height, the production of positive vorticity is also located on the same side of the storm as the favorable vertical pressure gradient, so that cyclonic vorticity and updraft production are positively correlated.

However, the picture becomes more complicated since there is evidence that storm rotation also effects storm propagation. Rotunno and Klemp (1985) used a numerical model initialized with unidirectional shear to simulate a supercell storm (actually, with unidirectional shear the model produces two supercells, one is a mirror image of the other–

they only looked at the cyclonically rotating storm). They took a closer look at the entire perturbation pressure equation which is given by:

$$-\nabla^2\pi = 2[\frac{\partial u}{\partial y}\frac{\partial v}{\partial x} + \frac{\partial u}{\partial z}\frac{\partial w}{\partial x} + \frac{\partial v}{\partial z}\frac{\partial w}{\partial y}] + (\frac{\partial u}{\partial x})^2 + (\frac{\partial v}{\partial y})^2 + (\frac{\partial w}{\partial z})^2 - w^2\frac{\partial^2 ln\overline{\rho}}{\partial z^2} - \frac{\partial B}{\partial z}. \quad (2.6)$$

The first three terms on the right hand side of (2.6) are the contribution to pressure from the fluid shear, the next four terms involve fluid extension, and the last term is the contribution from vertical buoyancy changes. They determined that the low pressure at mid-levels was driven primarily by the shearing terms in (2.6) and concluded that the rightward storm propagation was driven primarily by rotation generated along the storm's right flank. In addition to the perturbation pressure equation, they used equivalent potential vorticity and the Bjerkness circulation theorem to study the origins of updraft rotation. Their results indicated that there were two different mechanisms for generating updraft rotation. At mid-levels in the storm, the vertical vorticity originated from horizontal vorticity in the environment which was tilted into the vertical by the updraft.

Davies-Jones (1985) also looked at the origin of storm rotation using a Beltrami basic state flow (in which the vorticity and velocity vectors are everywhere parallel to each other). Using this basic state, he was able to obtain analytical solutions for the distribution of pressure (and hence the vertical pressure gradient force) which he compared to other conceptual models (in particular the one proposed by Rotunno and Klemp (1982)). His results showed that low pressure at the edge of the rotating updraft coincided with the region where the total wind was largest, not where $\mathbf{S} \cdot \nabla w$ (where $\mathbf{S}$ is the environmental shear vector) was negative as proposed by Rotunno and Klemp (1982). However, the results did agree with Rotunno and Klemp in that they produced an upward directed pressure gradient force along the storm's southern flank, and hence further storm development would be favored in that region. It is not clear what effect baroclinicity would have on the results since baroclinic effects were not included in the study.

Low levels

Doppler radar observations of supercell thunderstorms indicate that low-level rotation in the storm may be initiated by a different mechanism than mid-level rotation. This is suggested by observations which indicate that in some storms, a region of strong rotation in the lowest 2km of the storm develops independently from the region of mid-level rotation (Johnson et al., 1987; Wakimoto and Atkins, 1996; Wakimoto et al., 1997).

Idealized modelling studies have also investigated mechanisms for the development of low-level rotation in supercell storms. Klemp and Rotunno (1983) revisited their model simulation of the Del City storm (Klemp et al., 1981) and added a second grid with smaller grid spacing to take a closer look at the tornadic region of the storm. In their simulation, strong cyclonic vorticity developed first at midlevels in the storm, and was then followed by a large increase at low levels. Eventually the vorticity at low levels well exceeded that found at midlevels in the storm. They attributed this large increase in low- level cyclonic vorticity to the tilting and convergence of horizontal vorticity generated baroclinically along the storm outflow to the northeast of the mesocyclone.

In another study, Klemp and Rotunno (1985) also found that low-level rotation originated from baroclinically generated horizontal vorticity along the leading edge of the storm outflow. This vorticity was then transported into the updraft region and tilted into the vertical. To show baroclinically-generated vorticity was the source for low-level storm rotation, they performed a simulation where rain was not allowed to fall. The storm still propagated southward (to the right of the mean winds) and rotated cyclonically at mid-levels, but showed little indication of low-level rotation. From these experiments, they postulated that the primary importance of the mid-level rotation was to transport potentially cold air along the forward and left flanks of the storm where it can be evaporatively cooled until it sinks and produces a cold pool to the north and west of the low-level updraft. Solenoidal effects then generate horizontal vorticity which is of the proper sign to produce positive vertical vorticity when tilted into the vertical by the updraft.

Davies-Jones and Brooks (1993) further investigated the origins of low- level rotation using horizontally homogeneous model simulations of an idealized supercell. They ran simulations with and without precipitation processes and found that peak vertical vorticity values at low levels were 6 times greater in the simulation with precipitation. This indicates that the development of strong low-level rotation requires evaporative cooling, giving further support to the idea of baroclinically generated vorticity as a source for updraft rotation at low levels. In an extension to this study, Brooks et al. (1993, 1994) hypothesized that differences in precipitation structure in the storms were responsible for changes in low-level mesocyclone development. They argued that the precipitation structure in supercell storms was largely a function of the environmental mid-level winds and the strength of the mid-level mesocyclone. They did several model simulations and showed that if the mid-level winds were too strong, no precipitation fell near the updraft and no low level mesocyclone developed. If the mid-level winds were too weak, large amounts of precipitation fell near the updraft which generated strong low level outflow, undercutting the updraft and effectively 'killing off' the mesocyclone. They argued that this is the case with HP supercells, which usually form in environments with moderate/weak mid-level winds, and explains why HP supercells usually don't produce strong tornadoes. They also suggested that the development of a long-lived low level mesocyclone requires a 'balance' between the strength of mid-level winds (which tend to carry precipitation away from the updraft) and the strength of the mid-level mesocyclone (which tends to carry precipitation around the updraft).

Wicker and Wilhelmson (1995) also looked at the sources of vertical vorticity in the low-level mesocyclone in their simulation of a tornadic thunderstorm. They calculated backwards trajectories originating in the low level mesocyclone and found two main source regions of air–one from northwest of the mesocyclone, and another from the northeast. They found that air originating from northwest of the mesocyclone did not make a significant contribution to the large values of positive vertical vorticity found in the low-level mesocyclone. The air originating from the northeast traveled eastward into a strong gradient of equivalent potential temperature (θ_e) associated with the storm outflow boundary, and then southward

along this boundary into the mesocyclone. They concluded that the cyclonic vorticity in the low level mesocyclone originated from tilting and stretching of baroclinically generated horizontal vorticity in the inflow region to the northeast of the low-level mesocyclone.

In addition to the studies which have focused on the origins of storm rotation, there are other modeling studies which are of significance to the current study. Brooks and Wilhelmson (1992) were able to simulate a storm that had many features of observed LP storms using horizontally homogeneous initial conditions. The LP storm was produced in an environment normally associated with 'classic' supercells (and in one of their simulations, this sounding did produce a classical supercell), but a smaller temperature perturbation was used to initiate convection. Although this result supports the hypothesis of Bluestein and Parks (1993), it is disconcerting from a modeling standpoint since it shows that even the *qualitative* model results may be sensitive to the way convection is initiated. Brooks and Wilhelmson concluded that in some cases, the pre-convective environment must be known in great detail in order to make a *qualitatively* correct forecast.

Weisman and Bluestein (1985) were also able to simulate a storm that had many LP storm characteristics by artificially suppressing the rain process in the model. While this is not physically realistic, they did demonstrate that long-lived rotating updrafts can exist without rain. They also suggested that the role of microphysical parameters might be important in supercell storms.

McPherson and Droegemeier (1991) also found their model simulations of supercells to be sensitive to the way convection was initiated in the model. They changed the size and strength of the initial convective bubble that was used to initiate convection in horizontally homogeneous simulations. They found that storm evolution beyond about 75 minutes in their simulations to be sensitive to the size and strength of the initial convective bubble.

In summary, idealized horizontally homogeneous model simulations and theoretical studies have been able to show that the source of mid-level rotation in supercells storms is ambient vorticity in the environment, while the source for low-level rotation in the storm appears to be baroclinically generated vorticity along the storm outflow. They have also been able to explain why supercells move to the right of the mean environmental winds and

Category	Wind Speed (mph)	Wind Speed (ms^{-1})
F0	40-72	18-32
F1	73-112	33-50
F2	113-157	51-70
F3	158-206	71-92
F4	207-260	93-116
F5	261-318	117-142
F6	over 319	over 143

Table 2.1: Wind speeds associated with the tornado strength categories in the Fujita (F) scale.

acquire net cyclonic rotation. However, the source of rotation in tornadoes is still a matter of debate. Current theories of tornadogenesis will be presented in the next section.

2.3 Tornadoes and Tornadogenesis

In this section, observations of tornadoes and their relationship to their parent thunderstorms are discussed. Since tornadoes are a relatively short-lived, infrequent and small-scale phenomena, they are a challenge to study observationally. The strong winds associated with most tornadoes make observations near and inside the core nearly impossible. Thus much of what we know about tornadoes has come from photographs and video tape, Doppler radar, and surveys of tornado damage paths.

With the recent increase in computer capabilities, model simulations of both the parent thunderstorm and the associated tornadic circulations are now possible. In Section 2.3.2, an overview of these studies is given along with possible tornadogenesis mechanisms.

2.3.1 Observations

A commonly used scale for measuring tornado strengths is the Fujita scale or 'F' scale. It is based on *estimated* wind speeds based on the damage that occurs along the tornado's path. A summary of the wind speeds associated with categories in the F-scale is given in Table 2.1.

Recall the conceptual model of the classical supercell shown in Figure 2.2. In this model, tornadoes are usually associated with the mesocyclone. Indeed many observations of supercell tornadoes show the tornado originating out of a rotating, lowering of the cloud base (called the 'wall cloud') which is thought to be a visual manifestation of the low-level mesocyclone. This is supported by other observations which indicate that supercells which do not possess low level mesocyclones are less likely to produce tornadoes.

The most widely used tool used in observing tornadic storms is Doppler radar. Although most operational Doppler radars do not have the capability to resolve the tornadic circulation (due to the large sampling volumes used), they will sometimes detect a large value of azimuthal shear between two adjacent sampling volumes. This feature is known as a 'tornado vortex signature' (or TVS) and is thought to be a degraded image of the incipient tornado (Burgess et al., 1977), although there still has been no proven direct connection between the TVS and the tornado (Rotunno, 1986). A TVS is sometimes (but not always) observed aloft prior to tornadogenesis, although there is mounting evidence that in some cases the TVS develops and intensifies near the surface, or forms simultaneously over a large depth including the surface (Vasiloff, 1993). Some studies have indicated that as many as 50% of all TVS's develop at low-levels (Trapp and Mitchell, 1995).

Lemon and Doswell (1979) synthesized several observational data sets (including radar, aircraft, observer, and surface data) in order to document the transition of supercells into the tornadic phase. Their work produced the classical supercell conceptual model shown in Figure 2.2. In this study, they documented the importance of the rear-flank downdraft (RFD) in the transition of the storm into a tornadic supercell. They proposed the RFD forms as environmental air (about 7-10km above the surface) encounters the intense 'blocking' updraft. This air is forced downward and mixes with cloudy air below and then descends to the surface through evaporative cooling. Their observations indicated that shortly before the mesocyclone 'descends' to low levels, the center of circulation shifts from the updraft to the region of large vertical velocity gradients between the updraft and the rear-flank downdraft. They termed this a 'divided mesocyclone structure' since part of the mesocyclone is in updraft, part in downdraft. They noted that in most of the well doc-

umented storms, tornadoes reached the surface only after the mesocyclone developed this 'divided' structure. The tornadoes typically formed along the periphery of the mesocyclone in the updraft region. They also proposed that the RFD also contributes to the initial disruption of the updraft, and eventually leads to storm collapse.

Brandes (1978) used Doppler radar observations of the low-level wind fields in two different supercells to investigate the transition of the mesocyclone to the tornadic phase. The radar data showed evidence of 'mesovortex breakdown' (in which a downdraft forms in the core of the mesocyclone) with several smaller vorticity maxima forming around the edge of the parent mesocyclone. (Vortex breakdown and secondary vortex development will be discussed further in section 2.4.) One of the tornadoes appeared along the major axis (at a focal point) of an elliptical low-level mesocyclone. Brandes concluded that tornadogenesis coincides with an apparent 'breakdown' of the mesocyclone, and tornadoes may develop from secondary vortices that appear along the elongated horizontal axis of the mesocyclone. He also speculated that "... downdrafts and/or related wind surges from outside the parent mesocyclone could initiate a process similar to vortex breakdown and alter flow properties so that instabilities (tornadoes) will grow within the confines of an asymmetrical mesocirculation."

Barnes (1987a,b) analyzed damage paths created by several tornadoes for a series of storms which occurred near Oklahoma City on 30 April, 1970. Based on the damage paths and radar observations taken during the storm, he concluded that some of the mesocyclones produced several tornadoes simultaneously. He also speculated that some of the observed damage could have been produced from strong winds associated with the mesocyclones themselves.

Wakimoto and Lin (1997) also documented a tornado which formed as a result of vortex breakdown/secondary vortex development. They used Doppler radar data to document the tornadogenesis process in a storm near Garden City, Kansas, on May 16, 1995. The radar data was collected with the airborn ELDORA radar as part of the VORTEX (Verifications of the Origins of Rotation in Tornadoes EXperiment) project, providing an unprecedented view of the tornadogenesis process with high time and space resolution. Prior to tornado-

genesis, an occlusion downdraft formed at the center of the mesocyclone circulation. The mesocyclone circulation then appeared to breakdown into 3 (or maybe 4) vorticity centers which formed an annular ring of positive vorticity around the central downdraft. One of the vorticity centers developed into the Garden City tornado.

However, there are other observations which indicate that the link between the mesocyclone and tornado may not be clear in all cases. Forbes and Wakimoto (1983) documented a storm that occurred on 6 August, 1977 near Springfield, IL. The storm was associated with a bow-echo on radar, and produced a complex damage path which included 17 cyclonic tornadoes, 1 anticyclonic tornado, 10 downbursts, and 19 microbursts. Most of the tornadoes and downbursts occurred while the echo shape on radar was evolving from an arc shape into a comma shape (which indicates that this storm may have been an HP supercell which was evolving through the rotating comma head life cycle). At least 9 of the tornadoes were associated with the gust front. Many of the other tornadoes appeared to be associated with the southern side of the rotating comma head (mesocyclone) on radar. However, a survey of the damage provided evidence that several of these tornadoes associated with the mesocyclone may have formed from shear along the periphery of microbursts. From the damage survey, it appeared that the tornadoes formed just downstream and on the cyclonic shear side of microbursts. The authors suggested that these tornadoes may have formed from Kelvin-Helmholtz type instabilities along the edge of the microbursts, but point out that the proximity to the mesocyclone makes the genesis mechanism somewhat nebulous. The survey did reveal that the origin of weak tornadoes associated with thunderstorms may be varied.

Wakimoto and Atkins (1996) present observations taken during the VORTEX project in which a strong tornado (F3 strength) developed along the flanking line of a supercell thunderstorm. Previous observations have also documented cases of tornado development 3-5 km southeast of the mesocyclone along the flanking line of supercell storms (Burgess et al., 1977; Barnes, 1978a; Brandes, 1978) but it was generally thought that tornadoes forming in this region of the storm would be weak (F0-F1 strength). High resolution Doppler radar observations indicated that the tornado formed from a low-level shear feature along the

flanking line. The authors concluded that feature intensified due to vortex stretching which occurred under an intense updraft which was associated with a rapidly growing tower along the flanking line. Although the supercell possessed a low-level mesocyclone, there were no tornadoes associated with it. It is also interesting to note that the descent of the funnel cloud occurred *after* the tornado had already traveled about 1 km along its damage track.

Stumpf and Burgess (1993) recently documented a case of a bow-echo thunderstorm which moved through Norman, Oklahoma on 5-6 September, 1992. Most of the damage caused by the storm appeared to coincide with the paths of several small-scale rotation features which were detected along the gust front by Doppler radar. Several of the vortices were located along the leading edge of the bow-echo while another was located along the gust front beneath the mid-level mesocyclone. The vortices were short-lived with diameters of about 2km and were confined to the lower troposphere. They proposed calling these vortices 'Boundary Layer Vortices' (BLV) due to their relatively large size.

Other observations also indicate that tornadoes can sometimes form in storms which do not possess mesocyclones (Burgess and Donaldson, 1979; Holle and Main, 1980; Bluestein, 1985; Wilson, 1986; Wakimoto and Wilson, 1989; Szoke and Rotunno, 1993). These tornadoes have come to be known as 'non-supercell tornadoes' (NST) or as 'landspouts'. They are usually weak (F0-F1 strength) and are generally confined to the boundary layer (reaching heights of about 2km) sometimes reaching up to 600m in diameter (Brady and Szoke, 1989; Wakimoto and Wilson, 1989). A few cases of this type of tornado reaching F2-F3 intensity and developing high into the parent storm have been reported (Wilczak et al., 1992; Roberts and Wilson, 1995). Although the focus of the current study is tornadogenesis in supercells, it has been proposed that tornadoes which form along outflow boundaries in supercells or even tornadoes associated with the mesocyclone may be generated by mechanisms similar to the non-supercell tornadoes (Brandes, 1977), and a brief discussion of NST is included here.

NST usually develop along a boundary layer shear zone such as an outflow boundary, or in a region of two colliding boundaries. This type of tornado has even been observed to develop along a severe frontal rainband under synoptic conditions not conducive to tor-

nado development (Carbone, 1983). Doppler radar observations have also indicated that the tornadoes may originate from shear-induced Helmholtz instabilities along the boundary. Observations of NST along outflow boundaries (some showing as many as 3-7 rather equally spaced tornadoes occurring simultaneously) seem to support this idea (Burgess and Donaldson, 1979). Prior to tornadogenesis, several cyclonic circulations usually appear along the boundary (as seen on Doppler radar). These circulations are known as 'misocyclones'[3] and they range in size from 40m-2km and are generally confined to the boundary layer (i.e. extend 1-3km in the vertical). Several of these circulations have also been observed to merge into a larger circulation prior to tornadogenesis (Wilczak et al., 1992; Roberts and Wilson, 1995). It is generally observed that the tornado develops from the misocyclone circulations as these circulations intensify through vertical stretching when convective storms develop over them, or as they move under pre-existing convection (Wakimoto and Wilson, 1989; Brady and Szoke, 1989; Roberts and Wilson, 1995). However, tilting of baroclinically generated horizontally vorticity into the vertical may be a significant source of low-level vorticity when the mesoscale boundary is strongly baroclinic (Wilczak et al., 1992).

Also of interest is the structure and evolution of non-supercell tornadoes. Despite the generally weak circulations associated with NST and their parent misocyclones, both NST and misocyclones have been observed to be two-celled vortices in which a downdraft develops in the center of the circulation surrounded by a ring of updraft (Mueller and Carbone, 1987; Brady and Szoke, 1989; Wilczak et al., 1992; Wakimoto and Martner, 1992). Brady and Szoke (1989) used Doppler radar to document an F1 tornado which occurred 26 July, 1985 near Erie, Colorado. The tornado developed from a misocyclone circulation as described above, and had an average width of 520m (as seen on radar) during its lifetime. Instead of shrinking in size prior to its demise, the tornado expanded in time as it weakened reaching a diameter of 1.5km before tornadic strength winds were no longer detected. The weakened vortex persisted for more than 15 minutes after the tornado dissipated.

---

[3]The term 'misocyclone' was first used by Fujita (1981) to describe observed vortices with horizontal scales between 40m-4km.

In summary, observations suggest that there may be several different mechanisms for tornadogenesis. Possible mechanisms for tornadogenesis have also been investigated in numerical models. These numerical simulations are the subject of the next section.

2.3.2 Modelling Studies

Early simulations of tornadoes were constrained to simplified models of storms/vortices due to computational limitations. Leslie (1971) performed calculations with a model developed to numerically simulate laboratory experiments which produced concentrated vortices in rotating tanks. He found that the concentrated vortices produced in the simulations grew downward from the top of the tank until they reached the bottom boundary. Upon contact with the bottom boundary, the vortex would strengthen rapidly before reaching a steady state. Through these numerical experiments, Leslie was able to document the process by which the vortex built downward. He argued that as the vortex started to develop, it reached cyclostrophic balance at some height. Since the radial pressure gradient force and the centrifugal force 'balance' each other, little or no inflow is allowed radially into the vortex. However, air could enter the vortex from below as a rotationally induced upward pressure gradient drew air upward into the vortex, which behaved somewhat like a 'pipe'. The inflow into the lower part of the vortex created an area of convergence below the vortex which concentrated ambient vertical vorticity, eventually establishing cyclostrophic balance at a lower level. As this process continued, the vortex descended toward the surface (lower boundary). This process has come to be known as the 'dynamic pipe effect' (or DPE for short), and has been used to explain how the radar observed TVS extends to the ground and strengthens into a tornado.

Smith and Leslie (1978) extended this work by modifying the model of Leslie (1971) to specify a vertical profile of swirling velocity at the lateral boundary. The purpose of their work was to investigate different profiles of swirl to see how this affected vortex development. In all cases, the vortices grew downward as described by Leslie (1971). However, they found that the vortex extended to the lower boundary only if the ambient rotation occurred at sufficiently low-levels, otherwise a suspended vortex was maintained.

Trapp and Davies-Jones (1997) further investigated conditions under which the dynamic pipe effect could/could not occur. They used both an idealized axisymmetric model and a simplified analytical model to investigate this question. They argued that the importance of the DPE in tornadogenesis (in their model) depended on two things: the vertical distribution of convergence, and the vertical distribution of vertical vorticity. If convergence of vertical vorticity was greater aloft than near the surface, the DPE could occur. The DPE would be especially important in cases where the low-level convergence associated with the larger-scale flow was weak. In these cases, the vortex would have to develop its own convergence through the DPE in order to descend toward the surface. If there was insufficient low-level rotation, the vortex would remain aloft as was the case with Smith and Leslie (1978). Trapp and Davies-Jones also argued if the ambient vertical vorticity and convergence are relatively constant with height, the vortex could develop simultaneously over the depth of the boundary layer. In cases where convergence and vorticity are strongest near the surface, the vortex would develop from the ground upward.

Klemp and Rotunno (1983) were the first to investigate the transition of a supercell into its tornadic phase using a high resolution cloud model. They began by simulating a supercell (using horizontally homogeneous initial conditions) in a model with 1 km grid spacing. Once the supercell became well organized, they interpolated a subset of the 1 km grid to another grid with 250m horizontal grid spacing. The coarser grid information was then used to provide boundary conditions for the fine grid. The fine grid simulation produced a downdraft in the center of the mesocyclone and a ring of strong cyclonic vorticity around the center of circulation at low levels, which they suggested might be characteristic of the tornado cyclone (they never discussed the strength of the tangential winds so it is unclear whether the simulated vortex was of tornadic strength). Their analysis showed that the strong low-level vorticity was generated by tilting of horizontal vorticity present in the environment by the updraft, and also through tilting (by the updraft) of horizontal vorticity generated baroclinically along the leading edge of the forward flank downdraft. Once the vertical vorticity was generated through tilting, convergence acted to amplify it. An analysis

of the vertical pressure gradient term revealed that the downdraft was dynamically forced by the strong low-level rotation.

Although the primary focus of the simulations preformed by Davies-Jones and Brooks (1993) was low-level meso-cyclogenesis, they also combined their model results with previous studies to propose a possible mechanism for tornadogenesis. They suggested that the downdraft is essential to the development of low-level rotation and proposed the following scenario: 1) tilting of horizontal quasi-streamwise vorticity by the downdraft first produces anticyclonic vertical vorticity in the downdraft, 2) as this vertical vorticity is transported to low levels through subsidence, baroclinic generation of horizontal vorticity and continued tilting of horizontal vorticity into the vertical changes the sign of the vertical vorticity from anticyclonic to cyclonic at vertical levels less than 250m above the surface, 3) air flowing out the downdraft enters the updraft where the cyclonic vertical vorticity is enhanced through stretching, 4) convergence also aids to concentrate cyclonic vertical vorticity in a small region–the convergence is enhanced by the outflow.

Wicker and Wilhelmson (1993) used a primitive equation model with horizontally homogeneous initial conditions to investigate the effects of surface friction on tornadoes. The model had interactive nesting capabilities so both the parent thunderstorm and the tornadic circulations could be simulated. The smallest horizontal grid spacing used in the simulations was 120m. In the simulation run with the no-slip lower boundary condition, two intense vortices developed from the mesocyclone. Prior to the development of both 'tornado cyclones' (as they termed their intense vortices), the mesocyclone evolved into an elliptical shape. Each tornado cyclone lasted about 10 minutes and was about 1 km in diameter with maximum tangential velocities between 53-55 ms^{-1}. An analysis of the model data revealed that the two tornado cyclones developed differently. The first appeared to develop from the mesocyclone downward, as maximum values of vertical vorticity appeared aloft before they developed at the surface. The second appeared to develop from the boundary layer upward, since strong rotation was first seen in the boundary layer (0-2km above the surface), and then at higher levels. The inclusion of surface friction in the simulations created significant inflow into the base of the tornado cyclones. As a result, the diameter of

the tornado cyclones shrunk to half the size of those in the free-slip simulations, the surface wind speeds were 10-15% larger, and the updrafts around the tornadoes were 5 times larger at low levels.

In an extension to their 1993 study, Wicker and Wilhelmson (1995) reexamined the tornado cyclone simulations to try to determine the origins of the large vertical vorticity values near the surface. They calculated backwards trajectories from the second tornado cyclone and looked at the vertical vorticity along the trajectories. The air entering the tornado appeared to originate from two main regions–one from low levels to the northeast of the vortex, the other at higher levels (around 1 km) to the northwest of the vortex. The authors found that the vertical vorticity in the air originating in the downdraft to the northwest of the vortex remained negative until the parcel finished descending. The vertical vorticity then changed sign as the parcel moved upward as it entered the tornado. They attributed this sign change in the vertical vorticity to baroclinically generated horizontal vorticity along the parcel trajectory which was then tilted upward. However, their analysis was unable to conclusively identify the process(es) responsible for the generation of rotation next to the surface.

Walko (1993) did a series of highly idealized simulations with the RAMS model to explore possible mechanisms of tornadogenesis. The 'parent storm' was represented by a heating function (to generate upward vertical motion) and a low-level heat sink approximated the evaporatively cooled downdrafts. The simulations differed from each other in the initial low-level wind and thermal fields, and the presence or absence of the heat sink. The results from the experiments indicated that tilting of horizontal vorticity by the updraft alone could not produce a tornado extending to the surface. To produce a vortex which extended to the surface required either vertical vorticity to be present in the ambient environment, or to be generated by tilting of horizontal vorticity into the vertical by a downdraft. The author also argued that the tilting of horizontal vorticity by the downdraft must occur over a region several times larger than the tornado core radius. The tornado then formed as convergence concentrated the vorticity to the tornado scale.

Trapp and Fiedler (1995) also used a simplified model which allowed them to isolate and control thunderstorm features which are thought to play a role in tornadogenesis. Their model was based on the idea that low-level rotation develops primarily from baroclinically-generated horizontal vorticity; no ambient wind shear was included in the simulations. Convective updrafts and downdrafts were forced with prescribed buoyancy distributions. A region of negative buoyancy was fixed in the center of the domain and the updraft region was assigned a specific orbit around the downdraft so that horizontal vorticity generated by the outflow became streamwise in the storm-relative frame. The authors ran several sensitivity experiments changing the lower boundary condition (free slip/no slip), the strength of the central downdraft, the speed of the updraft, and model viscosity. They found tornadogenesis in the model occurred only for a small region of parameter space (updraft propagation rates, fluid viscosities, downdraft intensity). A circulation analysis was preformed in the simulations that did produce a vortex and revealed that downdrafts played an important role in tilting the horizontal vorticity into the vertical. This vorticity was then converged and stretched in the vertical to form the tornado vortex.

Grasso and Cotton (1995) used the RAMS model to simulate a tornadic storm starting with horizontally homogeneous initial conditions. They used the nested grids capability of the model in order to study the tornadic region of the storm (smallest horizontal grid spacing was 111m). The model produced an intense vortex which initially formed at mid-levels along the edge of the updraft region in the storm. A pressure deficit tube then formed and built downward into the sub-cloud layer. They proposed a scenario for tornadogenesis in which low-level vorticity is drawn upward into the base of the vortex, enriching the vertical vorticity to values large enough to reduce the pressure there. This allowed that pressure deficit tube to descend to the surface and form a tornado.

Most recently, Grasso (1996) used RAMS to simulate two classical supercells which produced tornadoes. A unique feature of this study was that the simulations were initialized with synoptic data. All convection in the simulations was initiated with resolved vertical motion and subsequent condensation/latent heating from the model microphysics; no warm bubbles or cumulus parameterizations were used. In both simulations, the storms were

initiated along a dryline in the southern plains. As the storms developed, nested grids were added to the simulations to better resolve the tornadic region of the storm (smallest horizontal grid spacing was 111m). One simulation produced a tornado of F2/F3 strength. The other simulation produced an F4 tornado with maximum tangential winds speeds of over $100ms^{-1}$. Grasso performed a circulation analysis on the tornadoes and found in both cases, the tornadoes started at the ground and worked their way upward (maximum vertical vorticity values were first seen near the surface and then at higher levels). Their results also indicated that the main source for near-surface rotation was positive tilting of horizontal vorticity into the vertical by the (forward flank) downdraft during the life of the tornado. This tilting occurred in the lowest few hundred meters above the surface. They also speculated that a potential source for low-level rotation could be horizontal wind shear associated with a bulge in the dryline which formed along the southern flank of the developing supercell. However, conclusive proof of this mechanism requires further investigation.

Lee and Wilhelmson (1997a,b) undertook an idealized modelling study to investigate shear instabilities along outflow boundaries in three dimensions, and their possible connection to tornadogenesis. The simulations consisted of releasing a 'cold pool' meant to represent a storm outflow from one side of the domain which then propagated into a region of southerly winds, creating a vortex sheet along the leading edge of the outflow. The simulations were conducted both with and without moist convective processes present and with different across-front shears and vertical stabilities. They then documented several stages in the evolution of the vortex sheet and the subsequent vortices that developed:

1. Vortex sheet development stage
2. Vortex sheet roll-up stage in which the vortex sheet broke down into several 'misocyclones' (vortices with dimensions between 40m-4km). In their case the initial scale of these 'horizontal shear instabilities' (or HSI) was about 1.5km which was half the predicted theoretical value.
3. Misocyclone interaction and merger stage, in which 2-3 misocyclones merged together creating vortices with scales on the order of 3km.
4. Early mature phase when the misocyclones intensified to tornadic strength as convective towers develop above them.
5. Late mature phase as rain-cooled downdrafts developed near the surface, enhancing the low-level convergence which intensified the vortices.

6. Dissipation stage as negatively buoyant air surrounded the low-level vortex, inhibiting upward vertical motion.

Their results also suggested that the strong convective updrafts which develop near the misocyclones were not just chance occurrences. Instead the misocyclones influenced the pattern of deep convection along the outflow boundary.

In summary, observations and modelling studies have suggested several possible mechanisms by which tornadoes may develop in severe storms. These mechanisms include:

- convergence of pre-existing low-level vorticity by a convective updraft (Wakimoto and Wilson, 1989; Walko, 1993)
- tilting of baroclinically generated horizontal vorticity into the vertical by the updraft, followed by amplification of the vertical vorticity through convergence (Klemp and Rotunno, 1983; Wilczak et al., 1992)
- tilting of baroclinically generated horizontal vorticity into the vertical by the downdraft, followed by amplification of the vertical vorticity through convergence (Davies-Jones, 1983; Davies-Jones and Brooks, 1993; Grasso, 1996)
- dynamic pipe effect (Leslie, 1971; Smith and Leslie, 1978)
- shear instability along an outflow boundary (or other mesoscale boundary) which is amplified through convergence as convective updrafts either develop or move overhead (Brady and Szoke, 1989; Roberts and Wilson, 1995; Lee and Wilhelmson, 1997a,b)
- vortex breakdown/instabilities in the mesocyclone (Brandes, 1987a,b; Wakimoto and Lin, 1997)

The main purpose of this study is to extend the work of previous modeling studies by examining the tornadogenesis process in a simulated HP supercell (starting with synoptic data on June 30, 1993), and comparing it to the proposed tornadogenesis mechanisms in classical supercells. In addition, a second simulation of a tornado produced by a classical supercell was performed in which vortex dynamics and stability of the simulated tornado is explored as it relates to the development of secondary vortices in tornadoes. A summary of previous studies of vortex stability and secondary vortices in tornadoes is given in the next section.

2.4 Secondary Vortices and Vortex Stability

2.4.1 Observations

Observations have shown that both the horizontal and vertical wind fields associated with tornadoes are highly asymmetric. Golden and Purcell (1977, 1978) analyzed video tapes of several different tornadoes in order to estimate wind speeds using photogrammetric analysis. They noted pronounced azimuthal asymmetries in the vertical motion field in the tornadoes with weak sinking motion on one side of the vortex, and maximum rising motion on the other. The primary rising/sinking maxima shifted around the vortex in time. They also observed dust bands extending into the vortex column base from the west/southwest. These dust bands were associated with a major inflow jet of air accelerating into the vortex at low levels (estimated wind speeds in the inflow jet ranged from $20ms^{-1}$ accelerating to $60ms^{-1}$ near the base of the vortex). They speculated that these inflow jets could be responsible for some of the observed spiral damage paths that sometimes extend outward from the edge of the vortex damage path for considerable distances. Damage surveys have also revealed the existence of microbursts along the periphery of some tornadoes (Fujita, 1978; Forbes 1978; Fujita, 1989; Fujita and Smith, 1993). These microbursts occur most frequently on the right side of the tornado track (looking down-track). Fujita and Smith (1993) documented one such case that occurred on October 3, 1979 near Windsor Locks, Connecticut, in which 8 microbursts occurred along the right-hand side of the 30km long tornado path as shown in Figure 2.9. In an extreme case, Fujita (1989) found evidence of 72 microbursts along the 40km long damage path left by the Teton-Yellowstone tornado on June 21, 1987. In addition to these asymmetries, Davies-Jones et al. (1978) analyzed the damage path from a well documented tornado (Union City, Oklahoma) and were able to surmise that there was a distinct wind speed minimum on one side of the vortex. Similar conclusions were reached by Golden and Purcell (1978).

Observations of tornadoes and surveys of damage paths have also revealed a different type of flow asymmetry in some tornadoes–the development of several smaller vortices

within the main tornado vortex. Evidence of these smaller vortices was first seen in early aerial damage surveys in which it was noticed that distinct circular/cycloidal marks were left on the ground by some tornadoes (Van Tassel, 1955; Prosser, 1964). A closer inspection of these surface marks revealed that they were actually bands of debris deposit 5-10cm high (Fujita, 1970). Fujita (1970, 1971) connected these cycloidal marks with multiple-vortex tornadoes, and proposed the terms 'suction spots' or 'suction vortices' to describe the smaller vortices which sometimes form in the parent tornado vortex.

Since the early 1970s, many multiple-vortex tornadoes have been documented on video tape (Fujita et al., 1970; Agee et al., 1975; Blechman, 1975; Fujita, 1975; Agee et al., 1977; Forbes, 1978; Pauly and Snow, 1988). These studies have found the following common characteristics associated with suction vortices and the parent tornado:

- Suction vortices usually rotate cyclonically around the parent vortex, although cases of stationary suction vortices (with respect to the ground) have been reported.
- Suction vortices tend to form on one side of the tornado, and usually dissipate before making a full revolution around the parent vortex. The preferred quadrant for the formation of suction vortices in the parent vortex varies from tornado to tornado (Forbes, 1978).
- The most severe damage (and most deaths) caused by intense tornadoes appears to be linked to the paths of suction vortices. When F5 damage (the highest observed level on the F-scale) occurs, it tends to be confined to narrow swaths which coincide with the paths of the suction vortices (Fujita, 1970, 1975).
- Anywhere between 2-5 suction vortices have been observed rotating around the parent vortex at any one time, although it is often difficult to visually distinguish a suction vortex from the parent vortex (Fujita and Smith, 1993).
- The diameter of the suction vortices is at least 1 order of magnitude smaller than the diameter of the parent vortex (Fujita and Smith, 1993). Observed damage paths associated with suction vortices have been observed to be between 20-140m in diameter (Forbes, 1978).
- Many suction vortices reside in the surface boundary layer and do not extend through the depth of the PBL (Agee et al., 1975, 1977). Those that do extend through the PBL (or higher) tend to tilt away from the vertical as one moves upward away from the surface (Agee et al., 1977; Pauly and Snow, 1988).
- Multiple vortices appear to be favored over uniform surfaces. Trees and buildings tend to disrupt the multiple vortices (Blechman, 1975; Forbes, 1978).
- In many cases, the intersection between inflow jets or downbursts and the tornado path mark an increase in tornado intensity or the onset of multiple vortices (Forbes, 1978).
- There is also some observational evidence that there may occasionally be even smaller vortices within the suction vortices (Agee et al., 1977; Forbes, 1978; Snow, 1982).

- Suction vortices rotate around the parent vortex at speeds that are less than the the maximum tangential wind speeds at the edge of the core (Agee et al., 1975; Forbes, 1978).
- Observations also suggest that it is possible for suction vortices to interact with one another. Unevenly spaced suction vortices can become paired and revolve around each other as they revolve around the parent vortex (Forbes, 1978).

Forbes (1978) documented many cases of multiple-vortex tornadoes and noted that three types of suction vortex decay have been observed:

1. All suction vortices disappear in the parent vortex.
2. One suction vortex becomes dominant and takes over as the new central vortex.
3. The tornado diffuses.

In addition Golden and Purcell (1977) noted that although multiple- vortex tornadoes *tend* to be more intense and destructive than single vortex tornadoes, they are not always accompanied by unusually high wind speeds.

Observations also indicate that some mesocyclones may possess multiple vortices or multiple vorticity centers. Radar observations have shown multiple vorticity maxima in rings surrounding the centers of some mesocyclones (Brandes, 1978). Wakimoto and Lin (1997) documented a tornado which developed from one of three vorticity maxima along the periphery of a mesocyclone. There have also been numerous eye-witness accounts describing multiple tornadoes occurring simultaneously in one storm with the tornadoes 'moving in different directions in different parts of the city' (revolving around a single point) (Fujita et al., 1970; Barnes, 1987a,b).

It is clear from observations that the flows associated with tornadoes (especially multiple-vortex tornadoes) are very complex. To help shed some understanding on tornado dynamics, laboratory experiments and analytical/modeling studies of idealized vortex flows have been carried out. These studies will be discussed in the following sections.

2.4.2 Laboratory Studies

In this section, laboratory simulations of tornado-like vortices are presented. Laboratory simulations can isolate the important physical parameters in tornado maintenance

and dynamics using highly simplified idealized flows, and can provide great insight into the dynamics of actual tornadoes provided that the conditions of geometrical and dynamical similarity are closely met (Church et al. 1979). Early laboratory studies of tornadoes consisted of rotating water tanks in which meridional flow was driven by draining fluid from either the bottom or the top of the cylindrical tank. Fluid was then allowed to reenter the tank through the lateral boundaries or by injecting buoyant fluid into the bottom of the tank. However, these experiments suffered from the presence of the lateral tank wall which induced flow constraints not found in atmospheric flows associated with thunderstorms/tornadoes (Davies-Jones, 1974).

Ward (1972) took a somewhat different approach to tornado modeling. Ward's simulator used an exhaust fan at the top of a circular chamber as a proxy to the convective updraft. A fine-mesh honeycomb structure was placed below the exhaust fan at the top of the chamber to prevent fan-induced vorticity from entering the chamber, and to remove rotation from the outflow, divorcing the vortex from the fan. Air was allowed to flow into the chamber over a limited depth at the bottom of the chamber. Before entering the convective region of the chamber, the confluent low-level inflow passed through a rotating screen so that air entering the convective portion of the chamber possessed angular momentum. The updraft radius, inflow depth, volume flow-rate and the rotation rate of the screen could all be varied in the experiments, allowing many different types of vortex behavior to be simulated. Ward was able to produce: 1) a characteristic surface pressure profile, 2) 'bulging deformation in the vortex core' (i.e. vortex breakdown), and 3) multiple vortices. He also found that the simulated vortex was very sensitive to the geometrical features of the larger-scale flow. As the 'configuration ratio' ($2r_o h^{-1}$) was decreased (where h is the depth of the inflow layer and r_o is the radius of the updraft), the radius of the vortex core became progressively smaller. When the configuration ratio was held fixed, the radius of the vortex core became larger as the initial angular momentum of the inflow was increased.

Davies-Jones (1973) later reanalyzed Ward's results to show that the nondimensional radius of the turbulent vortex core in Ward's laboratory experiments depended only on a nondimensional quantity called the 'swirl ratio'. There are a number of different ways

the swirl ratio (S) can be expressed. In laboratory tornado models, the swirl ratio can be written as:

$$S = \frac{\tan\theta}{2a} \tag{2.7}$$

where a is the aspect ratio ($a = \frac{h}{r_0}$ where h is the inflow depth and r_0 is the updraft radius), and θ is the swirl angle ($\theta = arctan(\frac{v_0}{u_0})$ where v_0 and u_0 are the vertically averaged tangential and radial velocities (respectively) within the inflow layer at r_0). Using conservation of mass and assuming axial symmetry, the swirl ratio can also be written as:

$$S = \frac{v_0}{\overline{w}} \tag{2.8}$$

where $\overline{w}$ is the average vertical velocity inside r_0 at height h.

The swirl ratio can also be expressed in terms of physical quantities necessary for vortex development and maintenance. It can be written either in terms of the circulation, $M = r_0 v_0$, and the volume flow rate, $Q = r_0 u_0 h$, or in terms of the ambient vertical vorticity, ω, and the horizontal convergence, φ, as:

$$S = \frac{r_0 M}{2Q} = \frac{r_0 \omega}{2\varphi h}. \tag{2.9}$$

In all instances, the swirl ratio can be thought of as a measure of the strength of the ambient rotation compared to the strength of the ambient convergence.

The results from Davies-Jones (1973) have subsequently been tested in the laboratory by several different investigators (Church and Snow, 1979; Church et al., 1979; Baker and Church, 1979; Snow et al., 1980; Pauly et al., 1982; Snow, 1982; Monji, 1985) using tornado vortex chambers similar to that developed by Ward (1972), and in laboratory simulations of dust devils (Mullen and Maxworthy, 1977). These studies documented the changes in vortex structure as functions of the swirl ratio, the radial Reynolds number ($Re_r = \frac{Q}{\nu}$ where ν is the kinematic viscosity), and the aspect ratio ($a = \frac{h}{r_0}$). These studies all concluded that the swirl ratio (S) was the most important non-dimensional parameter for determining the structure of the vortex, suggesting that S is the principal dynamic similarity variable

(Church and Snow, 1993). Figure 2.10 depicts the laboratory vortex evolution as the swirl ratio is increased. For very small values of S ($S \leq 0.1$), a ring-like zone of separated flow develops along the lower boundary in the inflow region. This prevents low-level angular momentum from reaching the center of the vortex chamber, and no concentrated vortex forms at the surface (Figure 2.10a). As S is increased slowly, the vortex develops aloft and builds downward, contacting the surface when $S \approx 0.1$. At this point the vortex is termed a 'one-celled' vortex since upward vertical velocities extend everywhere inside the core radius with the maximum vertical velocities along the center (Figure 2.10b). At low swirl values, the initial response of the vortex is to contract as S is increased. However, as S increases, the core structure of the vortex undergoes a very dramatic change at some level. This sudden change is referred to as a 'vortex breakdown' and occurs as an adverse axial pressure gradient develops in the vortex core. The breakdown is marked by a free stagnation point which becomes the leading edge of the vortex breakdown. Immediately upstream of the free stagnation point is an inner circulation associated with the breakdown known as a 'breakdown bubble'. The flow associated with the breakdown bubble is unsteady and can take many different forms (Faler and Leibovich, 1977). The core radius of the vortex abruptly increases (often by a factor of five or more (Church and Snow, 1979)) downstream of the breakdown as upward moving air diverges and flows around the breakdown bubble. Downstream of the breakdown point, the axis of the vortex core contains weaker, decelerating upflow surrounded by an annular region of stronger, accelerating upflow. As the flow in the center of the core continues to decelerate, a second stagnation point (vortex breakdown) develops. Downstream of this second breakdown the core can be stagnant or can contain a downdraft[4](Figure 2.10c). Air in the central downdraft contains little (if any) rotation, so the vertical vorticity downstream of the second stagnation point is concentrated in the annular updraft region. Vortex breakdown has been observed in some tornadoes (Davies-Jones, 1983; Lugt, 1989; Pauly and Snow, 1989).

---

[4]Results from some laboratory experiments show a central downdraft upstream of the first vortex breakdown, indicating that the second stagnation point can be included in the structure of the breakdown bubble (Pauly, 1989).

As S is increased further, the first vortex breakdown moves downward toward the surface and the one-celled vortex beneath it intensifies. The most intense stage of the vortex (at the surface) occurs when the leading edge of the breakdown lies just above the surface. It is at this point that the largest pressure deficits, strongest winds, and strongest vertical accelerations are experienced in the surface layer. This condition has been termed a 'drowned vortex jump' by Maxworthy (1972) and occurs in the laboratory around $S \approx 0.45$. Further increases in S mark the penetration of the vortex breakdown to the surface, followed by radial expansion of the core and penetration of the central downdraft to the surface. At this point the vortex has a 'two-celled' structure in which the central downdraft is surrounded by an annular updraft region through the depth of the vortex (Figure 2.10d). After the downdraft reaches the surface, the annular shear zone becomes thinner and has a greater velocity difference across it. For very large values of S, (S=2-2.5), the core expands until it fills the updraft hole. At this stage the updraft is confined to a narrow annulus, and the downdraft becomes stronger and larger until it occupies most of the convective region.

After vortex breakdown has occurred, helical disturbances can develop in the annular updraft region downstream of the breakdown. These helical disturbances take the form of smaller vortices spinning about their own axis while at the same time circling the center of the parent vortex (except the m=1 mode (where m is the azimuthal wavenumber) which is stationary with respect to the parent vortex). These smaller vortices have been labeled as 'suction vortices', 'subsidiary vortices', or 'secondary vortices', and occur in the laboratory around $S \approx 0.5$. For the duration of this dissertation, we will use the term 'secondary vortices' (abbreviated by SV). The initial disturbance (m=1) takes the form of a single helical vortex which winds around the central (decelerating) upflow downstream of the first breakdown point. This disturbance can extend upward through the depth of the vortex chamber, or can be confined to the region between the first and second breakdowns (Church et al., 1979). The axis of the disturbance is oriented along the local vorticity vector of the parent circulation, and the m=1 mode does not rotate about the parent vortex. If S is increased slightly, the single helical vortex gives way to a vortex pair. In the laboratory, the m=2 mode (i.e. 2 secondary vortices) occurs around S=1. When the downdraft extends all

the way to the surface, the SV increase in size and tend to extend through a deeper vertical layer. Further increases in S produce higher order multiple vortex patterns (Figure 2.10e). Modes as high as m=6 have been produced in the laboratory, but the higher modes are difficult to maintain. Note that the laboratory experiments suggest there are two subsets of secondary vortices–one set associated with the initial vortex breakdown, and another set associated with the penetration of the central downdraft to the surface.

As was discussed above, the most important non-dimensional parameter for dynamic similarity in laboratory experiments is the swirl ratio (S). In the laboratory, the quantities needed to calculate the swirl ratio are based on the geometry of the vortex chamber and other parameters controlled by the experimenter, such as the volume flow rate through the chamber and the angular momentum of the air entering the chamber. In the atmosphere, calculation of a swirl ratio for an actual tornado is not so straight forward. There are no boundaries constraining the geometry of the flow, and detailed measurements of the flow structure outside the vortex are difficult to come by. To get around these problems, a crude measure of the swirl ratio, called the 'poor man's swirl ratio' (Forbes, 1978) is used. This is given by

$$S_{pm} = \frac{v_{max}}{w_{max}} \tag{2.10}$$

where v_{max} is the maximum wind speed measured below cloud base in the tornado, and w_{max} is the maximum vertical velocity measured in the tornado (below cloud base). Measurements are made either using dual Doppler radar or photogrammetry. Calculations of the swirl ratio from (2.10) using wind speed estimates from observed tornadoes indicate that multiple-vortex tornadoes are favored at swirl ratios between 1.25-2.5 (Forbes, 1978).

In addition to the structure of the main parent vortex, several studies have investigated some of the properties of the secondary vortices. The following are characteristics of secondary vortices simulated in the laboratory:

- Secondary vortices occupy the volume *inside* the region of maximum winds (Church et al., 1979). The center of the SV lies about $\frac{4}{5}$ of the parent vortex core radius from the center of the parent vortex. The outer wind maximum of the SV is located at the same radial position as that of the parent vortex (Monji, 1985).
- Secondary vortices are accompanied by extremes of low-pressure–much lower than the central pressure of the primary vortex (Ward, 1972). Pressure measurements

have shown pressure deficits in the SV can be 2-3 times greater than central pressure deficit in the parent vortex (Pauly et al., 1989).

- There is generally an inverse relationship between number and size of the SV (Ward, 1972). The larger the number of SV, the smaller their core radius, although the SV are not all of the same size or strength (even though parent vortex is axisymmetric) (Pauly et al., 1989)
- The core size of the SV is about 20% that of parent vortex (Monji, 1985), although the size of stronger SV can be only 10-15% of parent vortex core radius (Pauly et al., 1989).
- SV rotate around the parent vortex at about half the speed of the tangential winds in the parent vortex (Ward, 1972; Monji, 1985). In other words, the SV are in retrograde motion with respect to the parent vortex.
- Maximum tangential velocities in SV are about 25% larger than the tangential velocities of the parent vortex (Monji, 1985).

All the laboratory experiments presented above used some variant of the Ward vortex chamber which creates a vortex through convergence of angular momentum. Recently, a new type of tornado vortex chamber has been developed which is designed to model vortices which develop from highly helical flows (as is thought to be the case in the atmosphere). Rothfusz (1986) and La Due (1993) present vortex simulations using the University of Oklahoma tornado vortex chamber. This vortex chamber has been modified from the Ward design by including several inflow layers which can be oriented in different directions to create veering flow. The goal of the design is to create a highly helical flow with no net vertical circulation, so that any vertical circulation in the chamber is created through the vertical tilting of ambient horizontal vorticity in the flow. These preliminary studies have shown that this type of vortex chamber can produce some of the observed features associated with the tornadic region of supercell thunderstorms included a mesocyclone-like circulation in which a smaller tornado-like vortex is embedded (Rothfusz, 1986), and a kind of rear-flank gust front with a region of anticyclonic curvature (La Due, 1993).

Despite their success in simulating many observed features in tornadoes and dust devils, laboratory experiments are not without their problems. One potential problem found in most laboratory studies is that the similarity requirements are not satisfied with the Reynolds number (Re). Atmospheric values are several orders of magnitude larger than the value in the laboratory (Church et al., 1979). Church et al. (1979) investigated the

critical swirl ratio needed for a given vortex transition (such as the transition from a one-celled vortex to a two-celled vortex, or the transition between multiple vortex states) as a function of Reynolds number. They found that the critical swirl ratio decreased as the Reynolds number was increased, and that an asymptotic limit of critical S was reached at high values of *Re*. So although the behavior of the vortex core is somewhat sensitive to *Re*, it is much less sensitive to changes in *Re* than to changes in S. From the work of Church et al. (1979) and others, it does not appear that the lack of Reynolds number similarity in the tornado vortex chamber is a major problem provided that *Re* is sufficiently large so that the flow is turbulent. Another potential drawback in laboratory studies is that the circulation and the volume flow rate can be varied independently. This is probably not the case in the atmosphere (Pauly et al., 1989), but the relationship between these two quantities in tornadic thunderstorms is not well understood.

An important question left unanswered by laboratory studies is the physical mechanism responsible for the development of secondary vortices. The nature of the two-celled vortices produced in the laboratory studies suggests that inertial[5]instability in the annular shear zone may be the mechanism that gives rise to SV (Church et al., 1979). This idea is explored further in the analytical and idealized numerical studies of vortices presented in the next section.

2.4.3 Analytical/Numerical Modeling Studies

In this section, previous analytical and numerical modeling studies of tornado-like vortices are presented. Since the interest in this section is secondary vortices produced by tornadoes, attention will be restricted to those analytical and numerical studies which have focused on vortex stability characteristics and secondary vortex development. The fact that the flow in laboratory vortex experiments is very close to axisymmetric suggests that the development of secondary vortices cannot be explained by an external forcing mechanism,

---

[5]The type of instability referred to as 'inertial instability' by Church et al. (1979) is usually referred to as 'barotropic instability' by the atmospheric science community.

but could arise from an instability in the flow. Laboratory studies have shown that secondary vortices occur only after the vorticity field in the vortex becomes concentrated in a narrow ring. This suggests barotropic instability could occur in the vortex.

This idea was first explored by Rayleigh (1880) who discovered that two-dimensional vortex flows (in which the tangential velocity is a function of radius) were stable to two-dimensional disturbances if the vertical vorticity ($\omega = r^{-1}\partial(rv)/\partial r$) was a monotonic function of r. Put another way, the flow was stable if the radial vertical vorticity gradient did not change sign anywhere in the flow. In a later study, Rayleigh (1916) showed that the same flow was stable to axisymmetric perturbations if $r^{-3}\partial(r^2v^2)/\partial r > 0$. Howard and Gupta (1962) extended Rayleigh's analysis to three-dimensional flows in which the vertical velocity was also a function of radius. They found the flow was stable to axisymmetric disturbances if $r^{-3}\partial(r^2v^2)/\partial r(\partial w/\partial r)^{-2} > 0.25$. No general stability criteria could be found for three-dimensional disturbances in these flows.

Since laboratory vortex flows are better understood (and better measured) than tornadoes, most numerical and analytical studies of tornado dynamics have been designed to numerically simulate laboratory vortices. Rotunno (1977) developed an axisymmetric numerical model to simulate Ward's (1972) laboratory vortices. Model tests showed that the numerical model could reproduce laboratory surface pressure patterns, and the core size dependence on the swirl ratio. Numerical tests were also performed to evaluate the role of viscous diffusion in the model. Results indicated that for very large viscosities, the core region was larger and the vorticity gradients at the edge of the core were not as strong. However, if the Reynolds number was large enough (i.e. viscosity was small enough), the core radius size was independent of Re as was also found in the laboratory. Tests with different lower boundary conditions indicated that a frictional lower boundary tended to decrease the core size.

In a further study, Rotunno (1979) extended his 1977 study by incorporating finer grid spacing and a no-slip lower boundary into the model. The purpose of this study was to document the simulated vortex behavior at different values of the swirl ratio with particular interest in the ground-vortex interactions. The simulations were able to reproduce many

of the boundary layer features observed in laboratory vortices, and showed that the vortex structure was mainly a function of the swirl ratio (S). Other vortex features observed in the laboratory were also simulated in the model including vortex breakdown and a drowned vortex jump. The model results showed that the flow upstream of the vortex breakdown was indeed supercritical, and that the flow downstream was subcritical, supporting large amplitude inertial waves. The simulated breakdown was characterized by a separation of the flow off the axis and the establishment of standing waves. Evidence was also presented that the breakdown itself was related to the breaking of large-amplitude inertial waves. The presence of the frictional lower boundary induced radial convergence into the vortex near the lower boundary. This lead to increased tangential velocities near the surface which were 50% larger than the free-slip simulations.

Snow (1978) proposed that multiple vortices in intense tornadoes arise from inertial (barotropic) instability in a two-celled vortex. To investigate this possibility, Snow tested the stability of a rotating flow which contained strongly sheared azimuthal velocity with respect to linear two-dimensional non-axisymmetric disturbances. The basic state vortex consisted of a cylindrical shear layer (in which the tangential velocity was only a function of radius) which surrounded a central stagnant core. The basic states chosen in this study were absolutely stable to axisymmetric disturbances. The results indicated that as the radial shear of the tangential velocity was increased, the most unstable disturbance transitioned to progressively higher azimuthal wavenumbers (denoted by 'm') which is in qualitative agreement with laboratory studies. (However, the m=1 mode was stable for all basic states considered.) The disturbances always traveled in the direction of the basic-state rotation, and were restricted to angular frequencies ranging from 50-100% of the basic-state angular frequency. In the case of a non-rotating core, the disturbances rotated about the central axis at half the angular frequency of the air flow at the edge of the core. When rotation was added to the core, the disturbances moved more slowly and their growth rates were reduced (the long wavelength disturbances were actually stabilized). The effects of shear-layer thickness on the stability of the flow were also investigated. The results indicated that as the thickness of the shear layer was decreased, progressively higher order modes were

excited (the most unstable mode shifted from lower wavenumbers to higher wavenumbers), and the growth rate of the most unstable mode increased. The streamlines associated with the most unstable disturbance in two different cases were also reconstructed. The disturbances took the form of smaller vortices having strong cyclonic cores which were located within the core region of the parent vortex.

Rotunno (1978) considered the stability of an idealized vortex flow which consisted of a central downdraft (with no rotation) surrounded by an irrotational updraft ring containing constant angular momentum. This study essentially generalized the cylindrical vortex sheet model to include a central downdraft surrounded by an annular updraft ring. The linear stability of the flow was investigated by deriving a dispersion relationship for the system, and then considering several limiting cases as well as the full case. Without any vertical motion in the vortex, azimuthal waves m=1,2 (where m is the azimuthal wavenumber) were stable for all vertical wavelengths. For axisymmetric disturbances (m=0), results showed that the larger vertical wavenumbers were the most unstable, their growth rates increasing with increasing vertical velocity (which in this model also implied increasing radial gradients of vertical velocity). When the full characteristic equation was considered (for non-zero vertical velocities) azimuthal wavenumbers m=1,2 were also found to be unstable for disturbances with sufficiently large vertical wavenumbers indicating that the radial shear in the vertical velocity destabilized these modes.

The possibility that secondary vortices arise from barotropic instability was also investigated by Staley and Gall (1979) who examined the stability of a tangential wind profile observed in an actual multiple-vortex tornado. They used a linear stability analysis based on the barotropic vorticity equation to find growth rates and structures of any unstable waves. The results showed that the tornadic wind profile was indeed barotropically unstable, with disturbance e-folding times on the order of a few seconds (although the growth rates were very sensitive to the basic state wind profile). The instability was confined between azimuthal wavenumbers m=1.2-5, although the largest growth rates were associated with m=2-5. These wavenumbers lie in the range of the number of secondary vortices observed in a tornado at any one time.

Gall (1983) further investigated the stability of vortex flows by using a simple vertically-integrated axisymmetric model (based on laboratory experiments) to generate axisymmetric basic states for different swirl ratios. The stability of these basic state flows was then tested using a linear primitive equation model where disturbances had both azimuthal and vertical structure. The results indicated that if S was high enough for a central downdraft to develop in the vortex, the flow was unstable. In all other cases the vortex was stable. At low values of S, only azimuthal wavenumbers m=1,2 were unstable. As S was increased, the most unstable azimuthal wavenumber shifted to higher wavenumbers (first 4, then 5, etc.). In this study, m=3 was always stable, probably because the simple model used to generate the basic states could not reproduce all vortex states simulated in the laboratory. The stability analysis also revealed that there were two 'modes' of instability: one (mode 1) in which only m=1,2 were unstable, and a second (mode 2) in which higher wavenumbers were unstable. The two modes could be distinguished by their energetics. Mode 1 (which occurred at low S) gained most of its energy from the radial shear of the vertical wind, while mode 2 (which occurred at higher S) gained most of its energy from the radial shear of the tangential wind. This implies that at large S, the nondivergent barotropic model gives an accurate estimate of the stability of the basic state. However, mode 1 also existed in the barotropic model in which there was no energy source from the vertical wind. Thus it cannot be said that model 1 arises from the radial shear of the vertical wind; but once excited, it draws most of its energy from the vertical velocity shear. The effect of eddy viscosity on the instabilities was also investigated. The results indicated that increasing the value of eddy viscosity in the model did not change the qualitative aspects of the instabilities–the most unstable wavenumber still increased as S increased, but the point at which the transitions occurred between unstable waves occurred at higher values of S. The growth rates of the disturbances were also reduced as the eddy viscosity was increased.

Walko and Gall (1984) extended the work of Gall (1983) by investigating the stability of axisymmetric basic states without making any drastic simplifying assumptions about the structure of the basic state vortex as was done in previous studies. Two different numerical models were used: the first model was patterned after laboratory studies and was used to

generate a collection of steady-state axisymmetric basic state vortices for a range of swirl ratios. The second model was designed to investigate the stability of the basic state flows by simulating the behavior of small-amplitude linear perturbations superimposed on the basic state flows. The results from this study reproduced many of the results found in Gall (1983) and other modeling studies including: 1) the vortex flow at low swirl ratios is stable, 2) as S increased the vortex became unstable (after a central downdraft developed) and the wavelength of maximum instability decreased (i.e. m increased) as S is increased, 3) the linear perturbations had a helical (clockwise) tilt with height and were centered near the radius of maximum vertical vorticity, 4) the energetics of the disturbances depended only on the radial distributions of the tangential and vertical velocities, 5) the disturbances rotated clockwise around the basic-state vortex and were in retrograde motion with respect to the parent vortex at low levels, and 6) increasing the model viscosity lead to lower linear growth rates, and longer wavelengths (smaller m) of maximum instability. In addition to previous modeling studies, the authors were also able to show that the disturbances tilt radially outward with height, and that the disturbance amplitude varies in the axial direction (the level of maximum perturbation amplitude was found at lower vertical levels for high values of S). The strong similarities between the linear perturbations and secondary vortices produced in laboratory vortices indicated that linear stability analysis is a valid approach to this problem.

The stability of vortex flows generated in the laboratory was also investigated by Rotunno (1984). This study extended previous studies in that it presented full three-dimensional numerical simulations of flows which occur in Ward-type vortex chambers, including the development of secondary vortices. The behavior of the simulated vortex as a function of swirl ratio was documented in the model and found to agree well with laboratory experiments. Vortex stability and the structure of the secondary vortices was then investigated in the model. To investigate the stability of the vortex flows, some special numerical calculations were made for one case. The full three-dimensional model was used to simulate the evolution of a vortex in which secondary vortices were produced (in this case m=2). A two-dimensional version of the three-dimensional model was then run in which

the radial profile of the tangential winds was the same as in the three-dimensional case, but no secondary vortices developed in the flow. This was in agreement with previous linear stability analyses of two-dimensional vortices in which m=1,2 were always stable. The implication is that the instabilities are a three-dimensional phenomenon, and that the radial gradients of the vertical velocity play an instrumental role in the stability of the vortex. An examination of the structure and evolution of the secondary vortices revealed that the secondary vortices had central pressures that were about 1.5 times lower than the central pressure of the parent vortex. The simulated SV also had other characteristics which have been observed in the laboratory including: 1) the center of rotation of the SV occurred near the 'zero line' in the vertical velocity field of the parent vortex (which was also the location of the maximum vertical vorticity) and the SV propagated along the boundary between the updraft and downdraft, 2) the SV tilted clockwise with height although they were embedded in counterclockwise flow, indicating that the SV take the shape of the vortex lines in the cylindrical shear layer within the parent vortex, and 3) the SV propagated at about half the azimuthally-averaged maximum rotation rate of the parent vortex at the lowest model level. Rotunno also pointed out that even though the Reynolds number in the model (based on the eddy viscosity) was much smaller than in laboratory studies ($Re \simeq$ 150 in the numerical model), the model was still able to reproduce observed features of laboratory vortices.

In summary, both laboratory and numerical simulations of idealized tornadic flows have indicated that a non-dimensional parameter called the 'swirl ratio' is the most important parameter governing vortex dynamics. When the swirl ratio is sufficiently high, the vortex develops a central downdraft (i.e. becomes a two-celled vortex). Idealized modeling studies of these two-celled vortices have indicated that the flow in the core of such vortices is unstable to three-dimensional disturbances, and that radial shears of both the vertical and tangential winds are important in the instability. These studies have provided much insight into basic vortex dynamics, and have provided strong evidence that certain vortex configurations are unstable. However, not all features observed in tornadoes have been reproduced in the laboratory or in axisymmetric numerical models (Church and Snow, 1993). This study will extend previous studies by documenting the evolution and characteristics of

secondary vortices produced within a parent vortex which is allowed to develop 'naturally' in relation to its parent storm without any axisymmetric constraints.

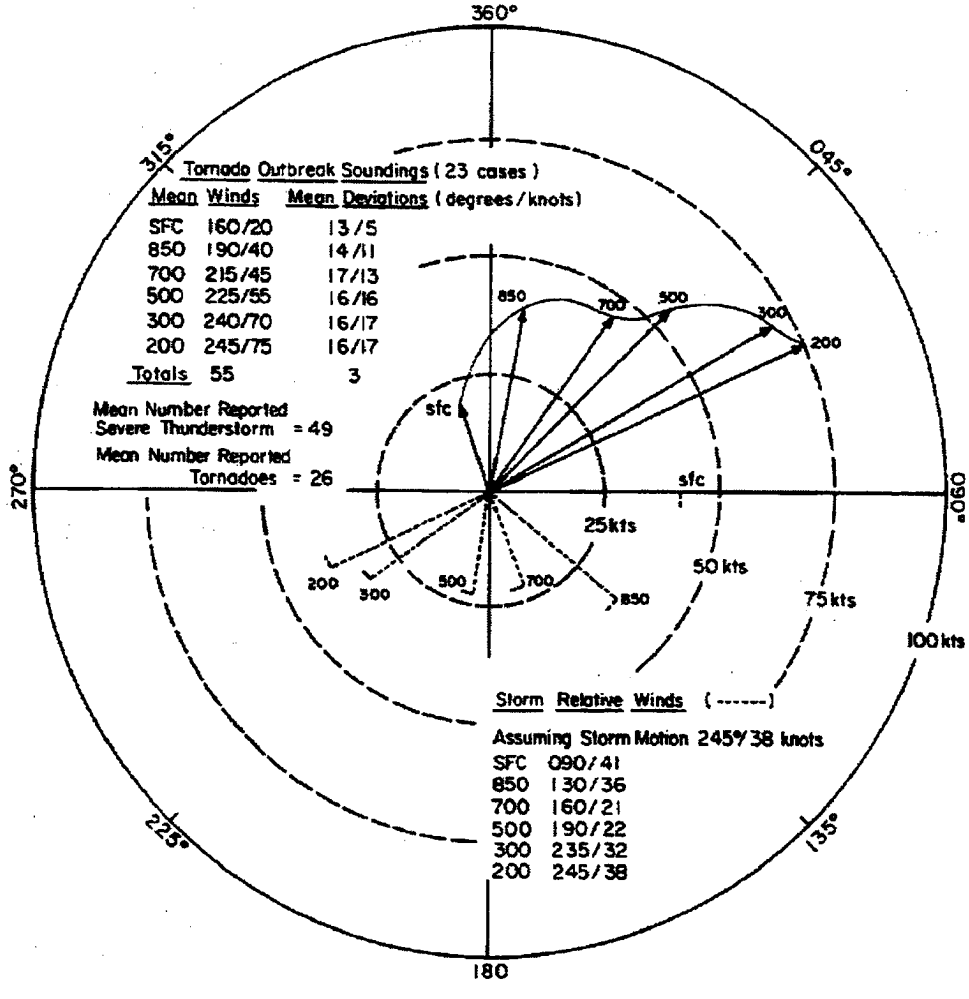

Figure 2.1: A composite hodograph for 23 tornado outbreaks. The estimated storm-relative wind vectors are indicated by the dashed lines beneath the hodograph [from Maddox (1976)].

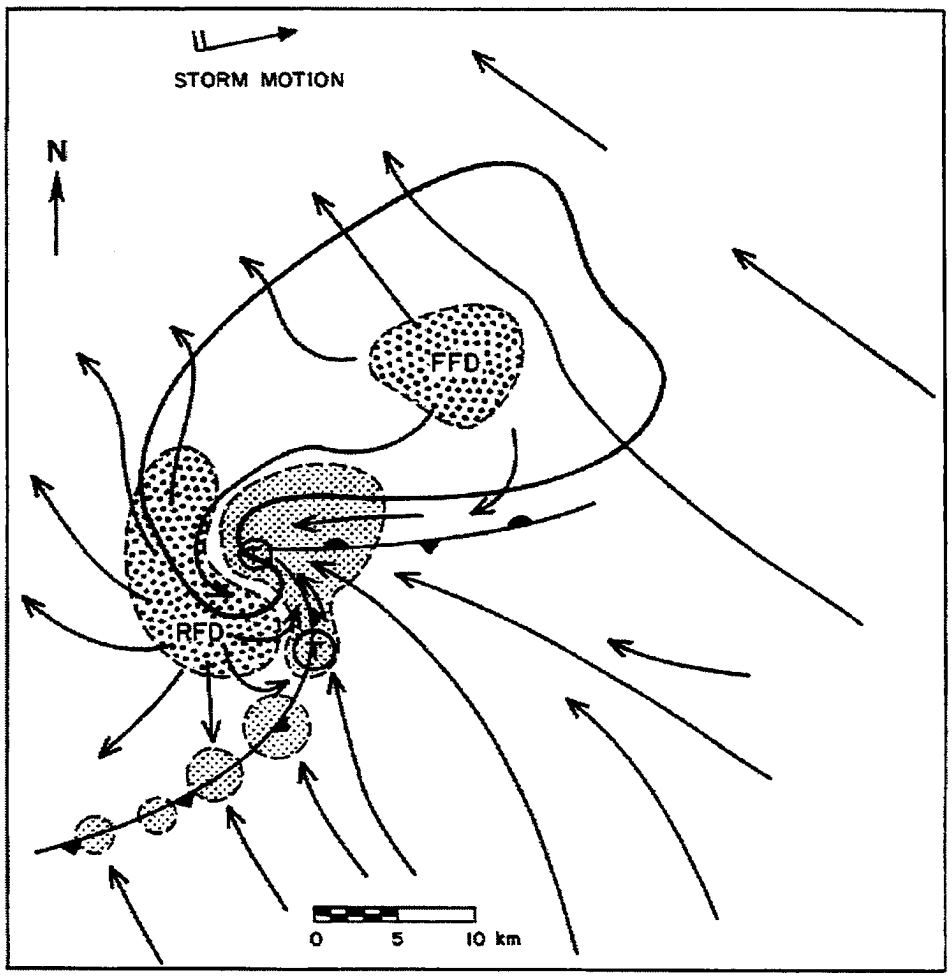

Figure 2.2: A shematic plan view of a tornadic classical supercell at the surface. The thick line denotes the radar echo at mid-levels. Surface downdraft postitions are denoted with coarse stippling, and surface positions of the updrafts are denoted with fine stippling. The positions of the storm outflow boundaries are indicated with frontal symbols. Low-level storm-relative streamlines are denoted by the arrows. Typical tornado postitions are shown by encircled T's. The most likely tornado postion is at the appex of the 'gustfront wave', although tornadoes may occur at the bulge in the gustfront which is also the favored location for new mesocyclone development [adapted from Lemon and Doswell (1979)].

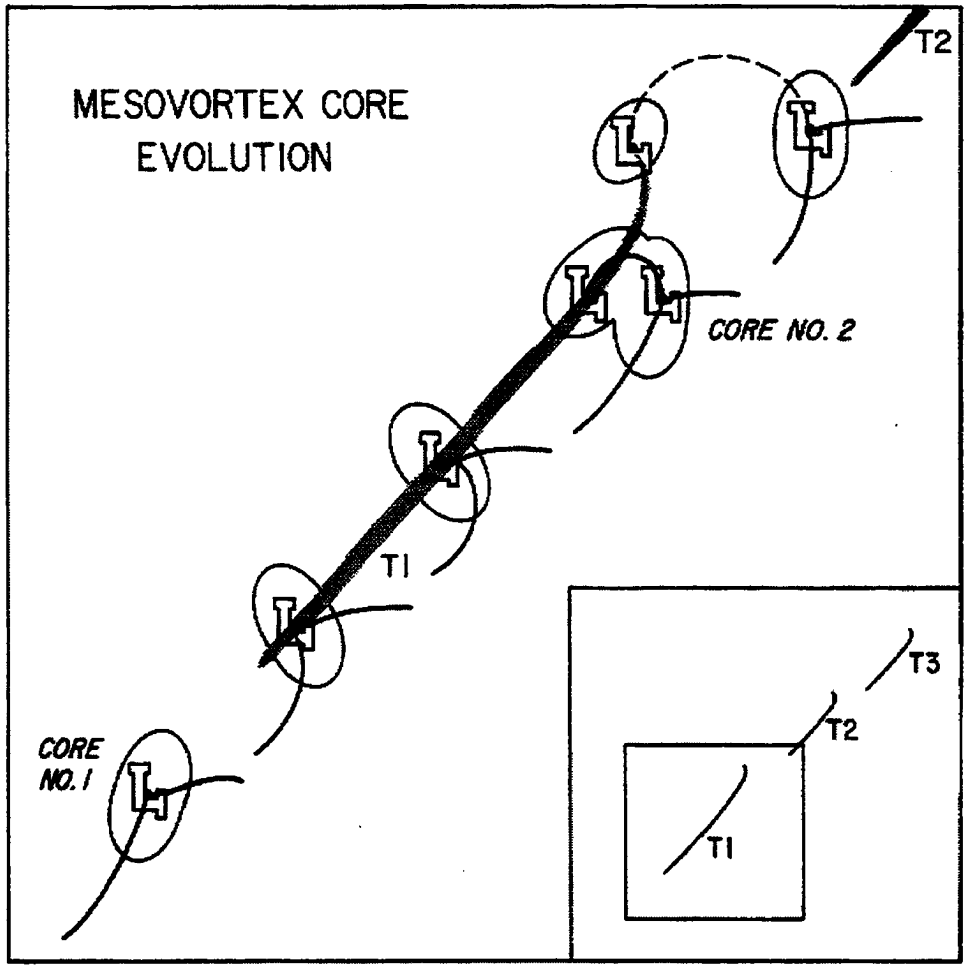

Figure 2.3: Conceptual model of mesocyclone core evolution. The low-level mesocyclone is denoted by an encircled L. Heavy lines denote the surface positions of the storm outflow boundaries. The tornado tracks are indicated by the shaded regions. The insert shows the tornado family tracks. The square indicates the region expanded in the figure [from Burgess et al. (1982)].

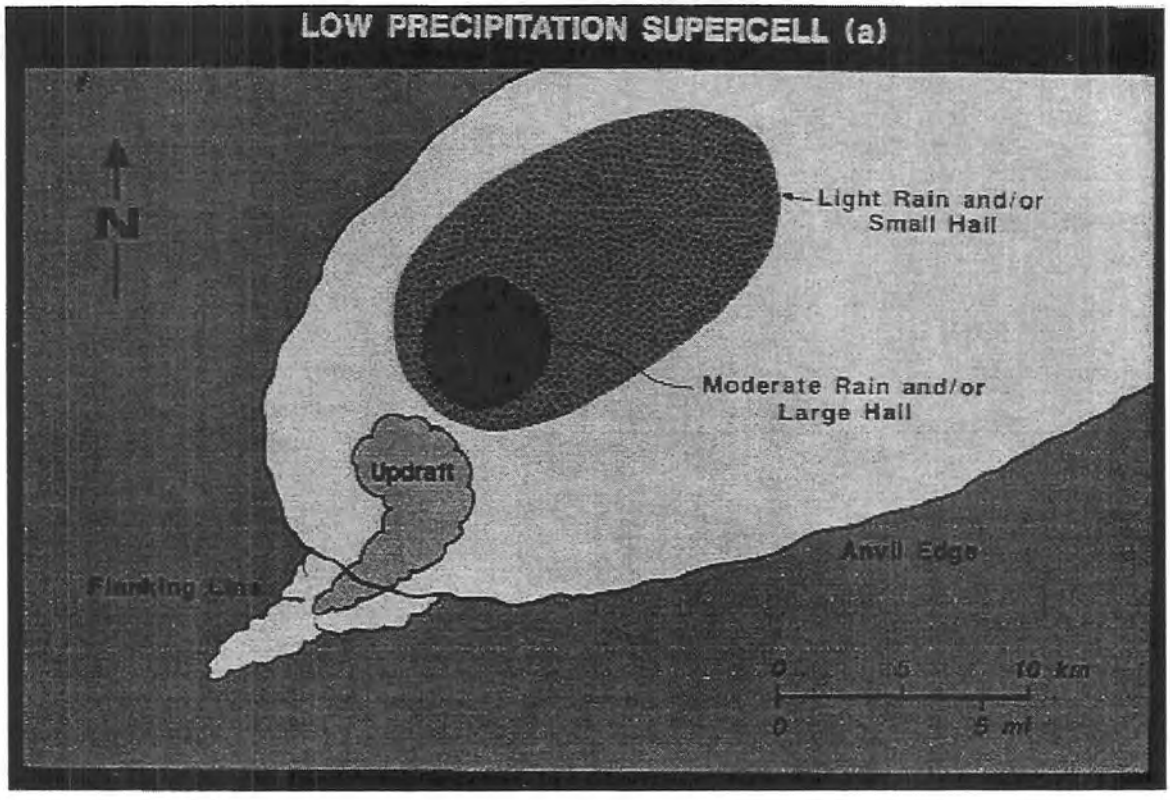

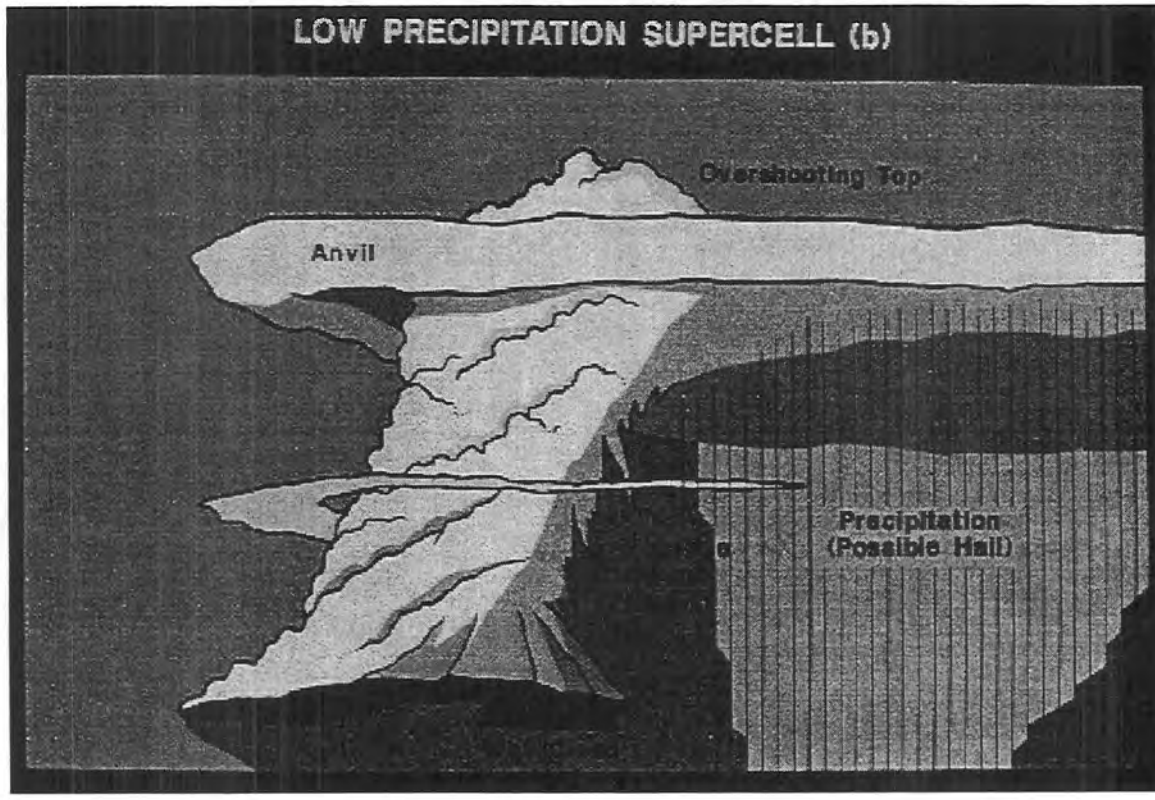

Figure 2.4: A conceptual model of a low-precipitation supercell. (a) The low-level precipitation structure and cloud features looking down from above. (b) Visual structures from an observer's point of view to the east of the storm [from Doswell and Burgess (1993)].

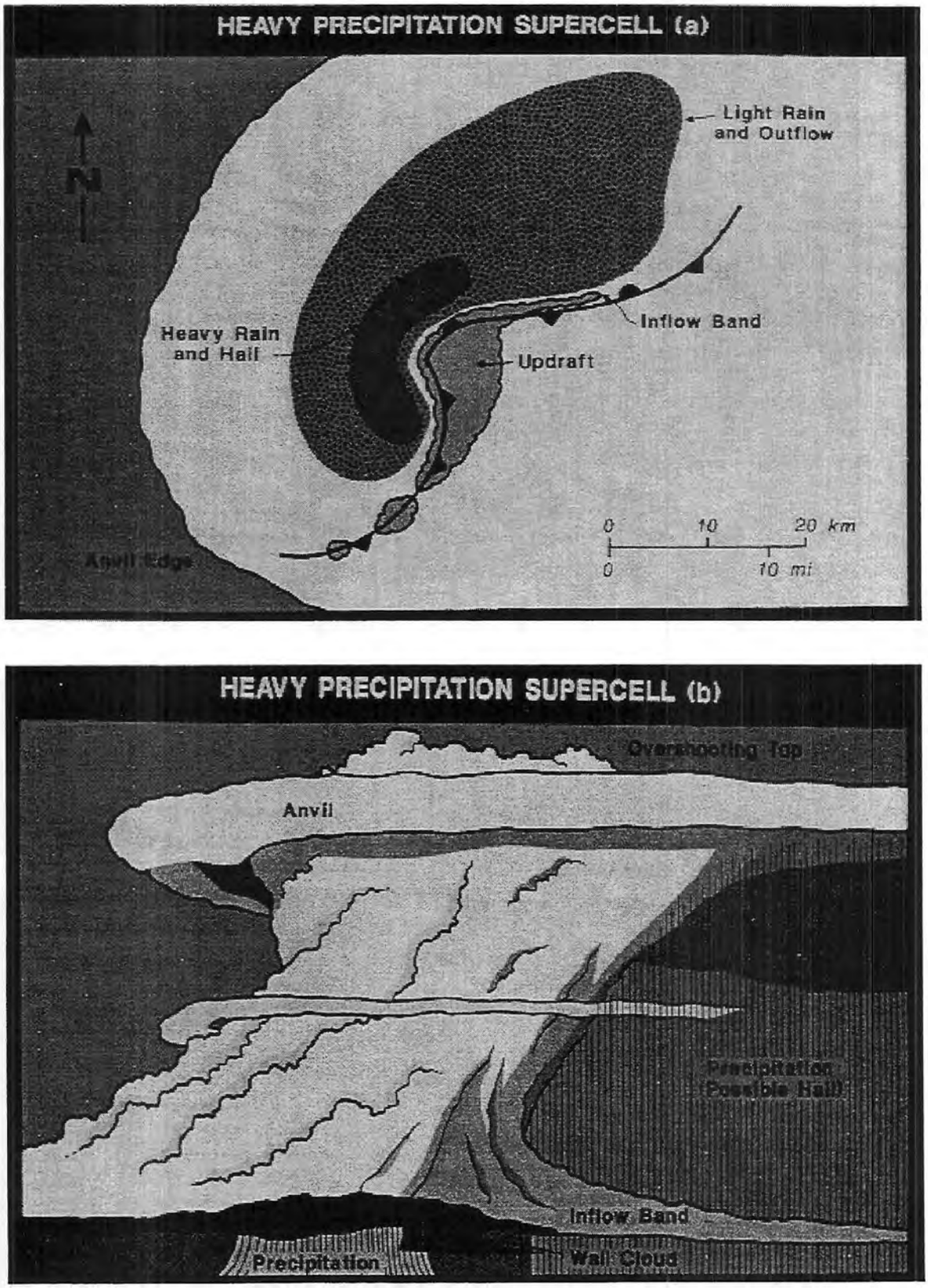

Figure 2.5: A conceptual model of a high-precipitation supercell. (a) The low-level precipitation structure and cloud features looking down from above. (b) Visual structures from an observer's point of view to the east of the storm [from Doswell and Burgess (1993)].

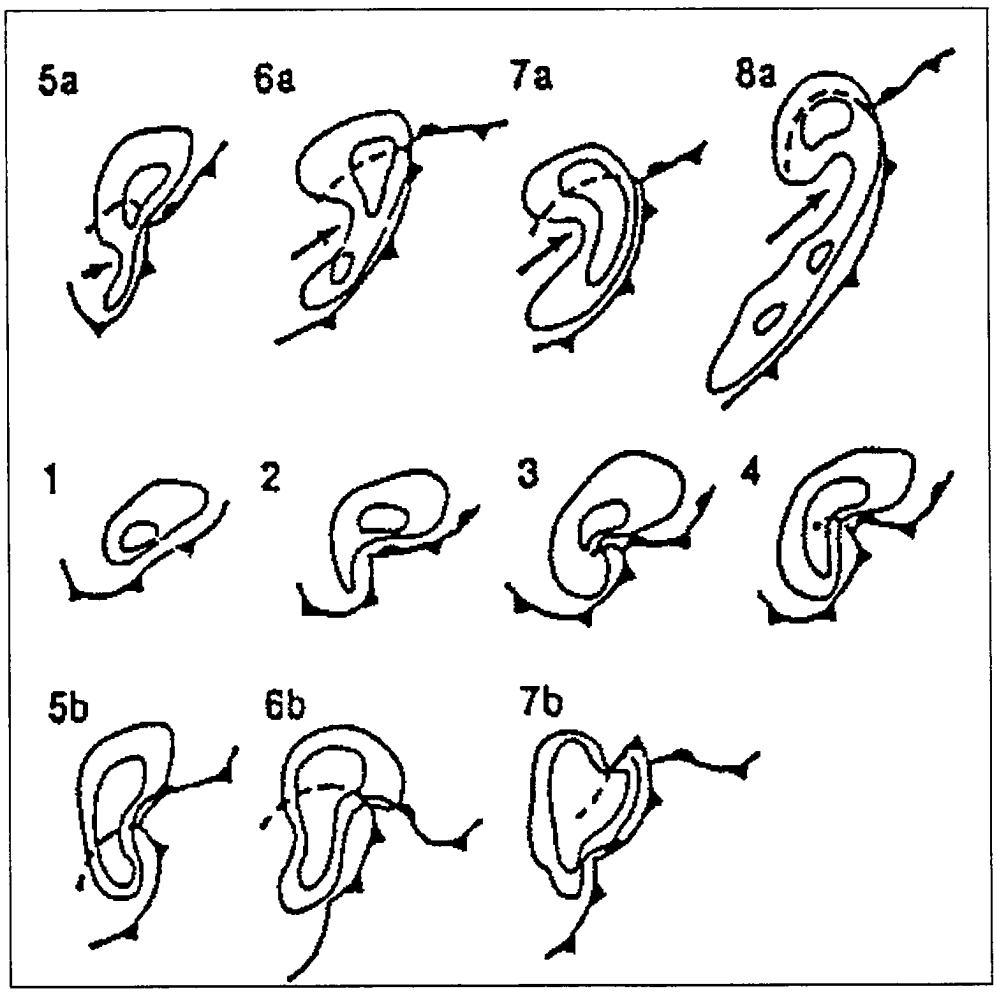

Figure 2.6: Possible life cycles (as seen on radar) of high-precipitation supercells. Frames 1-4 indicate the transition of a classical supercell into an HP supercell. HP supercells may then evolve into a bow-echo with a rotating comma head (5a-8a), or may produce cyclic mesocyclones along the storms' southern flank (5b-7b) in a manner similar to classical supercells. Arrows denote the location of the rear inflow jet in 5a-8a [from Moller et al. (1990)].

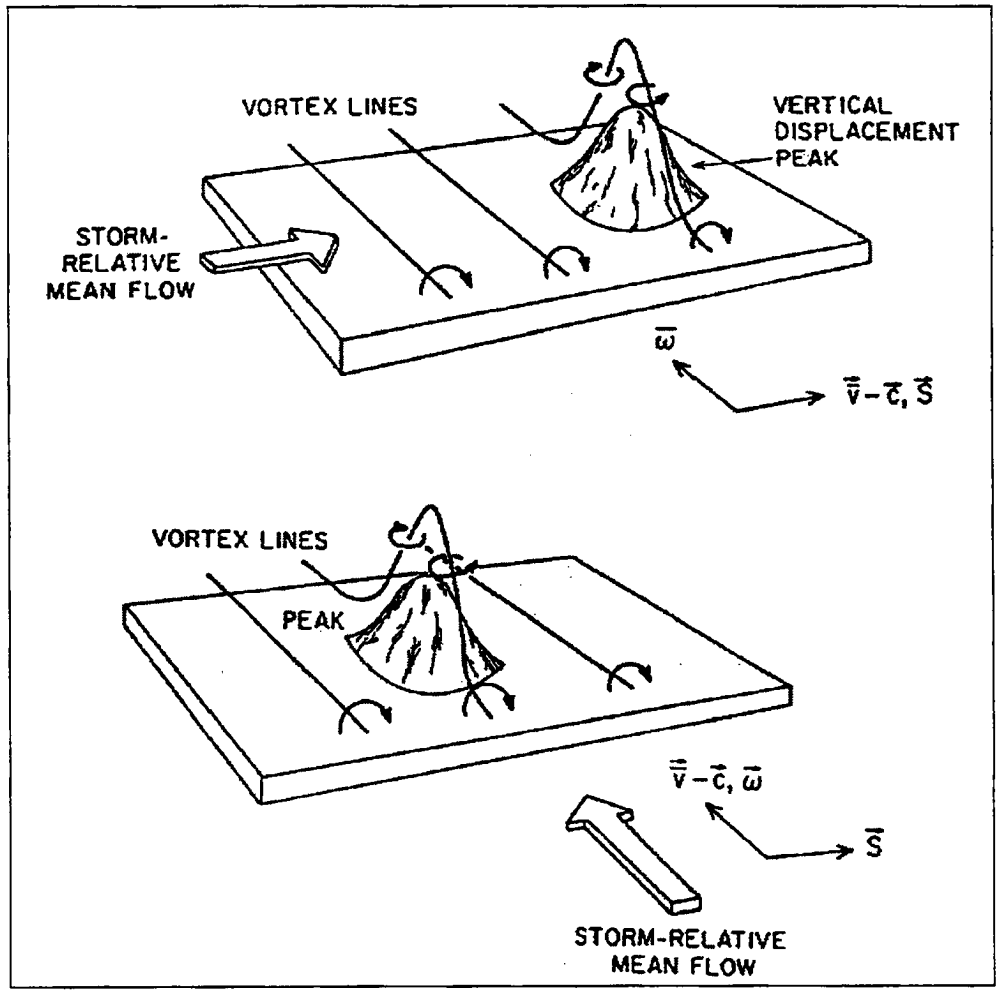

Figure 2.7: An idealized conceptual model showing the importance of streamwise vorticity in the development of thunderstorm rotation. In linear theory, streamlines and vortex lines follow the isentropic (or moist isentropic) surfaces, and the thunderstorm can be thought of as a 'bump' in the isentropic surfaces. In the upper panel, the storm-relative flow is perpendicular to the vorticity vectors, so the updraft (i.e. the side of the 'bump' facing the inflow) is not correlated with vorticity of either sign. In the bottom panel, the storm-relative flow is parallel to the vorticity vector, so the updraft is positively correlated with vertical vorticity [from Davies-Jones (1984)].

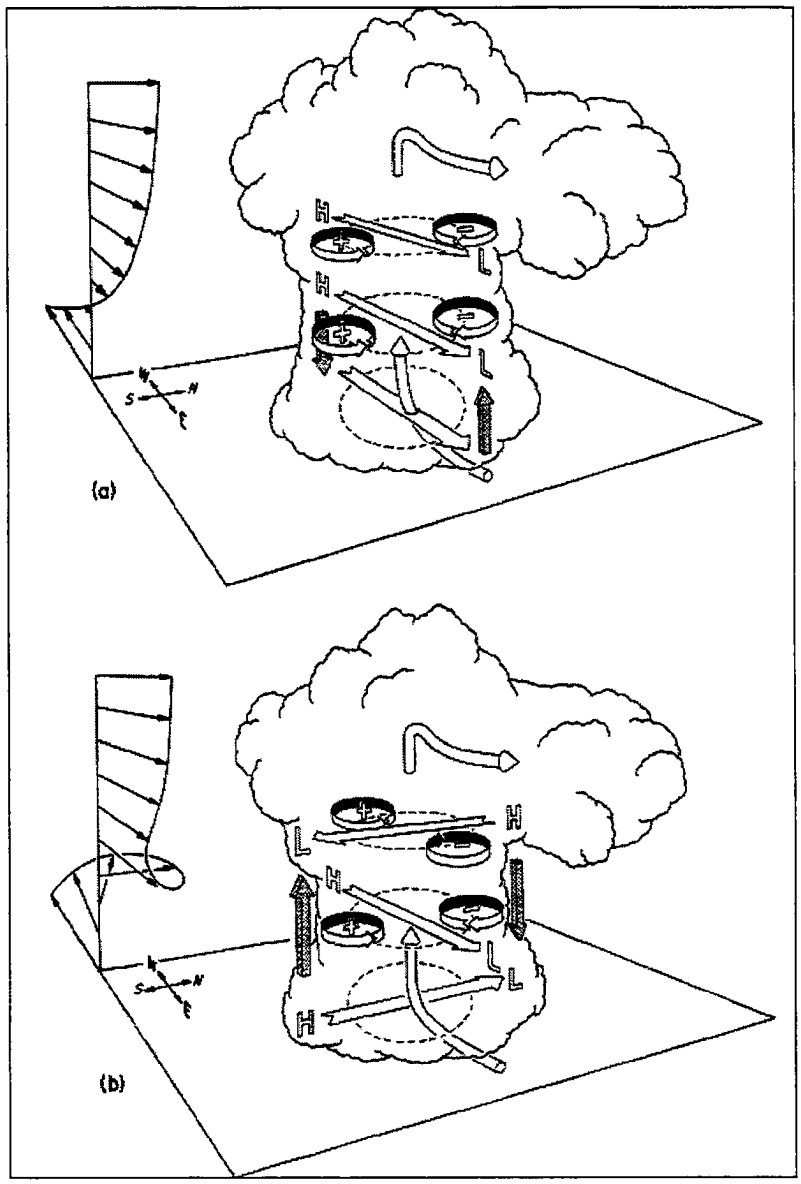

Figure 2.8: Illustration of how the storm updraft interacts with the environmental wind shear creating pressure perturbations in the storm. In (a) the shear vector does not change direction with height. In (b), the shear vector turns clockwise with height, creating an upward vertical pressure gradient force along the southern flank of the storm. The direction of the vertical (horizontal) pressure gradient force is denoted with the shaded (clear) arrows. Cyclonic (anticyclonic) rotation is indicated by the '+' ('-') loops [from Klemp (1987)].

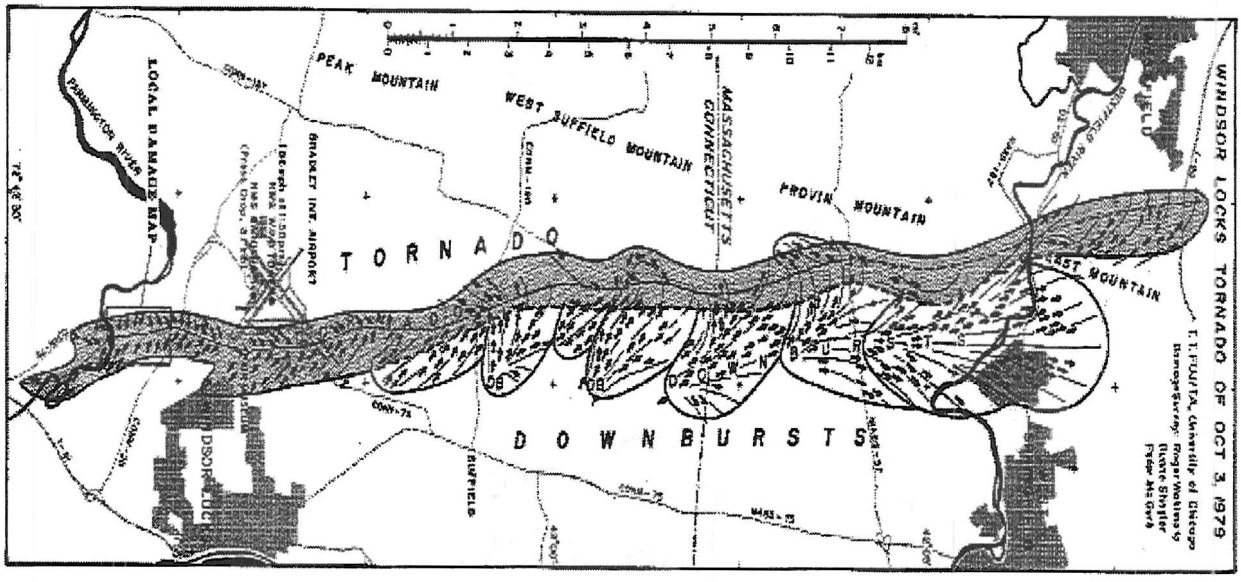

Figure 2.9: Damage path of the Windsor Locks (Connecticut) tornado which occurred on October 3, 1979. The tornado traveled from south (left) to north (right). Seven microbursts were mapped on the right-hand side of the tornado track [from Fujita and Smith (1993)].

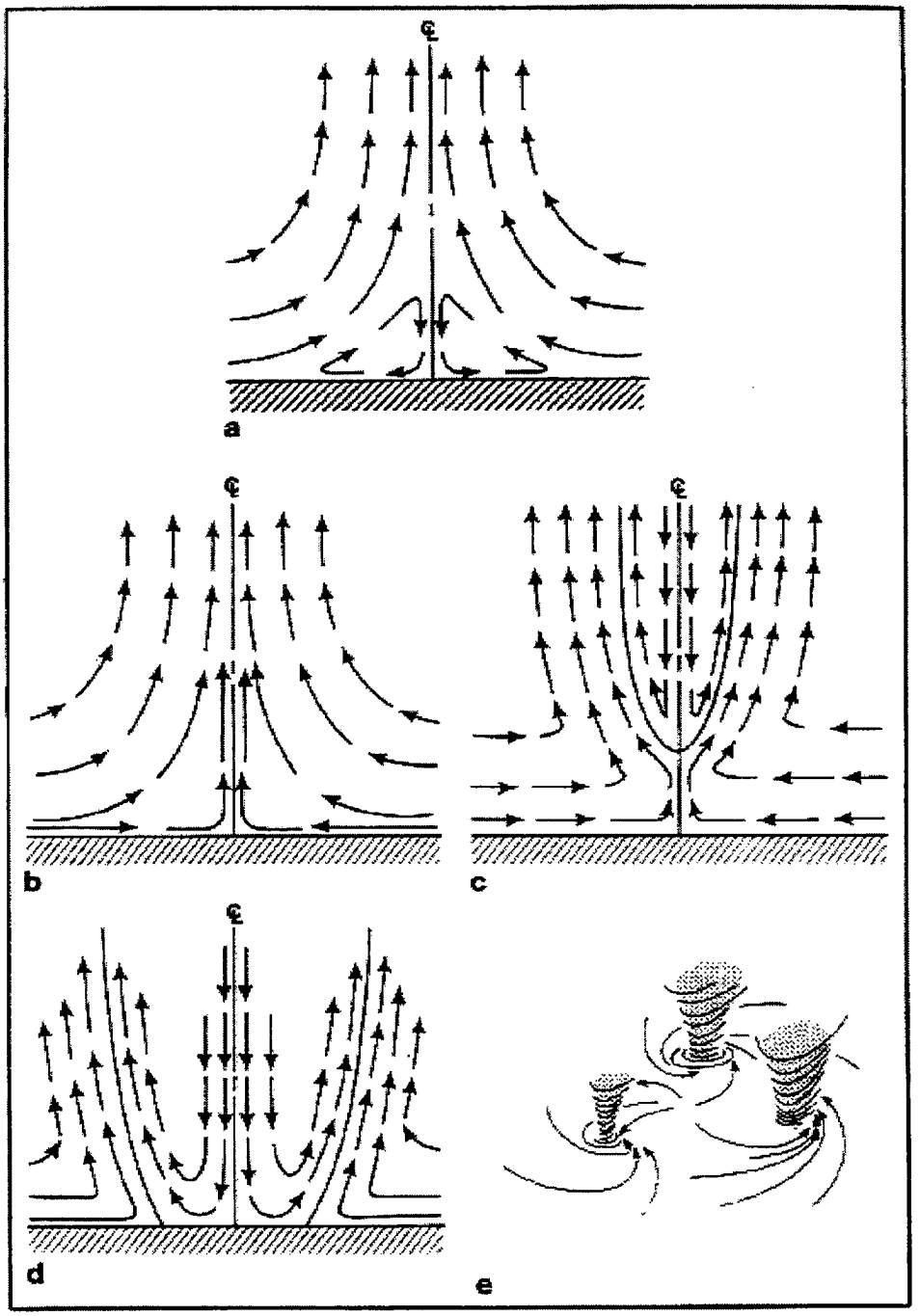

Figure 2.10: Effect of increasing swirl ratio on vortex flow. (a) Weak swirl–flow in the boundary layer separates and passes around the corner region; (b) one-cell vortex; (c) vortex breakdown; (d) two-cell vortex with downdraft pentrating to the surface; (e) multiple vortices [from Davies-Jones (1981)].

Chapter 3

CASE OVERVIEWS

3.1 June 30, 1993 Case

This section overviews the meteorological observations of the June 30-July 1 case. This case was the second day of a thirteen consecutive day period in which heavy rain fell somewhere in the midwest, leading to the extensive flooding which occurred in mid/late July. The previous evening (June 29), a derecho-type Mesoscale Convective Complex (MCC) formed over northeast Iowa, and produced heavy rains and strong winds as it moved southeastward over Iowa. By 6a.m. June 30 (the time the simulation was started), the system had moved into Illinois and Indiana. However, new convective cells formed to the west of the system during the early morning hours of June 30, so that by sunrise, rain was again falling over much of the eastern half of Nebraska and northeast Kansas.

At upper levels, the western US was dominated by a large scale trough while the eastern half of the country was under the influence of a weak ridge. This pattern produced weak southwesterly flow aloft across Nebraska, Kansas and Missouri. Although it is difficult to identify any significant 'shortwaves' embedded in the flow, there was significant divergence between 500-200mb (Figure 3.1) over Iowa, Missouri, and eastern parts of Nebraska and Kansas from 1200 UTC June 30 at least through 0000 UTC July 1. It was probably the upper level divergence which supported almost continuous convection over the midwest throughout the day. By 0000 UTC July 1, an upper-level jet streak was located SW-NE across Iowa, eastern Nebraska, and north central Kansas. This jet streak may have aided convective development during the late afternoon and evening hours. In addition, a strong low-level jet between 925-850mb was bringing gulf moisture northward into the central plains, providing additional fuel for thunderstorms as shown in Figure 3.2.

The surface synoptic situation the morning of the 30th was quite complex (Figure 3.3). A stationary front stretched from southeast Colorado to a weak area of low pressure in southwest Iowa. A 'warm' front (later analyzed as a stationary front) extended from the weak low in Iowa to another weak area of low pressure in western Indiana (probably a remnant of the previous MCC). These surface features remained quasi-stationary the rest of the day and into the nighttime hours. South of the frontal boundaries, the air was quite moist (dewpoints in the low to mid 70's) while north of the front, the air was considerably drier (dewpoints in the low 60's/upper 50s). Convective cells in Iowa which formed during the morning hours on the 30th produced an outflow boundary oriented east-west across northern Missouri and northeast Kansas as shown in Figure 3.4. This outflow boundary played an instrumental role in initiating the convective cell which developed into a supercell.

The storm of interest in this study began to develop between 2100 UTC-2130 UTC June 30 at the intersection between the stationary front and the outflow boundary in northeast Kansas. In the next hour, the storm evolved into a supercell (radar summary at 2235 UTC is shown in Figure 3.5) and severe weather began to be reported around 2330 UTC. By 0100 UTC July 1, this storm became the southern storm in a line of storms which extended from NE Kansas into central Iowa and the line eventually developed into a Mesoscale Convective Complex. However, according to the local storm reports, the storm maintained at least some of its supercell characteristics until about 0330 UTC July 1.

During the course of its life, the storm moved slowly to the east producing heavy rains (local reports of 3-5 inches in 2 hours in northeast Kansas), large hail, strong winds (60-70mph in some locations) and vivid lightning. The storm also produced several weak (F0-F1) tornadoes (6 confirmed) with many more reports of funnel clouds from the general public.

3.2 May 15, 1991 Case

A frequent precursor to severe storm development in the southern plains of the United States is the development of a strong east-west gradient of moisture in the boundary layer known as a 'dryline'. The dryline is also a region of strong convergence near the surface

and is frequently the focus for thunderstorm development. This was the case on May 15, 1991.

At 1200 UTC at the surface, an elongated area of weak low pressure centered in northeast Colorado stretched southward into eastern New Mexico and southwest Texas. The surface dewpoints at this time gave some indication of a dryline in this same region, although the moisture gradient is rather diffuse (Figure 3.6). During the morning hours, the trough of low pressure slowly moved eastward into western Kansas and the Texas and Oklahoma panhandles. By 2000 UTC, the dryline had intensified and was located along the center of the low pressure trough from southwest Kansas into the eastern portions of the Oklahoma and Texas panhandles (Figure 3.7). Dewpoint differences across the dryline were on the order of 20°C with dewpoints to the east of the dryline in the 16-20°C range and in the -2 to -7°C range to the west of the dryline. Surface winds ahead of the dryline were generally from the south/southeast becoming southwesterly behind the dryline. This supported strong moisture convergence which was observed in the dryline vicinity (Hane et al., 1993).

At upper levels, a cut-off low was centered over the Four Corners region as shown in Figure 3.8, creating strong upper-level divergence from southeast Colorado to southwest Texas. This provided the upper-level support for convection, as no other significant upper-level weather features moved over the region that day.

Convection began developing along the dryline between 1930 UTC - 2000 UTC. The strongest storms developed first in Colorado and Kansas, and then further south along the dryline as the afternoon progressed. By 2300 UTC, strong storms began developing in the Oklahoma and Texas panhandles as shown in Figure 3.9. As these storms intensified, they moved to the northeast away from the dryline. Severe weather began to be reported in western Oklahoma around 0230 UTC, and in the Texas panhandle starting about 0315 UTC. The storms produced strong winds, large hail and several tornadoes as they marched to the northeast. Most of the tornadoes reported were weak (F0) with two notable exceptions: an F3 was reported near Laverne, Oklahoma around 0235 UTC, and another F3 was reported near Shamrock, Texas around 0317 UTC.

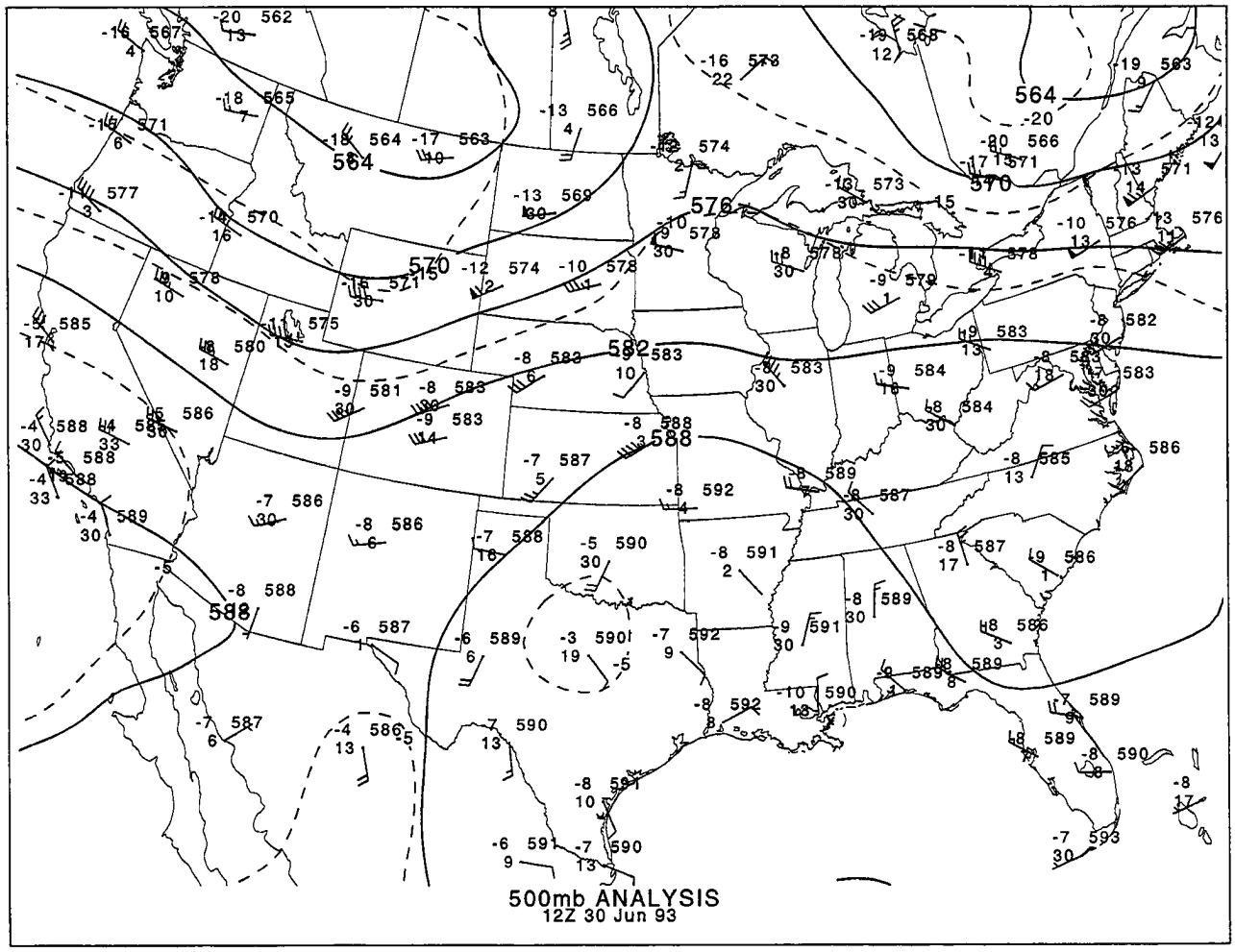

Figure 3.1: 500mb analysis at 1200 UTC June 30, 1993.

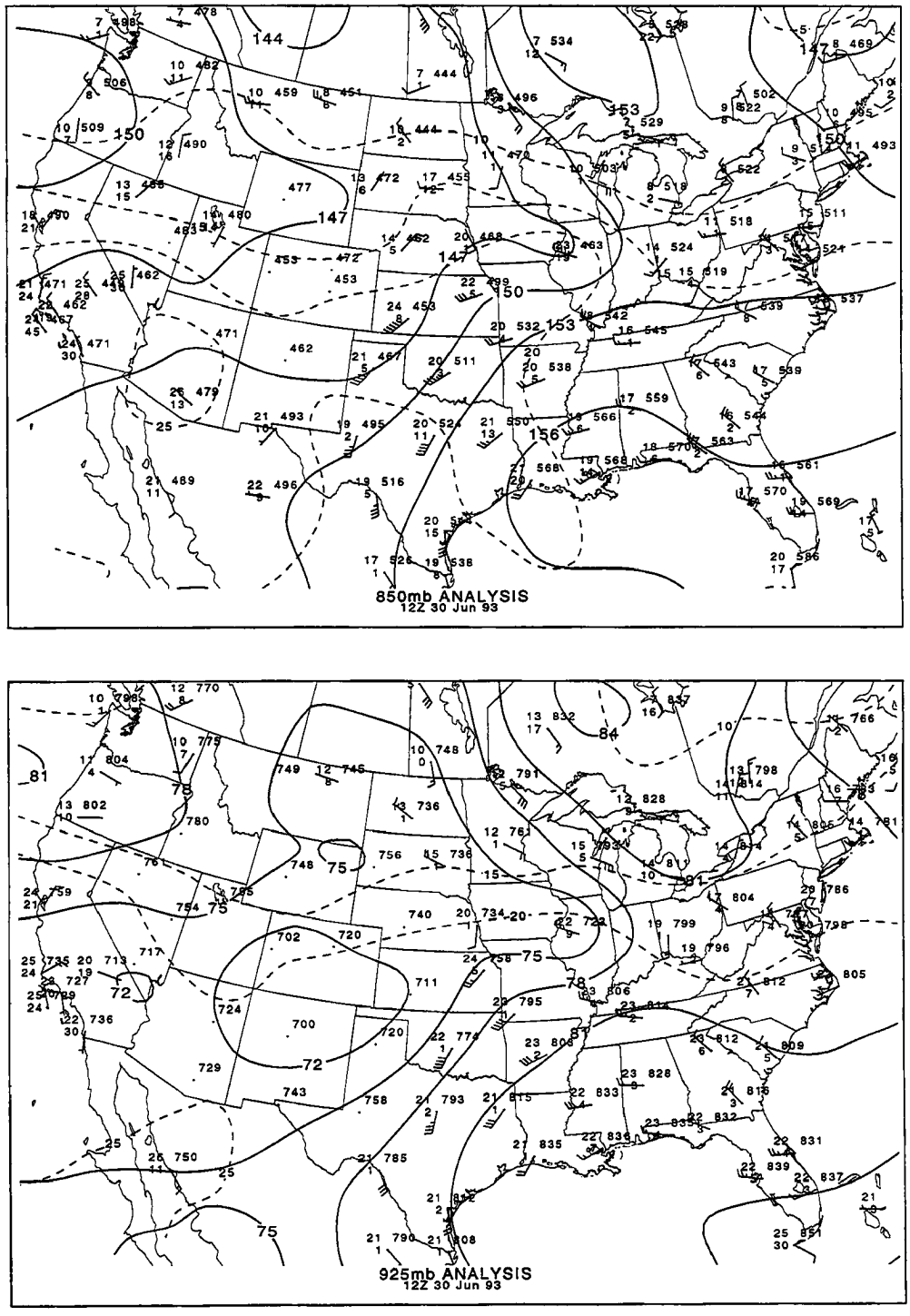

Figure 3.2: The 850mb analysis (top) and the 925mb analysis (bottom) at 1200 UTC 30 June, 1993.

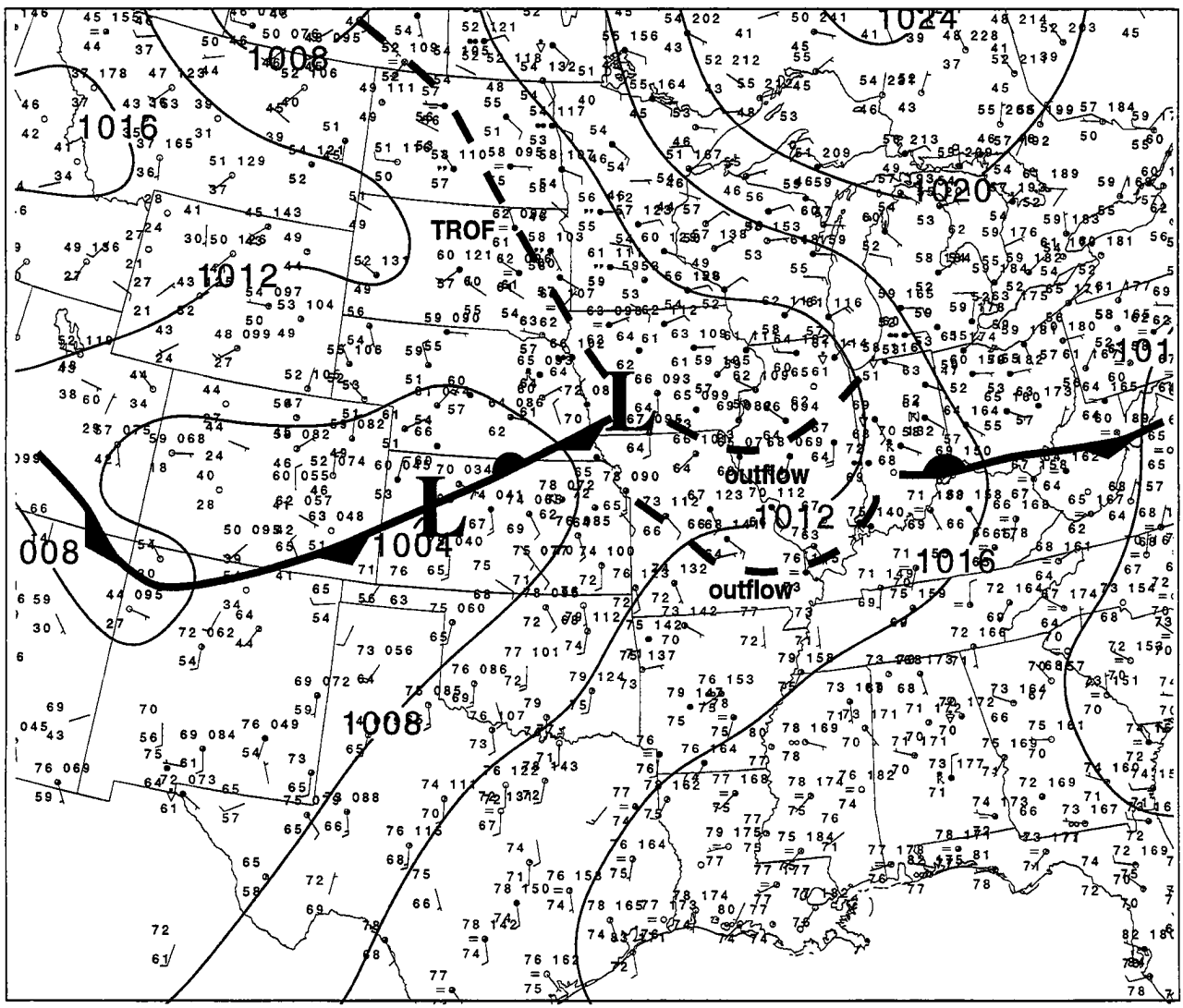

Figure 3.3: Surface analysis at 1200 UTC June 30, 1993.

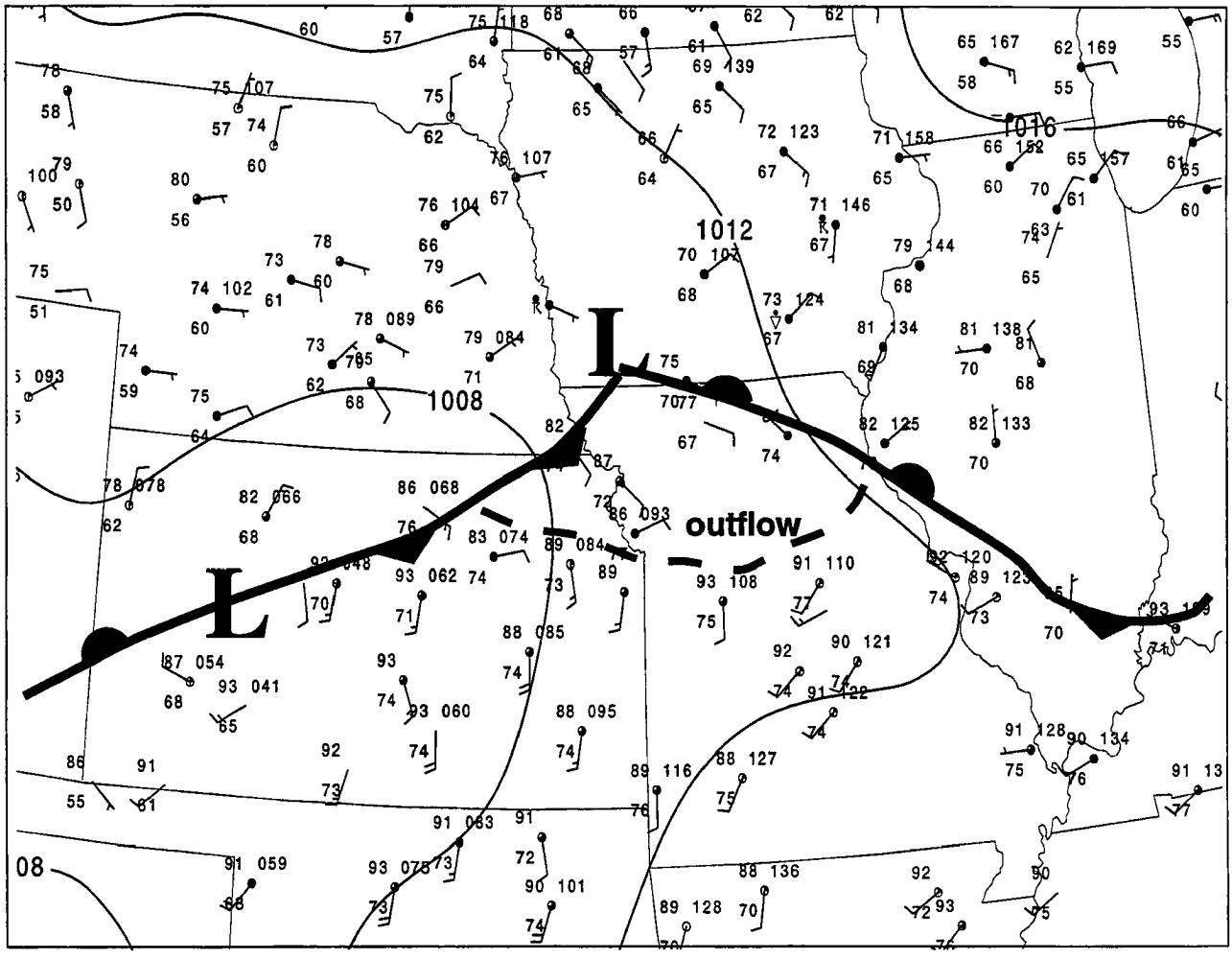

Figure 3.4: Surface analysis at 2000 UTC June 30, 1993. Note the outflow boundary that has moved into northern Missouri and northeast Kansas.

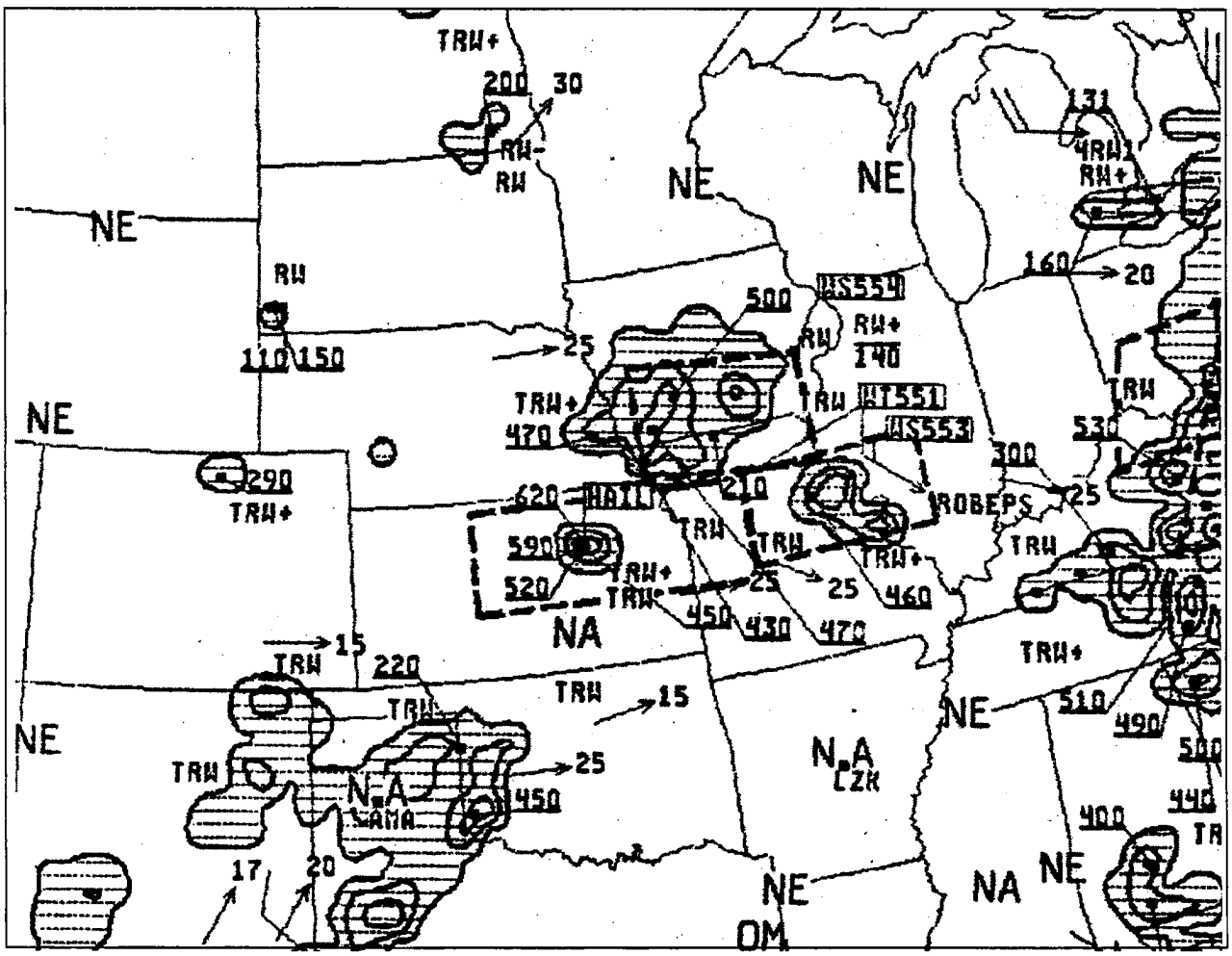

Figure 3.5: Radar summary at 2235 UTC June 30, 1993. The storm of interest in this study is the supercell developing in northeast Kansas.

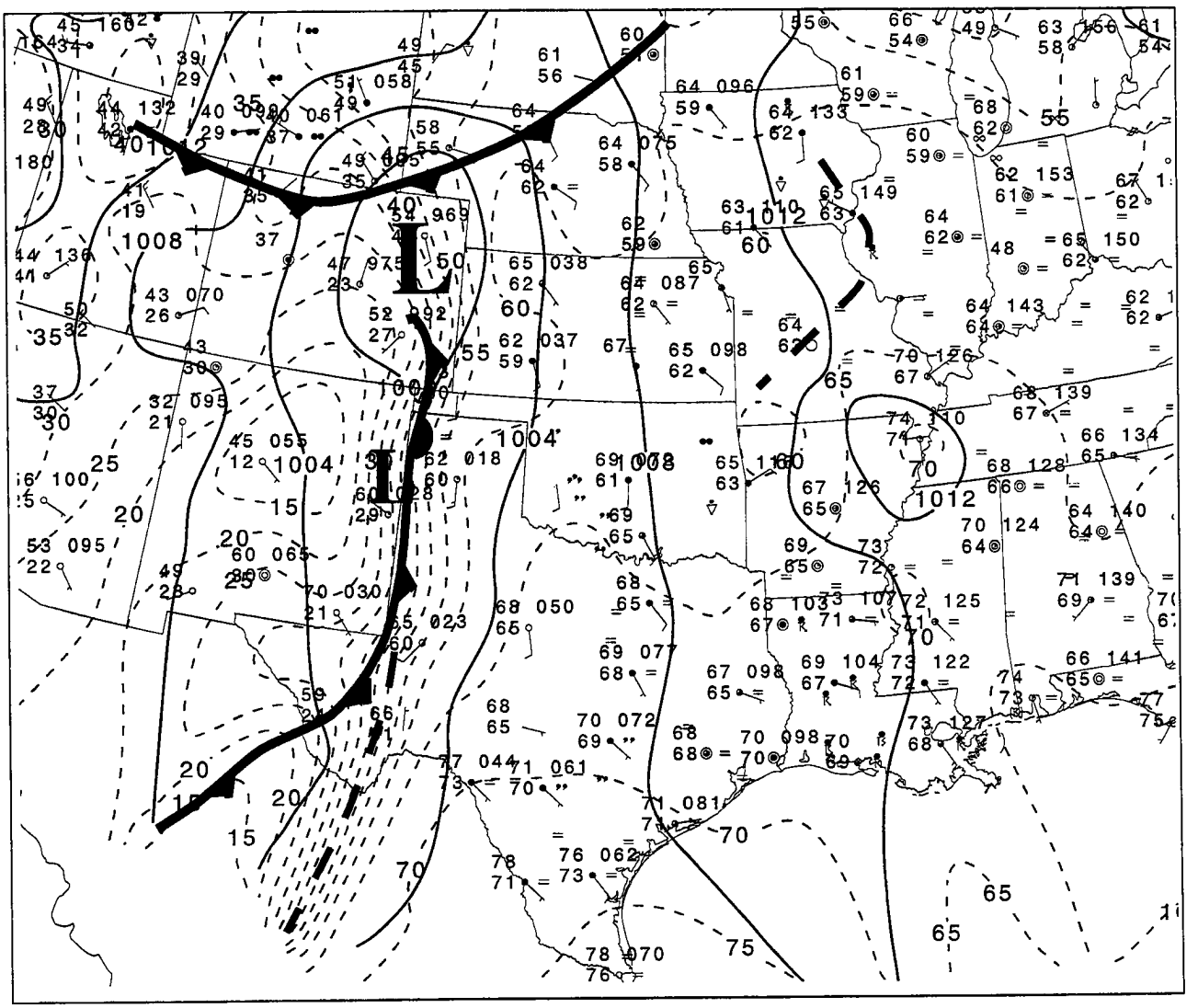

Figure 3.6: Surface analysis at 1200 UTC 15 May, 1991. Narrow dashed lines denote isodrosotherms (contour interval 4°F).

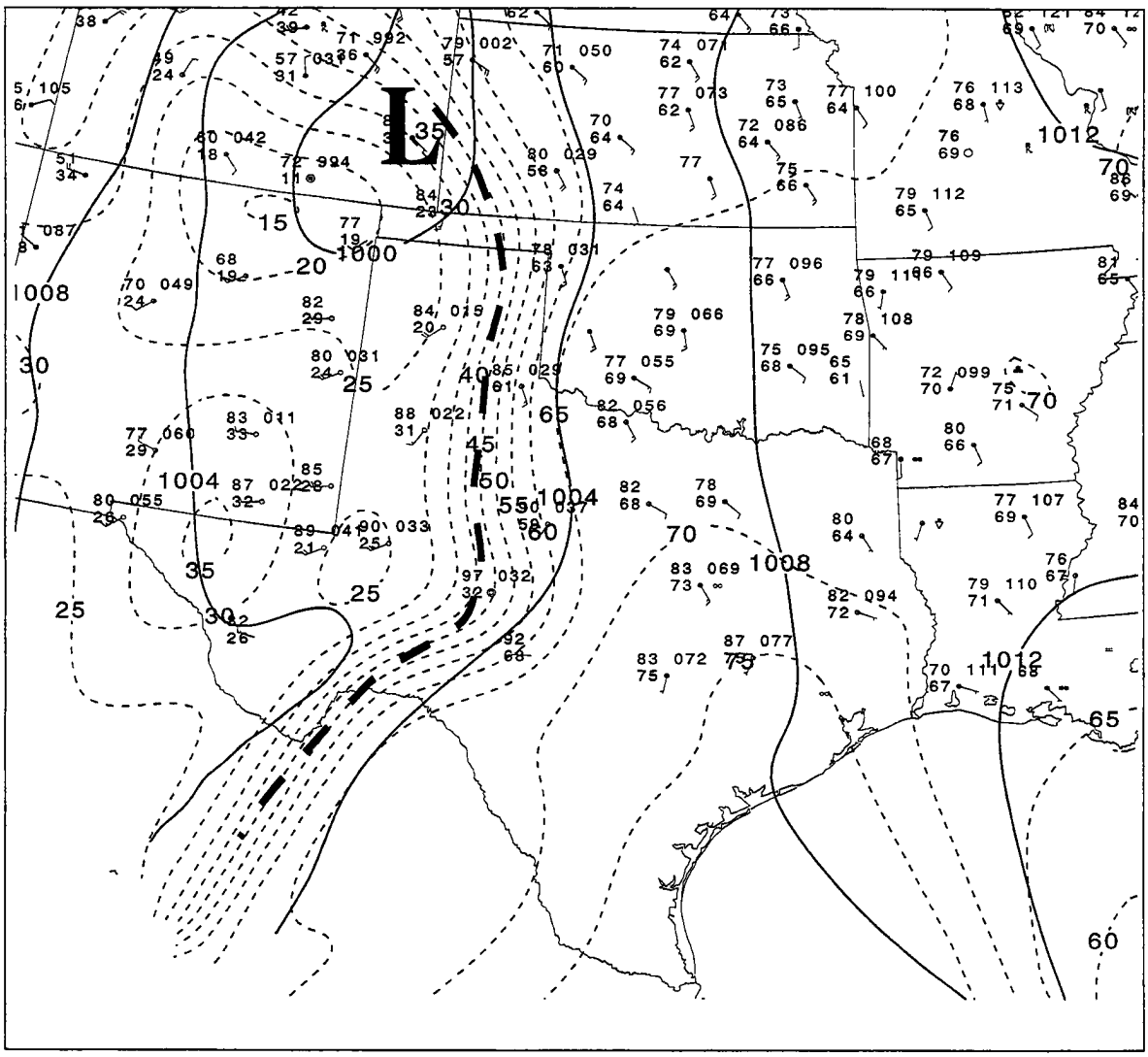

Figure 3.7: Surface analysis at 2000 UTC 15 May, 1991. Narrow dashed lines denote isodrosotherms (contour interval 4°F).

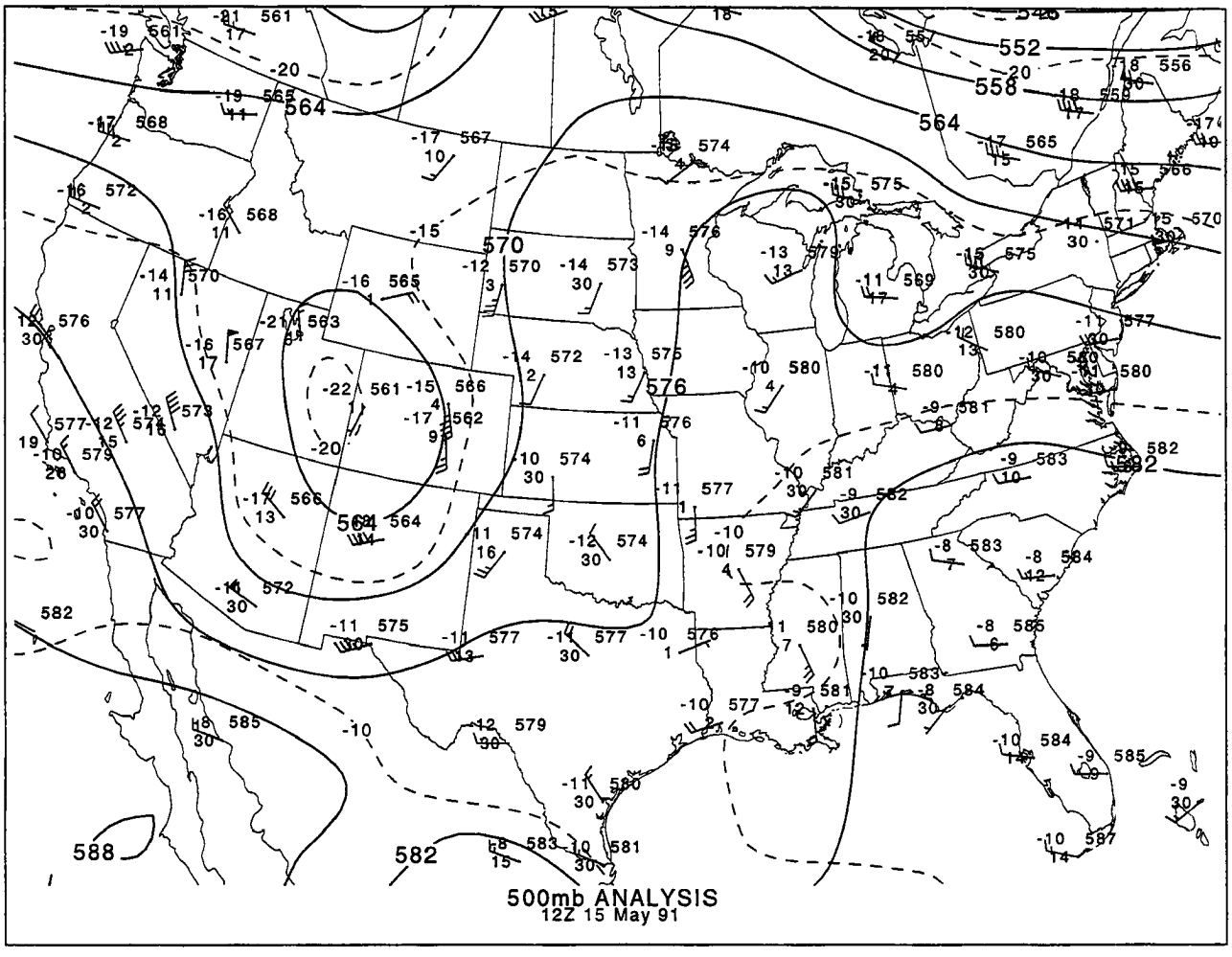

Figure 3.8: 500mb analysis at 1200 UTC May 15, 1991.

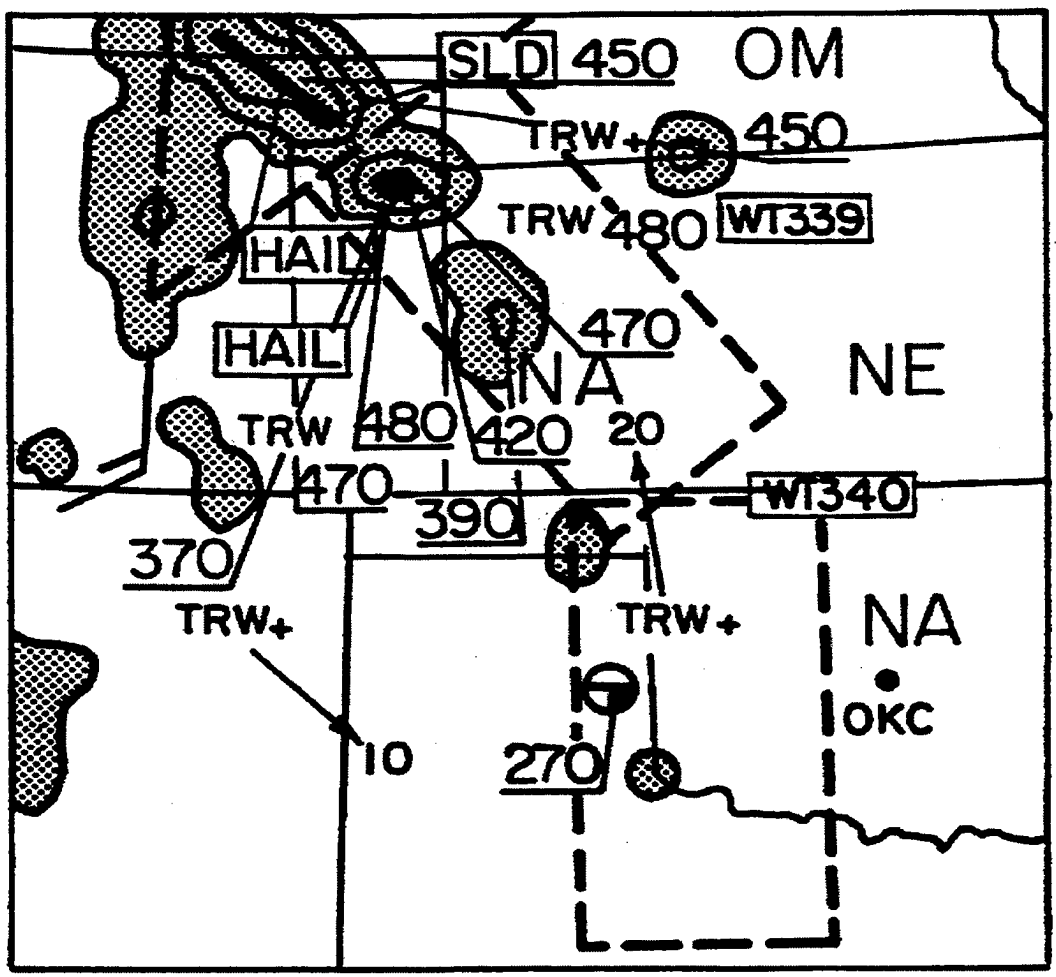

Figure 3.9: Radar summary at 2235 UTC, 15 May 1991.

Chapter 4

MODEL DESCRIPTION AND CONFIGURATION

In this section, we focus on the primitive equation model used to simulate the June 30, 1993 and May 15, 1991 cases. In Section 4.1, the basic model features are described with a focus on aspects of the model that are of particular importance to the simulations. For a more complete description of options available in the model, the reader is referred to Pielke et al. (1992). The data sets used to generate the initial model atmospheric fields and surface boundary conditions are discussed in Section 4.2. An explanation of the model configuration used in the simulations can be found in Section 4.3.

4.1 PE Model

The Regional Atmospheric Modeling System (RAMS) version 3b developed at Colorado State University was used for both simulations. The model utilizes a staggered Arakawa C grid (Arakawa and Lamb, 1981) with terrain-following sigma coordinates in the vertical (Tripoli and Cotton, 1980). For the simulations performed here, a second order accurate hybrid timestep scheme was used in which momentum fields were advanced using a leapfrog scheme, and scaler fields were advanced using a forward scheme. The non-hydrostatic/compressible forms of the basic model equations (Tripoli and Cotton, 1986) were used for the simulations. Subgrid-scale turbulence was parameterized using a deformation-K closure scheme following Smagorinsky (1963) with stability modifications made by Lilly (1962) and Hill (1974).

The radiation scheme used in the simulations was developed by Maher and Pielke (1977). This scheme calculates radiative fluxes which are functions of the vertical temperature and moisture distributions. The incoming solar (short-wave) radiation varies longitu-

dinally over the domain with time to account for the diurnal cycle. Clouds in this scheme are seen only as areas of very high water vapor content; the scheme does not account for the radiative characteristics of condensed water or ice species. This will lead to an overestimate of solar fluxes reaching the surface in cloudy regions and an underestimate of the long-wave cooling at the top of clouds. However, this scheme was chosen for use in these simulations due to computational considerations (it requires much less computational time than the other radiation scheme available in the model). These errors will probably not have a large impact on the simulations since supercell thunderstorms are largely dynamically (not radiatively) driven systems.

Condensed water species are represented with a single-moment bulk microphysics parameterization (Walko, et al., 1995). The microphysics package includes predictive equations for rain, pristine ice, snow, aggregates, graupel and hail. Cloud water is diagnosed as a residual. No cumulus parameterization was used in any of the simulations. All convection in the simulations was generated by resolved vertical motions, and subsequent condensation/latent heating.

The model also possesses a soil model (Tremback and Kessler, 1985) and a vegetation parameterization (Avissar and Pielke, 1989). The soil model is a multi-layer column model in which heat and moisture are exchanged vertically between soil layers. The top soil layer also exchanges heat and moisture with the atmosphere, while soil temperature and moisture in the lowest soil layer remain constant throughout the simulation. The vegetation parameterization classifies vegetation types into 18 different categories. Each category has its own value for leaf area index, roughness length, displacement height, and root parameters which are used to determine the exchange of heat and moisture between the vegetation and the atmosphere.

Another salient feature in the model is the two-way interactive grid nesting (Clark and Farley, 1984). This feature reduces memory and computational requirements by allowing the user to add greater horizontal resolution only over the region(s) of interest. The coarse grids supply the initial conditions to the fine grids at time zero (except those nested grids which have been initialized with synoptic data as specified by the user). At subsequent

times, the coarse grids provide the lateral boundary conditions to the fine grids. The two-way interaction is completed at each timestep when the nested grid variables are averaged back to the coarser grid. Nested grids may be added or removed at any time during the simulation. The model also has the ability to move the nested grids within a parent grid (Walko et al., 1995). This feature further reduces memory and computational requirements by allowing the user to specify a smaller nested grid and then 'follow' the phenomenon of interest.

Both the lateral and top boundary conditions for Grid #1 were provided with a Davies nudging scheme (Davies, 1976) in which boundary values of the horizontal winds (u, v), potential temperature (θ), water vapor mixing ratio (r), and perturbation Exner function (π) in the model were nudged toward observations. The user can control the strength of the nudging through a specified time scale at the outermost (or top) model grid point, or in the model interior if center nudging is to be preformed. The strength of the nudging is inversely proportional to the time scale at the outermost (top) boundary, and drops off following a hyperbolic function to the strength specified for the model interior over a distance specified by the user. In the simulations performed here, the time scale for both the lateral and top nudging regions was 1800s. The lateral boundaries were nudged over 5 grid points, while the top boundary was nudged over 3 grid points. Center nudging is also an option in the model and was used early in the June 30, 1993, simulation to incorporate an important surface feature which was not present at the time the model was initialized. This procedure will be discussed in more detail in Section 5.1.

4.2 Data Sets and Initial Conditions

A very important step to any model simulation is generating good initial conditions. RAMS contains an objective analysis and initialization package which generates model initial conditions and the time dependant lateral boundary conditions from real data. The data sets used are all available from the NCAR data archive. They include the NCEP (formerly NMC) spectral model analyses, and the upper air and surface observations. The NCEP spectral analyses are available for 0000 and 1200 UTC daily. The analyses include

temperature, geopotential height, relative humidity, and u and v wind components at 2.5° latitude/longitude grid intervals, at 'standard' pressure levels (1000, 850, 700, 500, 400, 300, 200, 150, 100, 70, and 50 mb). The upper air data set includes daily observations at 0000 UTC and 1200 UTC of pressure, height, temperature, relative humidity, wind speed and wind direction at both mandatory and significant levels. The surface data are available every 3 hours, but only the 0000 and 1200 UTC data are used in the RAMS objective analysis. The surface data set includes observations of surface temperature, pressure, wind speed, wind direction and relative humidity. In the June 30, 1993 simulation, wind profiler data were available and were also incorporated into the model initialization. The model objective analysis package takes these data sets, combines them, and then does a Barnes objective analysis (Barnes, 1964, 1973) on the data. The analyzed data are then interpolated to the model grid points along sigma-z terrain following coordinates below 4km, and to constant θ surfaces above 6km. Between 4km and 6km, a hybrid sigma-z/θ coordinate system is used. The initial model wind and temperature fields on Grid #2 at the lowest model level for the June 30 case are shown in Figure 4.1. The initialization captured the basic synoptic-scale features such as the low in south-east Colorado, the stationary front across Kansas and Nebraska, and remnants of an old storm outflow across Missouri and Illinois.

Several additional data sets were used to initialize the surface characteristics in these simulations. The model topography on Grid #1 was generated using the USGS 10′ data set, while on Grid #2, the USGS 30s data set was used. Sea-surface temperatures (SSTs) were provided by the 1° monthly mean values as given in the SST data set available at NCAR. Vegetation type and land-percentage were provided by the USGS 30s land use data set (Loveland et al. 1991). The original vegetation data set contains 159 different land-use categories (including water) which are converted to the 18 BATS categories used by the model. The vegetation type at each model grid point was determined by the dominant vegetation type in the grid cell. The land/water percentage in each grid box was calculated by counting the number of water pixels in each grid cell, and then dividing by the total number of pixels.

Soil moisture is probably the most difficult surface feature to initialize. Since no consolidated national soil moisture databases exist, soil moisture must be initialized by other means. In this study, an Antecedent Precipitation Index (API) was used (Wetzel and Chang, 1988). This procedure utilizes a regression scheme to determine soil moisture based on the previous three months of precipitation. Precipitation values are weighted more heavily as the date of the station report approaches the date of the model start time. In this particular case, the API probably *underestimates* soil moisture in the midwest in the June 30, 1993 case since the regression analysis is based on a 'normal' year of precipitation. Soil type is assumed constant throughout the model domain in the absence of any easily digestible soil databases.

4.3 Model Configuration

One of the largest obstacles to modelling tornadic supercells starting with synoptic data is the great range of spatial scales that need to be resolved (which can be computationally expensive). In both simulations presented here, 6 grids were required to capture both the synoptic scale evolution and scales down near the tornado scale[1]. The grid configurations used in the simulations are discussed below and summarized in Table 4.1.

4.3.1 June 30, 1993 Case

The grid configuration used in this simulation was designed to make the coarse grids (Grids #1 and #2) large enough so that it would be possible to simulate either the mature MCC that developed later in the evening of June 30, or to focus in on the individual thunderstorms which developed earlier in the day starting from the same initial conditions. (Grids #1 and #2 were the grids onto which the 1200 UTC synoptic data were interpolated and analyzed.) A schematic of the relative sizes of the grids is shown in Figure 4.2. Since

[1] One can argue that the horizontal grid spacing on Grid #6 (100-111m) in not sufficient to really resolve most tornadoes. To fully resolve a tornadic circulation 100m in diameter, grid spacing on the order of 20m would be needed, which would push the simulation beyond the memory limits of the available computing resources.

Grids #4-6 were moved during the simulation, they are plotted in their initial positions with respect to their parent grids.

The simulation was started at 1200 UTC June 30, 1993, and ended at 0100 UTC July 1. The simulation was run from 1200 UTC-2000 UTC with Grids #1-3 to capture the early evolution of the synoptic fields. Grid #4 was added at 2000 UTC at which point the microphysics parameterization was turned on. Grid #4 captured the development and evolution of the thunderstorm complex until 0000 UTC July 1 at which point Grids #5-6 were added. All six grids were then run until the end of the simulation at 0100 UTC.

4.3.2 May 15, 1991 case

A schematic of the relative sizes of the grids used in the May 15 case is shown in Figure 4.3. Since Grids #4-6 were also moved during this simulation, they are plotted in their initial positions with respect to their parent grids. This experiment was designed specifically to capture the evolution of a dryline in Texas and Oklahoma, and the subsequent development of deep convection along this dryline in the late afternoon.

This simulation was started at 1200 UTC May 15, 1991, and ended at 2200 UTC. Grids #1-3 were run from 1200 UTC-2000 UTC with the microphysics parameterization turned on since Grid #3 had sufficient horizontal resolution to possibly support deep cumulus convection. Grid #4 was added at 2000 UTC and followed the developing storm for 1 hour until 2100 UTC. Grids #5 and #6 were added at 2100 UTC, and all 6 grids were run until the end of the simulation at 2200 UTC.

	June 30 case	**May 15 case**
Grid 1	grid spacing: 120km	grid spacing: 60km
	44 x 34 points	45 x 45 points
	time step: 90s	time step: 90s
Grid 2	grid spacing: 40km	grid spacing: 20km
	44 x 50 points	53 x 83 points
	time step: 45s	time step: 30s
Grid 3	grid spacing: 8km	grid spacing: 5km
	42 x 42 points	42 x 92 points
	time step: 15s	time step: 5s
Grid 4	grid spacing: 1.6km	grid spacing: 1km
	57 x 57 points	47 x 47 points
	time step: 5s	time step: 1.5s
Grid 5	grid spacing: 400m	grid spacing: 333.33m
	90 x 90 points	47 x 47 points
	time step: 2.5s	time step: 1.5s
Grid 6	grid spacing: 100m	grid spacing: 111.11m
	62 x 62 points	62 x 62 points
	time step: 0.83s	time step: 0.75s
vertical grid spacing	starts at 80m -stretched to 1km at upper levels	starts at 100m -stretched to 1km at upper levels
soil layers	7 points at depths of 0cm (surface), 3cm, 6cm, 9cm, 18cm, 35cm, 50cm	11 points at depths of 0cm (surface), 4cm, 8cm, 12cm, 16cm, 20cm, 24cm, 28cm, 32cm, 40cm, 50cm

Table 4.1: Summary of the grid configurations used in the June 30 and May 15 simulations.

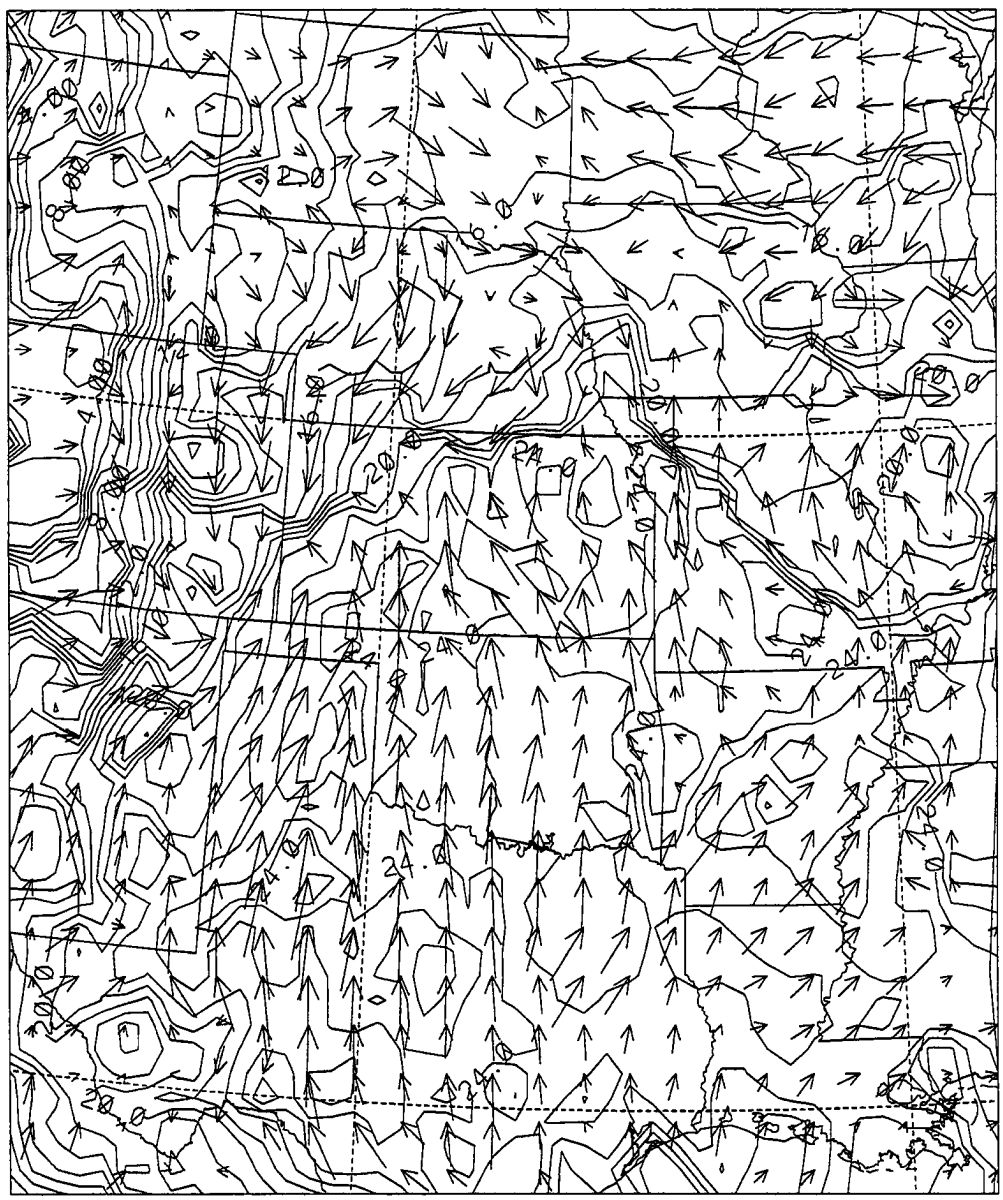

Figure 4.1: Model initialization of surface winds and temperature (in degrees Celcius) 50m above the surface at 1200 UTC June 30, 1993. Wind vectors are plotted at every other model grid point. A wind vector with the same length as the distance between 2 vector heads has a magnitude of $5ms^{-1}$. Temperature is contoured every 1°C.

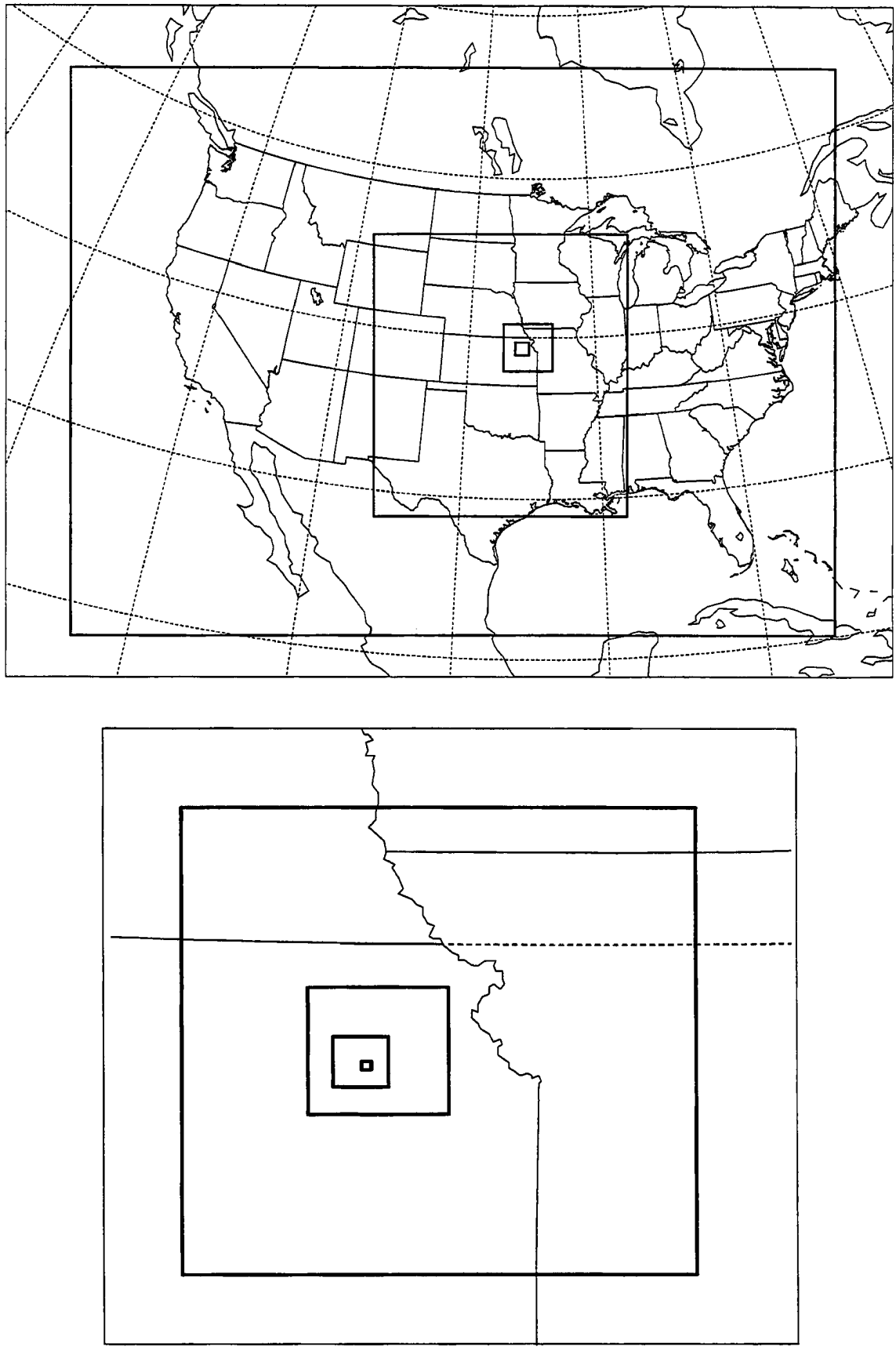

Figure 4.2: Grid configuration for the June 30, 1993 case (grid boundaries are denoted by the bold lines). The top figure shows the positions of Grids #1-3 and the initial postion of Grid #4. The bottom figure shows the initial positions of Grids #3-6. Grids #4-6 were moved during the simulation.

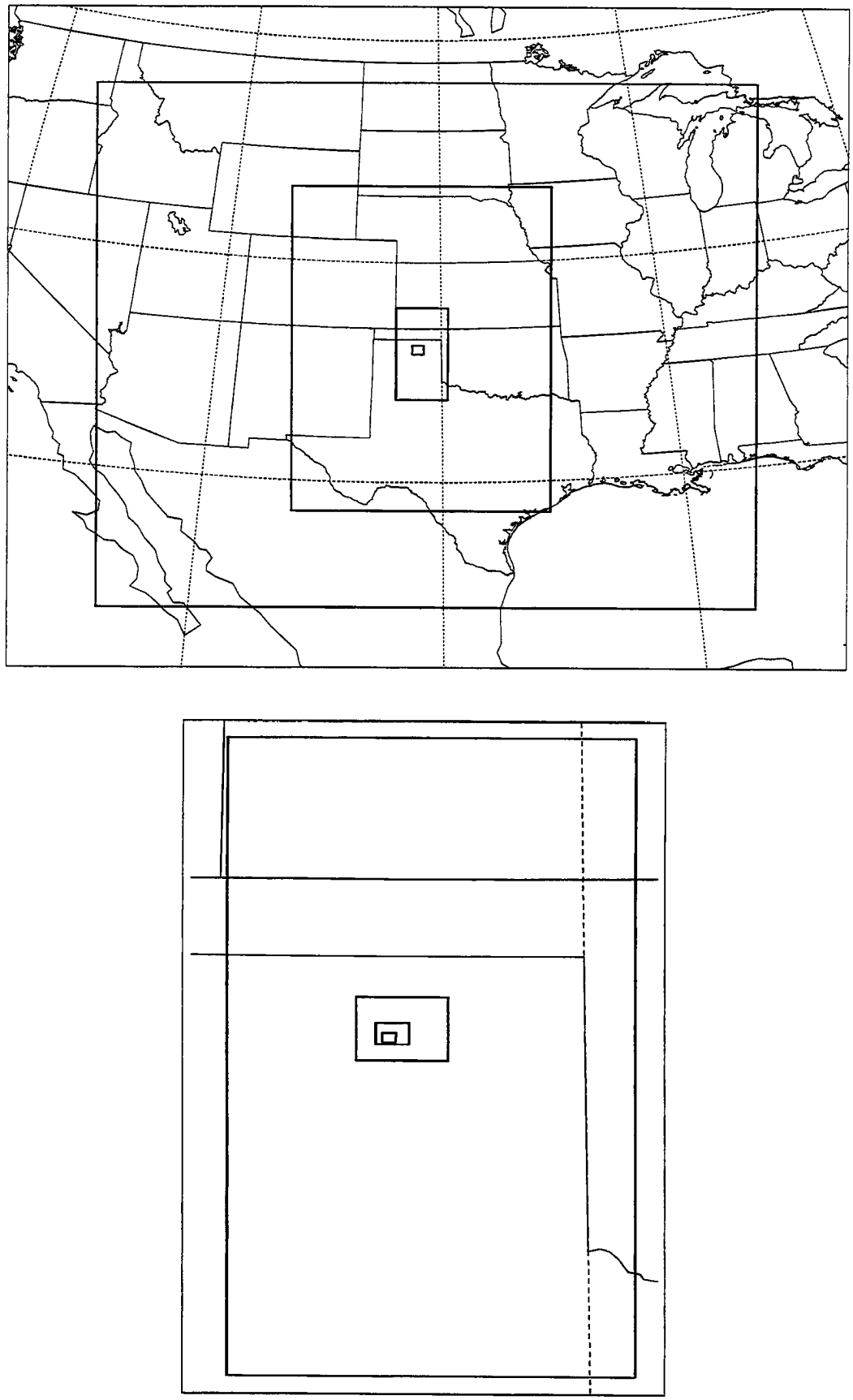

Figure 4.3: Grid configuration for the May 15, 1991 case (grid boundaries are denoted by the bold lines). The top figure shows the positions of Grids #1-3 and the initial postion of Grid #4. The bottom figure shows the initial positions of Grids #3-6. Grids #4-6 were moved during the simulation.

Chapter 5

SIMULATED JUNE 30, 1993 HP SUPERCELL

In this chapter, the structure and evolution of the simulated June 30, 1993 high-precipitation supercell is presented. The supercell which develops in the simulation starts out as a classical supercell, and then becomes part of a small thunderstorm complex which eventually develops into a single storm which has many characteristics of an HP supercell. The evolution of the supercell is discussed in section 5.1. An analysis of the storm's transition into a bow echo is presented in section 5.2 along with a discussion about a deep tropospheric gravity wave which is emitted from the storm just prior to its transition. A summary and discussion of the results is presented in section 5.3.

5.1 Storm Evolution and Structure

The June 30, 1993, simulation was started at 1200 UTC with 3 grids to capture the early evolution of the synoptic fields. However, the convection that was present early in the day over Nebraska and Iowa was never captured by the model (by either simulations starting with 3 grids using a cumulus parameterization, or simulations staring with 4 grids using explicit microphysics). Perhaps this is due to inadequate sampling of the moisture field in the cloudy regions, or the lack of any dynamic initialization in the model (i.e. vertical motion is zero everywhere at the beginning of the simulation). In the observations, this convection produced an outflow boundary which moved southward into northern Missouri and northeast Kansas during the late morning hours, where it intersected the stationary front. It was near this intersection point that the convection of interest later developed.

Simulations performed without the outflow boundary in the model fields failed to produce convection in northeast Kansas (although they did capture the convection which later

developed in southwestern Iowa). Stensrud and Fritsch (1994a,b) illustrated the importance of incorporating mesoscale features into simulations of convection. They presented results from a weakly forced MCC simulation in which outflow boundaries and other mesoscale features were detectable in the data, but were not sufficiently resolved in the standard synoptic analysis to be well defined in the model initialization. The data were reanalyzed and some 'bogus' soundings were added in order to better capture the three dimensional mesoscale environment (or their best estimate of the mesoscale environment). They found that the specification of a 'mesoscale' initial condition (i.e. one that included features like outflow boundaries and mesoscale pressure and wind features) greatly improved their simulation of a series of MCCs. The current simulation is a bit more complicated, since the outflow boundary did not begin to develop until 1800 UTC, at which point the simulation was already underway. To try to incorporate the outflow into the model simulation, interior nudging was preformed over a limited region from 1600-2000 UTC during the simulation. The horizontal extent of the nudging region is shown in Figure 5.1. The depth of the nudging region was $\sim$1km [1]since profiler data from the region indicated that the outflow depth was around 1km. Because thermodynamic data were available only at the surface, the surface data were allowed to influence the thermodynamic fields upward to a depth of 1km in the nudging region. Wind profiler data and surface winds were used to approximate the winds throughout the depth of the nudging region. The wind and temperature fields at z=38m at 2100 UTC (one hour after the nudging ended) is shown in Figure 5.2. The outflow boundary weakened in time, but persisted throughout the duration of the simulation (hereafter, this boundary will be denoted as B1).

Grid #4 was added at 2000 UTC at which time the microphysics was turned on in the model. Grid #4 was initially centered over the intersection point between the stationary front and the outflow boundary since boundary layer moisture convergence on Grid #3 was strongest in that region. Between 2125-2135 UTC, the first storm began to develop

---

[1]The nudging weight was constant through the first eight model levels (up to 847m), dropping off to zero by the eleventh model level (1658m).

near the intersection between the stationary front and B1 in northeast Kansas (similar to observations) where low-level convergence was strongest. Figure 5.3 shows the low-level model wind and condensate fields 20-30 minutes after convection was initiated on Grid # 4. Both the stationary front and the preexisting outflow boundary (B1) are visible in the wind field. The air to the south of the stationary front and outflow boundary in the simulation was very unstable with CAPE values of over $3000 J(kg)^{-1}$. A typical model sounding taken just south of the developing convection is shown in Figure 5.4. The shear vector turns clockwise with height below 800mb with nearly unidirectional shear above this level. This gives a Bulk Richardson number of approximately 10, indicating that supercells should be the preferred mode of convection (Weisman and Klemp, 1982,1984). To the north of B1, there are still considerable amounts of CAPE ($\sim 2500 J(kg)^{-1}$) and shear, but the boundary layer in this region is strongly capped. The storm moved slightly eastward along B1 during the first 20 minutes, and away from the intersection point where the first convective updrafts were initiated. At about 2148 UTC, the storm began to split in a manner similar to the horizontally homogeneous supercell simulations of Klemp and Wilhelmson (1978a,1978b), Thorpe and Miller (1978), Schlesinger (1980) and Wilhelmson and Klemp (1978,1981) as shown in Figure 5.5. The 'right moving' storm (hereafter denoted as S1) remained almost stationary, while the left moving storm moved to the north and weakened rapidly. Like previous simulations, the right moving storm rotated cyclonically, while the left moving storm rotated anticyclonically.

By 2240 UTC, S1 moved eastward along B1 and away from the stationary front. The convergence line that was associated with the old outflow boundary has now appeared to 'wrap around' S1 in a frontal wave-like pattern similar to mid-latitude cyclones. Part of the old outflow boundary is now associated with the forward flank gust front, another with the rear flank gust front. A similar evolution between a surface 'trough' and a supercell storm was described by Wakimoto et al. (1997) during the VORTEX 95 experiment.

Around 2227 UTC, additional convection began to develop north of the stationary front to the west of the S1 as shown in Figure 5.6. This convection was rooted in a convergence zone above the surface created by southerly flow associated with a low-level jet over-running

B1 (which by this time was being reinforced with cold air outflow from S1). The convergence zone extends westward from S1 until it meets westerly flow in the divergent region along the top of the stationary front to the west. The northeasterly flow associated with air rotating around the north side of S1 also helped to enhance convergence immediately west of S1. The region of convergence is about 1km deep (starting about 850m above the surface) which forced significant upward motion in a band extending west-southwest from S1 as shown in Figure 5.6. Although the air feeding these updrafts (at first) originates near the top of the boundary layer, the air is still moist enough to produce convection. The new convection first originates immediately northwest of S1, and works its way westward along the convergence zone in time until 2253 UTC when convective cells extend along an entire east-west line between S1 and the stationary front.

By 2307 UTC, two convective cells have become dominant; the cell associated with S1, and the cell that developed furthest west along the elevated convergence zone (hereafter denoted as S2) as shown in Figure 5.7. At 2334, both storms exhibited supercell characteristics including mid-level rotation and 'hook echo' patterns in the condensate fields. S1 began showing signs of developing into an HP supercell around 2348 as can be seen in Figure 5.8. There is significant precipitation falling to the west and southwest of the updraft which is characteristic of HP supercells, with precipitation rates approaching $12cm(hr)^{-1}$. Farther west at low levels, outflow from S2 has begun to wrap around the west side of the main updraft of S2. This outflow 'collides' with the outflow spreading out from S1 by 2348 and forms a new low-level convergence line extending south of S2 as shown in Figure 5.9. This helps to enhance the convection along the southern flank of S2.

The outflow from S2 has merged with B1 by 0000 UTC. During this time, S1 was moving to the east/southeast at $15ms^{-1}$ while the main updraft associated with S2 was propagating rapidly to the SE at about $25ms^{-1}$ allowing S2 to 'catch up' with the southern portion of the mid-level updrafts associated with the flanking line of S1 as shown in Figure 5.10. At low levels (below 3.5km), the condensate field associated with S2 shows two distinct maxima–one to the north, and another to the south (just north of the main updraft at this level). Above 4km, the southern maximum becomes dominant as can be seen in Figure

5.10. In some ways, S2 appears to undergo a slow 'splitting' process between 2307-0000 UTC somewhat similar to S1. The updraft is split by a downdraft below 4km, with the cyclonically rotating updraft propagating to the east/southeast, and the anticyclonically rotating updraft moving toward the north/northeast (denoted by S3–hereafter S2 will denote the right moving storm). However, S2-S3 do not 'split' in the classical sense in that the condensate fields associated with the updrafts do not completely separate at mid/upper levels until about 0027; instead the condensate field elongates in the north-south direction as shown in Figure 5.11. Also, shortly after the storm splits, the updraft associated with S3 was no longer rooted in the lower boundary layer as can be seen in Figure 5.10 (note the absence of an updraft associated with the northern portion of the condensate field at this level). The left-moving storm (S3) was weaker than the right mover (S2), but remained identifiable through the duration of the simulation.

Grids #5 and #6 were spawned in the simulation at 0000 UTC July 1. (Originally, only Grid #5 was added at this time to better capture the storm's transition into a bow-echo, but the low-level wind fields showed evidence of rotation developing around 0015 UTC. As a result, Grid #6 was also added at 0000 UTC over the region that rotation developed at low levels on Grid #5.) Grid #6 captures the evolution of the simulated tornadoes, and the results from this grid will be discussed in Chapter 6. Grid #5 captures the evolution of the supercell in more detail (as well as some of the gross features of the simulated tornadoes). Between 0000 UTC and 0100 UTC, some large changes take place in the structure of S1. S2 continued to propagate southeastward from 0000-0015 UTC until it merged with the southern end of the updraft associated with the flanking line of S1 between 0015-0021. At low levels (below about 3km), the updraft associated with S2 appeared to move smoothly to the southeast, while at middle and upper levels, both the vertical motion and condensate fields exhibited signs of discrete propagation. Time series of the vertical motion and condensate fields (not shown) indicated that S2 made two distinct 'jumps' to the south/southeast (one between 0000-0010:30 and another between 0010:30-0019:30) in which it appeared that one updraft (condensate maximum) dissipated while another formed to the south/southeast of it (this could also be seen in the vorticity field).

The end result at 0021 UTC was one large continuous updraft as shown in Figure 5.15. Shortly after this merger, S2 loses many of its supercell characteristics. The merger of the two updrafts produced a sudden increase in the depth and strength of convection in the region surrounding the merger point between 0015 and 0019:30 UTC. AT z=6.1km on Grid #5, updrafts increased from 16-18ms^{-1} at 0013:30 UTC to 28-32ms^{-1} at 0019:30, with maximum updrafts reaching 56ms^{-1} near the tropopause (storm tops in the simulation reached approximately 16-17km). The sudden and dramatic increase in convective intensity after cell merger has been observed by Simpson and Woodley (1971), Lemon (1976), and Houze and Cheng (1977). As quickly as the convection flares up near the updraft merger point, it quickly dies down and by 0021 UTC, updrafts in the region have dropped off to 14-18ms^{-1} at z=6.1 km.

At the same time that the cells are collapsing in the merger region between 0020 and 0030, the pressure drops over an elongated area surrounding the convective band. All during this time period, S1 (which now comprises the northern portion of the storm) has retained many of its supercell characteristics– most notably its rotating updraft. Although the cells along the convective line south of S1 are associated with large values of positive vertical vorticity, they do not display obvious signs of rotation. Thus the storm has become an elongated line of convection with one main mesocyclone at the northern end of the line (associated with S1) and a large flanking line extending to the south and west. The pressure field on Grid #5 at z=6.1km for several successive times is shown in Figure 5.12. The pressure drop occurs over a large depth of the troposphere and is associated with a gravity wave which is emitted from the storm system between 0020-0030 UTC. The gravity wave appears to be generated by the sudden burst and collapse of convection associated with the updraft merger since the largest wave amplitude originates from that region of the storm. The wave moves east/southeast away from the storm at about 31ms^{-1} and extends through the depth of troposphere with the largest amplitude (both in pressure and vertical velocity fields) occurring at mid-levels. This can be seen in Figure 5.13 which shows a time series of the model wind and pressure fields at a point originally east of the storm. At mid-levels, the wave passage is marked by upward motion of 5-6ms^{-1}, and a

pressure drop of 1.5 mb. A vertical cross section on Grid #4 taken through the center of the wave is shown in Figure 5.14. Like the pressure drop associated with the wave, the upward motion also extends through most of the troposphere. Although the upstream propagating wave is also visible upstream of the storm at later times (with careful inspection of the model fields), the downstream propagating wave has a much larger amplitude in both the vertical motion and pressure fields. This point will be discussed further later in this chapter. The pressure drop associated with the wave increases the horizontal pressure gradient over a large area–particularly at mid-levels where the pressure drop associated with the wave is largest. Although the increased pressure gradient force does not increase the total wind speed, it does turn the winds eastward behind the convective line over a large depth of the troposphere. This helps enhance convergence over a large region along the gust front, producing a more organized convective band by 0021 as shown in Figure 5.15. The convective band intensifies by 0030 as updrafts increase again to 25-30ms^{-1} (at z=6.1km) in the central portion of the line on Grid #5. Thus the pressure field associated with the gravity wave appears to help the storm become more organized.

The condensate and vertical vorticity maxima that developed along the central and southern portion of the storm appeared to move north/northeastward along the gust front between 0100-0030. Around 0030, a large condensate and vorticity maximum that originated in the central portion of the convective line (near the merger region between S1 and S2) appeared to 'merge' with the the condensate and vorticity maximum at the northern end of the storm which was associated with S1 (this is very evident in time loops of these fields). Some evidence of this can be seen in Figures 5.16 and 5.17 which show the evolution of the condensate and vorticity fields at z=2.5km on Grid #4. A similar evolution as noted by Lemon (1976) and Barnes (1978a,b) who used radar observations to document HP supercells where storms in the flanking line moved toward and merged with the main storm updraft (mesocyclone). From 0030-0037 UTC, the positive vertical vorticity along the gust front increased dramatically at low levels as the gust front accelerated eastward (not shown). Between 0030-0040, other condensate and vorticity maxima generated along the gust front also appeared to move northward and merge with the main mesocyclone

at the northern end of the convective line. As the vorticity centers along the gust front moved northward and merged with the positive vertical vorticity region associated with the mesocyclone, the mesocyclone grew in size and intensified (both with respect to increased maximum vertical vorticity and lower pressure) with time as can be seen in Figures 5.17 and 5.18, and the storm evolved into a rotating comma-head structure. This finding also supports the idea proposed by Lemon (1976) that the flanking line could be an important vorticity source for some rotating storms. Also during this time period, negative vertical vorticity develops along the southern end of the storm behind the convective line. Between 0030-0040, two distinct counter rotating vortices emerge at mid-levels in the storm. These counter rotating vortices are often referred to as 'book-end vortices', and are a common feature of bow-echoes (Rotunno et al., 1988; Schmidt, 1991; Weisman, 1993; Skamarock et al., 1994).

To demonstrate that the gust front could potentially be a vorticity source for the mesocyclone, a group of 20 particles was placed along the gust front in regions of large vertical vorticity at z=488m on Grid #5 at 0030 UTC. Each of the particles is meant to represent an air parcel originating in the boundary layer along the gust front. Note that the particles are originating below cloud base along the band of upward motion at the leading edge of the gust front. Three dimensional particle trajectories were then calculated until 0045 UTC. Horizontal projections of the initial and final locations of the particles are shown in Figure 5.19. All but the southern-most particles (in the initialization) ended up at various elevations in the mesocyclone (rotating comma-head structure) at the northern edge of bow. The parcels took a wide range of trajectories before reaching their final locations in the mesocyclone. Many of the particles were caught up in the convective updrafts along the flanking line and were carried into the mesocyclone at middle and upper levels. Vorticity calculated along these particle trajectories (not shown) indicated that there was positive vertical vorticity associated with the air parcels throughout the 15 minute period (i.e. these parcels carried positive vertical vorticity into the mesocyclone region). A few of the particle trajectories showed that the parcels first moved upward, and then got caught in a convective downdraft before entering the mesocyclone region below cloud base

(which was at approximately 1500m). The vertical vorticity associated with the parcels of 2 of these low-level trajectories changed from positive to negative as the parcels descended. However, the majority of parcels entering the mesocyclone from low levels in the flanking line had positive vertical vorticity values at least as large (most larger) upon entering the mesocyclone region than they had at their initialization.

As was discussed above, it appeared from a time series loop of the vertical vorticity field (at many different vertical levels) that vorticity (and condensate) maxima appeared to move northward along the gust front, and then merge with the main mesocyclone at the northern end of the storm. Horizontal particle motions calculated starting with particles positioned along the gust front at many levels between the surface and z=4km (not shown) indicated that most of the particles eventually ended up in the region of the mesocyclone at the northern end of the bow-echo. These horizontal particle movements indicate that longer-lived entities (such as individual stronger updrafts along the flanking line– which would also be more efficient tilters/stretchers of ambient horizontal vorticity) could be advected along the gust front and 'ingested' into the rotating comma-head structure of the storm. It should be noted the above analysis only points to one possible vorticity source for the mesocyclone. It is quite possible that there could be other sources (such as tilting in the downdrafts along the northwestern portion of the mesocyclone) of equal or greater significance than the flanking line source investigated here.

During the time period from 0030-0040 UTC, the winds behind the convective line accelerated eastward over a large depth of the troposphere (from the surface to about 6-7km). This marked the storm's transition into a bow-echo or rotating comma-head structure. Recall that this is one of the possible life cycles of an HP supercell as documented by Moller et al. (1990). Near the surface, the acceleration is particularly large along the south side of the mesocyclone with wind speeds reaching $28 ms^{-1}$ between 0033-0037 (on Grid #5) along the south side of the center of rotation (not shown). A vertical cross section taken through the center of the bow-echo on Grid #5 at several successive times is shown in Figure 5.20. Just prior to the transition, the updrafts along the center of the line begin to lean considerably toward the west (upshear)–especially in the lowest 7km above the surface (see

Figure 5.20a,c). The updrafts continued to lean westward with height until shortly after 0040 when the updrafts weakened significantly and became more upright as shown in Figure 5.20e , eventually leaning eastward (down-shear) with height. Although the storm does not have an extensive rear inflow jet extending far behind the convective line as there is with many large bow echoes, the system does have strong westerly storm-relative winds (average motion of the center of the bow during this period was eastward at $15ms^{-1}$) extending horizontally 10-15km behind the convective line and vertically between 2km-7km. Note that the only westerly storm-relative winds below 1.5km are associated with the leading edge of the gust front. Possible explanations for the transition of the system into a bow-echo will be discussed further below.

Another interesting feature in the simulation is that the storm draws in high valued θ_e air from the south/east over the lowest 3km of the atmosphere. Trajectory calculations (not shown) indicate that the main source of air entering the storm originates ahead of the gust front where the high θ_e air gets swept northeastward and eventually gets 'wrapped into' the east side of the storm as shown in Figure 5.21. This occurs from 0010-0040 UTC at which point the high θ_e inflow gets cut-off as the storm evolves into a bow-echo. After 0040, the storm updrafts weaken considerably, and the mesocyclone gets cut off from its vorticity source as the convection along the central portion of the bow dissipates. The low pressure center that was associated with the mesocyclone begins to fill, and the areal extent of the rotation broadens and the rotation weakens. The simulation was terminated at 0100 UTC July 1 since the simulated storm weakened considerably and the observed storm became part of a large and well organized squall line extending from northeast Kansas into eastern Iowa by this time (which could not be simulated with the grid configuration used in this study).

5.2 Further Analysis of Bow-echo Transition

In this section, the transition of the storm into a bow-echo/rotating comma head structure will be investigated further. Although there have been previous modelling studies of bow-echoes, these studies have been highly idealized (starting with a single idealized sound-

ing and initializing the entire model domain with it) and have focused on the long-lived Mesoscale Convective System (MCS) bow-echoes (Weisman et al., 1988; Weisman, 1993; Skamarock et al., 1994). It is not clear if the ideas presented in those studies are applicable to the smaller-scale HP supercell systems in more realistic three dimensional environments.

Previous studies suggest the following possible mechanisms for creating/enhancing inflow into the back side of storms:

1. Gravity wave dynamics

2. Cold pool dynamics

These possibilities will be investigated in the context of the model simulation below.

5.2.1 Gravity Waves

It was shown previously that a large amplitude gravity wave was emitted from the storm shortly before the storm transitioned into a bow-echo. Here we investigate the possible connection between the gravity wave and the storm's transition into a bow-echo. Previous idealized modeling studies of convection (usually squall lines) have shown that gravity waves generated by convective heating/cooling can have a significant impact on the environment surrounding the convection and on the evolution of the convection itself in some cases.

Nicholls et al. (1991) and Mapes (1993) both investigated the response of an atmosphere at rest to a prescribed localized heating source (meant to represent convection). Both studies found that several disturbances propagated horizontally away from the heat source (in both directions) at the gravity wave phase speed of internal linear gravity waves which is given by:

$$c = \frac{N}{m} \tag{5.1}$$

where c is the phase speed of the wave (for linear gravity waves, it is also the group velocity of the waves), N is the Brunt-Vaisala frequency, and m is the vertical wave number of the wave. By convention, m=1 corresponds to a wave with a half-wavelength equal to the

depth of the troposphere, m=2 corresponds to a wave with a vertical wavelength equal to the depth of the troposphere, etc. Note that from equation 5.1, the m=1 mode will travel twice as fast as the m=2 mode. However, the propagating disturbances were not true 'waves' in the sense that they would propagate through the fluid, leaving the fluid undisturbed after they pass. Instead, the disturbances left in their wake permanent vertical displacements of the isentropes, and perturbations in the horizontal winds (because of this, Mapes (1993) called these disturbances 'buoyancy bores' rather than gravity waves). The atmospheric response to a positive heating rate in the mid and upper troposphere and a negative heating rate at low-levels (meant to represent convective heating aloft with evaporative cooling at lower levels) is shown in Figure 5.22. The leading edge of the m=1 mode is characterized by deep tropospheric downward motion and horizontal winds which blow toward the storm in the lower troposphere, and away from the storm in the upper troposphere. The m=2 mode is characterized by downward motion in the upper half of the troposphere, and upward motion in the lower troposphere. Behind the m=2 mode, the horizontal winds in the middle troposphere are accelerated toward the storm, while the horizontal winds in the upper and lower troposphere are accelerated away from the storm. When the heating is turned off, bores of the opposite sense (i.e. the m=1 mode is associated with deep tropospheric upward motion, and the m=2 model is associated with upward (downward) motion in the upper (lower) troposphere) propagate away from the heating region. Mapes (1993) refers to the regions between the positive/negative couplet of the m=1,2 modes as 'buoyancy rolls'. Of course, in the real atmosphere, this picture becomes far more complicated since most long-lived convection forms in regions of strong vertical wind shear (which was neglected in their studies), N varies with height, gravity waves can propagate vertically as well as horizontally (Figure 5.22 was for the rigid lid solution) and convection (and hence the convective heating rate) is rarely (if ever) in 'steady state'. In a somewhat more realistic two dimensionally simulation of convection generated by a sea-breeze, Nicholls et al. (1991) found that deep tropospheric gravity waves were emitted by convection. However, unlike the idealized simulations, the waves were not emitted from the storm during the explosive development, but during the stage when the convection decreased in intensity. The wave

resembled an m=1 buoyancy roll, with the upward motion lagging the downward motion by approximately 60km. The magnitude of the downward motion in the wave was less than the upward motion at the back of the wave, but the downward motion was spread out over a larger area. They attributed this structure to some of the wave energy escaping vertically.

Schmidt and Cotton (1990) used a two dimensional version of RAMS to study the role of gravity waves on squall line structure and maintenance. The model was initialized horizontally homogeneously using a smoothed sounding taken from the CCOPE field experiment on a day when a long-lived bow-echo squall line developed. The sounding showed three distinct thermodynamic layers: a moist, stable boundary layer, a deep, nearly dry adiabatic layer extending above the boundary layer to 450mb, and an upper tropospheric stable layer extending up to the stratosphere. The authors then varied the vertical wind shear profile to investigate the effects of wind shear on the simulated squall line and how the gravity waves generated by the convection affected the squall line structure. They found the convection generated large gravity waves (single waves of either elevation or depression) in both the upper and lower level stable layers. (Since the current simulation had a well mixed boundary layer instead of a stable layer near the surface, the rest of the discussion of the Schmidt and Cotton study will focus on the upper-level waves.) In the no shear case, the upper level waves had a vertical wavelength twice the troposphere depth (similar to the m=1 wave presented by Nicholls et al. (1991) and Mapes (1993)), and were characterized by a region of weak downward motion followed by a region of stronger upward motion. The authors compared the no-shear simulation to a control simulation and found that the flow structures generated by the gravity waves could account for many of the observed flow features of the control case, including the rear to front flow (also known as the rear inflow jet) at mid-levels behind the storm. When vertical wind shear was introduced into the simulations, the phase speed and magnitude of the upstream propagating waves changed. The waves propagated more slowly upstream, and the vertical displacement of the isentropes behind the wave increased in the strong shear case. The authors proposed that this led to partial blocking of the ambient flow, and channeled upper tropospheric flow downward into mid-levels behind the storm, creating the rear inflow jet.

Pandya and Durran (1996) also investigated the role of gravity waves in generating observed mesoscale circulations in idealized two dimensional squall lines. They also argue that the upstream propagating gravity waves generated by the leading convective line are responsible for generating many of the flow features associated with squall lines (such as the front to rear flow, rear inflow jet, and the anvil-level outflow). They ran a control simulation in which they initialized their model horizontally homogeneously with a sounding taken ahead of an observed squall line, and then preformed several (dry) sensitivity studies to investigate how changes in a prescribed heating profile and changes in the environment effect the convectively generated gravity waves and the mesoscale circulations left in their wake. They found that dry simulations in which the prescribed heating profiles matched the heating profiles in the moist simulations (in which a convective storm was simulated) generated gravity waves which propagated upstream and produced mesoscale circulations which resembled mesoscale circulations behind observed squall lines. Sensitivity studies revealed that the gravity waves (and hence the mesoscale circulations left in their wake) were very sensitive to changes in the shape of the thermal forcing. In particular, they found that the generated gravity waves did not produce realistic mesoscale circulations unless the convective heating profile leaned upstream with height, and the region of low-level cooling was displaced rearward with respect to the low-level heating.

With these previous studies in mind, we now turn to the June 30 HP supercell simulation. While none of the aforementioned studies directly link gravity waves to bow-echoes, they do suggest that gravity waves may be responsible for generating a rear inflow jet into the back side of the storm (at least in squall lines). As was discussed previously, the storm emits a large amplitude gravity wave between 0020-0030 UTC shortly before the storm transitions into a bow-echo. Characteristics of the downstream propagating wave were shown earlier. To investigate the upstream propagating wave and its relationship to the convection, vertical east-west cross sections were taken at several locations along the evolving bow-echo on Grid #5. The upstream propagating wave emerged from the storm several minutes after the downstream propagating wave, and the wave amplitude (both in the vertical velocity and the pressure fields) was significantly smaller. A vertical cross sec-

tion through the center of the developing bow-echo at 0031:30 is shown in Figure 5.23. At this time, the upstream propagating wave is located between x=-90km and x=-80km and is characterized by a region of downward motion followed by a region of upward motion both of which extended through the depth of the troposphere. The trailing edge of the wave is located along the western edge of the storm at this time as can be seen by comparing Figures 5.23a,d. The main convective line is located between x=-70km to x=-80km and the updraft leans westward with height over the lowest 6km. The storm relative winds (the motion of the center of the bow which was eastward at $15ms^{-1}$ has been subtracted out) indicate that the winds behind the convective line have begun to accelerate below 6km in the region between the trailing edge of the gravity wave and the convective line.

By 0036, the convective line has moved eastward to x=-60km, while the position of the gravity wave has remained relatively unchanged as shown in Figure 5.24. The downward motion associated with the leading edge of the wave has increased from -$3ms^{-1}$ to -$1ms^{-1}$ since 0031:30, and the orientation of the phase lines now slope eastward with height indicating that some of the wave energy is propagating vertically. The trailing edge of the wave now lies outside storm, and the region of storm relative westerlies no longer extends to the trailing edge of the wave. The storm relative westerlies extend 10-15km behind the storm and have accelerated to a maximum of 14-$16ms^{-1}$ about 4km above the surface. The potential temperature field (Figure 5.24c) shows that the isentropes slope downward and toward the east in a region extending from the trailing edge of the wave to the convective updraft. A similar feature was observed in the 2-D high-shear simulations of Schmidt and Cotton (1990). They argued that this feature represented 'flow blocking' by the wave and was responsible for the development of the rear inflow jet as air moved adiabatically and was accelerated in the region where the isentropes were squeezed together. Some evidence of this can be seen in the present simulation (compare the θ=330K and the θ=306K contours between x=-80km to x=-65km), but it is not clear that the flow channeling argument can be made here since most of this region lies in the condensate field associated with the storm.

To get a better picture of the flow into the back side of the bow echo, backwards trajectories for 20 particles were calculated at several different levels starting from region of strongest inflow in the back of the storm. Six of the trajectories at each level starting from 0039 UTC (ending between 0019 - 0025 UTC) are shown in Figure 5.25. Backwards trajectories starting at z=2km and z=3.5km (Figure 5.25a,b) indicate that air flowing into the back side of the storm at these levels generally originated at higher levels to the north and west of the storm. This is consistent with the descending 'rear inflow jet' described in many MCS cases. As can be seen from Figure 5.25, air entering the northern two-thirds of the storm in strongly influenced by the cyclonic flow around the northern end of the storm. *All* of the trajectories starting from z=2km originate northwest of the storm, while at higher levels, air entering the southern one-third of the storm originates from almost due west. The parcel trajectories starting from z=4.3km and z=5.1km at the extreme northern and southern ends of the strong wind region actually originate from lower levels and appear to flow through a part of the storm updraft before entering the region of strong winds, while the air entering the central portion of the storm first ascends somewhat before descending into the storm. Comparing the slope of the parcel trajectories as they near the west side of the storm with the slope of the isentropes 10-15km west of the storm at 0036 UTC (see Figure 5.24c) shows that the two compare fairly well in the central portion of the storm. The trajectories show that the particles sink about 1km in the last 15km of their trajectories. Figure 5.24c also shows that the slope of the isentropes in that region of the storm is about 1km of descent to the east in 15km. Although this is not proof positive that flow blocking is going on east of the upstream propagating gravity wave, the possibility cannot be ruled out.

The same vertical cross section at 0040 UTC is shown in Figure 5.26. The storm has continued to move eastward while the wave position is nearly unchanged. Although the wave began propagating upstream shortly after it was emitted from the storm, it has turned into a standing wave (with respect to the surface). From the storm's perspective, the wave is propagating upstream at $15ms^{-1}$. The strong storm relative westerlies have moved eastward with the storm and it is now clear that these winds are not associated with

the gravity wave. In fact, the flow behind the wave is similar to the flow perturbations that would be expected behind the upward branch of the m=1 mode described by Nicholls et al. (1991) and Mapes (1993). While the wave appears to help drive the flow toward the storm in the upper troposphere, it interferes with the westerly flow behind the storm in the lower troposphere (where the strongest storm-relative westerlies develop).

Further evidence that the wave does not play a role in helping to accelerate the winds can be seen by taking a vertical cross section through the storm along the southern portion of the bow-echo. This portion of the storm remains relatively stationary (with respect to the surface) while the storm evolves into a bow-echo. A vertical cross section taken through the southern portion of the bow-echo at 0036 UTC is shown in Figure 5.27. Even though the standing wave is also present in this portion of the storm, strong inflow into the back side of the storm (in the lower troposphere) never develops in this region. A time series indicated that the winds into the back side of the storm in the upper troposphere did increase somewhat after the passage of wave, which is consistent with the the m=1 mode discussed earlier. Thus it is not obvious from the model results that the gravity waves emitted from the storm play any significant role in the storm's transition into a bow-echo.

5.2.2 Cold Pool Dynamics

The importance of the pool of evaporatively-cooled low-level air generated by thunderstorms has been the topic of much study over the last decade, especially in the transition of individual thunderstorms into larger convective complexes such as squall lines. Many idealized modelling studies have suggested that the characteristics of this 'cold pool' have a large effect on the subsequent evolution of the convection (Rotunno et al., 1988; Weisman et al., 1988; Lafore and Moncrieff, 1989; Fovell and Ogura, 1989; Skamarock et al., 1994). Although all these studies have focused on the squall lines (with characteristic horizontal scales an order of magnitude larger than supercells), some of the ideas may be applicable to the HP supercell simulation presented here.

A conceptual model showing the influence of the convectively-generated cold pool on the evolution of the convection is shown in Figure 5.28. As convection first develops, the

convective updrafts tilt down-shear in response to the ambient winds. As the cold pool beneath the storm strengthens, the convection becomes more upright, and then begins to tilt upshear (at midlatitudes, this would imply that most storms would tilt westward with height). It is only after the system begins to tilt upshear that the rear inflow jet and stratiform precipitation begin to develop behind the convective line. These studies have shown that the rear inflow develops in response to upshear-tilted updrafts in the convective line which then produced horizontal buoyancy gradients creating a circulation that draws air in from the rear of the storm. Idealized modelling studies have shown that the amounts of CAPE and wind shear in the environment determine the amount of tilting of the leading updraft, which then affects the characteristics of the rear inflow jet. Cases with very high shear and CAPE produced the strongest rear inflow jets and the strongest, longest lived convective lines. It is hypothesized that in these cases, the vorticity generated at the leading edge of the cold pool 'balances' the ambient vorticity, creating deep lifting at the leading edge of the gust front (Rotunno et al., 1988; Weisman et al., 1988).

Weisman (1993) expanded the previous idealized squall line studies to try to single out the dynamics of bow-echo squall lines. He found that the idealized bow-echoes were characterized by a strong, elevated rear-inflow jet which extended to the leading edge of the bow at 2-3km above the surface, with cyclonic and anticyclonic mid-level vortices on the northern and southern flanks of the bowed segment, respectively. The model results showed that the bow structure developed systematically as the cold pool strengthened over time, eventually producing a circulation that overwhelmed the ambient shear. As this happened, the leading edge of the cold pool accelerated, forcing the convective cells to be advected rearward over the cold pool and weaken. This generated horizontal buoyancy gradients (and hence horizontal pressure gradients) along the back edge of the rearward advecting cells which generated an elevated rear inflow jet that extended to the leading edge of the cold pool.

We will now examine the evolution of the low-level cold pool in the current simulation. The evolution of the pressure field at the lowest model level (z=38m) on Grid #5 is shown in Figure 5.29. The leading edge of the gust front closely follows the 30°C isotherm which

is denoted with the bold line. At 0019:30, there is generally weak high pressure behind the gust front (compared to the environment ahead of the gust front). The small, intense area of low pressure at x=-70km, y=18km is the first tornado in progress. The evolution of the tornado will be discussed in Chapter 6. Note the center of the weak high pressure developing behind the gust front near x=-82km, y=10km (denoted by the 'H'). By 0025, this area of high pressure has moved northeastward, intensified and increased in areal coverage as shown in Figure 5.29b. The pressure ahead of the gust front has dropped since 0019:30, and a meso-low has developed. This meso-low is associated with the large amplitude gravity wave being emitted from the storm at this time. Note that the horizontal pressure gradient has increased over a large area surrounding the gust front. The gravity wave propagated downstream away from the storm by 0030 UTC leaving the pressure ahead of the gust front slightly lower (by about 0.25mb) than it was before the wave passage. The region of high pressure behind the gust front continued to move northeastward and expand in area as shown in Figure 5.29c. Vertical cross sections taken through low levels in the storm indicated that the depth of the cold air also increased from 1km to 2km in the region of the expanding high pressure. During this time the horizontal pressure gradient continued to strengthen in the immediate vicinity of the gust front. The horizontal temperature gradient along the gust front also increased significantly (not shown). Between 0028:30 and 0030 UTC, the gust front began to accelerate rapidly toward the east and wrap around the mesocyclone. (Note that Grid #5 is moving during this time period so the x and y positions are changing along the axes in time.) Recall that this was the time that the updrafts along the center of the convective line began to lean westward with height (see Figure 5.20).

As the updrafts along the center of the bow began to lean westward with height, an area of low pressure developed at mid-levels behind the convective line. This can be seen in the vertical cross section of perturbation pressure taken through the center of the bow at 0031:30 UTC which is shown in Figure 5.30. Previous idealized modeling studies have shown that this pressure gradient develops in response to horizontal buoyancy gradients associated with the warm convective plume aloft, and cold air near the surface (Lafore and Moncrieff, 1989; Fovell and Ogura, 1989; Weisman, 1992, 1993), or equivalently, this

configuration of the buoyancy field supports a minimum in the hydrostatic pressure field at mid-levels (LeMone, 1983; LeMone et al., 1984). This creates a strong horizontal pressure gradient along the back side of the storm which accelerates the flow into the storm in this region. (Note the strong pressure gradient extends vertically from z=2km to z=6km and 10-15km behind the leading edge of the convective line. This is the region where the strong winds develop.)

By 0036 UTC, the high pressure area behind the gust front weakened as shown in Figure 5.29d. Vertical cross sections taken through low levels in the storm indicated that the weakening high pressure was associated with the collapse of the cold pool, as the cold air spread out along the surface. Even though the high pressure center behind the gust front had weakened, the horizontal pressure gradient along the gust front was still large, and the gust front continued to move rapidly eastward and wrap around the mesocyclone through 0055 UTC. By 0045, the storm looked very similar to an occluded midlatitude cyclone as shown in Figure 5.31.

Recall that S2 merged with the convection along the flanking line of S1 between 0015-0021 UTC. Both observational and modelling studies of cloud (updraft) merger have shown that precipitation increases significantly following merger (Simpson and Woodley, 1971; Tao and Simpson, 1984; Wescott, 1984). The precipitation rate at the lowest model level at several successive times is shown in Figure 5.32. Between 0019:30 and 0025:30, the precipitation rate increased significantly in the region surrounding x=-77km, y=13km. This occurs 5-10 minutes after the merger between S1 and S2 took place. The increase in precipitation rate is linked with the development of the mesohigh behind the gust front as can be seen in Figure 5.32 (the position of the mesohigh is marked with an 'H'). The precipitation maximum moves northeastward behind the gust front (parallels the movement of the mesohigh) and increases from $170mm(hr)^{-1}$ at 0025:30 to $190mm(hr)^{-1}$ at 0036. After 0045, maximum precipitation rates reach $210mm(hr)^{-1}$ along the southwest quadrant of the rotating comma head structure (not shown).

Although the simulated system is not nearly as large as long-lived squall lines and bow-echoes, some of the model results discussed above are consistent with previous idealized

modeling results of squall lines and bow-echoes. Shortly before the system transitions into a bow echo, the precipitation rate increases in a portion of the storm, strengthening the cold pool and increasing the high pressure behind the gust front. The pressure gradient increases along the leading edge of the gust front, and the gust front accelerates eastward. As the gust front surges eastward, the convective updrafts along the central portion of the flanking line tilt westward (upshear) with height. As the storms tilt westward, horizontal pressure gradients develop which generate an elevated rear inflow extending 10-15km behind the leading convective line. Although the rear inflow does not extend large distances behind the convective line in the HP supercell as it does in squall lines, it appears that the physical processes responsible for producing the strong elevated winds in the two systems are the same.

5.3 Summary and Discussion

This chapter has documented the evolution of a small convective cluster containing two supercells into an HP supercell which follows the bow-echo life-cycle with a rotating comma head structure. The initial storm (S1) develops at the intersection between an old outflow boundary and a stationary front, and maintains supercell characteristics during its entire lifetime. Other storms later develop to the west of the S1 and some of them also exhibit supercell characteristics at some point during their lifetime. One of these storms (S2) merges with storms along the flanking line of S1, producing a larger convective storm in which S1 becomes the main mesocyclone, and S2 (losing its supercell characteristics) becomes part of a large flanking line.

While the initial storm (S1) starts out as a classical supercell, it evolves into a large storm which has many characteristics of an HP supercell. The storm system exhibited both multi-cell and supercell characteristics which is often observed with HP supercells. Although the available radar summaries had insufficient time resolution to verify or refute the model results, other observations of HP supercells indicate that they are frequently parts of larger convective clusters (Moller et al. 1990). In the simulation, there is heavy precipitation to the west/southwest of the mesocyclone, and the storm evolves into a 'rotating comma head'

structure which has been documented as one of the possible life cycles of an HP supercell. The simulated storm also produced very heavy rain, strong winds, and weak tornadoes (as will be discussed in the next chapter), all of which are common features of HP supercells. The rotation of smaller cells along the gust front and into the main storm updraft has also been observed in some HP supercells. To the author's knowledge, this is the first model simulation of an HP supercell and its transition into a bow-echo.

The simulated bow-echo stage of the HP supercell life-cycle had several features in common with the idealized bow-echo squall line simulations of Weisman (1993) and Skamarock et al. (1994) including midlevel counter-rotating vortices, strong convective updrafts which lean upshear during the bow-echo stage, and an elevated rear inflow into the back side of the bow. An interesting feature seen in this simulation is that vorticity and condensate maxima along the flanking line moved northward along the flanking line and appeared to merge into the mesocyclone at the northern end of the convective line. Trajectory calculations also confirmed this. Thus the flanking line appears to be a source of vorticity for the mesocyclone in this case. In the long-lived simulated squall lines, the cyclonic vortex at the northern end of the line eventually becomes dominant. This is usually attributed to the convergence of earth's vorticity enhancing the cyclonic vortex (Skamarock et al., 1994) over a period of 6-10 hours. In the present simulation, the cyclonic vortex at the northern end of the line also becomes dominant, but over a time scale of less than an hour, which isn't a long enough time for the convergence of planetary vorticity to make a significant contribution. It is proposed that positive vorticity which is generated along the flanking line and advected into the mesocyclone could contribute to the dominance of the cyclonic vortex.

In the model simulations, it appears that the interaction between convective cells was important in the transition of the storm into a rotating comma-head structure (the environmental conditions ahead of the storm did not change significantly either just prior to, or during the transition.) Shortly after merger of S2 with the flanking line of S1, the precipitation rate increased significantly, increasing the pressure behind the gust front. This led to an acceleration of the gust front and caused convective cells along the center of the

flanking line to lean westward with height, creating horizontal pressure gradients which accelerate the winds into the back side of the bow. This evolution is similar to the idealized bow-echo squall line simulations of Weisman (1993), but on a much smaller scale. Although HP supercells are frequently a part of larger convective clusters, this is not always the case. Documentation exists in the literature regarding possible life cycles of HP supercells, but there is no breakdown as to whether HP supercells which are parts of larger convective clusters are more likely to evolve into bow-echoes than those which are relatively isolated. However, one could envision other processes (besides cell merger) which could increase the precipitation and/or evaporation and strengthen the cold pool beneath the storm.

Since the storm evolution into a bow-echo structure occurred in the hour following the addition of Grids #5 and #6, the simulation begs the question: 'is this the actual evolution of the system, or did the sudden addition of Grid #5 cause the solution to deviate into the bow-echo life cycle of an HP supercell?' To answer this question, the simulation was run from 0000 UTC to 0100 UTC without Grids #5-6 to see if the storm would evolve similarly in Grid #4. The Grid #4 results (not shown) looked like a 'smoothed out' version of the Grid #5 results (as expected, since Grid #4 has coarser grid spacing and is not able to capture as many details as Grid #5), indicating that the evolution of the storm into a bow-echo was not a result of the addition of finer grids during the simulation.

Even though the storm emits a very large amplitude deep tropospheric gravity wave just prior to the storm's transition into a bow-echo, the gravity wave does not appear to contribute to the strong inflow behind the storm (even though some idealized squall line simulations have linked gravity wave propagation upstream of the convective line to the development of the rear inflow jet behind the convective line). In the present simulation, the upstream propagating gravity does not propagate very far from the convective line before becoming a standing wave (with respect to the surface). The upstream wave had a much smaller amplitude than the downstream propagating wave and resembled the upward branch of the m=1 mode discussed by Nicholls et al. (1991) and Mapes (1993). Perhaps environments which allow the propagation of the gravity waves upstream away from the storm marks the difference between environments which can support the larger MCC systems (in

which deep tropospheric convectively generated gravity waves can propagate large distances upstream of the convection) and environments which support isolated storms and smaller convective clusters (in which deep tropospheric gravity waves cannot propagate upstream of the convection). However, this idea requires further investigation.

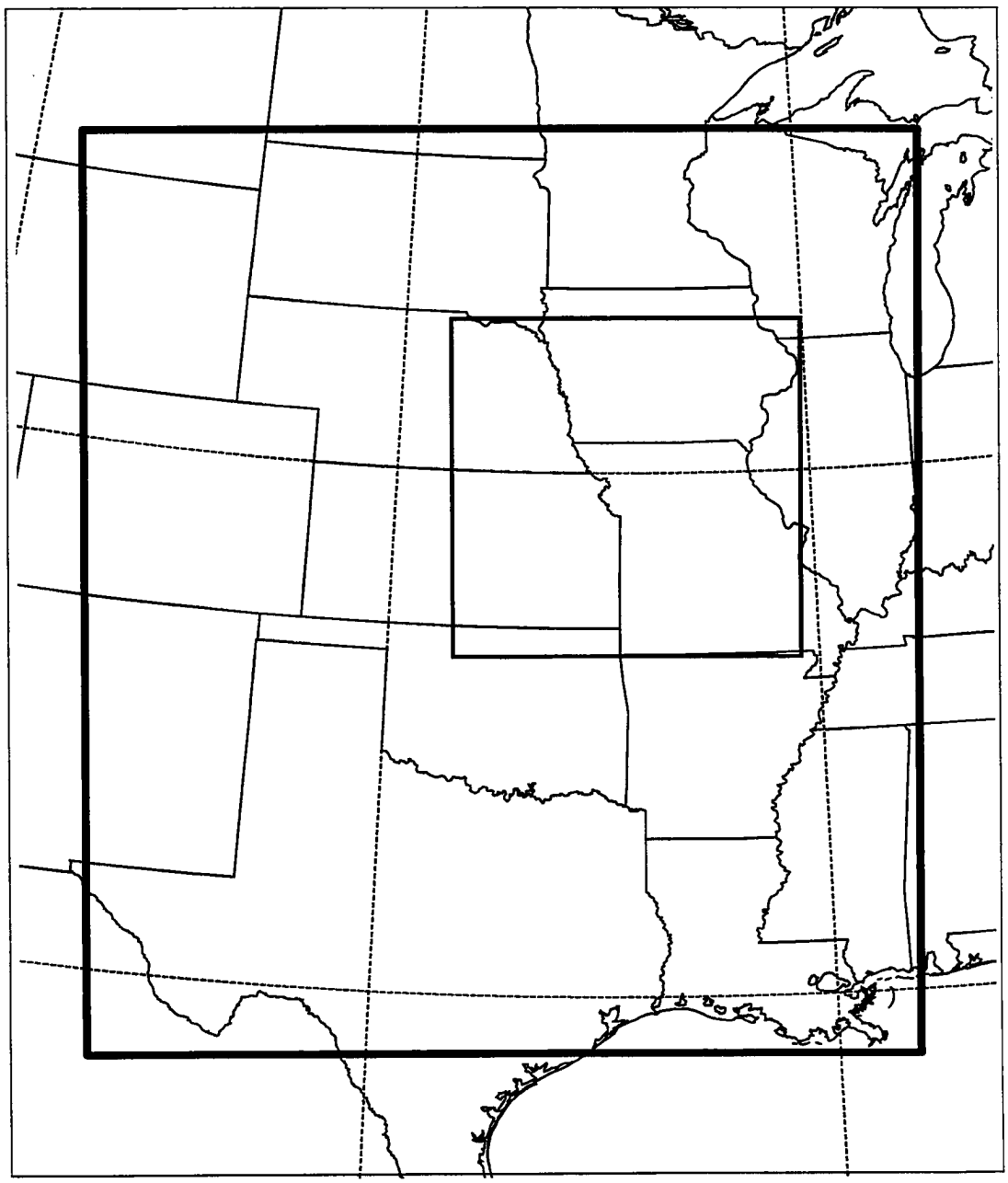

Figure 5.1: Areal outline of the interior nudging region used in the simulation. The bold outline denotes the boundaries of Grid #2. The finer outline denotes the boundaries of the nudging region used in the simulation.

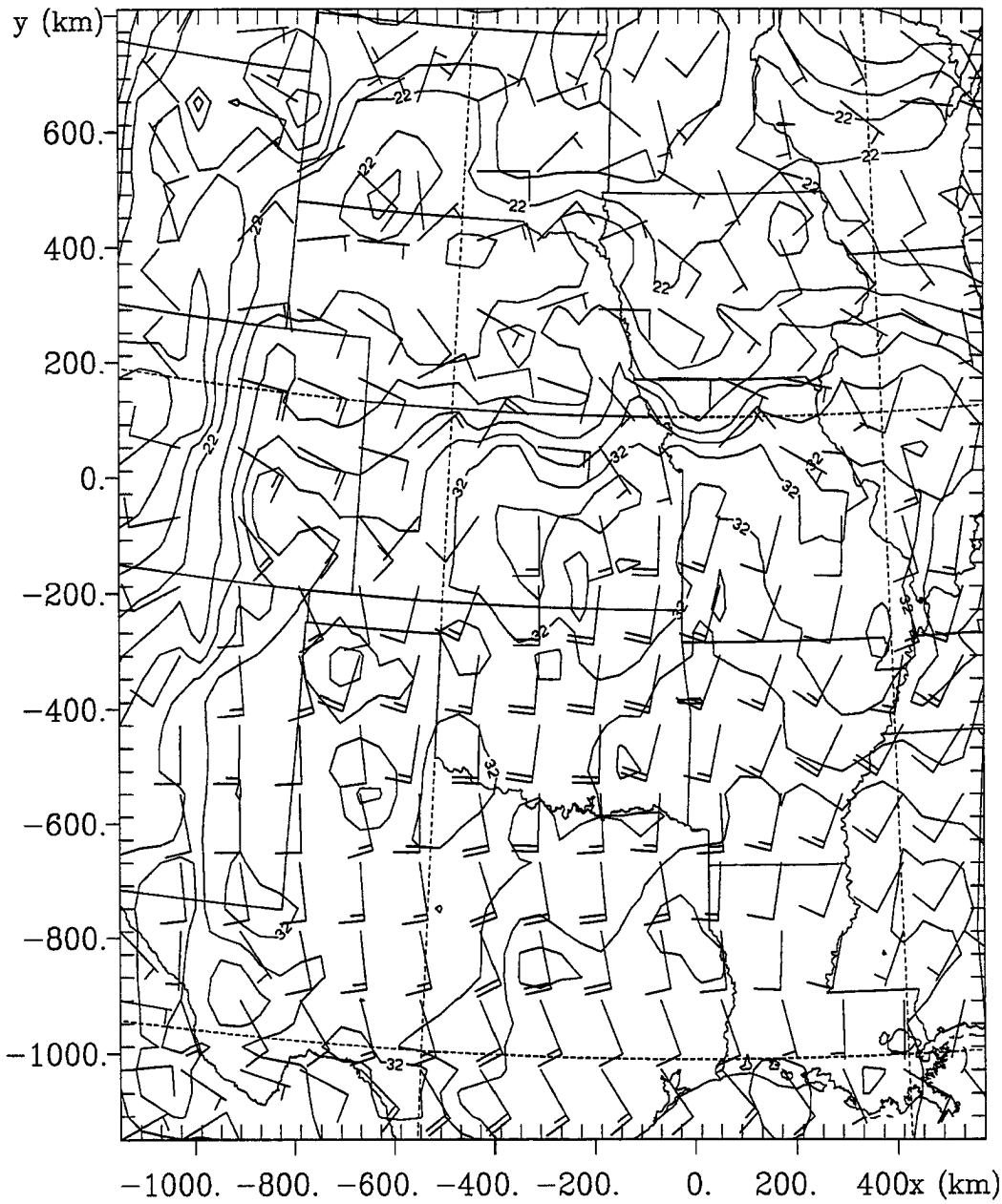

Figure 5.2: Winds and temperature field on Grid #2 at 38m above the surface at 2100 UTC one hour after interior nudging was turned off in the simulation. Wind barbs are plotted at every third model grid point. The short (long) flag on the wind barb represents $2ms^{-1}$ ($4ms^{-1}$). Temperature is contoured every 2°C.

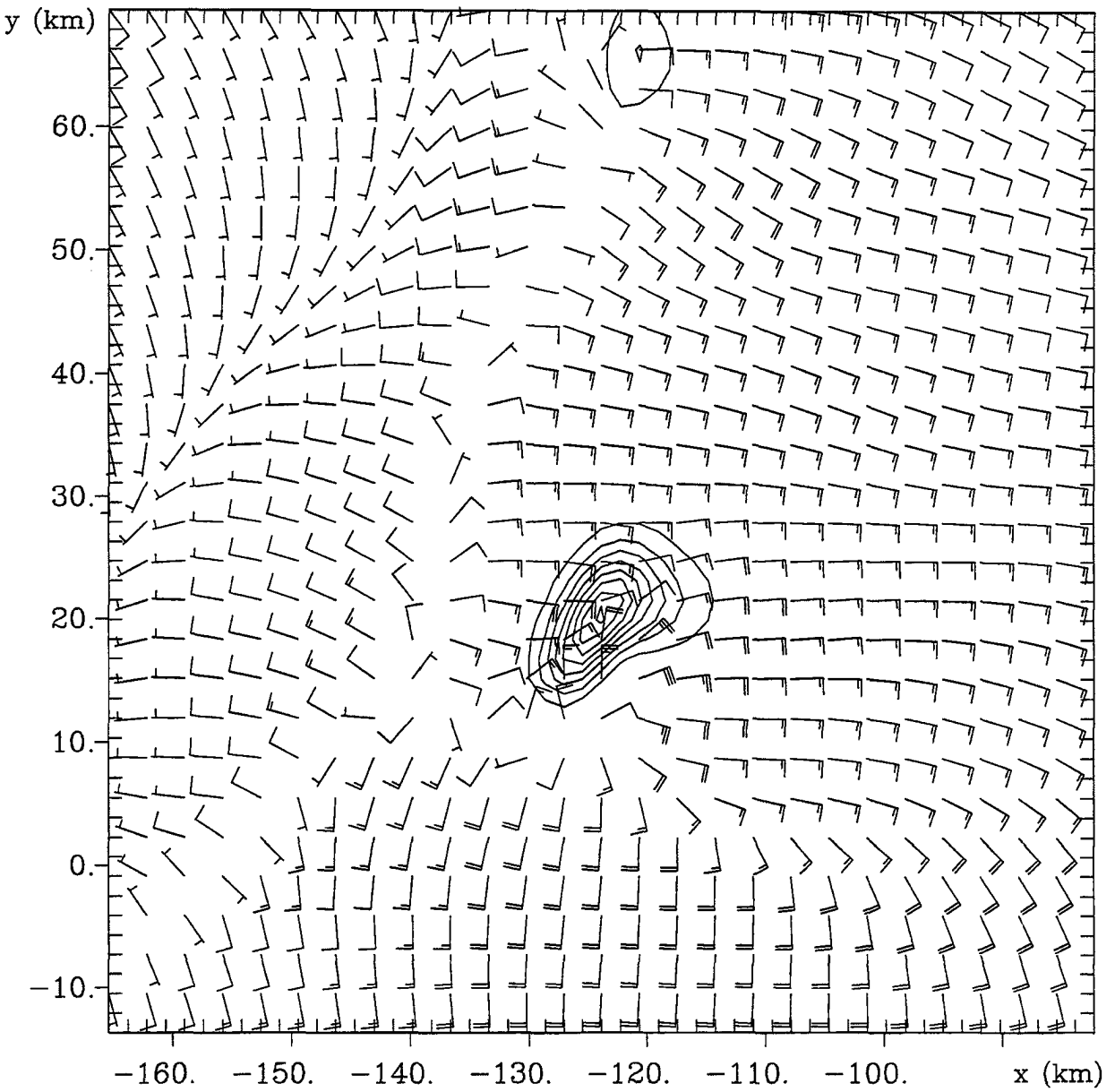

Figure 5.3: Winds and condensate mixing ratio 38m above the surface at 2148 UTC, 20-30 minutes after convection is initiated on Grid #4. Wind barbs are plotted at every other model grid point. The short (long) flag on the wind barb represents $2ms^{-1}$ ($4ms^{-1}$). Condensate mixing ratio is contoured every $0.25g(kg)^{-1}$.

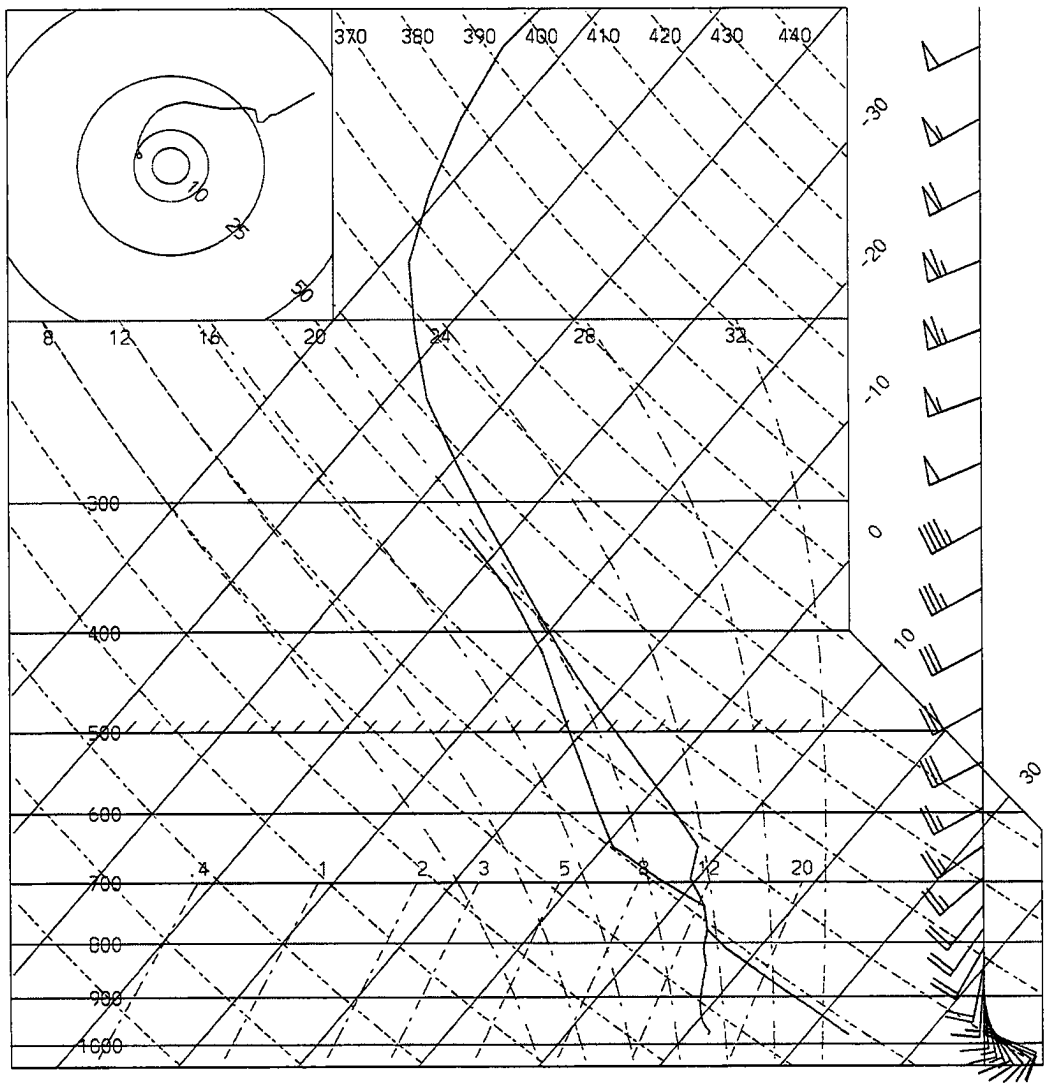

Figure 5.4: A vertical sounding and hodograph taken at 2040 UTC on Grid #4. Convection began to develop in the simulation just north of this point about 20 minutes later.

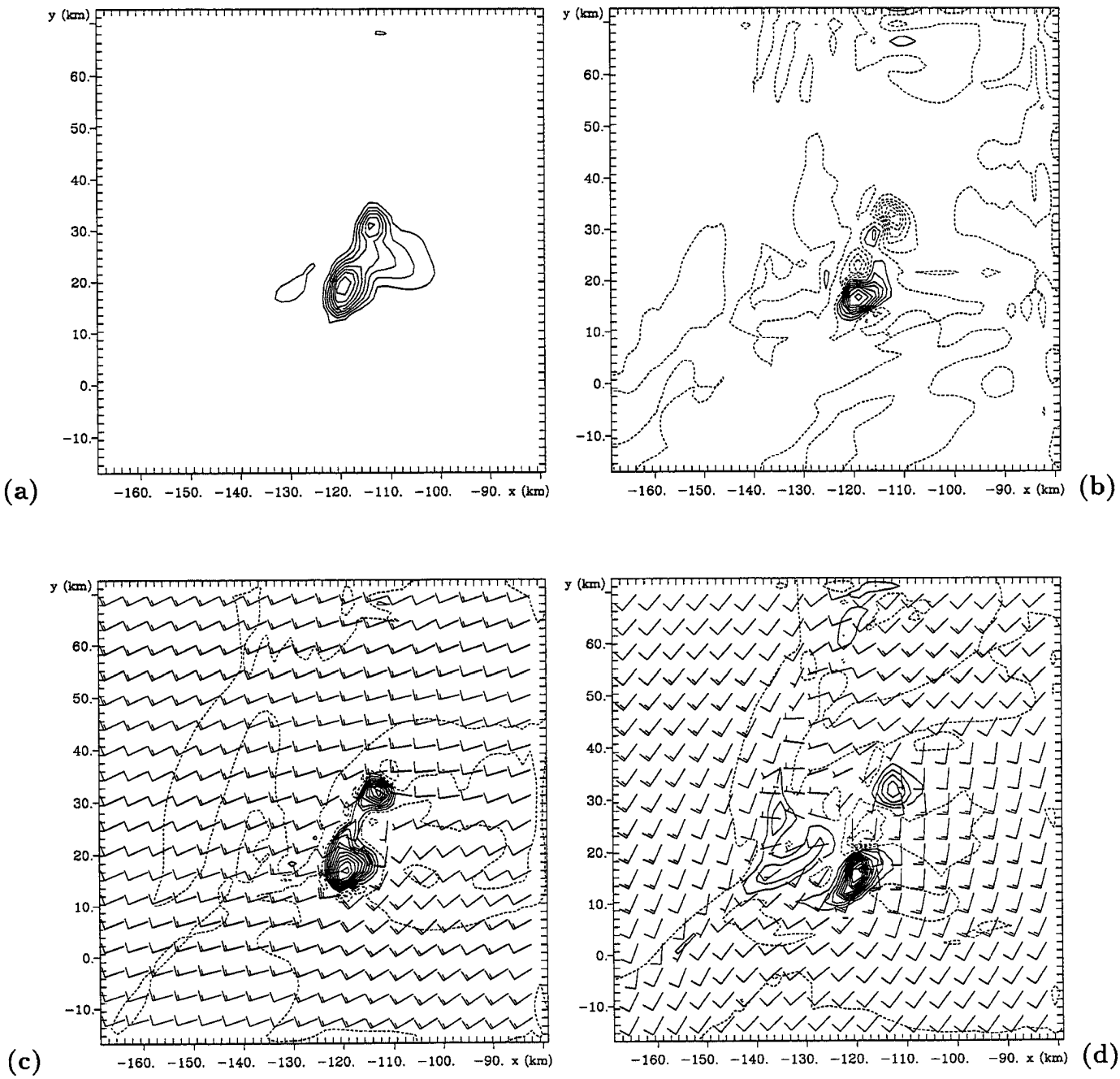

Figure 5.5: Model fields on Grid #4 at 2200 UTC shortly after the first storm splits. (a) Condensate field at z=4.3km, (b) vertical vorticity field at z=4.3km, (c) vertical velocity field overlayed with horizontal winds at z=4.3km, (d) vertical velocity field overlayed with horizontal winds at z=1.7km. Condensate mixing ratio is contoured every $1g(kg)^{-1}$. Vorticity contour interval is 0.001 s^{-1}. Vertical velocity is contoured every $2ms^{-1}$ at z=4.3km, and every $1ms^{-1}$ at z=1.7km. Wind barbs are plotted at every third grid point. The short (long) flag on the wind barb represents $5ms^{-1}$ ($10ms^{-1}$). Dashed contours indicate negative values.

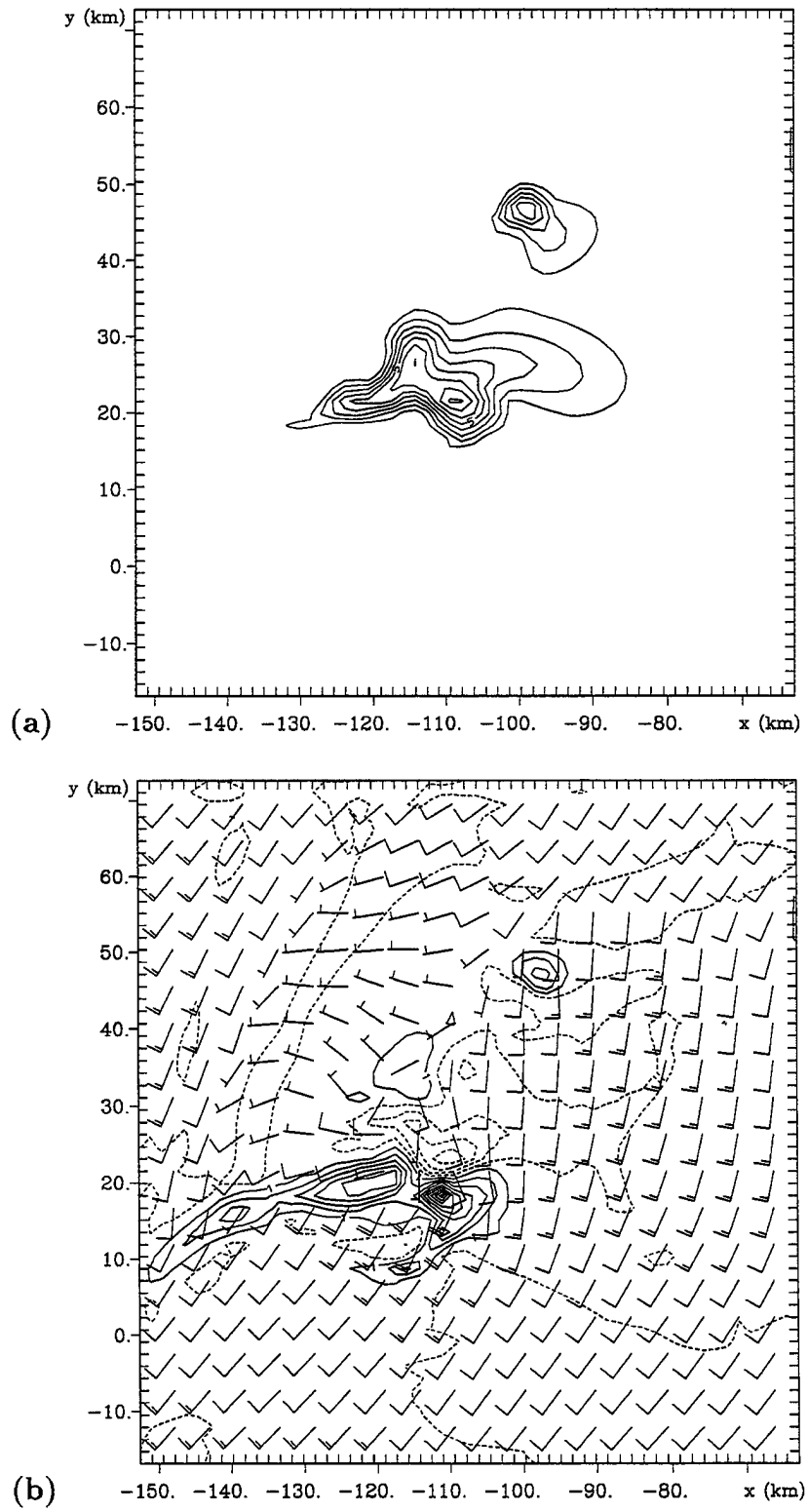

Figure 5.6: Condensate field on Grid #4 at 2227 UTC at z=4.3km (a), and vertical velocity field overlayed with horizontal winds at 2227 UTC at z=1.7km (b). Condensate contour interval is $1g(kg)^{-1}$. Vertical velocity is contoured every 1 ms^{-1} (dashed contours indicate negative values. Wind barbs are plotted at every third grid point. The short (long) flag on the wind barbs indicates $5ms^{-1}$ ($10ms^{-1}$).

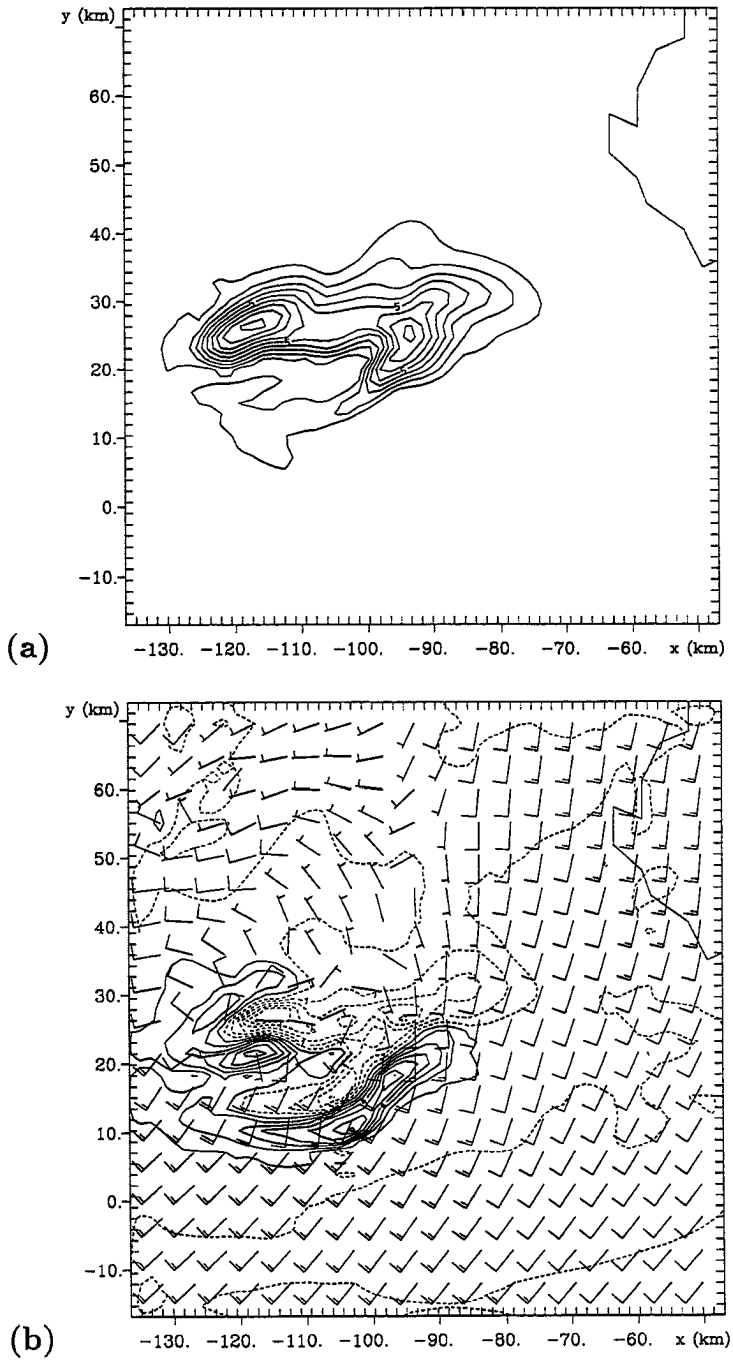

Figure 5.7: Continued storm evolution on Grid #4 at 2307 UTC. (a) Condensate field at z=4.3km, (b) vertical velocity field overlayed with horizontal winds at z=1.7km. Condensate mixing ratio contour interval is $1g(kg)^{-1}$. Vertical velocity is contoured every $1ms^{-1}$ (dashed contours indicate negative values). Wind barbs are plotted at every third grid point. The short (long) flag on the wind barbs indicates $5ms^{-1}$ ($10ms^{-1}$).

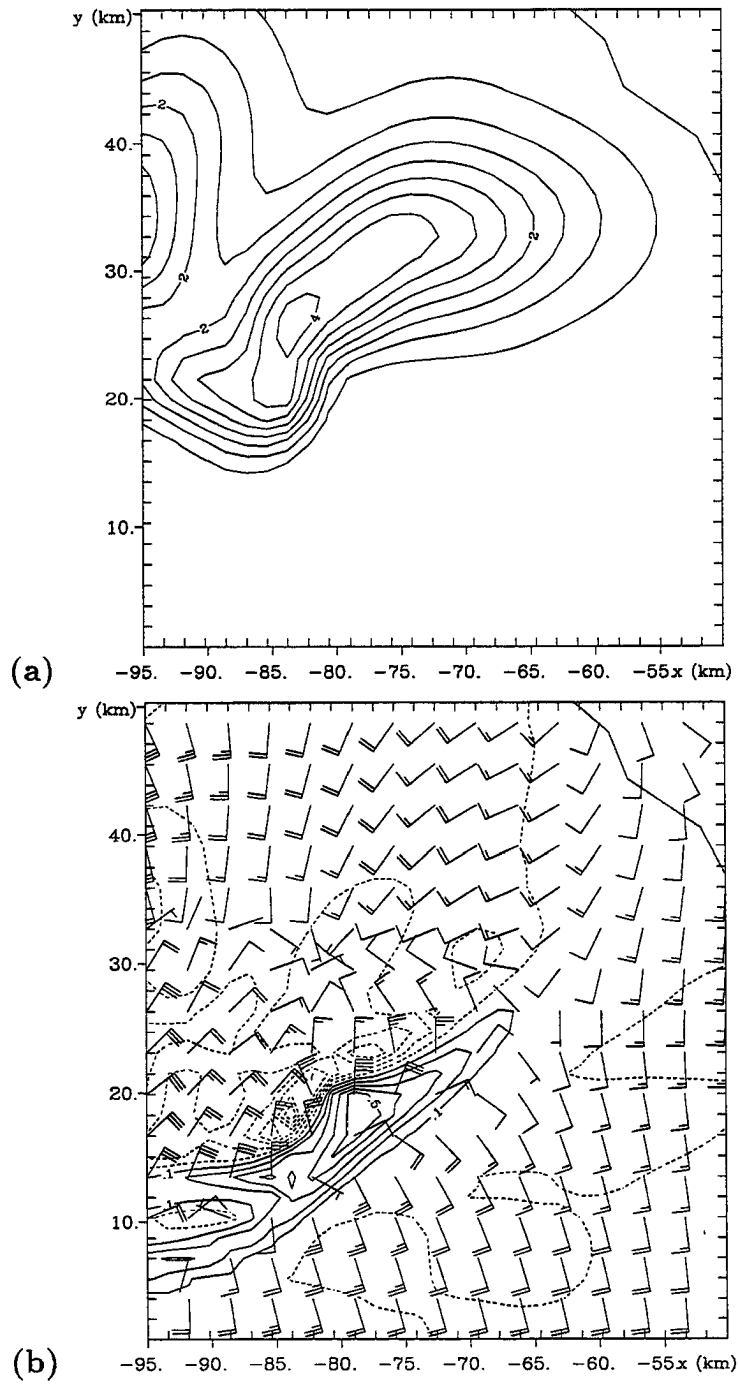

Figure 5.8: Condensate field on a subset of Grid #4 (zoomed in on S1) at 2348 UTC (a), and vertical velocity field overlayed with horizontal winds z=38m (b). Condensate mixing ratio contour interval is $0.5g(kg)^{-1}$. Vertical velocity is contoured every 10 $(cm)s^{-1}$ (dashed contours indicate negative values). Wind barbs are plotted at every other grid point. The short (long) flag on the wind barbs indicates wind speeds of $2ms^{-1}$ ($4ms^{-1}$). Note that there is heavy precipitation to the west of the updraft.

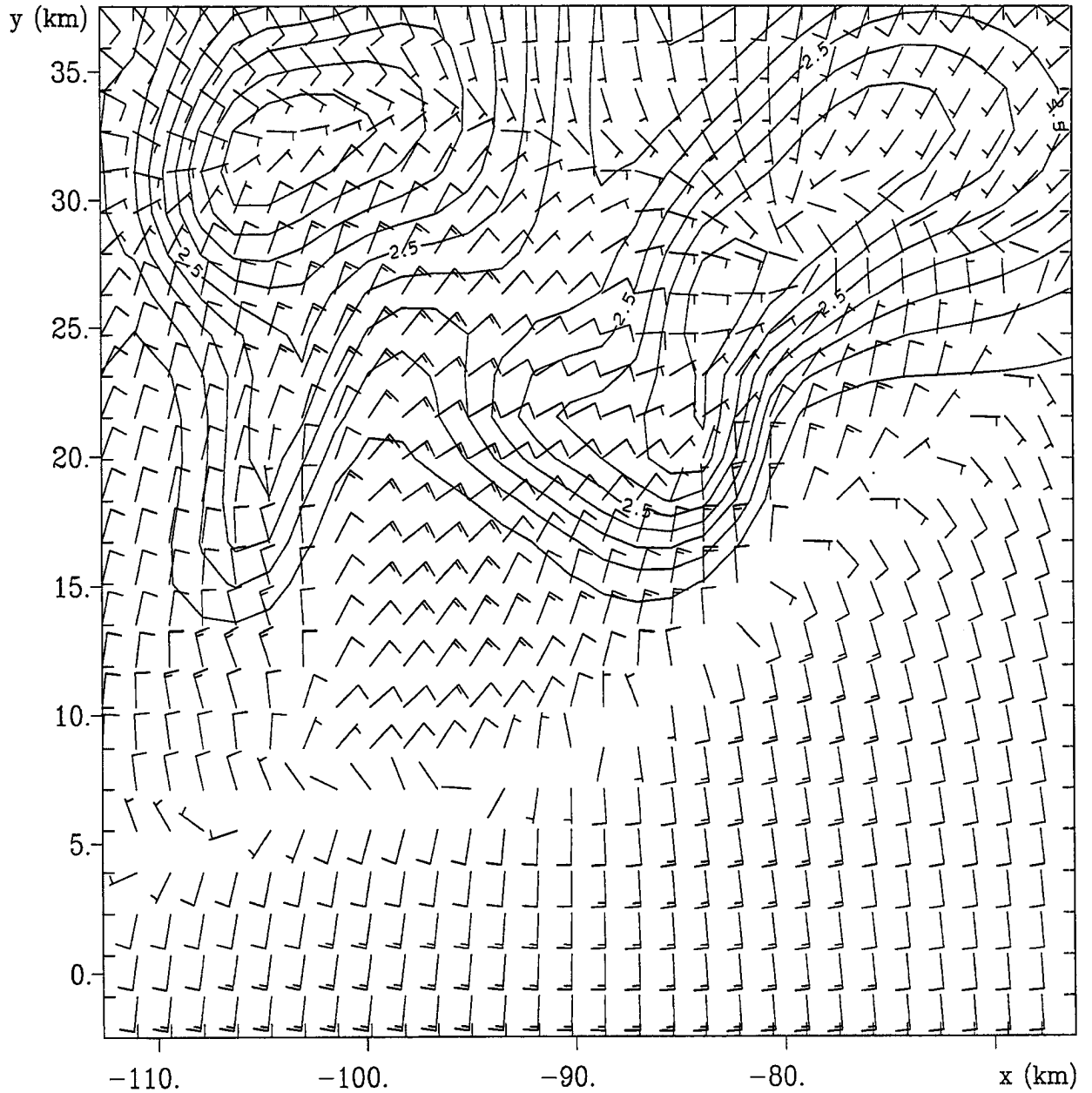

Figure 5.9: Horizontal winds and condensate fields 125m above the surface at 2348 UTC for a subset of Grid #4 (zoomed in on the area surrounding S1 and S2). Note the convergence zone extending south of S2 (the western storm). Wind barbs are plotted at every model grid point. The short (long) flag on the wind barb represents $5ms^{-1}$ ($10ms^{-1}$). Condensate mixing ratio is contoured every $0.5g(kg)^{-1}$.

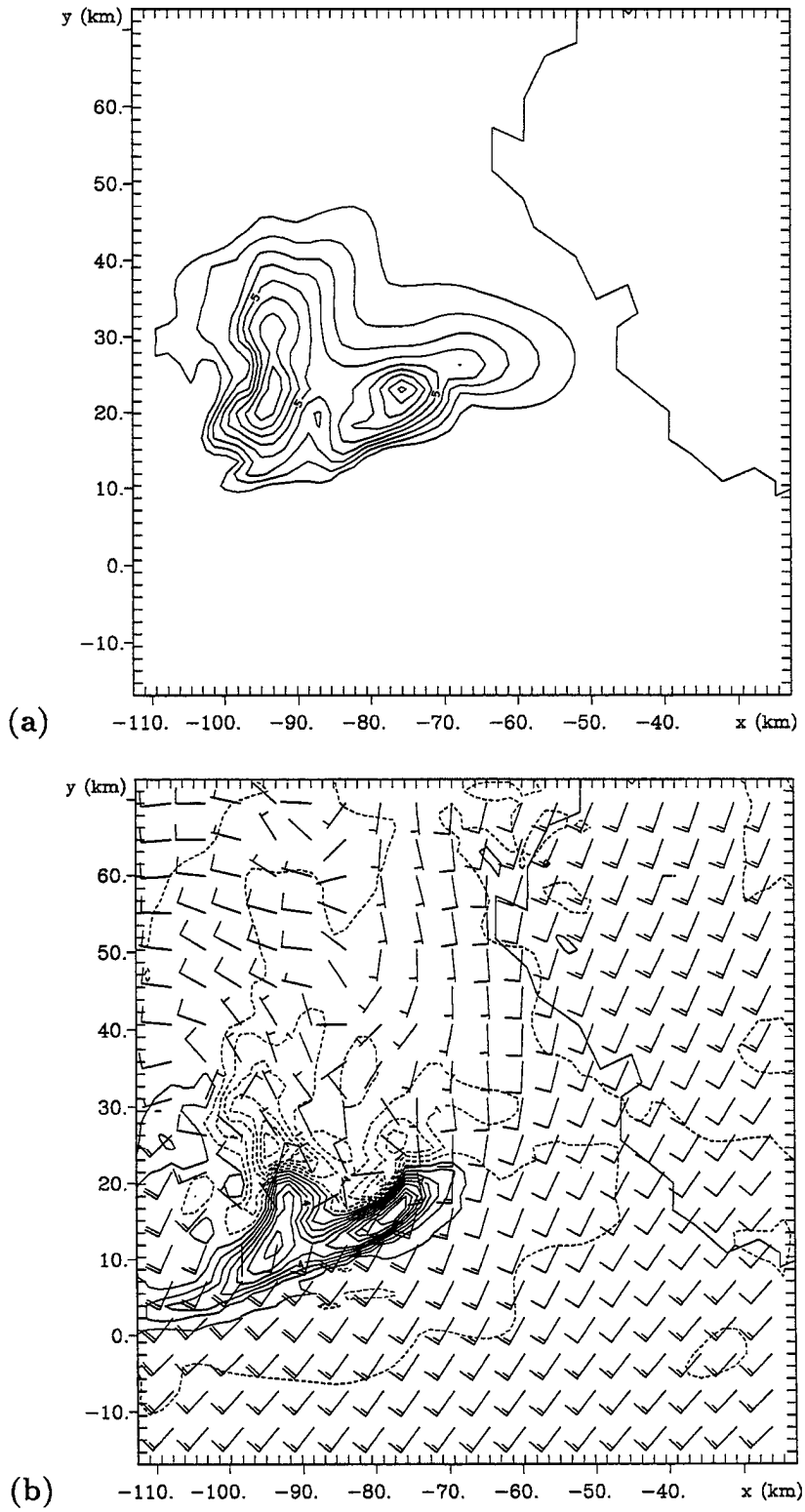

Figure 5.10: Storm evolution on Grid #4 at 0000 UTC July 1. (a) Condensate field at z=4.3km, (b) vertical velocity field overlayed with horizontal winds at z=1.7km. Condensate mixing ratio contour interval is $1g(kg)^{-1}$. Vertical velocity is contoured every $1ms^{-1}$ (dashed contours indicate negative values). Wind barbs are plotted at every third grid point. The short (long) flag on the wind barbs indicates $5ms^{-1}$ ($10ms^{-1}$).

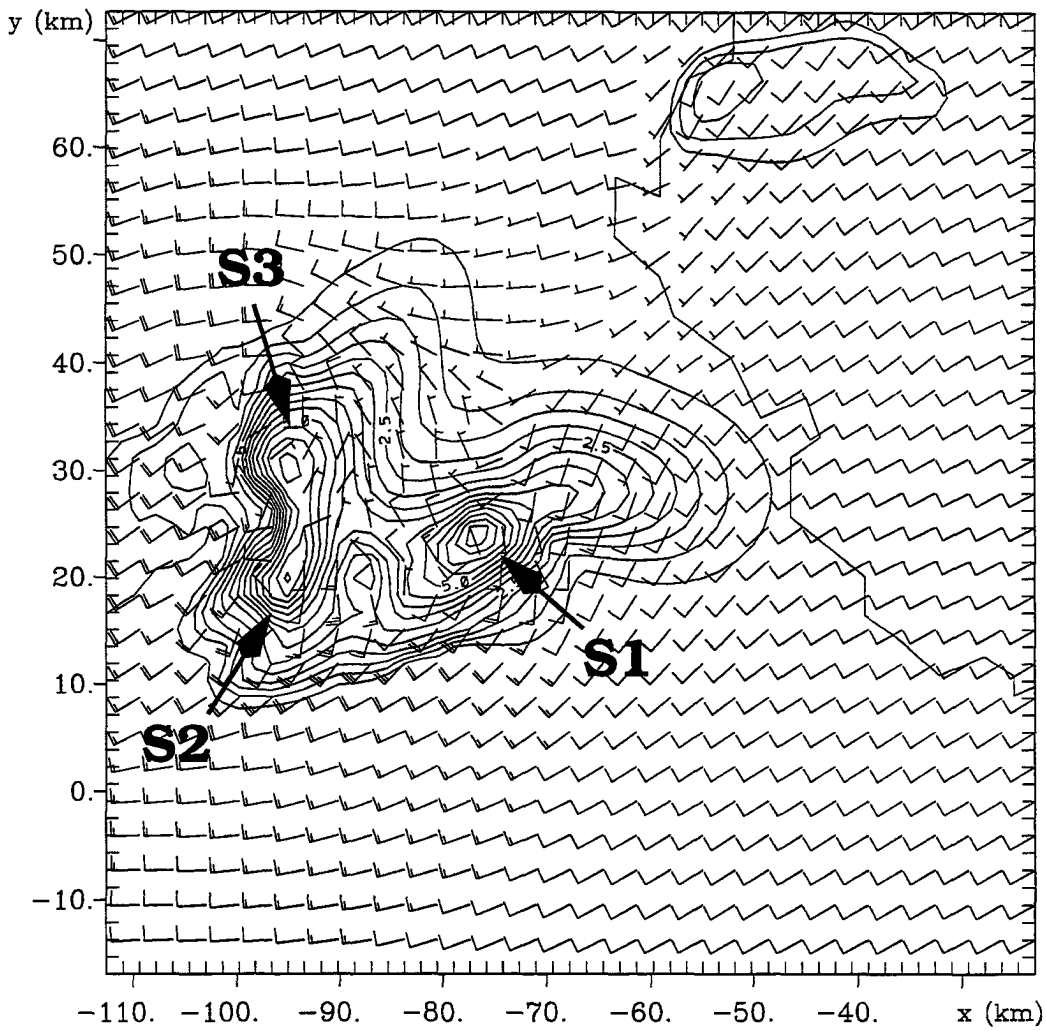

Figure 5.11: Condensate field overlayed with wind barbs at 0000 UTC at z=2.9km on Grid #5. Note that S1 and S2 are rotating cyclonically, while S3 is rotatating anticyclonically. Condensate mixing ratio is contoured every $0.5g(kg)^{-1}$. The short (long) flag on the wind barbs denotes a speed of 5 ms^{-1} (10 ms^{-1}). Wind barbs are plotted at every other grid point.

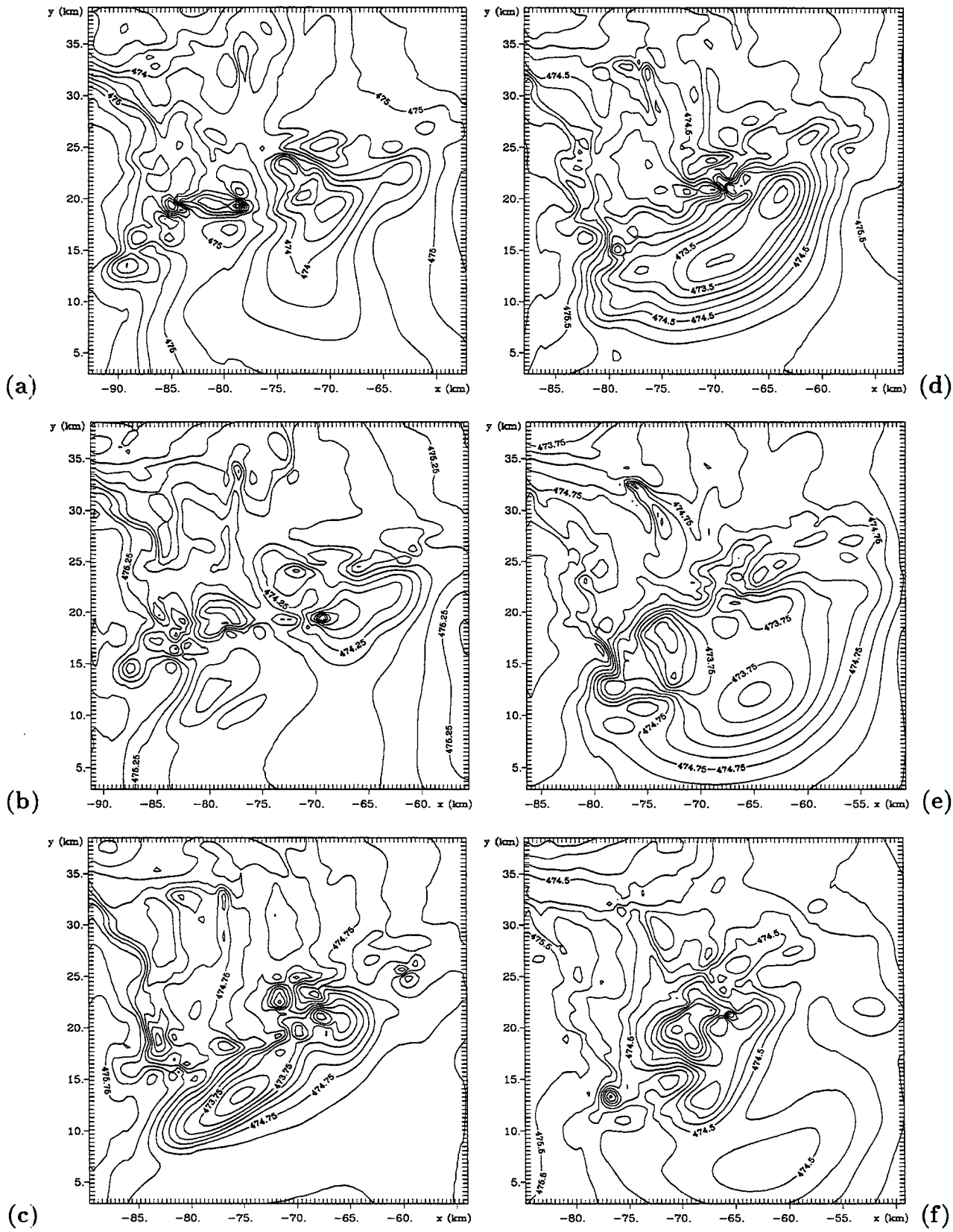

Figure 5.12: Evolution of the pressure field (contour interval 0.25mb) 6.1km above the surface at (a) 0013:30 UTC, (b) 0016:30 UTC, (c) 0019:30 UTC, (d) 0022:30 UTC, (e) 0025:30 UTC, (f) 0028:30 UTC. Note the large gravity wave that propagates away from the storm between 0020-0030 UTC.

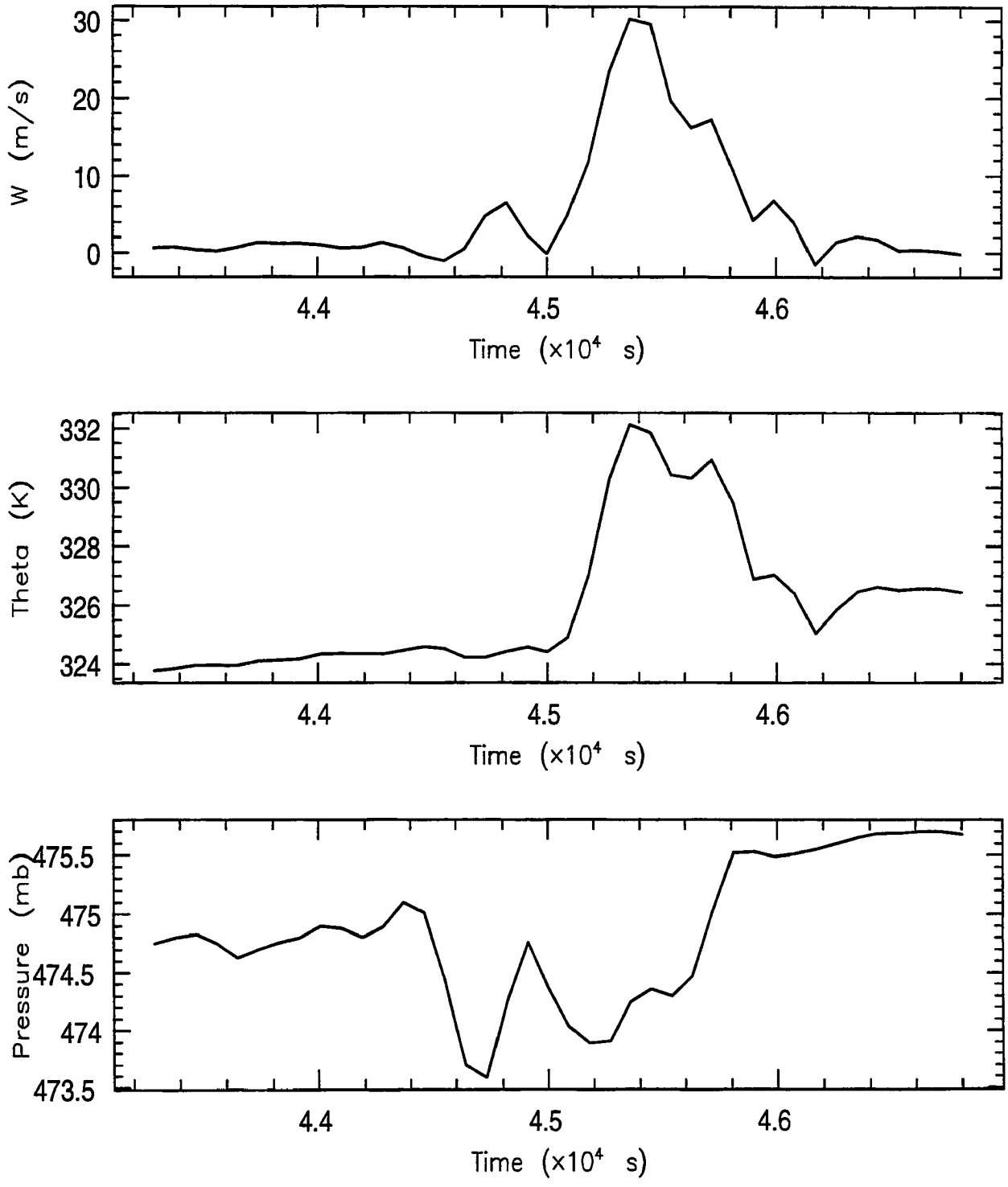

Figure 5.13: Time series of vertical motion, potential temperature, and pressure at z=3km at a point on Grid #4 which is downstream of the storm when the gravity wave is emitted. The gravity wave passes the point between approximately 0020-0030 UTC (44400s-45000s). The storm passes the point around 0037 UTC (45400s).

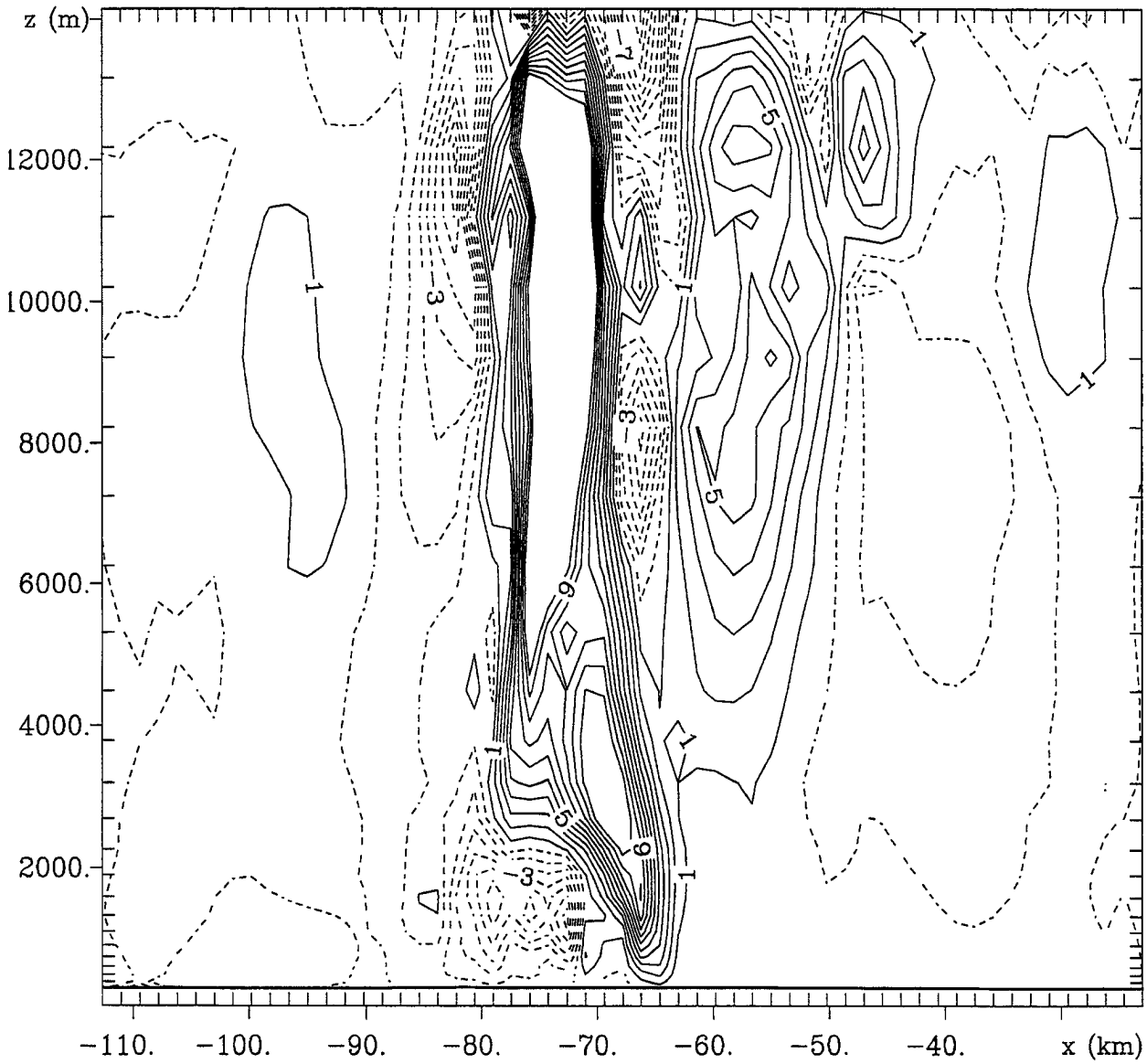

Figure 5.14: A vertical cross section of the vertical motion field on Grid #4 at 0030 UTC through the center of the gravity wave. Vertical motion is contoured every $1ms^{-1}$ (some of the contours in the convective tower have been omitted for clarity). The gravity wave is located at x=-58km. The storm is located between x=-65km to x=-80km. Dashed contours denote negative values.

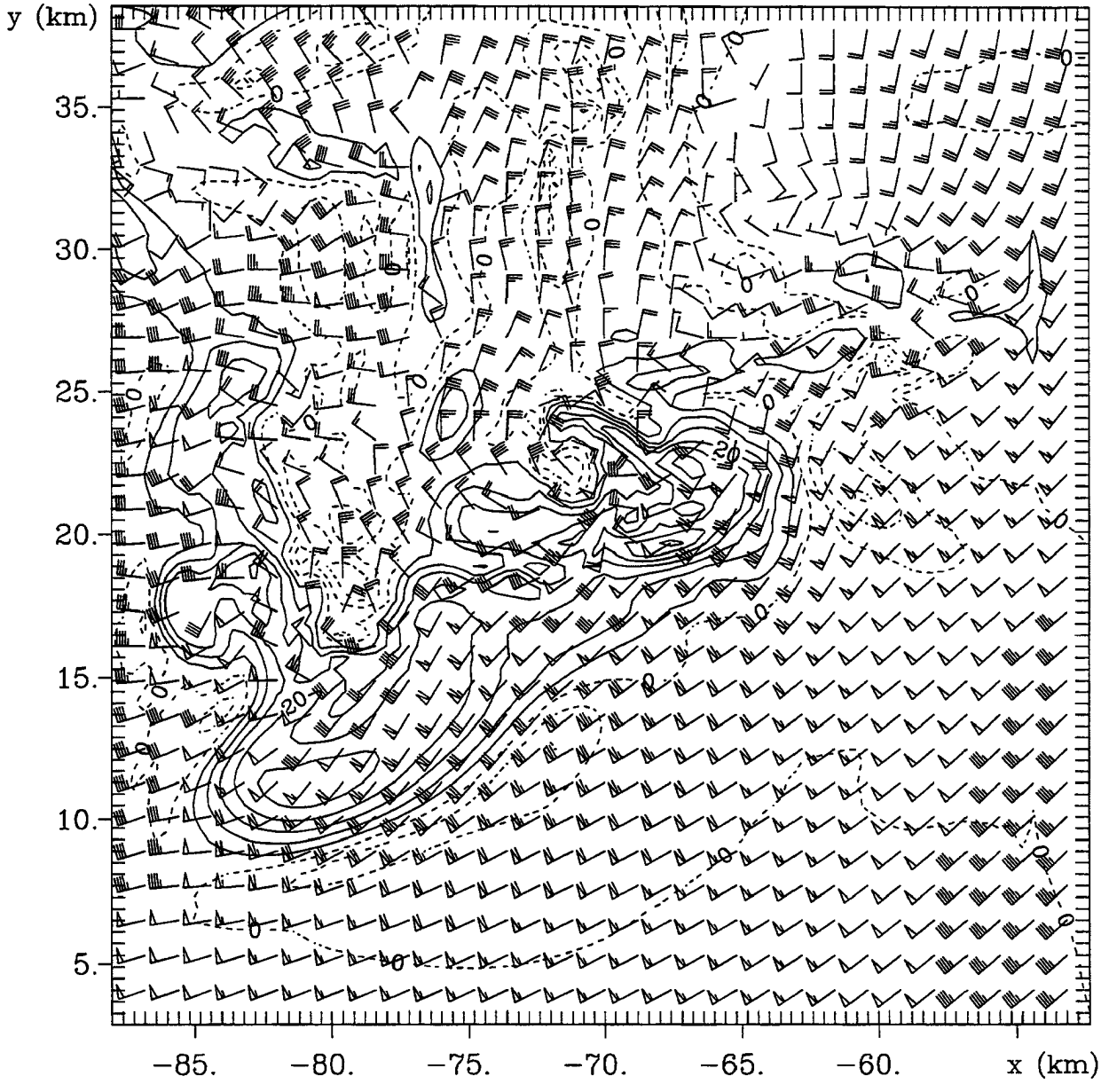

Figure 5.15: Horizontal cross section of horizontal winds (barbs) and vertical velocities (contours) 6.1km above the surface at 0021 UTC on Grid #5. Wind barbs are plotted at every third model grid point. The short (long) flag on the wind barb represents $5ms^{-1}$ ($10ms^{-1}$). The open flag on the wind barb represents a wind speed of $50ms^{-1}$. Vertical velocity is contoured every $5ms^{-1}$. Dashed contours denote negative vertical velocities.

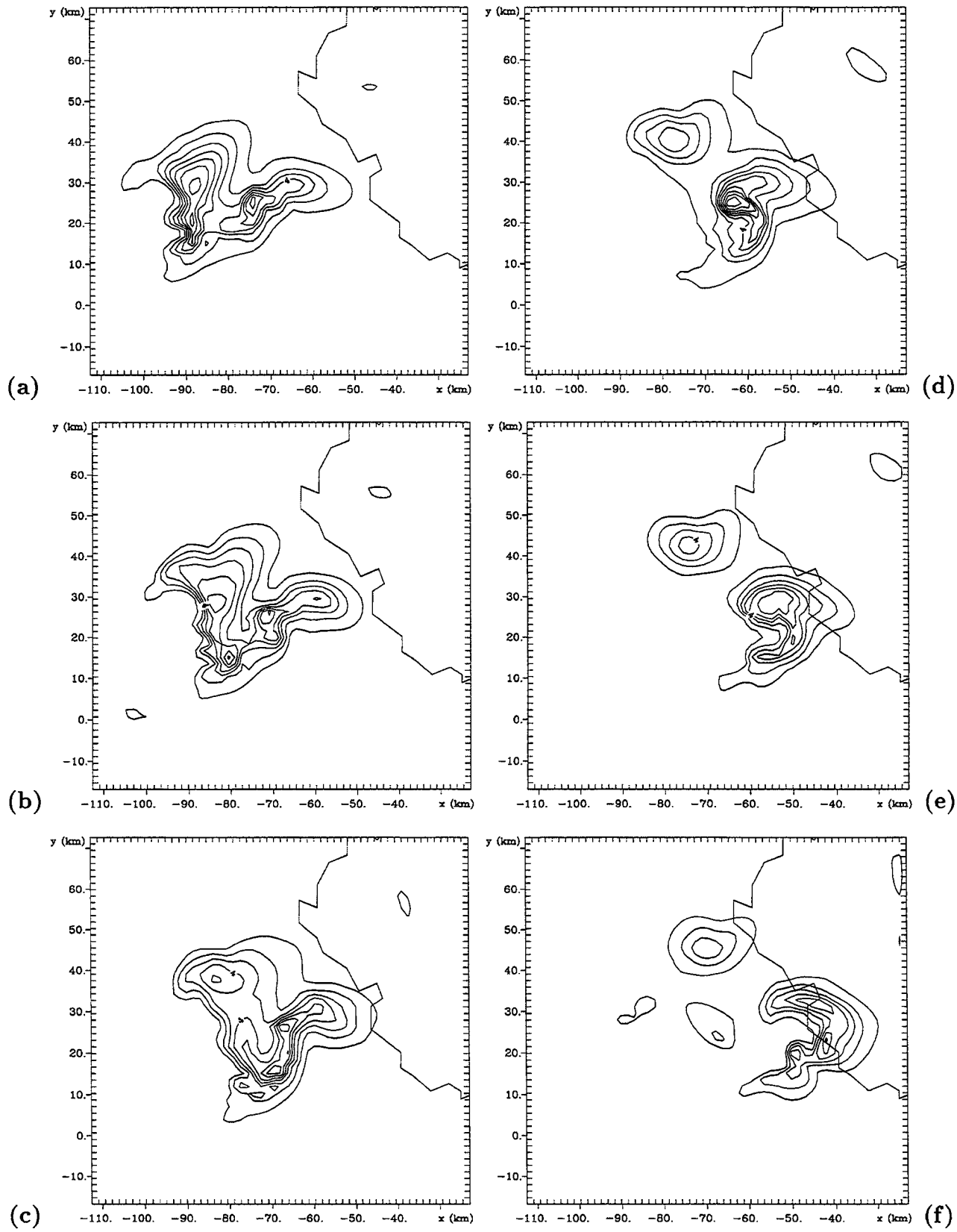

Figure 5.16: Evolution of the condensate field (contour interval $1g(kg)^{-1}$) at 2.5km above the surface on Grid #4 at (a) 0010:30 UTC, (b) 0019:30 UTC, (c) 0030 UTC, (d) 0040:30 UTC, (e) 0049:30 UTC, (f) 0100 UTC.

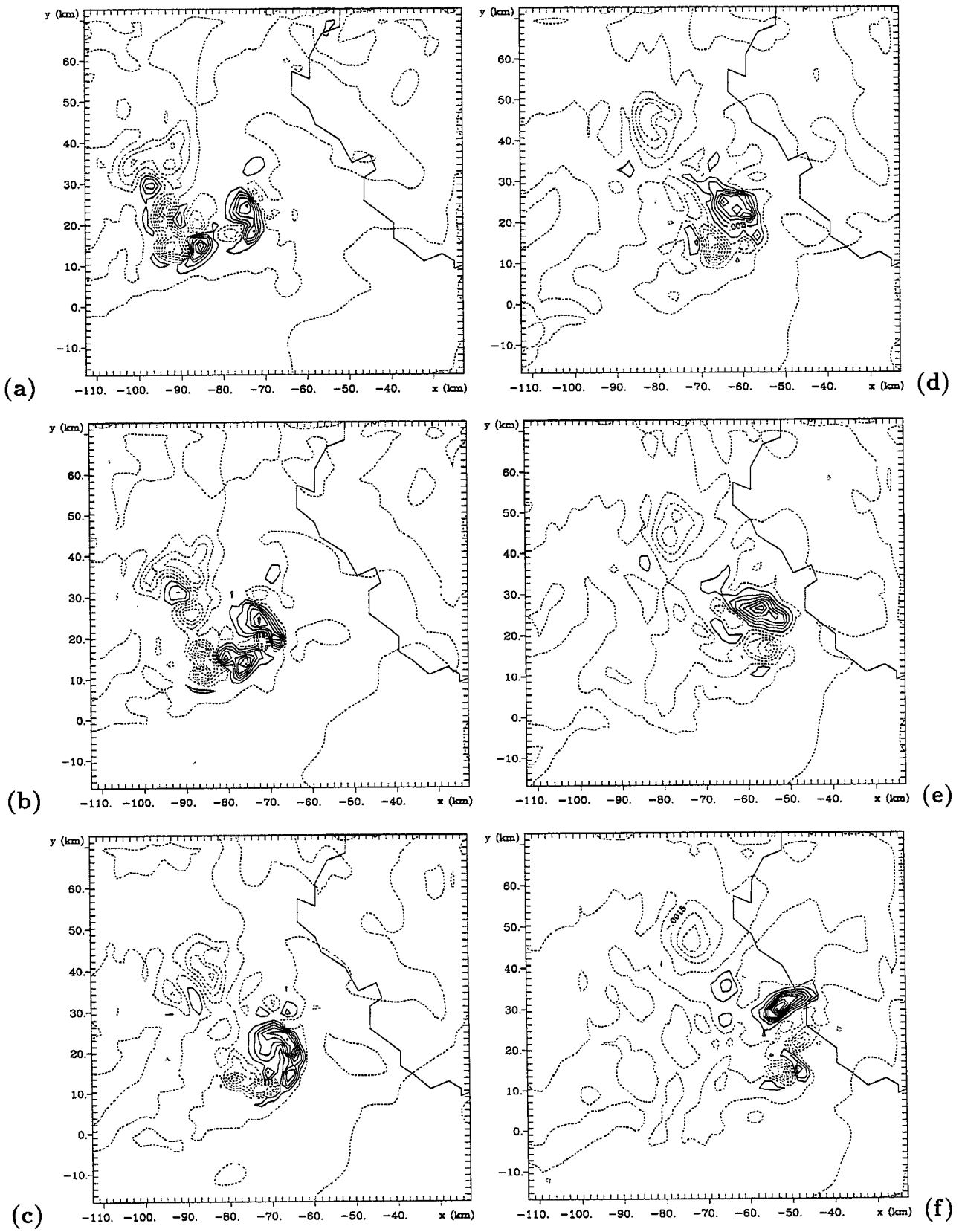

Figure 5.17: Evolution of the vertical vorticity field (contour interval $1.5\times10^{-3}s^{-1}$) at 2.5km above the surface on Grid #4 at (a) 0010:30 UTC, (b) 0019:30 UTC, (c) 0030 UTC, (d) 0040:30 UTC, (e) 0049:30 UTC, (f) 0100 UTC. Dashed contours indicate negative values.

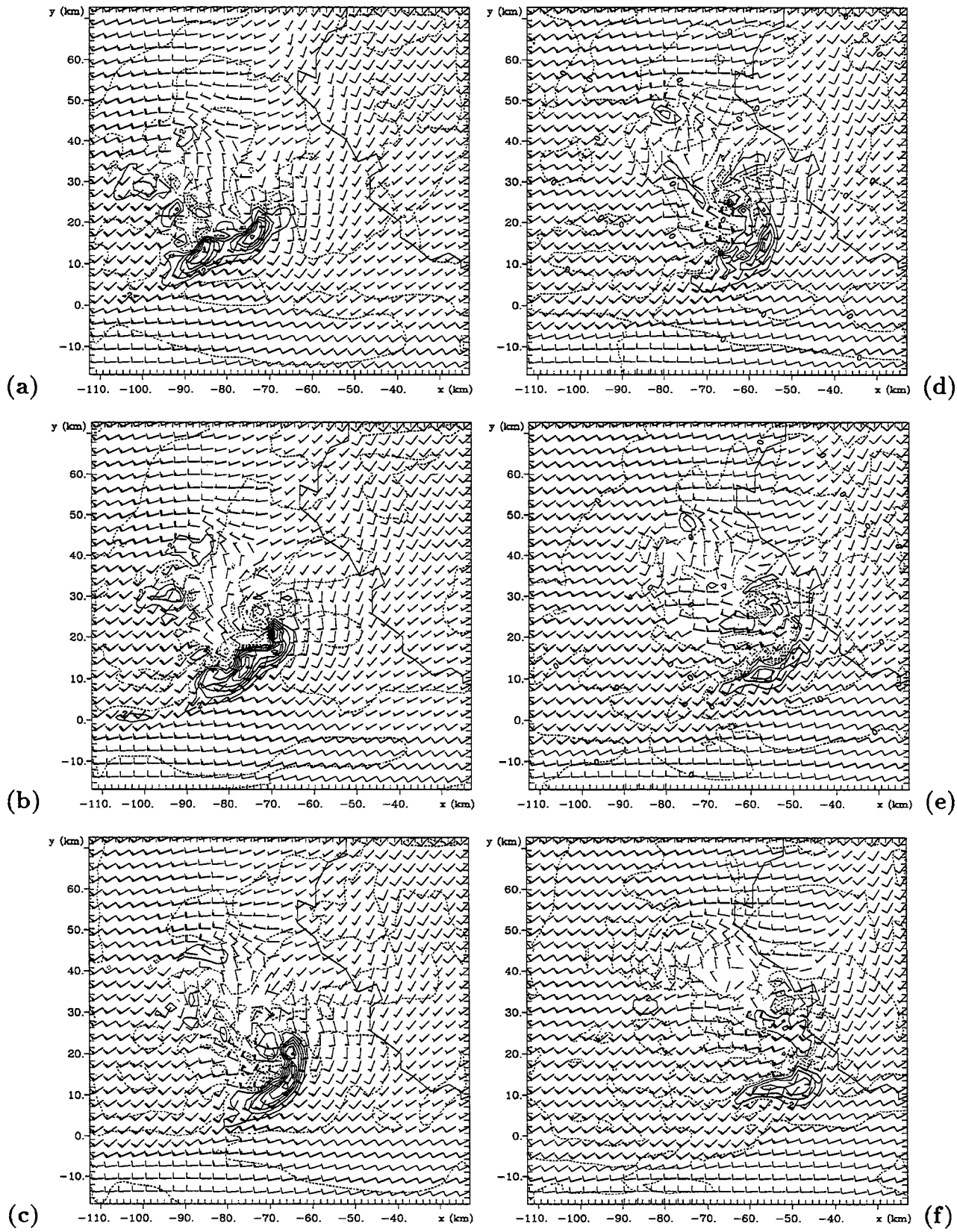

Figure 5.18: Evolution of the vertical and horizontal velocity fields at 2.5km above the surface on Grid #4 at (a) 0010:30 UTC, (b) 0019:30 UTC, (c) 0030 UTC, (d) 0040:30 UTC, (e) 0049:30 UTC, (f) 0100 UTC. Vertical velocity is contoured every $2ms^{-1}$. Dashed contours denote negative values. Wind barbs are plotted at every other grid point. The short (long) flag on the wind barb denotes a horizontal velocity of $5ms^{-1}$ ($10ms^{-1}$).

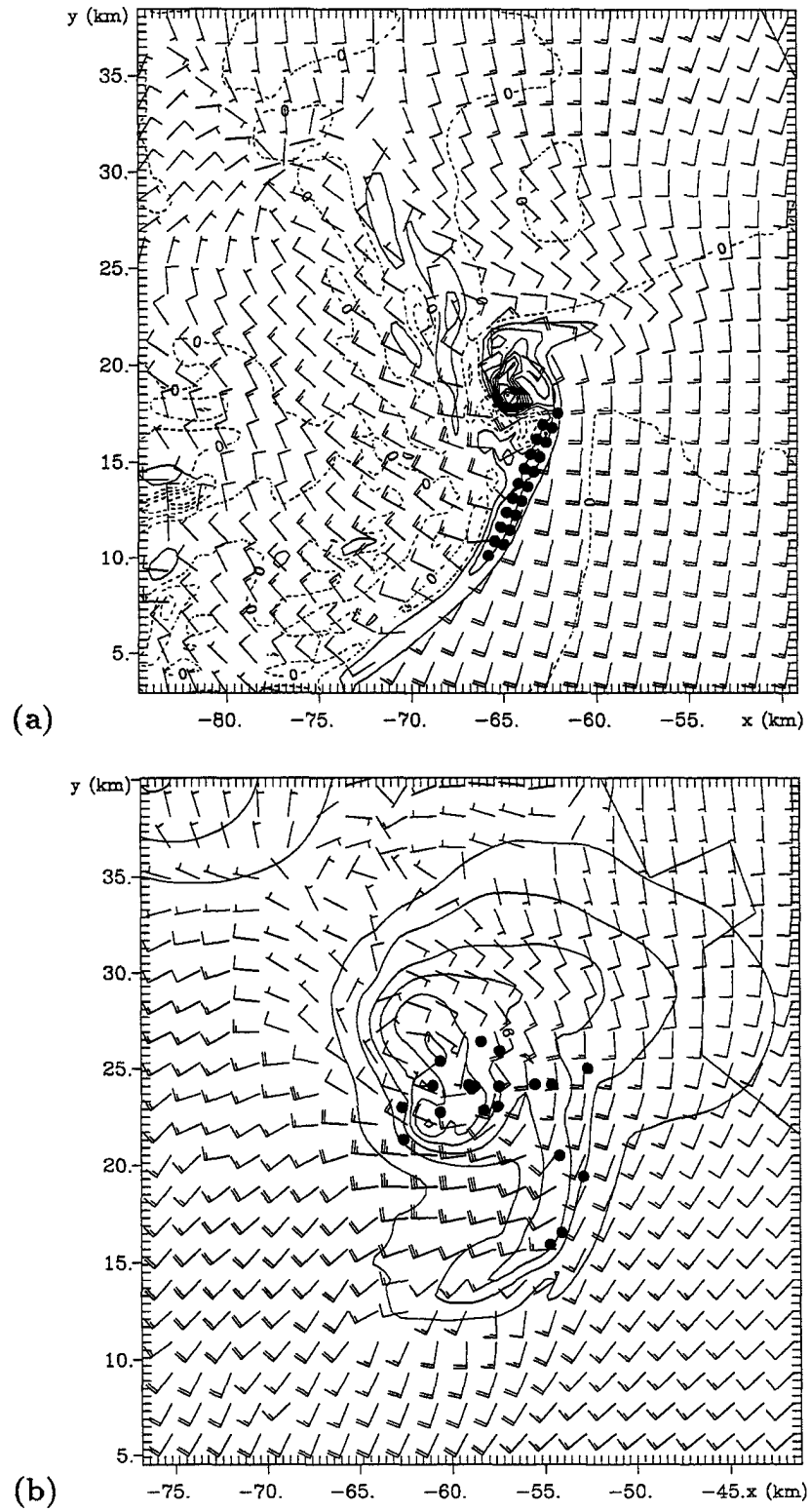

Figure 5.19: Horizontal projections of the inital (a) and final (b) locations of the 20 particles released from the flanking line on Grid #5. (a) Initial particle positions at z=488m overlayed on the vertical vorticity and horizontal wind fields. The particles were all initalized along the flanking line at z=488m as shown. Vertical vorticity is contoured every $5.0\times10^{-3}s^{-1}$. (b) Horizontal projection of the final particle positions overlayed with the total condensate and horizontal wind fields at z=2km at 0045 UTC. Condensate is contoured every $1.5g(kg)^{-1}$. Wind barbs are plotted at every fourth model grid point. The short (long) flag on the wind barb represents a wind speed of $5ms^{-1}$ ($10ms^{-1}$).

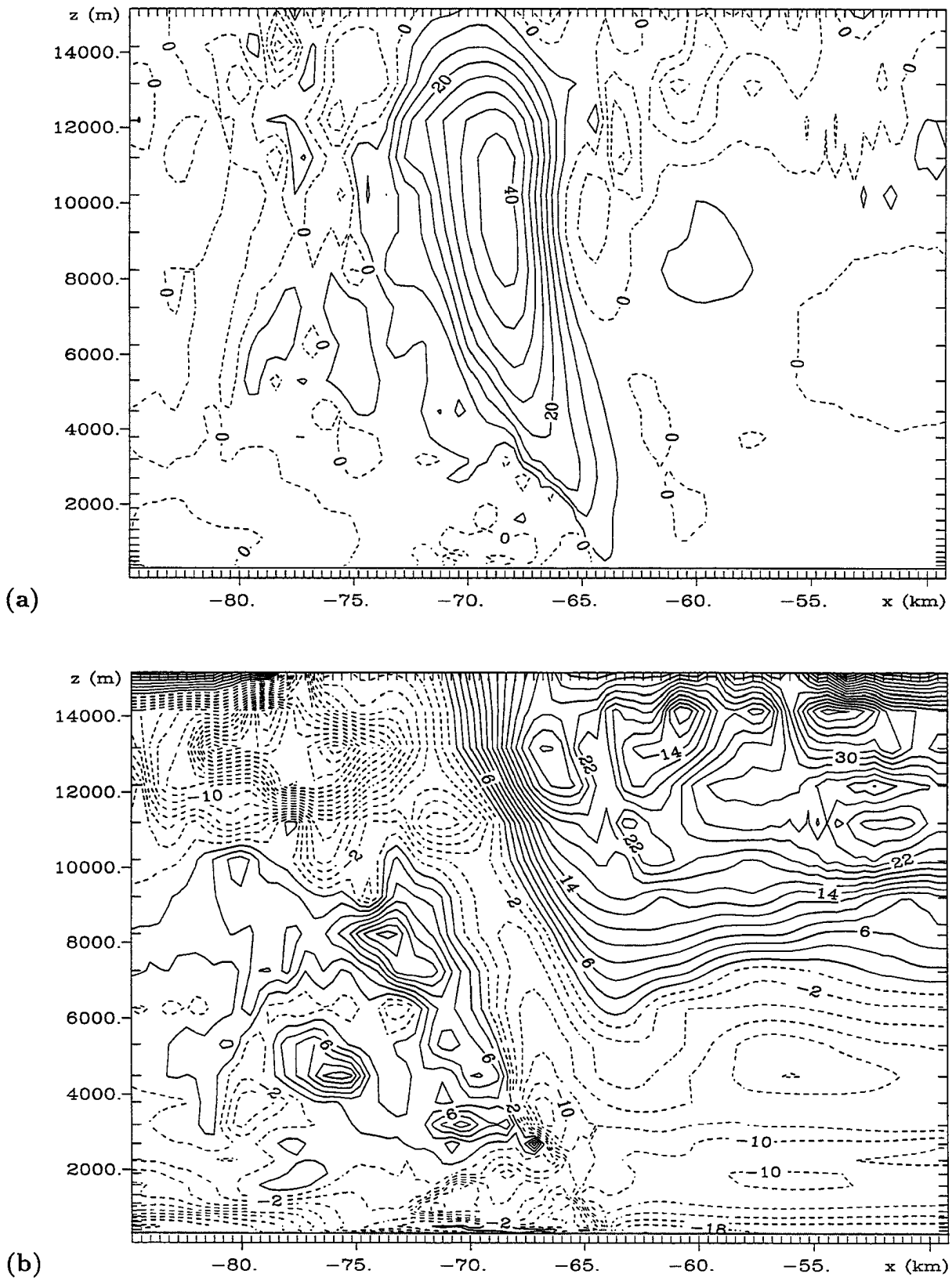

Figure 5.20: Vertical cross sections (looking north) through the center of the bow echo on a subset of Grid #5 (zoomed in on the storm). (a) Vertical velocity, (b) storm-relative u at 0028:30 UTC, (c) vertical velocity, (d) storm-relative u at 0037:30 UTC (time of strongest u winds), (e) vertical velocity, (f) storm-relative u at 0045 UTC. Contour interval is $5ms^{-1}$ for the vertical velocity, $2ms^{-1}$ for the storm-relative u. Dashed contours denote negative values.

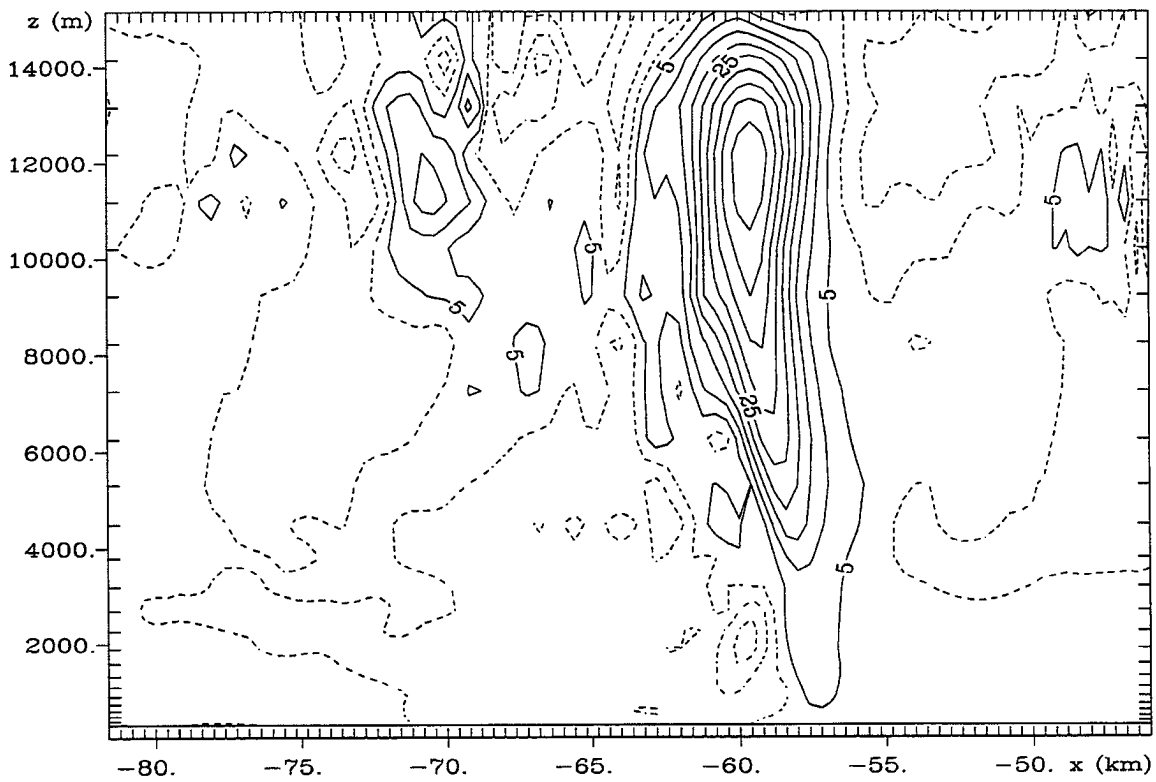
z (m)
14000.
12000.
10000.
8000.
6000.
4000.
2000.
−80.
−75.
−70.
−65.
−60.
−55.
−50. x (km)

(c)

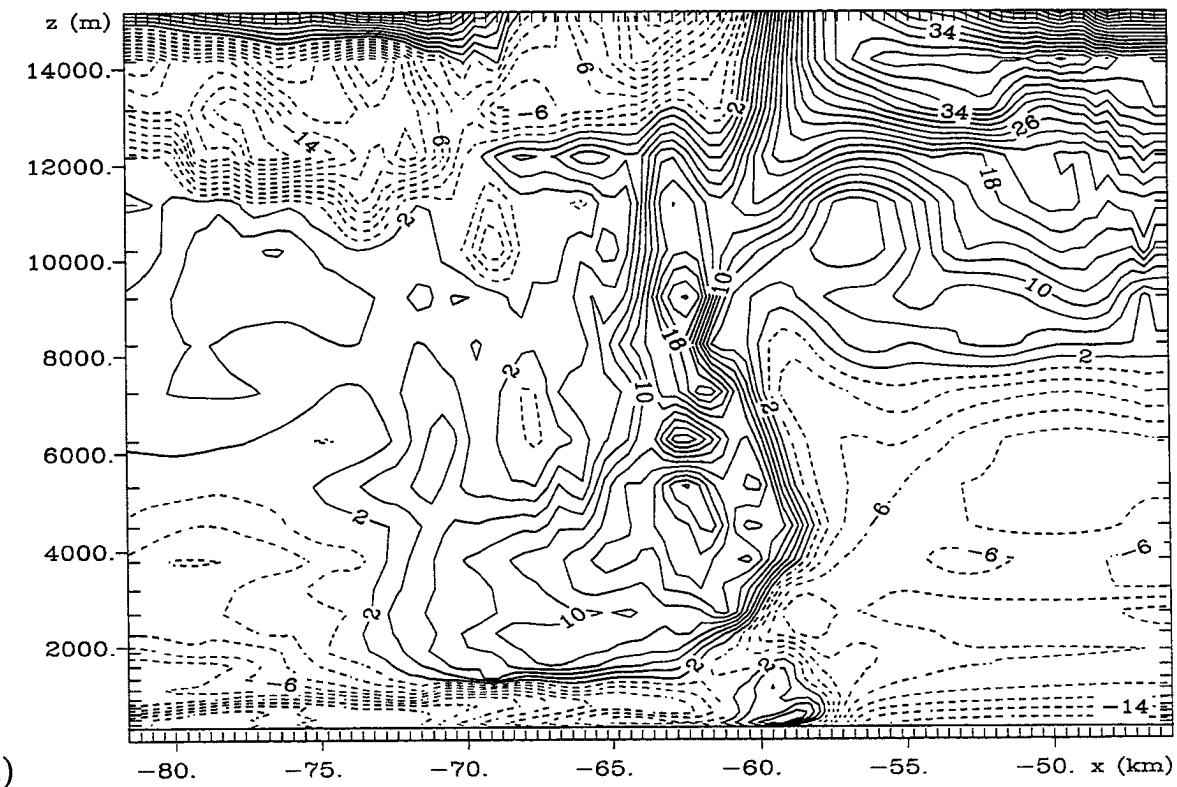
z (m)
14000.
12000.
10000.
8000.
6000.
4000.
2000.
−80.
−75.
−70.
−65.
−60.
−55.
−50. x (km)

(d)

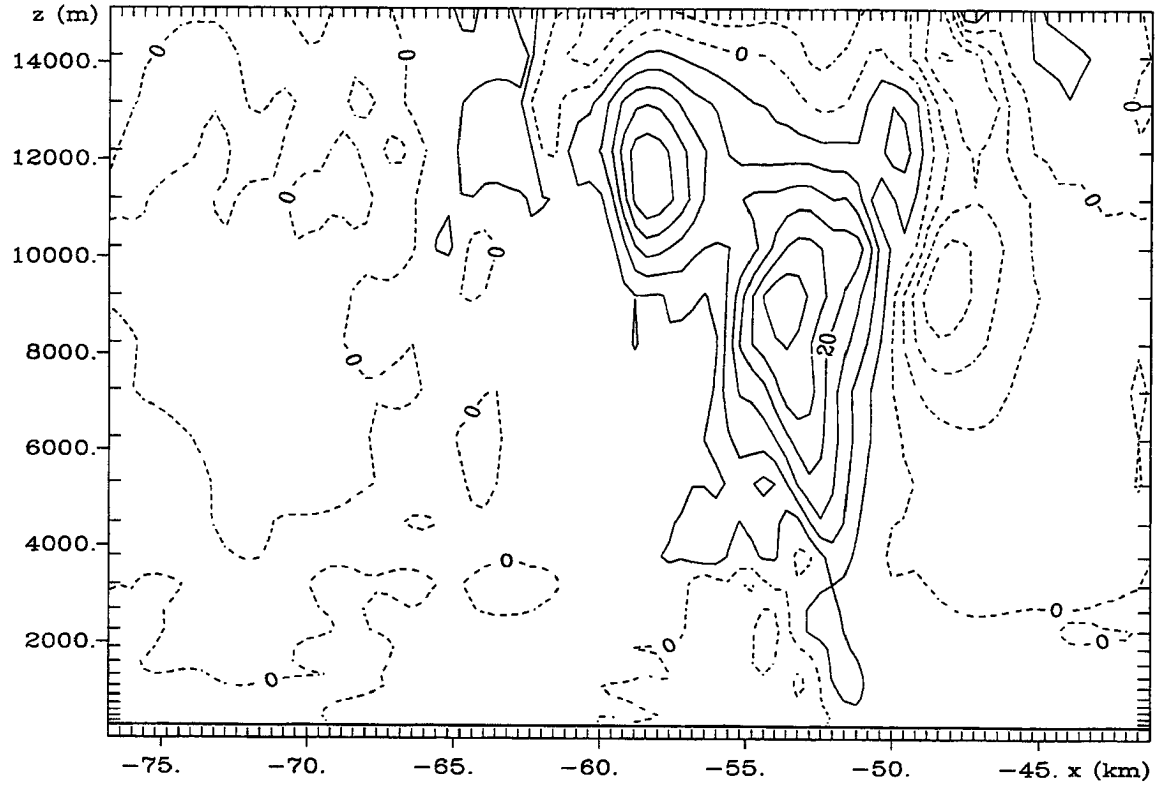
z (m)
14000.
12000.
10000.
8000.
6000.
4000.
2000.
0
20
−75.
−70.
−65.
−60.
−55.
−50.
−45. x (km)

(e)

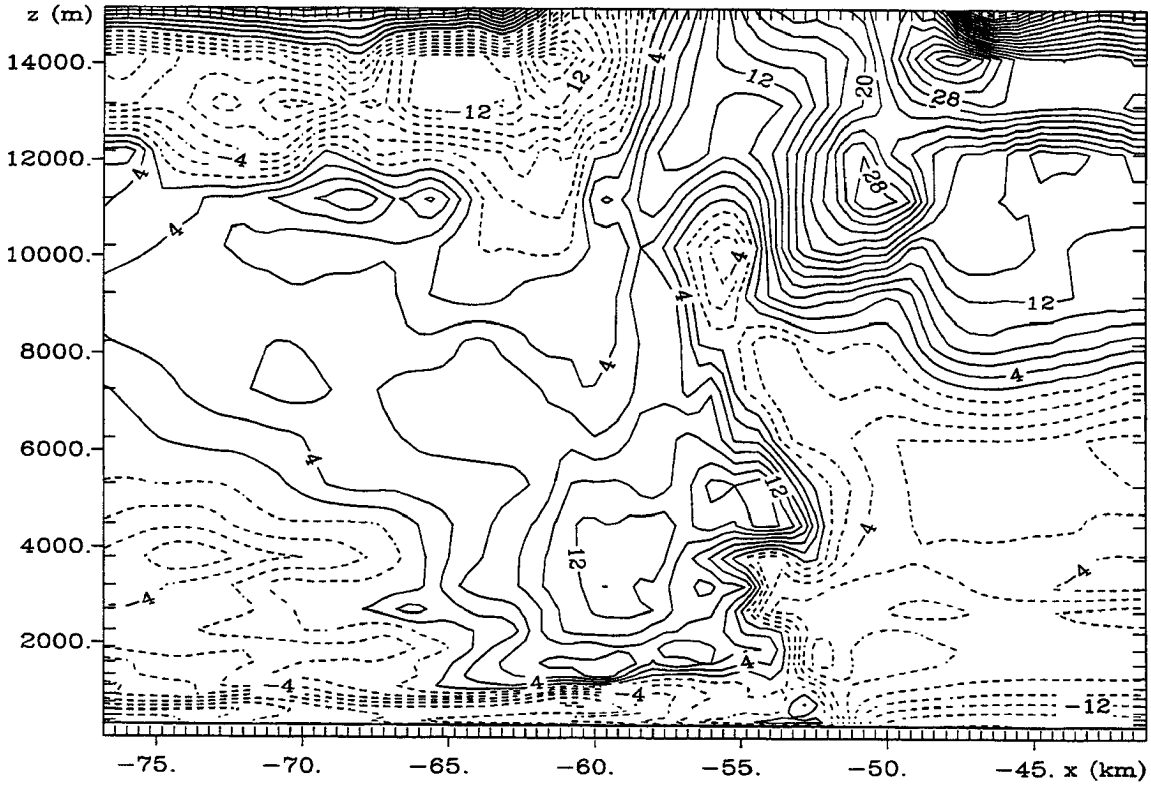
z (m)
14000.
12000.
10000.
8000.
6000.
4000.
2000.
4
12
20
28
−4
−12
−75.
−70.
−65.
−60.
−55.
−50.
−45. x (km)

(f)

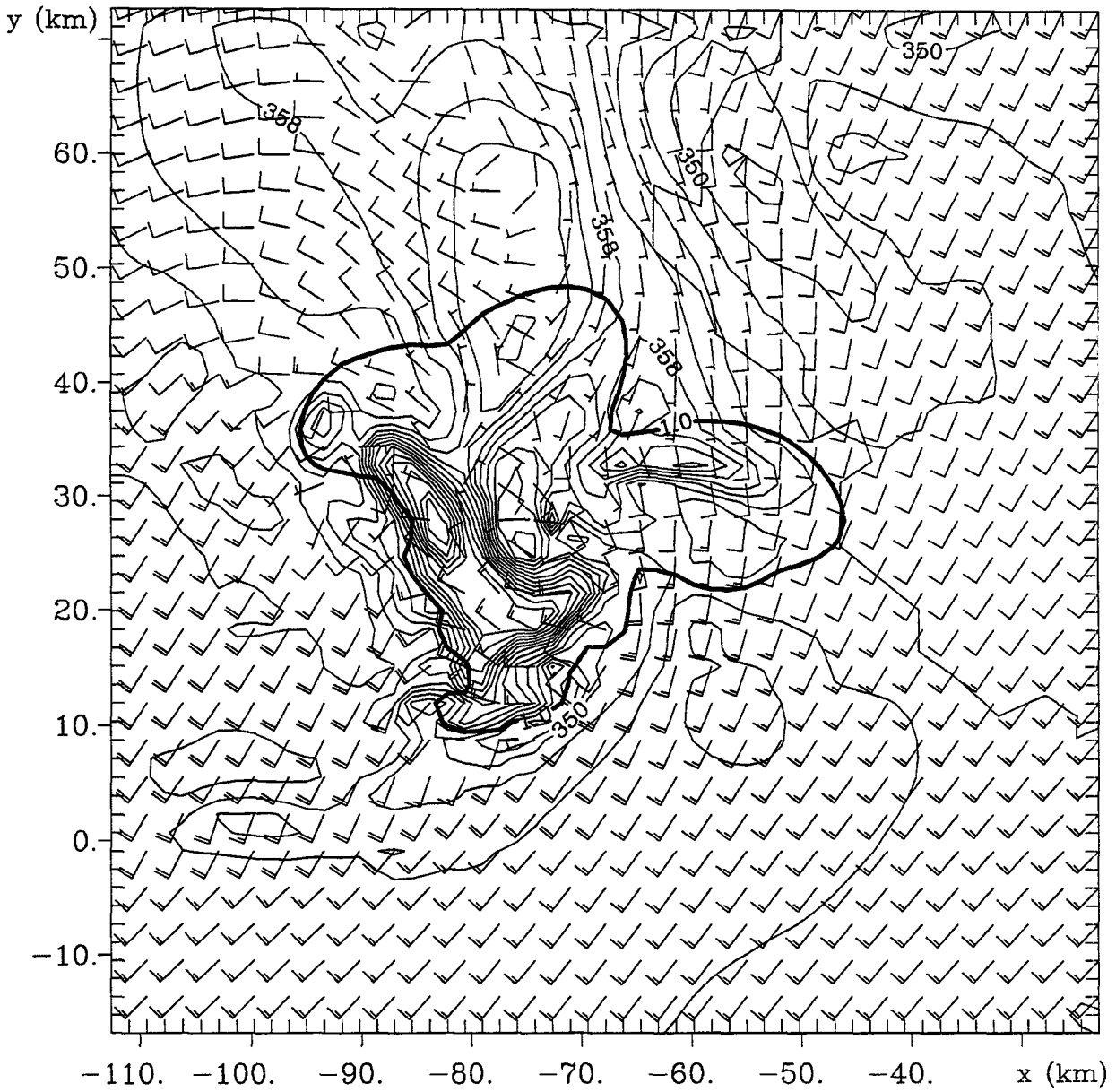

Figure 5.21: Horizontal cross section at z=1.7km of equivalent potential temperature (contour interval 2K) overlaid with the horizontal winds on Grid #4 at 0025:30 UTC. The contour in bold is the $1g(kg)^{-1}$ condensate mixing ratio line. The wind barbs are plotted at every other grid point. The short (long) flag on the wind barb denotes a velocity of $5ms^{-1}$ ($10ms^{-1}$).

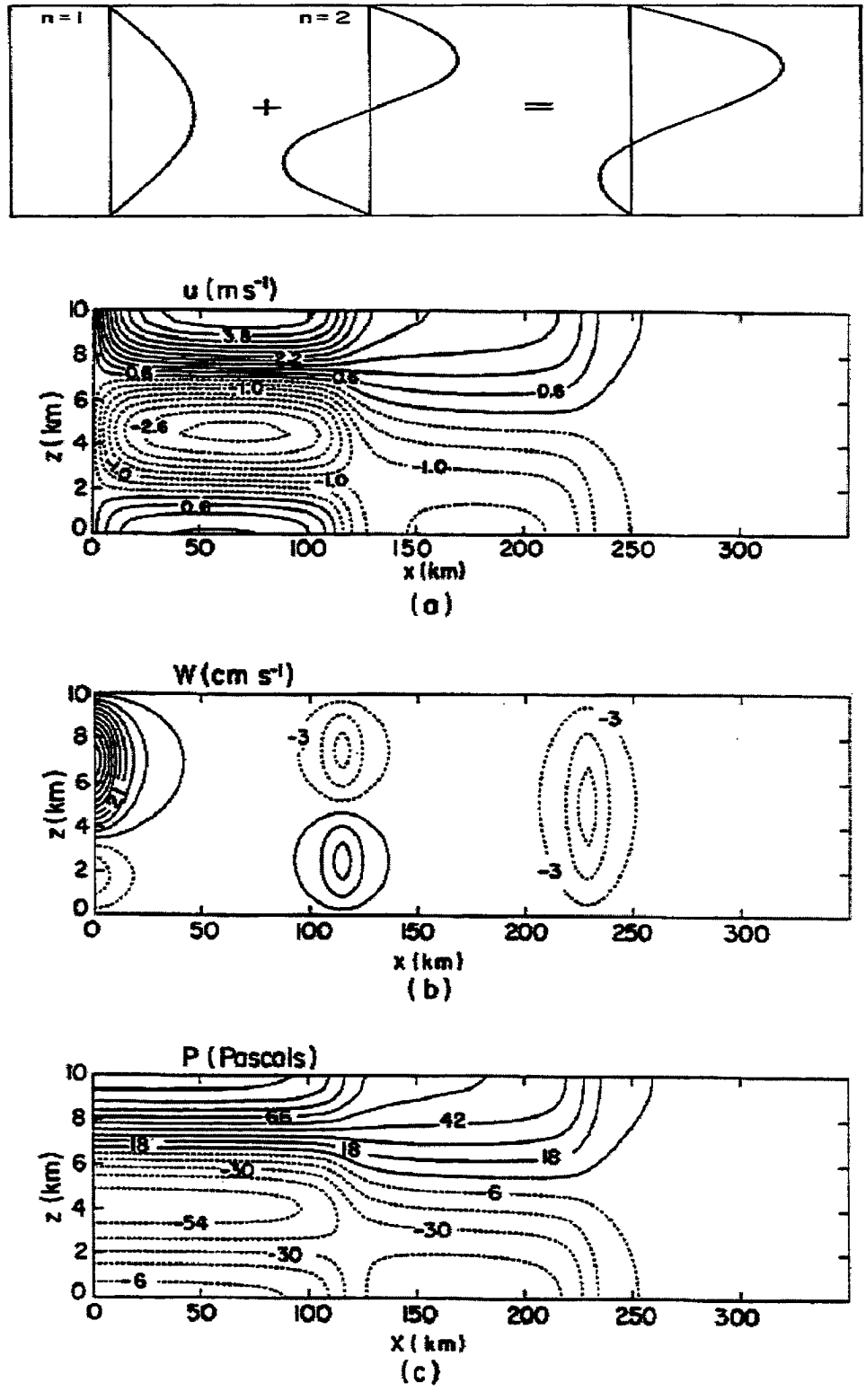

Figure 5.22: Rigid-lid solution for superpostion of m=1 and m=2 modes. The heating profile is given in the top panel (maximum rate is 1.0 $J(kg)^{-1}s^{-1}$), and the heat source is stationed at x=0. Also shown is the atmospheric response in (a) u winds (contour interval $0.4ms^{-1}$), (b) vertical velocity (contour interval $6(cm)s^{-1}$), and (c) pressure (contour interval 12 pascals) [adapted from Nichols et. al., 1991].

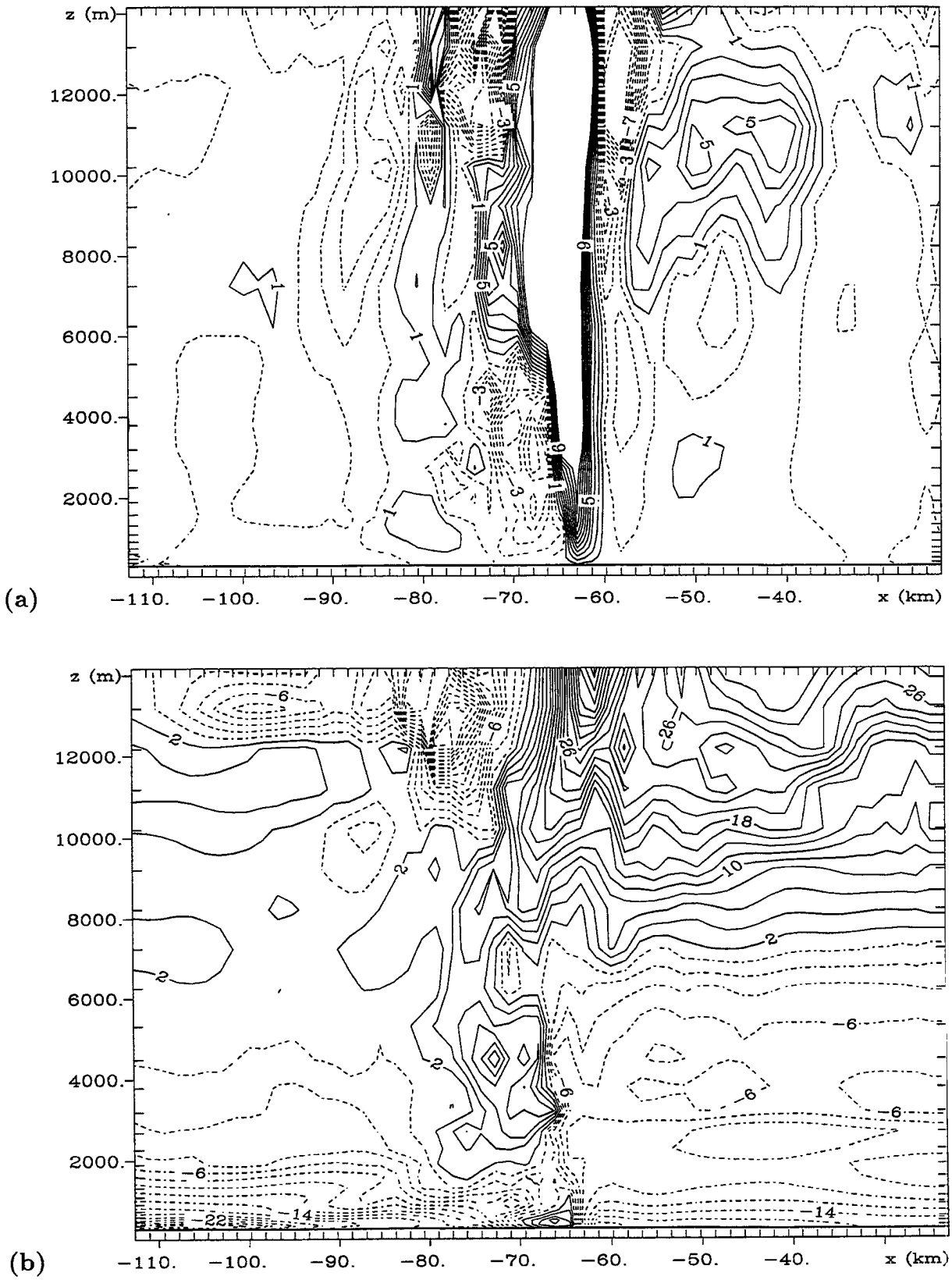

Figure 5.23: Vertical cross sections (looking north) through the center of the bow echo on Grid #5 at 0031:30 UTC for (a) vertical velocity, (b) storm-relative u, (c) potential temperature, (d) total condensate mixing ratio. Contour interval is $1ms^{-1}$ for the vertical velocity, $2ms^{-1}$ for the storm-relative u, 2K for the potential temperature, and $1g(kg)^{-1}$ for the condensate mixing ratio. Dashed contours denote negative values. Note the gravity wave between x=-90km and x=-80km.

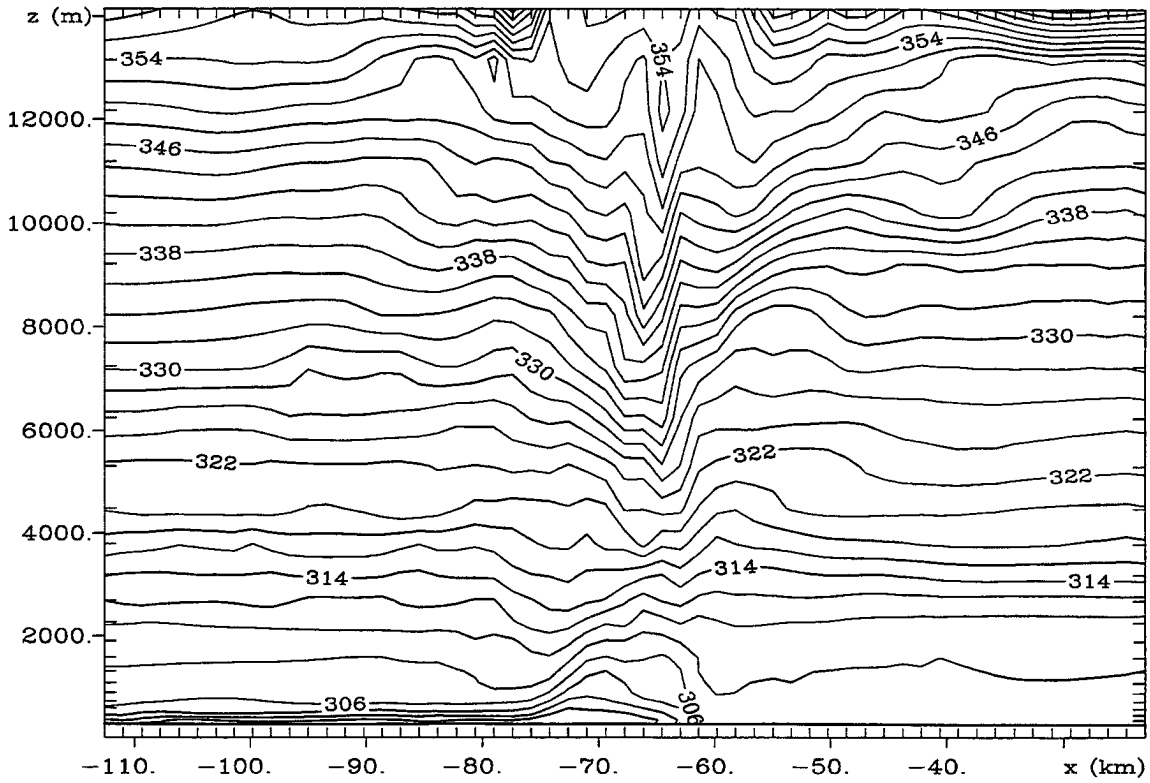
z (m)
12000.
10000.
8000.
6000.
4000.
2000.
354
346
338
330
322
314
306
−110.
−100.
−90.
−80.
−70.
−60.
−50.
−40.
x (km)

(c)

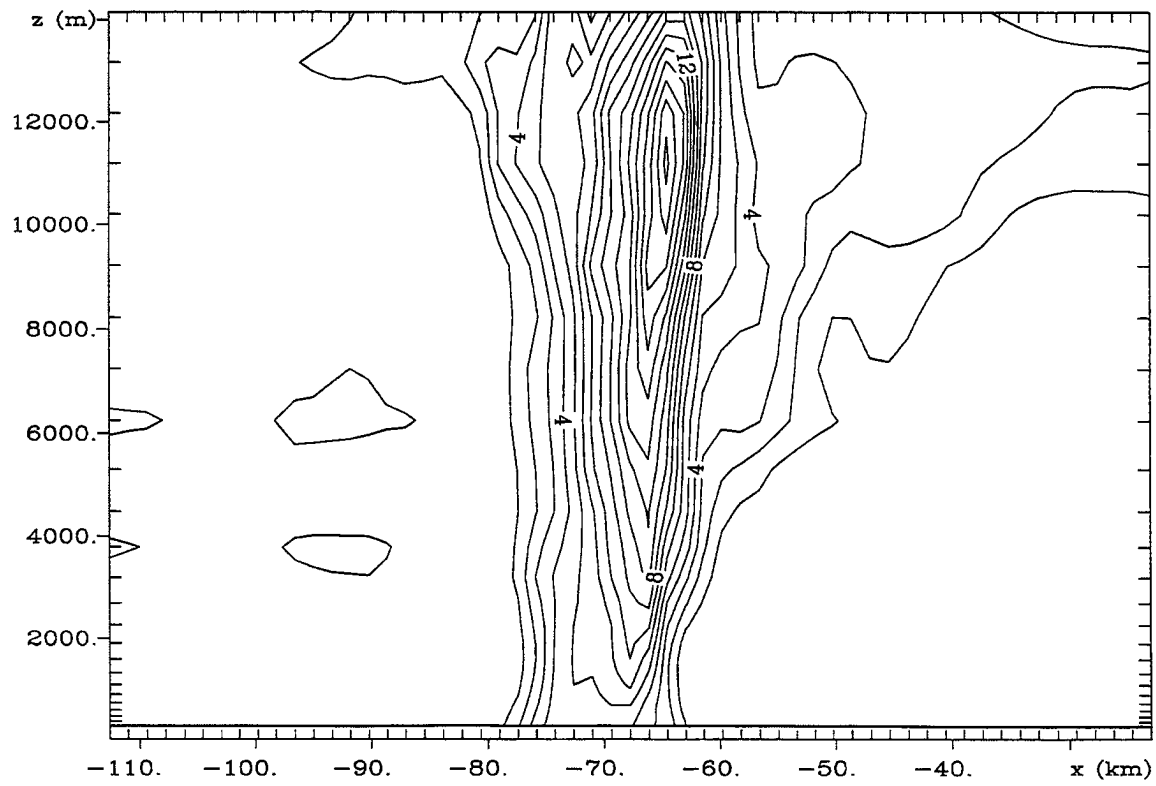
z (m)
12000.
10000.
8000.
6000.
4000.
2000.
12
8
4
−110.
−100.
−90.
−80.
−70.
−60.
−50.
−40.
x (km)

(d)

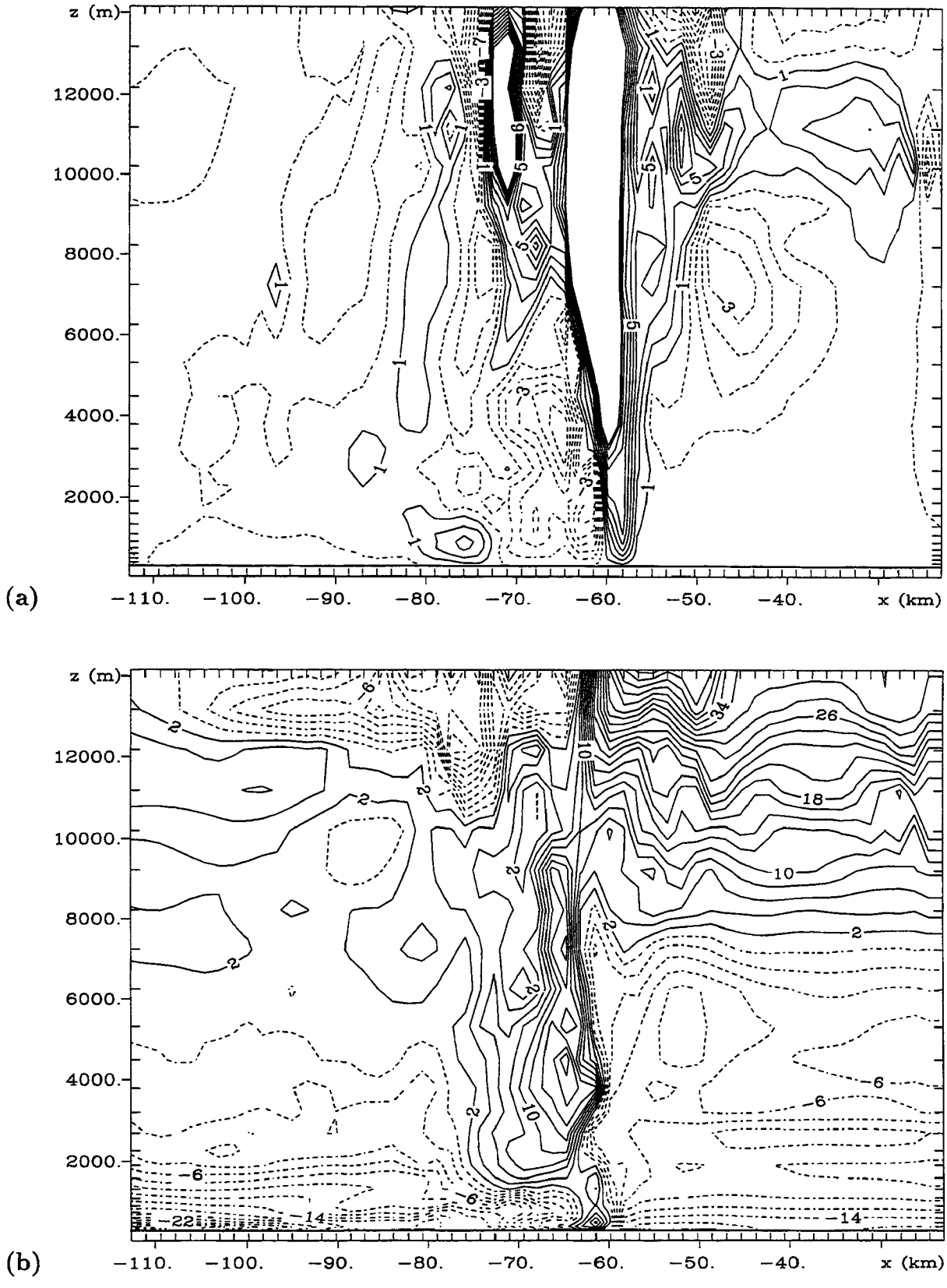

Figure 5.24: Vertical cross sections (looking north) through the center of the bow echo on Grid #5 at 0036 UTC for (a) vertical velocity, (b) storm-relative u, (c) potential temperature, (d) total condensate mixing ratio. Contour interval is $1ms^{-1}$ for the vertical velocity, $2ms^{-1}$ for the storm-relative u, 2K for the potential temperature, and $1g(kg)^{-1}$ for the condensate mixing ratio. Dashed contours denote negative values. Note the gravity wave between x=-90km and x=-80km.

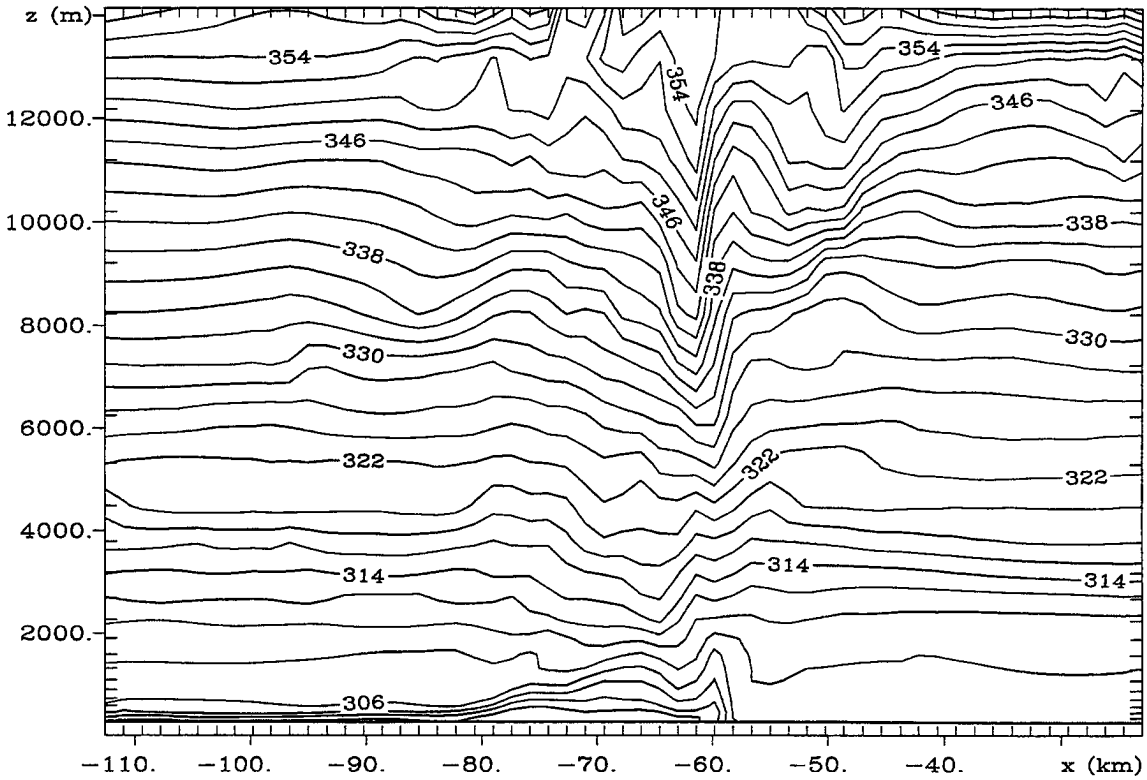
z (m)
12000.
10000.
8000.
6000.
4000.
2000.
354
346
338
330
322
314
306
−110.
−100.
−90.
−80.
−70.
−60.
−50.
−40.
x (km)

(c)

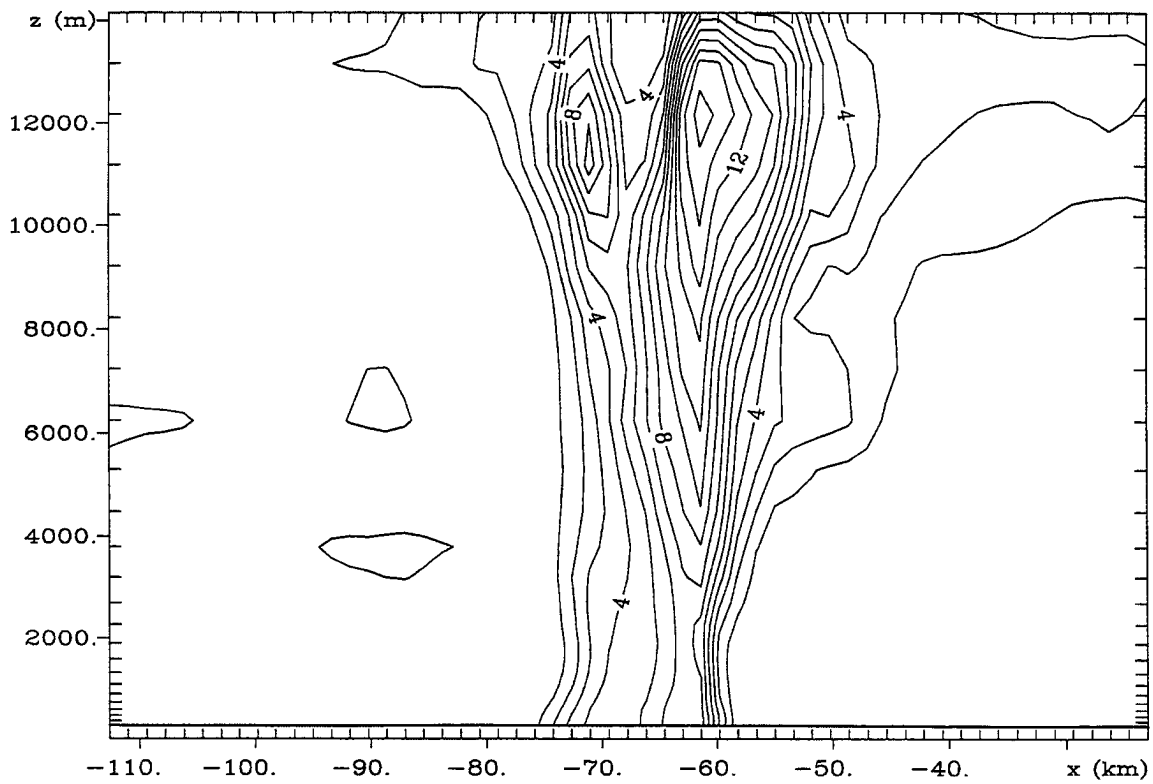
z (m)
12000.
10000.
8000.
6000.
4000.
2000.
4
8
12
−110.
−100.
−90.
−80.
−70.
−60.
−50.
−40.
x (km)

(d)

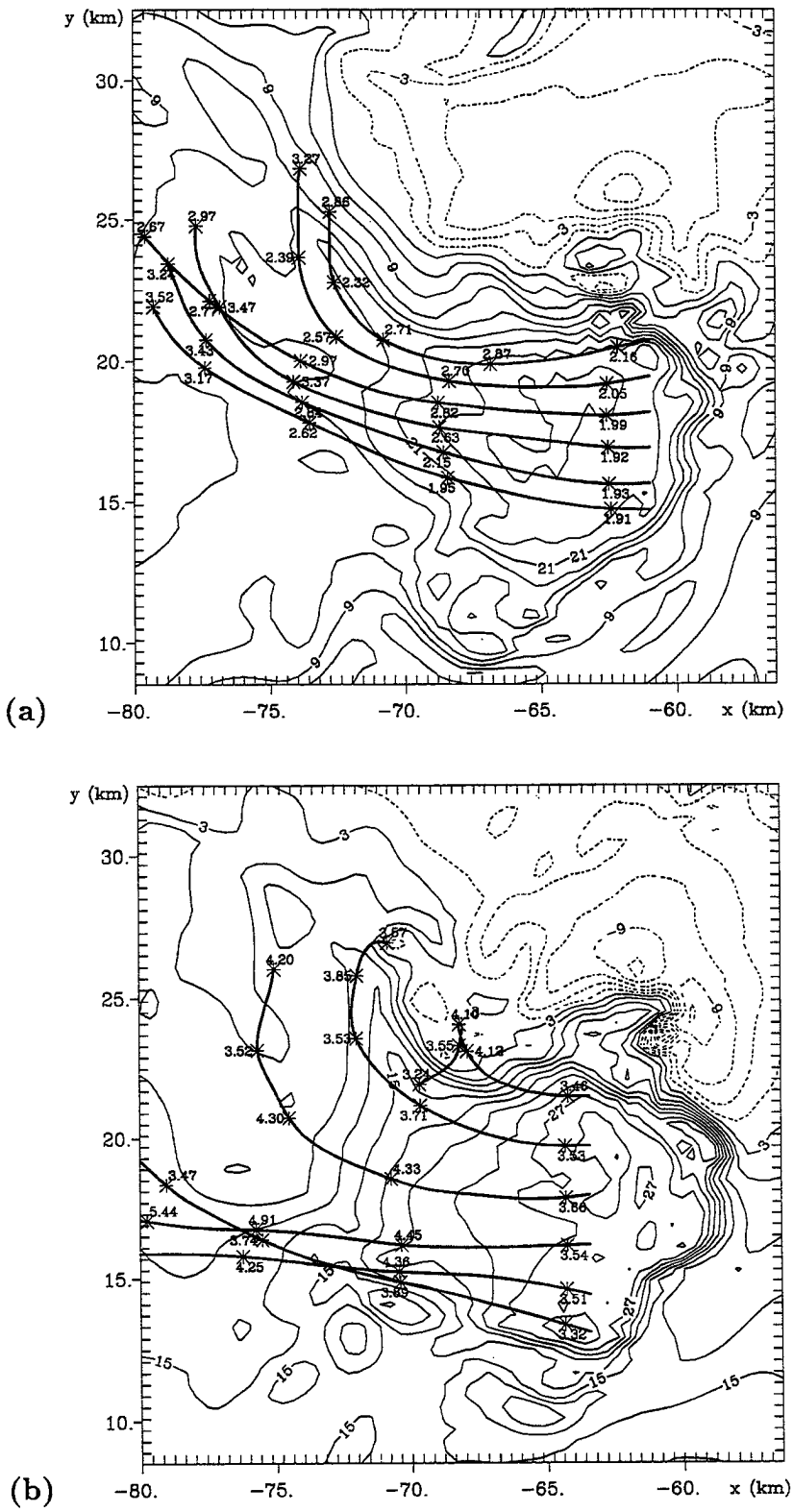

Figure 5.25: Horizontal cross sections of the u velocity component overlayed with projections of the backwards trajectories of 6 particles released from the region of strong winds west of the convective line on Grid #5 at (a) z=2km, (b) z=3.5km, (c) z=4.3km, (d) z=5.1km. The particles were released in a line in the region of strongest winds at each level, and then followed backwards in time. The height (in km) of the particles at various times (particle position denoted by the astericks) is indicated by along the trajectories. Contour interveral for u is $3ms^{-1}$.

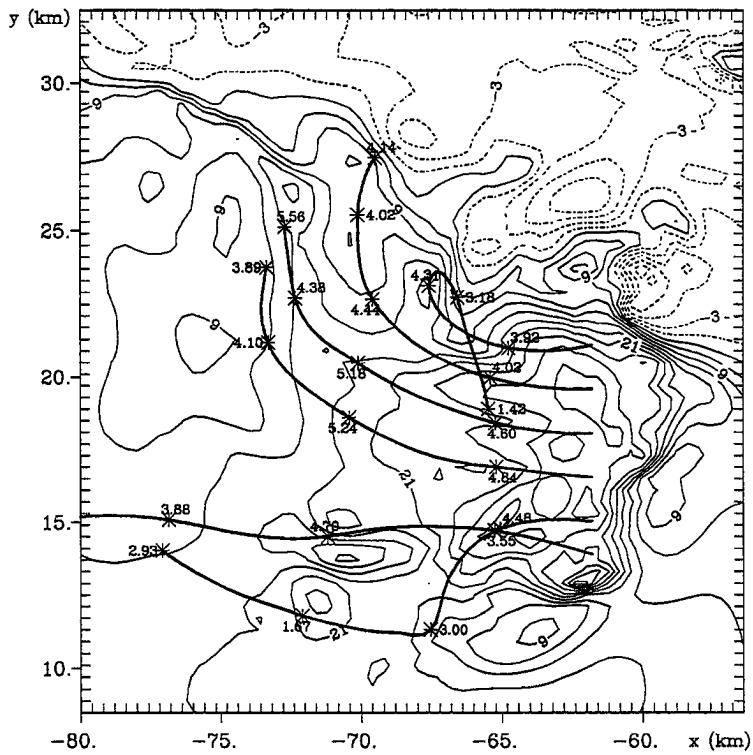
y (km)
30.
25.
20.
15.
10.
-80.
-75.
-70.
-65.
-60.
x (km)

(c)

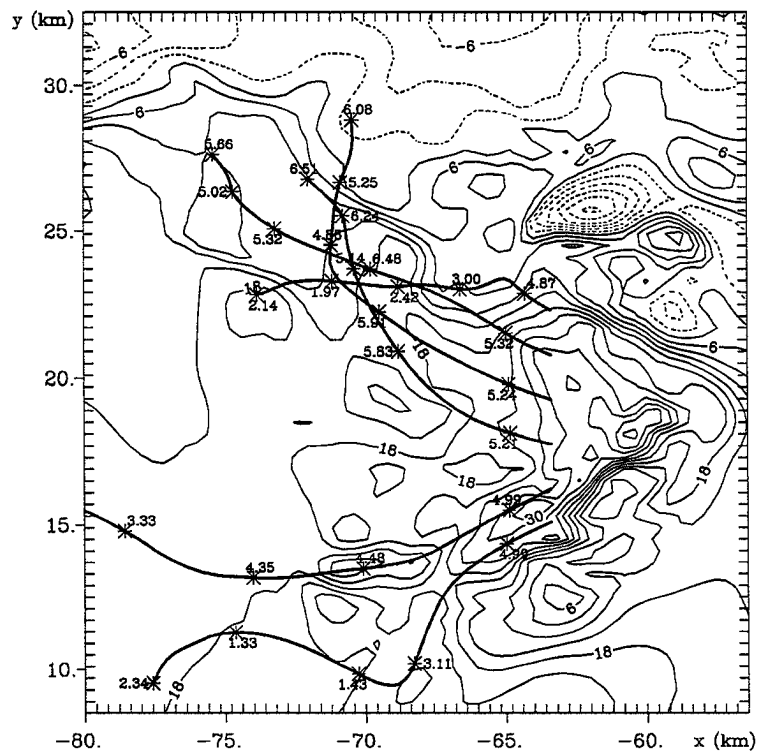
y (km)
30.
25.
20.
15.
10.
-80.
-75.
-70.
-65.
-60.
x (km)

(d)

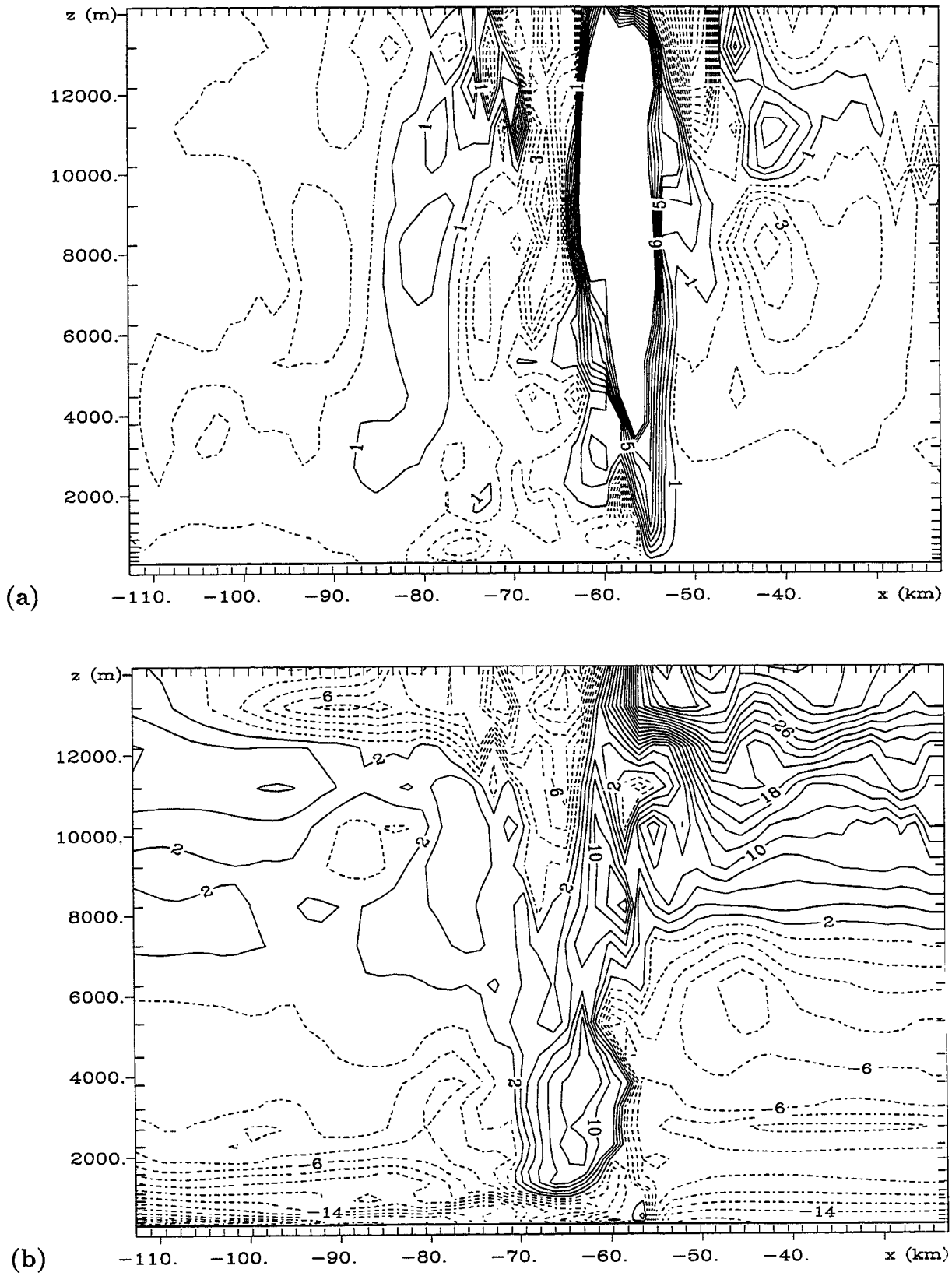

Figure 5.26: Vertical cross sections (looking north) through the center of the bow echo on Grid #5 at 0040:30 UTC for (a) vertical velocity, (b) storm-relative u, (c) potential temperature, (d) total condensate mixing ratio. Contour interval is $1ms^{-1}$ for the vertical velocity, $2ms^{-1}$ for the storm-relative u, 2K for the potential temperature, and $1g(kg)^{-1}$ for the condensate mixing ratio. Dashed contours denote negative values. Note the gravity wave between x=-90km and x=-80km.

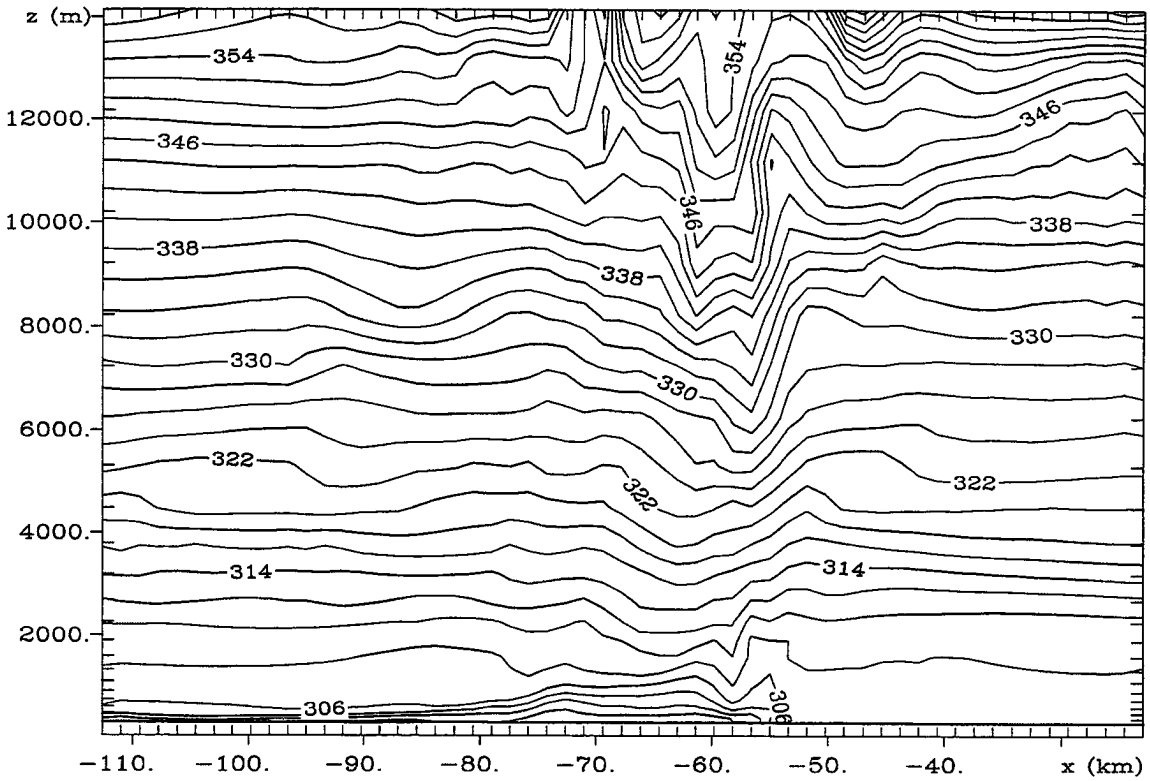
z (m)
12000.
10000.
8000.
6000.
4000.
2000.
354
346
338
330
322
314
306
−110.
−100.
−90.
−80.
−70.
−60.
−50.
−40.
x (km)

(c)

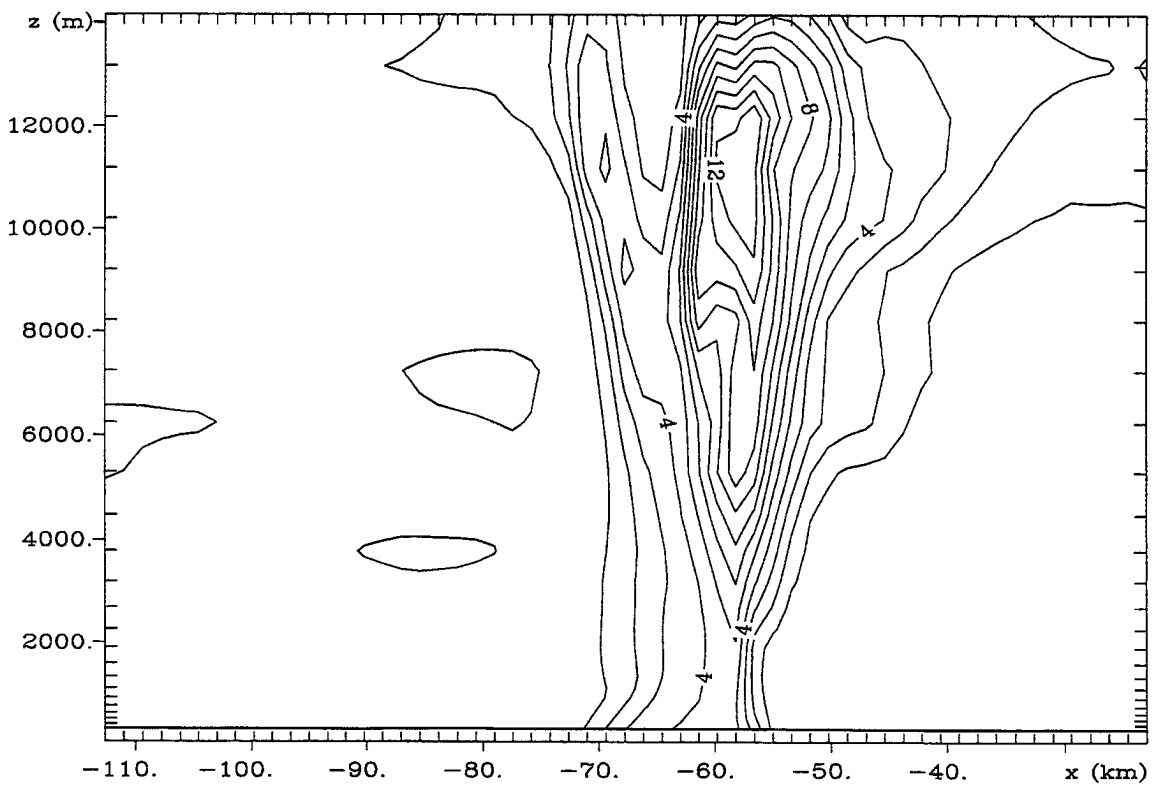
z (m)
12000.
10000.
8000.
6000.
4000.
2000.
4
8
12
4
4
4
4
−110.
−100.
−90.
−80.
−70.
−60.
−50.
−40.
x (km)

(d)

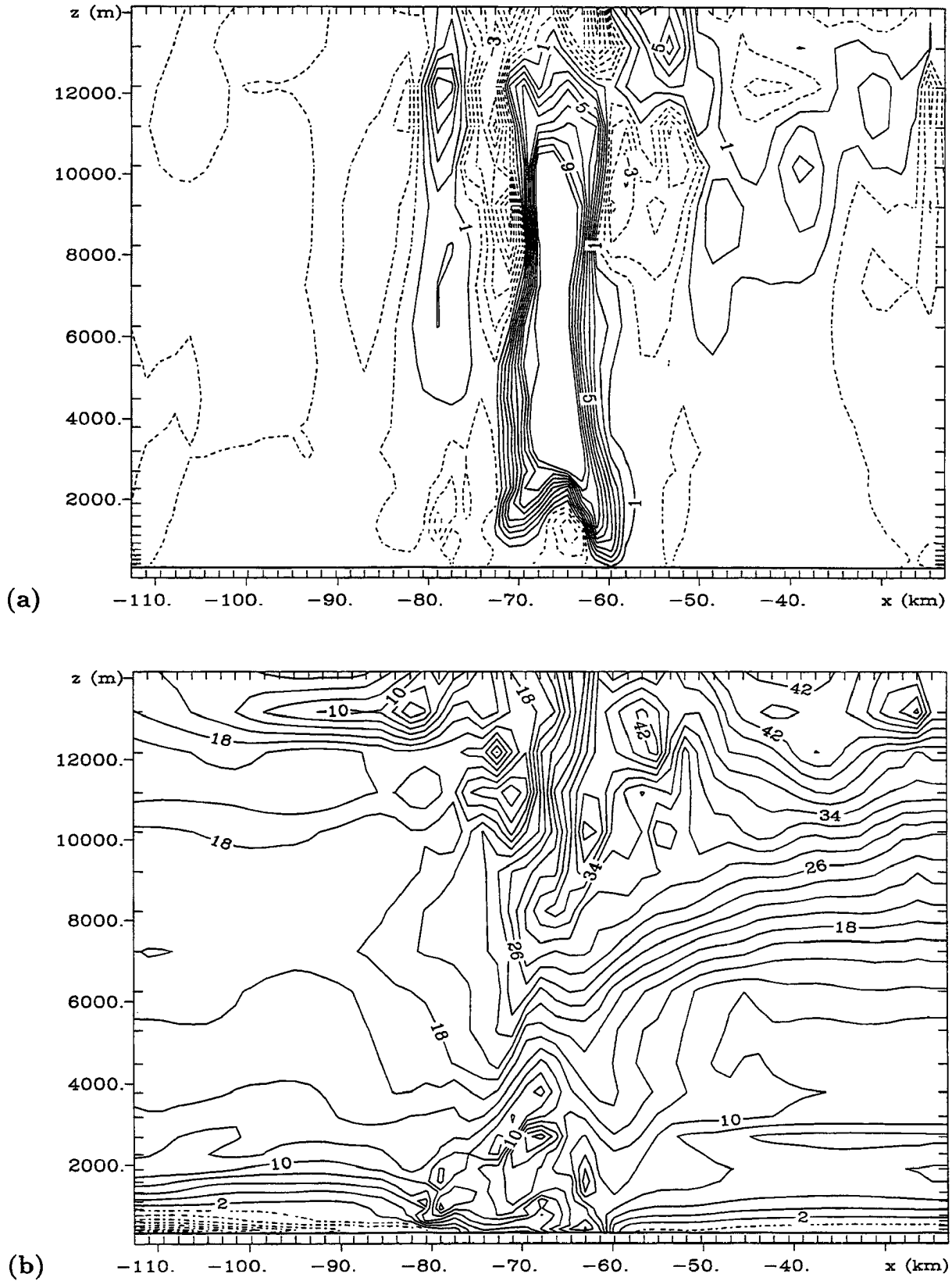

Figure 5.27: Vertical cross sections through the southern portion of the bow echo on Grid #5 at 0036 UTC for (a) vertical velocity, (b) u velocity. Contour interval is $1ms^{-1}$ for the vertical velocity, $2ms^{-1}$ for u. Dashed contours denote negative values. Note the gravity wave to the west of the storm between x=-90km to x=-75km.

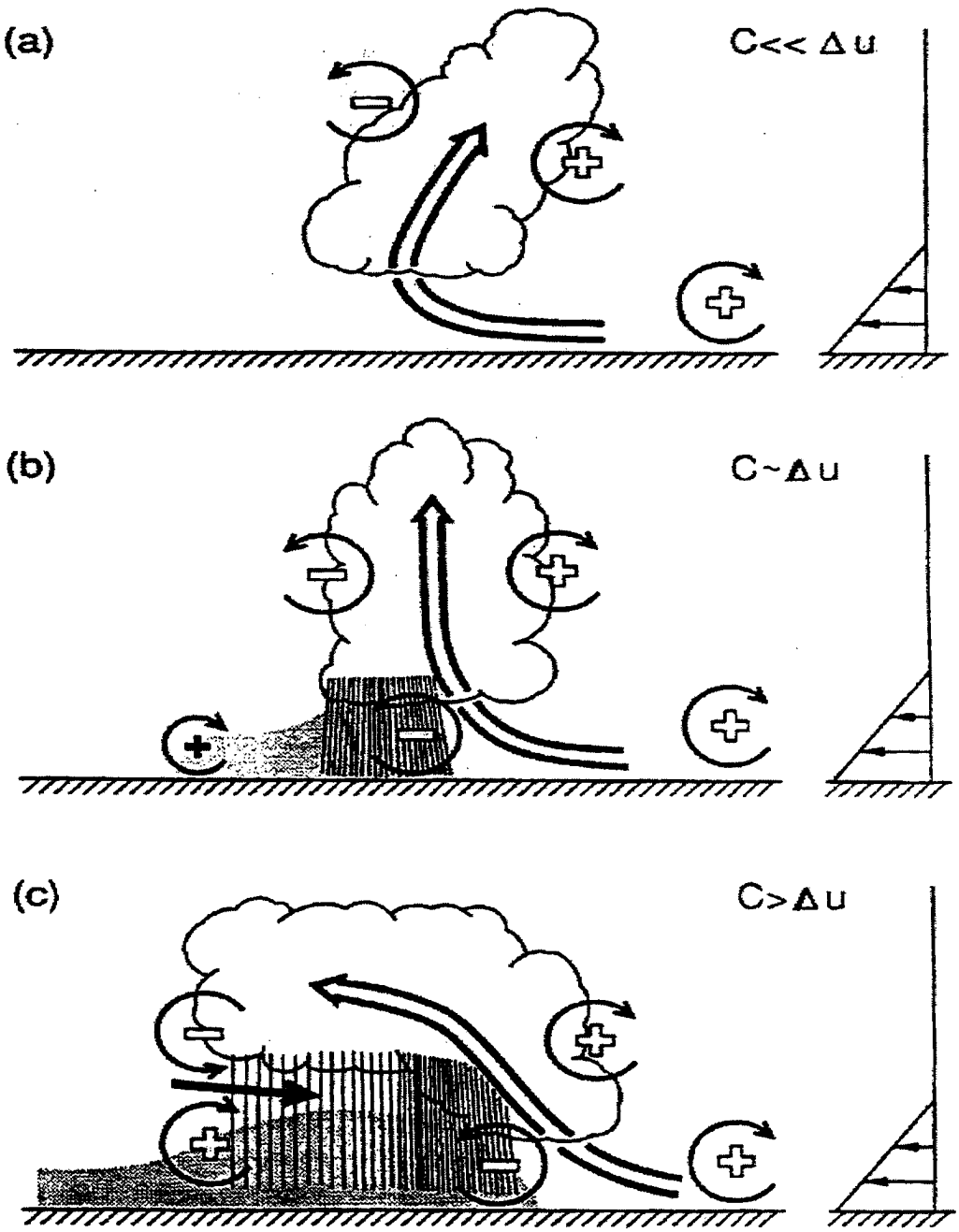

Figure 5.28: A conceptual model of the three stages in the evolution of a convective system. The system first tilts (a) downshear, then becomes (b) vertical, and eventually tilts (c) upshear in response to the strengthening cold pool [from Weisman, 1992].

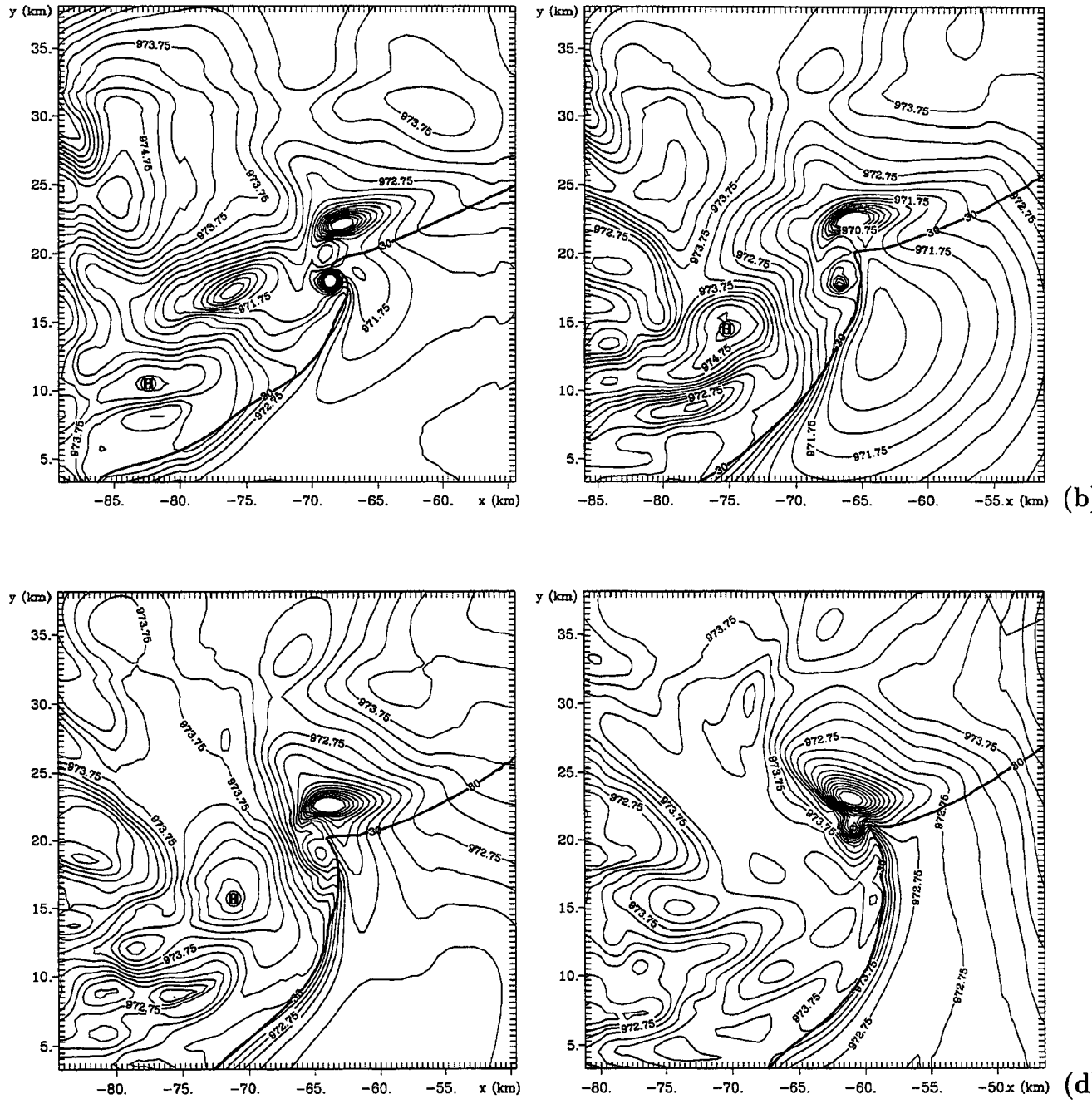

Figure 5.29: Horizontal cross sections showing the pressure field (in mb) at z=38m on Grid #5 at (a) 0019:30 UTC, (b) 0025:30 UTC, (c) 0030 UTC, (d) 0036 UTC. Contour interval for the pressure is 0.25mb. The bold line denotes the 30°C isotherm which is close to the leading edge of the gust front. The circled 'H' in (a),(b),(c) denotes the center of a region of high pressure behind the gust front.

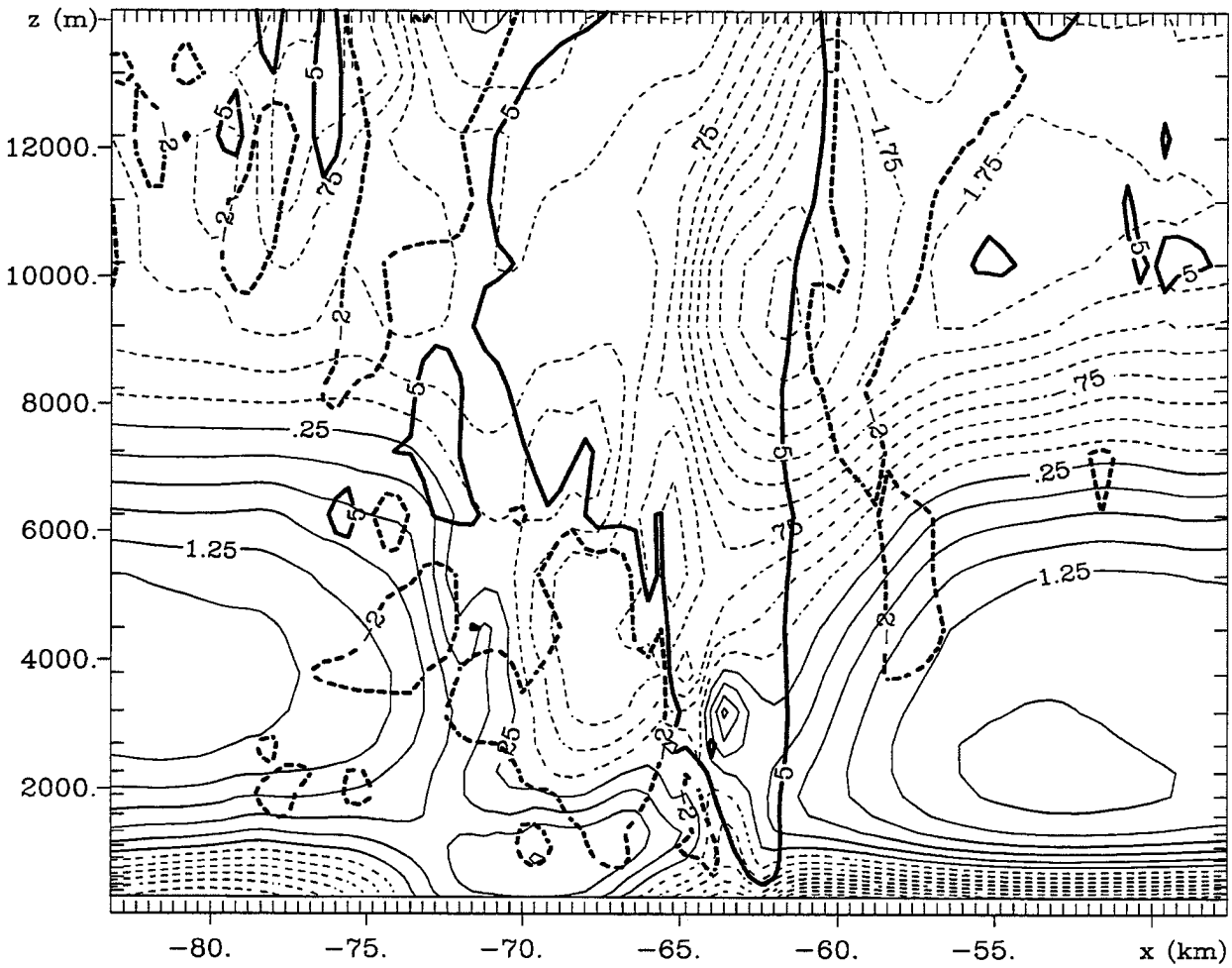

Figure 5.30: Vertical east-west cross section (looking north) of perturbation pressure (in mb) and vertical velocity at 0031:30 UTC on Grid #5. Pressure is contoured every 0.25 mb. Dashed contours denote negative values. The bold solid line denotes the $5ms^{-1}$ vertical velocity contour. The dashed bold contour denotes the -$2ms^{-1}$ vertical velocity contour. Note the large horizontal pressure gradient between z=2km to z=6km along the west side of the storm.

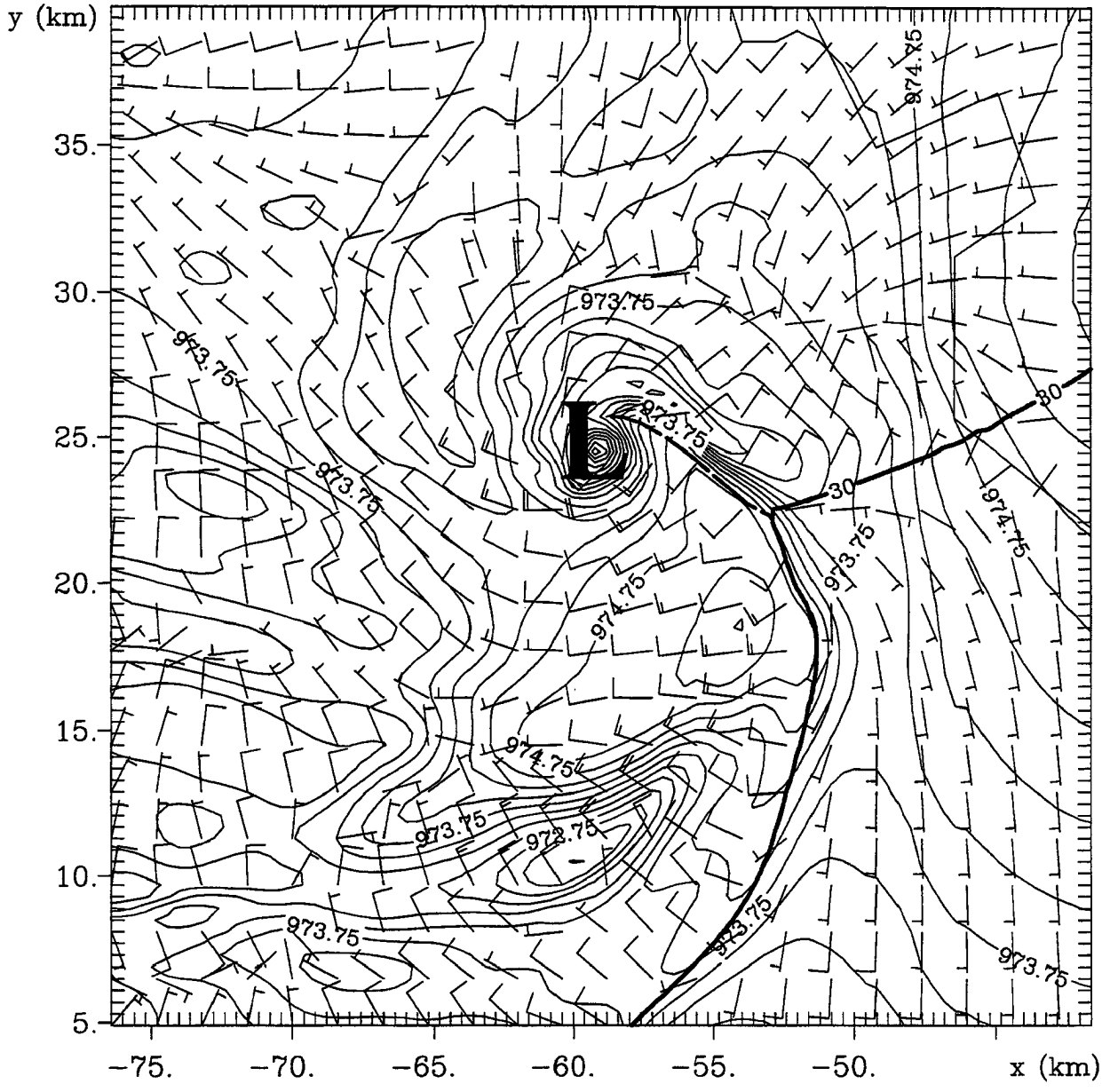

Figure 5.31: Winds and pressure (in mb) 38m above the surface at 0045 UTC on Grid #5. The storm had evolved into a rotating comma head strucure and the convection was weakening at this time. The bold solid line denotes the 30°C isotherm which lies close to the leading edge of the gust front. The bold dashed line respresent the position of the occlusion. Note that the surface pressure and temperature pattern associated with the storm resembles an occluded midlatitude cyclone. Wind barbs are plotted at every fourth model grid point. The short (long) flag on the wind barb represents $5ms^{-1}$ ($10ms^{-1}$). Pressure is contoured every 0.25 mb.

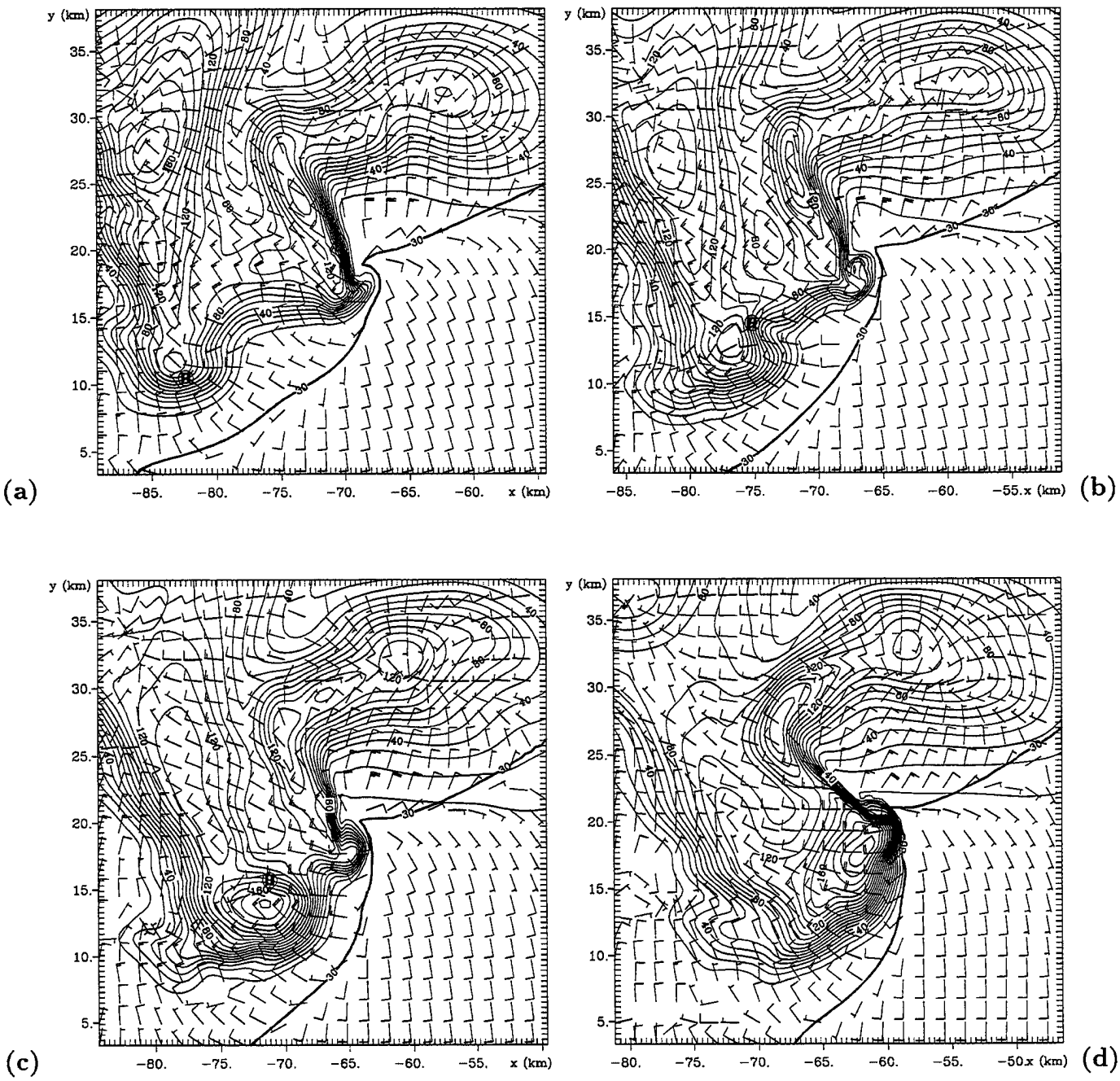

Figure 5.32: Horizontal cross sections showing the precipitation rate (in $mm(hr)^{-1}$) overlayed with the horizontal winds at z=38m on Grid #5 at (a) 0019:30 UTC, (b) 0025:30 UTC, (c) 0030 UTC, (d) 0036 UTC. The contour interval is $10mm(hr)^{-1}$. The bold line denotes the 30°C isotherm which is close to the leading edge of the gust front. The circled 'H' in (a),(b),(c) denotes the center of a region of high pressure behind the gust front. Wind barbs are plotted at every fourth model grid point. The short (long) flags on the wind barbs denote a wind speed of $5ms^{-1}$ ($10ms^{-1}$).

Chapter 6

JUNE 30, 1993 SIMULATED TORNADOES

In this chapter, the genesis, evolution and structure of the simulated tornadoes is presented. Unless otherwise stated, the results shown will be from Grid #6 which has grid spacing on the order of 100m in both the 30 June, 1993 and 15 May, 1991 cases. Arguably, 100m grid spacing is not sufficient to resolve all tornadoes–particularly weak, short-lived tornadoes which are typically about 50-100m in diameter (with 100m grid spacing, the smallest feature can be considered 'well resolved' has a spatial scale of 400m), although cases have been reported of weak tornadoes which develop along outflow boundaries having diameters (as measured by the distance between wind maxima in Doppler radar measurements) between 500-600m (Brady and Szoke, 1989; Wakimoto and Wilson, 1989). The focus of this chapter is on the process(es) that lead to the generation of the tornado. These processes are controlled by the parent thunderstorm and act on scales several times larger than the core radius of the tornado. As for the tornadoes themselves, many modelling studies have shown (and the author has personally experienced) that simulated features tend to become smaller in horizontal scale and more intense (i.e. the velocities associated with a feature will tend to become stronger) when smaller grid spacing is used. Thus it is very likely that if smaller grid spacing was used in the simulation, the simulated tornadoes would shrink somewhat in size (hopefully only down to scales that are observed) and become more intense. Due to computational and time limitations, 100m grid spacing was the smallest grid spacing that could be used in the present simulations.

Another question that sometimes arises in tornado studies is 'when does a vortex become a tornado?'. This question can always be raised in modeling studies of tornadoes (in which there is no visual funnel cloud or observable damage path), and sometimes arises

in observational studies and damage surveys (Forbes and Wakimoto, 1983). Here we will define a vortex a 'tornado' for the duration of time when the following three conditions are simultaneously met on Grid #6:

1. A closed circulation (ground relative) exists at the lowest model level (z=38m).
2. Tornadic strength winds ($\geq 18ms^{-1}$) exist somewhere within the closed circulation.
3. The maximum vertical vorticity at the lowest model level exceeds $0.1s^{-1}$.

While this definition is admittedly somewhat arbitrary, the need for each of the conditions became apparent during the course of the analysis. For example, during the spin-up of the first tornado in the 30 June case, there were times when there was a closed circulation associated with large vertical vorticity values at z=38m, but the maximum wind speeds associated with this feature were less than $18ms^{-1}$ (the minimum on the 'F' scale). There were other times during the spin up of both tornadoes when conditions 2 and 3 where met, but a closed cyclonic circulation did not exist at the surface. This difficulty in distinguishing a tornado from horizontal wind shear features associated with strong 'straight line winds' has also been encountered in some damage surveys in which it could not be determined if the damage was caused by a tornado, or by straight line winds (Forbes and Wakimoto, 1983; Fujita and Smith, 1993). The third condition is by far the most arbitrary of the three. Since the tornadoes form in environments already rich in vertical vorticity, this condition was set to help distinguish vertical vorticity associated with the tornado from other vertical vorticity features present in the storm and the near-storm environment.

With these definitions and limitations in mind, we now turn to the model results of the simulated tornadoes. The June 30, 1993 simulated HP supercell spawned two weak tornadoes (F0/F1 strength) and the evolution and structure of these tornadoes is presented is Section 6.1. The tornado produced by the simulated May 15, 1991 classical supercell will be discussed in the following chapter. Circulation and vorticity analyses were performed for both of the June 30 tornadoes, and these results are discussed in Section 6.3.1. A comparison of the tornadogenesis process(es) between the present simulation and previous studies is presented in Section 6.4.

6.1 Development and Evolution of T1

Grid #6 was added to the simulation at 0000 UTC July 1 (at the same time that Grid #5 was added). It was decided to add Grid #6 at this time since it was apparent about 20-25 minutes into the simulation with Grid #5 that the model was trying to spin-up a small scale vortex. Once Grid #6 was added, it remained a part of the simulation until the simulation was terminated at 0100 UTC July 1. As was mentioned above, the simulated June 30 HP supercell produced two tornadoes. Tornado 1 (hereafter denoted as T1) develops between 0018-0019:30 UTC along the flanking line of S1 (recall that this is near the time when S2 began to merge with S1). The vortex spins up along the southeast flank of the shear zone associated with the outflow from S1 which is shown in Figure 6.1. The shear zone extends up to a height of about 5km, and tilts westward and becomes oriented more east-west with height. At low levels, some evidence of a cyclonic circulation can be seen near the point where the shear zone turns from a north-south to more of an east-west orientation as can be seen in Figure 6.1. Note the circulation associated with the main mesocyclone to the north-northwest of this region.

Before going into details of the formation of T1, a more general perspective of the tornado and its position in the storm at 0019:30 UTC is shown in Figure 6.2. The main mid-level mesocyclone associated with S1 (the eastern storm) lies to the north-northwest of the tornado. Note the condensate that is wrapping around the south side of the tornadic circulation forming a hook pattern.

Some Grid #5 fields at 0006 UTC (prior to the development of T1) at three different levels are shown in Figures 6.3, 6.4, and 6.5. At the surface (Figure 6.3), a region of convergence extends from the main storm updraft southward along the leading edge of the gust front. Although this region is associated with vertical vorticity, the values are small at this time, and there is no evidence of a distinct closed cyclonic circulation along the flanking line. At z=2km (Figure 6.4), the convergence along the flanking line is still visible, but now the cyclonic circulation associated with the mesocyclone is visible to the northwest. Vertical vorticity values along the flanking line are larger at this level than at the surface

due to stretching of vertical vorticity (created by tilting at low levels along the leading edge of the gust front) by convection. At z=4.3km (Figure 6.5), the largest vertical vorticity values are now associated with the mesocyclone. Note that the circulation associated with the mesocyclone at this level lies along the vertical velocity gradient between an updraft and downdraft. This feature is often observed before supercells become tornadic (Lemon and Doswell, 1979). There is strong southwesterly flow in the region above the low-level gust front at this level, and a region of convergence exists where this flow meets the north-northwesterly flow wrapping around the mesocyclone. The fields on Grid #6 look very similar to Grid #5 at this time and are not shown.

Seven and half minutes later (at 013:30 UTC), some very significant changes have occurred in the flow field along the flanking line of S1 as can be seen in Figures 6.6 and 6.7. A downdraft has developed along and rotated around the southern end of the shear zone. The downdraft originates around z=5km and from the model tendency fields appears to be dynamically-driven, similar to the rear flank downdraft in Klemp and Rotunno (1983). The air feeding into the downdraft between 4-5km originates from air that is wrapping around the southern edge of the mesocyclone to the northwest. At the lowest model level (Figure 6.6), the vertical vorticity has increased in the region of strong vertical velocity gradients where the downdraft has reached the surface. The surface pressure in this region has also begun to fall, and a cyclonic circulation is beginning to take form.

To get a closer look at the developing vortex, Grid #6 fields at three different vertical levels at 0013:30 UTC are shown in Figure 6.8. Note that the largest vertical vorticity values are located at the lowest model level in the vertical velocity gradient between the updraft and the northern tip of the downdraft. There is a broad cyclonic circulation around this vorticity maximum, but the wind speeds are below tornadic strength at this time. It is also interesting to note that between 1-2km, the vorticity maxima associated with the developing vortex do not coincide with the southern portion of the elongated closed circulation evident in the wind fields. Instead the vortex appears to be developing along the southeast flank of this circulation feature.

The same Grid #6 fields at 0016:30 UTC (three minutes later) are shown in Figure 6.9. The downdraft has intensified over the last three minutes, and the strength of the updrafts has increased as well at z=38m and z=1km. The maximum value of vertical vorticity has increased dramatically at the lowest model level and is still positioned in the vertical velocity gradient near the northern tip of the downdraft. Vertical vorticity values at z=1km have also increased over the last 3 minutes, while the values at z=2km have remained relatively unchanged. The winds at the lowest model level have increased to tornadic strength along the southwestern portion of the vortex, but a closed cyclonic circulation has not yet developed.

The vortex develops into a tornado (as defined above) between 0016:30 UTC and 0018 UTC (model fields were only displayed every 90s during the simulation) and reaches maximum intensity (as measured by the strongest surface winds) in the simulation at 0019:30 UTC. Grid #6 fields at 0019:30 UTC are shown in Figure 6.10. Maximum ground-relative winds near the surface reach only $28 ms^{-1}$ (with a maximum surface pressure deficit of -5mb) which classifies this tornado as F0 strength. Note that tornadic-strength winds only occur along the southern half of the vortex. This flow asymmetry of stronger tangential winds occurring on one side of the tornado has also been inferred from observed damage paths (Davies-Jones et al., 1978). At the lowest model level, the vertical velocity field associated with the vortex consists of a central downdraft surrounded by an updraft ring similar to the two-celled vortices produced in the laboratory discussed in Chapter 2. The strengths of both the updrafts and downdrafts have increased at all levels during the last three minutes, along with the maximum values of vertical vorticity. Also note that closed cyclonic circulations exist at z=38m and z=1km, but not at z=2km. At z=1km, the center of circulation lies in the updraft side of the updraft/downdraft gradient. The simulated vortex is about 1km in diameter. This is a bit large for typical F0 tornadoes which are usually on the order of 100m in diameter, although diameters over 600m have been measured by Doppler radar (Brady and Szoke, 1989; Wakimoto and Wilson, 1989).

A north-south vertical cross section taken through the center of the vortex on Grid #5 at 0019:30 UTC is shown in Figure 6.11. Since the vortex was leaning almost due

northward with height, this cross section shows the vertical structure of the entire vortex (due to the small size of Grid #6, the tornado leans out of Grid #6 between z=3.5-4km). The largest values of vertical vorticity and perturbation pressure associated with the vortex occur in the lowest 1km of the tornado. Not surprisingly, the strongest winds associated with the vortex are also found in the lowest 1km above the surface. Note that the center of the cyclonic circulation lies in the updraft side of the updraft/downdraft gradient in the lowest 3km above the surface similar to the supercell tornado observations of Lemon and Doswell (1979). The vortex clearly extends upward to a height of about 5km, although the wind and vorticity fields indicate that the vortex may extend above 7km.

By 0022:30 UTC, the updraft and downdraft have continued to spiral around each other and have weakened somewhat during the last 3 minutes as shown in Figure 6.12. At z=38m, there is no longer a closed updraft ring surrounding the central downdraft in the tornado, and an updraft/downdraft couplet circle the vortex clockwise with height. The vertical vorticity has not changed much in magnitude at z=38m and z=1km, but has increased significantly at z=2km and a closed cyclonic circulation is now clearly visible at this level as well. Note that the tornadic strength winds again are only found along the southern side of the tornado.

As was discussed in Chapter 2, the non-dimensional parameter that most influences the structure of laboratory vortices is the swirl ratio (S). Typical values of S have not been calculated for many types of tornadoes, but estimates of S for multiple-vortex tornadoes in the atmosphere range from 1.25-2.5 (Forbes, 1978). To see how the swirl ratio in this case compares with observations and laboratory studies, the swirl ratio for T1 was calculated using (2.10). (Since T1 formed along the gustfront, it was difficult to estimate an updraft radius.) Swirl ratios for T1 ranged between 1.2-1.5 which lie at the lower end of the range estimated for multiple-vortex tornadoes. Although multiple vortices did not develop in T1, T1 did have a two-celled structure over the lowest few hundred meters above the surface.

The tornado T1 lasted from about 0018-0025 UTC in the simulation. Throughout its life, the tornado did not appear to be associated with the mesocyclone. This can be seen in Figure 6.13 which shows the wind and vorticity fields at 3km above the surface late in the

tornado's life cycle. The tornado is several kilometers south of the mesocyclone in the region of positive vertical vorticity extending south/southeast of the mesocyclone (associated with the position of the low-level gust front). It is interesting to note the wave #3 pattern that can be seen in the wind and vorticity fields superimposed on the mesocyclone circulation at this time. Wakimoto and Liu (1997) observed a similar wave pattern on a mesocyclone which was observed during the VORTEX experiment. In their case, one of the vorticity 'lobes' embedded in the mesocyclone eventually developed into a tornado. However, this does not appear to be the case here. During the later part of its life, the tornado slowly expanded in time, the low pressure center associated with the vortex slowly filled. The wind field also became more diffuse until wind speeds in the region were no longer of tornadic strength and a closed circulation was no longer visible. While very intense tornadoes have occasionally been observed to dissipate this way and there is one documented case of a non-supercell dissipating this way (Brady and Szoke, 1989), most tornado observations indicate that in the later portion of the tornado life cycle, the tornado actually shrinks in size as the winds associated with the tornado weaken. Perhaps the model cannot capture the later portion of the life cycle properly due to the relatively coarse grid spacing used (i.e. the model did not allow the tornado to shrink in size because the smaller spacial scale could not be resolved with the current grid configuration). Or perhaps the diffusion in the model is too large to allow the simulated tornado to become smaller. However, these ideas require further investigation which is beyond the scope of this study.

Although this simulated tornado is not consistent with observations in every regard, the model simulation does a remarkable job of reproducing many observed features of tornadoes despite its limitations, and brings to light some interesting features that are difficult to observe in actual tornadoes. T1 does not appear to be associated with the mesocyclone but rather forms along the flanking line to the south-southeast of the mesocyclone. This is the second most likely location for tornadoes to form in supercells as was shown in Figure 2.2. At low levels, the vortex forms on the updraft side of the vertical velocity gradient created by the updraft and a spiraling downdraft–not in region of strongest low-level convergence prior to the development of the downdraft. A time series of the vertical vorticity field at

Instead, a downdraft wraps around the updraft in the region where the gust front takes a southerly turn. There is a small region of large positive vertical vorticity (and low pressure) embedded in a larger region of positive vertical vorticity associated with the shear zone. However, this feature lies to the north of the surface vorticity maximum, and does not have vertical continuity below this level indicating that it is not connected with the region of large vertical vorticity at lower levels. At higher levels (z=4.3km shown in Figure 6.17) the shear zone is no longer clearly evident, but there is a a broad region of cyclonic rotation associated with the mid-level mesocyclone. The flow above the low-level shear feature is from the south at this level with a band of upward motion extending from the center of the mesocyclone to the south/southeast above the surface shear zone. Several local maxima can be seen in the vertical vorticity field at the level, but none of these maxima show any evidence of having vertical continuity with the maximum near the surface.

To get a closer look at the region in which T2 develops, Grid #6 fields at 0037:30 UTC (just prior to T2) are shown in Figure 6.18. Near the surface (Figures 6.18a,b) two local vertical vorticity maximum are embedded in an elongated shear zone extending along the northern edge of the gust front. Although there is very strong shear and convergence in this region, there is no distinct closed circulation at this time. Positive vertical motion extends along and immediately north of the leading edge of the gust front, while downward motion dominates behind the gust front. At 1.1km (Figures 6.18c,d), the vorticity maxima that were present at z=38m can no longer be seen and instead, two strips of positive vertical vorticity coinciding with two updraft bands are evident–one extending east-west along the northern side of the outflow and another extending more north-south along the eastern portion of the gust front. The flow at z=2km (Figures 6.18e,f) looks somewhat similar to the flow at z=1.1km, but the two updraft regions are completely separated by a downdraft. This downdraft originates between z=3-4km and appears to wrap around the southern and eastern sides of the mesocyclone. A local maxima can be seen in the vertical vorticity field at this level, but as mentioned previously, there is no vertical continuity between this feature and the vorticity maxima near the surface. However, there is vertical continuity between

the band of vertical vorticity to the south of the maximum at this level and the bands at lower levels.

A vortex quickly wraps up along the low-level shear zone and meets the criteria for a tornado (as given above) 1.5 minutes later at 0039 UTC. At z=38m (Figure 6.19a,b), the western vorticity maximum has intensified and become dominant, and a closed circulation about 500m in diameter has developed in connection with this feature. The strongest winds in the tornado again lie along the southern side of the vortex, with maximum wind speeds reaching $30ms^{-1}$ (with a maximum pressure deficit of -6mb), which classifies this tornado as an F1. (The straight line winds associated with the strong shear zone reached a maximum of $34ms^{-1}$ prior to the development of T2.) The strongest values of vertical vorticity near the surface lie in the updraft side of an updraft/downdraft gradient, but there is no evidence of a 'spiraling downdraft' at this level prior to the development of T2 as there was in the case of T1. At 1.1km (Figure 6.19c,d), a weak vorticity maximum now exists above the maximum at z=38m. A downdraft completely separates the two updraft regions that were present at this level earlier, and the vertical velocities in the region just to the west of T2 have increased to from $22ms^{-1}$ to $26ms^{-1}$. As was the case near the surface, the vorticity maximum at this level also lies along the eastern side of the updraft near the updraft/downdraft gradient. Several vorticity maxima are also present at z=2km (Figure 6.19e,f), but only the the weak maximum at x=-60km, y=23km appears to be connected with the lower-level features.

By 0040:30 UTC, a central downdraft has developed at the center of the vortex from z=38m to z=1.1km as shown in Figure 6.20a,c. At low levels (z=38m), the downdraft is surrounded by a ring of updraft while at z=1.1km, the northern portion of the vortex is embedded in downdraft. The vorticity field associated with the vortex at z=38m has also evolved from a single maximum into a vorticity ring (Figure 6.20b) with vertical vorticity values approaching zero at the center, and the size of the vortex has expanded to a diameter of about 1km. The vertical vorticity maximum at z=1.1km has also intensified, and a closed cyclonic circulation has now developed at this level. At z=2km, the main updraft has strengthened considerable in the last 1.5 minutes from $12ms^{-1}$ to $21ms^{-1}$.

From the vertical velocity fields at z=1.1km and z=2km between 0039 UTC and 0040:30 UTC, it appears an updraft 'pulse' began somewhere between the surface and z=1.1km, and is moving upward in time. The vertical vorticity maximum at z=2km has intensified somewhat since 0039 UTC but still remains significantly weaker than the maximum found at lower levels, and although a region of convergence has developed in the vicinity of the vorticity maximum, there is still no evidence of a closed cyclonic vortex at this level.

A vertical north-south cross section (looking west) taken through the center of the vortex on Grid #5 at 0040:30 UTC is shown in Figure 6.21. Although the tornado is embedded in a broad region of relative low pressure which extends into the upper troposphere, the tornado itself is largely a boundary layer feature. The tornado is nearly vertical (tilting slightly to the north above about z=1.5km) and extends somewhere between 2-3km above the surface. As was the case with T1, the largest vertical vorticity values associated with T2 are in the lower boundary layer. Although significant values of vertical vorticity lie to the north of the tornado at mid-levels, horizontal and vertical cross sections taken at many times during the evolution of the vortex (on both Grids #5 and #6) indicated that these regions of large vertical vorticity are not directly connected with T2, but are rather connected with the shear zone (which also sheared the mesocyclone into an east-west oriented ellipse) created by the deep surge of westerly winds which extended further north at mid-levels than at upper and lower levels.

From 0040:30 UTC to 0042 UTC, the low-level vortex continued to expand as shown in Figure 6.22. At z=38m (Figure 6.22a,b), the tornado still consists of a two-celled vortex (the central downdraft is completely surrounded by a ring of updraft), and there is now evidence that the vorticity at the center of the vortex ring has changed sign from positive to negative. At z=1.1km (Figure 6.22c,d), the vorticity maximum has again increased in intensity, and the downdraft region along the northern side of the vortex has weakened and expanded in size. The central downdraft now extends upward to z=2km as can be seen in Figure 6.22e. The vertical vorticity at this level has also increased greatly in magnitude from $0.045s^{-1}$ to $0.15s^{-1}$ during the last 1.5 minutes and a closed cyclonic circulation has now developed in association with this maximum.

The swirl ratio for T2 was also calculated using (2.10). (Since T2 also formed along a continuous updraft line, it was difficult to estimate an updraft radius.) Swirl ratios for T2 ranged between 1-1.3 which lie in the same range as the values found for T1. Although (like T1) multiple vortices did not develop in T2, T2 also had a two-celled structure over the lowest few hundred meters above the surface.

The tornado T2 lasted from about 0039-0045 UTC in the simulation. As was the case with T1, T2 slowly expanded in size in time. As the vortex expanded, the pressure field began to fill and the winds associated with the tornado weakened. Possible explanations for this evolution were given with the discussion of T1 above. T2 developed along a cyclonic shear zone created by a strong westerly wind surge associated with the storm's transition into a bow-echo/rotating-comma head structure. The position of T2 along the cyclonic shear side of a low-level wind maximum and along the southern periphery of the 'rotating comma head' portion of the storm (mesocyclone) is very similar to the 6 August, 1977 Springfield, Illinois case investigated by Forbes and Wakimoto (1983) which was discussed in Chapter 2. It is interesting to note that T2 developed in a region that was completely embedded in precipitation. The position of T2 with respect to the rotating comma head structure in the storm has also been observed in other HP supercells (Przybylinski, 1989, 1990).

Like T1, it was evident from time series of the model fields at many levels that the tornado T2 developed first in the lower boundary layer and then developed upward in time. The position of T2 relative to the mesocyclone raises the possibility that T2 is somehow connected with the mesocyclone. The evolution of the mesocyclone also appears to be affected by a surge of westerly winds along its southern flank, and evolves from a circular shape into an elliptical shape. The position of T2 appears to be along the southeast apex of the elliptical circulation at low-levels as shown in Figure 6.23. Although this feature lies in the vicinity of the mesocyclone, its direct connection with the mid-level mesocyclone is somewhat nebulous since the mesocyclone did not extend downward to this level prior to onset of the strong westerly winds. On the other hand, the fact that T2 appears to be a boundary layer feature and developed in a narrow zone of strong cyclonic shear also

raises the possibility that T2 developed as a result of an instability along the shear zone. These possibilities will be investigated further when the tornadogenesis process is discussed in Section 6.3.

6.3 Tornadogenesis

6.3.1 Circulation and Vorticity

An important question in the tornadogenesis process is 'How do large values of vertical vorticity get concentrated into a small region near the surface?' To help answer this question, two useful tools are the circulation and vorticity equations. Circulation and vorticity analysis have also been used in other severe storms/tornado studies by Davies-Jones (1982a), Davies-Jones and Brooks (1993), Klemp and Rotunno (1983), Wicker and Wilhelmson (1995), Trapp and Fiedler (1995) and Grasso (1996).

Vorticity is defined mathematically as the curl of the momentum field. Taking the curl of the momentum equation gives the three-dimensional vorticity equation:

$$\frac{\partial \vec{\omega}}{\partial t} + \mathbf{V} \cdot \nabla \vec{\omega} = -\underbrace{\vec{\omega} \nabla \cdot \mathbf{V}}_{A} + \underbrace{(\vec{\omega} \cdot \nabla)\mathbf{V}}_{B} - \underbrace{\nabla \alpha \times \nabla p}_{C} - \underbrace{\nabla \times (2\vec{\Omega} \times \mathbf{V})}_{D} + \underbrace{\nabla \times \mathbf{D}}_{E} \qquad (6.1)$$

where $\vec{\omega}$ is the three dimensional vorticity vector. Term A is referred to the stretching or convergence term, term B is the tilting term, term C is the solenoidal term, D is the coriolis term, and E is the diffusion term. Some care must be taken in interpreting some of these terms however, since flows which tilt a vortex tube will also stretch it (Davies-Jones 1982b).

Circulation is a macroscopic measure of rotation and is defined as:

$$C = \oint \mathbf{V} \cdot \vec{\tau} ds, \qquad (6.2)$$

where C is the circulation about a simple closed curve, $\mathbf{V}$ is the three-dimensional velocity vector, $\vec{\tau}$ is the unit vector tangent to the curve at any point (positive direction counterclockwise around the curve). Using Stokes' theorem, (6.2) can also be written as:

$$C = \int_s \vec{\omega} \cdot \mathbf{n} d\sigma \tag{6.3}$$

where s is the open surface bounded by the curve, $\vec{\omega}$ is the three-dimensional vorticity vector and $\mathbf{n}$ is the unit vector normal to the element of surface area $d\sigma$ at any given point. Put into words, the circulation is the integrated flux of vorticity through the surface.

In the analysis presented here, we will consider how the circulation changes in time following a material curve. Taking the total time derivative of (6.2) yields:

$$\frac{dC}{dt} = \oint \frac{d\mathbf{V}}{dt} \cdot \vec{\tau} ds. \tag{6.4}$$

Again using Stokes' theorem, (6.4) can be written as:

$$\frac{dC}{dt} = \int_s \nabla \times \frac{d\mathbf{V}}{dt} \cdot \mathbf{n} d\sigma. \tag{6.5}$$

The equations used to calculate the time rate of change of circulation in the model can be found by substituting the model momentum equation into (6.4). This gives:

$$\frac{dC}{dt} = \oint [\underbrace{-\theta_{ov} \nabla \pi}_{A1} + \underbrace{(\frac{\theta'_v}{\theta_{ov}} - r_c) g\mathbf{k}}_{B1} - \underbrace{2\vec{\Omega} \times \mathbf{V_H}}_{C1} + \underbrace{\mathbf{D}}_{D1}] \cdot \vec{\tau} ds \tag{6.6}$$

where θ_{ov} is the arbitrary reference state virtual potential temperature, θ'_v is the perturbation virtual potential temperature, π is the perturbation Exner function ($\pi = c_p(\frac{p'}{p_o})^{\frac{R}{c_p}}$), r_c is the total condensate mixing ratio, $\vec{\Omega}$ is the angular velocity of the earth, and $\mathbf{D}$ is the velocity tendency due to diffusion. Term A1 in (6.6) is the contribution due to pressure forces along the material curve, term B1 is the contribution due to buoyancy, term C1 is the coriolis term, and D1 is the contribution from diffusion. Note that the buoyancy term can change the circulation only if a portion of the curve lies in the vertical plane. Since θ_{ov} is only a function of the vertical coordinate in the model, if the material curve lies only in the horizontal plane the pressure term (A1) can be written as an exact differential and its integral around the curve vanishes. Thus the pressure term can also act to change the circulation only when a portion of the curve extends in the vertical. Because θ'_v and π are

functions of the reference state which is defined at the beginning of the model integration (6a.m. CDT time in this case), their actual values at the time the circulation analysis was performed (after 6p.m. CDT) may give counterintuitive results. For example, the model buoyancy tendency for a sinking air parcel late in the simulation may be positive (even though the parcel is negatively buoyant when compared to the local environment) simply because the environment has warmed during the simulation. Since the sum of terms A1 and B1 is independent of the basic state, the two terms were combined into one 'baroclinic' term in the analysis presented here. The coriolis term (C1) will only act to change the circulation if the material curve is converging/diverging, or if the curve is changing its orientation such that a larger portion of the surface bounded by the curve lies in the plane perpendicular to $\vec{\Omega}$. A converging material curve in the horizontal plane will have a positive coriolis tendency (since the coriolis force acts to the right of the wind vector) and diverging material curve will have a negative tendency. Diffusion (D1) can provide a positive or negative tendency to the circulation depending on the structure of the wind field and the shape of the material curve. The circulation tendency due to diffusion for a material curve with cyclonic (anticyclonic) circulation which lies near the surface will be negative (positive) since surface friction acts to slow the winds. For a material curve which lies in the vertical plane, the diffusion tendency can be positive or negative. Although diffusion will still act to slow down the winds near the surface (or perhaps increase them aloft, depending on the situation), this can provide either a positive or negative tendency to the circulation depending on the vertical wind shear relative to the curve.

Substituting the curl of the model momentum equation into (6.5) yields an alternate expression for the time rate of change of circulation in the model which is given by:

$$\frac{dC}{dt} = \int_s [-\nabla\theta_{ov}\times\nabla\pi+\nabla\times(\frac{\theta'_v}{\theta_{ov}}-r_c)g\mathbf{k}-2\vec{\Omega}(\nabla\cdot\mathbf{V})+(2\vec{\Omega}\cdot\nabla)\mathbf{V}-2\mathbf{V}\cdot\nabla\vec{\Omega}+\nabla\times\mathbf{D}]\cdot\mathbf{n}d\sigma. \quad (6.7)$$

As was the case in (6.6), the first two terms on the right hand side of (6.7) can only make a contribution to the circulation tendency if a portion of the curve extends vertically.

For the circulation analysis presented here, we will be using (6.4) and (6.6) since the momentum form of the equations is easier to calculate from the model output. Grid #5 fields were used for these calculations due to the small size of Grid #6. The initial material curve consisted of a circle of radius 1km (composed of 4000 individual massless particles) which was centered on the vertical vorticity maximum associated with the tornado at the lowest model level. The curve was initialized at a time shortly after the tornadic strength winds were established near the surface on Grid #5. The material curve was then advected backwards in time using the model wind fields which were stored every 5 seconds during the simulation, and the circulation was diagnosed using (6.2). Particles were redistributed around the curve every 15 seconds to keep successive particles from getting too far apart (which would introduce additional error into the circulation calculations). Momentum tendencies were also saved every 5 seconds during the simulation and the circulation tendency was calculated using (6.6). The circulation could then be 'prognosed' using the initial circulation calculated by (6.2) and the circulation tendency calculated from (6.6). If the prognosed and diagnosed circulations match reasonably well, then the physical processes responsible for changes in the circulation around the material curve can be determined.

While the circulation analysis gives useful information about the larger scale processes which help to spin up the tornado, it does not give any information about the vorticity changes an individual parcel experiences as it enters the tornado, or why such large values of vertical vorticity are attained near the surface. To help answer these questions, a vorticity analysis was also performed. The analysis consisted of calculating the vorticity components and tendencies along the trajectories of 20 particles which are meant to represent 20 air parcels, and the terms 'particle' and 'parcel' will be used interchangeably throughout the text. Like the circulation analysis, the particles were initialized in a circle inside the region of large vertical vorticity associated with the tornado at the lowest model level. The radius of the circle for the vorticity analysis was 800m, which lies inside the material curve used for the circulation calculations. Backwards trajectories were then calculated for each particle using the model wind fields that were saved every 5 seconds during the simulation, and the vorticity components and tendencies were calculated along the parcel trajectories. The

vorticity tendencies were then used to calculate a 'prognosed' vorticity using the initial vorticity values calculated with the actual wind fields. If the prognosed and diagnosed vorticity components match closely, the physical processes responsible for the large vertical vorticity values near the surface can be identified.

6.3.2 June 30–T1

Circulation Analysis

The material curve used for the circulation analysis of T1 was initialized at 0021 UTC (44460s) as shown in Figure 6.24d (recall that the path of the material curve was computed backwards in time so the curve was actually 'initialized' at the final time shown in the Figure). The position of the material curve was calculated backwards in time until 0003 UTC, after which time the calculation was terminated because a portion of the curve was advected out of the Grid #5 domain.

As shown in Figure 6.24a, most of the material curve at 0003 UTC (43380s) lies in the horizontal plane within the lowest model layer (between the surface and z=38m). A small portion of the curve extends upward into the vertical (maximum height 330m) inside the storm. By 0009 UTC (43740s), the vertical portion of the curve has descended toward the surface (maximum height now 200m) and the entire curve has converged toward the developing tornado. In the next 6 minutes, the material curve continued to converge and the vertical portion of the curve continued to descend until 0015 UTC (44100s) when most of the curve was in the horizontal plane in the lowest model layer except for a small portion northwest of the developing vortex. The vertical portion of the curve continued to descend until 0017 UTC (44220s) at which point the entire material curve was in the horizontal plane. From 0017 UTC to 0021 UTC (44220s-44460s), the curve converged horizontally into the tornado.

A time series of the prognosed and diagnosed circulations and circulation tendencies for the material curve is shown in Figure 6.25. The prognosed and diagnosed circulations match reasonably well until the last 200 seconds of the calculation. However, the trends in the

two curves remain the same despite the divergence of the curves. From 0003 UTC (43380s) to about 0013 UTC (44000s), the circulation around the material curve increases by 50% only to decrease to near its original value from 0013 UTC (44000s) to 0021 UTC (44460s). The net result is that from 0003 UTC until 0021 UTC (the time at which the material curve surrounded the tornado), there is very little change in the circulation associated with the material curve, indicating that the circulation at 0021 UTC was already present in the environment at 0003 UTC.

The tendencies show some somewhat unexpected results. The increase in circulation in the first half of the analysis is due to two terms: coriolis and diffusion. It is interesting to note that the coriolis term (and sometimes the diffusion term) has been neglected in many of the prior circulation analyses since it is generally assumed to be small (Klemp and Rotunno, 1983; Wicker and Wilhelmson, 1995; Davies-Jones and Brooks, 1993). However, the importance of the coriolis term is relative, since the magnitude of this term would be the same for *any* material curve with the same size and convergence rate at the same latitude. To illustrate this point, the change in circulation due only to coriolis tendency for T1 will be calculated below. From (6.7), changes in circulation due to the coriolis tendency can be written as

$$\frac{dC}{dt} = \int_s -2\vec{\Omega}(\bigtriangledown \cdot \mathbf{V})d\sigma \tag{6.8}$$

where all terms have been defined above. For simplicity, we will assume the material curve lies in the horizontal plain at all times. If this is the case, then only the local vertical component of $2\vec{\Omega}$ need be considered. This is given by $f = 2\vec{\Omega}\sin\phi$ where ϕ is the latitude. The storm in this case is located near 42°N giving $f = 9.77 \times 10^{-5}s^{-1}$. Assuming that f and $\bigtriangledown \cdot \mathbf{V}$ are constant over the time period under consideration, (6.8) can be written as

$$\frac{dC}{dt} = -f \bigtriangledown \cdot \mathbf{V}A \tag{6.9}$$

where A is the area bounded by the material curve at some time t. Using the relationship

$$\nabla \cdot \mathbf{V} = \frac{1}{A}\frac{dA}{dt}, \tag{6.10}$$

(6.9) becomes

$$\frac{dC}{dt} = -f\frac{dA}{dt} \tag{6.11}$$

or

$$\int_{C1}^{C2} dC = -f \int_{A1}^{A2} dA. \tag{6.12}$$

A computer program was used to calculate the horizontal area bounded by the material curve at the beginning and end of the circulation analysis. The area bounded by the curve at 0003 UTC (A1) was $2.227 \times 10^8 m^2$ (same as a circle with a radius of 8.4km) while the area bounded by the curve at 0021 UTC was $3.142 \times 10^6 m^2$. Substituting these values and the value for f into (6.12) gives a change in circulation over the time period due only to the coriolis tendency of $\triangle C = 2.145 \times 10^4 m^2 s^{-1}$. (Note that this value is very close to the change in circulation from the coriolis term shown in Figure 6.25). This would be the change in circulation due to the coriolis term for *any* material curve starting with an average radius of 8.4km which converged to a radius of 1km over some time period at $\phi = 42°$N, regardless of the magnitude of the initial circulation or the magnitudes of the other circulation tendencies. Thus the coriolis tendency would only be significant for weak tornadoes in which the magnitude of the circulation stays below $\sim 2 \times 10^5 m^2 s^{-1}$ while the curve converges over distances similar to those in this case. If a plot similar to Figure 6.25 were made for a strong tornado in which the circulation was an order of magnitude (or more) larger than T1, the coriolis tendency would appear as a relatively flat line (and hence negligible). In more general terms, the magnitude of the coriolis tendency to the circulation would be limited by the largest horizontal area over which the tornado could draw air during its lifetime (see 6.12). This would depend on several factors, including the magnitude of the convergence and the properties of the flow extending many kilometers away from the tornado. Thus it is not clear that the coriolis term can be neglected in a

circulation analysis in all cases, although it is unlikely that this term alone could provide enough circulation to spin up a tornado over realistic time periods.

The diffusion tendency to the circulation is initially positive from 0003 UTC (43380s) to about 0013 UTC (44000s) and then becomes negative until the end of the calculation. Recall from above that a portion of the curve lies in the vertical plane from 0003 UTC (43380s) to 0017 UTC (44220s) which corresponds closely with the time period that diffusion was making a positive contribution to the circulation. There are several possible reasons for this. First, from an inspection of the horizontal vorticity vectors in the region of the vertical segment of the curve, it could be inferred that the circulation in the vertical segment of the curve was slightly negative. The vorticity vectors at the lowest model levels were 'poking through' the curve as to contribute to positive circulation. The vorticity vectors at higher model levels poked through the curve in the opposite direction, making a negative contribution to the circulation, giving a net circulation around the vertical part of the curve that was slightly negative. Thus if diffusion were acting to decrease the wind speeds along the vertical segment of the curve, this would give a positive contribution to the circulation tendency (diffusion would be making the circulation less negative). Another possibility is that down-gradient diffusion is acting to change the wind speed along the vertical segment of the curve in such a way as to increase the circulation.

The baroclinic term makes a negligible contribution to the changes in circulation. Early in the circulation analysis, the baroclinic term is slightly negative leveling off to near zero as the material curve becomes horizontal at later times. This result is similar to the idealized vortex simulation of Walko (1993), but differs from the findings of Rotunno and Klemp (1985) and Davies-Jones and Brooks (1993) who showed that the buoyancy term (also referred to as the baroclinic or solenoidal term) dominated the circulation changes in their circulation analyses of a simulated low-level mesocyclone/tornado vortex. It also differs from the findings of Grasso (1996) who inferred that baroclinicity was important in changing the circulation along the material curves in his tornado simulations. This result is somewhat surprising since intuitively, one would think that since HP supercells can produce copious amounts of precipitation, they have the potential to generate regions of strong baroclinicity

and hence the baroclinic circulation tendencies would likely be quite large. Although the simulated storm does produce regions of strong baroclinicity, the wind fields are such that the vertical portion of the material curve does not lie in these regions.

One of the current theories of tornadogenesis for weak tornadoes not associated with the mesocyclone is that convergence of preexisting vertical vorticity can 'spin up' the vortex (Brady and Szoke, 1989). Since the material curve as described above lies chiefly in the horizontal plane throughout the analysis, we will explore the possibility that convergence of low-level vorticity alone can account for the large vertical vorticity associated with the tornado at low levels. For this calculation, we will assume that circulation is constant (considering there was very little change in the circulation between the beginning and end times from the material curve calculations, this is a good approximation), and that the only process that can change vertical vorticity is convergence of relative vorticity. The time rate of change of vorticity is then given by:

$$\frac{dln(\bar{\omega})}{dt} = - \bigtriangledown \cdot \mathbf{V} = - \frac{dln(A)}{dt} \tag{6.13}$$

where $\bar{\omega}$ is the area average vertical vorticity bounded by the material curve, and A is the area bounded by the curve. The relationship between the change of area bounded by the curve and the convergence was utilized since the area could be easily calculated when the material curve was placed on the model grid.

To make the calculation simpler, we will also ignore the vertical portion of the curve and assume that the curve lies in the horizontal plane at all times. Since the initial vertical portion of the material curve was neglected, the area bounded by the curve and the area integrated vorticity were calculated using a computer program at various times during the analysis. The cross sectional horizontal area bounded by the curve at 0003 UTC (43380s) was approximately $2.227 \times 10^8 m^2$ and the area averaged vertical vorticity was $4.73 \times 10^{-4} s^{-1}$. Note that this gives a circulation value which is somewhat larger than that calculated from integrating the wind field around the entire material curve again indicating that the vertical portion of the curve was making a small negative contribution to the total circulation around the curve at this time. The area bounded by the curve at 0021 UTC (44460s) was

$3.142 \times 10^6 m^2$. Using (6.13), the area average vorticity at 0021 UTC due only to convergence of low-level relative vorticity would be approximately $0.0335 s^{-1}$. The area average vorticity calculated from the circulation analysis at 0021 UTC (44460s) is $0.0176 s^{-1}$ which is the same order of magnitude as that which could be attained only through convergence. [For comparison purposes, convergence of planetary vorticity would give an area average vorticity of $3.74 \times 10^{-4} s^{-1}$.] Thus it appears possible that the tornado could 'spin up' from the convergence of preexisting low-level vorticity. If this is true, it raises a few issues such as 'what is the significance of the downdraft in the tornado formation?', and 'which processes create vertical vorticity at low-levels?'. To help answer these questions, vertical vorticity and the vorticity tendencies were calculated along parcel trajectories which entered the vortex near the surface. These results are presented in the next section.

Vorticity Analysis

The vorticity was calculated along parcel trajectories for 20 particles which were initialized in a circle at low levels in the vortex (inside the area bounded by the circulation curve). Like the circulation analysis, the particles were initialized at the lowest model level (z=38m) at 0021 UTC. The trajectories were then calculated backwards in time until 0001:30 UTC at which point the calculations were terminated because some of the particles were advected out of Grid #5.

The trajectories for 10 of these particles (where every other trajectory is plotted) are shown in Figure 6.26. As is evident from the trajectories, parcels entering the vortex at low-levels originate from two main areas: one to the southeast of the tornado at low-levels in the environment, the other to the northwest of the tornado in the storm downdraft. This pattern is even more pronounced when all 20 particles are plotted since the two 'outliers' are two of the ten particles plotted in Figure 6.26. Parcels originating in the downdraft enter the tornado at low-levels along the western and southern sides of the vortex, while those parcels originating in the environment enter the low-levels of the tornado along the eastern and northern sides. One of the parcels originates north of the vortex and enters the northern side of the tornado. The path of this parcel indicates that the parcel spends some

time in the region along the forward flank gust front before entering the vortex. Another parcel originates south of the vortex, and its path indicates that it spends some time along the rear flank gust front before entering the tornado from the south.

Since most of the trajectories entering the tornado at low levels originate from two main regions, a 'typical' particle was chosen from each region and their vertical vorticity evolutions are shown in Figures 6.27 and 6.29. Figure 6.27 displays the time evolution of vertical vorticity and vertical vorticity as a function of height for particle #14 which originates at low-levels in the environment to the southeast of the developing tornado. The time series of the vertical vorticity along the parcel trajectory (Figure 6.27a) indicates that the parcel's vertical vorticity remains slightly positive (but very near zero) until the parcel nears the developing vortex when its vertical vorticity increases exponentially. The plot of the vertical vorticity tendencies along the parcel's trajectory (Figure 6.28) indicates that tilting of horizontal vorticity (in this case the east-west component of horizontal vorticity) is responsible for the initial increase in the parcel's vertical vorticity, which is then amplified exponentially by convergence.

Figure 6.29 shows the time evolution of vertical vorticity as function of height for particle #10 which originates in the downdraft to the northwest of the tornado. The parcel's vertical vorticity starts out negative and remains negative until about 44200s (0017 UTC) when the parcel's vertical vorticity becomes positive, and then increases exponentially shortly thereafter as shown in Figure 6.29a. A plot of the vertical vorticity verses height shows that the parcel's vertical vorticity remains negative until the parcel nears the end of its descent as shown in Figure 6.29b. [Note that even though the parcel descends below the lowest model level, the vorticity at the surface is zero (lower boundary condition) so the vorticity of points below the first model level are interpolated downward from the values at the first model level.] Similar results were reported in the simulations of low-level mesocyclones by Davies-Jones and Brooks (1993) who also postulated that a similar process could occur in tornadogenesis. The vorticity tendencies along the parcel trajectory are shown in Figure 6.30. As the parcel nears the surface, divergence weakens the magnitude of the vertical vorticity. Since the vertical vorticity is negative at this time, the convergence

term makes a positive contribution to the vorticity tendency (i.e. makes the vertical vorticity less negative). Shortly before 44200s (about 0017 UTC–shortly before the vertical vorticity changes sign), tilting of horizontal vorticity (in this case the east-west component) starts to become positive and large. After 44300s (0018:30 UTC), convergence takes over and the vorticity amplifies exponentially. It is also interesting to note that although the coriolis term made a significant contribution to changes in the circulation around the material curve, the convergence of planetary vorticity does not make any significant contribution to the vertical vorticity along any of the parcel trajectories calculated here.

Although most of the particles originate to the northwest and southeast of the tornado, the two particles that originate to the north/south of the vortex are briefly discussed here for completeness. Particle #3 originates north of the developing vortex in the cold air behind the forward flank gust front. Shortly after 0009 UTC, the particle enters the baroclinic zone associated with the forward flank gust front and begins moving southwestward toward the vortex. The parcel remains in a weak downdraft just behind the gust front as it moves southwestward, and its vertical vorticity remains negative. However, during this time period, horizontal vorticity (pointing to the southwest) is being generated through baroclinicity as was found in the simulation of Rotunno and Klemp (1985). The horizontal vorticity gets tilted into the vertical as the parcel enters a weak updraft region north of the developing vortex. Convergence then acts to increase the vertical vorticity as the parcel moves southward. Particle #13 starts out in the warm environmental air to the south-southeast of the tornado. This parcel moves northwestward and enters the baroclinic zone associated with the rear flank gust front around 0015 UTC. As it enters the gust front, the horizontal vorticity is tilted into the vertical, and the parcel acquires positive vertical vorticity. The parcel then moves northward along the gust front toward the tornado as its vertical vorticity steadily increases due to convergence.

From the above analysis, it is clear that the large values of positive vertical vorticity associated with most of the parcels at the lowest model level in the simulated tornado are generated through tilting of horizontal vorticity into the vertical, followed by rapid amplification through convergence. In the trajectories originating to the southeast of the

vortex, horizontal vorticity is tilted into the vertical as the parcels encounter the low-level updraft associated with the gust front and developing vortex. For parcels originating northwest of the vortex, the tilting occurs just above the surface (below z=50m) in the downdraft.

Summary of Tornadogenesis Process for T1

The tornado T1 formed at the southern end of a shear zone present near cloud base in the storm. Although there was significant vertical vorticity associated with this feature in the storm, there was no evidence in the model results that the high values of vertical vorticity built downward in time as proposed by the dynamic pipe effect theory (Leslie, 1971). Instead the tornado developed first near the ground and then developed upward in time to a height of 5-6km. However, it is possible that the shear feature helped drive the downdraft which played a role in the tornadogenesis process.

The vorticity analysis revealed that the vertical vorticity which was converged into the tornado at the lowest model level along most of the parcel trajectories was created through tilting of horizontal vorticity into the vertical by both the updraft and the downdraft. (Recall that the lowest model level is 38m above the surface in these simulations.) A few of the trajectories indicated that a small percentage of the parcels spent time in the vicinity of the forward and rear flank gust fronts where tilting of baroclinically-generated horizontal vorticity and convergence also act to increase the vertical vorticity of the parcels.

From the circulation analysis presented above, it is evident that the circulation associated with T1 was already present at low-levels 15-20 minutes before the tornado developed. Although the baroclinic term associated with the downdraft made a negligible contribution to the circulation in this case, the downdraft played an important role in tilting horizontal vorticity into the vertical just above the surface in the near-tornado environment where horizontal convergence could then act to amplify it.

6.3.3 June 30–T2

Circulation Analysis

The material curve used for the circulation analysis of T2 was initialized at 0039 UTC (45540s) as shown in Figure 6.31d. The material curve was advected backwards in time until 0021 UTC, after which time the calculation was terminated because a portion of the curve was advected out of the Grid #5 domain. Recall that the storm goes through its transformation into a bow echo during this time period, and T2 develops along the northern edge of the shear zone created by the strong storm outflow.

Figure 6.31 shows the position of the material curve at four times during its evolution. At 0021 UTC (Figure 6.31a) most of the material curve lies in the horizontal plane within the lowest model layer (between the surface and z=38m) and extends over a large area enclosing T1 which was in progress. Note that about two-thirds of the curve lies inside the storm. The curve extends into the vertical plane in several locations including a narrow region along the northeastern portion of the curve, another narrow region along the southwestern portion of the curve, and a wider region along the northwestern side of the curve. The maximum height of the curve at this time was 410m along the northeastern part of the curve. From 0021 UTC to 0027 UTC, the material curve contracted and the vertical portions descended as shown in Figure 6.31b. The curve still encloses T1, and the flow around T1 is starting to distort the curve south of T1. The curve continues to contract and descend during the next 10 minutes, and by 0036 UTC it encloses part of the shear zone created along the northern edge of the storm outflow. The curve at this time is nearly horizontal with only two areas of the curve extending into the vertical to about 100m. The curve continues to shrink in size and the vertical portions continue to descend until 0039 UTC when the material curve surrounds the developing vortex[1]T2 at z=38m (Figure 6.31d).

---

[1]Recall from the discussion of the evolution of T2 that shortly after 0036 UTC there were 2 low-level vorticity maxima present along the shear zone. The eastern maxima weakened at the expense of the western

A time series of the prognosed and diagnosed circulations and the circulation tendencies for the material curve is shown in Figure 6.32. The prognosed and diagnosed circulations match reasonably well except near the end of the calculation, but show similar trends throughout the analysis. From 0021 UTC (44460s) to about 0024 UTC (44640s), the circulation around the material curve increases slightly and then slowly decreases until about 45200s (0033 UTC) after which time it drops off rapidly until the end of the analysis at 45540s (0039 UTC). The net result is that from 0021 UTC until 0039 UTC (the time at which the material curve surrounded the tornado), the circulation around the material curve decreased by 36%.

From the circulation tendencies shown in Figure 6.32 it is clear that the diffusion tendency, which was negative throughout the analysis, dominated the evolution of the material curve in this case. The fact that the vast majority of the material curve resided in the lowest model layer throughout the analysis suggests that surface stresses were responsible for this.

The coriolis tendency again makes a positive contribution to the circulation tendency (as it must if the curve is converging horizontally near the surface at midlatitudes as was discussed above), and accounts for most of the brief increase in the circulation early in the analysis. The relative contribution is smaller than it was in the analysis of T1 because the total circulation is larger in this case than it was in the case of T1.

Like T1, the baroclinic term is again almost negligible in the circulation analysis of T2. The baroclinic tendency makes a very small positive contribution to the changes in circulation early in the analysis, leveling off to zero as the curve becomes completely oriented in the horizontal plane. A closer look at the vertical segments of the curve revealed that all three of the the vertical segments resided in a baroclinic zones. The segment along the southern portion of the curve was located in the strong baroclinic region along the rear flank gust front. However, this baroclinic zone creates a circulation that would give

---

maximum, and it was the western maximum which developed into T2. This maximum was just developing at 0039 UTC on Grid #5 shown in Figure 6.31d.

a negative contribution to the circulation around the material curve. The segment along the northeastern portion of the curve resides in a weak baroclinic zone north of the forward flank gust front, and the segment along the northwestern part of the curve resides in another weak baroclinic zone. These baroclinic zones do generate solenoids which make a positive contribution to the circulation around the material curve. Although these baroclinic zones are weaker than that along the rear flank gust front, the area swept out by the vertical segments of the material curve to the northeast and northwest are larger than the vertical segment to the south, giving a small net positive contribution to the circulation due to baroclinicity.

In summary, the circulation analysis for T2 presented above indicates that the circulation at 0039 UTC (the time the material curve surrounded just the tornado) originates from the environmental circulation that was already present at 0021 UTC. The circulation tendencies indicated that the circulation around the tornado at 0039 UTC is *less* than the circulation present at 0021 UTC due to surface stresses acting to slow the winds near the surface.

Vorticity Analysis

To understand how such large values of vertical vorticity were created near the surface in T2, the vertical vorticity was calculated along parcel trajectories for 20 particles. The particles were initialized in a circle (inside the area bounded by the circulation curve) at the lowest model level (z=38m) at 0039 UTC. The trajectories were then calculated backwards in time until 0020 UTC at which point the calculations were terminated because some of the particles were advected out of Grid #5.

The trajectories for 10 of the particles (where every other particle is plotted) are shown in Figure 6.33. As was the case in T1, the trajectories entering T2 at low-levels originate from two main areas: one to the northeast of the tornado and the other to the west of the tornado. Both of these regions are inside the storm. The region to the northeast was in forward flank downdraft of S1 (before it transitioned into a bow-echo). Parcels originating from this region entered the north and west sides of the low-level vortex. The particles

coming from the west were originally located along the west side of S1 at 0021 UTC in a region of northwesterly winds associated with outflow from a storm to the west of S1. These parcels entered the tornado along the south and east sides of the vortex. It should be noted that there was one 'outlier' (not shown in Figure 6.33) which originated in the warm environmental air to the south of the forward flank gust front, entering the storm in the 'crook' of the kidney-bean type structure in the low-level precipitation field, eventually ending up on the east side of the tornado.

From Figure 6.33, it is evident that the particles originating northeast of the tornado came from different vertical levels. Most of the parcel trajectories originated in a downdraft (some as high as 500m above the surface), sinking down near the surface before moving southward toward the tornado. A few others originated near the surface, staying in the lowest model layer through the duration of the trajectory calculation. The vertical vorticity of these surface parcels did not become significant until the parcels entered the updraft region just east of the developing tornado when horizontal vorticity could be tilted into the vertical by the updraft, and then enhanced through convergence.

A time series of the vertical vorticity following one of the northeast downdraft parcels (particle #4) is shown in Figure 6.34a. The vertical vorticity started out negative at 0020 UTC (44400s) and changed sign around 0026 UTC (44750s) when the parcel had descended down to z=80m. This initial increase in vertical vorticity early in the trajectory analysis was caused by tilting of horizontal vorticity into the vertical as can be seen from the vertical vorticity tendencies which are shown in Figure 6.35. The vertical vorticity then leveled off at a small positive value until about 0037 UTC (45400s) when the vertical vorticity decreased again to near zero (some of the other particle's vertical vorticity dropped to slightly negative values again at this point). During this time the tilting term became slightly negative, and the vertical vorticity decreased. To see why this happened, the particle position was placed on top of the the model vertical velocity and horizontal vorticity fields (not shown). Around 0034 UTC, the parcel was moving into a region of slightly stronger downdrafts, and the vertical velocity gradient was such as to tilt the north-south component of horizontal vorticity downward. Around 0037 UTC (45400s), the parcel began to exit the

other side of the downdraft, and the vertical velocity gradient changed sign causing the tilting term to change sign and the vertical vorticity increased again. After about 0038 UTC (45500s), convergence became large and the vertical vorticity increased exponentially until the end of the calculation.

The particles which moved toward the tornado from the west also originated from different vertical levels. Some of the particles started in a weak downdraft, and slowly descended while moving eastward toward the tornado. These trajectories were surrounded to the north/south by other particle trajectories which started near the surface and stayed in the lowest model layer throughout the trajectory calculation. The time series of vertical vorticity for one of these low-level trajectories (particle #8) is shown in Figure 6.36a. Note that the vertical vorticity of the parcel is positive along the entire trajectory. This parcel (and all the others that start at low-levels to the west of the vortex) start and spend considerable time in a weak cyclonic shear zone associated with outflow from a storm west of S1. Around 0037 UTC (45400s), the vertical vorticity starts to increase exponentially. The vertical vorticity tendencies for the parcel (Figure 6.37) indicate that the large increase in the parcel's vertical vorticity is first caused by tilting of horizontal vorticity into the vertical (both the east-west and north-south components), followed by an exponential increase due to convergence.

Figure 6.38 shows the time evolution of vertical vorticity, and vertical vorticity as a function of height for particle #13 which originates in the downdraft to the west of the tornado. The parcel's vertical vorticity starts out negative and decreases somewhat between 0032:30 UTC (45150s) and 0036 UTC (45350s). After 0036 UTC, the vertical vorticity starts to increase and then changes sign just after 45400s (0037 UTC). A plot of the vertical vorticity verses height shows that the parcel's vertical vorticity starts out negative and does not change sign until the parcel nears the end of its descent in the downdraft as shown in Figure 6.38b. The vorticity tendencies again indicate that tilting of horizontal vorticity into the vertical (here tilting of the north-south component is much larger than tilting of the east-west component, but both are making a positive contribution) causes the vertical vorticity to increase and change sign, followed by amplification from convergence.

As was mentioned above, there was one particle (particle #16) that originated east of the tornado in the warm environmental air ahead of the storm. The vertical vorticity evolution of this parcel is discussed here briefly for completeness. This parcel starts with vertical vorticity values near zero (but slightly positive) as it moves northward toward the forward flank gust front. Shortly after 0027 UTC, the parcel enters the convergence region just ahead of the forward flank gust front, and the vertical vorticity of the parcel starts to increase due to convergence. The parcel then moves westward toward the storm with the environmental air along the forward flank gust front while its vertical vorticity slowly increases through convergence. Around 0035 UTC (45300s), the parcel enters the strong convergence region where the strong storm outflow from the west meets the northerly winds from what was the forward flank downdraft, and the vertical vorticity of the parcel amplifies rapidly as it moves eastward toward the tornado.

With the exception of particle #16, the large values of positive vertical vorticity at the lowest model level at the end of the parcel trajectories in the simulated tornado are generated through tilting of horizontal vorticity into the vertical, followed by rapid amplification through convergence. In the trajectories originating near the surface both to the west and northeast of the vortex, horizontal vorticity was tilted into the vertical as the parcels encountered the low-level updraft associated with the convergence zone created by the strong storm outflow. It is conceivable that the low-level parcels originating west of the tornado could have acquired vertical vorticity through convergence alone. However, the tendencies along the parcel trajectories indicated that tilting did play a role in increasing the parcels' vertical vorticity. For parcels originating in the downdraft to the west of the tornado, the tilting occurred in the lowest 50m above the surface in the downdraft. For parcels originating in the downdraft to the northeast of the tornado, the positive tilting of horizontal vorticity first occurred 80-200m above the surface, and then again as the parcels neared the end of their descent just above the surface.

As was mentioned above, the tornado T2 formed along a strong cyclonic shear zone created by the strong storm outflow associated with the storm's transition into a bow-echo. The fact that the tornado only develops upward to a height of 2-3km and develops very

quickly suggest a shear instability mechanism may have played a role it its development. Shear instability along thermal boundaries has been suggested as a possible mechanism for tornadogenesis in previous studies as was presented in Chapter 2. A brief recap of the theory behind shear instabilities is present here. For a more complete discussion on the stability of shear flows, the reader is referred to Drazin and Reid (1981).

Most of the work to date on shear instability has been done on two-dimensional shear parallel flows. The pioneering work was done by Rayleigh (1880) who showed that a necessary (but not sufficient) condition for shear instability is that an inflection point in the velocity profile must occur somewhere in the flow (or the vorticity gradient must change sign somewhere in the flow). In two dimensions, vorticity is conserved following air parcel motion so vorticity can increase in an area only through accumulation of pre-existing vorticity by differential advection. Batchelor (1967) illustrates this process for a two-dimensional vortex sheet. When a small sinusoidal disturbance is introduced in the wind field across the vortex sheet, the wind field concentrates vorticity in some areas, and depletes it in others. The vorticity concentrations induce a wind field which further acts to concentrate the vorticity in these regions leading to exponential growth of the disturbance.

However, outflow boundaries (and other mesoscale boundaries) in the atmosphere along which shear instabilities might develop are three-dimensional, and it is unclear how the results from two-dimensional studies would apply in three dimensions since tilting and stretching of vorticity can act to change the vorticity of an air parcel. Lee and Wilhelmson (1997a,b) undertook an idealized modelling study to investigate shear instabilities along outflow boundaries in three dimensions and the possible connection to tornadogenesis. They documented several stages in the evolution of the vortex sheet and the subsequent vortices that developed:

1. Vortex sheet development stage

2. Vortex sheet roll-up stage in which the vortex sheet broke down into several 'misocyclones' (weak vortices with dimensions between 40m-4km –see Chapter 2 for further

discussion). In their case, the initial scale of these 'horizontal shear instabilities' (or HSI) was about 1.5km which was half the predicted theoretical value.

3. Misocyclone interaction and merger stage, in which 2-3 misocyclones merged together creating vortices with scales on the order of 3km.

4. Early mature phase when the misocyclones intensified to tornadic strength as convective towers developed above them.

5. Late mature phase as rain-cooled downdrafts developed near the surface, enhancing the low-level convergence which intensified the vortices.

6. Dissipation stage as negatively buoyant air surrounded the low-level vortex, inhibiting upward vertical motion.

The present case is much more complicated, since moist convection has been ongoing, and rain-cooled downdrafts were already occurring both north and south of the shear zone prior to tornadogenesis. However, it may be helpful to take a closer look at the low-level vertical vorticity field to see if it is possible to detect a process similar to that found by Lee and Wilhelmson (1997a,b) occurring in the simulation.

The vertical vorticity field at z=350m on Grid #5 at several different times is shown in Figure 6.40. From these plots, it is clear that the necessary condition for instability is met–the vorticity gradient does change sign in the region along the northern edge of the strong storm outflow. However, prior to tornadogenesis at 0036 UTC (Figure 6.40a), there is little evidence of a periodic 'roll-up' along the east-west segment of the boundary (although there is along the north-south segment of the boundary). Instead, there is a region of high vertical vorticity approximately 4km long in the area where the outflow boundary turns toward the west. By 0037:30 UTC (Figure 6.40b), this zone of high vertical vorticity narrows and strengthens. Although not revealed in Figure 6.40b due to the $0.03s^{-1}$ cutoff in the vertical vorticity contours, two distinct vertical vorticity maxima are present in this region at 0037:30 UTC, located about 1km apart. Ninety seconds later at 0039 UTC (the time at which the circulation and vorticity analyses were preformed), the western maximum

has intensified at the expense of the eastern maximum as shown in Figure 6.40c. There is now evidence that smaller regions of concentrated vertical vorticity are beginning to emerge, and by 0040:30 UTC (Figure 6.40d), these periodic local maxima in the vertical vorticity field are readily visible. However, by this time tornadogenesis has already taken place. Thus although there is evidence that shear instabilities do develop along the outflow boundary, it is unclear if shear instability was involved in the tornadogenesis process in this case.

Summary of Tornadogenesis Process for T2

The tornado T2 formed on a strong cyclonic shear zone along the northern periphery of the strong storm outflow following the storm's transition into a bow-echo. There was evidence that horizontal shear instabilities did occur along the outflow boundary, but it could not be determined if they played a significant role in the tornadogenesis process. Although the tornado forms along the southern portion of the rotating comma-head feature of the storm (mesocyclone), there is no obvious connection between them. The tornado developed near the ground and then ascended in time to a height of about 2km.

The circulation analysis presented above indicated that T2 developed largely from the circulation already present at low-levels in the environment 15-20 minutes before the tornado developed. Although the baroclinic term associated with the downdraft air on the whole was negligible, the weak baroclinicity along the northeastern and western vertical segments of the material curve was acting to generate horizontal streamwise vorticity, increasing the circulation very slightly along those portions of the material curve.

The vorticity analysis revealed that the vertical vorticity which was converged into the tornado at the lowest model level along most of the parcel trajectories was created through tilting of horizontal vorticity into the vertical by both the updraft and the downdrafts. Although the parcels originating at low-levels to the west of the tornado had positive vertical vorticity throughout their trajectories (at least over the duration of the calculations), the vertical vorticity tendencies along these trajectories indicated that tilting did play a significant role in increasing the vertical vorticity as the parcels neared the vortex. Only the

single parcel originating to the east of the tornado had increases in vertical vorticity only due to convergence.

6.4 Comparison of Tornadogenesis Processes with Previous Studies

The two tornadoes that developed in the simulated HP supercell both developed along thermal boundaries associated with the storm, and did not appear to be directly associated with the storm's mesocyclone. In this regard, these tornadoes may have more in common with the non-supercell tornadoes (NST) than with 'supercell tornadoes'. Despite this, there are some similarities between the tornadogenesis process for the two tornadoes simulated here, and those found in previous studies of classical supercell storms.

From the analysis presented above, it was concluded that horizontal convergence of positive low-level vertical vorticity was responsible for the development of the low-level vortex in both T1 and T2. Positive values of vertical vorticity in the near-tornado environment were generated largely by tilting of horizontal vorticity into the vertical in both downdrafts and updrafts (the lowest model level in the simulations was at z=38m). A few of the parcel trajectories which originated from low-levels also revealed that convergence alone could account for the large vertical vorticity values near the tornado if the parcel started out with positive vertical vorticity, although these parcels were few and far between. It is difficult to speculate which 'source' is the most important for generating large values of low-level vertical vorticity early in the simulation. However, it is unlikely that tilting in the updraft can account for the early development of the low-level vortex. In the absence of the strong updrafts (and horizontal convergence) associated with the tornado, parcels which acquire vertical vorticity through tilting in the updraft would be advected upward large distances before acquiring large values of vertical vorticity (and thus can account for the development of the mid-level mesocyclone in the thunderstorm). The only other processes which could then possibly explain the initial development of the vortex are: 1) horizontal convergence of parcels near the surface which already have positive vertical vorticity, or 2) parcels with positive vertical vorticity brought down near the surface from above in downdrafts. This second possibility was first suggested by Davies-Jones (1982a) who proposed that tilting

of horizontal vorticity into the vertical in storm downdrafts could be an important vertical vorticity source for tornadoes, and could explain how large values of vertical vorticity reach the surface. Walko (1993) reached a similar conclusion in some highly idealized model simulations in which tilting in a downdraft followed by convergence produced an intense vortex near the surface.

In the simulation presented here, downdrafts also appeared to play a significant role in the development of both tornadoes as the vertical vorticity of parcels entering the tornado from the downdrafts became positive (or was increased) through tilting of horizontal vorticity into the vertical by the downdraft gradient as the parcels were exiting the downdraft. Similar results were found in the simulation of two classical supercell tornadoes by Grasso (1996). The results presented here are also similar to Grasso (1996) in that the tornadoes developed first near the surface, then upward into the storm.

In the simulated tornadoes presented here, the tilting in the downdraft occurred in the lowest 50-200m above the surface. In the tornadoes produced by classical supercell simulations of Grasso (1996), the tilting took place over the lowest 250-300m above the surface. Davies-Jones and Brooks (1993) [2]also found that tilting occurred in the lowest 200-300m above the surface for air entering the low-level mesocyclone in their simulation. Both of these previous studies also found that tilting of baroclinically-generated horizontal vorticity into the vertical was important in their simulations. However, this process does not appear to be occurring in the simulation of T1 presented here (and only to a very small extent in T2). Walko (1993) also found that baroclinically-generated horizontal vorticity did not play a role in the development of an intense vortex in his simulation. Thus baroclinically-generated horizontal vorticity in the downdraft does not appear to be prerequisite for tornado development. However, if present, it may certainly aid in the development of a tornado by changing the direction of the three-dimensional vorticity vector, making it easier for a parcel to acquire vertical vorticity through tilting in either an updraft

---

[2]Care must be taken here since Davies-Jones and Brooks were investigating the low-level mesocyclone, not a tornado. They only speculated that a similar process could be occurring in tornadogenesis.

or downdraft. Such a parcel would certainly have an 'advantage' to parcels which did not undergo this process in spinning up a tornado through tilting/convergence. Perhaps the extent to which parcels experience baroclinic generation of horizontal vorticity of the correct sign for positive tilting in the downdraft plays some role in determining the strength of the tornado (i.e. T2 was stronger than T1, and the tornadoes simulated by Grasso (1996) and the May 15 case to be presented in the next chapter were both stronger than either T1 or T2). However, this idea requires further investigation.

Unlike the results of Rotunno and Klemp (1983) and Wicker and Wilhelmson (1995), neither of the vorticity/trajectory analyses presented here showed a significant contribution from tilting of baroclinically-generated horizontal vorticity along the leading edge of the forward flank downdraft in parcels entering the tornadoes at low levels. Only 5-8% of the parcels in the trajectory analyses of T1 (an additional analysis was also carried out using 50 particles) showed evidence of spending time in the forward flank downdraft. Over 90% of the parcels entering T1 at low-levels originated either in the downdraft west of T1, or in the environment to the southeast of T1. The percentages are similar for parcels entering T2 from its two main source regions to the west and northeast of the vortex. (It should be noted here that the definition of 'forward flank downdraft' becomes somewhat obscure during the bow-echo portion of the storm's evolution.) It is also clear that since both tornadoes started near the surface and developed upward that the dynamic pipe effect did not play a role in the genesis process, despite the presence of rotation aloft prior to the development of both tornadoes.

Although T2 develops along a strong shear boundary, it is unclear if a shear instability was involved in its development. The strong shear zone does show evidence of smaller pools of vertical vorticity developing at semi-regular intervals (the first stage of horizontal shear instabilities according to the results of Lee and Wilhelmson (1997a)), but this occurs after T2 had already developed. In addition, the merger of several of these smaller regions of high vertical vorticity into a larger region was not observed to occur in the present simulation as it did in the simulations of shear instabilities preformed by Lee and Wilhelmson (1997a,b) and in some observations of NST development along mesoscale boundaries (Wilson, 1986;

Wilczak et al., 1992; Roberts and Wilson, 1995). Instead T2 appears to develop in the region of strongest low-level convergence along the shear zone.

The analysis presented above suggests a possible alternate interpretation to the role of the mesocyclone in the tornadogenesis process. Perhaps the role of the mesocyclone is to create a dynamically driven downdraft and a region of strong convergence near the surface. The downdraft acts to tilt horizontal vorticity into the vertical creating positive vertical vorticity as air parcels near the surface, which is then amplified through strong surface convergence below the mesocyclone. The strong updraft associated with the mesocyclone then draws the vortex up into the storm.

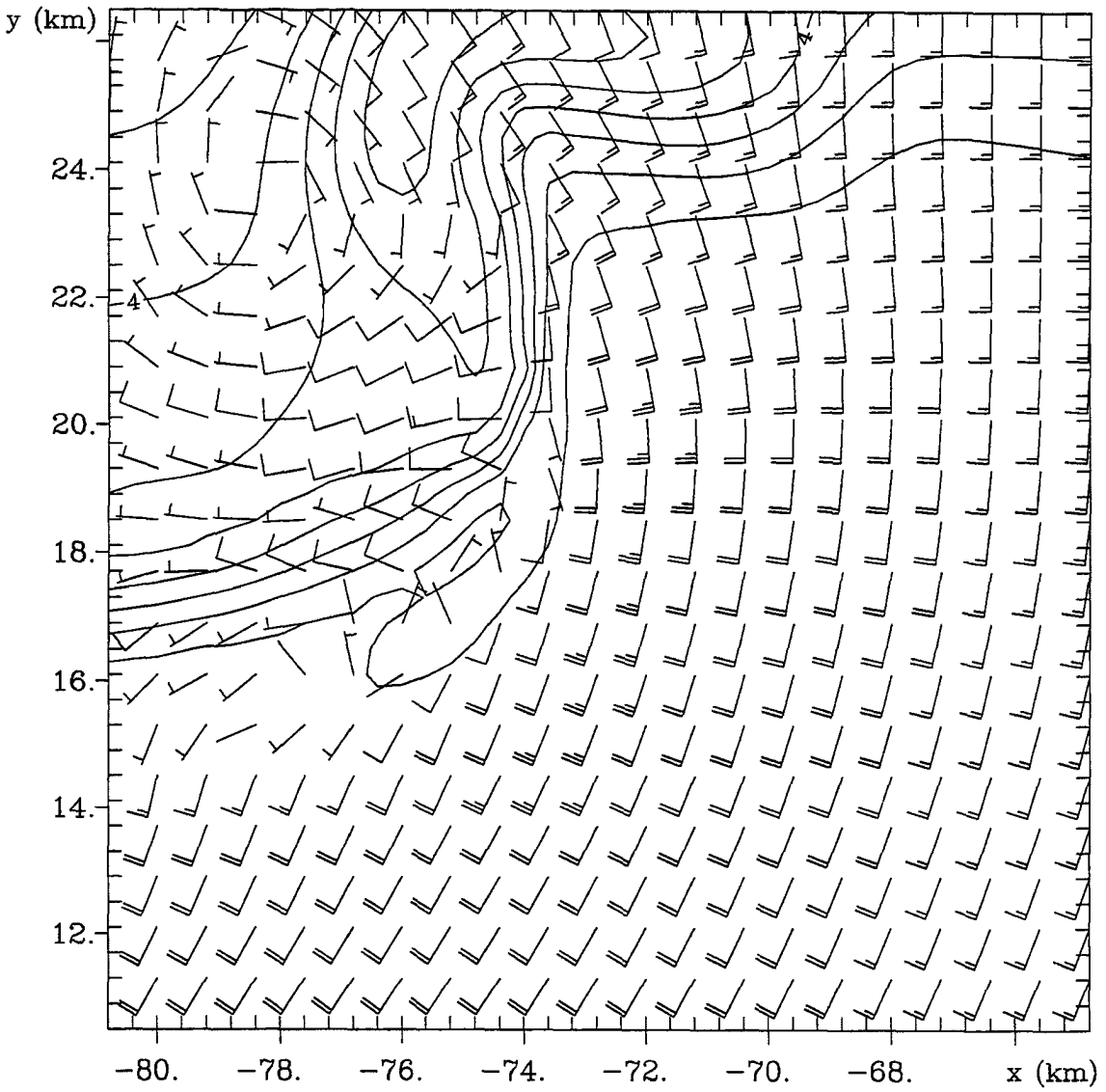

Figure 6.1: Condensate field overlaid with horizontal wind barbs at z=1.65km on a subset of Grid #5 at 0007:30 UTC (prior to T1) showing the position of strong horizontal shear along the flanking line in which T1 later develops. Condensate mixing ratio is contoured every $1g(kg)^{-1}$. Wind barbs are plotted at every other grid point. The short (long) flag on the wind barbs denotes a wind speed of $5ms^{-1}$ ($10ms^{-1}$).

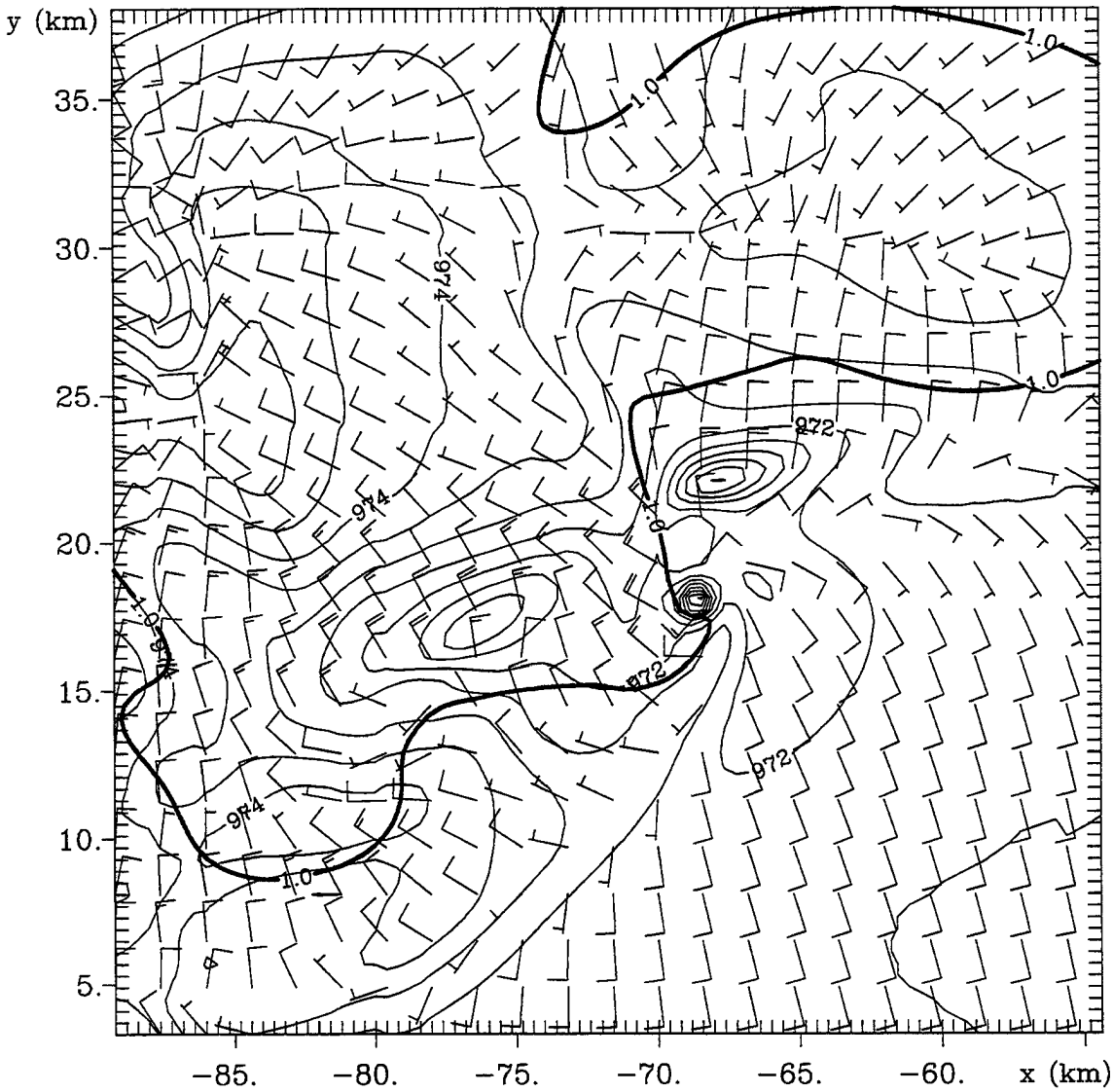

Figure 6.2: Pressure overlaid with horizontal wind barbs at z=38m on Grid #5 at 0019:30 UTC (when T1 was occurring) showing the position of T1 with respect to the rest of the storm. Pressure is contoured every 0.5mb. The bold contour denotes the $1g(kg)^{-1}$ condensate mixing ratio line. Wind barbs are plotted at every fourth grid point. The short (long) flag on the wind barbs denotes a wind speed of $5ms^{-1}$ ($10ms^{-1}$).

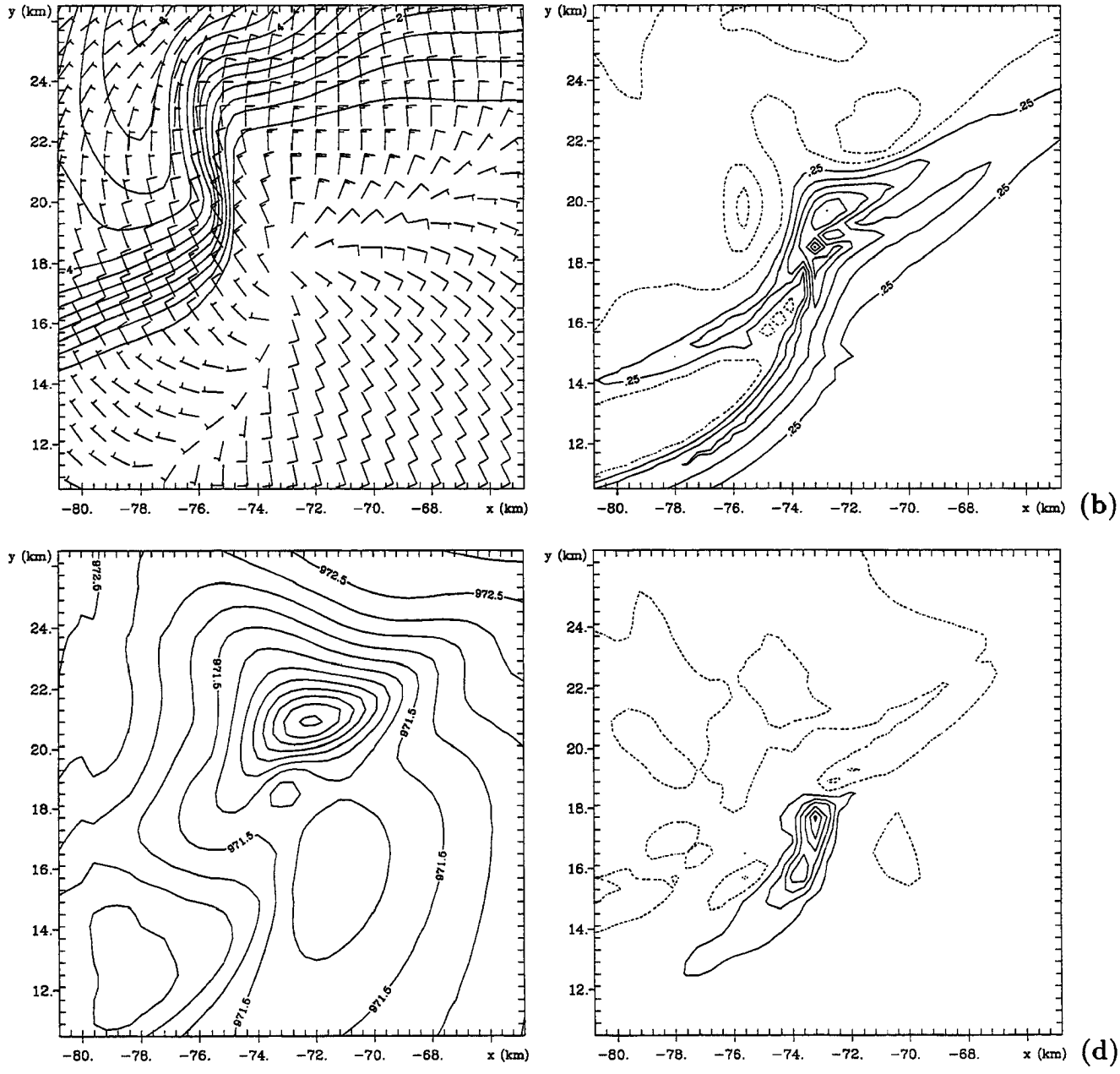

Figure 6.3: Grid #5 fields 38m above the surface at 0006 UTC. (a) Condensate field (contour interval $0.5g(kg)^{-1}$) overlayed with horizontal wind barbs, (b) vertical velocity (contour interval $0.25ms^{-1}$), (c) pressure (contour interval 0.25 mb), (d) vertical vorticity (contour interval 0.0025 s^{-1}). Dashed contours denote negative values. Wind barbs are plotted at every other grid point. The short (long) flag on the wind barb represents a wind speed of $5ms^{-1}$ ($10ms^{-1}$).

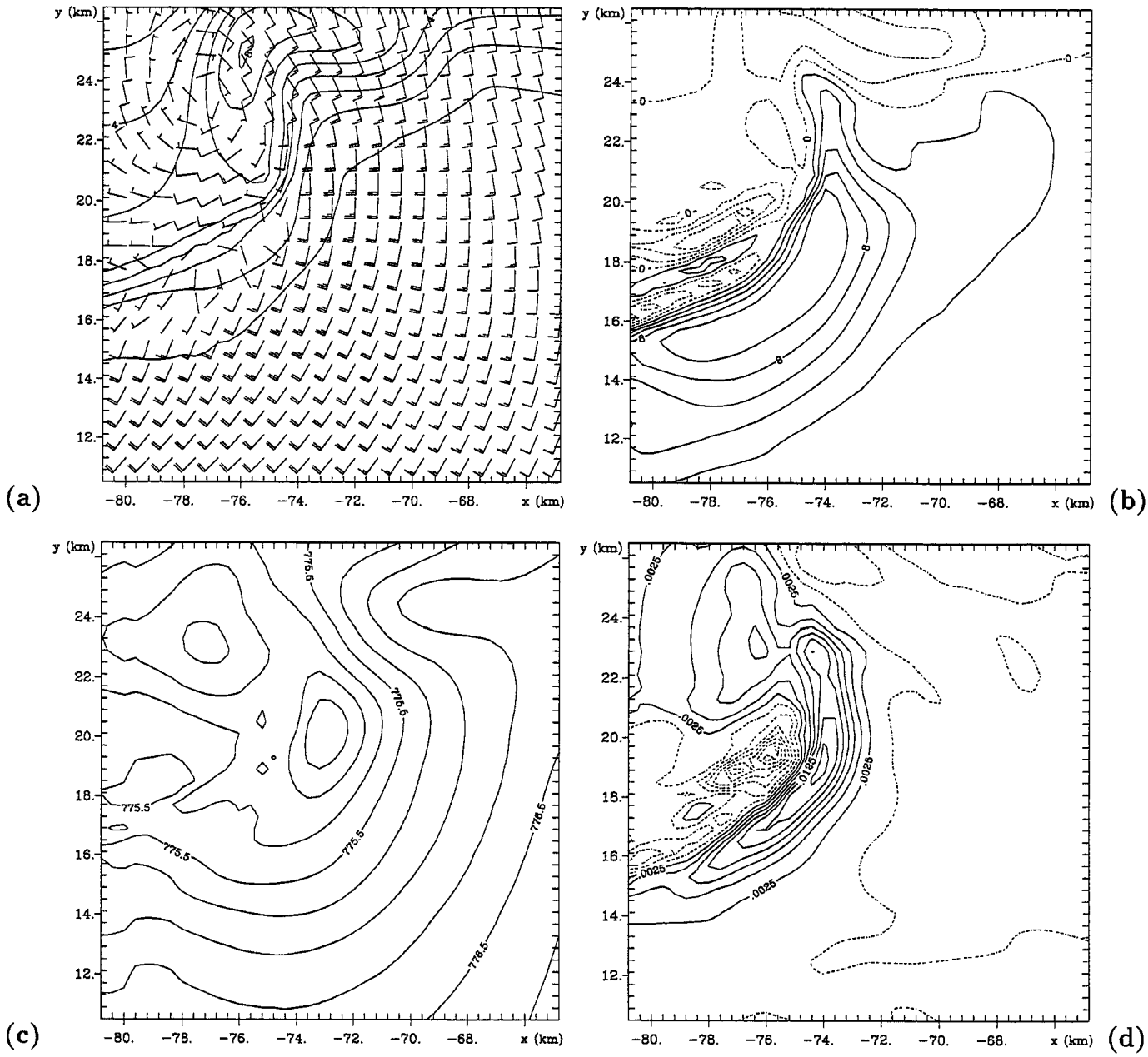

Figure 6.4: Grid #5 fields 2km above the surface at 0006 UTC. (a) Condensate field (contour interval $1g(kg)^{-1}$) overlayed with horizontal wind barbs, (b) vertical velocity (contour interval $2ms^{-1}$), (c) pressure (contour interval 0.25 mb), (d) vertical vorticity (contour interval 0.0025 s^{-1}). Dashed contours denote negative values. Wind barbs are plotted at every other grid point. The short (long) flag on the wind barb represents a wind speed of $5ms^{-1}$ ($10ms^{-1}$).

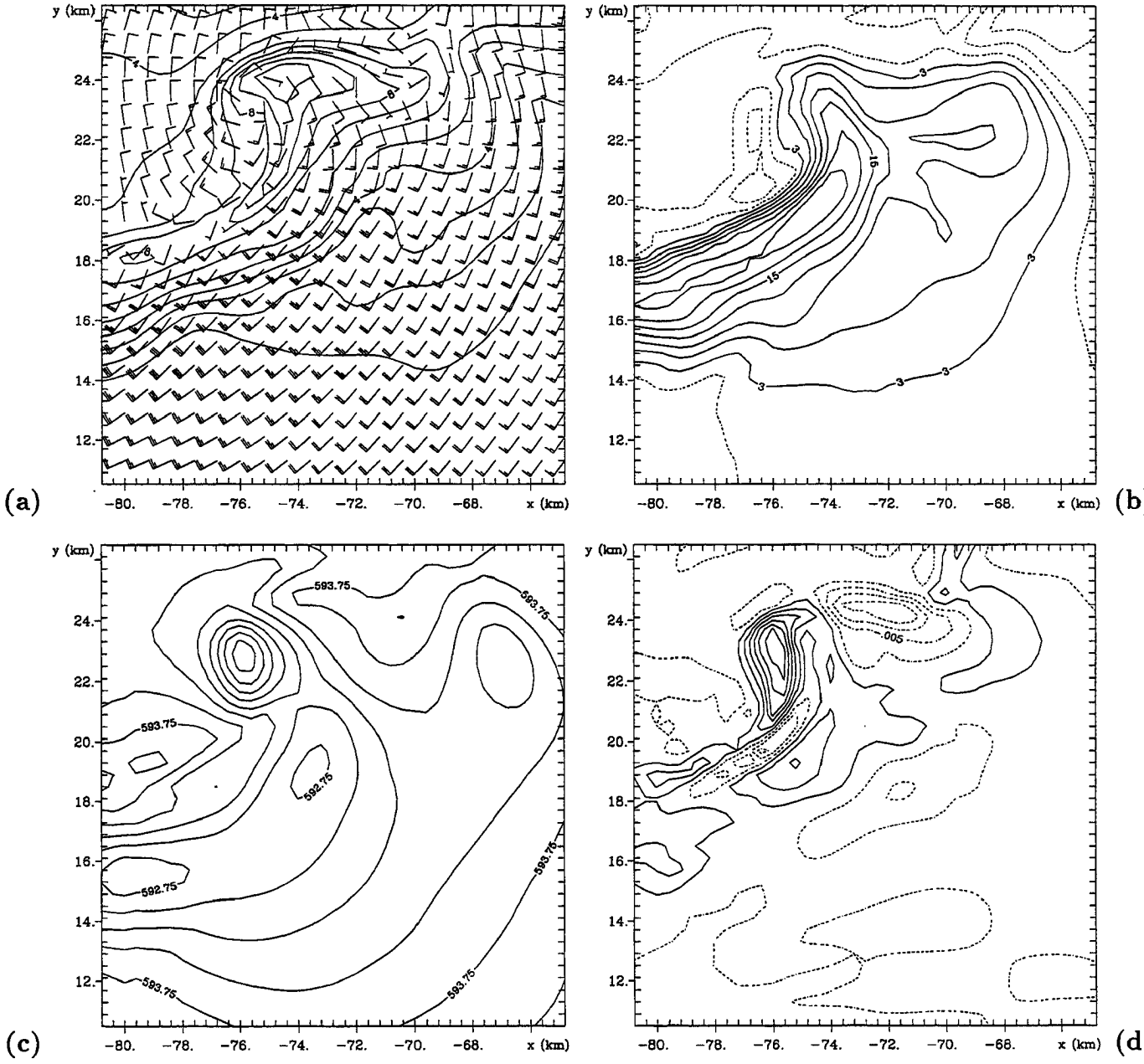

Figure 6.5: Grid #5 fields 4.3km above the surface at 0006 UTC. (a) Condensate field (contour interval $1g(kg)^{-1}$) overlayed with horizontal wind barbs, (b) vertical velocity (contour interval $3ms^{-1}$), (c) pressure (contour interval 0.25 mb), (d) vertical vorticity (contour interval 0.005 s^{-1}). Dashed contours denote negative values. Wind barbs are plotted at every other grid point. The short (long) flag on the wind barb represents a wind speed of $5ms^{-1}$ ($10ms^{-1}$).

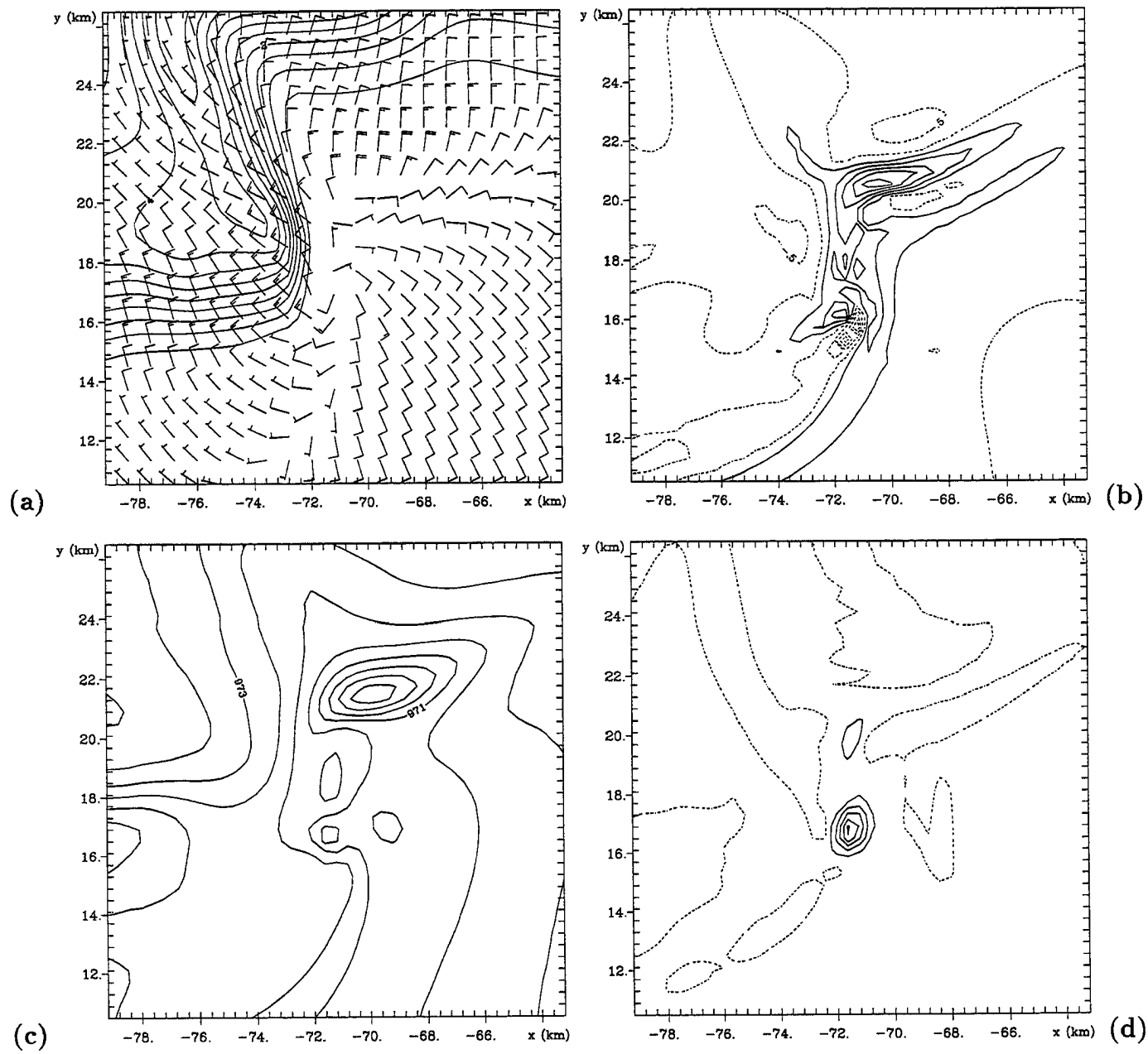

Figure 6.6: Grid #5 fields 38m above the surface at 0013:30 UTC. (a) Condensate field (contour interval $0.5g(kg)^{-1}$) overlayed with horizontal wind barbs, (b) vertical velocity (contour interval $0.5ms^{-1}$), (c) pressure (contour interval 0.5 mb), (d) vertical vorticity (contour interval 0.0075 s^{-1}). Dashed contours denote negative values. Wind barbs are plotted at every other grid point. The short (long) flag on the wind barb represents a wind speed of $5ms^{-1}$ ($10ms^{-1}$).

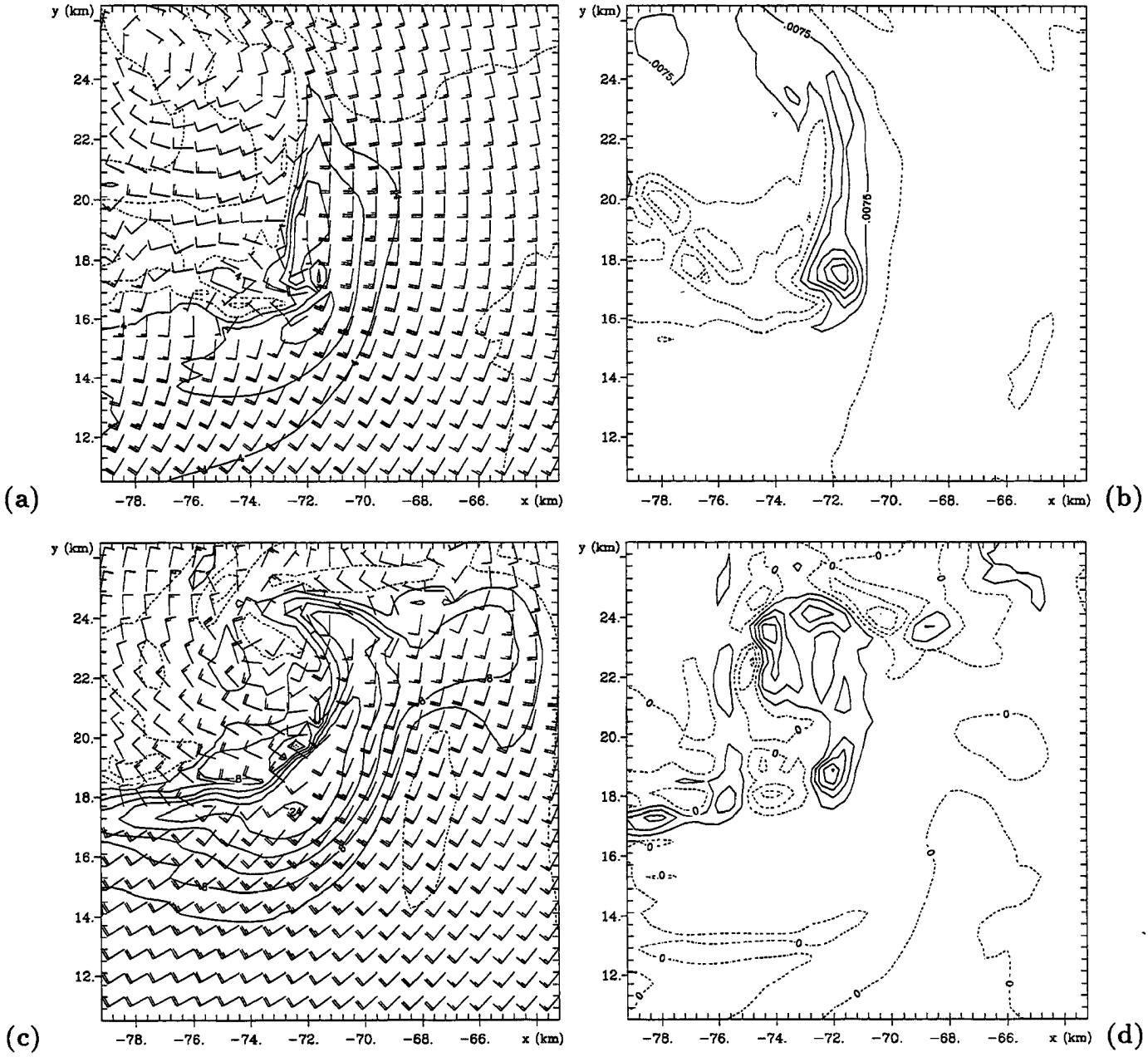

Figure 6.7: Grid #5 fields at 0013:30 UTC. (a) Vertical velocity overlaid with the horizontal winds at z=2.0km, (b) vertical vorticity at z=2.0km, (c) vertical velocity overlaid with the horizontal winds at z=4.3km, (d) vertical vorticity at 4.3km. Vertical velocity is countoured every $4ms^{-1}$. Vertical vorticity is contoured every $0.0075s^{-1}$. Dashed contours denote negative values. Wind barbs are plotted at every other grid point. The short (long) flag on the wind barb represents a wind speed of $5ms^{-1}$ ($10ms^{-1}$).

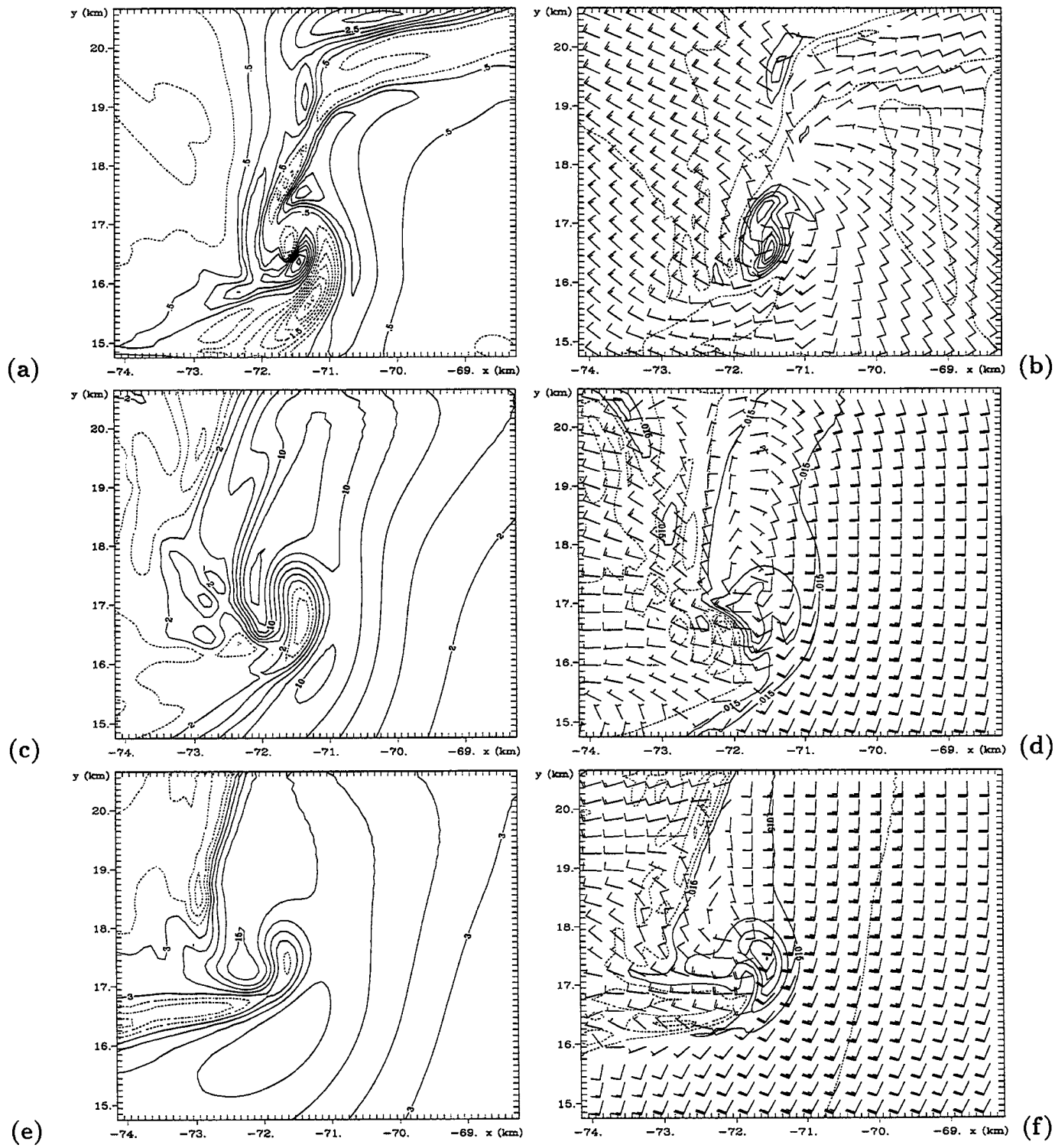

Figure 6.8: Grid #6 fields at 0013:30 UTC. (a) Vertical velocity (contour interval $0.5ms^{-1}$) at z=38m, (b) vertical vorticity at z=38m overlaid with the horizontal winds, (c) vertical velocity (contour interval $2ms^{-1}$) at z=1.1km, (d) vertical vorticity at z=1.1km overlaid with the horizontal winds, (e) vertical velocity (contour interval $3ms^{-1}$) at z=2km, (f) vertical vorticity at z=2km overlaid with the horizontal winds. The vertical vorticity is contoured every $0.015s^{-1}$. Wind barbs are plotted at every third grid point. The short (long) flag on the wind barb represents a wind speed of $5ms^{-1}$ ($10ms^{-1}$).

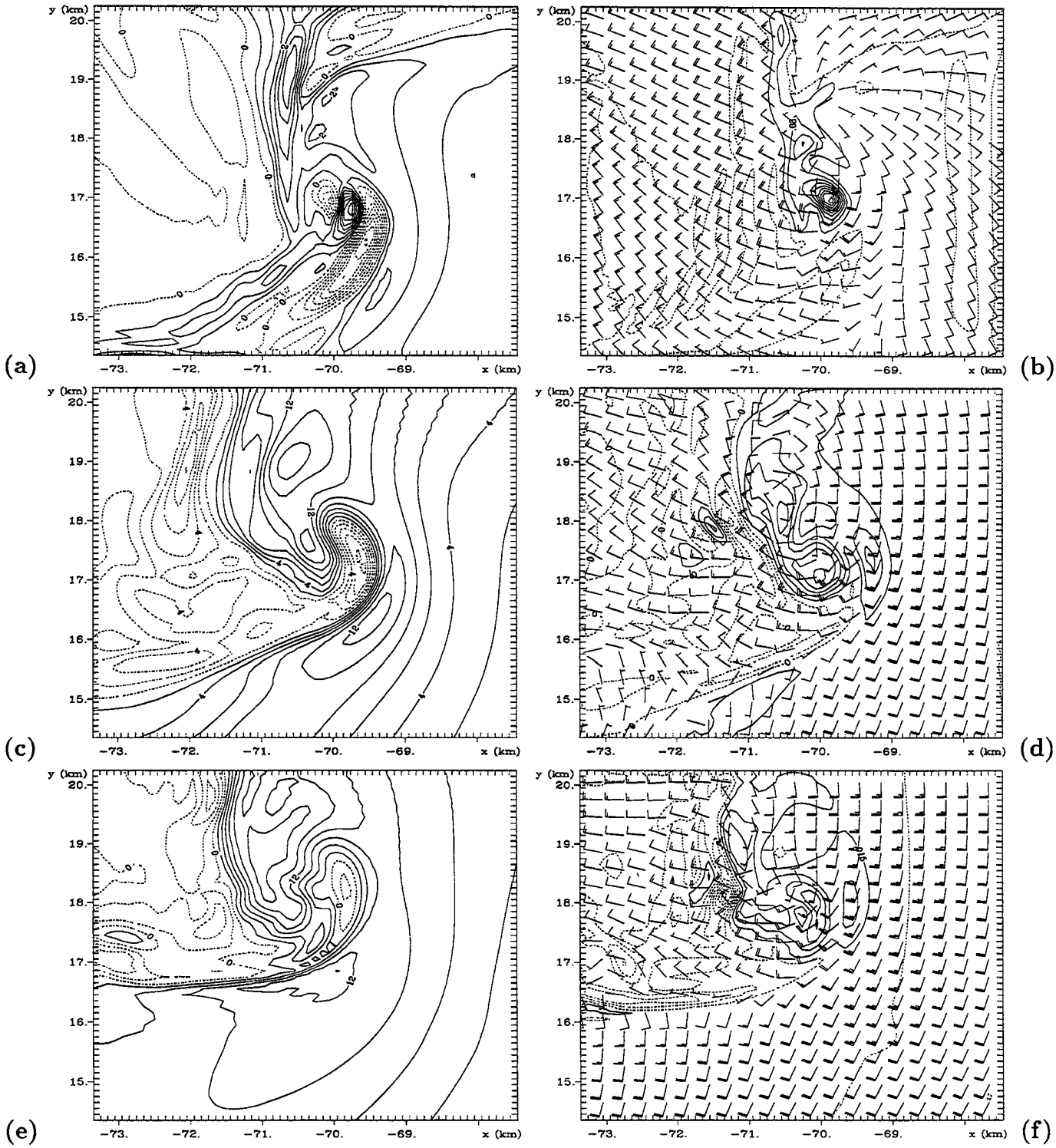

Figure 6.9: Grid #6 fields at 0016:30 UTC. (a) Vertical velocity (contour interval $0.5ms^{-1}$) at z=38m, (b) vertical vorticity at z=38m overlaid with the horizontal winds, (c) vertical velocity (contour interval $2ms^{-1}$) at z=1.1km, (d) vertical vorticity at z=1.1km overlaid with the horizontal winds, (e) vertical velocity (contour interval $3ms^{-1}$) at z=2km, (f) vertical vorticity at z=2km overlaid with the horizontal winds. The vertical vorticity is contoured every $0.015s^{-1}$. Wind barbs are plotted at every third grid point. The short (long) flag on the wind barb represents a wind speed of $5ms^{-1}$ ($10ms^{-1}$).

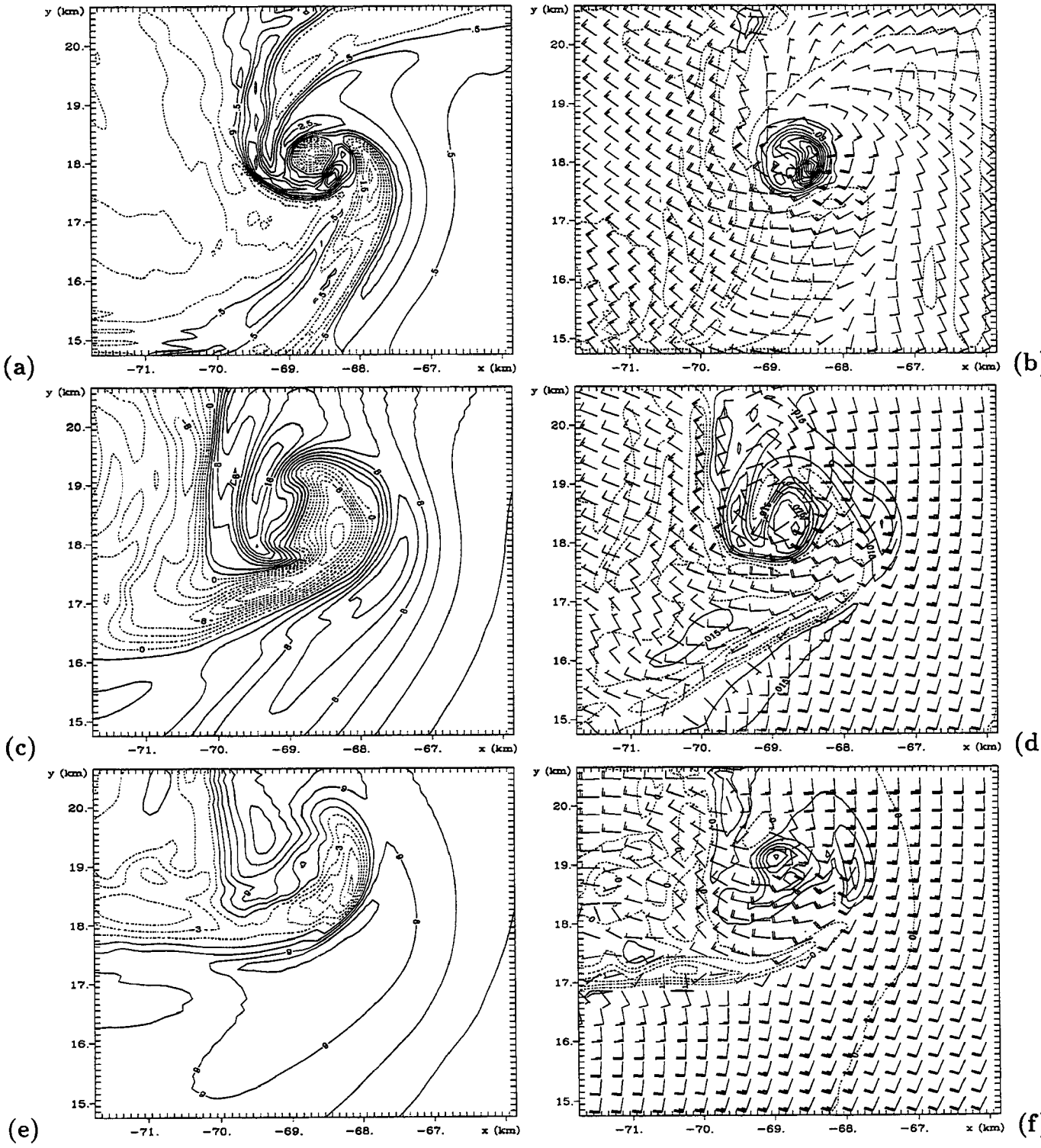

Figure 6.10: Grid #6 fields at 0019:30 UTC. (a) Vertical velocity (contour interval $0.5ms^{-1}$) at z=38m, (b) vertical vorticity at z=38m overlaid with the horizontal winds, (c) vertical velocity (contour interval $2ms^{-1}$) at z=1.1km, (d) vertical vorticity at z=1.1km overlaid with the horizontal winds, (e) vertical velocity (contour interval $3ms^{-1}$) at z=2km, (f) vertical vorticity at z=2km overlaid with the horizontal winds. The vertical vorticity is contoured every $0.015s^{-1}$. Wind barbs are plotted at every third grid point. The short (long) flag on the wind barb represents a wind speed of $5ms^{-1}$ ($10ms^{-1}$).

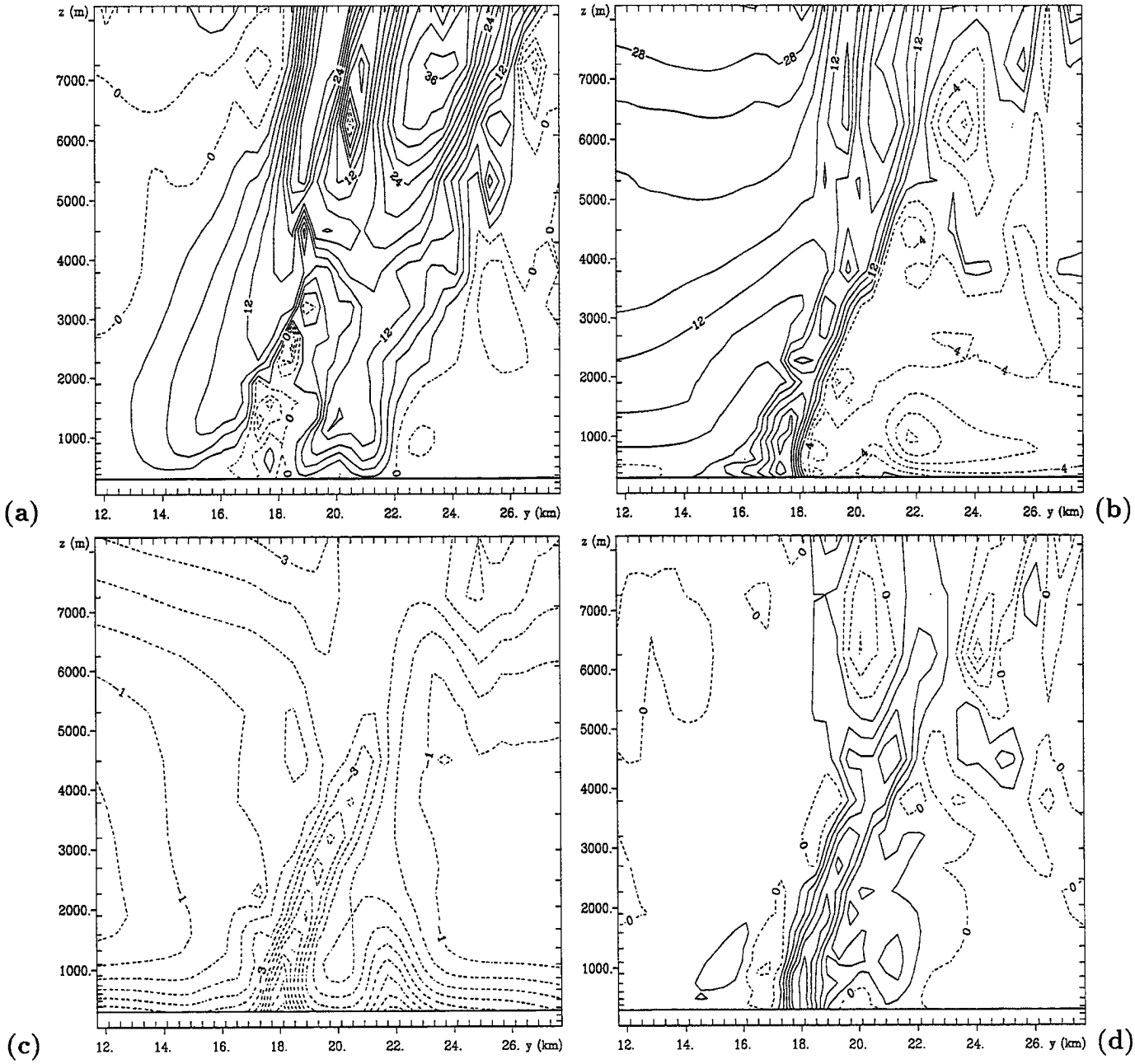

Figure 6.11: Vertical north-south cross section through T1 (looking west) on Grid #5 at 0019:30 UTC (time when T1 was strongest). (a) Vertical velocity (contour interval $3ms^{-1}$), (b) u-wind component (contour interval $4ms^{-1}$), (c) perturbation pressure (contour interval 0.5 mb), (d) vertical vorticity (contour interval 0.01 s^{-1}). Dashed contours denote negative values.

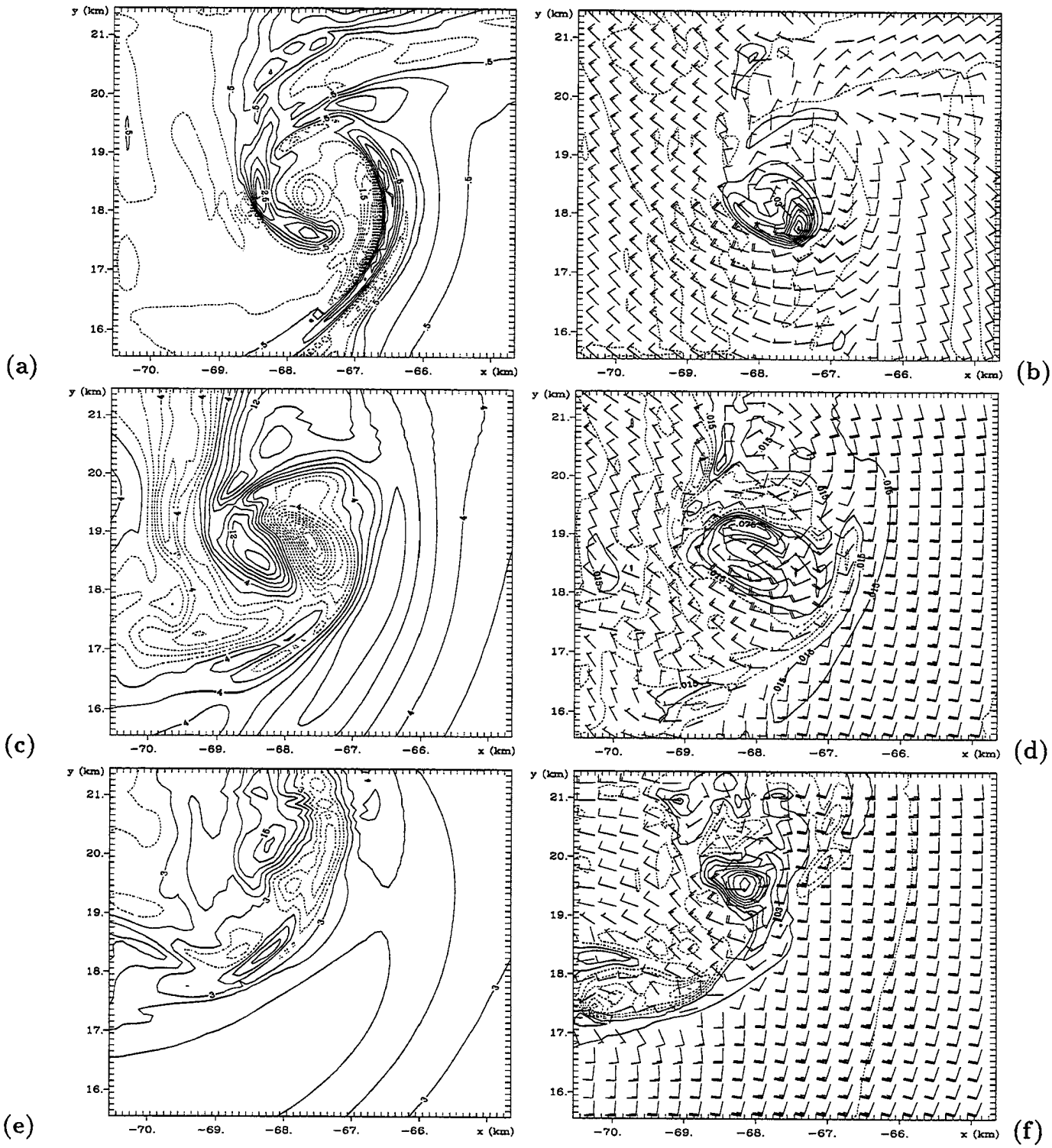

Figure 6.12: Grid #6 fields at 0022:30 UTC. (a) Vertical velocity (contour interval 0.5 ms^{-1}) at z=38m, (b) vertical vorticity at z=38m overlaid with the horizontal winds, (c) vertical velocity (contour interval $2ms^{-1}$) at z=1.1km, (d) vertical vorticity at z=1.1km overlaid with the horizontal winds, (e) vertical velocity (contour interval $3ms^{-1}$) at z=2km, (f) vertical vorticity at z=2km overlaid with the horizontal winds. The vertical vorticity is contoured every $0.015s^{-1}$. Wind barbs are plotted at every third grid point. The short (long) flag on the wind barb represents a wind speed of $5ms^{-1}$ ($10ms^{-1}$).

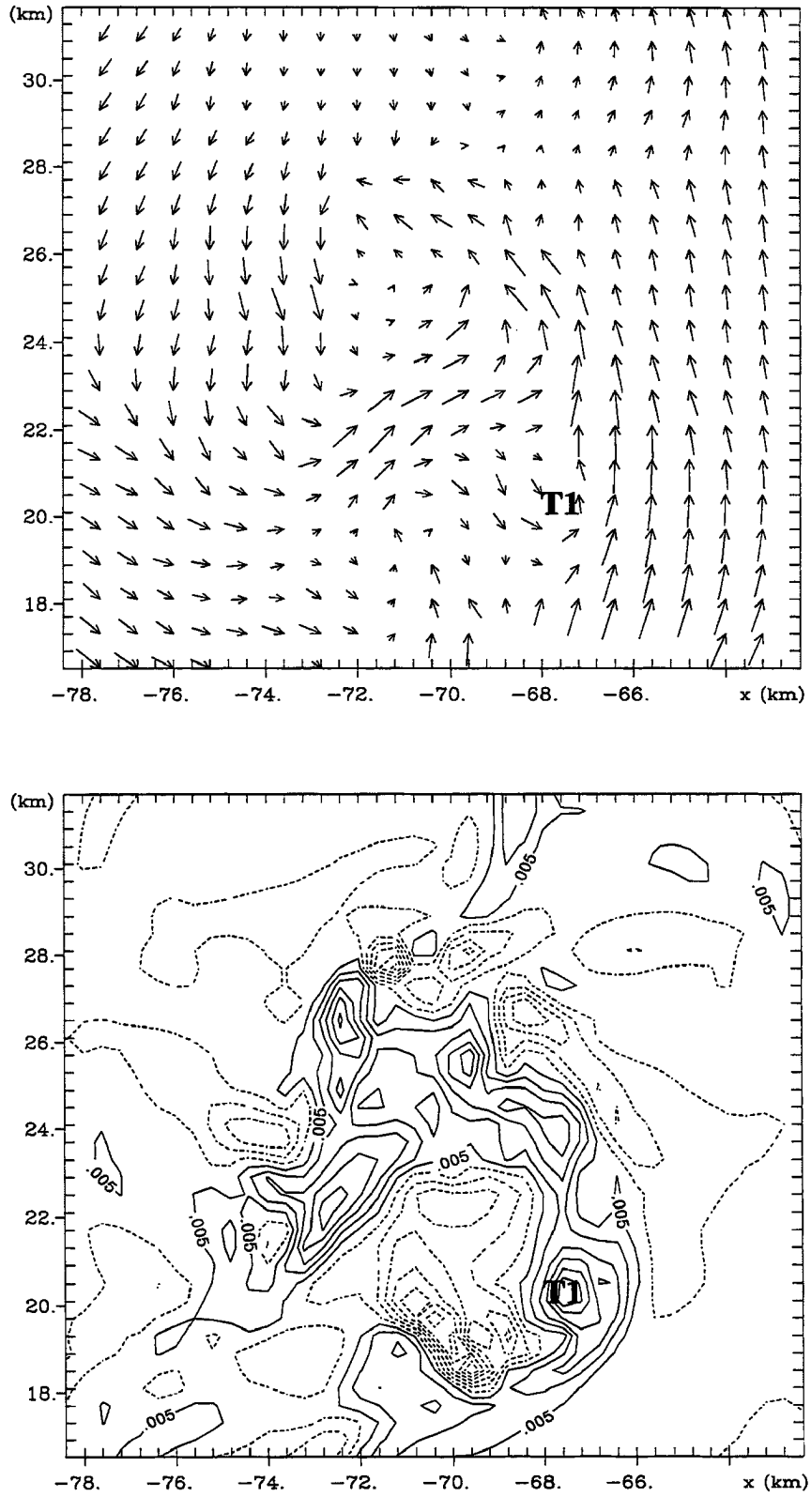

Figure 6.13: Horizontal wind vectors (top) and vertical vorticity (bottom) at 0024 UTC at 3km above the surface on a subset of Grid #5. Velocity vectors are plotted at every other grid point. A vector which has a length equal to the distance between vectors has a magnitude of $20ms^{-1}$. The vorticity contour interval is 0.005 s^{-1}. The position of the tornado is denoted by 'T1'. Note the wave 3 pattern on the mesocyclone.

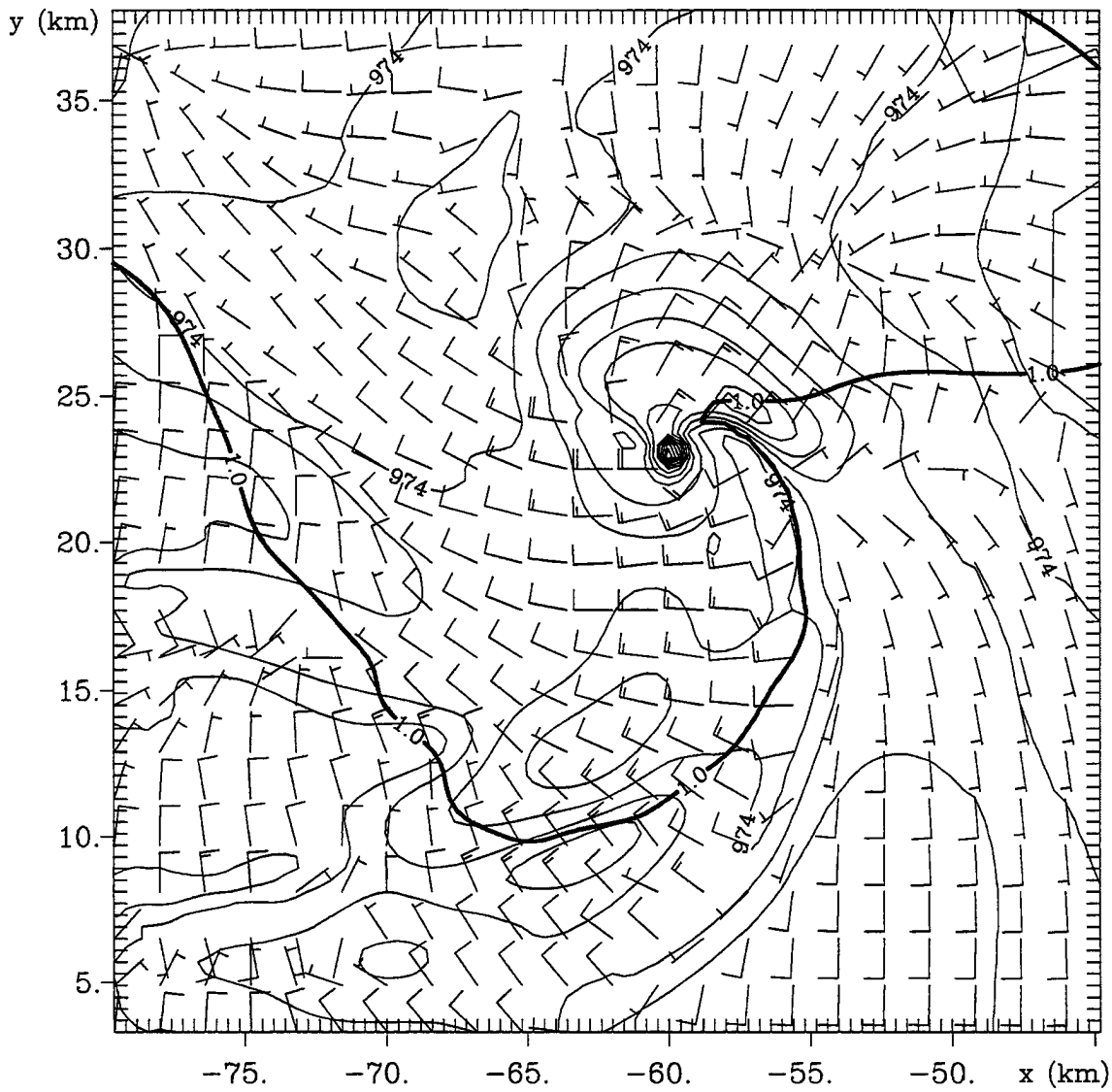

Figure 6.14: Pressure overlaid with horizontal wind barbs at z=38m on Grid #5 at 0040:30 UTC (when T2 was occurring) showing the position of T2 with respect to the rest of the storm. Pressure is contoured every 0.5mb. The bold contour denotes the $1g(kg)^{-1}$ condensate mixing ratio line. Wind barbs are plotted at every fourth grid point. The short (long) flag on the wind barbs denotes a wind speed of $5ms^{-1}$ ($10ms^{-1}$).

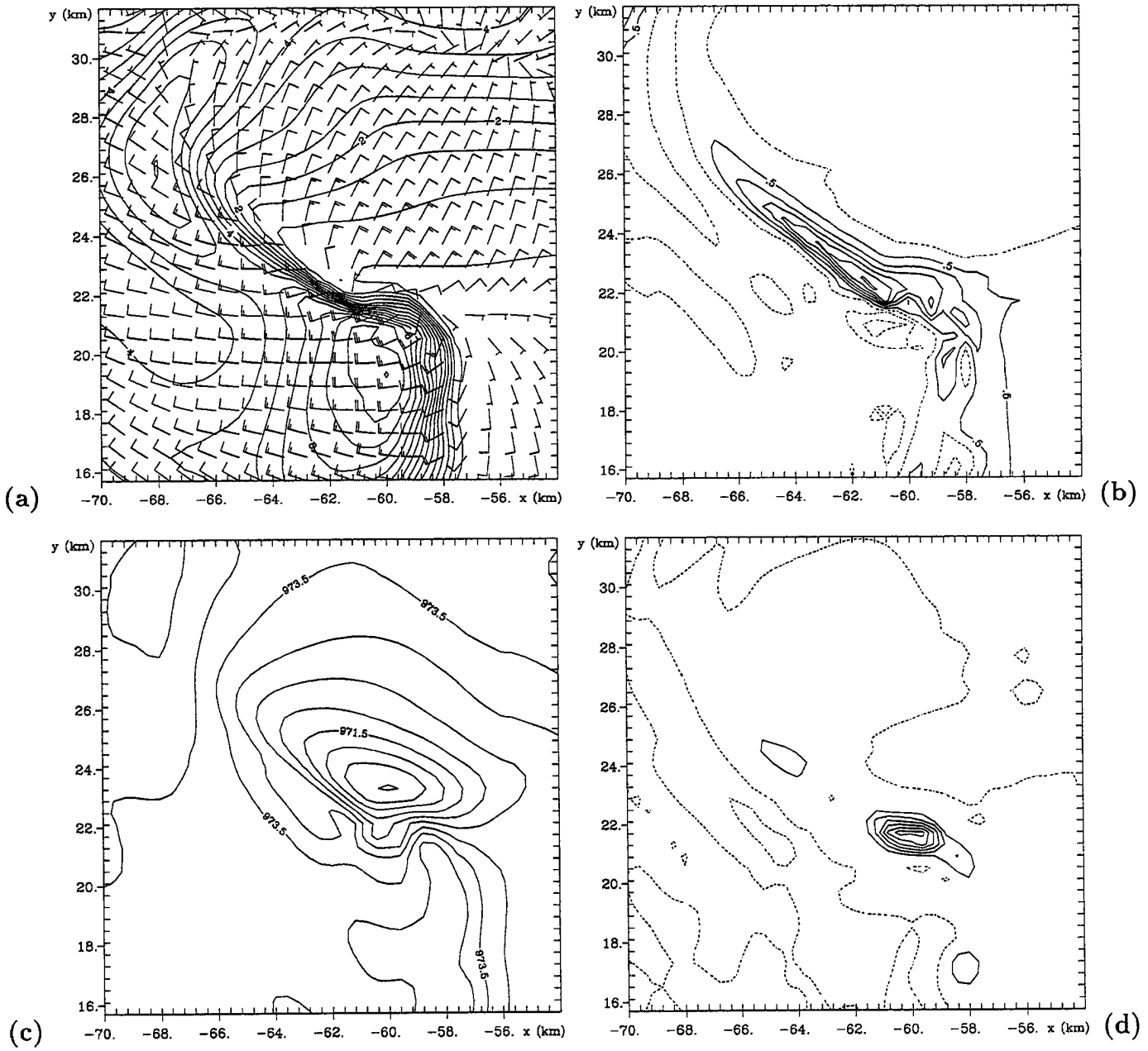

Figure 6.15: Grid #5 fields 38m above the surface at 0037:30 UTC. (a) Condensate field (contour interval 0.5 $g(kg)^{-1}$) overlayed with horizontal wind barbs, (b) vertical velocity (contour interval $0.5ms^{-1}$), (c) pressure (contour interval 0.5 mb), (d) vertical vorticity (contour interval $0.0075s^{-1}$). Dashed contours denote negative values. Wind barbs are plotted at every other grid point. The short (long) flag on the wind barb represents a wind speed of $5ms^{-1}$ ($10ms^{-1}$).

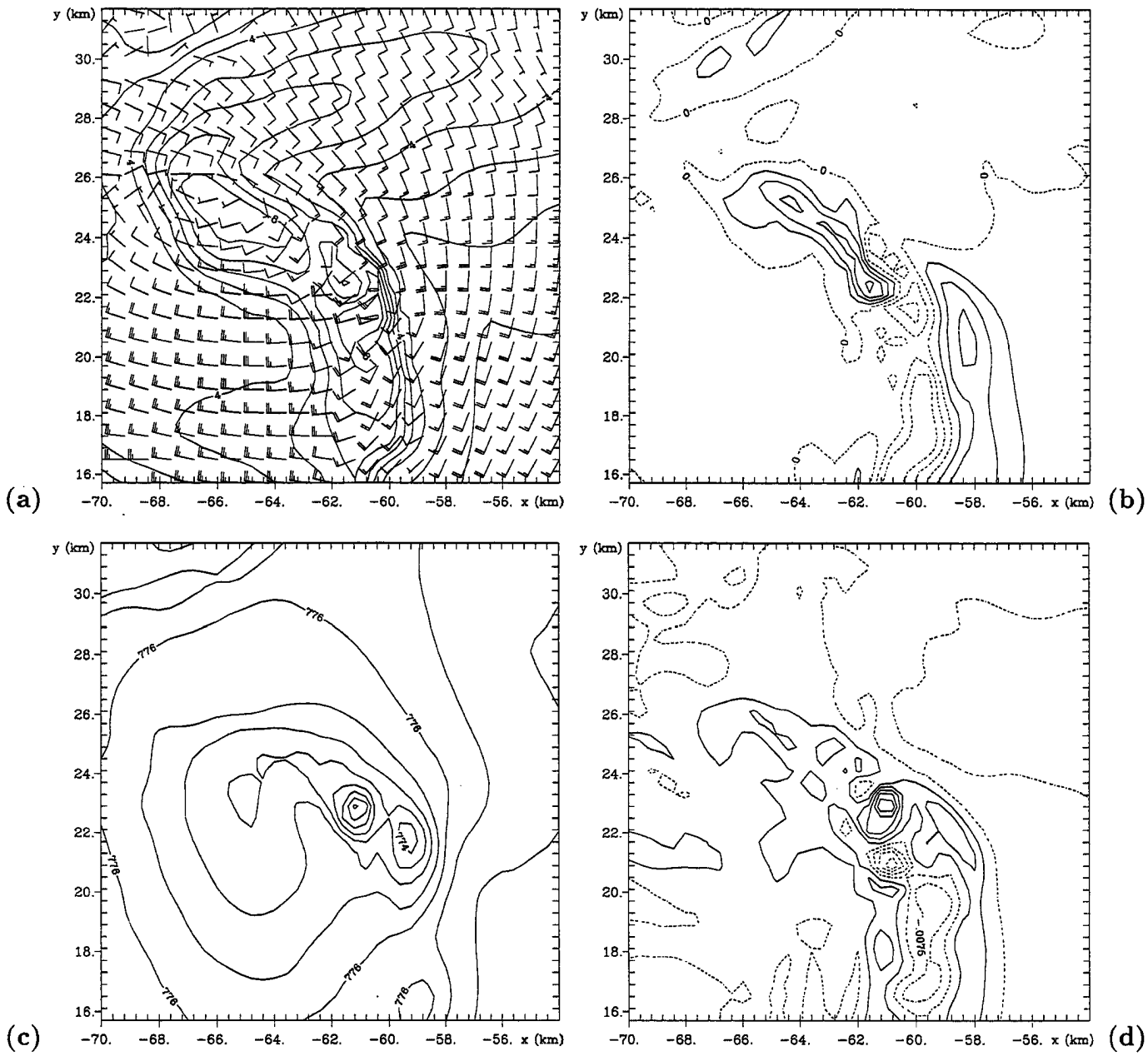

Figure 6.16: Grid #5 fields 2km above the surface at 0037:30 UTC. (a) Condensate field (contour interval $1g(kg)^{-1}$) overlayed with horizontal wind barbs, (b) vertical velocity (contour interval $4ms^{-1}$), (c) pressure (contour interval 0.5 mb), (d) vertical vorticity (contour interval $0.0075s^{-1}$). Dashed contours denote negative values. Wind barbs are plotted at every other grid point. The short (long) flag on the wind barb represents a wind speed of $5ms^{-1}$ ($10\ ms^{-1}$).

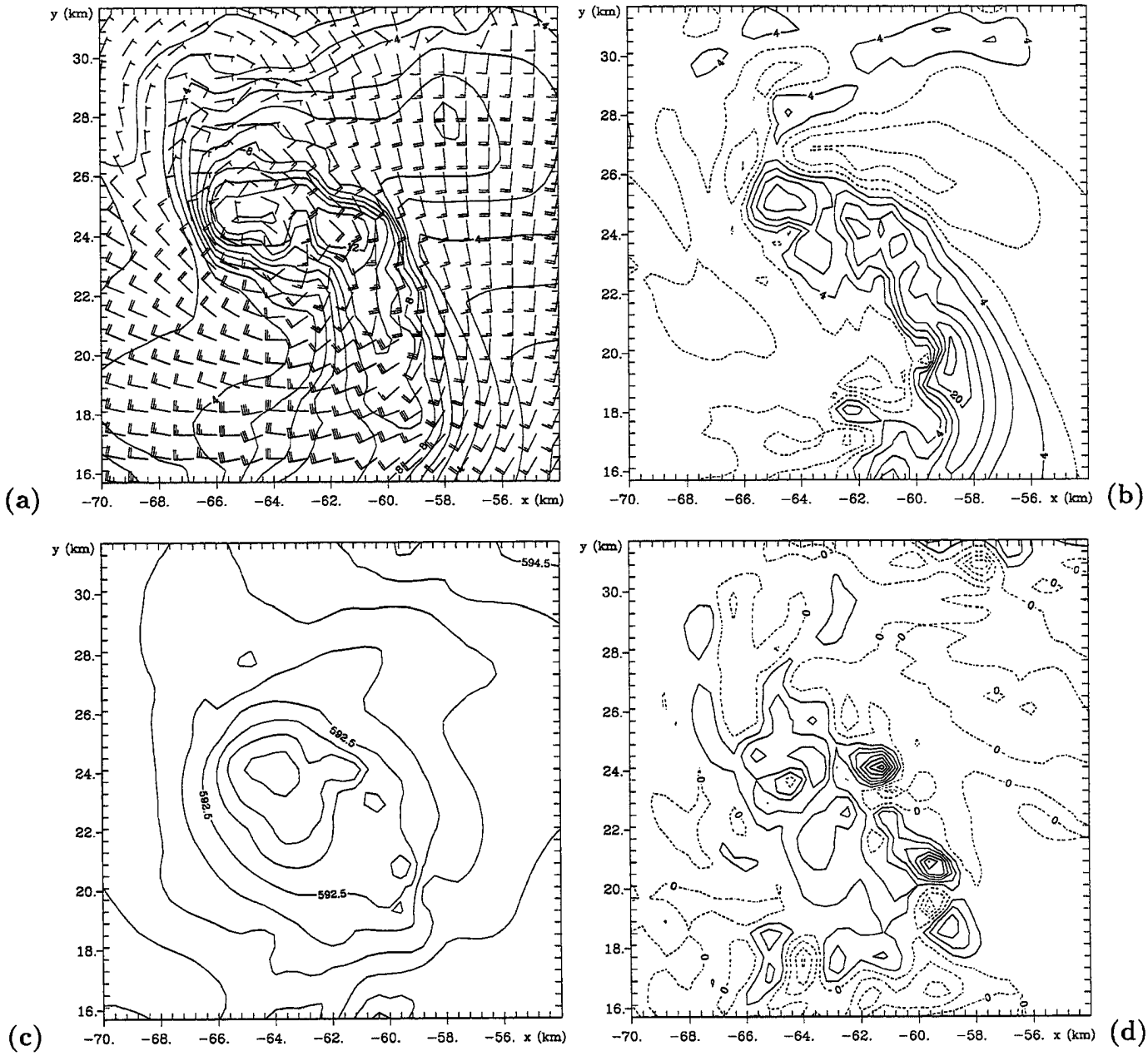

Figure 6.17: Grid #5 fields 4.3km above the surface at 0037:30 UTC. (a) Condensate field (contour interval $1g(kg)^{-1}$) overlayed with horizontal wind barbs, (b) vertical velocity (contour interval $4ms^{-1}$), (c) pressure (contour interval 0.5 mb), (d) vertical vorticity (contour interval 0.0075 s^{-1}). Dashed contours denote negative values. Wind barbs are plotted at every other grid point. The short (long) flag on the wind barb represents a wind speed of $5ms^{-1}$ ($10ms^{-1}$).

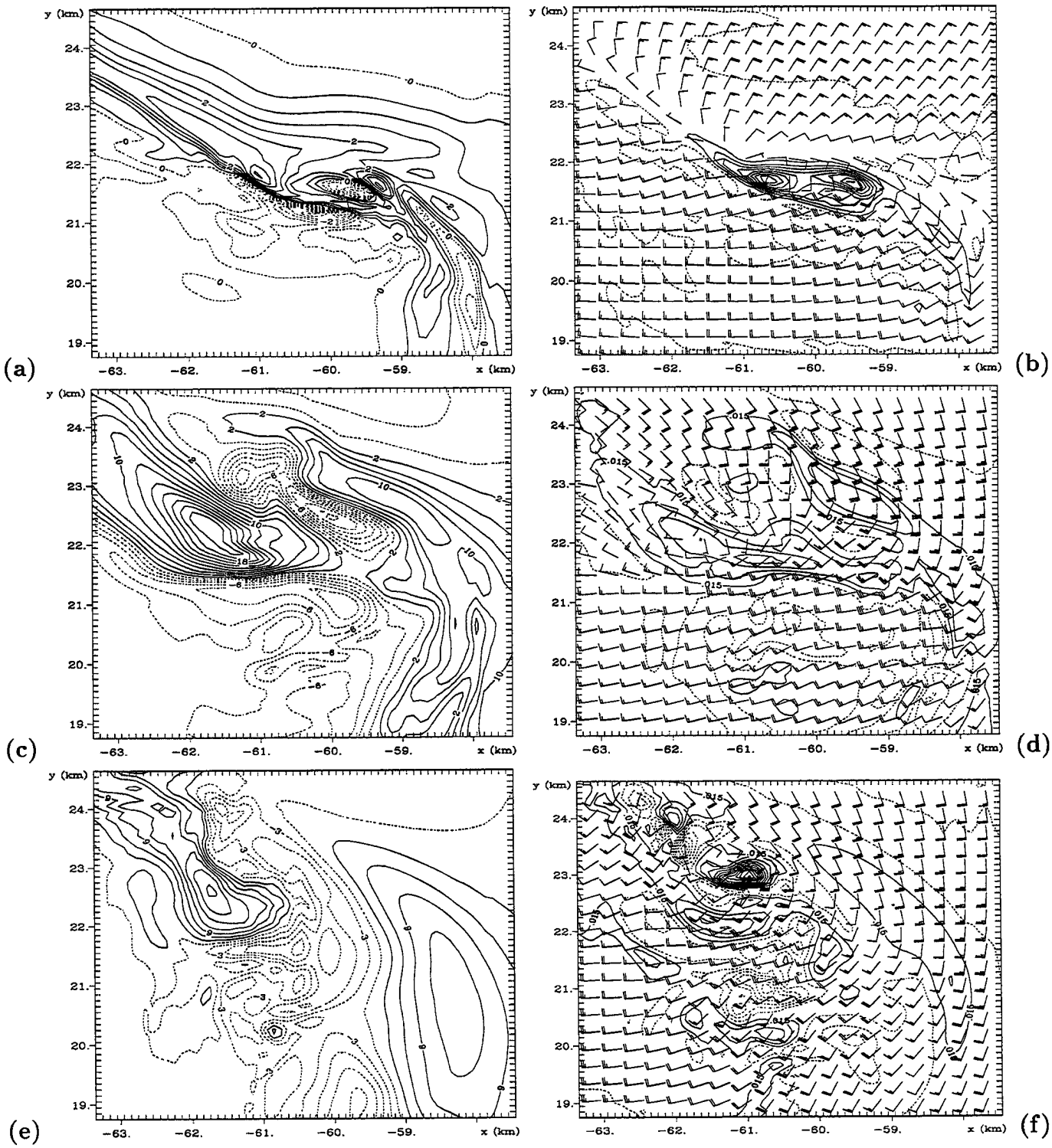

Figure 6.18: Grid #6 fields at 0037:30 UTC. (a) Vertical velocity (contour interval $0.5ms^{-1}$) at z=38m, (b) vertical vorticity at z=38m overlaid with the horizontal winds, (c) vertical velocity (contour interval $2ms^{-1}$) at z=1.1km, (d) vertical vorticity at z=1.1km overlaid with the horizontal winds, (e) vertical velocity (contour interval $3ms^{-1}$) at z=2km, (f) vertical vorticity at z=2km overlaid with the horizontal winds. The vertical vorticity is contoured every $0.015s^{-1}$. Wind barbs are plotted at every third grid point. The short (long) flag on the wind barb represents a wind speed of $5ms^{-1}$ ($10ms^{-1}$).

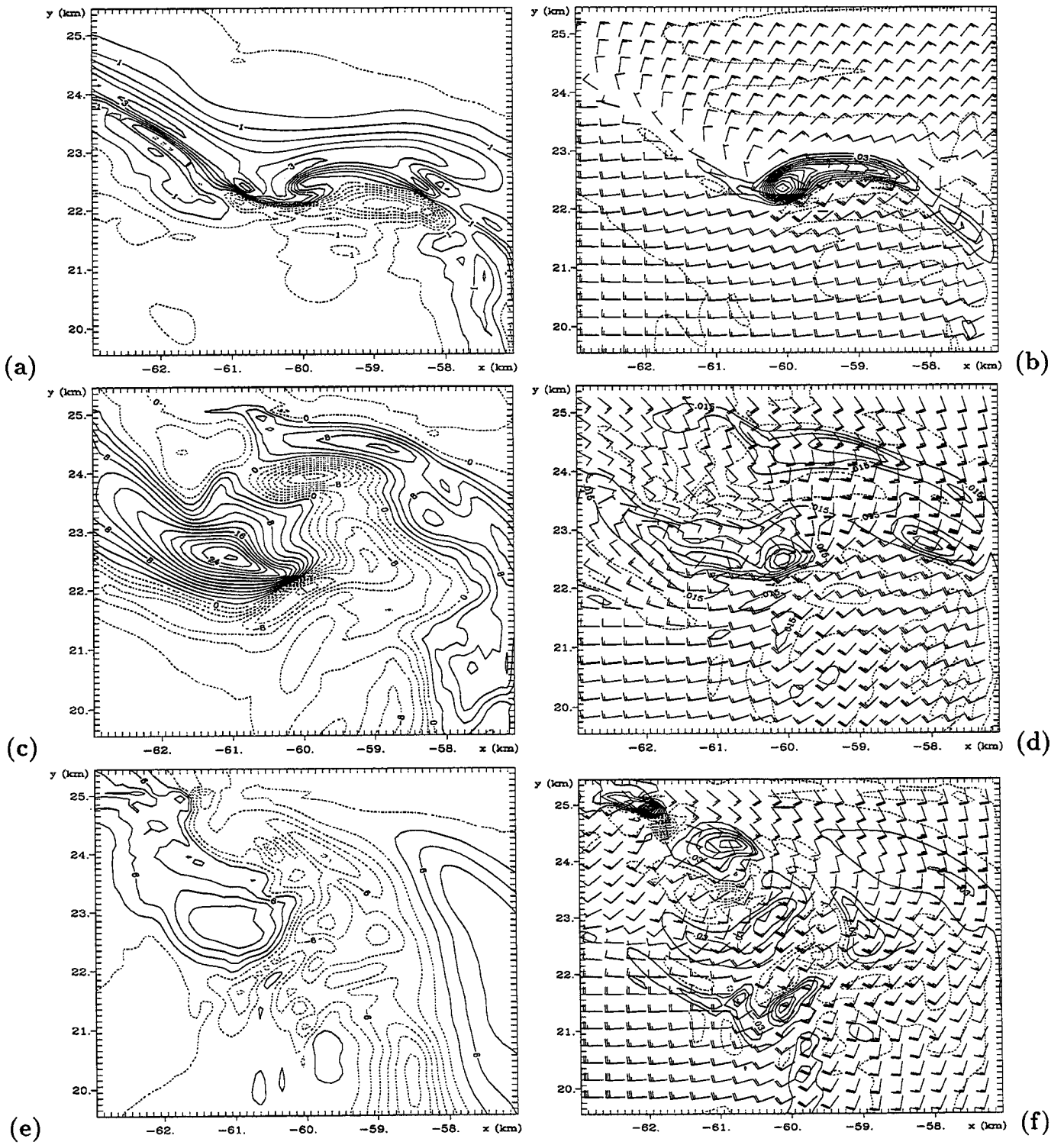

Figure 6.19: Grid #6 fields at 0039 UTC. (a) Vertical velocity (contour interval $0.5ms^{-1}$) at z=38m, (b) vertical vorticity at z=38m overlaid with the horizontal winds, (c) vertical velocity (contour interval $2ms^{-1}$) at z=1.1km, (d) vertical vorticity at z=1.1km overlaid with the horizontal winds, (e) vertical velocity (contour interval $3ms^{-1}$) at z=2km, (f) vertical vorticity at z=2km overlaid with the horizontal winds. The vertical vorticity is contoured every $0.015s^{-1}$. Wind barbs are plotted at every third grid point. The short (long) flag on the wind barb represents a wind speed of $5ms^{-1}$ ($10ms^{-1}$).

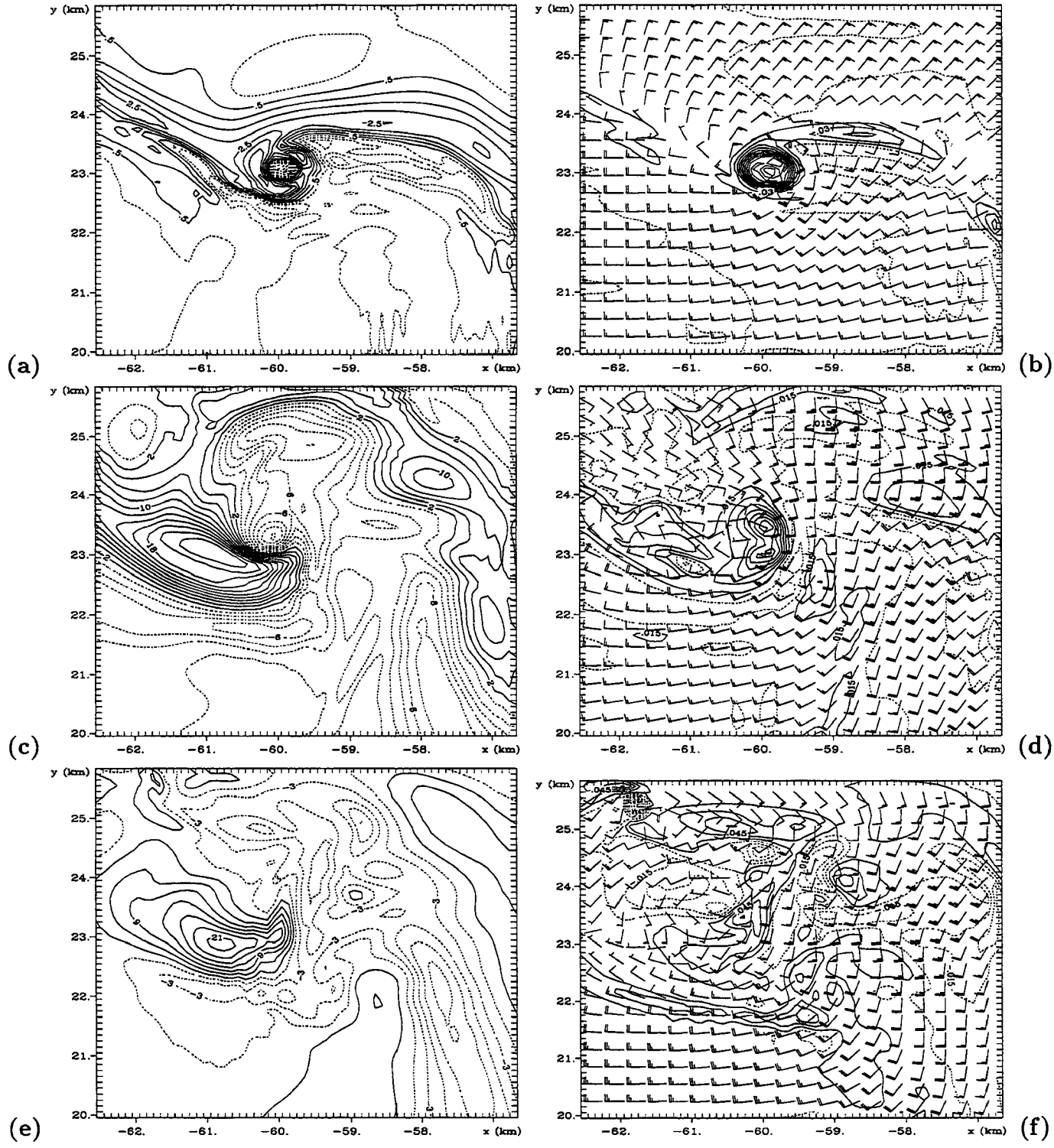

Figure 6.20: Grid #6 fields at 0040:30 UTC. (a) Vertical velocity (contour interval $0.5ms^{-1}$) at z=38m, (b) vertical vorticity at z=38m overlaid with the horizontal winds, (c) vertical velocity (contour interval $2ms^{-1}$) at z=1.1km, (d) vertical vorticity at z=1.1km overlaid with the horizontal winds, (e) vertical velocity (contour interval $3ms^{-1}$) at z=2km, (f) vertical vorticity at z=2km overlaid with the horizontal winds. The vertical vorticity is contoured every $0.015s^{-1}$. Wind barbs are plotted at every third grid point. The short (long) flag on the wind barb represents a wind speed of $5ms^{-1}$ ($10ms^{-1}$).

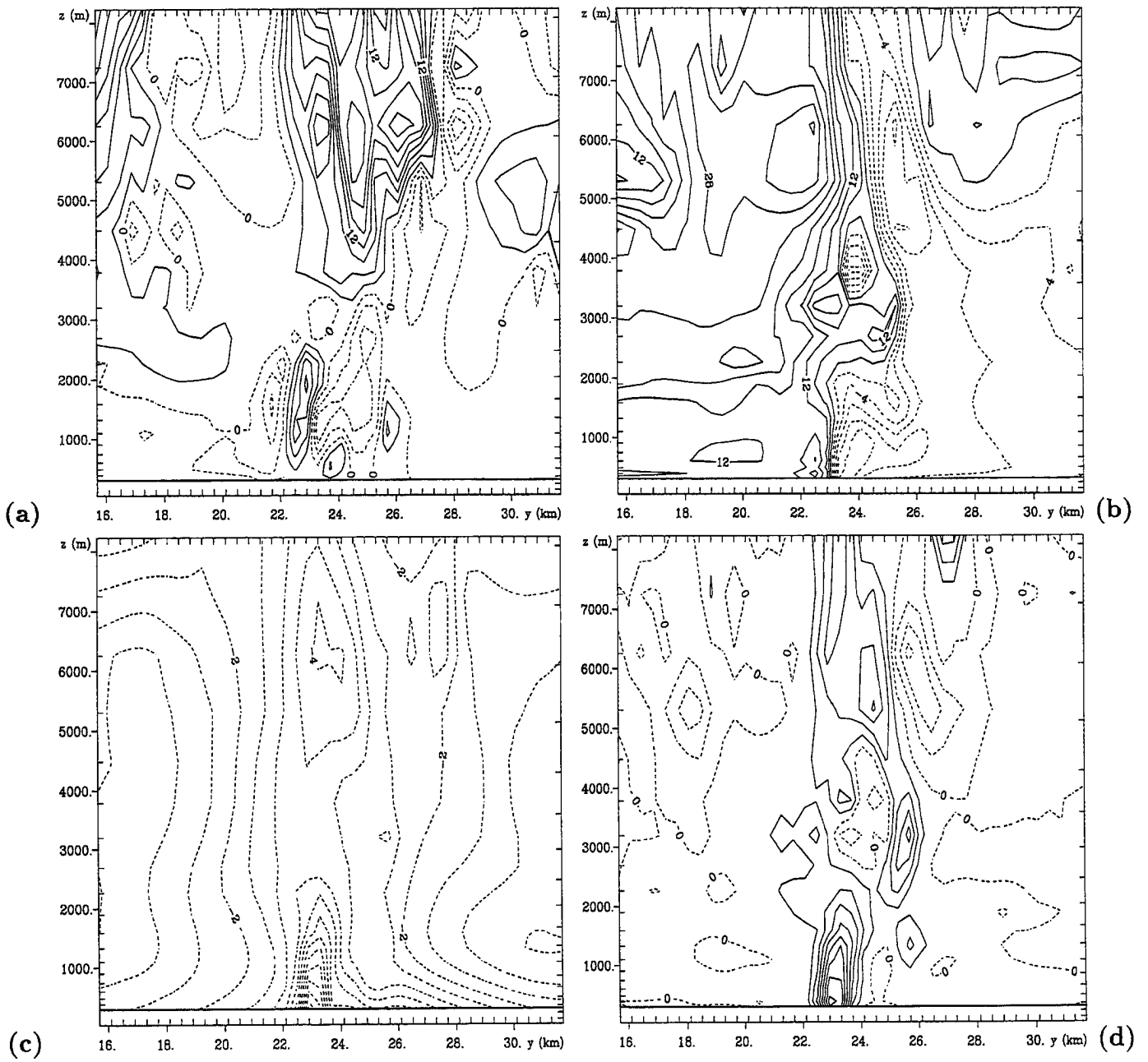

Figure 6.21: Vertical north-south cross section through T2 (looking west) on Grid #5 at 0040:30 UTC (time when T2 was strongest). (a) Vertical velocity (contour interval $3ms^{-1}$), (b) u-wind component (contour interval $4ms^{-1}$), (c) perturbation pressure (contour interval 0.5 mb), (d) vertical vorticity (contour interval $0.01s^{-1}$). Dashed contours denote negative values.

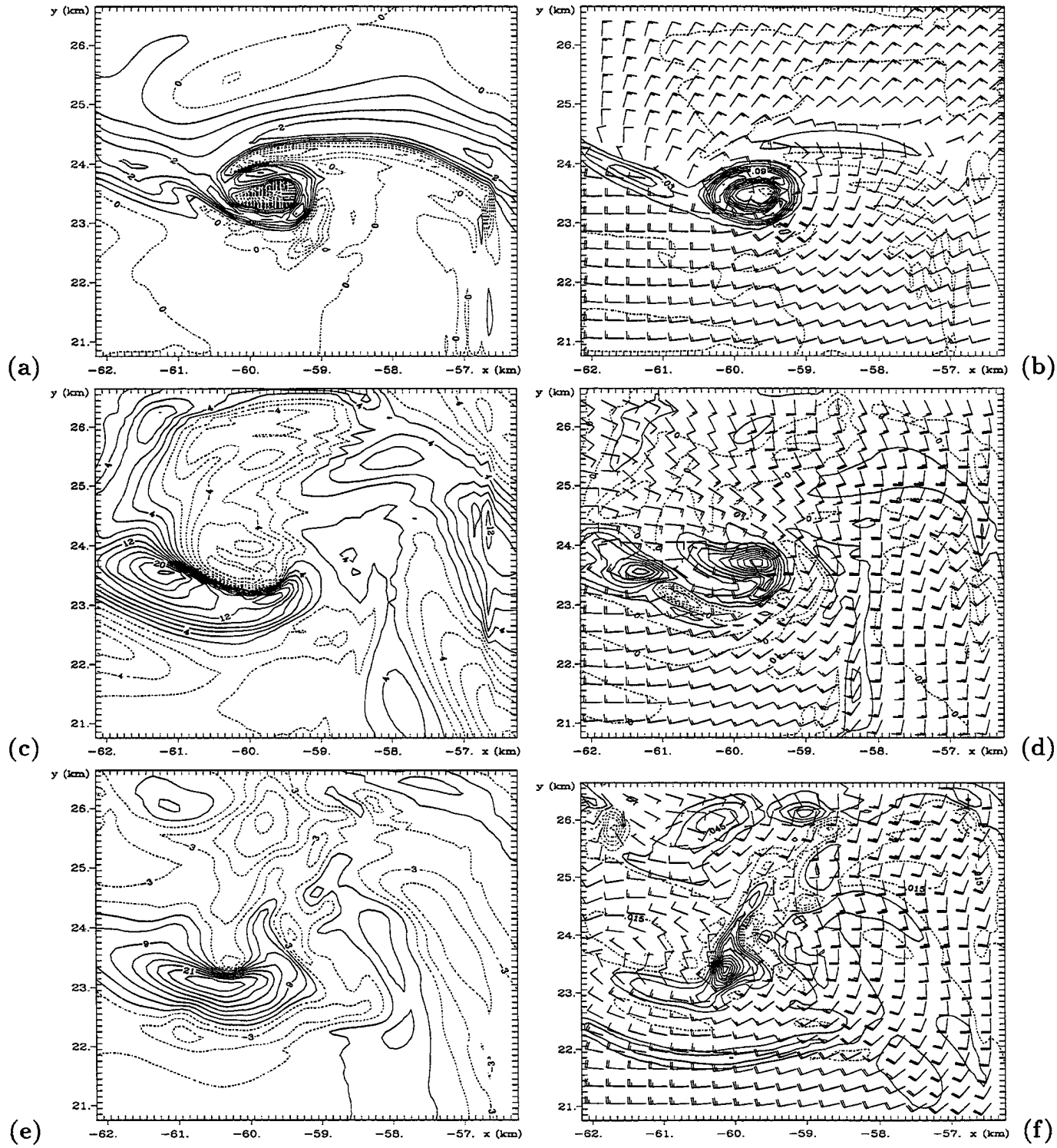

Figure 6.22: Grid #6 fields at 0042 UTC. (a) Vertical velocity (contour interval $0.5ms^{-1}$) at z=38m, (b) vertical vorticity at z=38m overlaid with the horizontal winds, (c) vertical velocity (contour interval $2ms^{-1}$) at z=1.1km, (d) vertical vorticity at z=1.1km overlaid with the horizontal winds, (e) vertical velocity (contour interval $3ms^{-1}$) at z=2km, (f) vertical vorticity at z=2km overlaid with the horizontal winds. The vertical vorticity is contoured every $0.015s^{-1}$. Wind barbs are plotted at every third grid point. The short (long) flag on the wind barb represents a wind speed of $5ms^{-1}$ ($10ms^{-1}$).

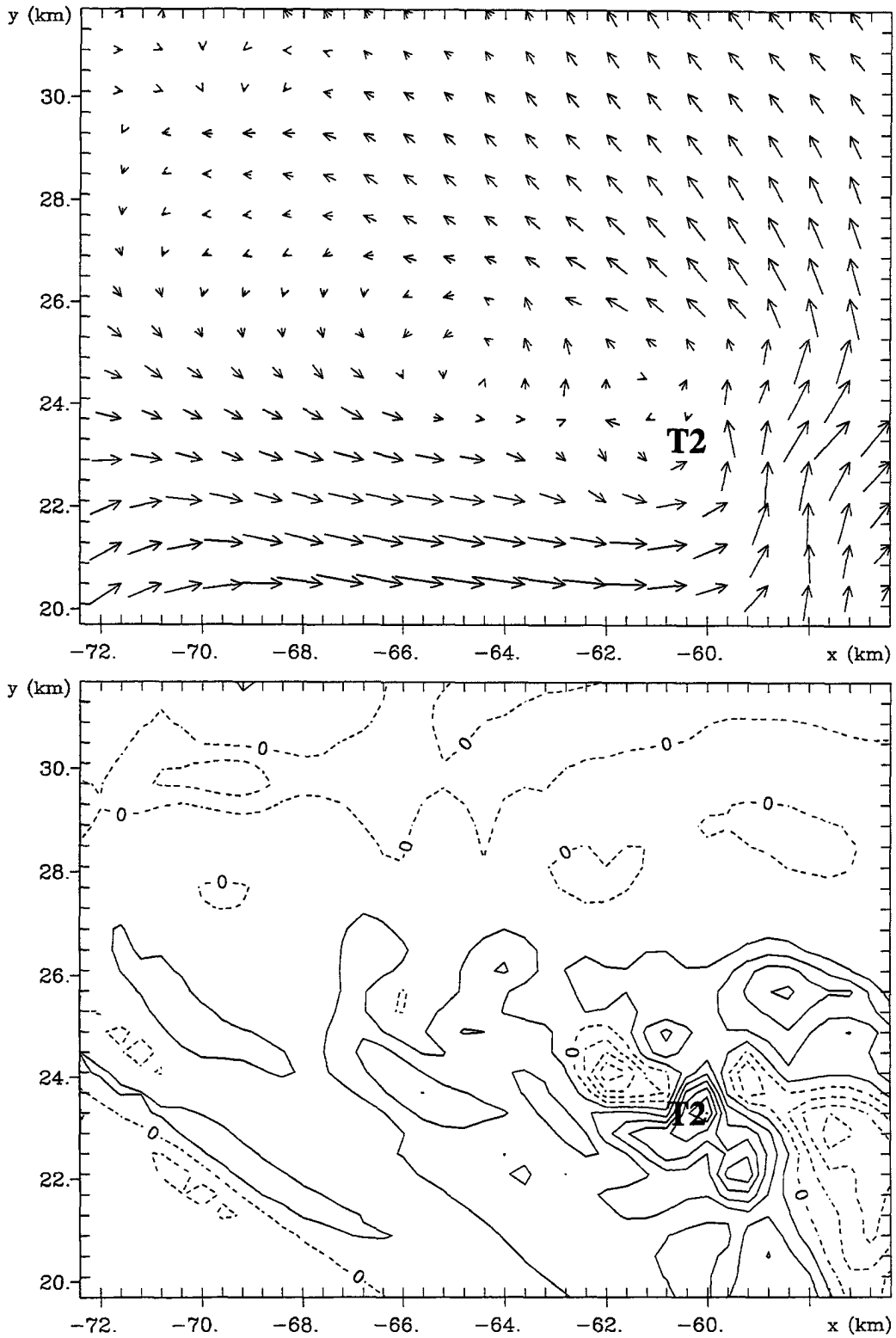

Figure 6.23: Horizontal wind vectors (top) and vertical vorticity (bottom) at 0040:30 UTC at 1.7 km above the surface on a subset of Grid #5. Velocity vectors are plotted at every other grid point. A vector which has a length equal to the distance between vectors has a magnitude of $20ms^{-1}$. The vorticity contour interval is 0.005 s^{-1}. The position of the tornado is denoted by 'T2'.

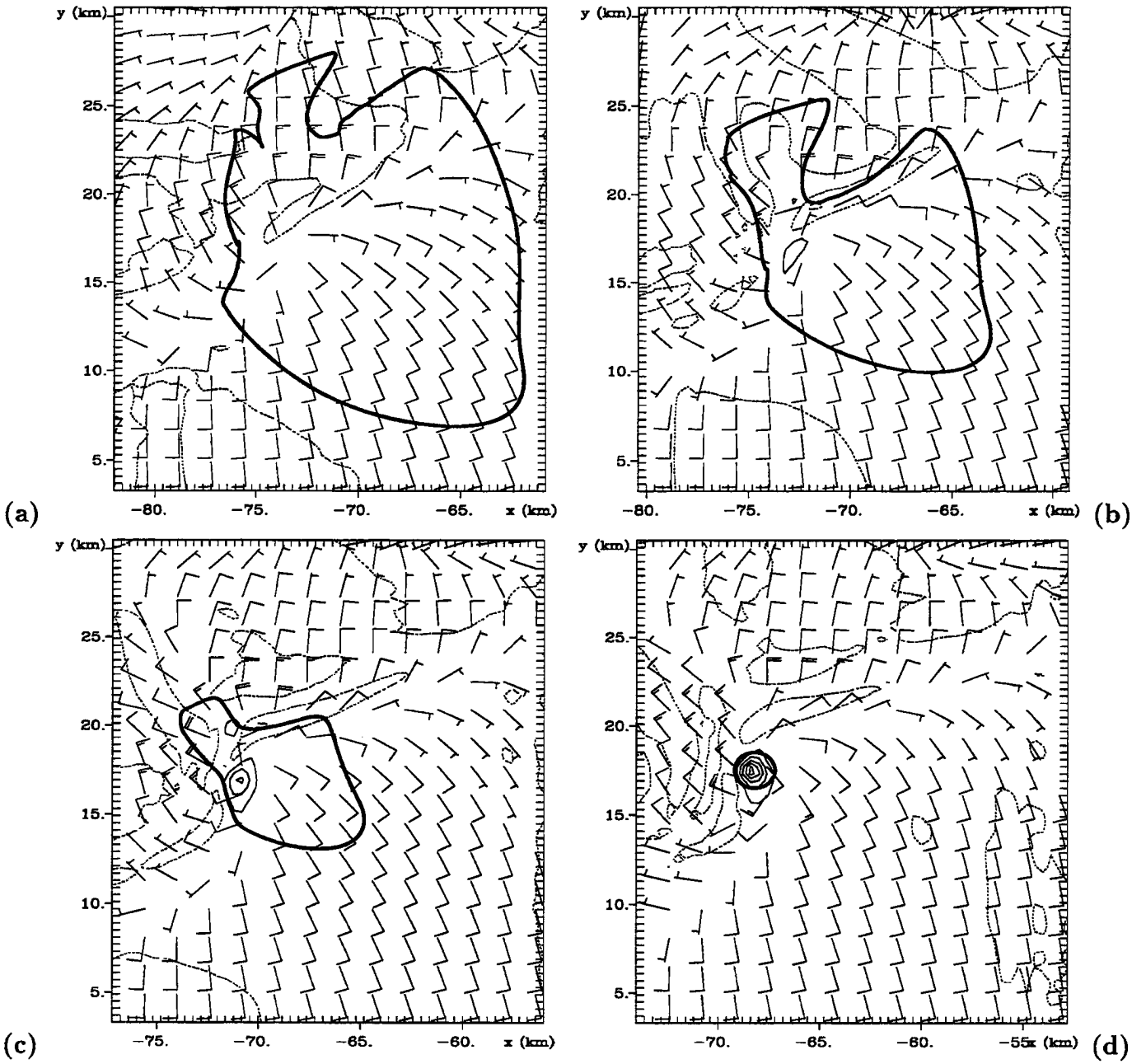

Figure 6.24: Position of the material curve for T1 with respect to the storm on a subset of Grid #5 at (a) 0003 UTC, (b) 0009 UTC, (c) 0015 UTC, (d) 0021 UTC. Colors denote the height of the material curve above the surface: red–surface to 38m, cyan–39m to 125m, purple–126m to 227m, green–228m to 350m, blue–351m to 500m, yellow–above 500m. Vertical vorticity is contoured every 0.0075 s^{-1}. Dashed contours denote a value of zero. Wind barbs are plotted at every fourth grid point. The short (long) flag on the wind barb represents a wind speed of $5ms^{-1}$ ($10ms^{-1}$).

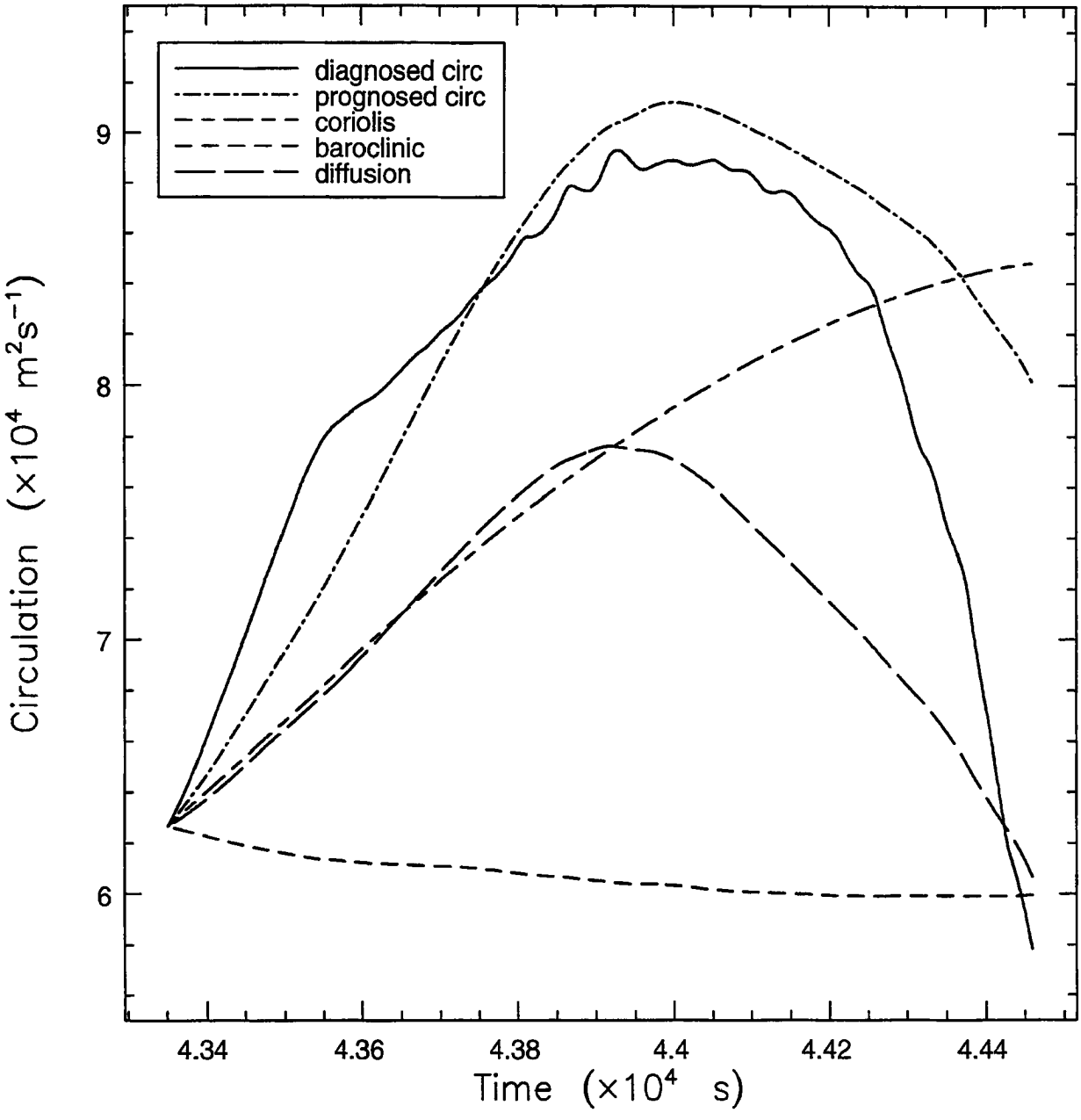

Figure 6.25: Time evolution of the circulation for a material curve initialized at 0021 UTC at z=38m around T1. The diagnosed circulation is plotted with the solid curve. The prognosed circulation and contributions to circulation from the tendencies in the circulation equation are denoted with dashed/dotted lines as denoted in the legend.

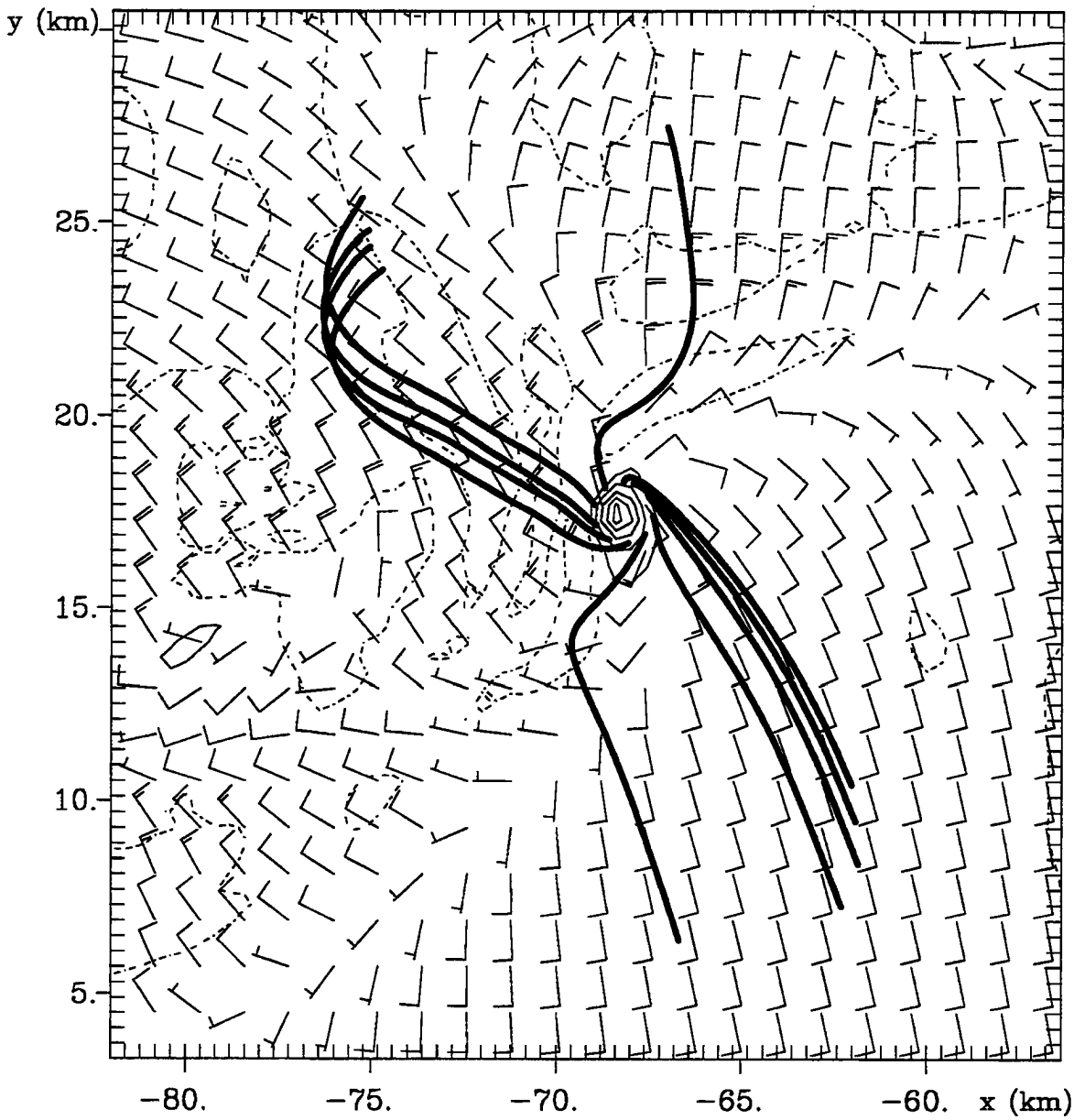

Figure 6.26: Parcel trajectories on a subset of Grid #5 for T1 overlayed on the horizontal wind and vertical vorticity at z=38m at 0021 UTC. Colors denote the height of the particles above the surface: red–surface to 38m, cyan–39m to 125m, purple–126m to 227m, green–228m to 350m, blue–351m to 500m, yellow–above 500m. Vertical vorticity is contoured every $0.0075s^{-1}$. Dashed contours denote a value of zero. Wind barbs are plotted at every third grid point. The short (long) flag on the wind barb represents a wind speed of $5ms^{-1}$ ($10\ ms^{-1}$).

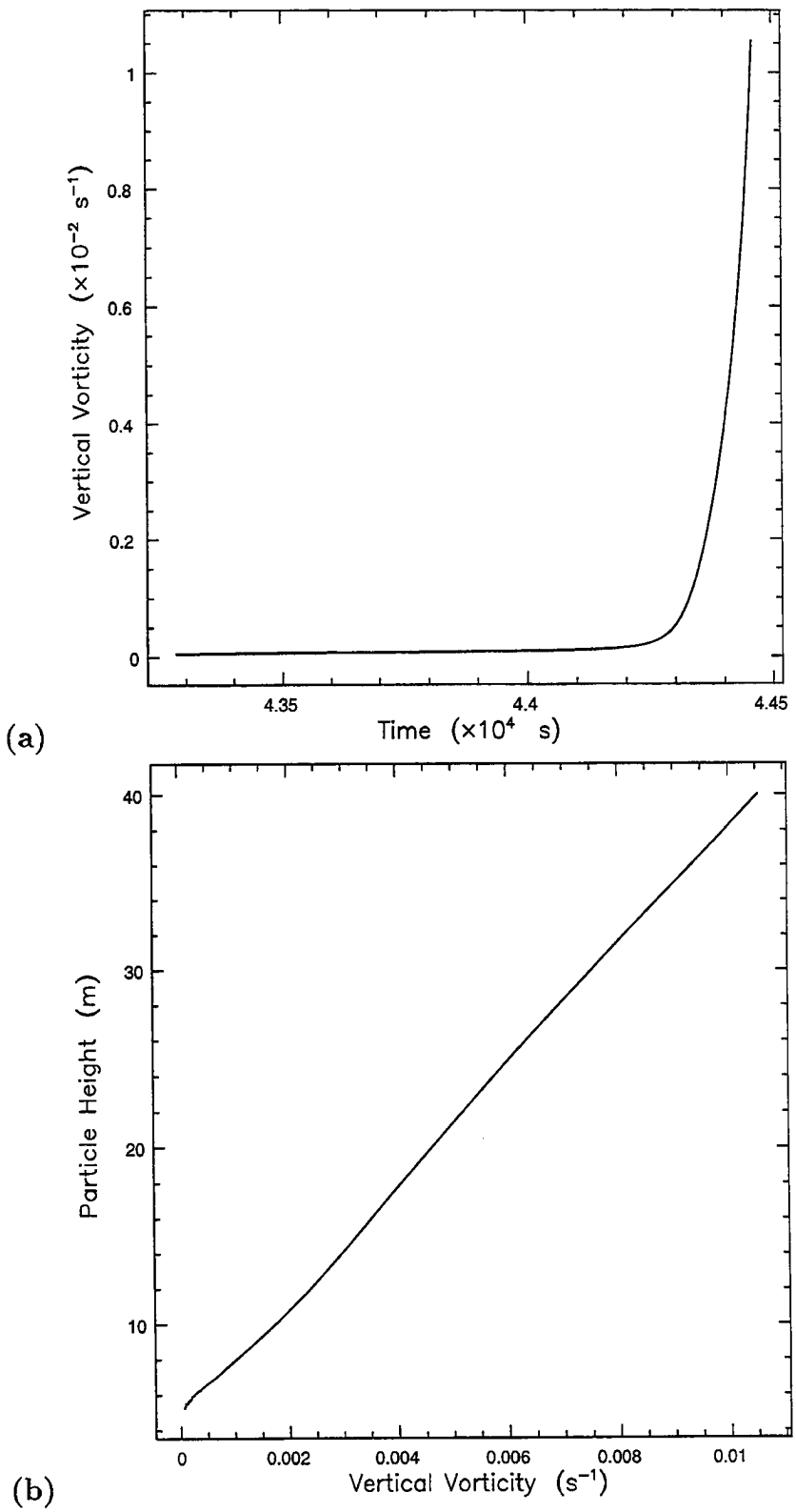

Figure 6.27: Evolution of the vertical vorticity along the trajectory of particle #14. This particle originated at low levels southeast of T1. (a) The time evolution of the vertical vortcity along the trajectory. (b) Vertical vorticity as a function of particle height along the trajectory.

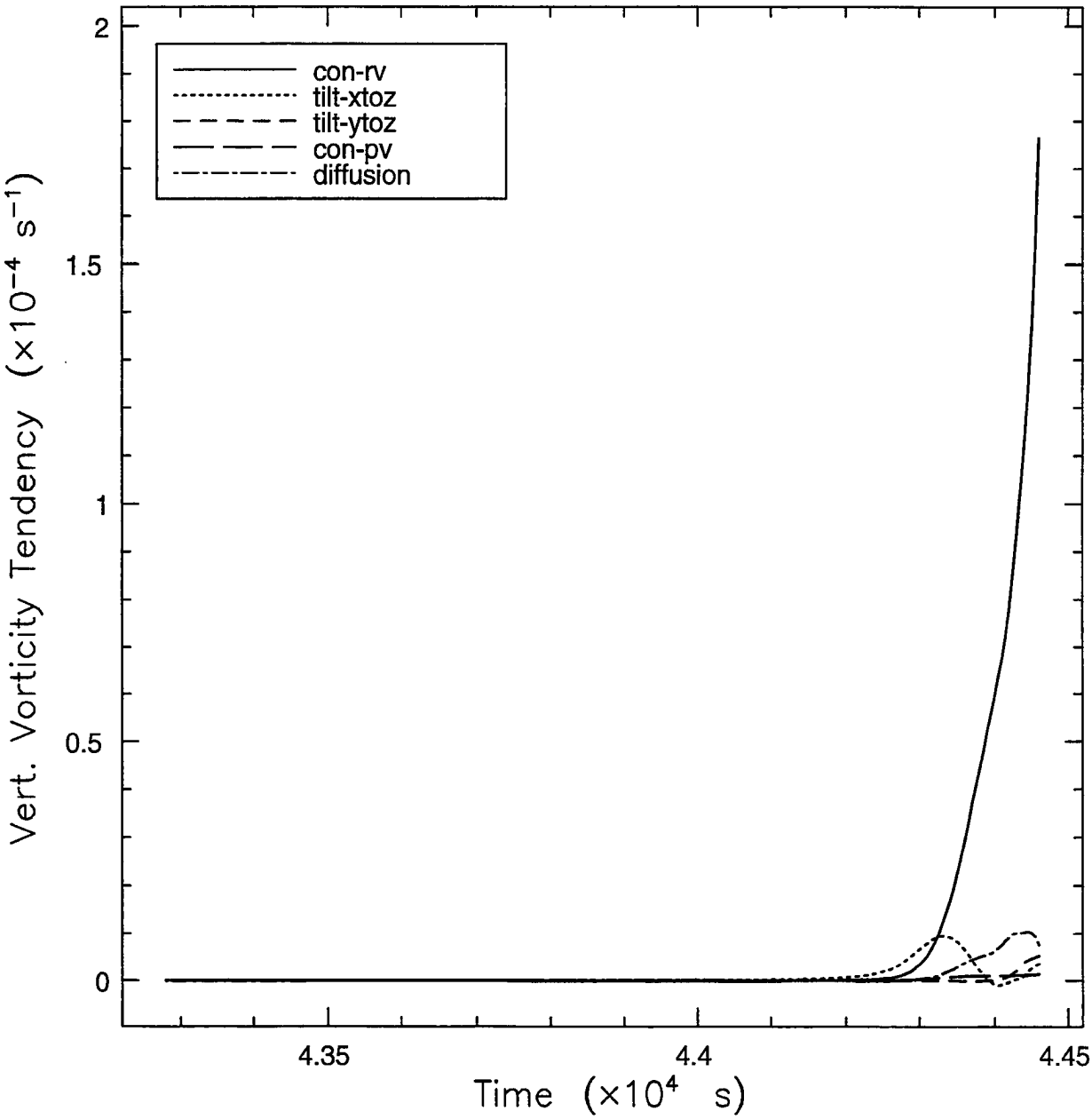

Figure 6.28: Time evolution of vertical vorticity tendencies following the trajectory of particle #14. This particle originated at low levels southeast of T1. The changes in vertical vorticity due to the various tendencies in the vertical vorticity equation are denoted with dashed/dotted lines as denoted in the legend. The abbreviations are as follows: con-rv–convergence of relative vertical vorticity, tilt-xtoz–tilting of the east-west component of the horizontal vorticity into the vertical, tilt-ytoz–tilting of the north-south component of the horizontal vorticity into the vertical, con-pv–convergence of planetary vorticity, diffusion–tendency due to surface stresses and turbulent mixing in the model.

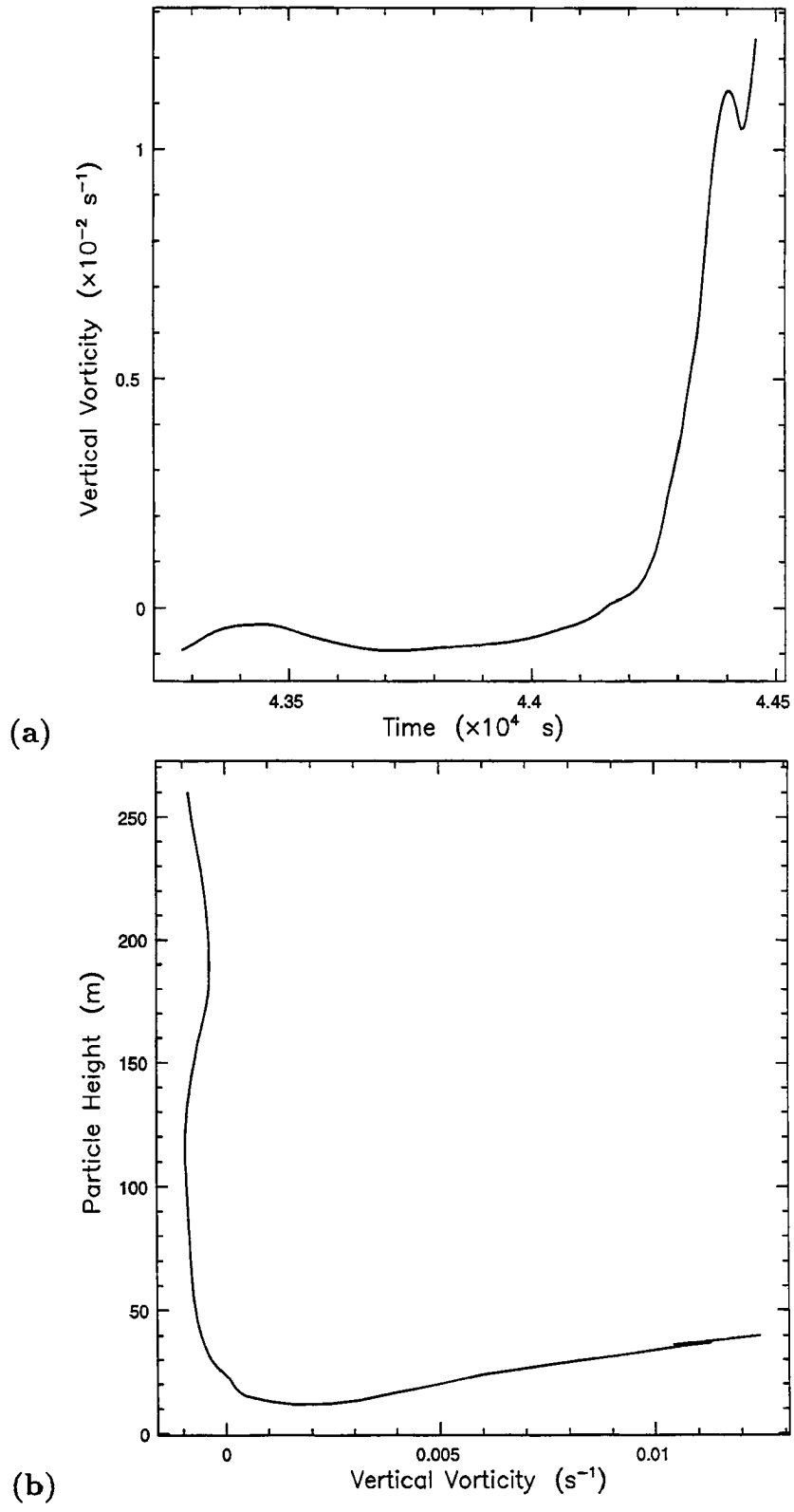

Figure 6.29: Evolution of the vertical vorticity along the trajectory of particle #10. This particle originated in the downdraft to the northwest of T1. (a) The time evolution of the vertical vortcity along the trajectory. (b) Vertical vorticity as a function of particle height along the trajectory.

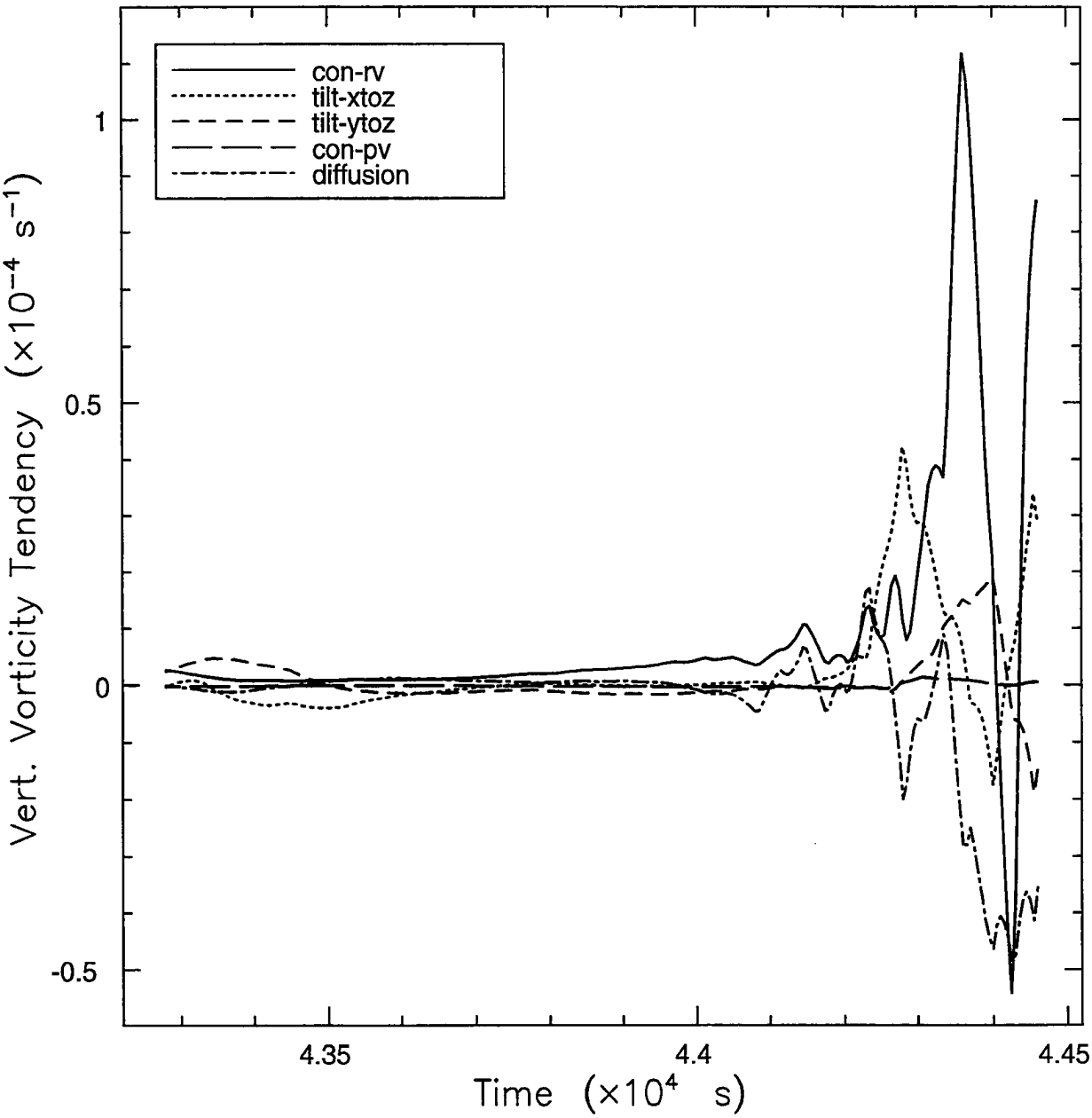

Figure 6.30: Time evolution of vertical vorticity tendencies following the trajectory of particle #10. This particle originated in the downdraft to the northwest of T1. The changes in vertical vorticity due to the various tendencies in the vertical vorticity equation are denoted with dashed/dotted lines as denoted in the legend. The abbreviations are as follows: con-rv–convergence of relative vertical vorticity, tilt-xtoz–tilting of the east-west component of the horizontal vorticity into the vertical, tilt-ytoz–tilting of the north-south component of the horizontal vorticity into the vertical, con-pv–convergence of planetary vorticity, diffusion–tendency due to surface stresses and turbulent mixing in the model.

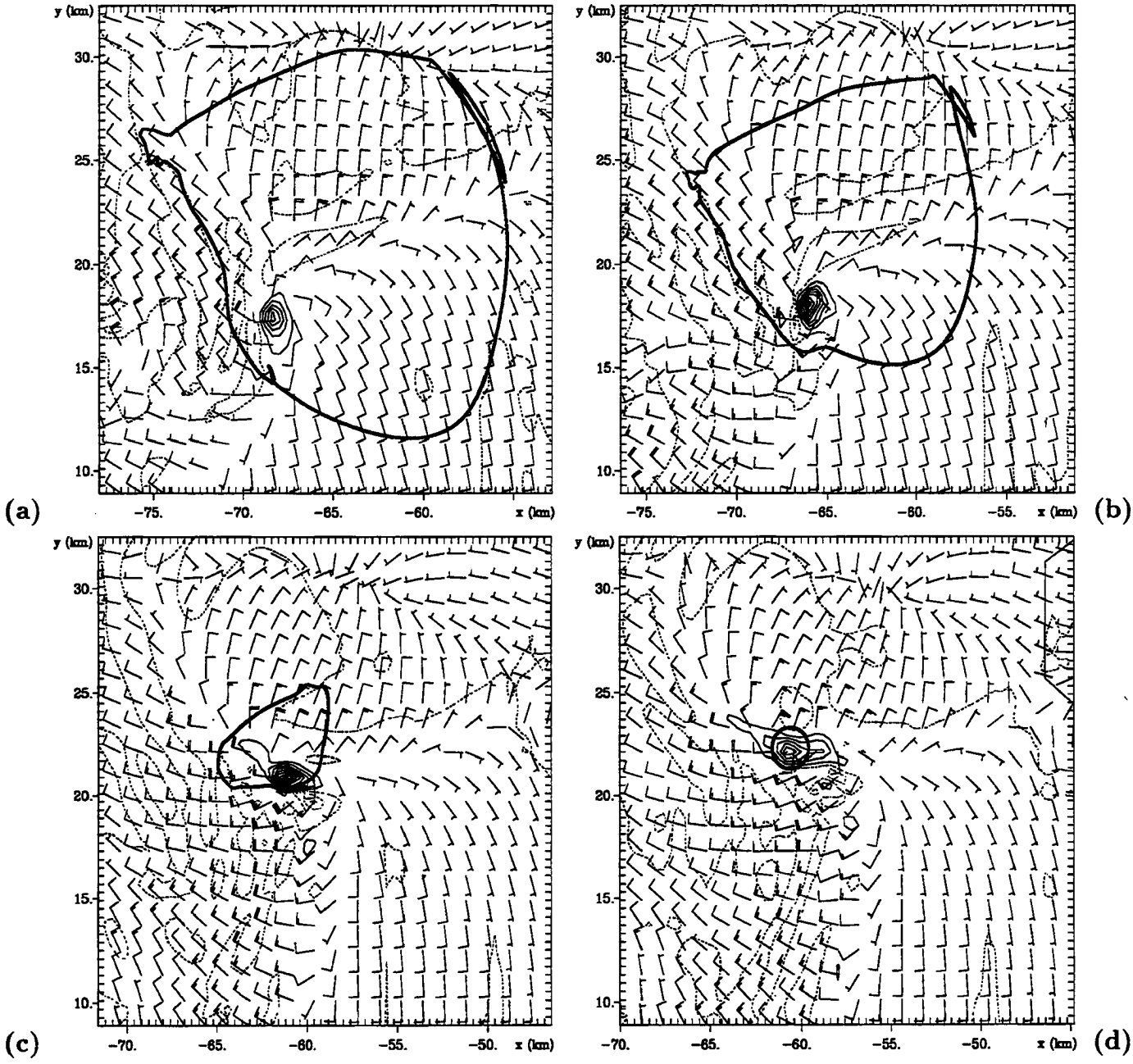

Figure 6.31: Position of the material curve for T2 with respect to the storm on a subset of Grid #5 at (a) 0021 UTC, (b) 0027 UTC, (c) 0036 UTC, (d) 0039 UTC. Colors denote the height of the material curve above the surface: red–surface to 38m, cyan–39m to 125m, purple–126m to 227m, green–228m to 350m, blue–351m to 500m, yellow–above 500m. Vertical vorticity is contoured every 0.0075 s^{-1}. Dashed contours denote a value of zero. Wind barbs are plotted at every fourth grid point. The short (long) flag on the wind barb represents a wind speed of $5ms^{-1}$ ($10ms^{-1}$).

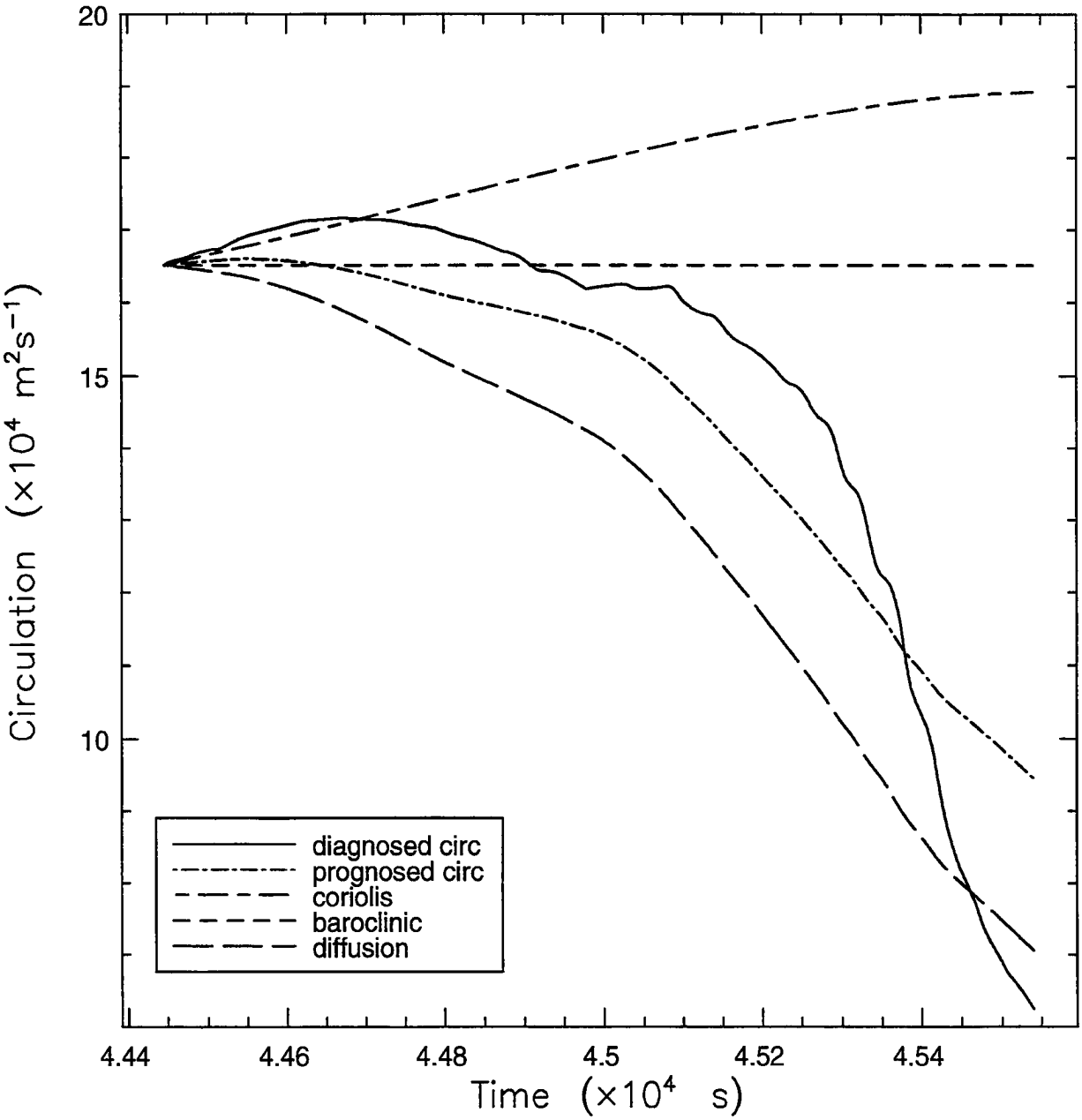

Figure 6.32: Time evolution of the circulation for a material curve initialized at 0039 UTC at z=38m around T2. The diagnosed circulation is plotted with the solid curve. The prognosed circulation and contributions to circulation from the tendencies in the circulation equation are denoted with dashed/dotted lines as denoted in the legend.

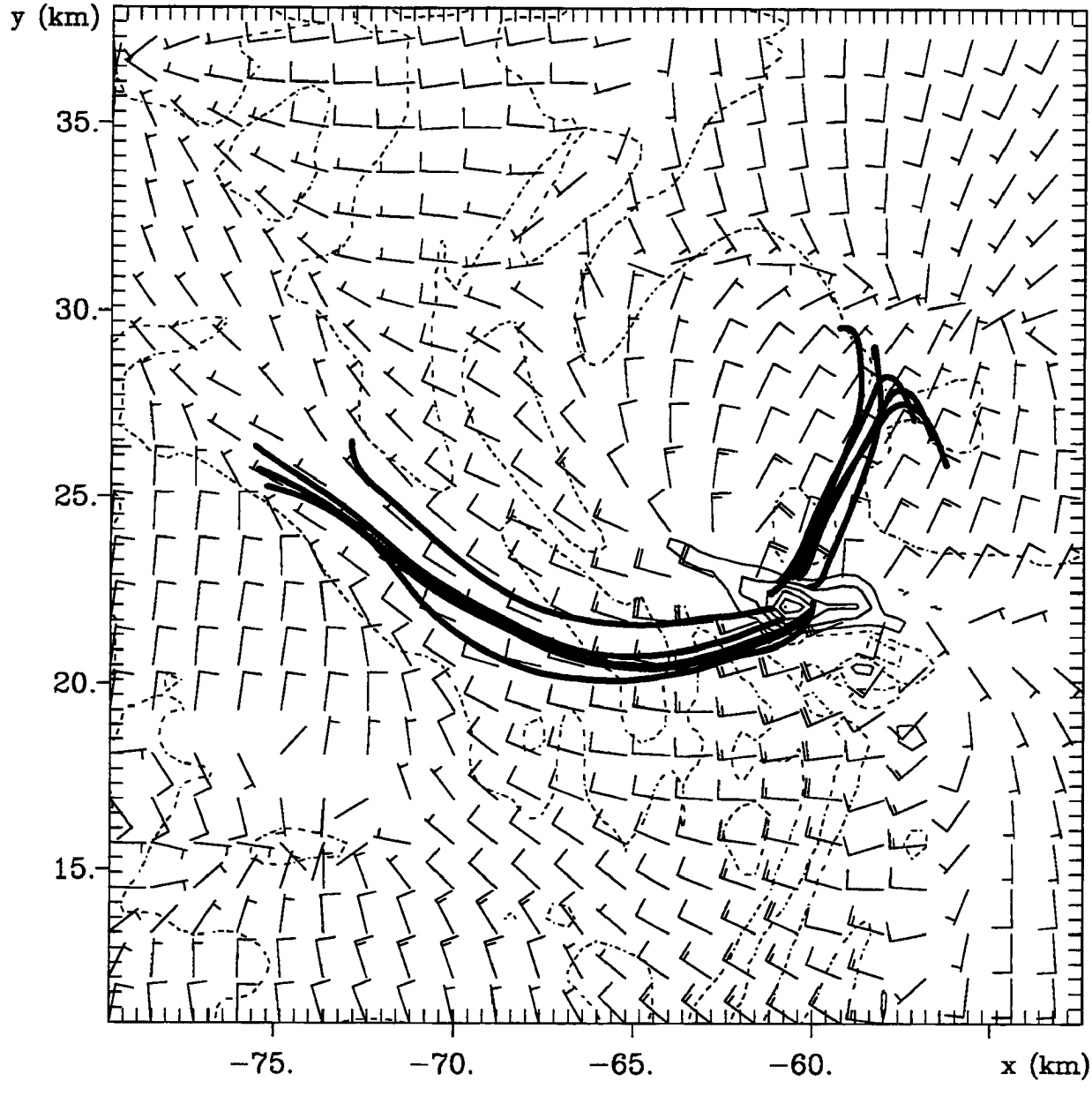

Figure 6.33: Parcel trajectories on a subset of Grid #5 for T2, overlayed on the horizontal wind and vertical vorticity at z=38m at 0039 UTC. Colors denote the height of the particles above the surface: red–surface to 38m, cyan–39m to 125m, purple–126m to 227m, green–228m to 350m, blue–351m to 500m, yellow–above 500m. Vertical vorticity is contoured every $0.0075s^{-1}$. Dashed contours denote a value of zero. Wind barbs are plotted at every third grid point. The short (long) flag on the wind barb represents a wind speed of $5ms^{-1}$ ($10\ ms^{-1}$).

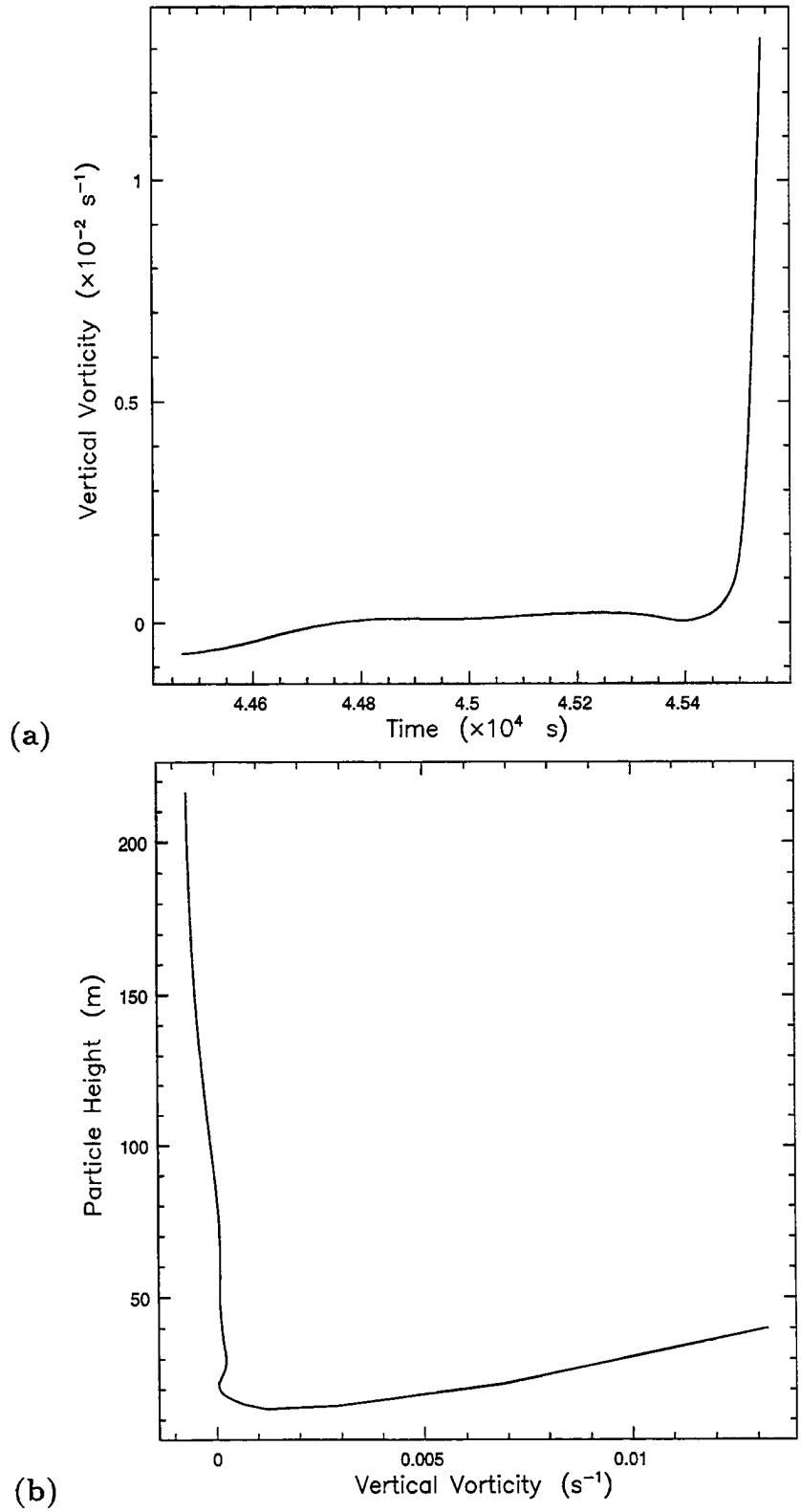

Figure 6.34: Evolution of the vertical vorticity along the trajectory of particle #4. This particle originated in a downdraft to the northeast of T2. (a) The time evolution of the vertical vortcity along the trajectory. (b) Vertical vorticity as a function of particle height along the trajectory.

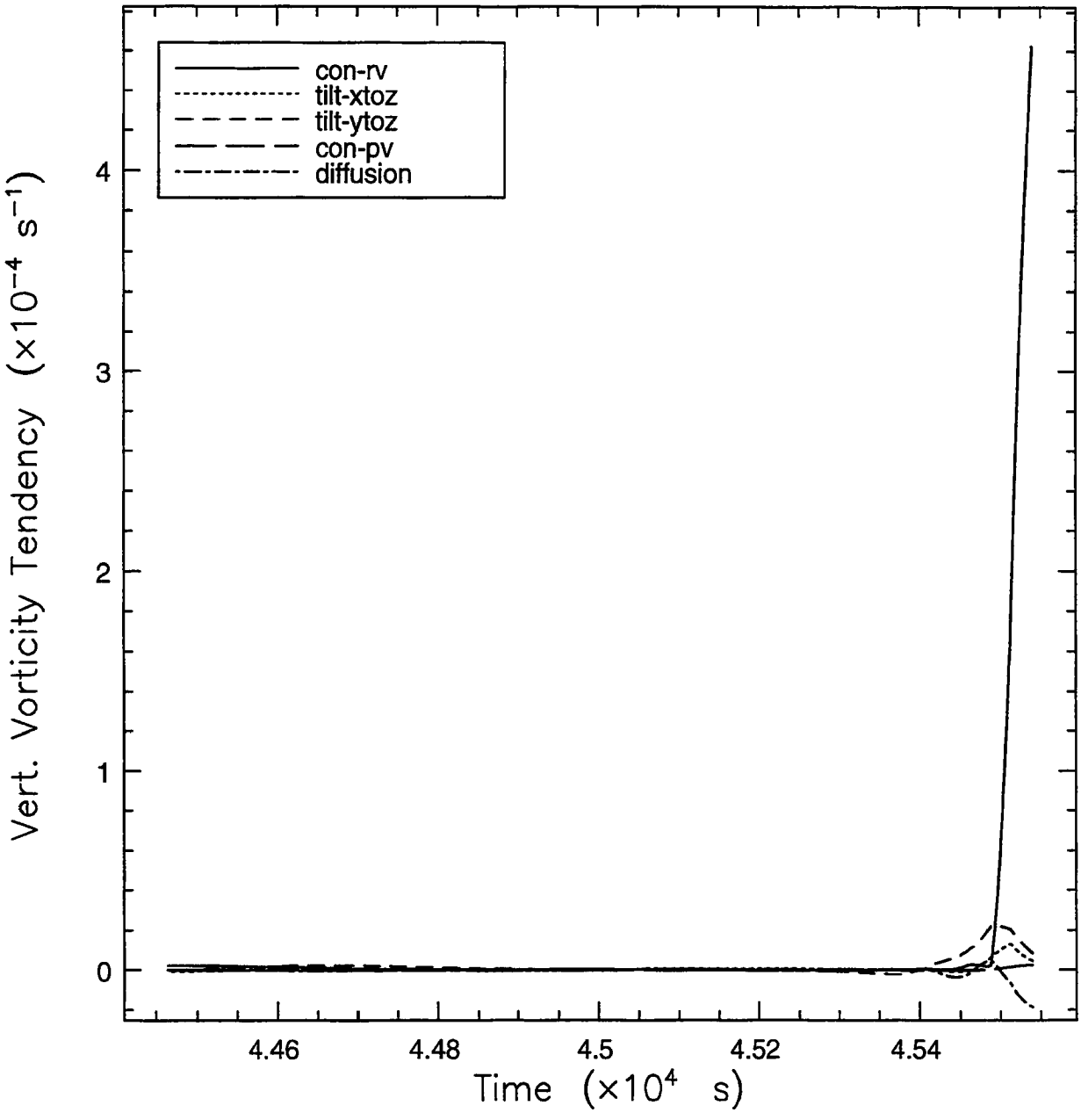

Figure 6.35: Time evolution of vertical vorticity tendencies following the trajectory of particle #4. This particle originated in a downdraft to the northeast of T2. The changes in vertical vorticity due to the various tendencies in the vertical vorticity equation are denoted with dashed/dotted lines as denoted in the legend. The abbreviations are as follows: con-rv–convergence of relative vertical vorticity, tilt-xtoz–tilting of the east-west component of the horizontal vorticity into the vertical, tilt-ytoz–tilting of the north-south component of the horizontal vorticity into the vertical, con-pv–convergence of planetary vorticity, diffusion–tendency due to surface stresses and turbulent mixing in the model.

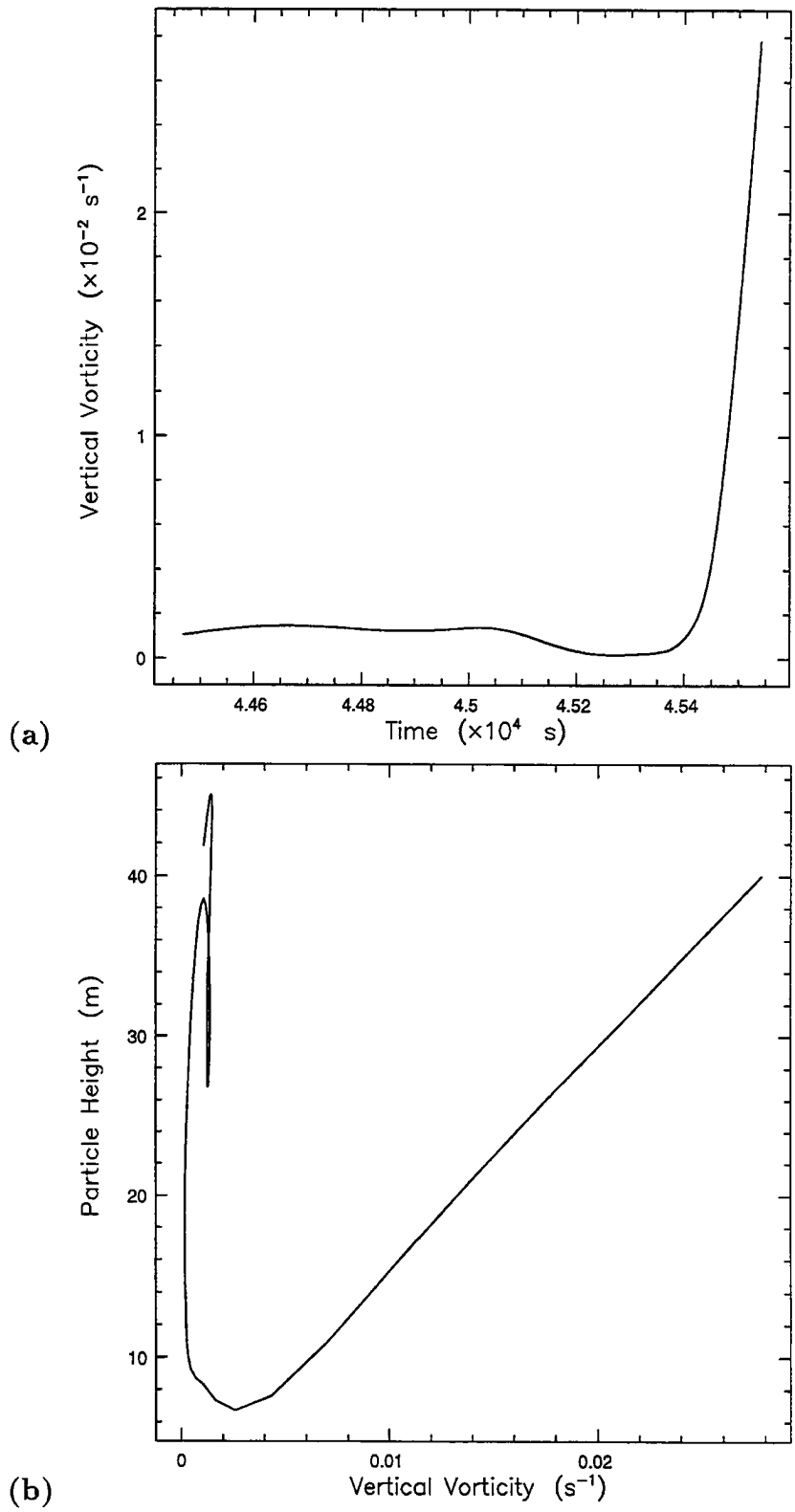

Figure 6.36: Evolution of the vertical vorticity along the trajectory of particle #8. This particle originated at low levels to the west of T2. (a) The time evolution of the vertical vortcity along the trajectory. (b) Vertical vorticity as a function of particle height along the trajectory.

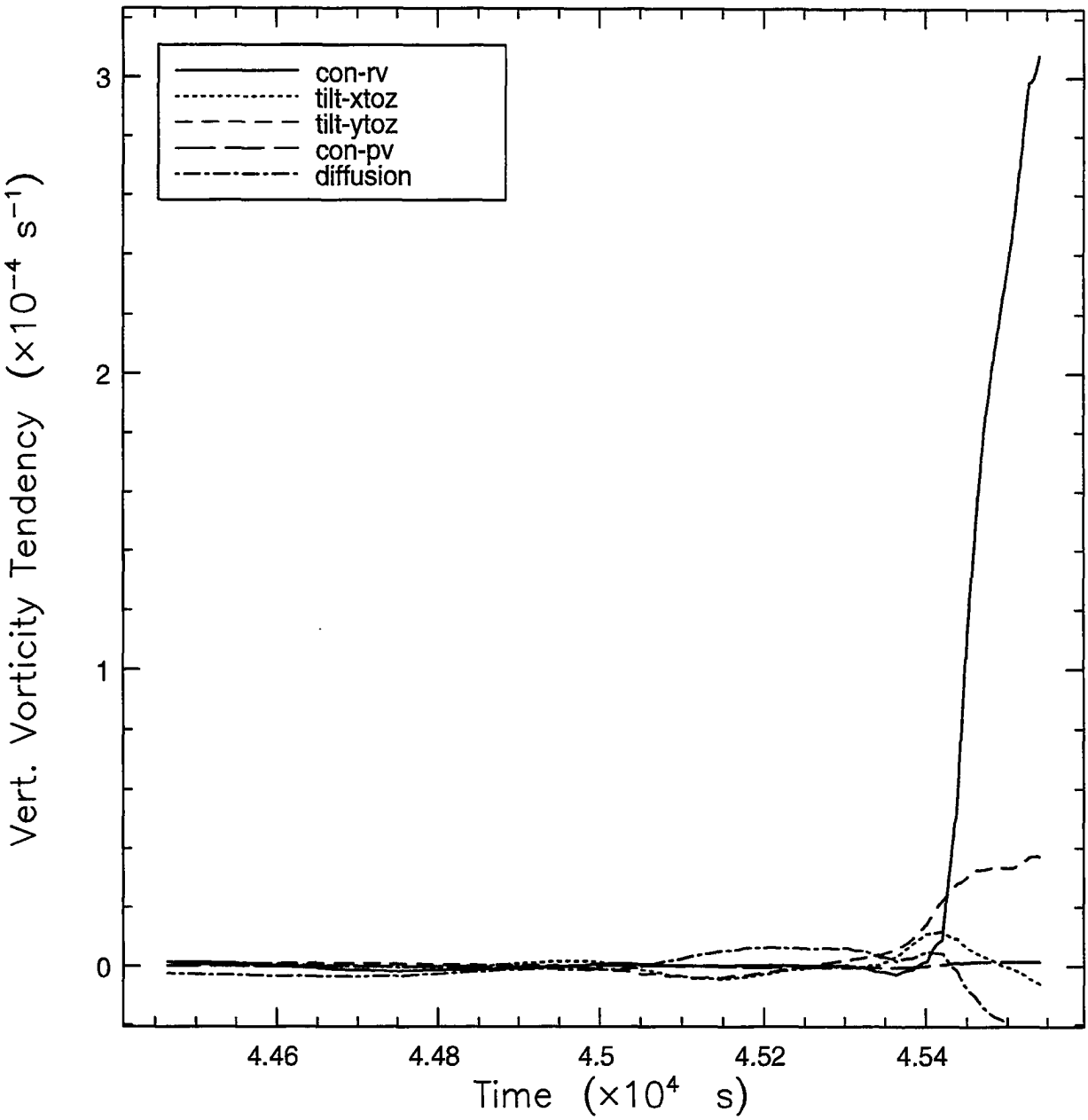

Figure 6.37: Time evolution of vertical vorticity tendencies following the trajectory of particle #8. This particle originated at low levels to the west of T2. The changes in vertical vorticity due to the various tendencies in the vertical vorticity equation are denoted with dashed/dotted lines as denoted in the legend. The abbreviations are as follows: con-rv–convergence of relative vertical vorticity, tilt-xtoz–tilting of the east-west component of the horizontal vorticity into the vertical, tilt-ytoz–tilting of the north-south component of the horizontal vorticity into the vertical, con-pv–convergence of planetary vorticity, diffusion–tendency due to surface stresses and turbulent mixing in the model.

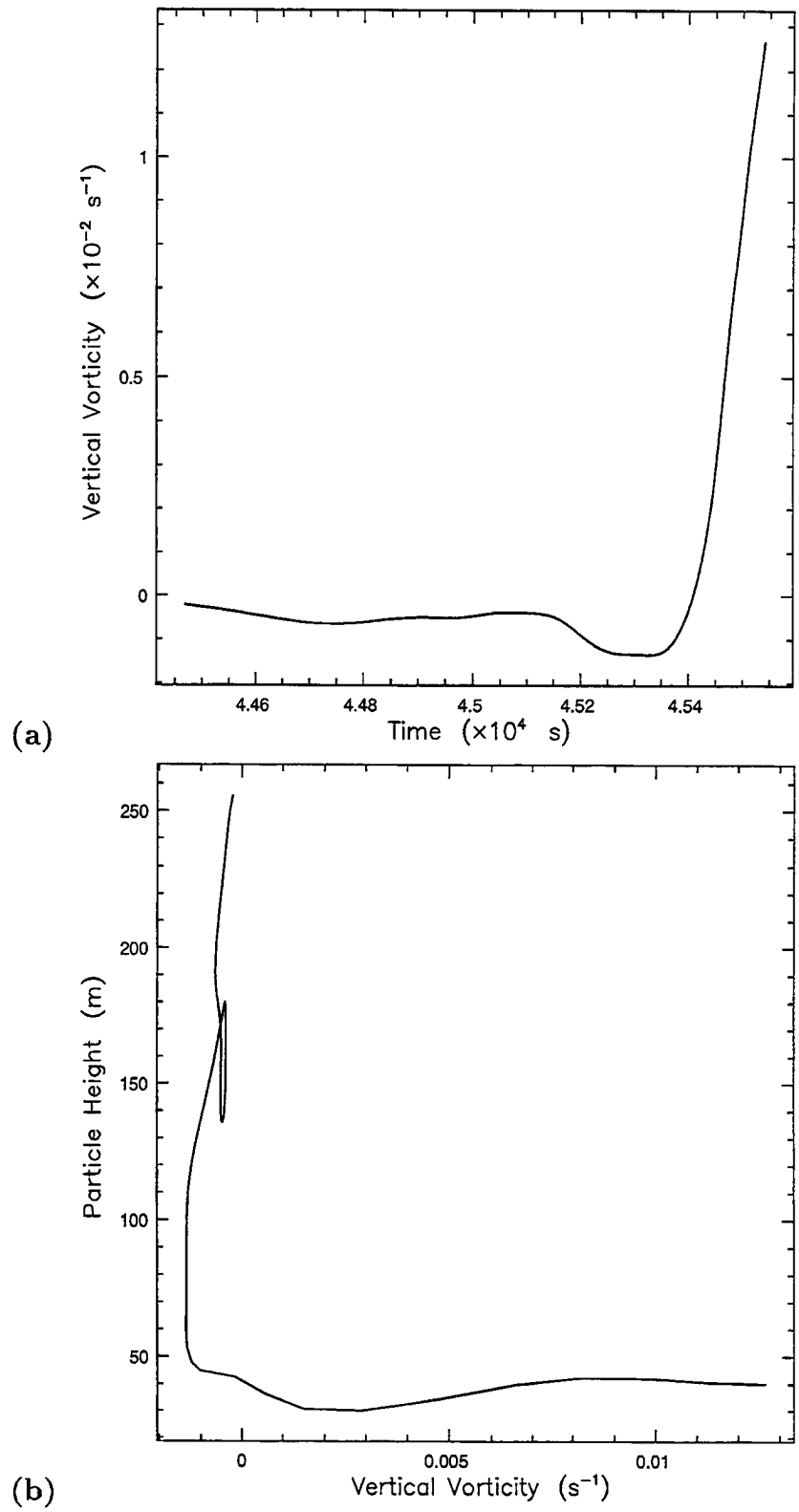

Figure 6.38: Evolution of the vertical vorticity along the trajectory of particle #13. This particle originated in a downdraft to the west of T2. (a) The time evolution of the vertical vorticity along the trajectory. (b) Vertical vorticity as a function of particle height along the trajectory.

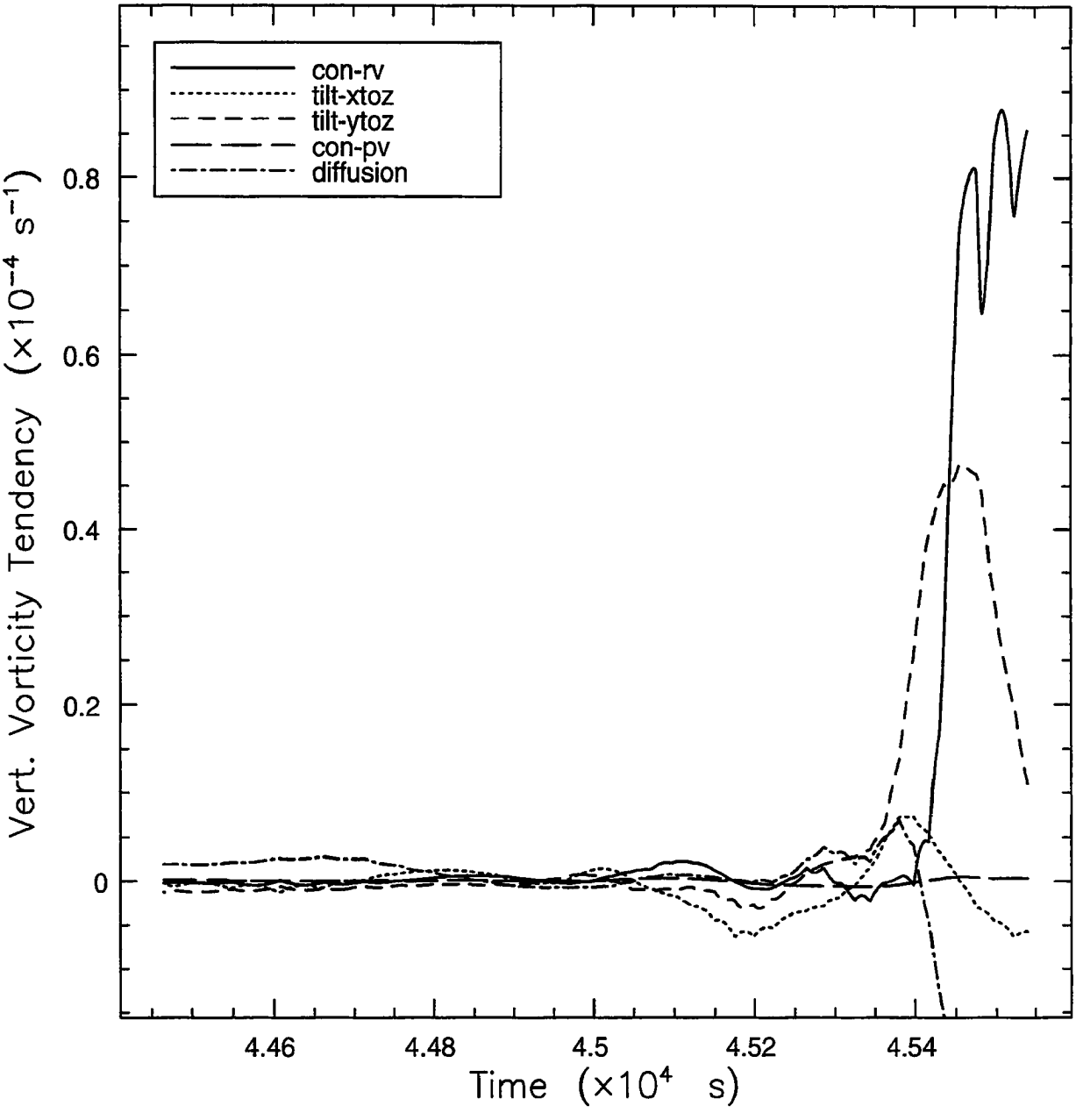

Figure 6.39: Time evolution of vertical vorticity tendencies following the trajectory of particle #13. This particle originated in a downdraft to the west of T2. The changes in vertical vorticity due to the various tendencies in the vertical vorticity equation are denoted with dashed/dotted lines as denoted in the legend. The abbreviations are as follows: con-rv–convergence of relative vertical vorticity, tilt-xtoz–tilting of the east-west component of the horizontal vorticity into the vertical, tilt-ytoz–tilting of the north-south component of the horizontal vorticity into the vertical, con-pv–convergence of planetary vorticity, diffusion–tendency due to surface stresses and turbulent mixing in the model.

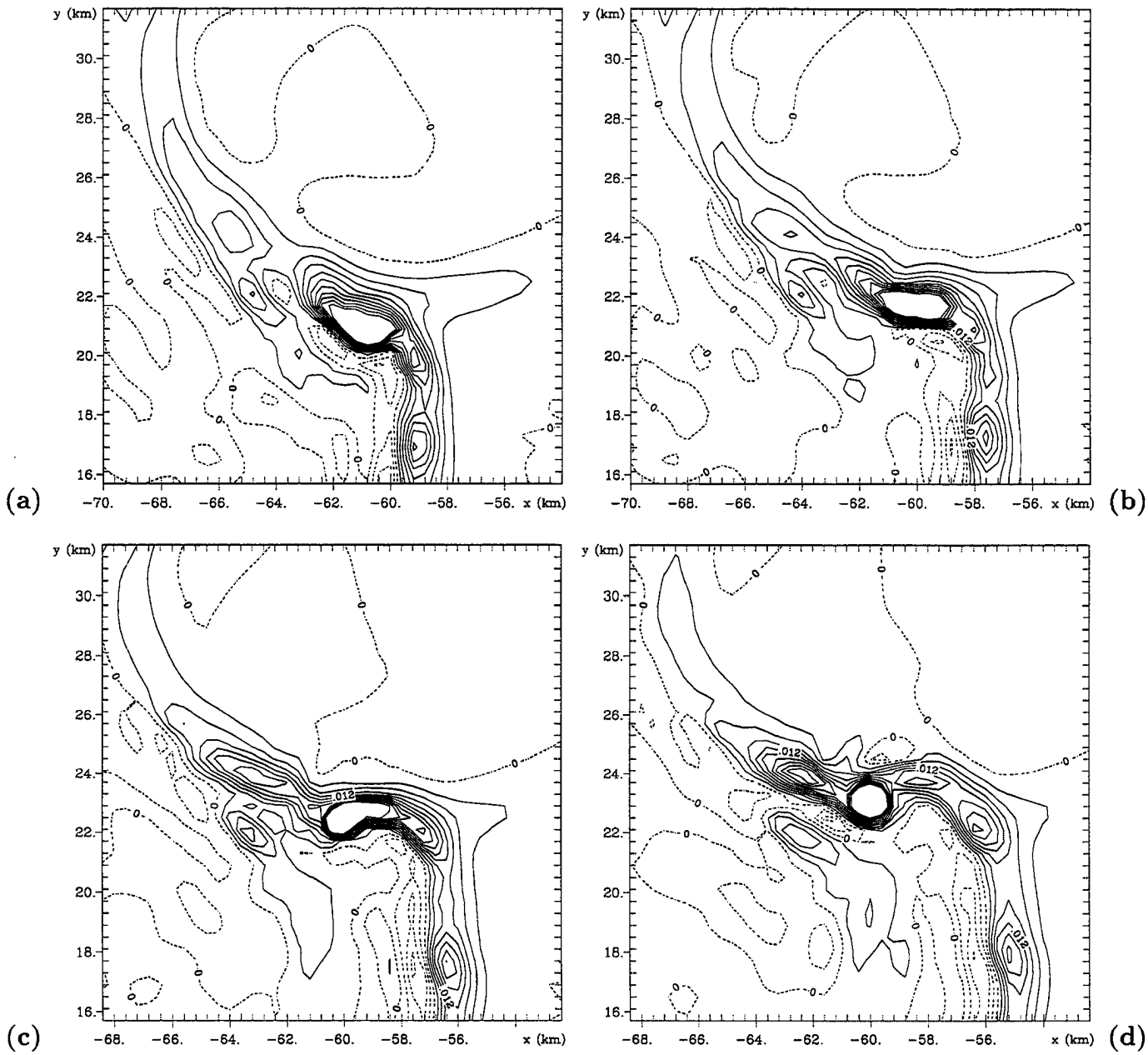

Figure 6.40: Evolution of the vertical vorticity field at z=350m on a subset of Grid #5 at (a) 0036 UTC, (b) 0037:30 UTC, (c) 0039 UTC, (d) 0040:30 UTC. Vertical vorticity is contoured every $0.003s^{-1}$ to a maximum of $0.03s^{-1}$. Dashed contours denote negative values.

Chapter 7

SIMULATED SECONDARY VORTICES–MAY 15, 1991 CASE

In this chapter, the model results from the May 15, 1991, simulation will be presented. This case was also simulated by Grasso (1996) who focused on the evolution of the dryline, the supercell storm evolution, and the initial development of the tornado. The simulation was run again in this study in order to confirm that the tornadogenesis process was similar to that found in Grasso (1996) following some changes made to the microphysical package in the model. In addition, the simulation was performed for a longer time period in order to investigate the evolution of the tornado (the simulation performed by Grasso (1996) was terminated shortly after the tornado developed since the focus of that study was the tornadogenesis process). The simulated tornado in this study lasted for 50 minutes, and was still going strong when the simulation was terminated at 2200 UTC. During the last 10-15 minutes of the simulation, the vortex expanded in size and smaller vortices developed along the annular shear zone of the main vortex. Since this is the first numerical simulation of secondary vortices produced in a non-axisymmetric vortex which is free to evolve with the parent thunderstorm, the purpose of this chapter is to document the evolution and characteristics of these 'secondary vortices' (which for brevity will be abbreviated as 'SV'). Comparisons with observations, laboratory experiments and previous idealized modeling studies will also be made.

In order to provide some continuity, a brief overview of the simulation prior to the development of the secondary vortices is also presented. For more details pertaining to the evolution of the mesoscale features in the simulation and the genesis of the tornado, the reader is referred to Grasso (1996).

7.1 Overview of May 15, 1991 Simulation

The May 15, 1991, simulation was started at 1200 UTC with 3 grids to capture the early evolution of the synoptic features. Of particular importance on this day was the development of a dryline in western Oklahoma and Texas which provided the forcing necessary to initiate the afternoon convection. The evolution of the near surface dryline in the model on Grid #3 is shown in Figure 7.1. Between 1700 UTC and 2000 UTC, the boundary layer moisture gradient strengthens significantly in the Texas panhandle as winds east of the dryline back and strengthen in time. This creates a narrow north-south band of strong low-level convergence extending across northern Texas into the Oklahoma panhandle. The air east of the dryline was very moist (mixing ratios up to $18g(kg)^{-1}$) as warm, moist air was advected north/northwestward into the region throughout the day.

As the low-level convergence along the dryline increased during the afternoon, the vertical velocity along the dryline also intensified, pumping the moist air east of the dryline into the upper boundary layer. Figure 7.2 shows the evolution of the water vapor field about 2km above the surface. Between 1900 UTC - 1930 UTC, water vapor mixing ratios increased significantly above the dryline indicating that the circulation associated with the dryline had now developed upward to this level. The upper boundary layer above the dryline continued to moisten during the next half hour and shortly after 2000 UTC, convection developed along the dryline on Grid #3. This is somewhat surprising considering that the horizontal grid spacing on Grid #3 is 5km and no cumulus parameterization was used. Thus the convection was initiated from resolved vertical motions created by the dryline on Grid #3. This early development of convection at z=1959m is shown in Figure 7.3. Between 2000 UTC - 2030 UTC, vertical motions above the dryline at z=1959m increased from $2ms^{-1}$ to $9ms^{-1}$, and a storm began to develop in the northern Texas panhandle.

Grid #4 (with 1km grid spacing) was spawned at 2000 UTC over the region where convection developed on Grid #3. This grid was added to the simulation in order to resolve the development and evolution of the storm. As the storm developed, it began moving northeastward away from the dryline and Grid #4 was moved to the northeast following the

storm. Although the storm exhibited signs of rotation early in its development, the storm never 'split' as in horizontally homogeneous simulations of supercells where convection is initiated with a warm bubble. The structure of the storm at 2108 UTC is shown in Figure 7.4. The simulated storm exhibited many characteristics of classic supercells including a rotating updraft, a hook echo, and a rear flank downdraft. Early indications of low-level rotation can also be seen near the surface at this time as shown in Figure 7.4c.

Grids #5-6 were added at 2100 UTC since fields on Grid #4 were indicating that the model was trying to develop a low-level circulation shortly after 2100 UTC. Around 2106 UTC, the first evidence of a developing vortex can be seen at z=50m on Grid #6 as shown in Figure 7.5. The pressure dropped over a small region and a closed circulation developed near the surface to the southeast of the main mid-level mesocyclone. The maximum wind speeds associated with the vortex at this time were $24ms^{-1}$ which is already tornadic strength. During the next 10 minutes, the surface pressure associated with the vortex continued to drop, reaching a maximum pressure deficit of 20mb at 2118 UTC (although the maximum tangential wind speeds were not reached at this time).

In the early stages of its life, the vortex was roughly 1km wide near the surface. Around 2116 UTC, a central downdraft was established at the center of the vortex which was surrounded by an annular region of updraft. From this time on, the vortex core (marked by the radius of maximum winds) slowly expanded in size. A few minutes later, the vorticity structure in the vortex changed from a central maximum to a vorticity 'ring' with a relative minimum at the center. This structure can also be seen in Figure 7.6 which shows the low-level tornado structure on Grid #6 at 2126 UTC. The strong central downdraft surrounded by an annular updraft is clearly visible, as is the vertical vorticity 'ring'. The maximum wind speed associated with the vortex at this time was $44ms^{-1}$ (which was typical of the vortex from 2110 UTC - 2130 UTC) which classifies this tornado as a strong F1.

Between 2130 UTC and 2140 UTC, the vortex was disrupted by a strong downdraft surge. The downdraft originated to the west of the tornado, and proceeded to wrap around the southern and eastern sides of the vortex. During this time the vortex weakened considerably with the maximum pressure deficit decreasing to 10mb, and maximum tangential

winds dropping off to $28ms^{-1}$ by 2141 UTC. After 2141 UTC, the vortex began recovering, and its structure at 2142 UTC is shown in Figure 7.7. The tornado still contains a central downdraft, but the downdraft is no longer completely surrounded by a ring of updraft, and the vertical vorticity field now takes the form of a semicircular vorticity strip. It is interesting to note that although the vortex still has a distinct pressure minimum associated with it, this pressure minimum does not correspond to the center of circulation in the vortex which is located about 1km to the northwest of the pressure minimum at this time.

During the next three minutes (2142-2145 UTC), the central pressure in the vortex drops and the tangential wind speeds increase as the vortex again becomes well established in the simulation. Over the course of the next 10 minutes, smaller vortices develop within the main vortex. These smaller 'secondary' vortices are the topic of the next section.

7.2 Evolution and Structure of the Secondary Vortices

As was mentioned above, the low-level vortex intensified around 2145 UTC following a brief disruption from a strong downdraft, and in the process, the diameter of the vortex core increased to 2km. Although tornadoes of this size have been observed, they are extremely rare (Davies-Jones, 1983). However, there is good observational evidence that secondary vortex development occurs over a range of scales in vortices associated with thunderstorms[1]from mesocyclones to suction vortices in tornadoes. Radar observations have shown multiple vorticity maxima in rings surrounding the centers of mesocyclones (Brandes, 1978) some of which have developed into tornadoes (Wakimoto and Lin, 1997). This pattern of several smaller vorticity maxima surrounding the mesocyclone core was also seen in the June 30 simulation presented earlier (see Figure 6.13). There have also been numerous eye-witness accounts describing multiple tornadoes occurring simultaneously in one storm with the tornadoes 'moving in different directions in different parts of the city' (revolving around a single point) (Fujita et al., 1970; Barnes, 1987a,b). Secondary vortex

[1]There is also observational evidence which indicates that 'secondary vortices' can also be found in hurricane eye-walls, but a complete discussion of hurricanes is beyond the scope of this text.

development can also occur in 'suction vortices' embedded within tornadoes. Observations of tornado damage paths have occasionally shown smaller cycloidal damage swaths within the larger cycloidal damage swaths produced by suction vortices (Agee et al., 1977; Forbes, 1978; Snow, 1982). In light of these observations, we believe the results from the present simulation are physically relevant to the development of secondary vortices within vortices produced by thunderstorms–including suction vortices in tornadoes–despite the fact that the vortex in the present simulation is larger than a 'typical' tornado. For generality, the main vortex (tornado) will be referred to as the 'parent vortex' or 'primary vortex' (PV), and the smaller sub-vortices will be referred to as 'secondary vortices' (SV).

A total of six secondary vortices developed within the parent vortex in roughly a ten minute time period between 2146-2156 UTC. A summary of some of the characteristics of the secondary vortices is given in Table 7.1. Just prior to the onset of the secondary vortices, the parent vortex again developed a well-defined two-celled structure. This can be seen in the vertical velocity field at z=800m which is shown in Figure 7.8. Prior to 2146 UTC, the vortex does not have a 'closed ring' structure in the vertical motion field (except at the lowest model level). Although there is evidence of a central downdraft, the updraft does not form a complete ring around it until 2146 UTC as shown in Figure 7.8a,b. After 2146, the central downdraft intensifies from less than $-2ms^{-1}$ to $-16ms^{-1}$ at 2147:30 UTC (Figure 7.8d) at z=800m.

Commencement of secondary vortex development occurs as both the central downdraft/updraft ring and a well-defined vertical vorticity ring become well established in throughout lowest 1.5km of the parent vortex. The secondary vortices are most visible in the pressure field, and the evolution of the pressure at the lowest model level (z=50m) is shown in Figure 7.9. (Note that the time interval between successive frames in Figure 7.9 is not constant.) The secondary vortices have been labeled SV1-SV6 for convenience. The first secondary vortex (SV1) develops along the eastern side of the parent vortex around 2147 UTC as shown in Figure 7.9b. Each successive SV develops along the east/southeast side of the parent vortex (in the *interior* of the parent vortex) and each is associated with a pressure minimum. As the SV rotated counter-clockwise around the parent vortex, the cen-

tral pressure associated with the SV decreased reaching a minimum as the SV approached the northernmost point of their trajectory. Most of the SV quickly dissipated as they rounded the northwest side of the parent vortex. SV1 (although one of the weaker SV) has the longest lifetime, completing almost $\frac{3}{4}$ of a revolution around the parent vortex before it could no longer be detected in the pressure field. SV2-SV5 completed about $\frac{1}{2}$ of a revolution, and the last secondary vortex (SV6) was only able to complete roughly $\frac{1}{4}$ of a revolution before it quickly dissipated. Another interesting feature is that as the stronger SV dissipate (SV3, SV4, and SV6 to a lesser extent), the central pressure associated with the SV changes from a relative 'low' to a relative 'high' (see Figures 7.9e-h). This will be discussed further below. The secondary vortices could be detected in the pressure field up to z=1.5km, but had a distinct pressure minimum only up to z=800m (except for SV2 which could only be detected up to z=500m). Between z=1-1.5km, the pressure minimum took the form of an open wave. The final secondary vortex (SV6) dissipated shortly after 2154 UTC, but wave-like disturbances could be seen in the pressure field until 2156 UTC.

The evolution of the vertical velocity field at z=50m throughout the period of secondary vortex development is shown in Figure 7.10. The position of the pressure center associated with each SV is denoted by a dot, and downdrafts outside the vortex core are denoted by D1 and D2. By 2146:30, the parent vortex is a well established two-celled vortex (i.e. the vortex core is dominated by a central downdraft surrounded by an annular region of updraft) as shown in Figure 7.10b. The secondary vortices developed near the interface between the central downdraft and the updraft ring in a region of strong radial gradients of vertical velocity as shown in Figures 7.10c-i. The only exception is the final secondary vortex (SV6) which appears to develop in a region completely dominated by updraft as shown in Figure 7.10j, although still in the vicinity of strong radial vertical velocity gradients. As the SV develop, each is associated with a local vertical velocity maximum which lies in the annular updraft ring of the parent vortex, and azimuthally lags the SV pressure center as can be seen in Figures 7.10d-j.

Another interesting feature in the SV evolution is that the stronger secondary vortices (SV3-SV6) develop a strong central downdraft prior to dissipation. This can be seen in

Figures 7.10h-m. SV3 is one of the strongest secondary vortices, and the central downdraft associated with SV3 reaches $-14ms^{-1}$ at z=50m (with a maximum of $-24ms^{-1}$ at z=384m), and can be seen up to heights of 1132m. As the downdrafts develop, the secondary vortices expand, and the pressure minimum that defines the secondary vortex fills. In some cases (SV3 and SV4), the pressure perturbation actually changes sign from a relative 'low' to a relative 'high' (compare Figures 7.10h and 7.9f, and Figures 7.10j and 7.9g,h). As SV3 dissipates, the central downdraft that was associated with it becomes the new central downdraft of the parent vortex. This also occurred with SV6 (Figures 7.10l-m) and at low levels with SV4 (Figures 7.10i,j). The downdrafts associated with the secondary vortices tend to persist after the low-level pressure features are no longer visible. (See Figures 7.10k-m – the secondary vortices are still labeled, but there is no dot associated with them indicating that no distinct pressure feature could be seen, although waves in the pressure field were still evident.)

A close inspection of Figure 7.10 reveals that during and immediately prior to the period that the secondary vortices were produced, the strength of both the central downdraft, and the updraft along the southern and eastern portions of the annular updraft ring increased. The intensification of the central downdraft can be seen in Figures 7.8 and 7.11. The increase in the updraft strength could be seen from near the surface to a height of about 800m, and at most levels, the updraft velocities doubled in the three minute period from 2147-2150 UTC. The strengthening of the updraft appears to coincide with the evolution of a downdraft (D2) which wraps around the outside of the parent vortex (see Figures 7.10b-i). This downdraft originates about 1.5km above the surface, approaches the vortex from the west and then proceeds to wrap around the southern and eastern sides of the vortex between 2145-2151 UTC. Downdrafts wrapping around the right side of tornadoes (facing the direction of motion) have often been observed (Fujita and Smith, 1993), and the intersection of these downdrafts with the tornado path at low levels frequently marks intensification of the vortex or the transition to multiple vortices (Forbes, 1978). Note that the updraft appears to strengthen from the tip of the downdraft to the south side of the vortex where the downdraft exists, as can be seen in Figures 7.10d-j. Also of interest is

that from 2148-2151 UTC, the strongest part of the central downdraft appears to 'follow' the location of the leading edge of the outside downdraft D2 as shown in Figure 7.11. This suggests that the central downdraft and the downdraft outside the core are somehow connected. This will be discussed further in the next section.

Also of interest in the evolution of the secondary vortices is the evolution of the vertical vorticity field at z=50m which is shown in Figure 7.12. (Note that the time interval between successive frames in Figure 7.12 is not constant.) The first evidence of a vertical vorticity 'ring' becomes visible around 2146:30 UTC after the parent vortex has developed a well-defined two-celled structure. The vorticity ring becomes better defined by 2147 when the first secondary vortex (SV1) begins to develop (Figure 7.12c). Between 2147-2147:45 UTC, the vorticity ring expands slightly and the vertical vorticity values in the interior of the ring drop to less than $0.03s^{-1}$. The secondary vortices develop and evolve in the strong vertical vorticity gradient along the interior of the vorticity ring. Each secondary vortex is associated with a local vertical vorticity maxima which lies within the vorticity ring of the parent vortex (at the same azimuth but slightly larger radius than the pressure center), and rotates about the parent vortex as can be seen in Figure 7.12d-m. These local vorticity maxima can be clearly distinguished in the vertical vorticity field up to z=800m. Between 2147-2156 UTC, the largest values of vertical vorticity (and also the largest radial vertical vorticity gradients) associated with the parent vortex occur along the southeast/east sides of the vorticity ring, and it is in this region of the parent vortex that the secondary vortices first develop.

Between 2150-2151:45 UTC, the vorticity ring of the parent vortex 'breaks' as shown in Figure 7.12f-h. This break extends throughout the lowest 1km of the vortex, and occurs as SV3 reaches maximum intensity along the northern quadrant of the parent vortex. Following the development of a central downdraft in SV3, SV3 develops its own vorticity ring as can be seen in Figure 7.12h. However, the vorticity ring associated with the parent vortex quickly becomes reestablished soon after SV3 dissipates.

The evolution of the vortex-relative wind speeds at the lowest model level is shown in Figure 7.13. (Note again that the time interval between successive frames in Figure

7.13 is not constant). As the secondary vortices develop, each develops a local wind speed maximum embedded in the annular wind speed maximum of the parent vortex. Maximum wind speeds in the secondary vortices exceed that of the parent vortex by as much as 25%, although speed excesses betweem 16-20% are more common. The vortex-relative wind fields (not shown) revealed that most of the secondary vortices developed well-defined closed circulations which were 400-500m in diameter. It is also interesting to note that after the parent vortex 'settles down' again following the dissipation of the secondary vortices, the near surface maximum wind speeds in the parent vortex reach $54ms^{-1}$ at 2156:30. These are the strongest winds associated with the parent vortex at any point in its lifetime, and puts the tornado into the F2 category.

Another distinguishing feature of the secondary vortices is their vertical structure. The vertical structures of the pressure field associated with two of the simulated secondary vortices (SV3 and SV4) are shown in Figures 7.14 and 7.15. Well-defined pressure centers are denoted with dots, open waves in the pressure field are denoted by dashed lines. As can be seen in Figures 7.14 and 7.15, SV3 and SV4 have a well-defined pressure minimum up to z=800m, above which the pressure minimum takes the form of an open wave. Above z=1.5km, no evidence of the secondary vortices could be detected. The secondary vortices tilt azimuthally with height, with the pressure center (and circulation) at z=800m lagging the pressure center (and circulation) near the surface. There is also evidence that SV3 tilts radially outward as well as shown in Figure 7.14, but no distinct radial tilt could be detected in SV4 (see Figure 7.15). A similar vertical structure could also be seen in the vertical vorticity field, (and to a lesser extent in the vertical velocity field) with the local vorticity maxima associated with the secondary vortices at higher levels azimuthally lagging the local maxima near the surface.

Between 2152-2152:45 UTC, the central downdraft in the parent vortex again intensifies, reaching a maximum of $-28ms^{-1}$ at z=651m. Around 2153 UTC, the updraft ring 'breaks' throughout depth of the vortex (with the exception of the first model level at z=50m), first on the north side and then on the northeast side of the parent vortex. These regions of the parent vortex now become embedded in downdraft as the pattern of a spiral-

ing updraft/downdraft becomes established once again in the vertical velocity field. (The spiraling updraft/downdraft pattern is displayed in Figure 7.8a.) This change in vortex structure marks the end of the secondary vortex production in the parent vortex. Although SV6 had just developed at 2153 UTC, it quickly dissipated as it rotated into the region of the parent vortex where the annular updraft no longer existed (Figures 7.10k,l). Following the dissipation of SV6, no other distinct secondary vortices develop, although there is still evidence of weak disturbances embedded in the parent vortex until 2156 UTC. By 2156:45, an annular updraft ring is reestablished at z=50, but it never reestablishes at higher levels.

7.3 Comparison of Model Results with Observations, Laboratory Studies and Previous Modeling Work

Since the size of the parent vortex and the secondary vortices in the simulation are larger than what is observed in a 'typical' tornado, it is important to establish that the results are still physically relevant. For the results to be credible, the simulated parent vortex and secondary vortices should have properties similar to those observed in actual tornadoes and simulated in the laboratory. To this end, the following section provides a comparison of the parent vortex and secondary vortices in the present simulation with observations, laboratory studies, and previous modeling work.

Laboratory and other numerical studies of tornadoes have shown that secondary vortices do not form in the parent vortex until vortex breakdown occurs, and the parent vortex develops a two-celled structure with a well-defined annular updraft (Church and Snow, 1979; Church et al., 1979; Baker and Church, 1979; Snow et al., 1980; Pauly et al., 1982; Snow, 1982; Monji, 1985). A similar evolution occurs in the current simulation. Although there is a significant downdraft associated with the parent vortex prior to secondary vortex development, the secondary vortices do not begin to occur until a well defined annular updraft (and vertical vorticity) ring develops over the lowest 1km of the parent vortex. Both laboratory studies and field observations also indicate that the parent vortex core usually broadens with height (Snow, 1982). This was also observed in the simulation. The annular updraft region, central downdraft, and vertical vorticity ring all became larger with height (not

shown). Prior to the development of the secondary vortices in the simulation, the parent vortex expanded in response to the strengthening of the central downdraft. Forbes (1978) also noted that in the Parker, Indiana tornado, the diameter of the tornado progressively increased prior to secondary vortex formation.

The secondary vortices in the simulation developed along the east/southeast quadrants of the parent vortex and then rotated cyclonically around the parent vortex. Most of the secondary vortices (with perhaps the exception of SV1) dissipated before making a complete revolution around the parent vortex. This is frequently observed in multiple vortex tornadoes (Forbes, 1978). In the simulation, as many as 3 secondary vortices can be seen in the parent vortex at any given time which is also comparable with observations which have noted between 2-5 secondary vortices rotating around the parent vortex at any given time (Fujita and Smith, 1993).

As was mentioned earlier, the main problem with the current simulation is that the space and time scales of the simulated tornado and secondary vortices are large compared with observations of 'typical' tornadoes. However, if the relative time/space scales between the parent vortex and the secondary vortices match observations and/or laboratory studies, it provides more evidence that the relationship between the parent vortex and the secondary vortices in the simulation is correct.

Observations indicate that secondary vortices are one order of magnitude smaller than the diameter of the parent vortex (Fujita and Smith, 1993). Laboratory measurements have indicated that a typical core size of the secondary vortices is about 20% that of the parent vortex (Monji, 1985), although stronger secondary vortices can be only 10-15% of the parent core radius in diameter (Pauly et al., 1989). In the present simulation the size of the parent vortex core diameter is around 2km, while the secondary vortices are typically 400m in diameter. Thus in the simulation, the diameter of the secondary vortices is about 20% of the parent vortex core diameter. This puts the relative size of the simulated secondary vortices in the same range as those simulated in the laboratory, and in the general neighborhood of suction vortices in observed tornadoes.

The speed of the secondary vortices relative to the parent vortex in the simulations also matches observations and laboratory studies. With the exceptions of SV1 and SV6, the secondary vortices typically make about half a revolution around the parent vortex during their lifetimes which is typically 3 minutes (see Table 7.1). This gives an average angular velocity of the secondary vortices of around $0.017s^{-1}$. Using a core radius of 2km for the parent vortex, the average speed of the secondary vortices about the center of the parent vortex is about $17ms^{-1}$. Since the average tangential wind speed around the parent vortex at the radius of maximum winds is roughly $36ms^{-1}$, the secondary vortices in the simulation are moving around the parent vortex at about 47% of the tangential wind speeds in the parent vortex. Thus the secondary vortices are in retrograde motion with respect to the parent vortex. This is in agreement with laboratory studies (Ward, 1972; Monji, 1985) and theoretical studies (Snow, 1978; Gall, 1983; Walko and Gall, 1984; Rotunno, 1984) in which the secondary vortices rotate around the parent vortex at about half the speed of the parent vortex maximum tangential winds.

The vertical structure of the simulated secondary vortices is also similar to both observations and laboratory studies, and to that predicted by theory. Tornado observations indicate that many secondary vortices do not extend through the depth of the planetary boundary layer, and most tilt away from the vertical with height (Agee et al., 1975, 1977). Observations of mesocyclones indicate that the local vorticity maxima which sometimes develop along the periphery of the mesocyclone have a similar vertical structure (Brandes, 1978). Laboratory studies (Church and Snow, 1979; Church et al., 1979, Baker and Church, 1979; Snow et al., 1980; Pauly et al., 1982; Snow, 1982; Monji 1985) and theoretical studies (Rotunno, 1978; Gall, 1983; Walko and Gall, 1984) also show that secondary vortices take the form of helical disturbances which wind counter-clockwise with height around the parent vortex. Although the secondary vortices in the present simulation do not extend through the depth of the planetary boundary layer, their vertical structure indicates that they also wind counterclockwise about the parent vortex.

The vertical velocity and pressure fields in the simulation indicated that the secondary vortices developed *inside* the radius of maximum winds of the parent vortex. This result

agrees with the laboratory simulations presented by Church et al. (1979) and Monji (1985), and the numerical simulations of Gall (1983), Walko and Gall (1984) and Rotunno (1984). Each secondary vortex in the present simulation was associated with a local minimum in pressure, and a local maximum in vertical vorticity, vertical velocity, and tangential wind speed. The local maxima associated with the secondary vortices were all embedded within the annular maximum associated with the parent vortex. This also agrees with the laboratory simulation of a multiple-vortex tornado presented by Monji (1985).

As the secondary vortices developed in the simulation, each developed a distinct updraft maximum. As SV3-SV6 dissipated, they expanded in size as they produced a strong local downdraft. Lewellen (1993) reported on the results of a large-eddy simulation of an idealized symmetrical vortex. In Lewellen's simulation, three secondary vortices developed, each having their own updraft and downdraft. Agee et al. (1975) also found that observed secondary vortices tend to expand in size as they reach maximum intensity and then dissipate. Although this does not prove that the observed secondary vortices develop a central downdraft as they dissipate, it does not rule out the possibility.

As was discussed in Chapter 2, the most important non-dimensional parameter for dynamic similarity in laboratory experiments is the swirl ratio (S). Estimates of the swirl ratio for multiple-vortex tornadoes in the atmosphere range from 1.25-2.5 (Forbes, 1978). To see how the swirl ratio in the present simulation compares with observations and laboratory studies, the swirl ratio for the simulated parent vortex is calculated two different ways.

1. The swirl ratio (S1) is calculated using (2.10) where v_{max} and w_{max} are determined from values along the radius of maximum winds throughout the depth of the boundary layer (about 2km).

2. The swirl ratio (S2) is calculated using (2.8) where r_0 (the updraft radius) is assumed to be 2.5km (roughly the radius of the mesocyclone just above cloud base) and the inflow depth (h) is assumed to be the depth of the boundary layer (about 2km).

Values of S1 calculated from 2145-2157 UTC ranged between 1.1-1.7, while values of S2 ranged from 1.9-2.3. Both values of S1 and S2 lie in the observational range for

multiple-vortex tornadoes, and in the laboratory range for secondary vortices. Values of S2 started near 1.9 at 2145 UTC and generally increased from 2145-2149 UTC. However, neither S1 nor S2 showed any significant increase just prior to the onset of the secondary vortices. Thus the significance of the swirl ratio in predicting the onset of multiple vortices in non-axisymmetric tornadic flows is unclear.

7.4 Summary and Discussion

One drawback of the laboratory models and idealized numerical/theoretical models is that the 'basic state' or parent vortex is confined to be axisymmetric so when secondary vortices develop, they are fairly evenly distributed around the parent vortex. Observations of tornadoes indicate that most tornadic flows are *not* axisymmetric, and when secondary vortices do occur they usually develop in a preferred quadrant of the parent vortex and dissipate before making a complete revolution around the parent vortex. A unique feature of the present simulation is that the parent vortex is free to evolve with the parent thunderstorm without any constraints of axisymmetry. With this constraint removed, the simulation was able to reproduce the development of secondary vortices on one side of the parent vortex and dissipation on the other. Of course, this begs the question of 'why does this occur?' A complete answer to this question is beyond the scope of the this study, but the model results do suggest a few possibilities.

Theoretical and idealized modeling studies have suggested that secondary vortices are a manifestation of a shear instability in the flow of the parent vortex (Rotunno, 1978; Staley and Gall, 1979; Gall, 1983; Walko and Gall, 1984; Rotunno, 1984). These instabilities are unique in that both the radial shears of vertical and tangential velocities are important to the development of the instabilities (Gall, 1983; Rotunno, 1984; Walko and Gall, 1984). Thus one possible reason for the transient nature of the secondary vortices is that the parent vortex is only 'unstable' in one region of the vortex due to flow asymmetries. The secondary vortices would develop in this region, and then dissipate as they moved into a region of the parent vortex that was not unstable. Although no generalized stability criterion exists for three dimensional vortical flows (Howard and Gupta, 1962; Rotunno, 1984), the model

results do support this idea. The secondary vortices begin to develop almost immediately after the parent vortex develops a two-celled structure (i.e. a strong central downdraft, and an updraft and vertical vorticity ring) over the depth of the boundary layer. An inspection of Figure 7.12 indicates that the largest values of vertical vorticity (i.e. radial shear of the tangential wind) can consistently be found along the southeast quadrant of the parent vortex. The largest radial gradients of the vertical vorticity in the interior of the vorticity ring are also found in this region of the parent vortex (recall that the necessary condition for instability of two-dimensional flow is that the radial vertical vorticity gradient must change sign somewhere in the flow). These features in the vertical vorticity field are even more evident between z=200-800m which look very similar to Figure 7.12d (although the actual vertical vorticity values are somewhat smaller at higher levels). The secondary vortices begin to dissipate as they move into the northern portion of the parent vortex where the vertical vorticity (and radial vertical vorticity gradient) values are smaller. Note that the necessary condition for barotropic instability is still met in the region of the parent vortex in which the secondary vortices dissipate.

In the first three minutes of the time period in which secondary vortices existed, the secondary vortices also developed in the portion of the parent vortex where the upward vertical velocities and radial vertical velocity gradients were largest (Figure 7.11). However, later in the period, the secondary vortices continued to develop along the southeastern/eastern quadrants of the parent vortex even though the radial vertical velocity gradients weakened significantly in that region (although the magnitude of the upward vertical velocities does not change). The secondary vortices dissipate as they pass through the northern portion of the parent vortex where the upward vertical velocities and radial vertical velocity gradients are usually weakest (this feature in the parent vortex becomes more noticeable with height). However, the significance of the parent vortex annular updraft in the development and evolution of the secondary vortices becomes apparent following the demise of the updraft ring. As SV6 propagated into the northeast quadrant of the parent vortex where a portion of the updraft ring had been replaced by a region of downdraft, SV6 quickly dissipated and no additional secondary vortices developed.

Other features which appear to impact the development of the secondary vortices in the simulation are the outer downdrafts (D1 and D2). Downdrafts which wrap cyclonically around low-levels of tornadoes have been observed (Fujita, 1978; Forbes, 1978; Fujita, 1989; Fujita and Smith, 1993), and when these downdrafts intersect the path of the tornado, the tornado frequently produces suction vortices (Forbes, 1978). It is clear from Figure 7.11 that the minimum in the central downdraft inside the vortex core tends to follow the leading edge of D2 around the vortex (this also occurs with D1 to some extent–see Figure 7.11b), although it is difficult to say for certain if the central downdraft is somehow driving D1 and D2 or visa-versa. It is possible that the importance of the outer downdrafts is to enhance convergence at low-levels along the southern and eastern sides of the parent vortex. Evidence for this is seen in the low-level convergence field which is shown in Figure 7.16. There is a persistent local maximum in the low-level convergence field along the southern/eastern portions of the parent vortex which coincides with the regions of the parent vortex influenced by D1 and D2. The secondary vortices tend to form in this region of maximum low-level convergence in the interior of the parent vortex. The enhanced convergence created by the outer downdrafts increases the upward vertical velocity in the parent vortex in those regions, increasing low-level convergence inside the core (and increasing the strength of the central downdraft through mass conservation). In addition, a time series of the horizontal velocity fields revealed that the downdrafts also provide an added tangential momentum source to the parent vortex (not shown). Thus the outer downdrafts also enhance the tangential velocities (and radial gradients of the tangential velocities) along the southern/eastern quadrants of the vortex. As a result of all this, the magnitude of the vertical and tangential velocities (and their radial gradients) are enhanced in the regions of the vortex affected by the outer downdrafts, making it more likely for instabilities to develop there.

At later times there is evidence that the demise of older secondary vortices helps to enhance the convergence along the southeastern portion of the parent vortex. Figure 7.16g-h shows the low-level wind and convergence fields shortly after SV3 developed a strong central downdraft. Divergence from the dissipating SV3 enhanced the wind speeds in the

core of the parent vortex, creating strong convergence along the southeast flank of the parent vortex.

A second possible reason for the transient nature of the secondary vortices could be due to the dynamics of the secondary vortices themselves. It is possible that the rapid spin-up of the secondary vortices could also lead to their demise. As was discussed in Chapter 2, two-celled vortices develop as an adverse axial pressure gradient develops in the vortex core. This adverse axial pressure gradient is driven by differential rotation in the vortex (i.e. rotation is stronger near the surface than it is aloft). It is possible that during the spin-up process, the convergence into the secondary vortices causes the rotation to 'overshoot' creating a strong adverse axial pressure gradient which drives a strong central downdraft in the core of the secondary vortex. This type of oscillatory vortex behavior was also simulated in an idealized study by Walko (1988). The strong divergence created as the downdraft impinges on the surface weakens the rotation in the secondary vortex (in some cases the central downdraft is strong enough to create a positive pressure perturbation), and the secondary vortex dissipates. Additional evidence that this process could be responsible of the demise of the secondary vortices was provided by Fiedler (1997). Although the genesis and dissipation of the secondary vortices was not the focus of that study, his model produced transient secondary vortices in a parent vortex that was initially axisymmetric. (The model updraft was driven by a prescribed axisymmetric buoyancy field, and the rotation source for the vortex was an imposed uniform, weak background rotation). His results showed that the secondary vortices developed a downdraft as they matured and decayed, and some of the secondary vortices attempted to develop their own small vorticity ring which expanded in time as they dissipated (similar to SV3).

Despite the success of the model in reproducing many observed features in multiple-vortex tornadoes and laboratory vortices, there are still some potential problems in the simulation. The most obvious shortcoming is the coarse grid resolution. Since the secondary vortices are barely resolved, it is possible that their evolution is not being fully captured in the present simulation. It should also be noted that a two-celled vortex was produced earlier in the simulation (around 2116 UTC), although no secondary vortices were

produced at that time. It is unclear if this was due to insufficient grid resolution, or to dynamical processes in the vortex. Another potential problem in these simulations is the effect of the model diffusion on the evolution of both the parent vortex and the secondary vortices. (The Reynolds number on Grid #6 is on the order of 100.) Other numerical simulations have indicated that the details of the 'corner flow' (i.e. the portion of the vortex near the surface where the streamlines abruptly turn upward) are very sensitive to the model viscosity (Lewellen, 1993). Idealized numerical studies have also shown that the core structure of the vortex is sensitive to diffusion under certain circumstances (Walko and Gall, 1986). However, Rotunno (1984) found that even though the effective viscosity in his simulations was high ($Re\sim$ 150), his model still reproduced most features observed in laboratory vortices. The effects of diffusion on the vortices simulated in this study are not clear and may require further investigation.

In summary, the above discussion shows that despite some inherent limitations in the simulation, the model was still able to reproduce many characteristics of both observed multiple-vortex tornadoes and multiple-vortex laboratory vortices. The model results support the idea that secondary vortices arise from instabilities in the parent vortex flow. In the simulation, the secondary vortices begin to develop almost immediately after the parent vortex develops a two-celled structure throughout the depth of the boundary layer. The secondary vortices develop in the region of the vortex that contains the largest radial gradients of vertical vorticity and vertical velocity–two quantities which have been shown in previous studies to be necessary ingredients for three-dimensional instabilities to develop in axisymmetric vortex flows. In the simulation, two different downdrafts also develop on the *outside* of the parent vortex during the period of secondary vortex development, and wrap around the southern and eastern sides of the parent vortex in time. The position of these downdrafts relative to the parent vortex coincides with the preferred regions for the development of the secondary vortices. The role of these downdrafts in the development of the secondary vortices may be to enhance radial gradients of both the vertical and tangential velocities in the parent vortex, thereby destabilizing or enhancing the instability of the flow in these regions.

	Duration	**Max. Pressure Deficit (wrt PV Core)**	**Max. Vertical Vorticity**	**Comments**
SV1	2147-2150 UTC	-1mb	$0.175s^{-1}$	-relatively weak -some evidence that the residual of SV1 develops into SV4
SV2	2148:45- 2151 UTC	+3.5mb (-1mb wrt local surroundings)	$0.175s^{-1}$	-forms further from PV center than other SV
SV3	2149-2152 UTC	-5.5mb	$0.275s^{-1}$	-intense -'breaks' PV vortex ring -develops central downdraft
SV4	2150:30- 2153:30 UTC	-3mb	$0.275s^{-1}$	-develops central downdraft
SV5	2152:30- 2154 UTC	-1mb	$0.275s^{-1}$	-develops central downdraft
SV6	2153-2154 UTC	-6mb	$0.325s^{-1}$	-intense -shortest lifetime of all the SV

Table 7.1: Summary of the characteristics of the secondary vortices in the May 15, 1991 simulation.

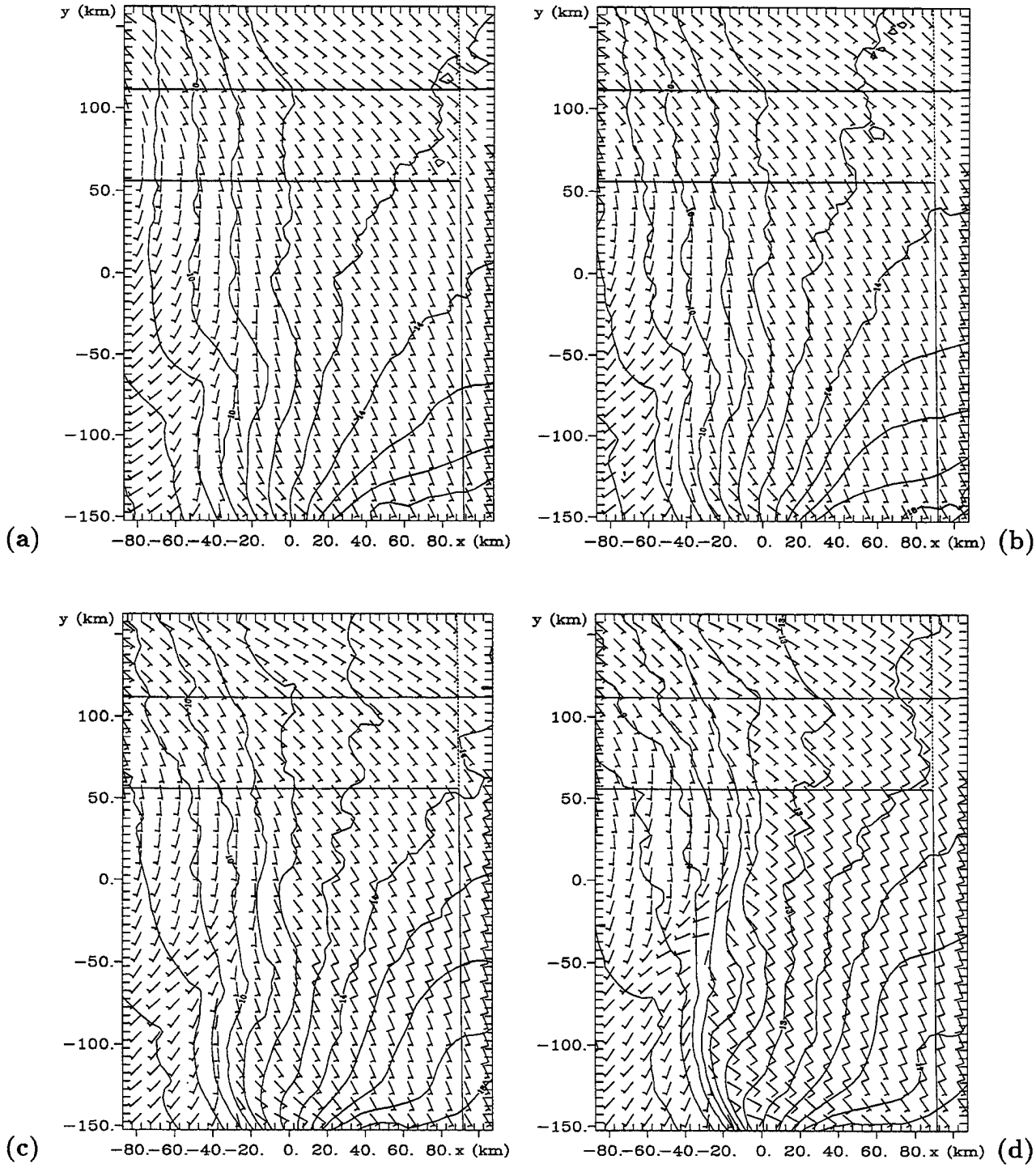

Figure 7.1: Evolution of the dryline at z=50m from 1700 UTC to 2000 UTC on a subset of Grid #3 at (a) 1700 UTC, (b) 1800 UTC, (c) 1900 UTC, (d) 2000 UTC. Water vapor mixing ratio is contoured every $1g(kg)^{-1}$. Wind barbs are plotted at every other model grid point. The short (long) flag on the wind barb denotes a wind speed of $5ms^{-1}$ ($10ms^{-1}$). The two straight lines running horizontally across the plot denote the boundaries of the Oklahoma panhandle.

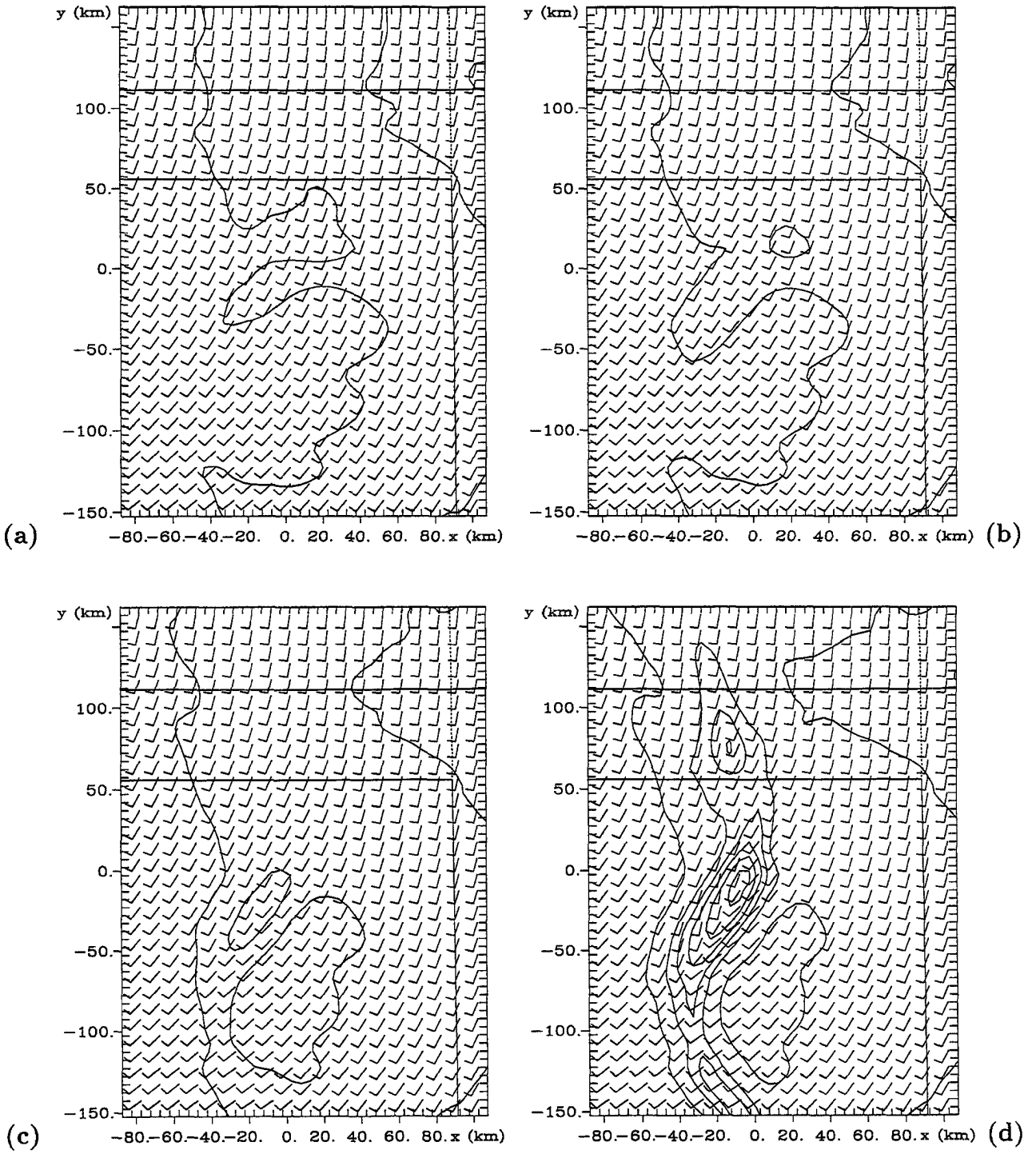

Figure 7.2: Evolution of the water vapor field at z=1959m from 1800 UTC to 1930 UTC on a subset of Grid #3 at (a) 1800 UTC, (b) 1830 UTC, (c) 1900 UTC, (d) 1930 UTC. Water vapor mixing ratio is contoured every $1g(kg)^{-1}$. Wind barbs are plotted at every other model grid point. The short (long) flag on the wind barb denotes a wind speed of $5ms^{-1}$ ($10ms^{-1}$). The two straight lines running horizontally across the plot denote the boundaries of the Oklahoma panhandle.

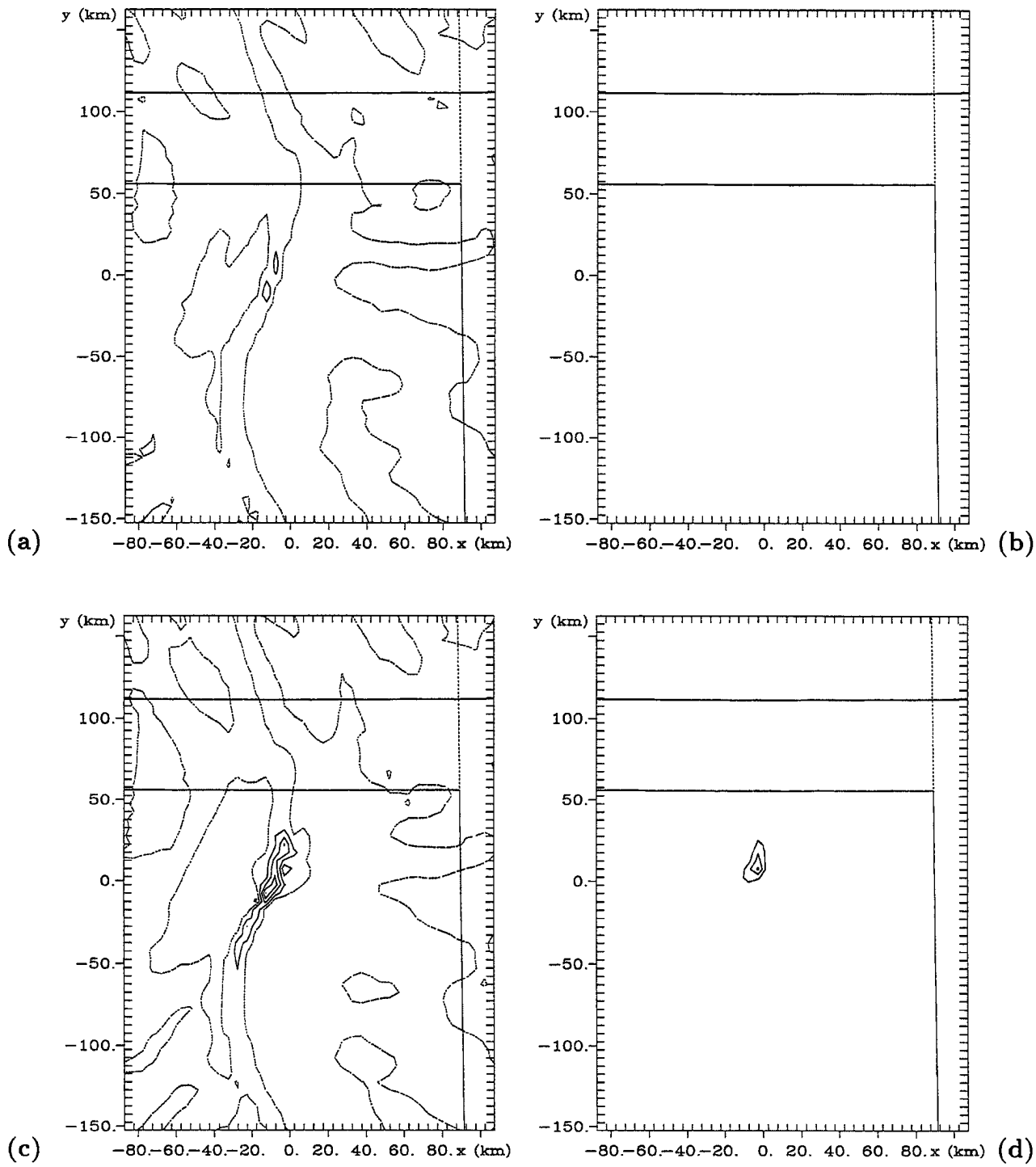

Figure 7.3: Evolution of the vertical velocity and condensate fields at z=1959m from 2000 UTC to 2030 UTC on a subset of Grid #3. Plotted are the vertical velocities at (a) 2010 UTC, (c) 2030 UTC, and the condensate mixing ratio at (b) 2010 UTC, (d) 2030 UTC. Condensate mixing ratio is contoured every $0.2g(kg)^{-1}$. Vertical velocity is contoured every $2ms^{-1}$. The dashed line in the vertical velocity plots denotes a value of zero. The two straight lines running horizontally across the plot denote the boundaries of the Oklahoma panhandle.

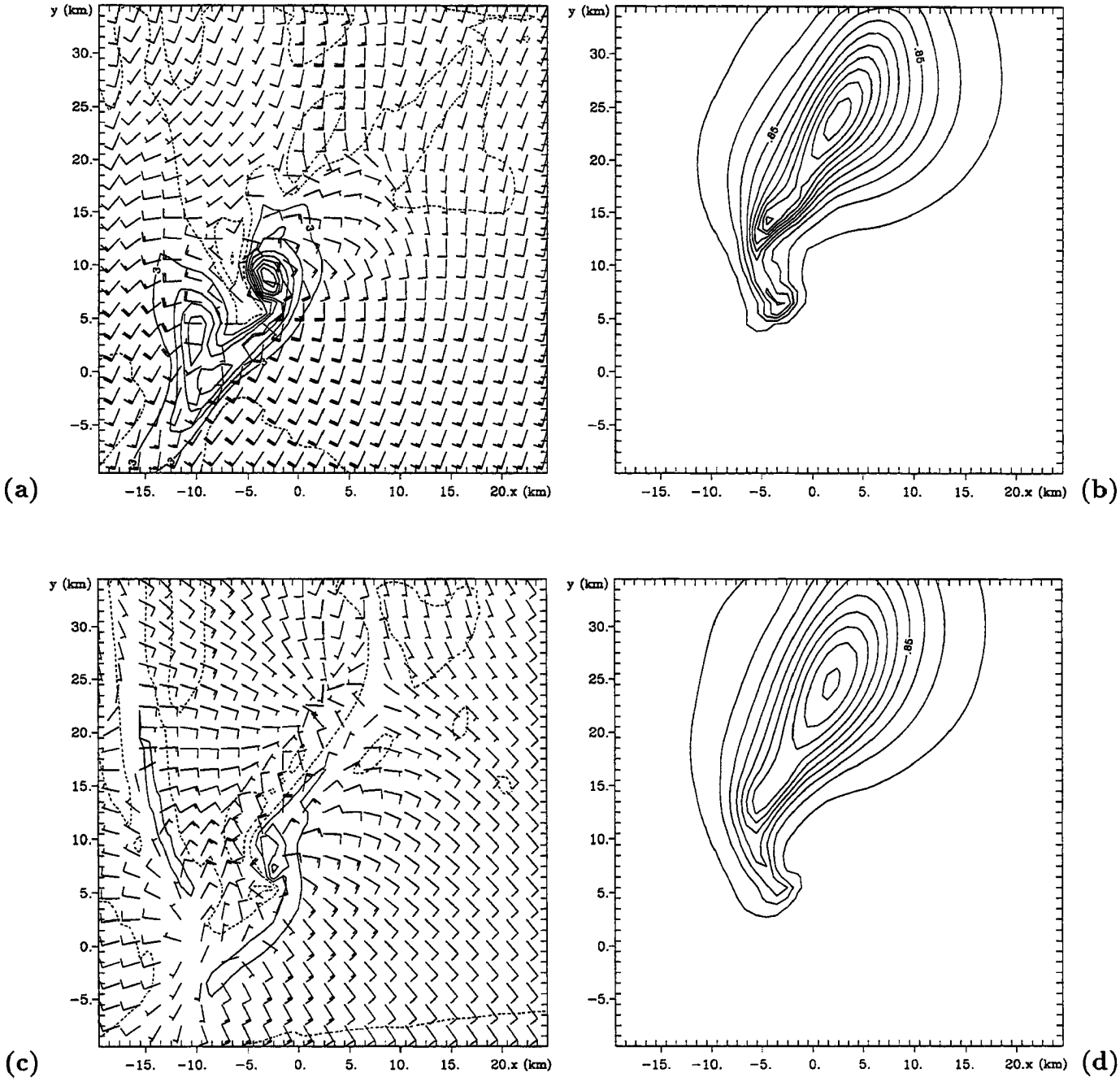

Figure 7.4: Structure of the supercell thunderstorm on Grid #4 at 2108 UTC. Plotted is the (a) vertical velocity at z=1959m (contour interval $3ms^{-1}$), (b) condensate mixing ratio at z=1959m (contour inverval $0.25g(kg)^{-1}$), (c) vertical velocity at z=50m (contour interval $0.5ms^{-1}$), (d) condensate mixing ratio at z=50m (contour inverval $0.25g(kg)^{-1}$). Dashed contours denote negative values. Wind barbs are plotted at every other model grid point. The short (long) flag on the barbs denotes a wind speed of $5ms^{-1}$ ($10ms^{-1}$).

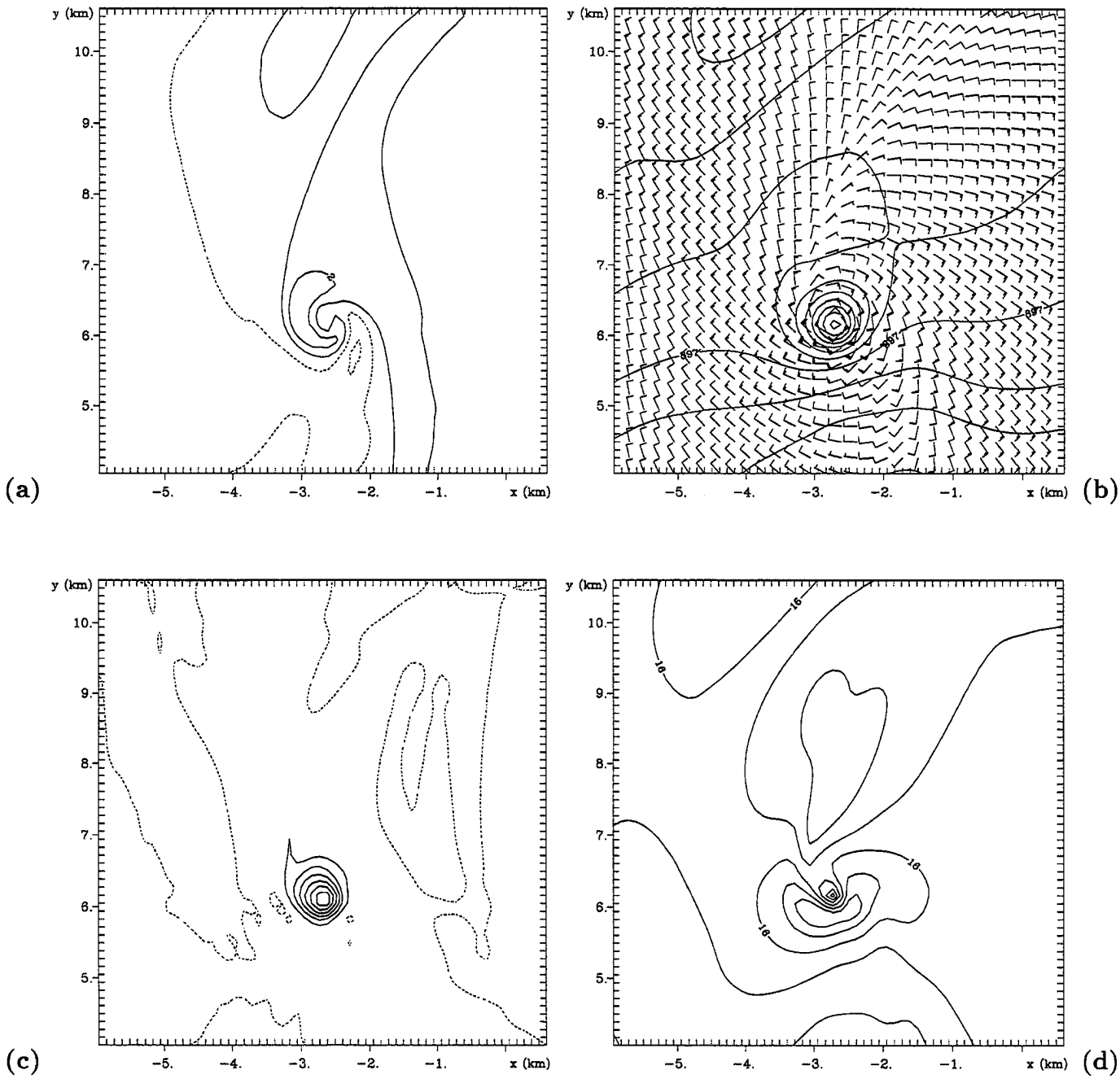

Figure 7.5: Structure of the simulated May 15, 1991 tornado at z=50m at 2106 UTC on Grid #6. Plotted is the (a) vertical velocity (contour interval $1ms^{-1}$), (b) pressure (contour interval 1mb) overlayed with the horizontal winds, (c) vertical vorticity (contour interval $0.03s^{-1}$), (d) wind speed (contour interval $4ms^{-1}$). Dashed contours denote negative values. Wind barbs in (b) are plotted at every other model grid point. The short (long) flag on the wind barb denotes a wind speed of $5ms^{-1}$ ($10ms^{-1}$).

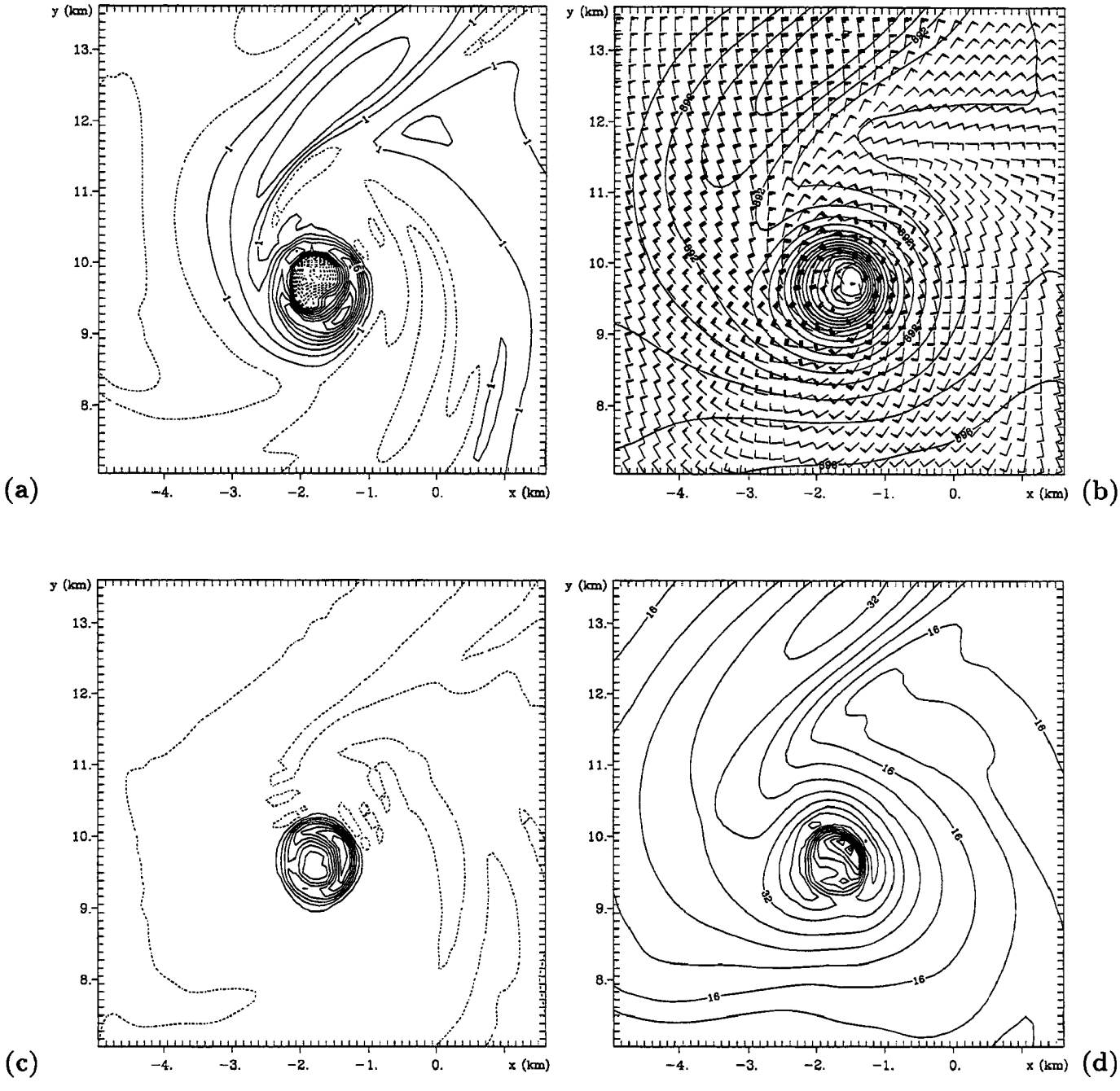

Figure 7.6: Structure of the simulated May 15, 1991 tornado at z=50m at 2126 UTC on Grid #6. Plotted is the (a) vertical velocity (contour interval $1ms^{-1}$), (b) pressure (contour interval 1mb) overlayed with the horizontal winds, (c) vertical vorticity (contour interval $0.03s^{-1}$), (d) wind speed (contour interval $4ms^{-1}$). Dashed contours denote negative values. Wind barbs in (b) are plotted at every other model grid point. The short (long) flag on the wind barb denotes a wind speed of $5ms^{-1}$ ($10ms^{-1}$).

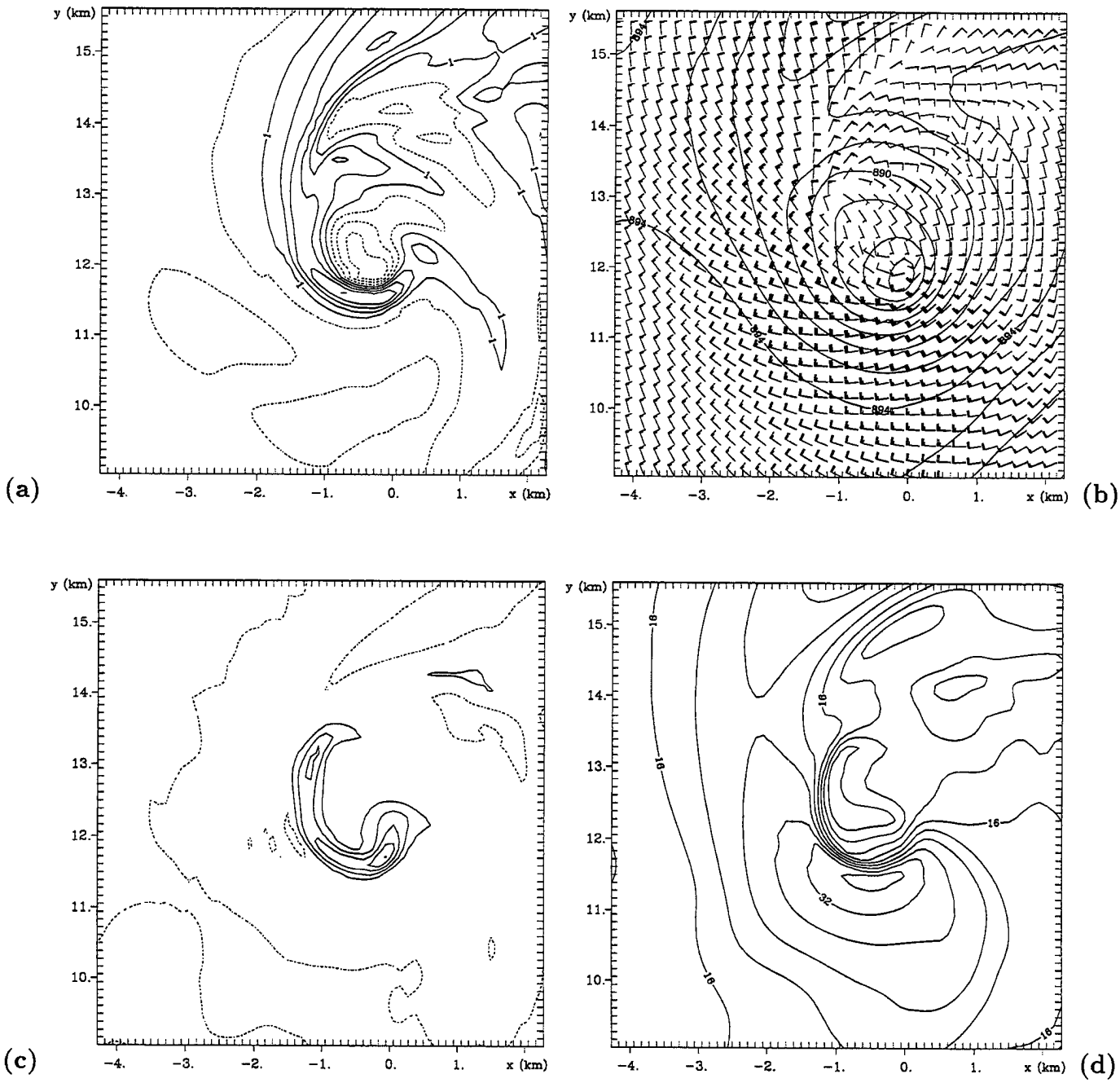

Figure 7.7: Structure of the simulated May 15, 1991 tornado at z=50m at 2142 UTC on Grid #6. Plotted is the (a) vertical velocity (contour interval $1ms^{-1}$), (b) pressure (contour interval 1mb) overlayed with the horizontal winds, (c) vertical vorticity (contour interval $0.03s^{-1}$), (d) wind speed (contour interval $4ms^{-1}$). Dashed contours denote negative values. Wind barbs in (b) are plotted at every other model grid point. The short (long) flag on the wind barb denotes a wind speed of $5ms^{-1}$ ($10ms^{-1}$).

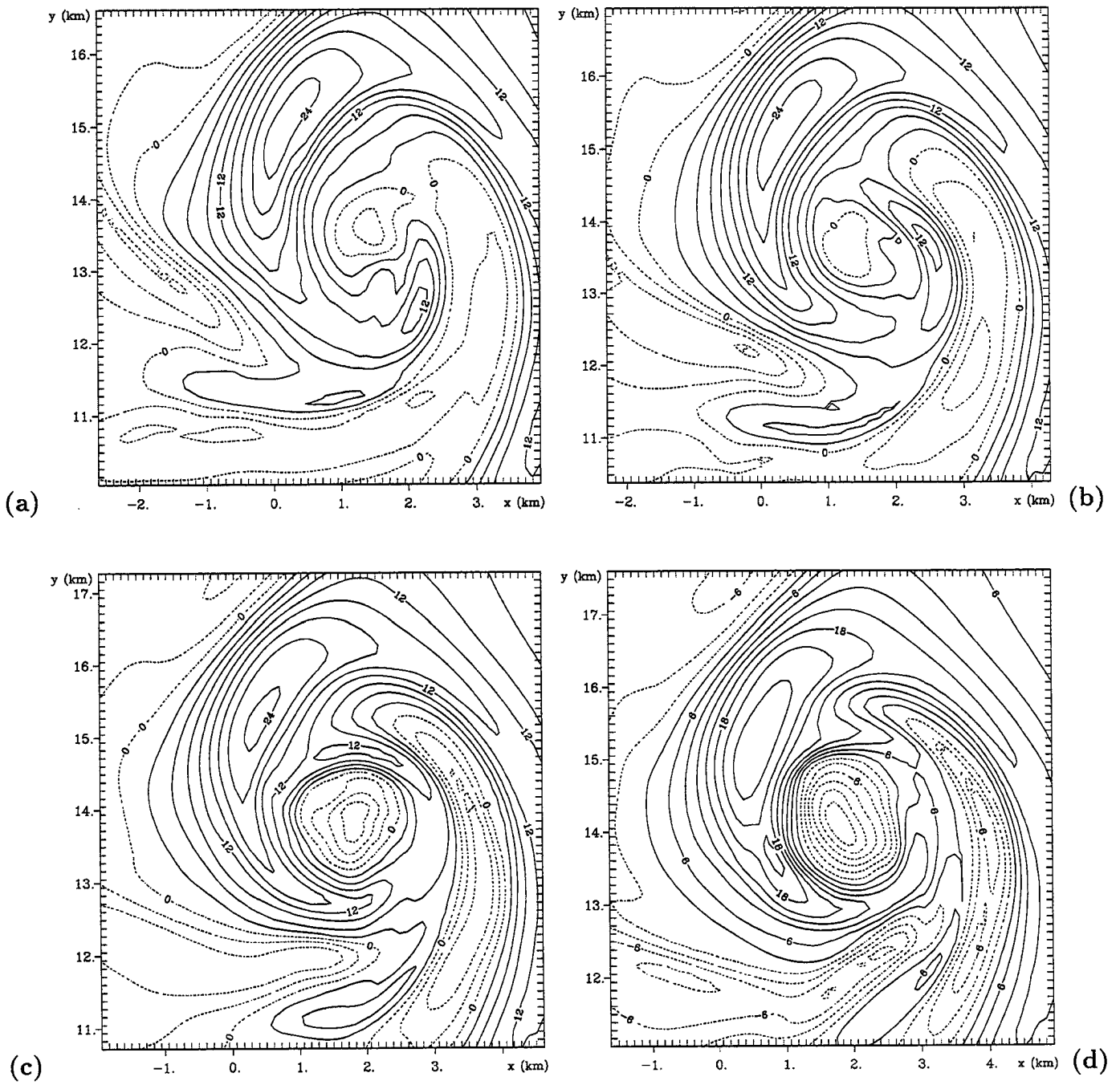

Figure 7.8: Early evolution of the vertical velocity field at z=800m prior to the period of secondary vortex development on Grid #6 at (a) 2145:15 UTC, (b) 2146 UTC, (c) 2146:45 UTC, (d) 2147:30 UTC. The contour interval is $3ms^{-1}$. Dashed contours denote negative values.

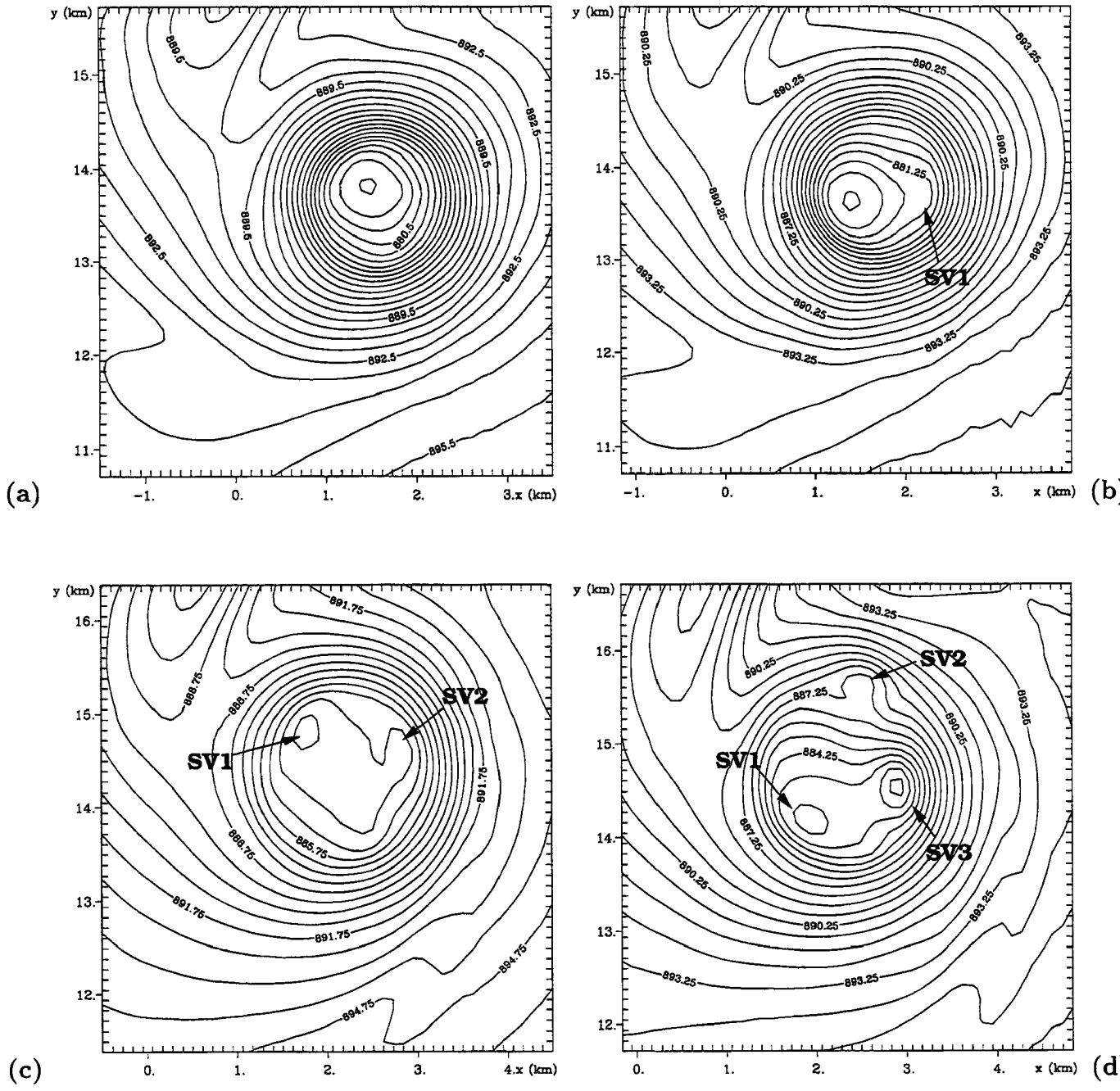

Figure 7.9: Evolution of the pressure field at the lowest model level (z=50m) on a subset of Grid #6 at (a) 2146:30 UTC, (b) 2147 UTC, (c) 2148:45 UTC, (d) 2149:45 UTC, (e) 2150:45 UTC, (f) 2151:45 UTC, (g) 2152:45 UTC, (h) 2153:45 UTC, (i) 2154 UTC, (j) 2154:45 UTC, (k) 2155:30 UTC, (l) 2156:15 UTC. Contour interval is 0.75 mb. The position and number of the secondary vorticies are denoted by the arrows and labels. The dashed lines denote weak disturbances in the pressure field.

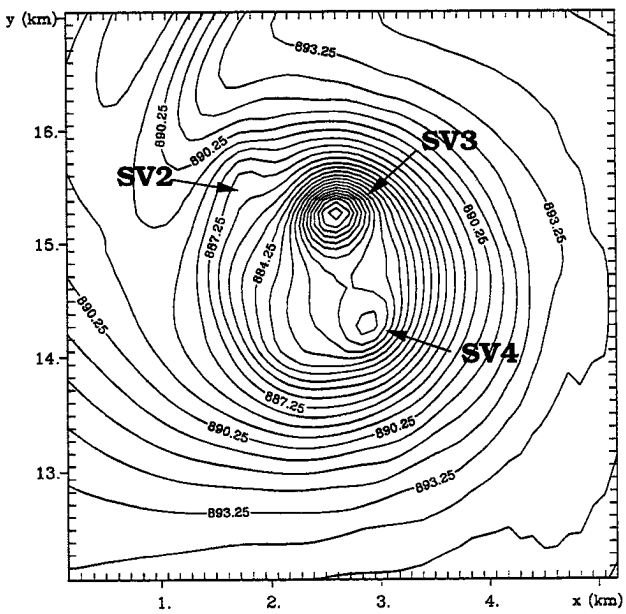
y (km)
16.
15.
14.
13.
SV2
SV3
SV4
893.25
890.25
887.25
884.25
1.
2.
3.
4.
x (km)

(e)

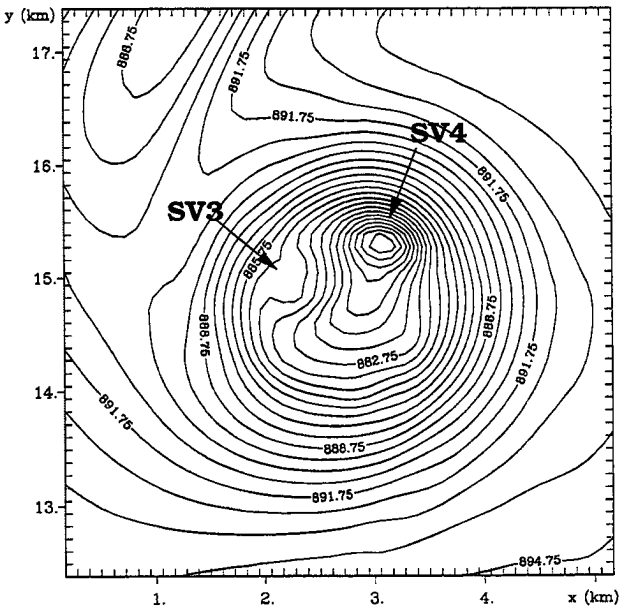
y (km)
17.
16.
15.
14.
13.
SV3
SV4
891.75
888.75
885.75
882.75
894.75
1.
2.
3.
4.
x (km)

(f)

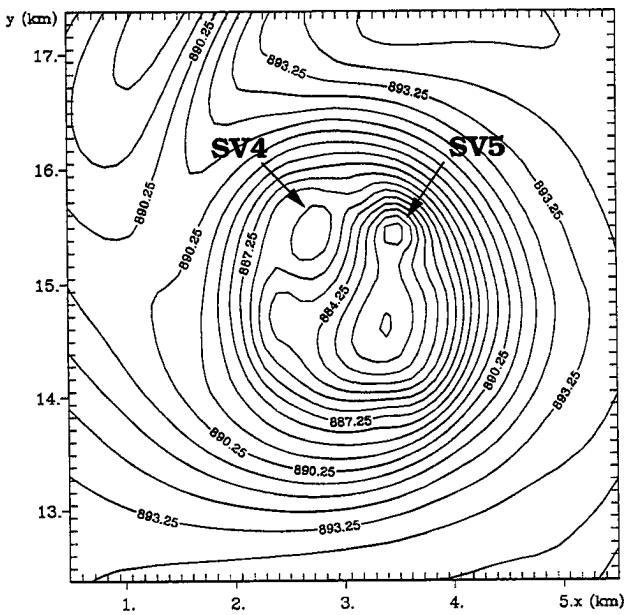
y (km)
17.
16.
15.
14.
13.
SV4
SV5
893.25
890.25
887.25
884.25
1.
2.
3.
4.
5.x (km)

(g)

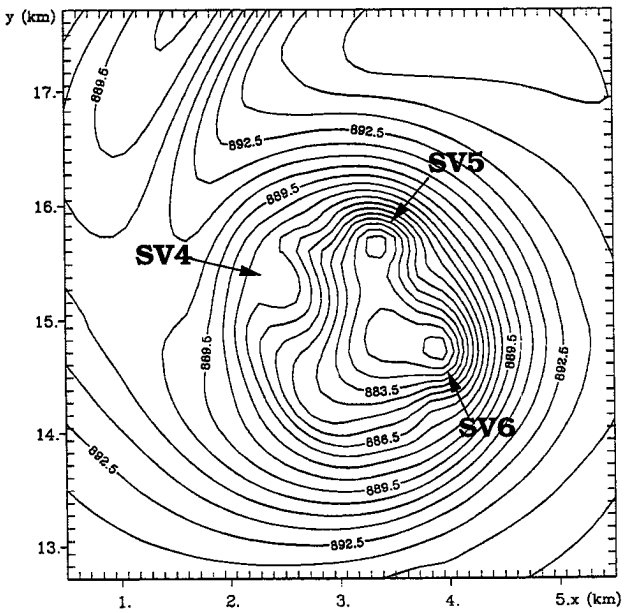
y (km)
17.
16.
15.
14.
13.
SV4
SV5
SV6
892.5
889.5
886.5
883.5
1.
2.
3.
4.
5.x (km)

(h)

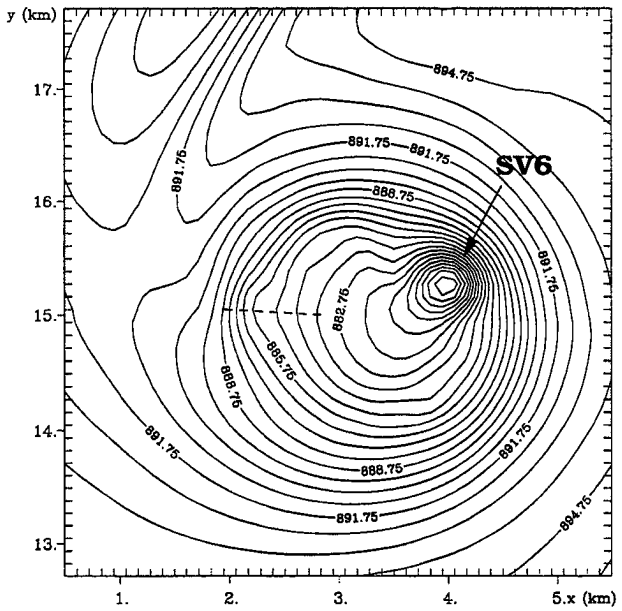
y (km)
17.
16.
15.
14.
13.
1.
2.
3.
4.
5.x (km)
SV6
894.75
891.75
888.75
885.75
882.75

(i)

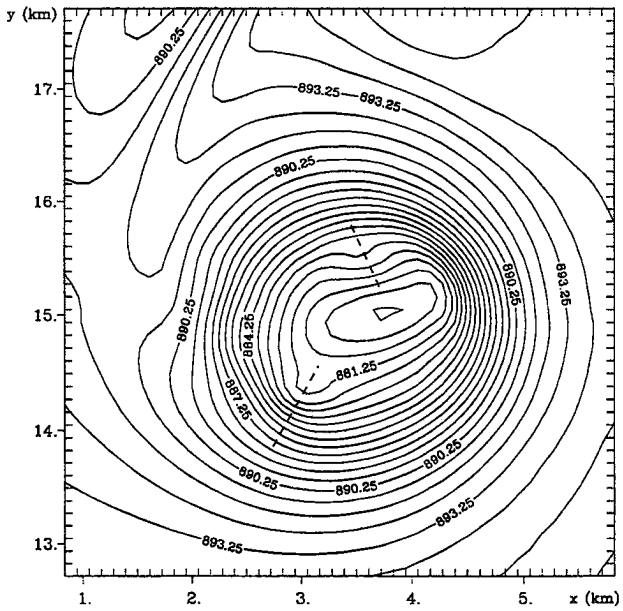
y (km)
17.
16.
15.
14.
13.
1.
2.
3.
4.
5.
x (km)
890.25
893.25
887.25
884.25
881.25

(j)

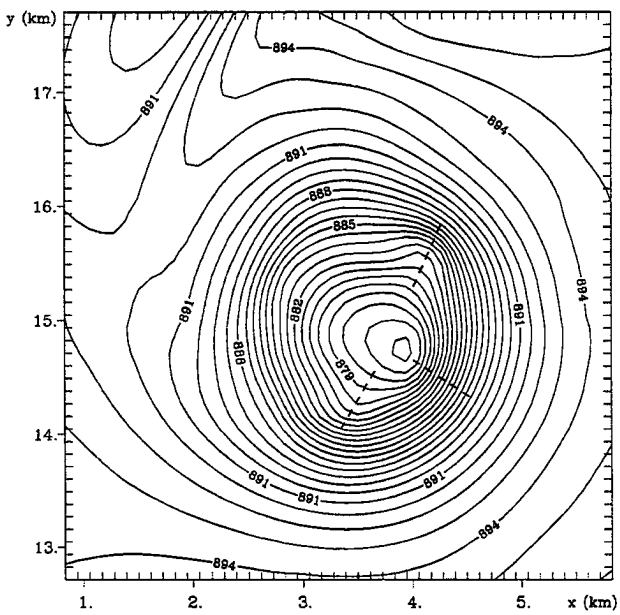
y (km)
17.
16.
15.
14.
13.
1.
2.
3.
4.
5.
x (km)
894
891
888
885
882
879

(k)

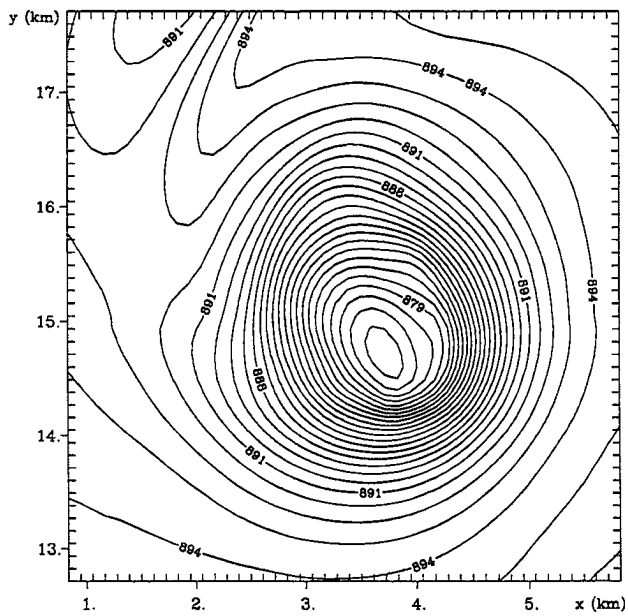
y (km)
17.
16.
15.
14.
13.
1.
2.
3.
4.
5.
x (km)
894
891
888
885
882
879

(l)

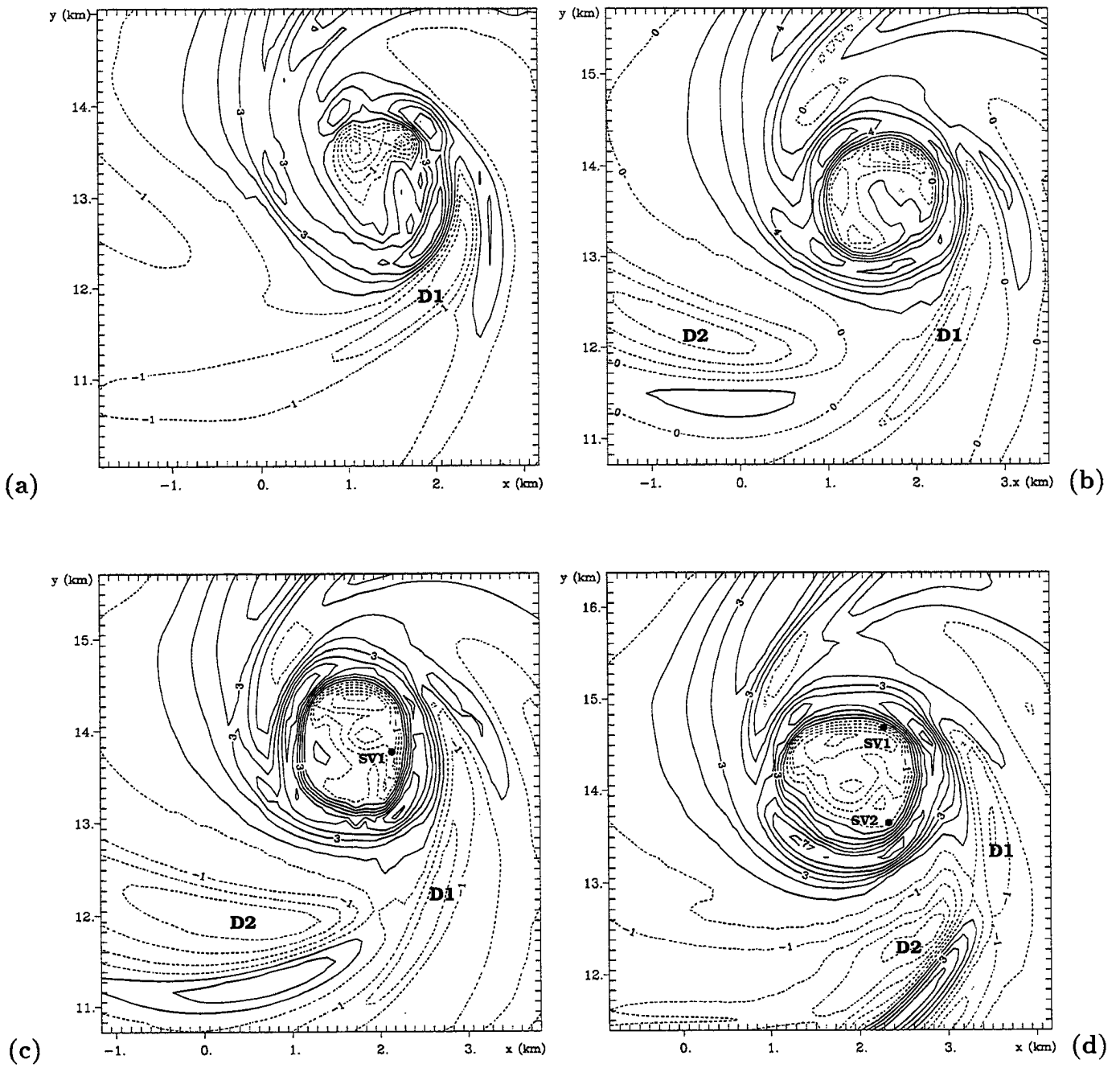

Figure 7.10: Evolution of the vertical velocity field at the lowest model level (z=50m) on a subset of Grid #6 at (a) 2145:30 UTC, (b) 2146:30 UTC, (c) 2147 UTC, (d) 2148 UTC, (e) 2148:45 UTC, (f) 2149:45 UTC, (g) 2150:45 UTC, (h) 2151:30 UTC, (i) 2152:15 UTC, (j) 2153:15 UTC, (k) 2154 UTC, (l) 2154:15 UTC, (m) 2154:45 UTC, (n) 2155:30 UTC, (o) 2156:15 UTC, (p) 2157 UTC. The contour interval is $1ms^{-1}$. Dashed contours denote negative values. The position of the pressure center associated with the secondary vortices are denoted by dots. Weak disturbances in the pressure field are denoted with dashed lines.

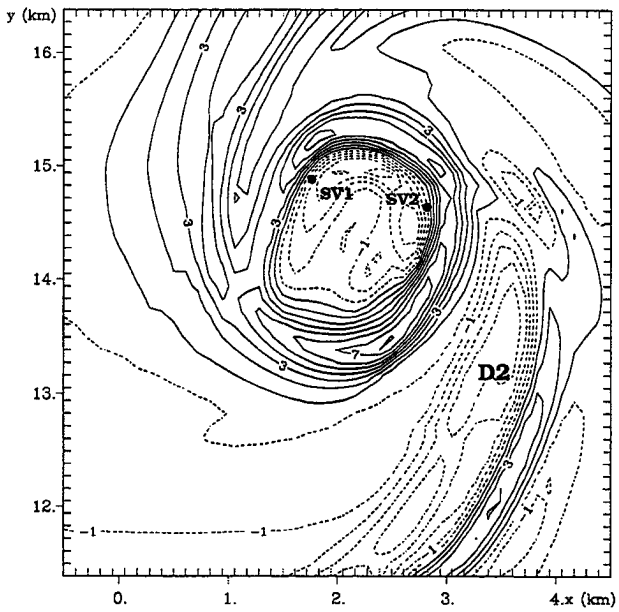
y (km)
16.
15.
14.
13.
12.
SV1
SV2
D2
0.
1.
2.
3.
4.x (km)

(e)

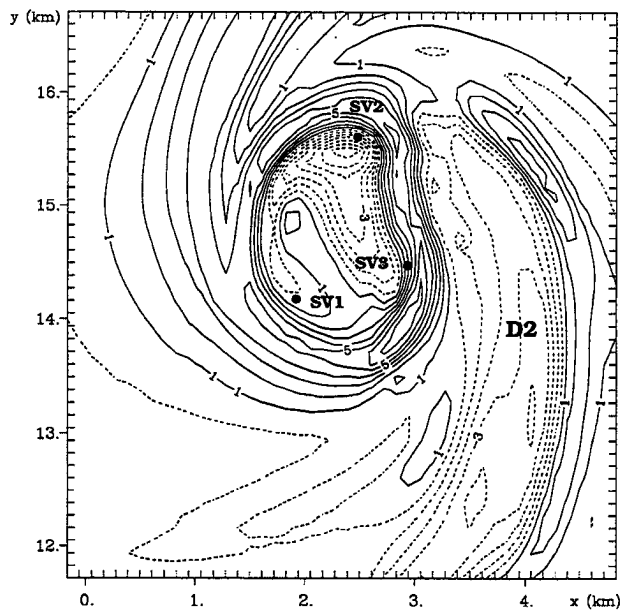
y (km)
16.
15.
14.
13.
12.
SV2
SV3
SV1
D2
0.
1.
2.
3.
4.
x (km)

(f)

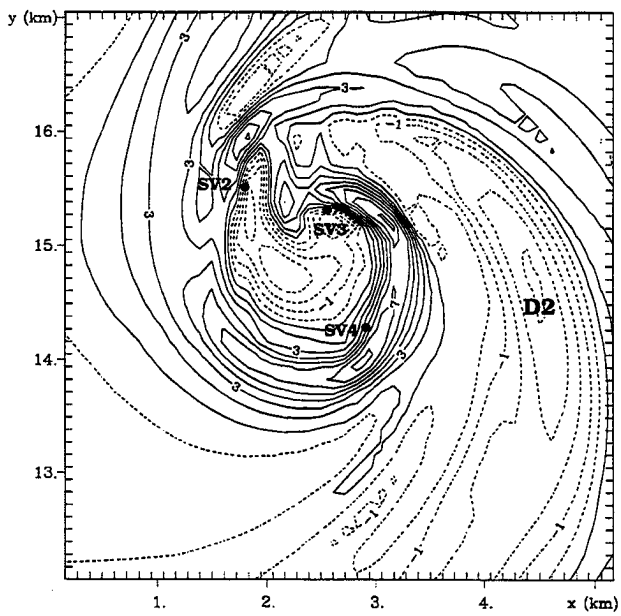
y (km)
16.
15.
14.
13.
SV2
SV3
SV4
D2
1.
2.
3.
4.
x (km)

(g)

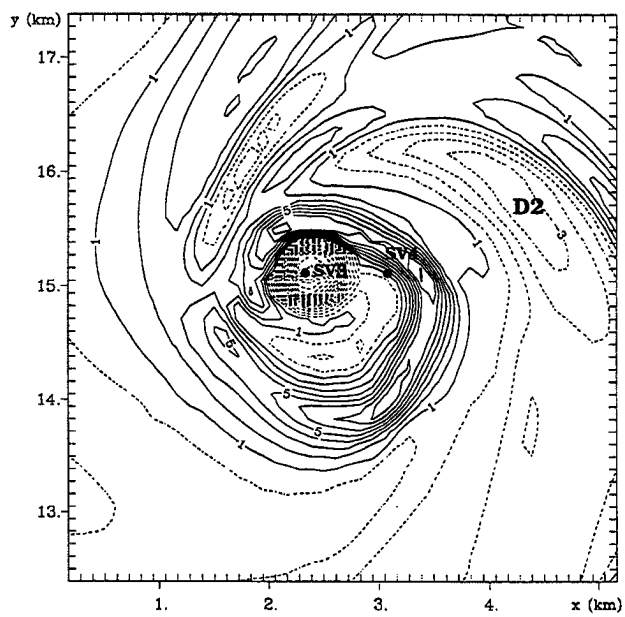
y (km)
17.
16.
15.
14.
13.
D2
SV4
SV3
1.
2.
3.
4.
x (km)

(h)

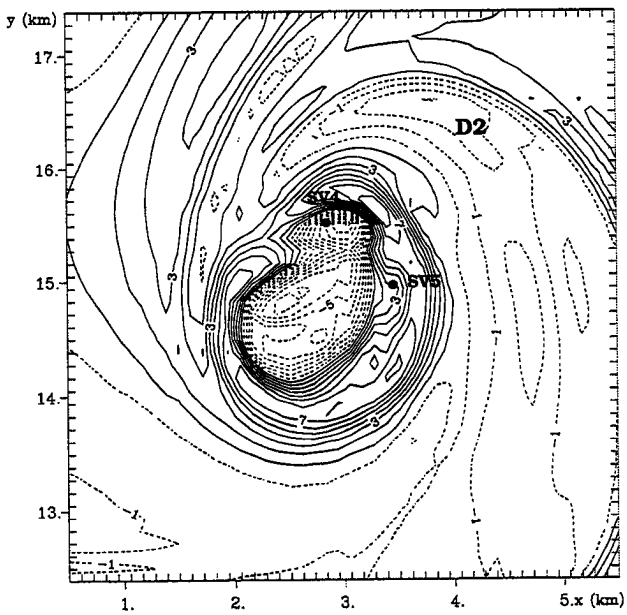
y (km)
17.
16.
15.
14.
13.
D2
SV4
SV5
SV6
1.
2.
3.
4.
5.x (km)

(i)

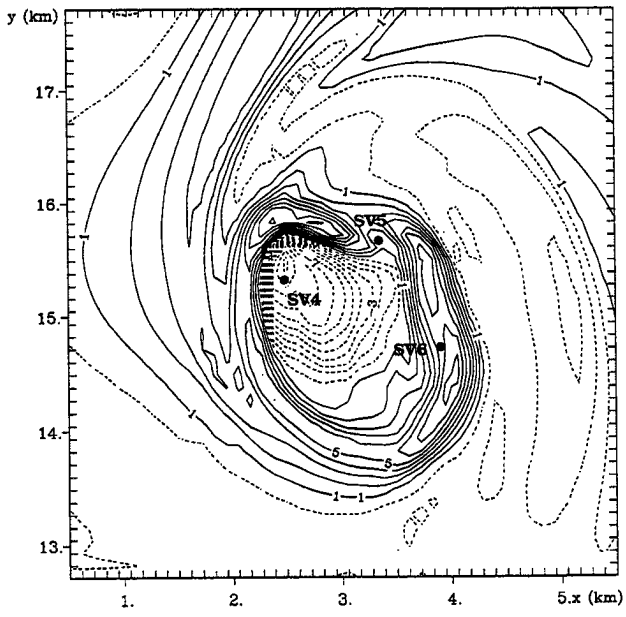
y (km)
17.
16.
15.
14.
13.
SV5
SV4
SV6
1.
2.
3.
4.
5.x (km)

(j)

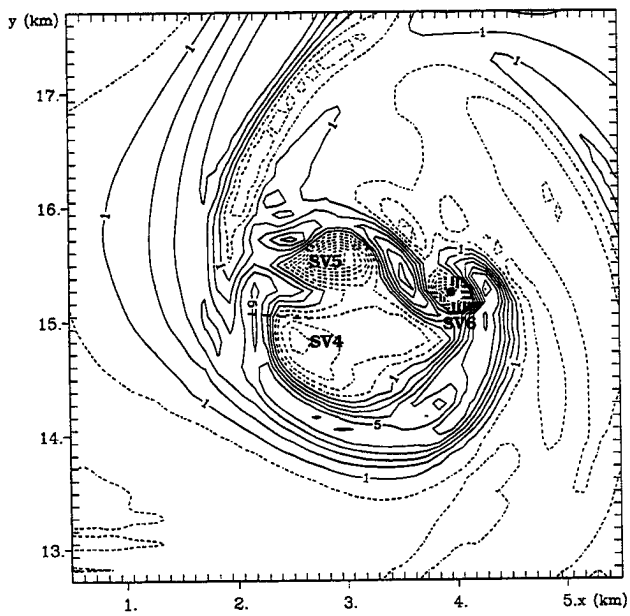
y (km)
17.
16.
15.
14.
13.
SV5
SV6
SV4
1.
2.
3.
4.
5.x (km)

(k)

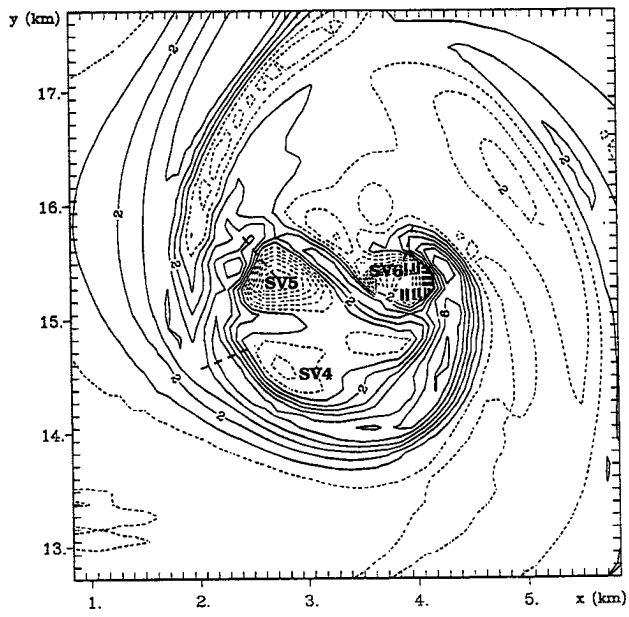
y (km)
17.
16.
15.
14.
13.
SV5
SV6
SV4
1.
2.
3.
4.
5.
x (km)

(l)

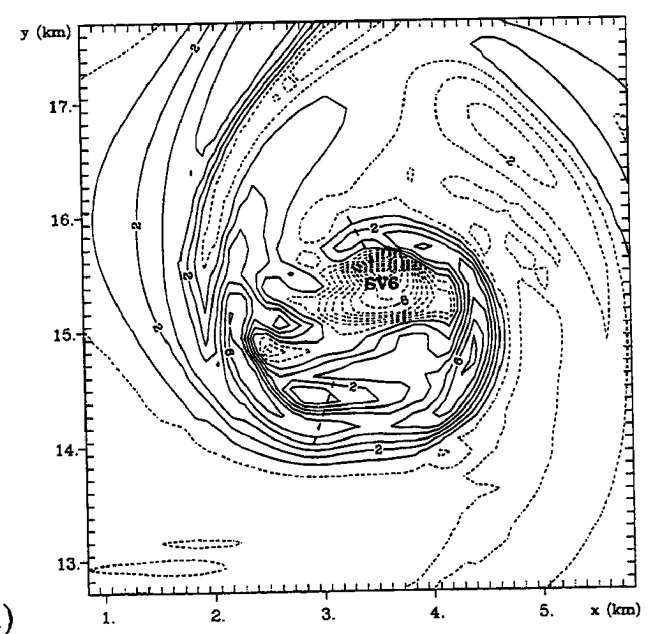
y (km)
17.
16.
15.
14.
13.
1.
2.
3.
4.
5.
x (km)
SV6

(m)

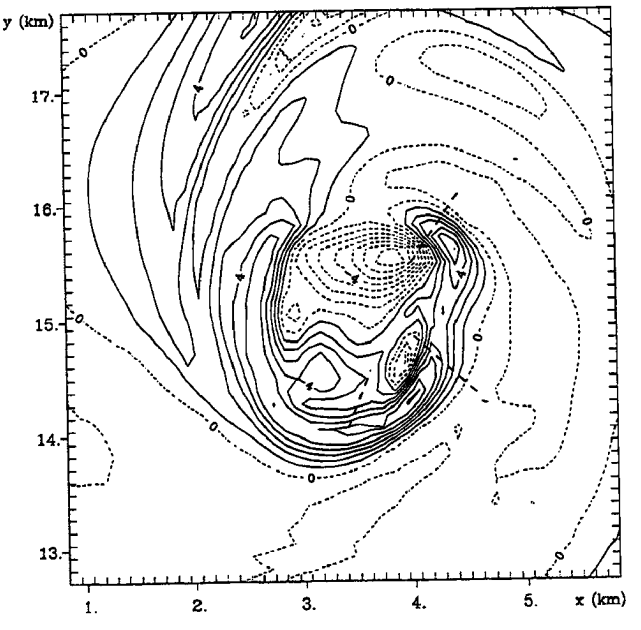
y (km)
17.
16.
15.
14.
13.
1.
2.
3.
4.
5.
x (km)

(n)

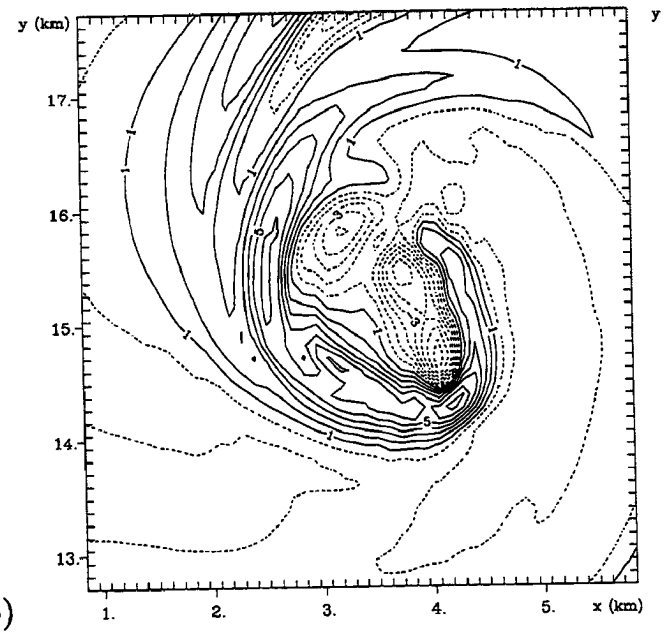
y (km)
17.
16.
15.
14.
13.
1.
2.
3.
4.
5.
x (km)

(o)

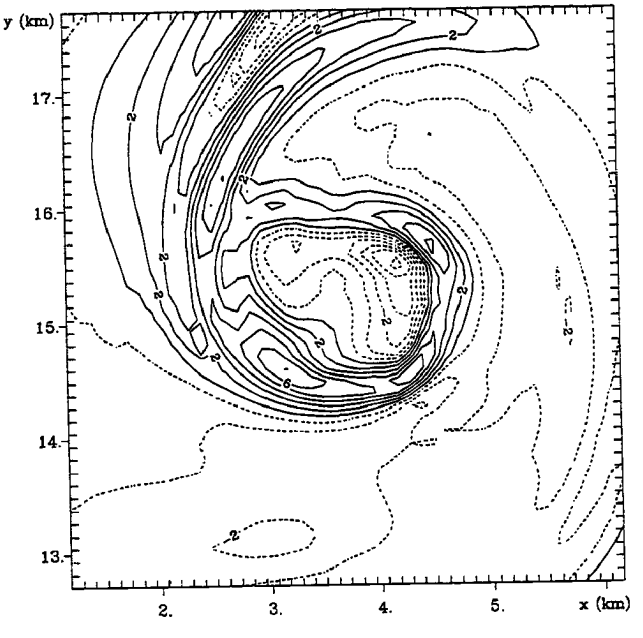
y (km)
17.
16.
15.
14.
13.
2.
3.
4.
5.
x (km)

(p)

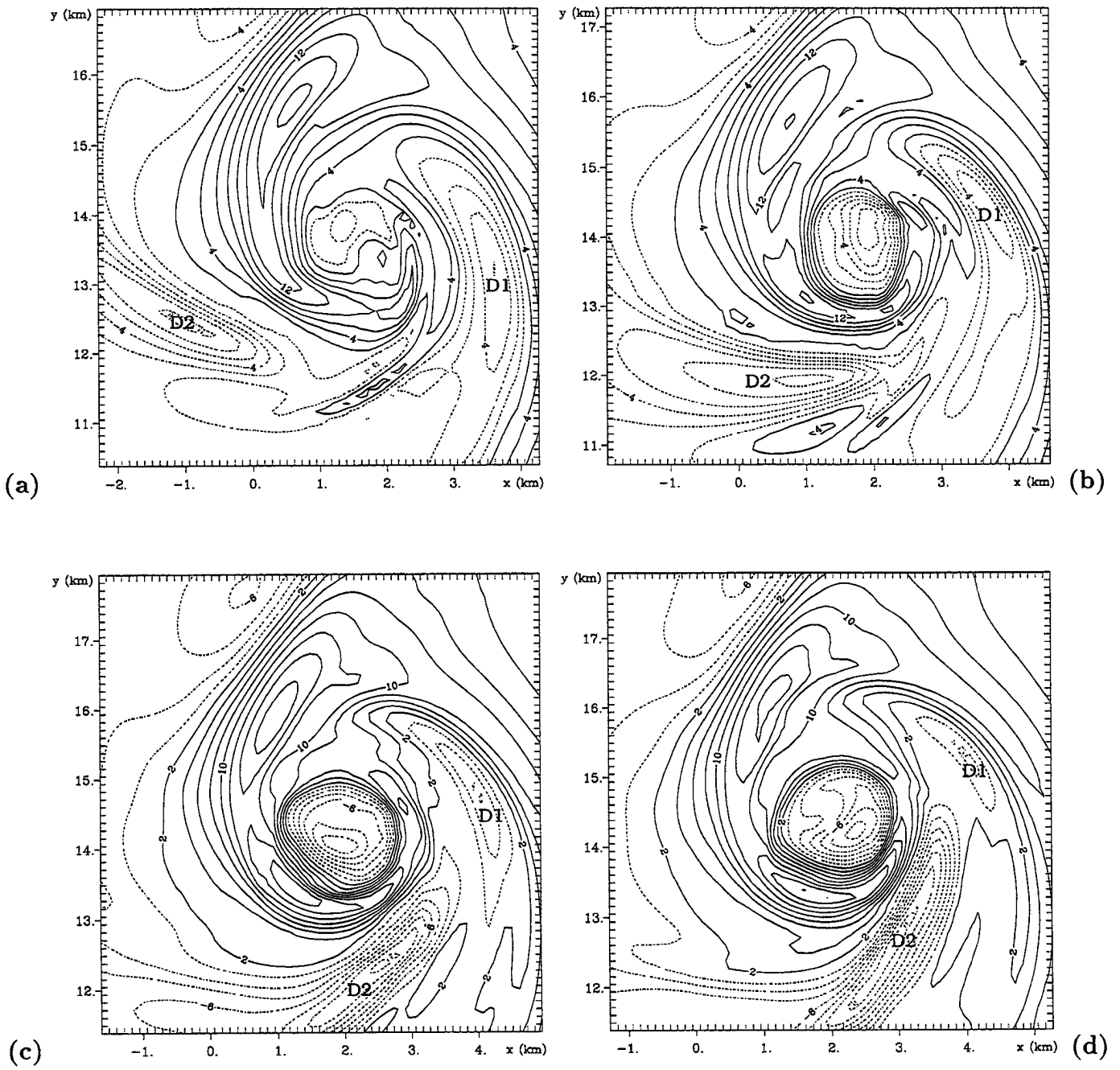

Figure 7.11: Evolution of the vertical velocity field at z=384m on a subset of Grid #6 at (a) 2146 UTC, (b) 2147 UTC, (c) 2148 UTC, (d) 2148:30 UTC, (e) 2149 UTC, (f) 2149:30 UTC, (g) 2150 UTC, (h) 2150:30 UTC. The contour interval is $2ms^{-1}$. Dashed contours denote negative values. The two outside downdrafts are denoted by D1 and D2. Note how the position of central downdraft follows the leading edge of D2.

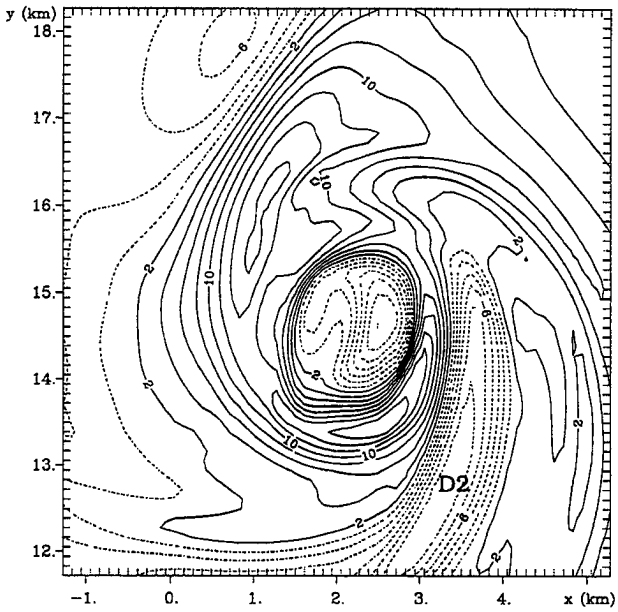
y (km)
18.
17.
16.
15.
14.
13.
12.
D2
−1.
0.
1.
2.
3.
4.
x (km)

(e)

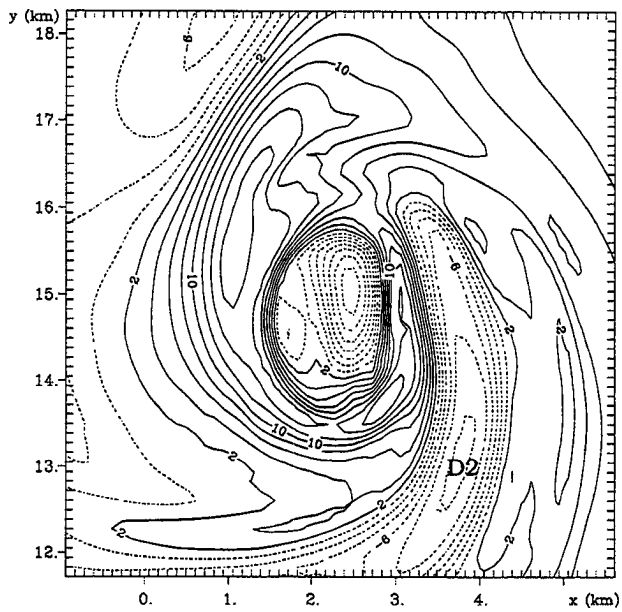
y (km)
18.
17.
16.
15.
14.
13.
12.
D2
0.
1.
2.
3.
4.
x (km)

(f)

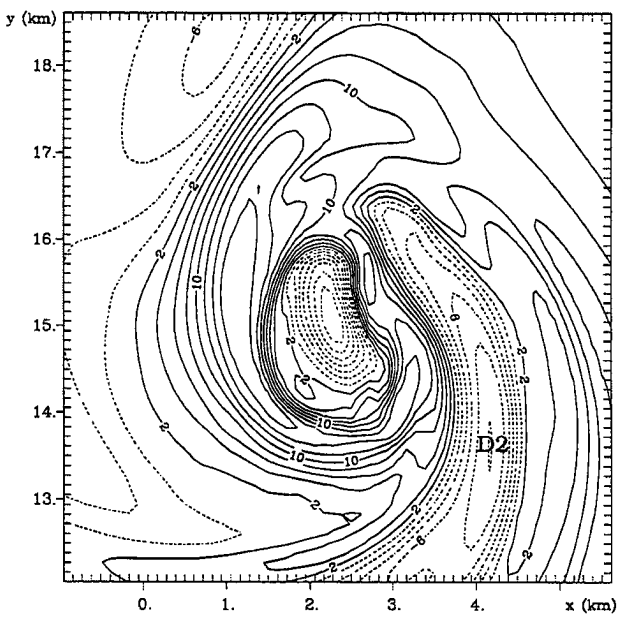
y (km)
18.
17.
16.
15.
14.
13.
D2
0.
1.
2.
3.
4.
x (km)

(g)

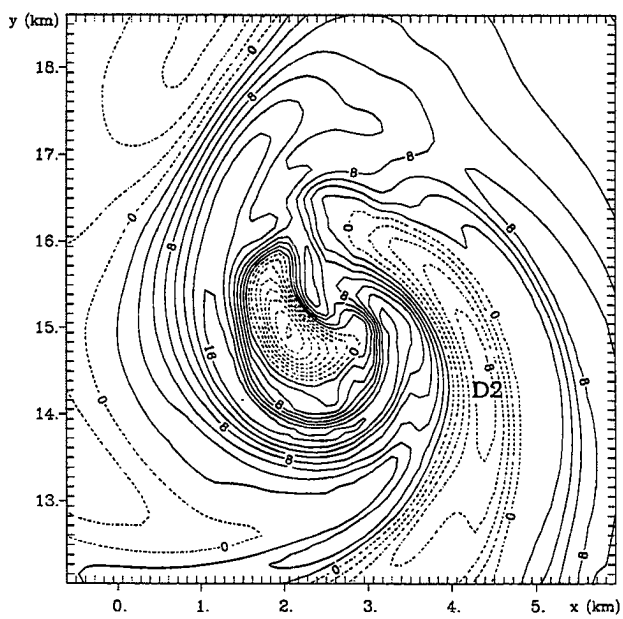
y (km)
18.
17.
16.
15.
14.
13.
D2
0.
1.
2.
3.
4.
5.
x (km)

(h)

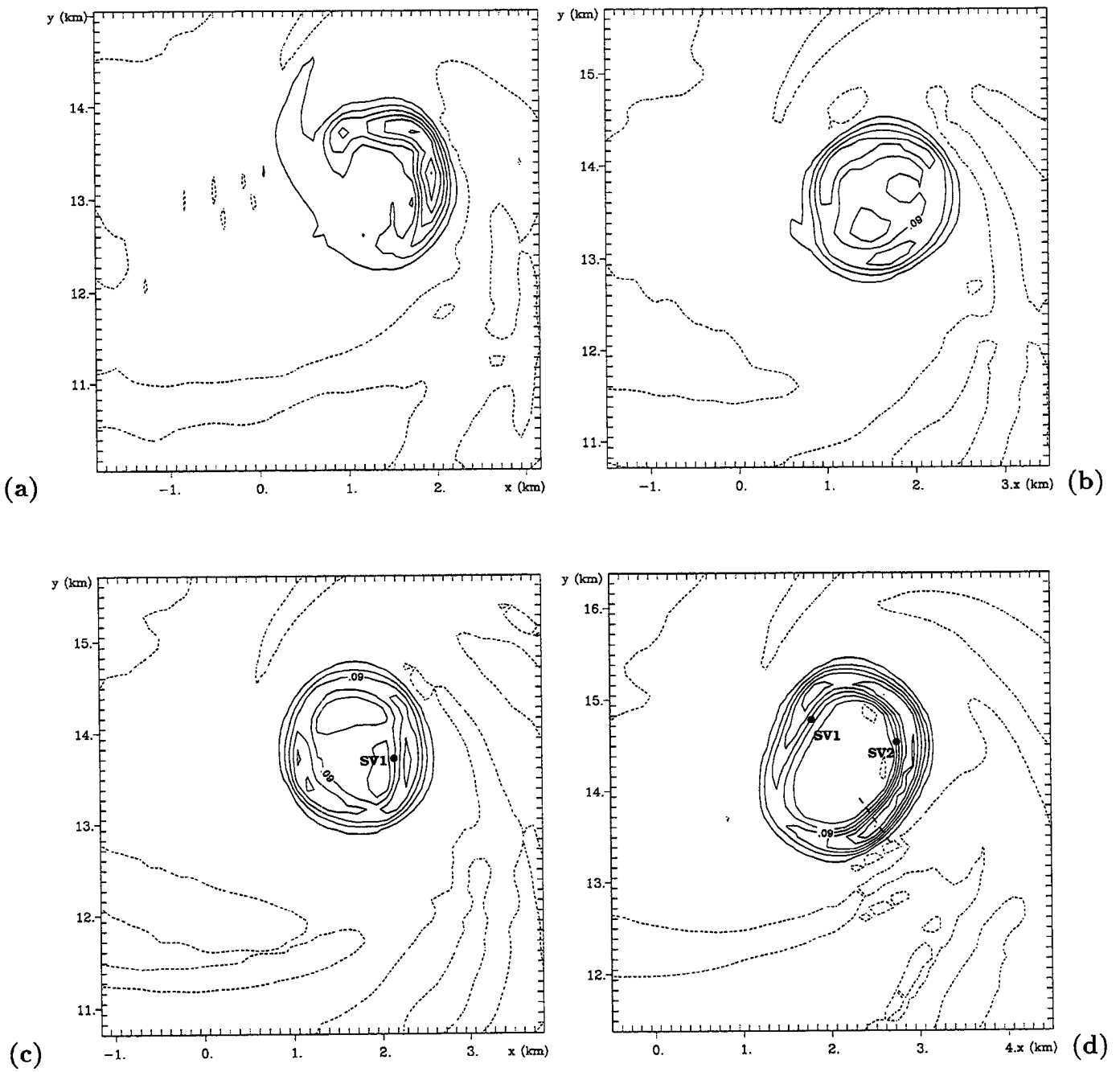

Figure 7.12: Evolution of the vertical vorticity field at the lowest model level (z=50m) on a subset of Grid #6 at (a) 2145:30 UTC, (b) 2146:30 UTC, (c) 2147 UTC, (d) 2148:45 UTC, (e) 2149:15 UTC, (f) 2149:45 UTC, (g) 2150:30 UTC, (h) 2151:15 UTC, (i) 2152 UTC, (j) 2152:30 UTC, (k) 2153:15 UTC, (l) 2153:45 UTC, (m) 2154 UTC, (n) 2154:15 UTC, (o) 2155:30 UTC, (p) 2156:15 UTC. The contour interval is $0.03s^{-1}$. Dashed contours denote a value of zero. The position of the pressure centers associated with the secondary vortices are denoted by dots. Weak disturbances in the pressure field are denoted with dashed lines.

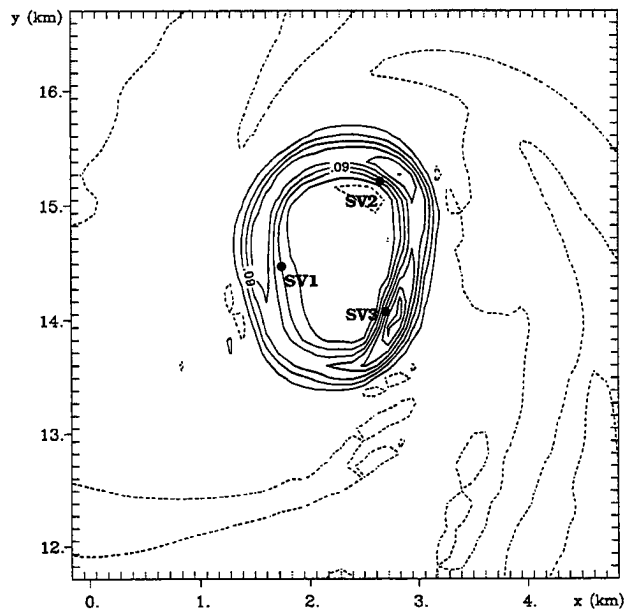
y (km)
16.
15.
14.
13.
12.
0.
1.
2.
3.
4.
x (km)
.09
.06
SV1
SV2
SV3

(e)

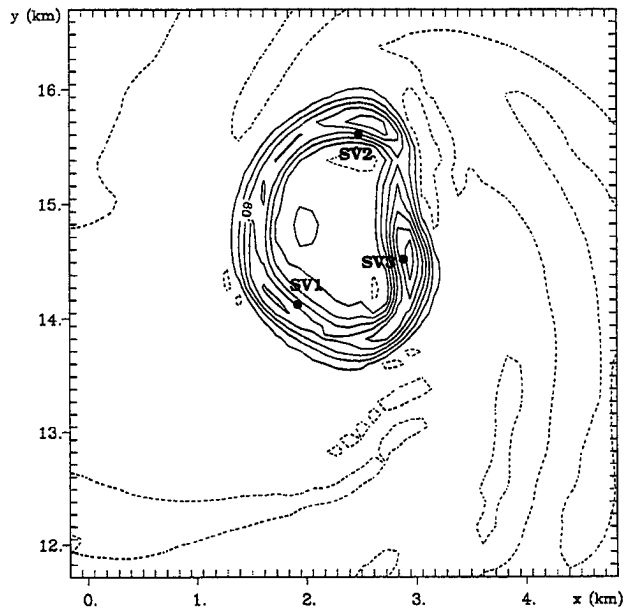
y (km)
16.
15.
14.
13.
12.
0.
1.
2.
3.
4.
x (km)
.08
SV1
SV2
SV3

(f)

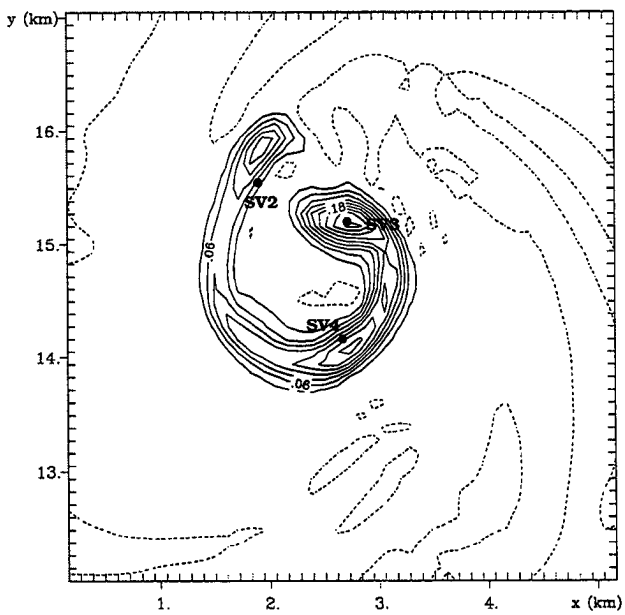
y (km)
16.
15.
14.
13.
1.
2.
3.
4.
x (km)
.18
.06
SV2
SV3
SV4

(g)

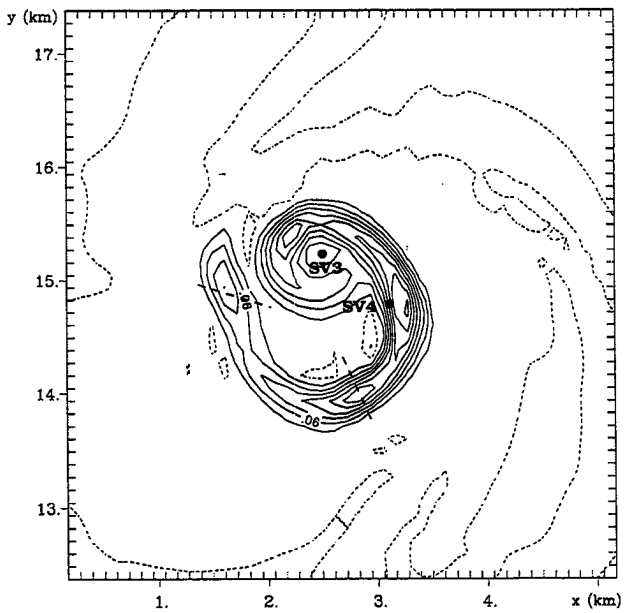
y (km)
17.
16.
15.
14.
13.
1.
2.
3.
4.
x (km)
.08
.06
SV3
SV4

(h)

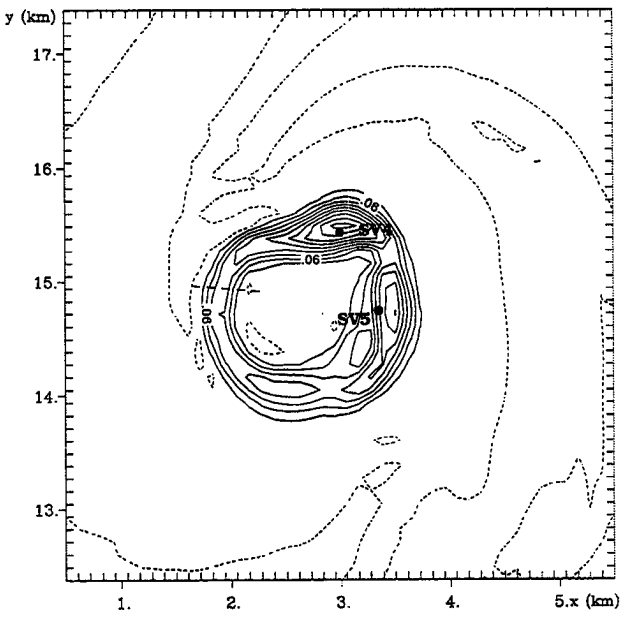
y (km)
17.
16.
15.
14.
13.
1.
2.
3.
4.
5.x (km)
SV4
SV5
.06
.06
.06

(i)

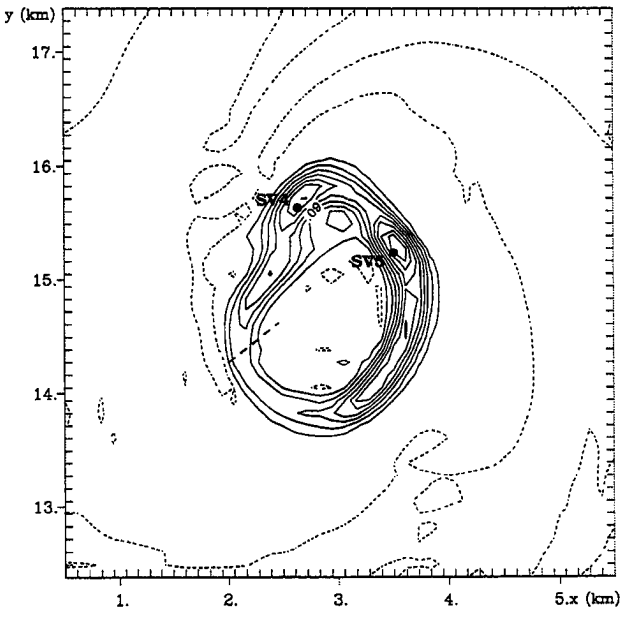
y (km)
17.
16.
15.
14.
13.
1.
2.
3.
4.
5.x (km)
SV4
SV5
.06

(j)

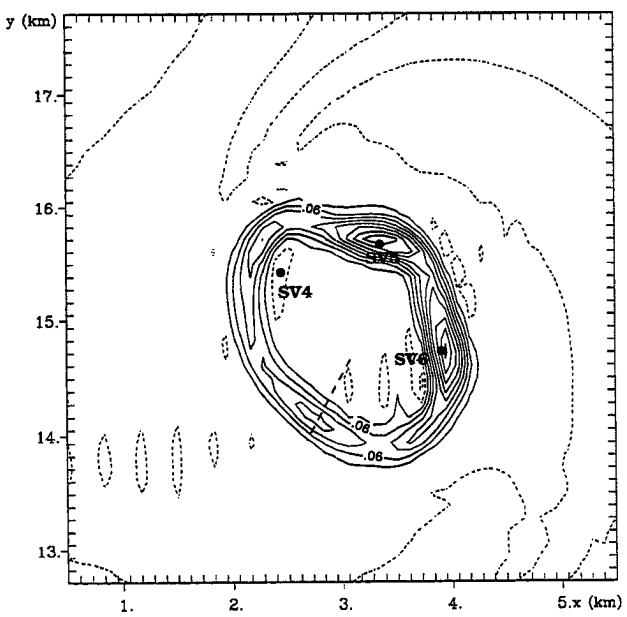
y (km)
17.
16.
15.
14.
13.
1.
2.
3.
4.
5.x (km)
SV4
SV5
SV6
.06
.06
.06

(k)

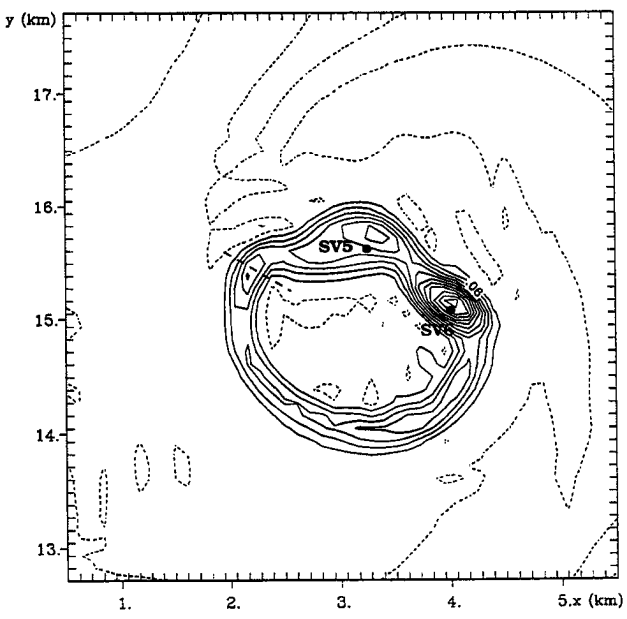
y (km)
17.
16.
15.
14.
13.
1.
2.
3.
4.
5.x (km)
SV5
SV6
.06

(l)

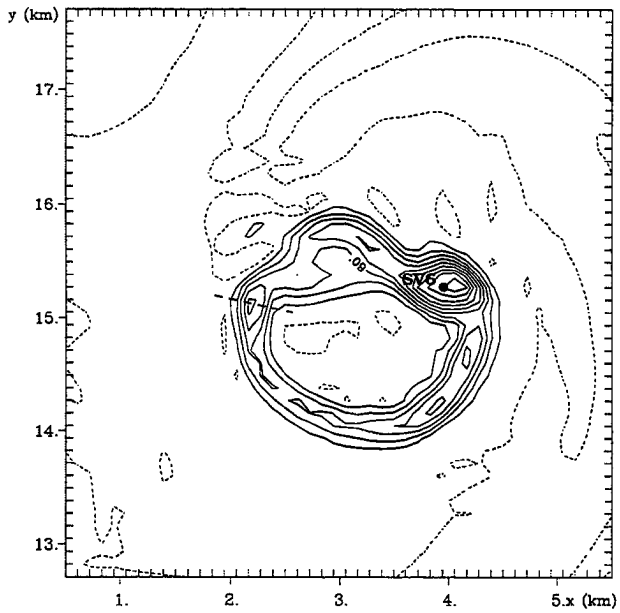
y (km)
17.
16.
15.
14.
13.
1.
2.
3.
4.
5.x (km)
.08
SV6

(m)

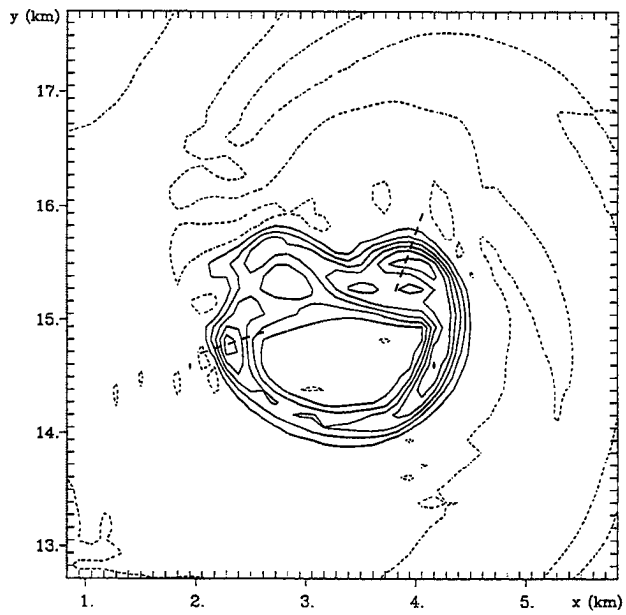
y (km)
17.
16.
15.
14.
13.
1.
2.
3.
4.
5.
x (km)

(n)

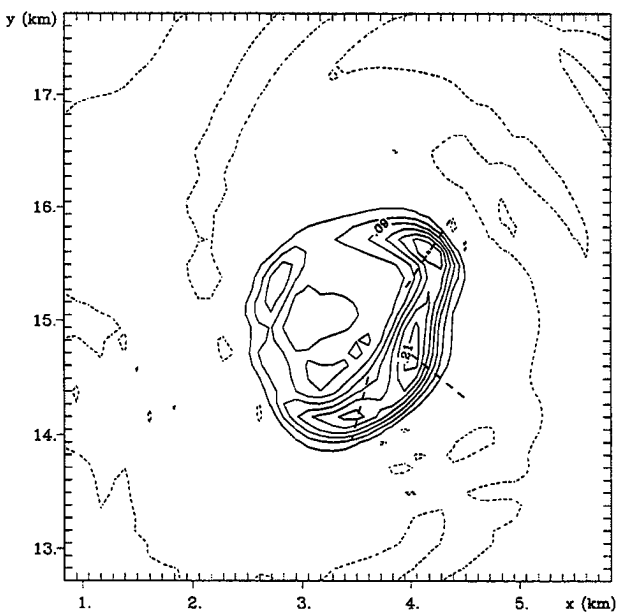
y (km)
17.
16.
15.
14.
13.
1.
2.
3.
4.
5.
x (km)
.09
.08
.07

(o)

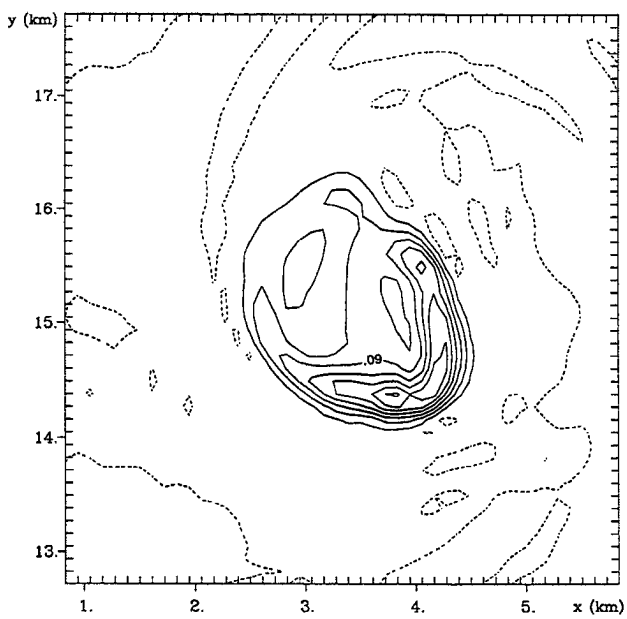
y (km)
17.
16.
15.
14.
13.
1.
2.
3.
4.
5.
x (km)
.09

(p)

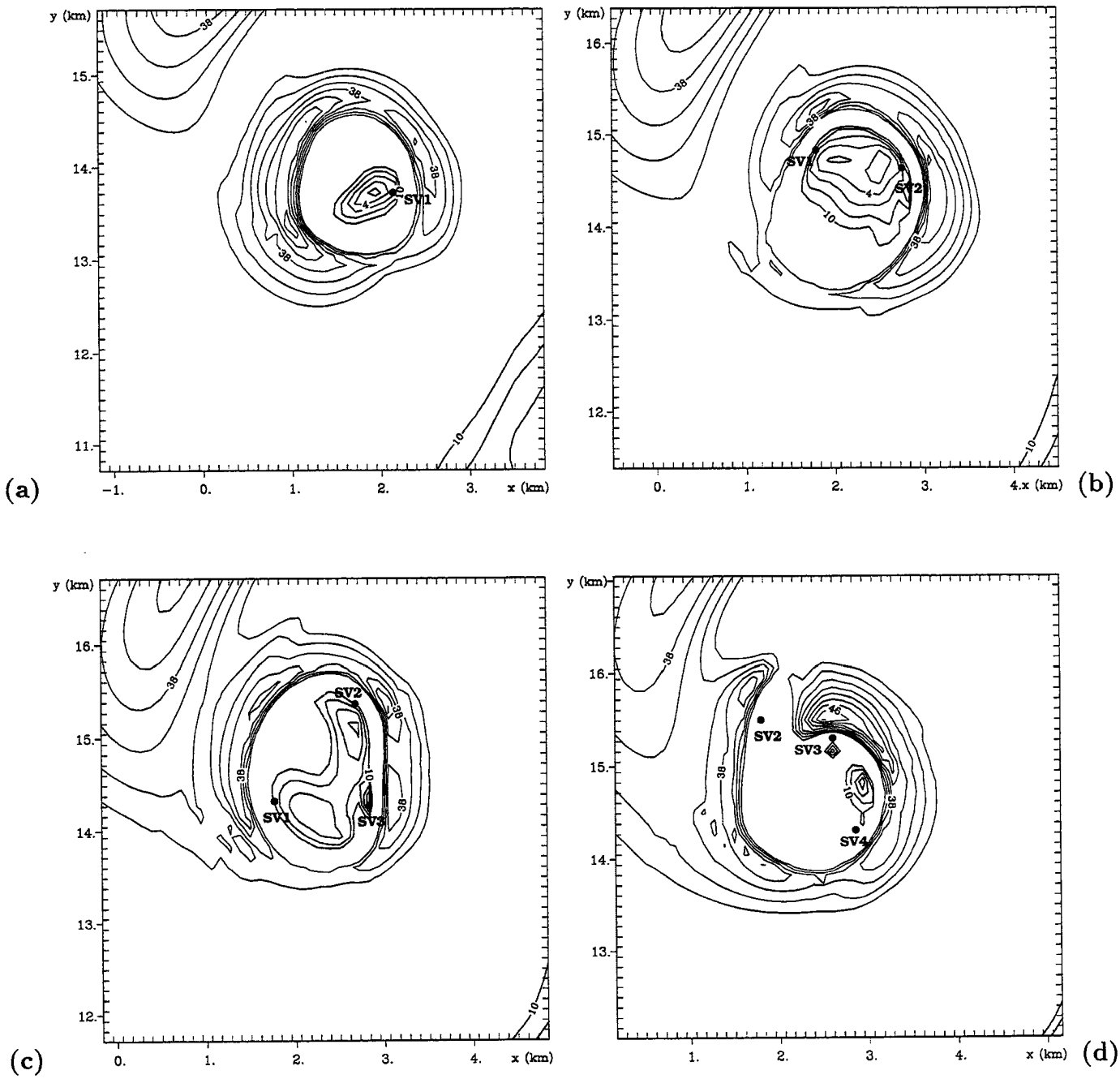

Figure 7.13: Evolution of the vortex-relative wind speed at the lowest model level (z=50m) on a subset of Grid #6 at (a) 2147 UTC, (b) 2148:45 UTC, (c) 2149:30 UTC, (d) 2150:45 UTC, (e) 2151:30 UTC, (f) 2152:30 UTC, (g) 2153:45 UTC, (h) 2154:15 UTC. Two different sets of contours are shown. The darker contours are wind speeds between $0 - 10ms^{-1}$. The lighter contours are wind speeds greater than $32ms^{-1}$. The contour interval for both sets of contours is $2ms^{-1}$. The position of the pressure centers associated with the secondary vortices are denoted by dots. Weak disturbances in the pressure field are denoted with dashed lines.

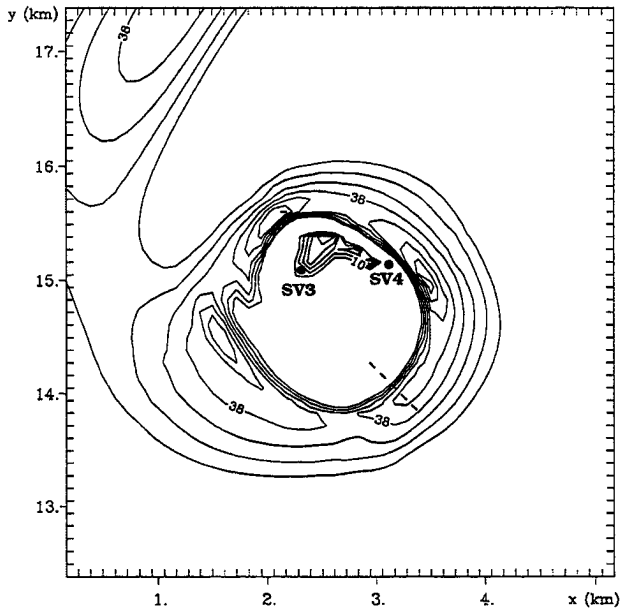
y (km)
17.
16.
15.
14.
13.
1.
2.
3.
4.
x (km)
SV3
SV4
38
10

(e)

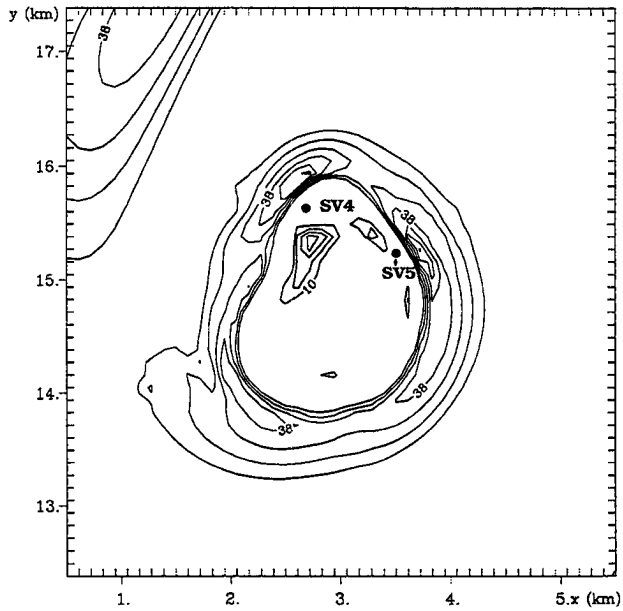
y (km)
17.
16.
15.
14.
13.
1.
2.
3.
4.
5.x (km)
SV4
SV5
38
10

(f)

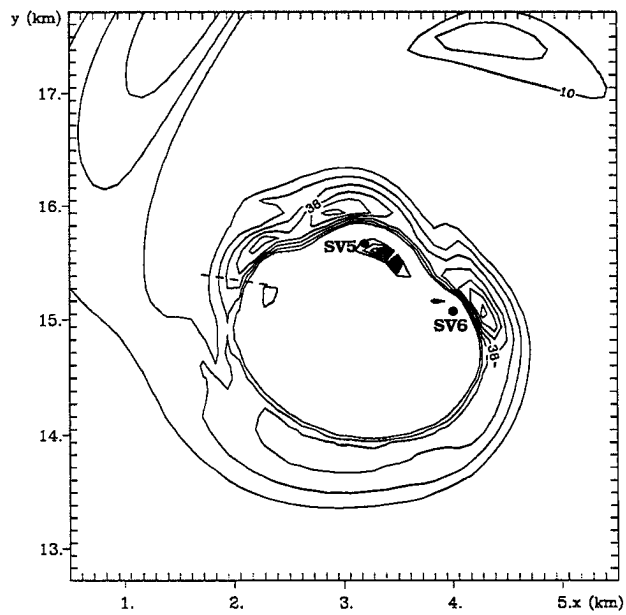
y (km)
17.
16.
15.
14.
13.
1.
2.
3.
4.
5.x (km)
SV5
SV6
38
10

(g)

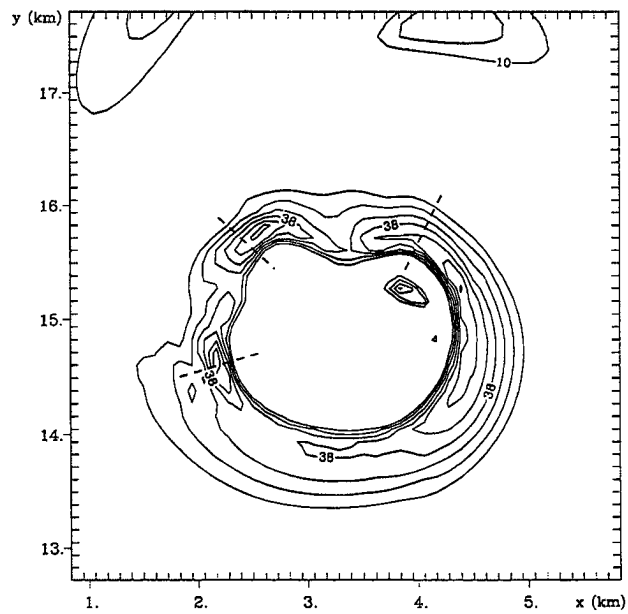
y (km)
17.
16.
15.
14.
13.
1.
2.
3.
4.
5.
x (km)
38
10

(h)

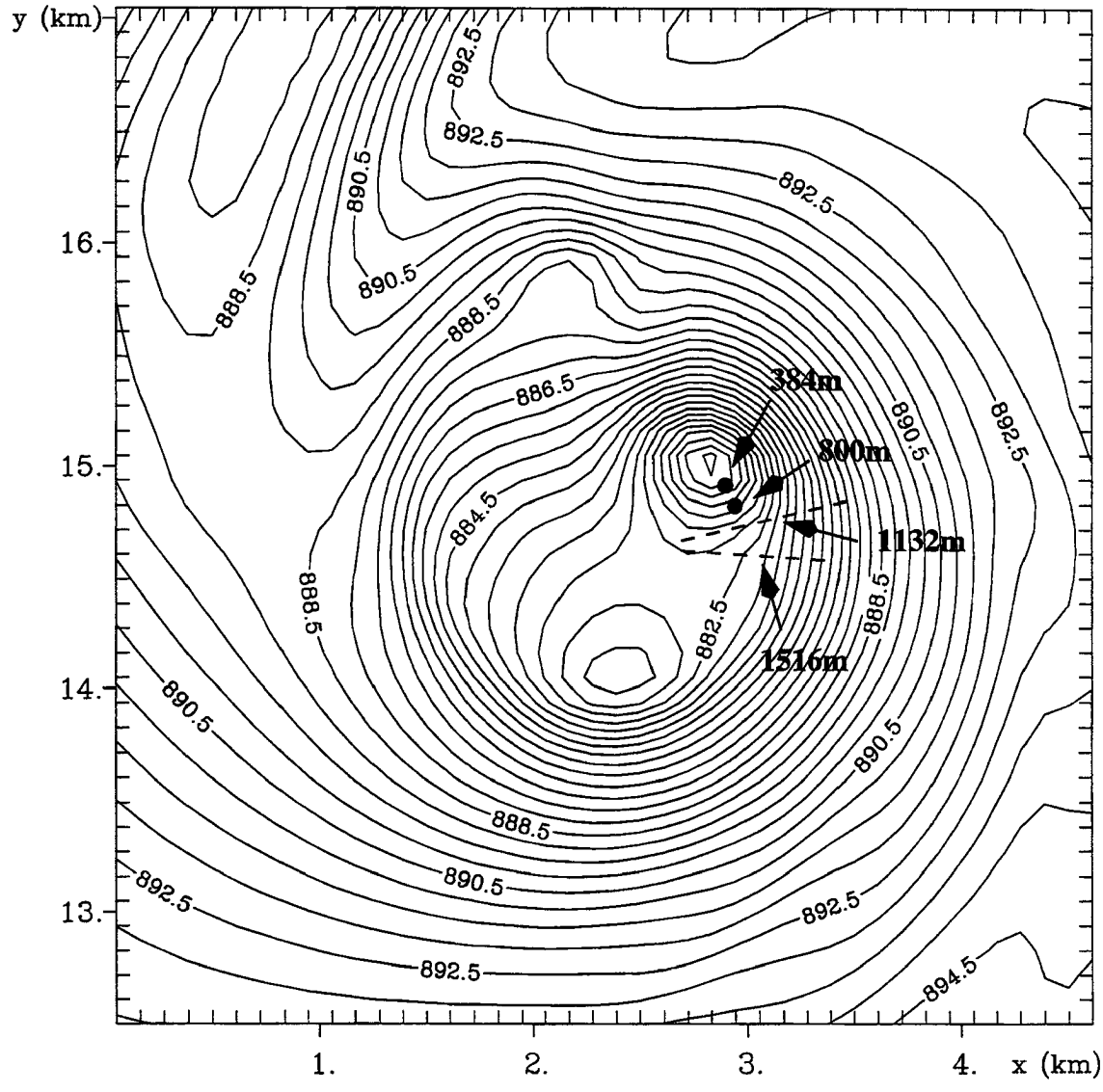

Figure 7.14: Vertical structure of the pressure field associated with SV3 at 2150:15 UTC. The pressure field on a subset of Grid #6 at z=50m is contoured every 0.5mb. The dots show the position of the pressure minimum associated with SV3 at the heights indicated on the figure. The dashed lines denote the positions of the minimum in the pressure waves at z=1132m and z=1516m.

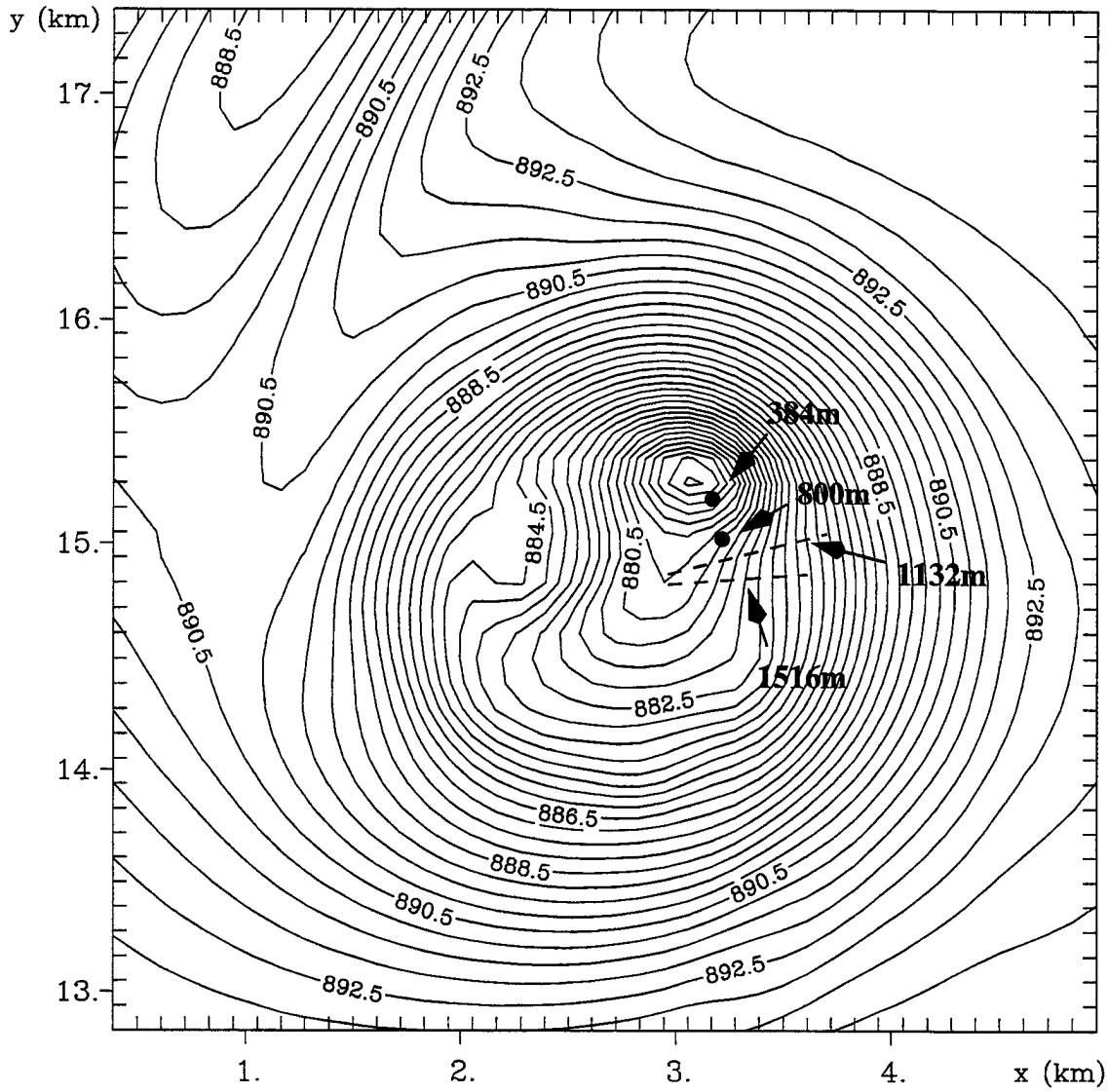

Figure 7.15: Vertical structure of the pressure field associated with SV4 at 2151:45 UTC. The pressure field on a subset of Grid #6 at z=50m is contoured every 0.5mb. The dots show the position of the pressure minimum associated with SV4 at the heights indicated on the figure. The dashed lines denote the positions of the minimum in the pressure waves at z=1132m and z=1516m.

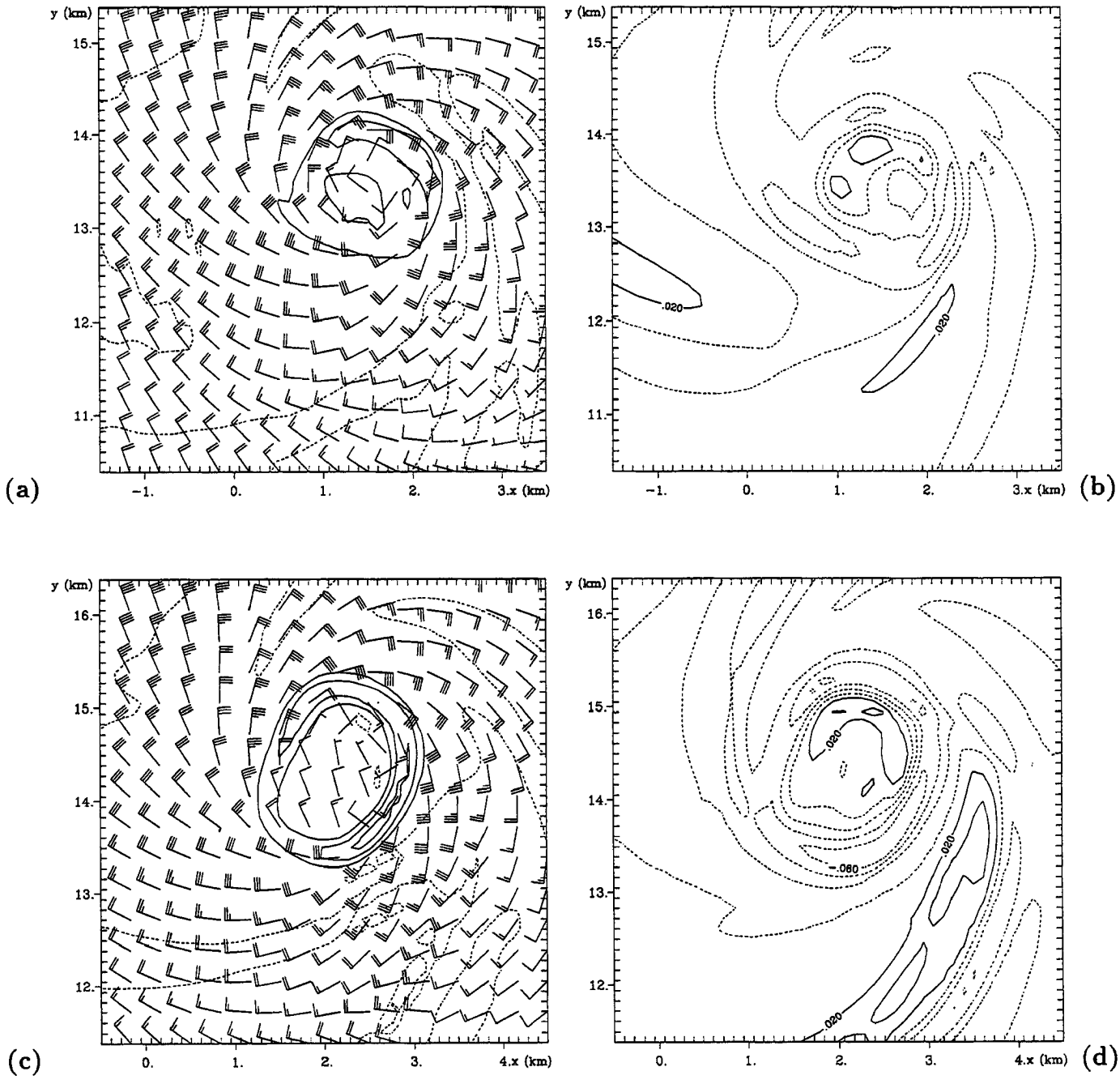

Figure 7.16: Evolution of the vortex-relative winds and the horizontal divergence field at the lowest model level (z=50m) on a subset of Grid #6. Plotted is the vertical vorticity field overlayed with the horizontal winds at (a) 2146 UTC, (c) 2148:45 UTC, (e) 2150:30 UTC, (g) 2152:30 UTC, and the horizontal divergence field at (b) 2146 UTC, (d) 2148:45 UTC, (f) 2150:30 UTC, (h) 2152:30 UTC. The vertical vorticity is contoured every $0.06s^{-1}$. The horizontal divergence is contoured every $0.02s^{-1}$. Dashed contours denote negative values (i.e. convergence). Wind barbs are plotted at every third model grid point. The short (long) flag on the wind barb denotes a wind speed of $5ms^{-1}$ ($10ms^{-1}$).

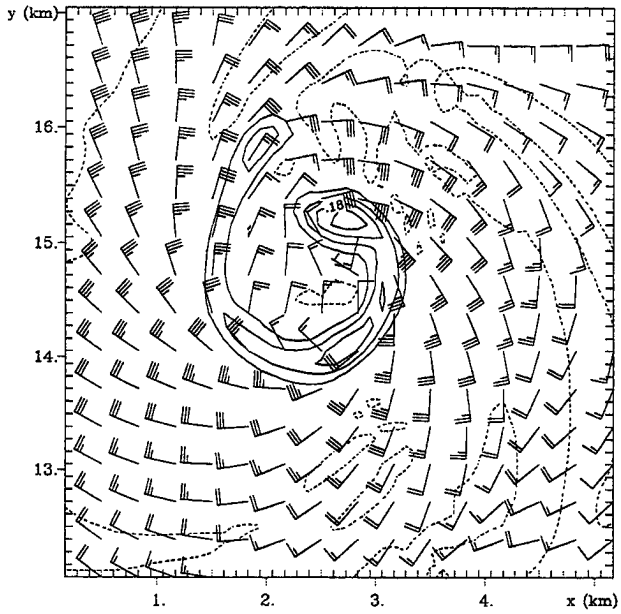
y (km)
16.
15.
14.
13.
1.
2.
3.
4.
x (km)
-.18

(e)

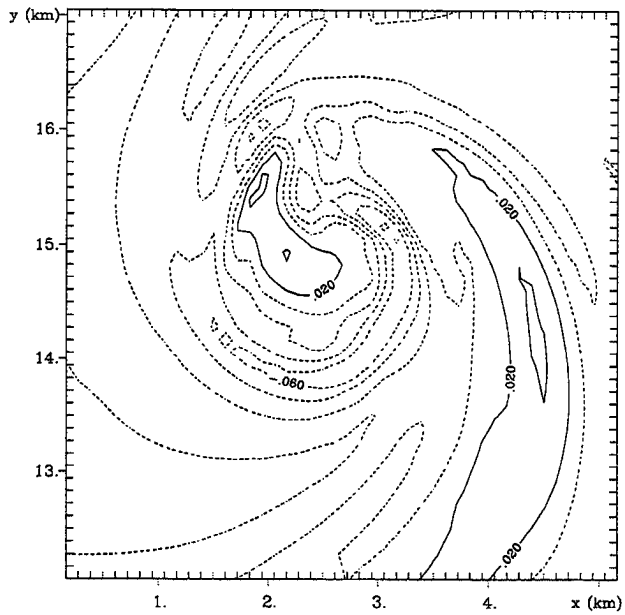
y (km)
16.
15.
14.
13.
1.
2.
3.
4.
x (km)
.020
.020
.060
.020
.020

(f)

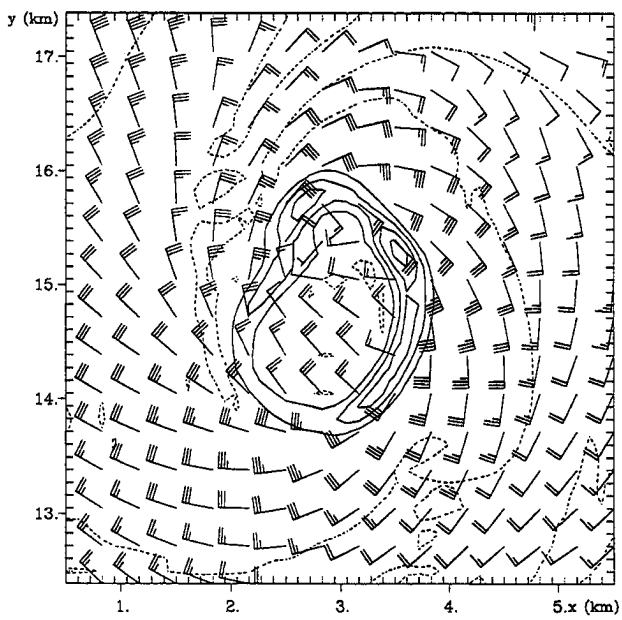
y (km)
17.
16.
15.
14.
13.
1.
2.
3.
4.
5.x (km)

(g)

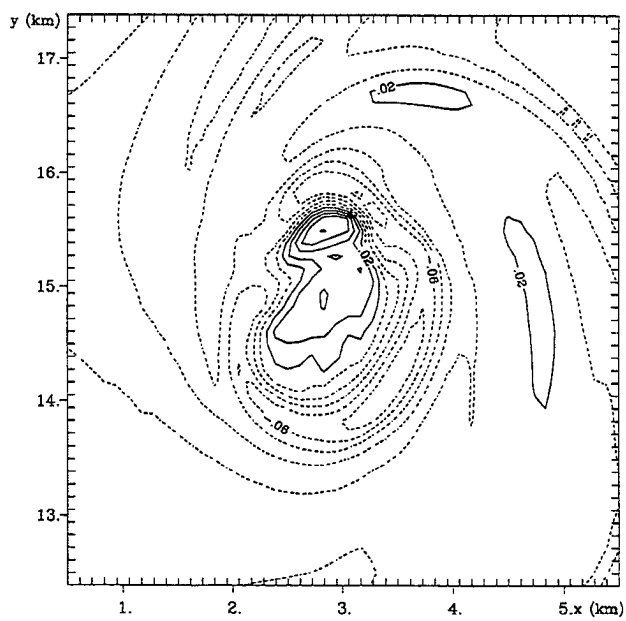
y (km)
17.
16.
15.
14.
13.
1.
2.
3.
4.
5.x (km)
.02
.02
.06
.02
.06

(h)

Chapter 8

SUMMARY, CONCLUSIONS, AND FUTURE WORK

A nested grid primitive equation model (RAMS version 3b) was used to study various aspects of tornadoes and the thunderstorms that produce them. These simulations were unique in that the model was initialized with synoptic data, and atmospheric flows ranging from the synoptic-scale down to the tornado-scale to be represented in the model through the use of telescoping nested grids. Two different case studies were simulated in this study: June 30, 1993, and May 15, 1991. A brief summary of each simulation and the major conclusions reached through the analysis of these simulations are presented below. Suggestions for future research are also provided at the end of the chapter.

8.1 June 30, 1993, HP Supercell Simulation

The June 30, 1993 simulation produced a small convective cluster containing two supercells which interact and evolve into an HP supercell. The HP supercell follows the bow-echo life-cycle with a rotating comma head structure. The initial storm (S1) develops at the intersection between an old outflow boundary and a stationary front, and maintains supercell characteristics during its entire lifetime. Other storms later develop to the west of the S1 and one of these storms (S2) merges with storms along the flanking line of S1, producing a larger convective storm in which S1 becomes the main mesocyclone, and S2 (losing its supercell characteristics) becomes part of a large flanking line.

The initial storm (S1) starts out as a classical supercell, but evolves into a large storm which has many characteristics of an HP supercell which include: both multi-cell and supercell behavior, production of very heavy precipitation, strong winds, weak tornadoes, and evolution into a 'rotating comma head' structure (bow-echo).

An analysis of the storm's transition into a bow-echo was presented, and the major findings are:

- The flanking line serves as a vorticity source for the simulated HP supercell. This was seen in the evolution of the vertical vorticity field at several levels, and was confirmed with trajectory calculations. The positive vorticity generated along the flanking line which is then advected northward into the mesocyclone contributes to the dominance of the cyclonic vortex in the bow-echo.

- The interaction between convective cells was important in the transition of the storm into a rotating comma-head structure in this case. Following the merger of S1 and S2, the precipitation rate increased, increasing the pressure behind the gust front. This lead to an acceleration of the gust front which triggered the storm's transition into a bow-echo.

- Although the storm emits a large amplitude deep-tropospheric gravity wave just prior to the storm's transition into a bow-echo, the gravity wave did not appear to contribute to the storm's transition.

8.2 June 30, 1993 Tornado Simulation

The June 30, 1993, simulated supercell produced two weak tornadoes. The first tornado (T1) developed in a vertical velocity gradient created at the interface of an updraft/downdraft along the flanking line of the storm to the southeast of the mesocyclone. Maximum wind speeds with T1 reached $28ms^{-1}$ with a maximum pressure deficit of 5mb near the surface. About twenty minutes later, a second tornado (T2) developed along a strong horizontal shear zone created by strong outflow beneath the rotating comma-head structure of the HP supercell. T2 had maximum wind speeds of $30ms^{-1}$ with a maximum pressure deficit of 6mb near the surface. An analysis of the tornadogenesis process was also performed, and the major conclusions are summarized below:

- Both tornadoes developed first near the surface, and then developed upward into the storm. T1 reached a depth of 5-6km, while T2 only reached a depth of about 2km.

- Neither tornado was clearly linked to the mesocyclone in the parent storm. T1 developed southeast of the mesocyclone and was clearly not associated with the mesocyclone at any point in its lifetime. The connection between T2 and the mesocyclone is more tenuous.

- Results from the circulation analyses revealed that the circulation associated with both tornadoes was already present at low-levels in the storm environment 15-20 minutes before the tornadoes developed.

- The baroclinic term associated with the downdraft made a negligible contribution to the circulation in this case, indicating that baroclinically-generated horizontal vorticity in the downdraft is not a prerequisite for tornado development in all cases. However, the downdraft did play an important role in tilting horizontal vorticity into the vertical just above the surface in the near-tornado environment where horizontal convergence could then act to amplify it.

In the June 30, 1993 simulation, downdrafts played a significant role in the development of both tornadoes as the vertical vorticity of parcels entering the tornado from the downdrafts became positive (or was increased) through tilting of horizontal vorticity into the vertical by the downdraft gradient as the parcels were exiting the downdraft. Similar results were found (although over a large depth) in the simulations of two classical supercell tornadoes by Grasso (1996). However, in Grasso's simulations, baroclinicity significantly increased the circulation around material curves converging toward the tornadoes, perhaps explaining why the tornadoes produced in his simulations were stronger than the tornadoes simulated in the June 30, 1993 case presented here. Despite this difference, all the tornadoes simulated in this study and those simulated by Grasso (1996) developed first near the surface, and then developed upward into the storm. These results suggest a possible alternate interpretation to the role of the mesocyclone in the tornadogenesis process. Perhaps the role of the mesocyclone is to create a dynamically driven downdraft and a region of strong convergence near the surface. The downdraft acts to tilt horizontal vorticity into the vertical, creating positive vertical vorticity as air parcels near the surface which is then

amplified through strong surface convergence below the mesocyclone. The strong updraft associated with the mesocyclone then draws the vortex upward into the storm.

8.3 Simulated Secondary Vortices–May 15, 1991 Case

The May 15, 1991, simulation produced a classical supercell which developed along the dryline in the Texas panhandle as was shown by Grasso (1996). This supercell in turn produced a tornado which lasted for 50 minutes in the simulation. During a ten minute period toward the end of the simulation, six secondary vortices developed within the main tornado vortex. The simulated secondary vortices had many features in common with multiple-vortex tornadoes and secondary vortices produced in laboratory vortices. The evolution and structure of the simulated secondary vortices was presented, and the major results are summarized below:

- The onset of secondary vortex production occurs shortly after the parent vortex develops a well-defined two-celled structure (as defined by a annular updraft and vertical vorticity ring) through the depth of the boundary layer. The end of the secondary vortex development occurs shortly after the two-celled structure breaks down along the north/northeast quadrant of the parent vortex.

- The secondary vortices develop along the southeast quadrant and in the *interior* of the parent vortex where the radial shears of the tangential wind, vertical vorticity, and vertical velocity are generally largest. This is also the region of the parent vortex where the low-level convergence is continually the greatest. The secondary vortices dissipate before making a complete revolution around the parent vortex.

- The secondary vortices wrap anticyclonically around the parent vortex with height. This is in agreement with observations, and theoretical and laboratory studies. The simulated secondary vortices also had many other characteristics in common with both observations and laboratory studies of the multiple-vortex phenomenon.

- The calculated swirl ratio in the simulation lies between 1.1-2.3 which is in both the observational range for multiple-vortex tornadoes and in the laboratory range for secondary vortices.

The model results support the idea that secondary vortices arise from instabilities in the parent vortex flow. In the simulation, two different downdrafts develop on the *outside* of the parent vortex during the period of secondary vortex development, and wrap around the southern and eastern sides of the vortex in time. The position of these downdrafts relative to the parent vortex coincides with the region of the secondary vortex development. The role of these downdrafts in the development of the secondary vortices may be to enhance radial gradients of both the vertical and tangential velocities in the parent vortex, thereby destabilizing or enhancing the instability of the flow in these regions.

8.4 Suggestions for Future Research

The results from these simulations and some of the limitations in the present study raised several issues which could be addressed in future work. A few suggestions are given below.

- It would be interesting to do further analysis on the vorticity source for the mesocyclone in the June 30, 1993 case both before and during the transition of the HP supercell into a bow-echo and compare the results with Weisman (1993). The flow around the storm is significantly different than the flow associated with classical supercells.

- In the HP supercell simulation, the upstream propagating deep tropospheric gravity wave was much weaker than the downstream propagating wave, and did not appear to contribute to the storm's transition into a bow-echo. This is in contrast to studies of mesoscale convective systems (MCS) which have shown that the upstream propagating gravity waves play a significant role in the development of the MCS. It would be interesting to investigate the possibility that environments which allow the propagation of the gravity waves upstream away from the storm mark the difference between

environments which can support the larger MCS systems and environments which support only isolated storms and smaller convective clusters.

- The most obvious drawback in the current simulations is that the grid spacing on Grid #6 (100m) is pushing the upper bound for resolving tornadic-scale motions. With continued increases in computer power, future simulations using even smaller grid spacings to better resolve tornadic flows should be possible.

- One problem in the tornado simulations (both the June 30 case and the May 15 case) is that the tornado continues to expand in time through most of its life cycle. This appears to be a feature in *all* model simulations to date in which both the parent thunderstorm and the tornado are simulated (Wicker and Wilhelmson, 1993, 1995; Grasso, 1996). The reason for this (be it physical or numerical) needs to be investigated.

- It would be interesting to construct an axisymmetric 'basic state' vortex in the May 15 simulation by taking azimuthal averages of model fields at a given radius, and then look at perturbations from the basic state during the period that the secondary vortices were developing. This may provide further insight into why the secondary vortices develop/dissipate where they do in the parent vortex.

- It would also be interesting to investigate how the secondary vortices affect the parent vortex. In the present simulation, 'eddy fluxes' created by the secondary vortices could be used to calculate tendencies in the parent vortex flow due to the secondary vortices.

Of course to really resolve the scales of most tornadoes produced in the atmosphere, primitive equation models would need to have grid spacings between 10-20m in both the horizontal and vertical directions. This provides a challenge for future modelling studies of severe storms and tornadoes.

References

Agee, E., C. Church, C. Morris, and J. Snow, 1975: Some synoptic aspects and dynamical features of vortices associated with the tornado outbreak of 3 April, 1974. *Mon. Wea. Rev.*, **103**, 318- 333.

Agee, E.M., J.T. Snow, F.S. Nickerson, P.R. Clare, C.R. Church, and L.A. Schaal, 1977: An observational study of the West Lafayette, Indiana, tornado of 20 March, 1976. *Mon. Wea. Rev.*, **105**, 893- 907.

Arakawa, A., and V.R. Lamb, 1981: A potential enstrophy and energy conserving scheme for the shallow water equations. *Mon. Wea. Rev.*, **109**, 18-36.

Avissar, R., and R.A. Pielke, 1989: A parameterization of heterogeneous land surfaces for atmospheric numerical models and its impact on regional meteorology. *Mon. Wea. Rev.*, **117**, 2113- 2136.

Baker, G.L., and C.R. Church, 1979: Measurements of core radii and peak velocities in modeled atmospheric vortices. *J. Atmos. Sci.*, **36**, 2413-2424.

Barnes, S.L., 1964: A technique for maximizing details in numerical weather map analysis. *J. Appl. Meteor.*, **3**, 396-409.

Barnes, S.L., 1968: On the source of thunderstorm rotation. *ESSA Tech. Memo. ERLTM-NSSL 38.* National Severe Storms Laboratory, Norman, OK. 28 pp.

Barnes, S.L., 1973: Mesoscale objective map analysis using weighted time-series observations. NOAA Technical Memorandum ERL NSSL-62, National Severe Storms Laboratory, Norman, OK, 38 pp.

Barnes, S.L., 1978a: Oklahoma thunderstorms on 29-30 April, 1970. Part II: radar-observed merger of twin hook echoes. *Mon. Wea. Rev.*, **106**, 685-696.

Barnes, S.L., 1978b: Oklahoma thunderstorms on 29-30 April, 1970. Part III: tornado characteristics inferred from damage tracks. *Mon. Wea. Rev.*, **106**, 697-703.

Barnes, S.L., and C.W. Newton, 1986: Thunderstorms in the synoptic setting. *Thunderstorm Morphology and Dynamics*, E. Kessler, ed., University of Oklahoma Press, Norman, Oklahoma, 75-112.

Batchelor, G.K., 1967: *An Introduction to Fluid Dynamics.* Cambridge University Press, 615pp.

Blechman, J.B., 1975: The Wisconsin tornado event of April 21, 1974: Observations and theory of secondary vortices. *Preprints, 9th Conf. on Severe Local Storms.*, Norman, OK, Amer. Meteor. Soc., 344-349.

Bluestein, H.B., and C.R. Parks, 1983: A synoptic and photographic climatology of low-precipitation severe thunderstorms in the southern plains. *Mon. Wea. Rev.*, **111**, 2034-2046.

Bluestein, H.B., 1984: Further examples of low-precipitation severe thunderstorms. *Mon. Wea. Rev.*, **112**, 1885-1888.

Bluestein, H.B., and G.R. Woodall, 1990: Doppler-radar analysis of a low-precipitation severe storm. *Mon. Wea. Rev.*, **118**, 1640-1664.

Bluestein, H.B., 1985. The formation of a 'landspout' in a 'broken-line' squall line in Oklahoma. *Preprints, 14th Conf. on Severe Local Storms*, Indianapolis, IN, Amer. Meteor. Soc., 267-270.

Brady, R.H., and E.J. Szoke, 1989: A case study of non-mesocyclone tornado development in northeast Colorado: Similarities to waterspout formation. *Mon. Wea. Rev.*, **117**, 843-856.

Brandes, E.A., 1977: Gust front evolution and tornadogenesis as viewed from Doppler radar. *J. Appl. Meteor.*, **16**, 333-338.

Brandes, E.A., 1978: Mesocyclone Evolution and Tornadogenesis: Some Observations. *Mon. Wea. Rev.*, **106**, 995-1011.

Brooks, H.E., and R.B. Wilhelmson, 1992: Numerical simulation of a low-precipitation supercell thunderstorm. *Meteor. Atmos. Phys.*, **49**, 3-17.

Brooks, H.E., C.A. Doswell III, and R. Davies-Jones, 1993: Environmental helicity and the maintenance and evolution of low-level mesocyclones. *The Tornado: Its Structure, Dynamics, Prediction, and Hazards, Geophys. Monogr.*, No.79, Amer. Geophys. Union, 97-104.

Brooks, H.E., C.A. Doswell III, and R. B. Wilhelmson, 1994: The role of mid-tropospheric winds in the evolution of maintenance of low-level mesocyclones. *Mon. Wea. Rev.*, **122**, 126-136.

Browning, K.A., 1964: Airflow and precipitation trajectories within severe local storms which travel to the right of the winds. *J. Atmos. Sci.*, **21**, 634-639.

Browning, K.A., 1968: The organization of severe local storms. *Weather*, **23**, 429-434.

Burgess, D.W., and E.B. Curran, 1985: The relationship of storm type to environment in Oklahoma on 26 April, 1984. *Preprints, 14th Conf. on Severe Local Storms*, Indianapolis, Amer. Meteor. Soc., 208-211.

Burgess, D.W., L.R. Lemon, and R.A. Brown, 1975: Tornado characteristics revealed by Doppler radar. *Geophys. Res. Lett.*, **2**, 183-184.

Burgess, D.W., R.A. Brown, L.R. Lemon, and C.R. Safford, 1977: Evolution of a tornadic thunderstorm. *Preprints, 10th Conf. on Severe Local Storms*, Omaha, Nebraska, Amer. Meteor. Soc., 84-89.

Burgess, D.W., and R.P. Davies-Jones, 1979: Unusual tornadic storms in eastern Oklahoma on 5 December, 1975. *Mon. Wea. Rev.*, **107**, 451-457.

Burgess, D.W., and R.J. Donaldson, Jr., 1979: Contrasting tornadic storm types. *Preprints, 11th Conf. on Severe Local Storms*, Kansas City, Missouri, Amer. Meteor. Soc., 189-192.

Burgess, D.W., V.T. Wood, and R.A. Brown, 1982. Mesocyclone evolution statistics. *Preprints, 12th Conf. on Severe Local Storms*, Amer. Meteor. Soc., 84-89.

Burgess, D.W., R.J. Donaldson, Jr., and P.R. Desrochers, 1993: Tornado detection and warning by radar. *The Tornado: Its Structure, Dynamics, Prediction, and Hazards, Geophys. Monogr.*, No.79, Amer. Geophys. Union, 203-221.

Calianese, E.J., Jr., A.R. Moller, and E.B. Curran, 1996: A WSR-88D analysis of a cool season, elevated high-precipitation supercell. *Preprints, 18th Conf. on Severe Local Storms*, San Francisco, CA, Amer. Meteor. Soc., 96-100.

Carbone, R.E., 1983: A severe frontal rainband. Part II: Tornado parent vortex circulation. *J. Atmos. Sci.*, **40**, 2639-2654.

Chen, C., and W.R. Cotton, 1983a: A one-dimensional simulation of the stratocumulus-capped mixed layer. *Bound. Layer Meteor.*, **25**, 289- 321.

Chen, C., and W.R. Cotton, 1983b: Numerical experiments with a one-dimension higher order turbulence model: Simulation of the Wangara day 33 case. *Bound. Layer Meteor.*, **25**, 375-404.

Church, C.R., and J.T. Snow, 1979: The dynamics of natural tornadoes as inferred from laboratory simulations. *J. Rech. Atmos.*, **13**, 111-133.

Church, C.R., J.T. Snow, G.L. Baker, and E.M. Agee, 1979: Characteristics of tornado-like vortices as a function of swirl ratio: A laboratory investigation. *J. Atmos. Sci.*, **36**, 1755-1776.

Church, C.R., and J.T. Snow, 1993: Laboratory models of tornadoes. *The Tornado: Its Structure, Dynamics, Prediction, and Hazards, Geophys. Monogr.*, No.79, Amer. Geophys. Union, 277-295.

Clark, T.L., and R.D. Farley, 1984: Severe downslope windstorm calculations in two and three spacial dimensions using anelastic interactive grid nesting: A possible mechanism for gustiness. *J. Atmos. Sci.*, **41**, 329-350.

Davies, H.C., 1976: A lateral boundary formulation for multi-level prediction models. *Tellus*, **102**, 405-418.

Davies-Jones, R.P., 1973: The dependence of core radius on swirl ratio in a tornado simulator. *J. Atmos. Sci.*, **30**, 1427-1430.

Davies-Jones, R.P., and E. Kessler, 1974: Tornadoes. *Weather Modification and Climate*, W.N. Hess, ed., John Wiley and Sons, New York, 552-595.

Davies-Jones, R.P., D. Burgess, L.R. Lemon, and D. Purcell, 1978: Interpretation of surface marks and debris patterns from the 24 May, 1973 Union City, Oklahoma tornado. *Mon. Wea. Rev.*, **106**, 12-21.

Davies-Jones, R.P., 1982a: Observational and Theoretical Aspects of Tornadogenesis. *Topics in Atmospheric and Oceanographic Sciences: Intense Atmospheric Vortices*, Bengtsson, Lighthill, ed., Springer-Verlag, Berlin, 175-189.

Davies-Jones, R.P., 1982b: A new look at the vorticity equation with application to tornadogenesis. *Preprints, 12th Conf. on Severe Local Storms*, Amer. Meteor. Soc., 249-252.

Davies-Jones, R.P., 1983: Tornado Dynamics. *Thunderstorm Morphology and Dynamics*, Edwin Kessler, ed., University of Oklahoma Press, 197-236.

Davies-Jones, R.P., 1984: Streamwise vorticity: the origin of updraft rotation in supercell storms. *J. Atmos. Sci.*, **41**, 2991-3006.

Davies-Jones, R.P., 1985: Dynamical interaction between an isolated convective cell and a veering environmental wind. *Preprints, 14th Conf. on Severe Local Storms*, Indianapolis, IN, Amer. Meteor. Soc., 216-219.

Davies-Jones, R.P., D. Burgess, and M. Foster, 1990: Test of helicity as a tornado forecast parameter. *Preprints, 16th Conf. on Severe Local Storms*, Amer. Meteor. Soc., 588-592.

Davies-Jones, R.P., and H. Brooks, 1993: Mesocyclogenesis from a theoretical perspective. *The Tornado: Its Structure, Dynamics, Prediction, and Hazards, Geophys. Monogr.*, No.79, Amer. Geophys. Union, 105-114.

Deal, R.L., Y.-L. Lin, M.S. Kulie, and D.S. Decroix, 1996: Observations and simulation of a long-lived tornadic storm: The 27 March, 1994 Cherokee County, Alabama supercell. *Preprints, 18th Conf. on Severe Local Storms*, Amer. Meteor. Soc., 245-249.

Doswell, C.A., III, The operational meteorology of convective weather, vol. II, storm-scale analysis, *NOAA Tech. Memo. ERL ESG-15.*

Doswell, C.A., III, and D.W. Burgess, 1993: Tornadoes and tornadic storms: A review of conceptual models. *The Tornado: Its Structure, Dynamics, Prediction, and Hazards, Geophys. Monogr.*, No.79, Amer. Geophys. Union, 161-172.

Doswell, C.A., III, A.R. Moller, and R. Przybylinski, 1990: A unified set of conceptual models for variations on a supercell theme. *Preprints, 16th Conf. on Severe Local Storms*, Kananaskis Park, Alberta, Canada, Amer. Meteor. Soc., 40-45.

Drazin, P.G., and W.H. Reid, 1981: *Hydrodynamic Stability.* Cambridge University Press, New York, 525 pp.

Droegemeier, K.K., S.M. Lararus, and R. Davies-Jones, 1993: The influence of helicity on numerically simulated convective storms. *Mon. Wea. Rev.*, **121**, 2005-2029.

Fiedler, B., 1997: Three-dimensional numerical simulations of tornadoes. *Preprints, 11th Conf. on Fluid Dynamics.*, Tacoma, WA, Amer. Meteor. Soc., 73-76.

Foote, G.B., and H.W. Frank, 1983: Case study of a hailstorm in Colorado: part III: Airflow from triple-Doppler measurements. *J. Atmos. Sci.*, **40**, 686-707.

Forbes, G.S., 1978: Three scales of motions associated with tornadoes. Ph.D. Dissertation, University of Chicago, 359pp.

Forbes, G.S., and R.M. Wakimoto, 1983: A concentrated outbreak of tornadoes, downbursts and microbursts, and implications regarding vortex classification. *Mon. Wea. Rev.*, **111**, 220-235.

Fovell, R.G., and Y. Ogura, 1989: Effect of Vertical Wind Shear on Numerically Simulated Multicell Storm Structure. *J. Atmos. Sci.*, **46**, 3144-3176.

Fujita, T.T., 1970: The Lubbock tornadoes: A study of suction spots. *Weatherwise*, **23**, 161-173.

Fujita, T.T., 1971: Proposed mechanism of suction spots accompanied by tornadoes. *Preprints, 7th Conf. on Severe Local Storms.*, Kansas City, MO, Amer. Meteor. Soc., 208-213.

Fujita, T.T., 1974: Jumbo tornado outbreak of 3 April, 1974. *Weatherwise*, **27**, 116-174.

Fujita, T.T., 1975: New evidence from April 3-4, 1974 tornadoes. *Preprints, 9th Conf. on Severe Local Storms.*, Norman, OK, Amer. Meteor. Soc., 252-255.

Fujita, T.T., 1978: Manual of downburst identification for Project Nimrod. *SMRP Res. Paper 156*, Univ. of Chicago, Chicago, IL, 104 pp.

Fujita, T.T., 1979: Objectives, operation, and results of project NIMROD. *Preprints, 11th Conf. on Severe Local Storms*, Kansas City, Missouri, Amer. Meteor. Soc., 259-266.

Fujita, T.T., 1981: Tornadoes and downbursts in the context of generalized planetary scales. *J. Atmos. Sci.*, **38**, 1511-1534.

Fujita, T.T., 1989: The Teton-Yellowstone tornado of 21 July, 1987. *Mon. Wea. Rev.*, **117**, 1913-1940.

Fujita, T.T., D.L. Bradbury, and C.F. Van Thullenar, 1970: Palm Sunday tornadoes of April 11, 1965. *Mon. Wea. Rev.*, **98**, 29-69.

Fujita, T.T., and B.E. Smith, 1993: Aerial survey and photography of tornado and microburst damage. *The Tornado: Its Structure, Dynamics, Prediction, and Hazards, Geophys. Monogr.*, No.79, Amer. Geophys. Union, 479-493.

Gall, R.L., 1983: A linear analysis of the multiple vortex phenomenon in simulated tornadoes. *J. Atmos. Sci.*, **40**, 2010-2024.

Golden, J.H., and D. Purcell, 1977: Photogrammetric velocities for the Great Bend, Kansas, tornado of 30 August, 1974: accelerations and asymmetries. *Mon. Wea. Rev.*, **105**, 485-492.

Golden, J.H., and D. Purcell, 1978: Airflow characteristics around the union city tornado. *Mon. Wea. Rev.*, **106**, 22-28.

Grasso, L.D., and W.R. Cotton, 1995: Numerical simulation of a tornado vortex. *J. Atmos. Sci.*, **52**, 1092-1203.

Grasso, L.D., 1996: Numerical simulation of the May 15 and April 26, 1991 tornadic thunderstorms. Ph.D. Dissertation, Colorado State University, 151pp.

Hane, C.E., C.L. Ziegler, and H.B. Bluestein, 1993: Investigation of the dryline and convective storms initiated along the dryline: field experiments during COPS-91. *Bull. Amer. Meteor. Soc.*, **74**, 2133-2145.

Hill, G.E., 1974: Factors controlling the size and spacing of cumulus clouds as revealed by numerical experiments. *J. Atmos. Sci.*, **31**, 646-673.

Holle, R.L., and M.W. Maier, 1980: Tornado formation from downdraft interaction in the FACE Mesonetwork. *Mon. Wea. Rev.*, **108**, 1010-1028.

Houze, R.A., and C-P. Cheng, 1977: Radar characteristics of tropical convection observed during GATE: Mean properties and trends over the summer season. *Mon. Wea. Rev.*, **105**, 964-980.

Howard, L.N., and A.S. Gupta, 1962: On the hydrodynamic and hydromagnetic stability of swirling flows. *J. Fluid Mech.*, **14**, 463-476.

Imy, D.A., and K.J. Pence, 1993: An examination of a supercell in Mississippi using a tilt sequence. *The Tornado: Its Structure, Dynamics, Prediction, and Hazards, Geophys. Monogr.*, No.79, Amer. Geophys. Union, 257-264.

Johns, R.H., and W.D. Hirt, 1987: Derechos: Widespread convectively induced windstorms. *Wea. Forecasting*, **7**, 588-612.

Johnson, K.W., P.S. Ray, B.C. Johnson, and R.P. Davies-Jones, 1987: Observations related to the rotational dynamics of the 20 May, 1977 tornadic storms. *Mon. Wea. Rev.*, **115**, 2463-2478.

Klemp, J.B., and R. Rotunno, 1983: A study of the tornadic region within a supercell thunderstorm. *J. Atmos. Sci.*, **40**, 359-377.

Klemp, J.B., and R.B. Wilhelmson, 1978a: The simulation of three-dimensional convective storm dynamics. *J. Atmos. Sci.*, **35**, 1070-1096.

Klemp, J.B., and R.B. Wilhelmson, 1978b: Simulations of right- and left-moving storms produced through storm splitting. *J. Atmos. Sci.*, **35**, 1097-1110.

Klemp, J.B., and R.B. Wilhelmson, and P.S. Ray, 1981: Observed and numerically simulated structure of a mature supercell thunderstorm. *J. Atmos. Sci.*, **38**, 1558-1580.

Knupp, K.R., and W.R. Cotton, 1982: An intense, quasi-steady thunderstorm over mountainous terrain. Part II: Doppler radar observations of the storm morphological structure. *J. Atmos. Sci.*, **39**, 343-358.

Kulie, M.S., Y.-L. Lin, R.L. Deal, and D.S. Decriox, 1996: A cloud-scale numerical simulation of the 28 November, 1988 Raleigh tornadic thunderstorm. *Preprints, 18th Conf. on Severe Local Storms*, Amer. Meteor. Soc., 283-287.

LaDue, J.G, 1993: Vortex formation from a helical inflow tornado vortex simulator. *The Tornado: Its Structure, Dynamics, Prediction, and Hazards, Geophys. Monogr.*, No.79, Amer. Geophys. Union, 307-316.

LaFore, J-P., and M.W. Moncrieff, 1989: Numerical Investigation of the Organization and Interaction of the Convective and Stratiform Regions of Tropical Squall Lines. *J. Atmos. Sci.*, **46**, 521-544.

LeMone, M.A., 1983: Momentum flux by a line of cumulonimbus. *J. Atmos. Sci.*, **40**, 1815-1834.

LeMone, M.A., G.M. Barnes and E. Zipser, 1984: Momentum flux by lines of cumulonimbus over the tropical oceans. *J. Atmos. Sci.*, **41**, 1914-1924.

Lee, B.D., and R.B. Wilhelmson, 1997: The numerical simulation of non-supercell tornadogenesis: Part I: Initiation and evolution of pre-tornadic misocyclone circulations along a dry outflow boundary. *J. Atmos. Sci.*, **54**, 32-60.

Lee, B.D., and R.B. Wilhelmson, 1997: The numerical simulation of non-supercell tornadogenesis: Part II: Evolution of a family of tornadoes along a weak outflow boundary. *J. Atmos. Sci.*, **54**, 2387-2415.

Lemon, L.R., 1976: The flanking line, a severe thunderstorm intensification source. *J. Atmos. Sci.*, **33**, 686-694.

Lemon, L.R., and C.A. Doswell III, 1979: Severe thunderstorm evolution and mesocyclone structure as related to tornadogenesis. *Mon. Wea. Rev.*, **107**, 1184-1197.

Leslie, L.M., 1971: The development of concentrated vortices: a numerical study. *J. Fluid Mech.*, **48**, 1-21.

Lewellen, W.S., 1993: Tornado vortex theory. *The Tornado: Its Structure, Dynamics, Prediction, and Hazards, Geophys. Monogr.*, No.79, Amer. Geophys. Union, 19-39.

Lilly, D.K., 1962: On the numerical simulation of buoyant convection. *Tellus*, **14**, 148-172.

Lilly, D.K., 1986: The structure, energetics and propagation of rotating convective storms. Part II: Helicity and storm stabilization. *J. Atmos. Sci.*, **43**, 126-140.

Loveland, T.R., J.W. Merchant, D.O. Ohlen, and J.F. Brown, 1991: Development of a land-cover characteristics database for the conterminous U.S. *Photo. Eng. Rem. Sens.*, **57**, 1453-1463.

Lugt, H.J., 1989: Vortex breakdown in atmospheric columnar vortices. *Bull. Amer. Meteor. Soc.*, **70**, 1526-1537.

Maddox, R. A., 1976: An evaluation of tornado proximity wind and stability data. *Mon. Wea. Rev.*, **104**, 133-142.

Maddox, R., L.R. Hoxit, and C.F. Chappel, 1980: A study of tornadic thunderstorm interactions with thermal boundaries. *Mon. Wea. Rev.*, **108**, 322-336.

Maher, Y., and R.A. Pielke, 1977: A numerical study of the airflow over irregular terrain. *Beitr. Phys. Atmos.*, **50**, 98-113.

Mapes, B.E., 1993: Gregarious tropical convection. *J. Atmos. Sci.*, **50**, 2026-2037.

Maxworthy, T., 1972: On the structure of concentrated, columnar vortices. *Astronaut. Acta*, **17**, 363-374.

McPherson, R.A., and K.K. Droegemeier, 1991: Numerical predictability experiments of the 20 May 1977 Del City, OK supercell storm. *Preprints, 9th Conf. on Numerical Weather Prediction.*, Denver, CO, Amer. Meteor. Soc., 734-738.

Moller, A.R., and C.A. Doswell III, 1988: A proposed advanced storm spotter's training program. *Preprints, 15th Conf. on Severe Local Storms*, Baltimore, MD, Amer. Meteor. Soc., 173-177.

Moller, A.R., C.A. Doswell III, and R. Przybylinski, 1990: High-precipitation supercells: A conceptual model and documentation. *Preprints, 16th Conf. on Severe Local Storms*, Kananaskis Park, Alberta, Canada, Amer. Meteor. Soc., 52-57.

Moller, A.R., C.A. Doswell III, M.P. Foster, and G.R, Woodall, 1994: The operational recognition of supercell thunderstorm environments and storm structures. *Wea. Forecasting*, **9**, 327-347.

Monji, N., 1985: A laboratory investigation of the structure of multiple vortices. *J. Meteorol. Soc. Jpn.*, **63**, 703-713.

Mueller, C.K., and R.E. Carbone, 1987: Dynamics of a thunderstorm outflow. *J. Atmos. Sci.*, **44**, 1879-1898.

Mullen, J.B., and T. Maxworthy, 1977: A laboratory model of dust devil vortices. *Dyn. Atmos. Oceans*, **1**, 181-214.

Nicholls, M.E., R.A. Pielke, and W.R. Cotton, 1991: Thermally forced gravity waves in an atmosphere at rest. *J. Atmos. Sci.*, **48**, 1869-1884.

Nelson, S.P., 1987: The hybrid multicellular-supercellular storm–an efficient hail producer. Part II: General characteristics and implications for hail growth. *J. Atmos. Sci.*, **44**, 2060-2073.

Nelson, S.P., and N.C. Knight, 1987: The hybrid multicellular-supercellular storm–an efficient hail producer. Part I: An archetypal example. *J. Atmos. Sci.*, **44**, 2042-2050.

Pandya, R.E., and D.R. Durran, 1996: The influence of convectively generated thermal forcing on the mesoscale circulation around squall lines. *J. Atmos. Sci.*, **53**, 2924-2951.

Pauly, R.L., C.R. Church, and J.T. Snow, 1982: Measurements of maximum surface pressure deficits in modeled atmospheric vortices. *J. Atmos. Sci.*, **39**, 369-377.

Pauly, R.L., and J.T. Snow, 1983: On the kinematics and dynamics of the 18 July, 1986 Minneapolis tornado. *Mon. Weather Rev.*, **116**, 2731-2736.

Pauly, R.L., 1989: Laboratory measurements of axial pressures in two-celled tornado-like vortices. *J. Atmos. Sci.*, **46**, 3392-3399.

Pielke, R.A., W.R. Cotton, R.L. Walko, C.J. Tremback, W.A. Lyons, L.D. Grasso, M.E. Nicholls, M.D. Moran, D.A. Wesley, T.J. Lee, and J.H. Copeland, 1992: A comprehensive meteorological modeling system-RAMS. *Metero. and Atmos. Phys.*, **49**, 69-91.

Prosser, N.E., 1964: Aerial photographs of a tornado path in Nebraska, May 5, 1964. *Mon. Wea. Rev.*, **92**, 593-598.

Przybylinski, R.W., 1989: The Raleigh tornado–28 November, 1988: A radar overview. *Preprints, 12th Conf. Weather Forecasting and Analysis.* Monterrey, CA, Amer. Meteor. Soc., 186-191.

Przybylinski, R.W., S. Runnels, P. Spoden, and S. Summy, 1990: The Allendale, Illinois tornado–January 7, 1989: One type of an HP supercell. *Preprints, 16th Conf. on Severe Local Storms*, Kananaskis Park, Alberta, Canada, Amer. Meteor. Soc., 516-521.

Przybylinski, R.W., J.T. Snow, E.M. Agee, and J.T. Curran, 1993: The use of volumetric radar data to identify supercells: A case study of June 2, 1990. *The Tornado: Its Structure, Dynamics, Prediction, and Hazards, Geophys. Monogr.*, No.79, Amer. Geophys. Union, 241-250.

Rasmussen, E.N., and J.M. Straka, 1996: Variations in supercell morphology. Part I: Hypothesis and observations. *Mon. Wea. Rev.*, submitted.

Rasmussen, E.N., and R.B. Wilhelmson, 1983: Relationships between storm characteristics and 1200 GMT hodographs, low-level shear, and stability. *Preprints, 13th Conf. on Severe Local Storms*, Amer. Meteor. Soc., J5-J8.

Rayleigh, Lord (J.W. Strutt), 1880: On the stability, or instability of certain fluid motions. *Proc. London Math Soc.*, **11**, 57-70.

Rayleigh, Lord (J.W. Strutt), 1916: On the dynamics of revolving flows. *Proc. Roy. Soc. London*, **A93**, 148-154.

Richardson, Y.P., and K.K. Droegemeier, 1996: An investigation of the dynamics governing organized multicell rotation and transition. *Preprints, 18th Conf. on Severe Local Storms*, Amer. Meteor. Soc., 195-199.

Roberts, R.D., and J.W. Wilson, 1995: The genesis of three non-supercell tornadoes observed with dual-Doppler radar. *Mon. Weather Rev.*, **123**, 3408-3436.

Rotunno, R., 1977: Numerical simulation of a laboratory vortex. *J. Atmos. Sci.*, **34**, 1942-1956.

Rotunno, R., 1978: A note the stability of a cylindrical vortex sheet. *J. Fluid Mech.*, **87**, 761-771.

Rotunno, R., 1979: A study in tornado-like vortex dynamics. *J. Atmos. Sci.*, **36**, 140-155.

Rotunno, R., 1981: On the evolution of thunderstorm rotation. *Mon. Weather Rev.*, **109**, 577-586.

Rotunno, R., 1984: An investigation of a three-dimensional asymmetric vortex. *J. Atmos. Sci.*, **41**, 283-298.

Rotunno, R., 1986: Tornadoes and tornadogenesis. *Mesoscale Meteorology and Forecasting*, Peter S. Ray, ed., Amer. Meteor. Soc., 414-433.

Rotunno, R., and J.B. Klemp, 1982: The influence of the shear-induced pressure gradient of thunderstorm motion. *Mon. Weather Rev.*, **110**, 136-151.

Rotunno, R., and J.B. Klemp, 1985: On the rotation and propagation of simulated supercell thunderstorms. *J. Atmos. Sci.*, **42**, 271-292.

Rotunno, R., J.B. Klemp, and M.L. Weisman, 1988: A Theory for Strong, Long-Lived Squall Lines. *J. Atmos. Sci.*, **45**, 463-485.

Rothfusz, L.P., 1986: A mesocyclone and tornado-like vortex generated by the tilting of horizontal vorticity: Preliminary results of a laboratory simulation. *J. Atmos. Sci.*, **43**, 2677-2682.

Schmidt, J.M., and W.R. Cotton, 1990: Interactions between upper and lower tropospheric gravity waves on squall line structure and maintenance. *J. Atmos. Sci.*, **47**, 1205-1222.

Schmidt, J.M., 1991: Numerical and observational investigations of long-lived, MCS-induced, severe surface wind events: the derecho. Ph.D. Dissertation, Colorado State University, 196pp.

Schlesinger, R.E., 1980: A three-dimensional numerical model of an isolated thunderstorm. Part II: Dynamics of updraft splitting and mesovortex couplet evolution. *J. Atmos. Sci.*, **37**, 395-420.

Simpson, J., and W.L. Woodley, 1971: Seeding cumulus in Florida: New 1970 results. *Science*, **172**, 117-126.

Skamarock, W.C., Weisman, M.L., and J.B. Klemp, 1994: Three-Dimensional Evolution of Simulated Long-Lived Squall Lines. *J. Atmos. Sci.*, **51**, 2563-2584.

Smagorinsky, J., 1963: General circulation experiments with the primitive equations. I. The basic experiment. *Mon Wea. Rev.*, **91**, 99-164.

Smith, R.K., and L.M. Leslie, 1978: Tornadogenesis. *Quart. J. R. Met. Soc.*, **104**, 189-199.

Smith, R.K., and L.M. Leslie, 1979: A numerical study of tornadogenesis in a rotating thunderstorm. *Quart. J. R. Met. Soc.*, **105**, 107-127.

Snow, J.T., 1978: On inertial instability as related to the multiple-vortex phenomenon. *J. Atmos. Sci.*, **35**, 1660-1677.

Snow, J.T., C.R. Church, and B.J. Barnhart, 1980: An investigation of the surface pressure fields beneath simulated tornado cyclones. *J. Atmos. Sci.*, **37**, 1013-1026.

Snow, J.T., 1982: A review of recent advances in tornado vortex dynamics. *Rev. Geophys.*, **20**, 953-964.

Stanford, J.L., 1987: *Tornado: Accounts of Tornadoes in Iowa,* second edition. Iowa State University Press, Ames, Iowa, 143pp.

Staley, D.O., and R.L. Gall, 1979: Barotropic instability in a tornado vortex. *J. Atmos. Sci.*, **36**, 973-981.

Stensrud, David J., and J.M. Fritsch, 1994: Mesoscale convective systems in weakly forced large-scale environments. Part II: Generation of a mesoscale initial condition. *Mon. Wea. Rev.*, **122**, 2068-2083.

Stensrud, David J., and J.M. Fritsch, 1994: Mesoscale convective systems in weakly forced large-scale environments. Part III: Numerical simulations and implications for operational forecasting. *Mon. Wea. Rev.*, **122**, 2084-2104.

Stumpf, G.J., and D.W. Burgess, 1993: Observations of low-tropospheric misocyclones along the leading edge of a bow echo thunderstorm. *Preprints, 26th Int. Conf. on Radar Meteorology*, Norman, OK, Amer. Meteor. Soc., 215-217.

Szoke, E.J., and R. Rotunno, 1993: A comparison of surface observations and visual tornado characteristics for the June 15, 1988, Denver tornado outbreak. *The Tornado: Its*

Structure, Dynamics, Prediction, and Hazards, Geophys. Monogr., No.79, Amer. Geophys. Union, 353-366.

Tao, W.-K., and J. Simpson, 1984: Cloud interactions and merging: numerical simulations. *J. Atmos. Sci.*, **41**, 2901-2917.

Thorpe, A.J., and M.J. Miller, 1978: Numerical simulations showing the role of the downdraught in cumulonimbus motion and splitting. *Quart. J. R. Met. Soc.*, **104**, 873-893.

Trapp, R.J., and B.H. Fiedler, 1995: Tornado-like vortexgenesis in a simplified numerical model. *J. Atmos. Sci.*, **52**, 3757-3778.

Trapp, R.J., and E.D. Mitchell, 1995: Characteristics of tornadic vortex signatures detected by WSR-88D radars. Preprints, *27th Conf. on Radar Meteorology*, Vail, CO, Amer. Meteor. Soc., 211-212.

Trapp, R.J., and R. Davies-Jones, 1997: Tornadogenesis with and without a dynamic pipe effect. *J. Atmos. Sci.*, **54**, 113-133.

Tremback, C.J., and R. Kessler, 1985: A surface temperature and moisture parameterization for use in mesoscale numerical models. *Proc. 7th Conf. on Numerical Weather Prediction*, Montreal, Quebec, Amer. Meteor. Soc., 433-434.

Tripoli, G.J., and W.R. Cotton, 1980: A numerical investigation of several factors leading to the observed variable intensity of deep convection over South Florida. *J. Appl. Meteor.*, **19**, 1037-1063.

Tripoli, G.J., and W.R. Cotton, 1986: An intense, quasi-steady thunderstorm over mountainous terrain. Part IV: Three-dimensional numerical simulation. *J. Atmos. Sci.*, **43**, 894-912.

Van Tassel, E.L., 1955: The North Platte Valley tornado outbreak of June 27, 1955. *Mon. Wea. Rev.*, **83**, 255-264.

Vasiloff, S.V., 1993: Single-Doppler radar study of a variety of tornado types. *The Tornado: Its Structure, Dynamics, Prediction, and Hazards, Geophys. Monogr.*, No.79, Amer. Geophys. Union, 223-232.

Vasiloff, S.V., E.A. Brandes, and R.P. Davies-Jones, 1986: An investigation of the transition from multicell to supercell storms. *J. Climate Appl. Meteor.*, **25**, 1022-1036.

Wakimoto, R.M., and J.W. Wilson, 1989: Non-supercell tornadoes. *Mon. Wea. Rev.*, **117**, 1113-1140.

Wakimoto, R.M., and B.E. Martner, 1992: Observations of a Colorado tornado. Part II: Combined photogrammetric and Doppler radar analysis. *Mon. Wea. Rev.*, **120**, 497-520.

Wakimoto, R.M., and N.T. Atkins, 1996: Observations on the origins of rotation: the Newcastle tornado during VORTEX 94. *Mon. Wea. Rev.*, **124**, 384-407.

Wakimoto, R.M., C. Liu, and H. Cai, 1997: The Garden City, Kansas storm during VORTEX 95. Part I: Overview of the storm's life cycle and mesocyclogenesis. *Mon. Wea. Rev.*, (submitted).

Wakimoto, R.M., and C. Liu, 1997: The Garden City, Kansas storm during VORTEX 95. Part II: The wall cloud and tornado. *Mon. Wea. Rev.*, (submitted).

Walko, R., 1988: Plausibility of substantial dry adiabatic subsidence in a tornado core. *J. Atmos. Sci.*, **41**, 3456-3471.

Walko, R., 1993: Tornado spin-up beneath a convective cell: required basic structure of the near-field boundary layer winds. *The Tornado: Its Structure, Dynamics, Prediction, and Hazards, Geophys. Monogr.*, No.79, Amer. Geophys. Union, 89-95.

Walko, R., W.R. Cotton, M.P. Meyers, and J.Y. Harrington 1995: New RAMS cloud microphysics parameterization. Part I: The single moment scheme. *Atmos. Res.*, **43**, 29-62.

Walko, R., and R. Gall, 1984: A two-dimensional linear stability analysis of the multiple vortex phenomenon. *J. Atmos. Sci.*, **41**, 3456-3471.

Walko, R., and R. Gall, 1986: Some effects of momentum diffusion an axisymmetric vortices. *J. Atmos. Sci.*, **41**, 3456-3471.

Ward, N.B., 1972: The exploration of certain features of tornado dynamics using a laboratory model. *J. Atmos. Sci.*, **29**, 1194-1204.

Weaver, J.F., and S.P. Nelson, 1982: Multi-scale aspects of thunderstorm gust fronts and their effects on subsequent storm development. *Mon. Wea. Rev.*, **110**, 707-718.

Weisman, M.L., 1992: The Role of Convectively Generated Rear-Inflow Jets in the Evolution of Long-Lived Mesoconvective Systems. *J. Atmos. Sci.*, **49**, 1526-1847.

Weisman, M.L., 1993: The genesis of severe, long-lived bow echoes. *J. Atmos. Sci.*, **50**, 645-670.

Weisman, M.L., and H.W. Bluestein, 1985: Dynamics of numerically simulated LP storms. *Preprints, 14th Conf. on Severe Local Storms*, Indianapolis, Amer. Meteor. Soc., 267-270.

Weisman, M.L., and J.B. Klemp, 1982: The dependence of numerically simulated convective storms on vertical wind shear and buoyancy. *Mon. Wea. Rev.*, **110**, 504-520.

Weisman, M.L., and J.B. Klemp, 1984: The structure and classification of numerically simulated convective storms in directionally varying wind shears. *Mon. Wea. Rev.*, **112**, 2479- 2498.

Weisman, M.L., J.B. Klemp, and R. Rotunno, 1988: Structure and Evolution of Numerically Simulated Squall Lines. *J. Atmos. Sci.*, **45**, 1990-2013.

Westcott, N., 1984: A historical perspective on cloud mergers. *Bull. Amer. Meteor. Soc.*, **65**, 219-226.

Wetzel, P.J, and J.T. Chang, 1988: Evapostranspiration from nonuniform surfaces: A first approach for short-term weather prediction. *Mon. Wea. Rev.*, **116**, 600-621.

Wicker, L.J., and R.B. Wilhelmson, 1993: Numerical simulation of tornadogenesis within a supercell thunderstorm. *The Tornado: Its Structure, Dynamics, Prediction, and Hazards, Geophys. Monogr.*, No.79, Amer. Geophys. Union, 75-88.

Wicker, L.J., and R.B. Wilhelmson, 1995: Simulation and analysis of tornado development and decay within a three-dimensional supercell thunderstorm. *J. Atmos. Sci.*, **52**, 2675-2703.

Wilczak, J.M., T.W. Christian, D.E. Wolfe, R.J. Zomora, and B. Stankov, 1992: Observations of a Colorado tornado. Part I: Mesoscale environment and tornadogenesis. *Mon. Wea. Rev.*, **120**, 497-520.

Wilhelmson, R.B., and J.B. Klemp, 1978: A numerical study of storm splitting that leads to long-lived storms. *J. Atmos. Sci.*, **35**, 1974-1986.

Wilhelmson, R.B., and J.B. Klemp, 1981: A three-dimensional numerical simulation of splitting severe storms on 3 April, 1964. *J. Atmos. Sci.*, **38**, 1581-1600.

Wilson, J.W., 1986: Tornadogenesis by non-precipitation induced wind shear lines. *Mon. Wea. Rev.*, **114**, 270-284.